MODELING OF DIESEL FUEL INJECTION PROCESSES

by

MANOLIS GAVAISES
Dipl. (Mech. Eng.)

Imperial College of Science, Technology & Medicine
Department of Mechanical Engineering
University of London

Thesis submitted for the degree of
Doctor of Philosophy
in the University of London
and for the
Diploma of Membership of the Imperial College

June 1997

Στο Θοδωρη

ABSTRACT

This study deals with the development and experimental validation of a mathematical model simulating the diesel fuel injection processes which include the flow within the fuel injection system and the development of the injected sprays. The model of the internal flow includes the one-dimensional wave propagation in typical hydraulic systems in the presence of various valves, slots, uniform pressure chambers, hole cavitation, and the three-dimensional flow characteristics in the sac volume and injection holes, while the spray model includes the two-phase turbulent flow processes with liquid sprays and the inter-phase transport.

The injection conditions are modeled by solving the wave dynamics in the fuel injection system using a phenomenological one-dimensional code, while the flow in the sac volume is treated as three-dimensional under non-cavitating conditions. For cavitating cases, correlations giving the discharge coefficient of the injection holes are used in order to predict the fuel injected. Both inclined and vertical injectors were modeled since different flow rates are predicted for different holes of multi-hole nozzles, depending on the position of the injection hole relative to the sac volume and the needle. A one-dimensional model is used for the calculation of the effective area of the injection holes in the presence of cavitating bubbles.

Following fuel injection, with velocity, size, effective area and level of turbulence calculated for each individual hole of multi-hole nozzles from the FIE model, a three-dimensional CFD spray model has been extended and used for the prediction of the spray characteristics. This model is based on the Eulerian-Lagrangian stochastic particle technique; the gas phase is simulated by solving numerically the full Navier-Stokes equations while the second phase (liquid) is modeled using a Lagrangian particle tracking approximation.

Spray sub-models are used to represent the various physical phenomena taking place during the spray development. Different jet-atomization models are implemented in order to predict the disintegration of the emerging from the injection hole liquid jet which include aerodynamic-induced atomization, jet turbulence-induced atomization and a newly developed model for the cavitation-induced atomization. The latter is combined with a proposed correlation simulating the radial distribution of droplets within the spray cone angle. Droplet secondary break-up phenomena are taken into

account as the droplets penetrate into the surrounding gas. These simulate a wide range of observed droplet aerodynamic-induced break-up regimes. A new model based on the maximum entropy formalism is used for the calculation of the droplet size distribution of the droplets formed during the aerodynamic break-up; thus, the need for a pre-assumed droplet size distribution function is eliminated. Droplet collisions are also taken into account. Droplet aerodynamic drag calculations are based on those of a distorted droplet. In addition, droplet-wall interaction models are implemented into the code in order to investigate the physics involved during the impingement of diesel sprays. Finally, various droplet evaporation models are implemented and applied in order to simulate the spray development inside the piston bowl of a DI diesel engine.

The computational results are extensively compared with experimental data which include the line pressure, needle lift, fuel injection rate and total fuel injected for the FIE model, fuel injected per injection hole for the hole cavitation flow model, LDV measurements for the validation of the three-dimensional sac volume flow model, and droplet mean and rms velocities, droplet sizes (obtained both with a PDA system and a Malvern particle sizer), spray tip penetration and global spray structure for the validation of the spray model. The test cases include different injection and chamber conditions varying from free atmospheric sprays in a quiescent or cross-flowing environment to impinging atmospheric diesel sprays and sprays injected inside the piston bowl of a DI diesel engine. The results have been found to predict satisfactorily the whole fuel injection process under all examined conditions.

Extensive parametric studies have been performed examining the effect of various design parameters of the fuel injection system on the nozzle exit characteristics. In addition, results obtained with the spray model have revealed the effect of the flow characteristics inside the fuel injection system and the relative importance of the various physical processes taking place during the spray development, on the structure of diesel sprays.

ACKNOWLEDGMENTS

When I first came to London from a theoretically oriented academic research group, I found myself in the middle of an international scientific community of applied research involving automotive industries, R&D's and experimental projects. This gradually convinced me of the new role of academics in this contemporary society. For me, London and Imperial College have been a new environment of challenge and motivation for my work. Far from being a typical recognition, I would like to thank the people who played a role in my research:

My supervisor Professor C. Arcoumanis for his valuable guidance and endless support in scientific, financial and mostly human terms.

All members of the Thermofluids Section and Laboratory of Internal Combustion Engines, which are too numerous to list here, for the exchange of useful information all these years. Special mention has to be given to Mr. H. Flora for instrumenting components of the experimental rig, to Dr. P. Cutter and Dr. A. Nagwaney for providing detailed information about their experimental results, and to Dr. J. Nouri for helping me with my first use of laser techniques; also, to Miss M. Kenny for being kind and helpful in many administrative matters which otherwise would have been such a pain to deal with. Finally, Dr. M. Sarantinos for his help on the post processing of the computational results and Dr. Y. Hardalupas for useful discussions.

The advanced diesel engine groups of Ford Motor Company at Dunton (UK) and Dearborn (US) for financial support and especially Mr. B. French, R. Horrocks, P. Bostock and Dr. Emad Abdul-Wahab for providing equipment and for useful discussions.

Professor G. Bergeles from the National Technical University of Athens who has kindly provided the CFD code used in the present investigation but mostly because he encouraged me to continue my studies and practically directed me to Imperial College.

My colleague and close friend Dr. A. Theodorakakos from the National Technical University of Athens for his assistance and cooperation on many other aspects apart from the use of the CFD code.

My family for their support and tolerance when the work piled up to my ears; especially my mother for taking care of almost everything for all of us.

My beloved Elpida for having and sharing common dreams.

Last but not at all least, I would like to dedicate this study to Thodoros Gavrilis who with his knowledge, experience and wisdom has always been an inspiration and precious companion to me.

CONTENTS

LIST OF FIGURES

LIST OF TABLES

CHAPTER 1

...from them, undoubtfully, we have inherited the need to find explanation, the agony which drive us to find the meaning of the existence. Agony which is the creator of all the myths, of all religions, all philosophies and of science itself

Zak Mono
(Le hazard et la necessite)

Introduction

1.1 Background

The 20th century can be generally characterized as the era of the major scientific achievements of the human race. The modern science, closely related with the semantic changes in the social, philosophical and political systems of the last 200 years, was initiated from the years of renaissance in the western European countries and reached its maximum theoretical achievements in the early 1900's with the formulation of the quantum physics and the theory of relativity. However, the years that followed the turmoil period after the 1st world war, and especially during and after the 2nd world war, have revealed the dramatic effects that technology can have on human lives. The technological developments were one of the main strategies of the countries during the cold war period, supported by government policies. Throughout these years, science has benefited from the development of experimental techniques, multi-purpose machines and computers which have dramatically changed the way of life in contemporary societies. The automotive industry and its applications - transportation - is one of the major sections that applied sciences have achieved large improvements and have contributed to a great extent to the way the building of all cities in the developed world is based on.

Internal combustion (IC) engines date back to the late 19th century when the first spark-ignition and compression-ignition (diesel) engines were developed. Since then, they have experienced a rapid development, closely related to the technologically oriented policy of contemporary years; through the developments resulting from continuous research by engine manufacturers as well as universities, this type of engine ensured its dominant role in the transportation of the 20th century.

However, as is the case with many other man's activities, the wide spread use of IC engines in transportation has given rise to environmental problems. The first well-

known case was the air pollution problem in the 1940's in Los Angeles, which resulted from atmospheric reactions of nitrogen oxides and hydrocarbon compounds present in the automotive exhaust gases. Since then it has been realized since then that automobiles in urban areas are the major cause of high concentrations of nitrogen oxides, hydrocarbons, carbon monoxide and soot. At the present time many cities around the world, including the capital of my native country, Greece, suffer from this type of environmental problem. A fairly recent blow to the automotive manufacturers was the oil crisis in the 1970's, when the oil prices became so high that the development of low fuel consumption engines was seen by the companies as the only way to go. The oil crisis not only highlighted the importance of engine efficiency, but also encouraged the extensive utilization of diesel engines in passenger cars, due to their well known superior fuel consumption efficiency. This trend has been much more visible in Europe than in the USA due to the much higher oil prices in the European countries.

Due to the side effects of air pollution on health, many countries have decided to introduce - and update on a few years basis - the emission standards for both spark ignition and diesel engines. A similar response has developed towards noise pollution, since IC engines are important noise sources especially in towns. Nowadays, engine manufacturers are focusing their efforts to develop engines which satisfy the existing emission legislations in all developed countries and start becoming a standard policy in the developing ones.

To obtain the desired engine performance, extensive research in universities and other research centers has been carried out over the last twenty years not only through the empirical-experimental way adopted as the standard development procedure through all these past years, but also on the theoretical side. The basic flow processes taking place in many mechanical or chemical applications, including IC engines were established in the late 1800's or early 1900's, where among other basic physical sciences, the equations describing the motion of fluids with heat transfer and chemical reactions were formulated. Due to their complexity, it was impossible to be solved analytically in the general 3-D transient case, making them practically unused. However, the technological revolution in the digital computers has influenced, among all other activities, the way of thinking and investigating the physics involved in particular applications. Up to now a large number of computer simulation programs has been developed or is under development; problems related to the motion of fluid flows have

been given special attention since these are involved in a wide range of applications, such as all kinds of different thermal engines, hydraulic machines, turbines, aviation, e.t.c as well as in air-water pollution problems all around the earth.

It is now clear that applied research involving the development of various simulation models is a very sound way to move forward in order to understand the physics involved in the various applications and, as a result, to design machines with the desired performance as well as to propose sensible solutions related to the environmental pollution problems. Experiments are performed to reveal the physics of some particular complex phenomena taking place in many areas of technological interest and provide information for validation of the computer models.

Diesel engines are one example of many other applications where computer models have been found to be applicable with promising results. Since it is well known that one of the major factors influencing engine performance is the fuel injection system, the present study has focused on the development of a computer model simulating the whole fuel injection process, starting from the modeling of the operation of the fuel injection system itself and ending to the simulation of the sprays injected into the engine cylinder.

In the following section, the general computational methods for fluid flows and diesel spray models are described followed by a summary of the most important contributions of the present investigation and the thesis outline.

1.2 Computational Methods in Fluid Mechanics

The starting step of all computational methods is a mathematical model of the physical processes to be simulated. However, this mathematical description usually neglects some less important phenomena in order to reduce the complexity of the final mathematical model. Generally, such models can be categorized into phenomenological and multi-dimensional; the former consists of zero-dimensional and one-dimensional models. The zero-dimensional models ignore spatial variations of flow parameters and are capable of predicting only their temporal variations. In one-dimensional models, the full three-dimensional forms of the governing equations are reduced to one-dimensional by ignoring or making assumptions about variations in the other two directions. The

multi-dimensional models are more complex but offer prediction of the spatial and temporal variation of the flow parameters.

Even when the mathematical model has been derived, the solution procedure of the governing equations remains a major problem. Unfortunately, analytical solutions in flow problems are limited to very simple geometries and flow types, which are usually of minor practical interest. The appearance of the digital computers in the 1940's and their rapid developments in the last 20 years have given rise to numerical solutions of the governing flow equations in cases where analytical ones can not be found. In general, these methods consists of discretization of the solution domain into a finite number of sub-domains, and approximations of the original equations by a system of simultaneous algebraic equations, linking the variables in these sub-domains. Solution of this system by a solution algorithm provides a set of numerical values at these sub-domains, which represents the approximate solution.

Among the various numerical techniques developed up to now in order to solve differential equations, the finite volume method is widely used in fluid motion problems and has its roots in the science of fluid mechanics; the first works date back to late 1960's and early 1970's. Since that time, a number of general and special-purpose computational fluid dynamics (CFD) codes have been developed, including the TEACH, the KIVA, the FIRE, the SPEED, the STAR, the FLUENT and many other commercial or in-house university codes. The code developed during the present investigation represents such an example.

Although CFD is now widely used in many applications, there are still a number of incomplete or non-universal mathematical models in fluid mechanics. Some topics include the modeling of turbulence, many types of two-phase flows and combustion. There are also a number of other processes in fluid mechanics which are incompletely understood and which do not have satisfactory models, including for example, sprays, as will be pointed out in this study.

Despite the fact the mathematical modeling of various processes is still under development, CFD can be used to investigate the effect that various geometries/design parameters of various systems have on the performance of the system. The CFD analysis is also widely used in cases where experimentation is difficult if not impossible to be applied. It is now generally accepted by the scientific/industrial community that models

can be used to improve the design procedure and to obtain physical information from a number of different applications.

The efforts made in the present thesis should be seen in the light of further assessments of models simulating the injection processes in diesel engines. These comprise a number of different problems, such as the fluid motion inside the fuel injection system, the onset of cavitation at the injection hole area and its effect on the disintegration of the emerging liquid, and then a number of other physical processes taking place during the motion of clouds of droplets, such as droplet secondary break-up, droplet-droplet interactions, droplet turbulent dispersion and in some cases droplet-wall interactions. Furthermore, when injected into a hot environment, heat transfer between the two phases is an additional process that complicates the mathematical analysis. A detailed literature review on previous works proposed to simulate all the aforementioned flow processes will be given in the corresponding chapters of the thesis.

1.3 Present Contribution

During the last few years, a lot of experimental and computational studies have been performed on both the characterization and the design of fuel injection systems and on the injected sprays. A number of different diesel fuel injection pumps and injection nozzles are used by the automotive industry, since the fuel injection system strongly affects both engine performance and pollutant emissions. Lately, a number of computer models have been published simulating the characteristics of sprays injected from various types of injectors. Most of these use a Lagrangian approach accounting for the trajectories of the liquid droplets. For such a solution, an initial condition is required; ideally, the actual flow conditions at the hole exit should be known for the representation of the following spray dispersion. However, these initial flow conditions are not usually known. The common assumption adopted in all previous models is the use of the measured fuel line pressure upstream of the nozzle as the actual injection pressure. Then the fuel flow rate is estimated assuming a constant discharge coefficient for the nozzle. Even in cases where the injection flow rate can be measured and given as input to the simulation, the detailed flow characteristics at the exit of the hole are still unknown parameters that influence the following spray development. The flow characteristics affecting the dispersion of the injected liquid have been previously

identified to be the liquid velocity, the velocity profile and the level of turbulence in the injection holes. In addition, if cavitation occurs in the injection holes, then the spray characteristics are dramatically altered from those of the non-cavitating cases. Thus, the two-phase nozzle flow has been identified to control the disintegration mechanism of the injected liquid jet. Also, the injection hole flow variations due to hole cavitation include an increase of the liquid velocity due to the volume of the injection holes occupied by bubbles and corresponding increase in the jet turbulence. Until now, only a few studies have been published on the modeling of the effect of this type of flow itself and on its subsequent influence on the liquid core disintegration. Usually, aerodynamic-induced or turbulence-induced atomization models are applied in order to predict the liquid core atomization. However, in the present study it is postulated that if cavitation occurs in the injection holes, which has proved to be the case under practical diesel engine conditions, then these models fail to predict the droplet size close to the injection holes. Also, most of the existing models do not take into account the injection velocity increment occurring in the injection holes due to the volume occupied by the bubbles. Thus, droplet velocities can be significantly underestimated.

It is the scope of the present investigation to develop a model simulating the flow in the fuel injection system, in the injection holes and the subsequent spray characteristics. For this type of modeling, no experimental or operating information is necessary, since the pump and the injector geometric characteristics are the only requirements. A phenomenological one-dimensional model is used for this type of simulation; this model is expensively validated against experimental data obtained during the present investigation. A set of model predictions for two different fuel injection systems are presented. Furthermore, in the present study more emphasis is given to the sac volume and injection holes flow characteristics. For non-cavitating (low injection pressure) conditions, a three-dimensional CFD code is used for the modeling of the flow in the sac volume and is validated against experimental data obtained in a large scale model of a multi-hole injection nozzle. For the transient solution, the calculated from the FIE model fuel flow rate just before the needle seat is used as a boundary condition to the code. For cavitating conditions, a phenomenological one-dimensional model is developed in order to describe the flow in the sac volume and the injection holes. For these cases, a series of experiments were performed giving useful data for the validation of the computer model. These include measurements of the total

fuel injected from each individual hole of the multi-hole injector used. The developed model can predict the flow rate of each of the injection holes of inclined injectors where the injection holes are asymmetrically located in the sac volume area. A model is used for the calculation of the hole area occupied by cavitating bubbles. These are calculated as a function of the sac volume pressure, back pressure, hole location relative to the sac area and hole geometry. Also, a hole turbulence model is used for the calculation of the average liquid turbulence kinetic energy in the injection hole and its dissipation rate.

One of the most challenging problems in fuel injection systems is to link the nozzle-hole flow with the spray characteristics. Having identified the flow conditions at the exit of the injection holes, a computational study on the prediction of the spray characteristics is performed. No experimental information is required for the model since all the flow characteristics can be simulated by the FIE model. The gas motion induced either by spray injection or by a cross stream of air is simulated by solving numerically the full Navier-Stokes equations. In the case of spray injection, source coupling terms are added expressing the mass, momentum and energy exchange between the two phases. The spray is simulated using a Lagrangian particle-tracking technique whereby the spray is modeled by a number of droplet parcels each of which contains a large number of droplets. It is assumed that the droplets in every parcel are identical and do not interact between them. Initially, the number of parcels injected is very small, since the nozzle flow determines the fuel injection rate and the initial droplet size (assumed to be equal to the hole effective area) and thus, the number of the liquid elements injected from the injection nozzle. Following their injection, a number of different phenomena, like liquid core atomization, droplet secondary break-up, droplet collisions, droplet turbulent dispersion, droplet evaporation and droplet deceleration have to be taken into account.

A number of different spray sub-models have been implemented into a previously developed CFD code. Initially, the liquid core which is assumed to consist of the injected fluid elements, disintegrates due to various forces involved. The three mechanisms of aerodynamic-induced atomization, jet turbulence-induced atomization and cavitation-induced atomization are all considered and it is revealed that hole cavitation controls/enhances atomization. Bubble collapsing was identified to be the factor responsible for the liquid core disintegration, in agreement with all the relevant experimental data published up to now. Although a detailed bubble dynamics model

would be required for the accurate representation of such flow phenomena, a simpler phenomenological approach is used here in order to take into account this effect. This is combined with a model calculating the droplet radial distribution in the spray cone angle. This is done since a number of experimental data show that the largest droplets are found close to the spray axis and the smaller at the edge of the spray. However, most models up to now distribute the droplets uniformly within the spray cone angle. The results of the proposed models are compared with the experimental data together with the results of other models available in the open literature.

Following the disintegration of the liquid core, the formed droplets penetrate into the surrounding gas. Droplet deceleration, secondary break-up, collisions, turbulent dispersion and evaporation all take place simultaneously in a diesel engine and different models are needed in order to account for all these phenomena. Since the injection velocities reach maximum values of over 300 m/s, a wide range of Weber numbers are calculated. It is well known from a number of different experiments that the secondary break-up mechanism is a function of the droplet Weber number. Also, completely different droplet deformation patterns have been observed for various ranges of Weber numbers. The most clear of them are classified as vibrating, bag, stripping and catastrophic break-up modes. The model used for the calculation of these flow processes combines experimental data and correlations available in the literature for the droplet deformation and the corresponding drag coefficient, the break-up time and the Sauter mean diameter of the formed droplets. The results of this model are combined with a proposed model calculating the droplet sizes and the number of droplets formed during the droplet break-up period; this model is based on the maximum entropy formalism and its use eliminates the need for the usually adopted assumption for droplet size distribution from which the droplet size is randomly sampled. Bimodal droplet size distributions like the case of stripping break-up are modeled by allowing more than one parcels to be formed during the droplet break-up. This approximation is not usually employed in other CFD spray models due to the large number of parcels required for the simulation and thus, the respective cost in computational time. However, in the present study it is postulated that this size distribution plays an important role in the spray structure. The frequently observed 'Christmas tree' spray structure can be attributed to this effect together with the variations in the injection pressure caused by the wave

dynamics of the flow in the FIE. Finally, correlations giving the droplet velocities as a function of their size after their secondary break-up are used.

The droplet deformation affects the liquid area in contact with the hot surrounding gas. This has an effect on the droplet evaporation rate; correlations for this liquid-gas interface surface are used accounting for the aforementioned effect. Very recent models calculating the temperature variation within the droplet by solving the one-dimensional heat conduction equations are compared with models estimating an average droplet temperature. However, the assumption of a spherical droplet seems not to be valid for most of their life time due to their deformation.

Finally, models accounting for droplet collisions and droplets turbulent dispersion are taken into account and their effect on the spray structure is evaluated.

Having identified the free spray characteristics, computational studies are performed for impinging diesel sprays. Available simulation models describing the dynamics of droplets during their impaction have been implemented in the developed code. The results of these models (each of which considers different physical processes) are compared with experimental data. Most of the experimental observations for such conditions are explained with the aim of the models used.

Finally, all the various FIE and spray sub-models are combined in order to predict the individual spray characteristics inside the piston bowl of a 1.9 l DI diesel engine. The model is validated against data reported in the open literature and confirmed that the model can be used to represent the characteristics of individual sprays as a function of both the injection characteristics and the gas motion inside the piston bowl of the combustion chamber.

1.4 Thesis Outline

The structure of the thesis is as follows. In Chapter 2 the equations describing the motion of the continuous phase are given; that comprises of the three-dimensional CFD code and of the one-dimensional model simulating the flow development in the fuel injection system. The derivation starts from the instantaneous transport equation for a general conserved property in a general curvilinear coordinate system; then, the ensemble-averaged form of these equations is given where the system of equations closes with the mathematical representation of the turbulence model. In addition, the

boundary conditions as well as the discrete form of the solved equations is given. For the case of the FIE flow simulation, the 3-D flow equations reduce to one direction only. In the presence of valves as well as other external geometric characteristics influencing the operation of the system, the various pressure losses are described. The numerical procedure allowing for any combination between the various elements comprising the FIE is given. Finally, this chapter closes with the derivation of a simple phenomenological cavitation model which predicts the effective injection velocity during the injection period in the presence of hole cavitation.

The spray model incorporating all the spray sub-models developed/implemented is described in Chapter 3. In this chapter, models for the liquid core atomization, droplet secondary break-up, droplet collisions, droplet impingement, droplet turbulent dispersion, droplet evaporation and droplet drag coefficient are described in detail together with the derivation of the mathematical representation of the general form of the Lagrangian spray model and the coupling terms between the gas and the liquid phases.

Chapter 4 describes the results obtained with the continuous phase simulation models. These include results for two different fuel injection systems for the validation of the FIE model and computational studies on the sac volume flow. Validation for the three dimensional CFD code is performed by comparing the computational results against measurements obtained during the present investigation on a purpose-built large scale transparent diesel injection nozzle. Parametric studies performed using the simulation models for both the FIE and the details of the geometry of the sac volume give a better understanding of the main design parameters of the system that have an influence on the nozzle exit characteristics.

Having validated the model calculating the nozzle exit characteristics which are then used as inputs to the CFD spray model, the validation of the dispersed phase model is given in Chapter 5. Comparison between the computational and experimental results is performed for different injection and surrounding gas conditions including free atmospheric sprays, either in a quiescent environment or in the presence of a cross flowing stream, impinging sprays and finally DI diesel engine sprays.

The conclusions of the present investigation are summarized in Chapter 6 together with suggestions for future work.

CHAPTER 2

Because it seems to me that the whole meaning of physical philosophy consists of this: from the phenomena of movements to derive the forces of nature and then with these forces to describe other, like the movements of starts and comets and the waves of the sea...

Isaac Newton
(principia)

Model of Continuous Phase

2.1 Introduction

In this chapter the model used for the simulation of the continuous phase (i.e. the flow in the fuel injection system, the flow in the sac volume and the gas motion) is described. The chapter is divided into two main sub-sections: first the CFD model is described followed by the presentation of the FIE computer model.

2.2 CFD Model of the Continuous Phase

This model was used for the simulation of the flow in the sac volume as well as for the prediction of the gas motion in the case of spray injection. It is a turbulent, three dimensional, transient and compressible model that can be applied to any geometry with moving boundaries. The full Navier-Stokes equations are numerically solved on a collocated curvilinear non-orthogonal Cartesian numerical grid using Cartesian velocity components. It is thus already clear that this model is not restricted to a specific application but can be applied to many liquid or gas flow processes. For the case of spray injection, this model was modified to account for the induced by the spray flow field through appropriate coupling terms which are given in Chapter 3. In what follows, the mathematical development of this model is given while more details can be found in the Ph.D. thesis of Theodorakakos (1997).

The basic equations describing the mass, momentum and scalar quantities conservation laws can be expressed in the following vector form, which is independent of the coordinate system used:

$$\frac{\partial \rho}{\partial t} + \mathrm{div}(\rho \vec{v}) = \dot{S}_{MASS}$$

$$\frac{\partial}{\partial t}(\rho \vec{v}) + \mathrm{div}(\rho \vec{v} \times \vec{v} - T) = \dot{S}_{MOMENT} \qquad (2\text{-}1)$$

$$\frac{\partial}{\partial t}(\rho \Phi) + \mathrm{div}(\rho \Phi \vec{v} - \vec{q}) = \dot{S}_{SCALAR}$$

Here ρ is the fluid density, $\vec{v}$ is the velocity vector and Φ is any scalar variable (i.e. temperature, concentration, turbulence kinetic energy e.t.c.). T is the stress tensor and $\vec{q}$ is the flux vector. The stress tensor for a Newtonian fluid is defined as:

$$T = -(p + \frac{2}{3}\mu \cdot \mathrm{div}(\vec{v}))I + 2\mu D \qquad (2\text{-}2)$$

where p is the pressure, μ is the dynamic viscosity of the moving fluid, I is the unit tensor and D is the deformation (rate of strain) tensor. The flux vector is usually given by the Fourier law as:

$$\vec{q} = \lambda \cdot \mathrm{grad}\Phi \qquad (2\text{-}3)$$

where the proportionality coefficient λ is called 'diffusivity' and is usually a property of the transporting fluid. Although all forms of the above differential equations describe the same laws and from the mathematical point of view any of them is valid, their form is of significant importance when they are integrated and discretized over a finite number of control volumes. When they are written in their strong conservation form, the resulting fluxes would cancel in pairs at the interior control volume cell faces when added together and only the boundary fluxes will remain. This procedure guarantees overall conservation of the transported quantity and this is why this type of expression of the differential form of the flow equations is usually referred to as 'strong conservation form'. When the differential equations are written in the weak conservation form and integrated over the control volumes there is no obvious discretization method which would guarantee overall conservation. In addition these terms, which are usually referred to as 'curvature terms', are quite sensitive to the grid

smoothness. Thus, it is clear that the strong conservation is the desirable form of the differential flow equations and this has been selected in this investigation.

The most common method to achieve the above form of equations in a general curvilinear coordinate system is to express both vector and tensor components on a spatially constant base; the obvious selection is then the Cartesian coordinate system since in this system the equations take their simplest possible mathematical form. In addition, their integration becomes relatively simple and the boundary conditions can be easily implemented. Thus, the Cartesian system has been adopted in this investigation.

2.2.1 Governing equations in a general coordinate system

The conservation equations of mass, momentum and any scalar quantity expressed in any coordinate system $y_i=y_i(x_1, x_2, x_3)$, where x_i is the Cartesian coordinate system, can take the form :

$$\begin{aligned}
&\frac{1}{J}\frac{\partial(J\rho)}{\partial t}+\frac{1}{J}\frac{\partial}{\partial x_j}\left(\rho u_m \beta_m^j\right)=s_{mass}\\
&\frac{1}{J}\frac{\partial(J\rho u_i)}{\partial t}+\frac{1}{J}\frac{\partial}{\partial x_j}\left[\left(\rho u_m u_i - T_{mi}\right)\beta_m^j\right]=s_u^i\\
&\frac{1}{J}\frac{\partial(J\rho\varphi)}{\partial t}+\frac{1}{J}\frac{\partial}{\partial x_j}\left[\left(\rho u_m \varphi - q_m\right)\beta_m^j\right]=s_\varphi
\end{aligned} \tag{2-4}$$

where J is the Jacobian of the coordinate transformation and β are the derivatives of the transformation which are defined as:

$$\beta_j^i = J\cdot\frac{\partial x_i}{\partial y_j} \tag{2-5}$$

The stress tensor and the flux vector can be written as:

$$\begin{aligned}
T_{mi} &= \frac{1}{J}\mu\cdot\left(\frac{\partial u_i}{\partial x_n}\beta_m^n+\frac{\partial u_m}{\partial x_j}\beta_i^j\right)-p\delta_{mi}=\tau_{mi}-p\delta_{mi}\\
q_m &= \frac{1}{J}\Gamma_\varphi\frac{\partial\varphi}{\partial x_n}\beta_m^n
\end{aligned} \tag{2-6}$$

where δ is the Kroneger's delta function and Γ is the diffusion coefficient of the scalar variable φ.

2.2.2 Model of turbulence

Turbulence is an important feature of fluid flows and has to be taken into account in the calculation; many studies in the past have extensively investigated the physics and the mathematical formulation of turbulent fluid flow, for example Tenekes and Lamley (1972), Launder and Spalding (1974), Hinze (1975), Landant et.al. (1992) and many others. In order to model mathematically the turbulent motion of fluids, it is generally accepted that the properties of any variable φ can be divided into a mean value and a fluctuating (turbulent) component:

$$\varphi = \bar{\varphi} + \varphi' \tag{2-7}$$

where

$$\bar{\varphi}' = \lim_{T\to\infty}\left(\frac{1}{T}\int_{to}^{to+T}\varphi' dt\right) = 0 \tag{2-8}$$

Under these assumptions and if the density and viscosity fluctuations are neglected (which is the case for flows with low Mach number and without chemical reactions), by introducing equation (2-7) into the transport equations (2-4) these take their time-averaged form:

$$\frac{1}{J}\frac{\partial(J\rho)}{\partial t} + \frac{1}{J}\frac{\partial}{\partial x_j}\left(\rho\bar{u}_m\beta_m^j\right) = s_{mass}$$

$$\frac{1}{J}\frac{\partial\left(J\rho\bar{u}_i\right)}{\partial t} + \frac{1}{J}\frac{\partial}{\partial x_j}\left[\left(\rho\bar{u}_m\bar{u}_i - \left(\bar{T}_{mi} - \rho\overline{u'_m u'_i}\right)\right)\beta_m^j\right] = \bar{s}_u^i \tag{2-9}$$

$$\frac{1}{J}\frac{\partial\left(J\rho\bar{\varphi}\right)}{\partial t} + \frac{1}{J}\frac{\partial}{\partial x_j}\left[\left(\rho\bar{u}_m\bar{\varphi} - \left(\bar{q}_m - \rho\overline{u'_m\varphi'}\right)\right)\beta_m^j\right] = \bar{s}_\varphi$$

Equations (2-9) have the same form as equations (2-4); however, they refer to a much longer time scale than equations (2-4) and thus they can be practically intergated to give the mean values of the flow properties. The extra terms that appear in these equations

are usually referred to as Reynolds stresses for the velocity and turbulent scalar fluxes for the scalar variables and are defined as:

$$T^t_{mi} = -\rho\overline{u'_m u'_i} \qquad q^t_m = -\rho\overline{u'_m \varphi'} \tag{2-10}$$

It should be mentioned that Reynolds stresses are at least an order of magnitude larger that the shear stresses of the molecular properties of the fluid. To close the system of equations it is necessary either to relate these extra terms directly to the mean flow properties or to supply additional equations from which they can be estimated; as a result, a wide variety of 'turbulence models' have been reported up to now in the literature. In the present investigation the two equation k-ε turbulence model has been adopted. According to this model, the following correlations can be used to calculate the Reynolds stresses and the turbulent scalar fluxes:

$$\begin{aligned} -\rho\overline{u'_m u'_i} &= \frac{1}{J}\mu_t \cdot \left(\frac{\partial \bar{u}_i}{\partial x_n}\beta^n_m + \frac{\partial \bar{u}_m}{\partial x_j}\beta^j_i\right) - \frac{2}{3}k\rho\delta_{mi} = \tau^t_{mi} - p_t\delta_{mi} \\ -\rho\overline{u'_m \varphi'} &= \frac{1}{J}\Gamma_{\varphi t}\frac{\partial \bar{\varphi}}{\partial x_n}\beta^n_m \end{aligned} \tag{2-11}$$

The turbulent viscocity and diffucivity coefficients are defined as:

$$\mu_t = C_\mu \rho \frac{k^2}{\varepsilon} \quad \text{and} \quad \Gamma_{\varphi t} = \frac{\mu_t}{Pr_\varphi} \tag{2-12}$$

where Pr_φ is the Prandl number. The part of the turbulent normal stress $p_t = \frac{2}{3}k \cdot \rho \cdot \delta_{mi}$ as well as the normal stress $\frac{2}{3}\mu \cdot \mathrm{div}\vec{u}$ are usually incorporated into the mean pressure. In the above equations k stands for the turbulent kinetic energy while ε is the dissipation rate of k. These are generally defined as:

$$k = \frac{1}{2}\overline{u'_i u'_i} \qquad \varepsilon = \frac{1}{J}\frac{\mu}{\rho}\cdot\overline{\left(\frac{\partial u'_i}{\partial x_n}\beta^n_j\right)\cdot\left(\frac{\partial u'_i}{\partial x_n}\beta^n_j\right)} \tag{2-13}$$

The transport equations for k and ε have exactly the same form as for any other scalar variable; in these equations the 'difussion' coefficients have the form:

$$k: \ \Gamma_k = \frac{\mu_t}{\sigma_k} \quad \text{and} \quad \varepsilon: \ \Gamma_\varepsilon = \frac{\mu_t}{\sigma_\varepsilon} \tag{2-14}$$

while the source terms are written as:

$$s_k = G - \rho \cdot \varepsilon = G - \frac{\rho^2 C_\mu}{\mu_t} k^2$$

$$s_\varepsilon = C_1 \frac{\varepsilon}{k} G - C_2 \rho \frac{\varepsilon^2}{k} + C_3 \cdot \rho \cdot \varepsilon \cdot \mathrm{div}\vec{u} = \frac{C_1 C_\mu \rho k}{\mu_t} G - \frac{C_2 C_\mu \rho^2 k}{\mu_t} \varepsilon + C_3 \cdot \rho \cdot \varepsilon \cdot \mathrm{div}\vec{u} \tag{2-15}$$

where G is the rate of production of turbulent kinetic energy which can be calculated as:

$$G = \tau_{ij}^t \frac{\partial \overline{u}_i}{\partial y_j} = \frac{1}{J^2} \mu_t \left(\frac{\partial \overline{u}_i}{\partial x_n} \beta_j^n + \frac{\partial \overline{u}_j}{\partial x_m} \beta_i^m \right) \cdot \left(\frac{\partial \overline{u}_i}{\partial x_n} \beta_j^n \right) - \frac{2}{3} (\nabla \vec{u})(\rho \cdot k + \mu \cdot \nabla \vec{u}) \tag{2-16}$$

Common values for the empirical coefficients introduced in the above equations are the following:

$C_\mu = 0.09$ $C_1 = 1.44$ $C_2 = 1.92$ $C_3 = -0.373$ $\sigma_k = 1.0$ $\sigma_\varepsilon = 1.3$

When the Reynolds and scalar turbulent stresses that derive from this k-ε model are introduced into equations (2-9) these finally take a form similar to that of the non-time averaged flow equations, where the coefficients μ and Γ have to be replaced from their effective values which are defined as:

$$\mu_{eff} = \mu_l + \mu_t \qquad \Gamma_{\varphi,eff} = \Gamma_{\varphi l} + \Gamma_{\varphi t} \tag{2-17}$$

where μ_l and μ_t are the laminar and turbulent viscocities, respectively. This characteristic of the model makes it attractive and it is one of the reasons that it is used in many CFD codes.

Equations (2.2.2-3) can be also written in the following form:

$$\frac{\partial(J\rho\varphi)}{\partial t}+\frac{\partial}{\partial x_1}(\rho U_1\varphi)+\frac{\partial}{\partial x_2}(\rho U_2\varphi)+\frac{\partial}{\partial x_3}(\rho U_3\varphi)$$
$$-\frac{\partial}{\partial x_1}\left[\frac{\Gamma_{\varphi,eff}}{J}\left(\beta_1^{12}+\beta_2^{12}+\beta_3^{12}\right)\frac{\partial\varphi}{\partial x_1}\right]-\frac{\partial}{\partial x_2}\left[\frac{\Gamma_{\varphi,eff}}{J}\left(\beta_1^{22}+\beta_2^{22}+\beta_3^{22}\right)\frac{\partial\varphi}{\partial x_2}\right] \qquad (2\text{-}18)$$
$$-\frac{\partial}{\partial x_3}\left[\frac{\Gamma_{\varphi,eff}}{J}\left(\beta_1^{32}+\beta_2^{32}+\beta_3^{32}\right)\frac{\partial\varphi}{\partial x_3}\right]= \quad s_\varphi^{CD1}+s_\varphi^{CD2}+Js_\varphi+Js_{\varphi 2}$$

where the following Table 2-1 summurises the corresponding source terms:

φ	$\Gamma_{\varphi,eff}$	s_φ
1	0	0
u_1	μ_{eff}	$-\left[\beta_1^1\frac{\partial(p+p_t)}{\partial x_1}+\beta_1^2\frac{\partial(p+p_t)}{\partial x_2}+\beta_1^3\frac{\partial(p+p_t)}{\partial x_3}\right]$
u_2	μ_{eff}	$-\left[\beta_2^1\frac{\partial(p+p_t)}{\partial x_1}+\beta_2^2\frac{\partial(p+p_t)}{\partial x_2}+\beta_2^3\frac{\partial(p+p_t)}{\partial x_3}\right]$
u_3	μ_{eff}	$-\left[\beta_3^1\frac{\partial(p+p_t)}{\partial x_1}+\beta_3^2\frac{\partial(p+p_t)}{\partial x_2}+\beta_3^3\frac{\partial(p+p_t)}{\partial x_3}\right]$
k	μ_{eff}/σ_κ	$G-\frac{\rho^2 C_\mu}{\mu_t}k^2$
ε	$\mu_{eff}/\sigma_\varepsilon$	$\frac{C_1C_\mu\rho\cdot k}{\mu_t}G-\frac{C_2C_\mu\rho^2 k}{\mu_t}\varepsilon+C_3\rho\cdot\varepsilon\cdot\nabla\vec{u}$
h	$\mu_l/\sigma_{T,l}+\mu_t/\sigma_{T,t}$	$\frac{\partial P}{\partial t}+G$

Table 2-1 : Source terms of the various variables involved into the simulation

where :

$$\beta_k^m = J\frac{\partial x_m}{\partial y_k} \qquad (2\text{-}19)$$

$$U_k=\left[\beta_1^k\left(u_1-u_{g1}\right)+\beta_2^k\left(u_2-u_{g2}\right)+\beta_3^k\left(u_3-u_{g3}\right)\right] \qquad (2\text{-}20)$$

where u_{g1}, u_{g2} and u_{g3} are the Cartesian velocity components of the transformed coordinate system (or in other words, the velocities of the numerical nodes). Also:

$$p_t = \frac{2}{3}(\rho \cdot k + \mu_{eff} \nabla \vec{u}) \tag{2-21}$$

$$\mu_{eff} = \mu_l + \mu_t = \mu_l + \frac{C_\mu \rho k^2}{\varepsilon} \tag{2-22}$$

$$h = c_p T \tag{2-23}$$

$$G = \frac{1}{J^2}\mu_t \left(\frac{\partial u_i}{\partial x_n}\beta_j^n + \frac{\partial u_j}{\partial x_m}\beta_i^m\right) \cdot \left(\frac{\partial u_i}{\partial x_n}\beta_j^n\right) - \frac{2}{3}(\nabla \vec{u})(\rho \cdot k + \mu \cdot \nabla \vec{u}) \tag{2-24}$$

The term $s_{\varphi 2}$ on the right hand side of equation (2-18) is due to any external source terms (for example the presence of liquid droplets). The terms s_φ^{CD1} and s_φ^{CD2} can be estimated as:

s_φ^{DC1}: ($\varphi = u_1, u_2, u_3, k, \varepsilon, h$)

$$\begin{aligned} s_\varphi^{DC1} = & \frac{\partial}{\partial x_1}\left[\frac{\Gamma_{eff}}{J}\left(\frac{\partial \varphi}{\partial x_2}\left(\beta_1^1\beta_1^2 + \beta_2^1\beta_2^2 + \beta_3^1\beta_3^2\right) + \frac{\partial \varphi}{\partial x_3}\left(\beta_1^1\beta_1^3 + \beta_2^1\beta_2^3 + \beta_3^1\beta_3^3\right)\right)\right] + \\ & \frac{\partial}{\partial x_2}\left[\frac{\Gamma_{eff}}{J}\left(\frac{\partial \varphi}{\partial x_1}\left(\beta_1^2\beta_1^1 + \beta_2^2\beta_2^1 + \beta_3^2\beta_3^1\right) + \frac{\partial \varphi}{\partial x_3}\left(\beta_1^2\beta_1^3 + \beta_2^2\beta_2^3 + \beta_3^2\beta_3^3\right)\right)\right] + \\ & \frac{\partial}{\partial x_3}\left[\frac{\Gamma_{eff}}{J}\left(\frac{\partial \varphi}{\partial x_1}\left(\beta_1^3\beta_1^1 + \beta_2^3\beta_2^1 + \beta_3^3\beta_3^1\right) + \frac{\partial \varphi}{\partial x_2}\left(\beta_1^3\beta_1^2 + \beta_2^3\beta_2^2 + \beta_3^3\beta_3^2\right)\right)\right] \end{aligned} \tag{2-25}$$

$s_{u_k}^{DC2}$: ($\varphi = u_1, u_2, u_3$)

$$\begin{aligned} s_{u_k}^{DC2} = & \frac{\partial}{\partial x_1}\left[\frac{\Gamma_{eff}}{J}\left(\frac{\partial u_1}{\partial x_1}\beta_1^1\beta_k^1 + \frac{\partial u_1}{\partial x_2}\beta_1^1\beta_k^2 + \frac{\partial u_1}{\partial x_3}\beta_1^1\beta_k^3\right)\right] + \\ & \frac{\partial}{\partial x_1}\left[\frac{\Gamma_{eff}}{J}\left(\frac{\partial u_2}{\partial x_1}\beta_2^1\beta_k^1 + \frac{\partial u_2}{\partial x_2}\beta_2^1\beta_k^2 + \frac{\partial u_2}{\partial x_3}\beta_2^1\beta_k^3\right)\right] + \end{aligned}$$

$$\frac{\partial}{\partial x_1}\left[\frac{\Gamma_{eff}}{J}\left(\frac{\partial u_3}{\partial x_1}\beta_3^1\beta_k^1+\frac{\partial u_3}{\partial x_2}\beta_3^1\beta_k^2+\frac{\partial u_3}{\partial x_3}\beta_3^1\beta_k^3\right)\right]+$$

$$\frac{\partial}{\partial x_2}\left[\frac{\Gamma_{eff}}{J}\left(\frac{\partial u_1}{\partial x_1}\beta_1^2\beta_k^1+\frac{\partial u_1}{\partial x_2}\beta_1^2\beta_k^2+\frac{\partial u_1}{\partial x_3}\beta_1^2\beta_k^3\right)\right]+$$

$$\frac{\partial}{\partial x_2}\left[\frac{\Gamma_{eff}}{J}\left(\frac{\partial u_2}{\partial x_1}\beta_2^2\beta_k^1+\frac{\partial u_2}{\partial x_2}\beta_2^2\beta_k^2+\frac{\partial u_2}{\partial x_3}\beta_2^2\beta_k^3\right)\right]+ \qquad (2\text{-}26)$$

$$\frac{\partial}{\partial x_2}\left[\frac{\Gamma_{eff}}{J}\left(\frac{\partial u_3}{\partial x_1}\beta_3^2\beta_k^1+\frac{\partial u_3}{\partial x_2}\beta_3^2\beta_k^2+\frac{\partial u_3}{\partial x_3}\beta_3^2\beta_k^3\right)\right]+$$

$$\frac{\partial}{\partial x_3}\left[\frac{\Gamma_{eff}}{J}\left(\frac{\partial u_k}{\partial x_1}\beta_1^3\beta_k^1+\frac{\partial u_k}{\partial x_2}\beta_1^3\beta_k^2+\frac{\partial u_k}{\partial x_3}\beta_1^3\beta_k^3\right)\right]+$$

$$\frac{\partial}{\partial x_3}\left[\frac{\Gamma_{eff}}{J}\left(\frac{\partial u_2}{\partial x_1}\beta_2^3\beta_k^1+\frac{\partial u_2}{\partial x_2}\beta_2^3\beta_k^2+\frac{\partial u_2}{\partial x_3}\beta_2^3\beta_k^3\right)\right]+$$

$$\frac{\partial}{\partial x_3}\left[\frac{\Gamma_{eff}}{J}\left(\frac{\partial u_3}{\partial x_1}\beta_3^3\beta_k^1+\frac{\partial u_3}{\partial x_2}\beta_3^3\beta_k^2+\frac{\partial u_3}{\partial x_3}\beta_3^3\beta_k^3\right)\right]$$

The terms β_k^m are the derivatives of the coordinates transformation which are given from the general form:

$$\beta_k^m = J\frac{\partial x_m}{\partial y_k} \qquad (2\text{-}27)$$

2.2.3 Discretization

In this section the disrcetisation of the described equations is given. The method used is that of the finite volumes in which the solved equations are integrated and appropriatelly discretised on the numerical grid and finally they are linearised to allow then to be solved numerically.

The following Figure 2-1 shows a general three dimensional computational (control) volume including references to all points that will be used latter. The only information required for this arbitrary volume is the coordinates of its nodes in the

Cartesian coordinate system; its volume can also be calculated from the coordinates of the nodes.

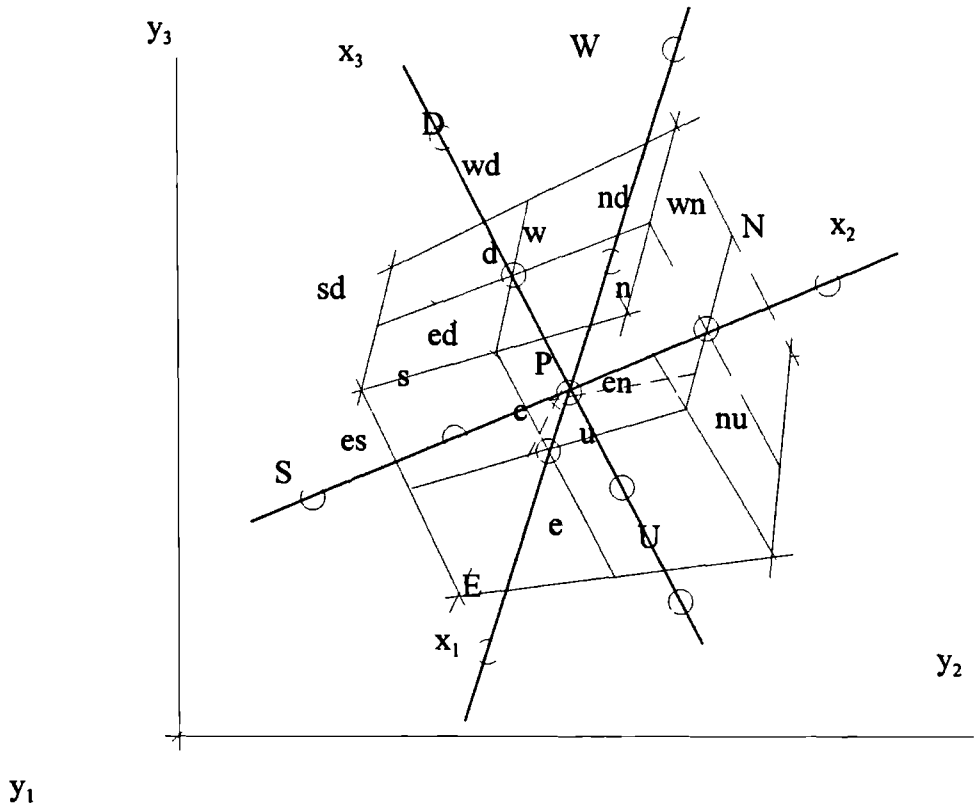

Figure 2-1 : Control volume and notation used for the discretization

By using the following notation (2-28) the infinitesimal increment of the Cartesian coordinate y^i along the constant x^j direction becomes:

$$\left(\delta y^i\right)_e^1 = y_E^i - y_P^i \qquad \left(\delta y^i\right)_e^2 = \left(y_n^i - y_s^i\right)_e \qquad \left(\delta y^i\right)_e^3 = \left(y_d^i - y_u^i\right)_n$$

$$\left(\delta y^i\right)_n^1 = \left(y_e^i - y_w^i\right)_n \qquad \left(\delta y^i\right)_n^2 = y_N^i - y_P^i \qquad \left(\delta y^i\right)_n^3 = \left(y_d^i - y_u^i\right)_n \qquad (2\text{-}28)$$

$$\left(\delta y^i\right)_d^1 = \left(y_e^i - y_w^i\right)_d \qquad \left(\delta y^i\right)_d^2 = \left(y_n^i - y_s^i\right)_d \qquad \left(\delta y^i\right)_d^3 = y_D^i - y_P^i$$

then, the derivatives of equations (2-27) can be estimated from the following correlations:

$$\beta_1^1 \approx \frac{1}{\delta x_2 \delta x_3}\left[(\delta y_2)_2(\delta y_3)_3 - (\delta y_2)_3(\delta y_3)_2\right] = \frac{1}{\delta x_2 \delta x_3} b_1^1$$

$$\beta_2^1 \approx \frac{1}{\delta x_2 \delta x_3}\left[(\delta y_1)_3(\delta y_3)_2 - (\delta y_1)_2(\delta y_3)_3\right] = \frac{1}{\delta x_2 \delta x_3} b_2^1$$

$$\beta_3^1 \approx \frac{1}{\delta x_2 \delta x_3}\left[(\delta y_1)_2(\delta y_2)_3 - (\delta y_1)_3(\delta y_2)_2\right] = \frac{1}{\delta x_2 \delta x_3} b_3^1$$

$$\beta_1^2 \approx \frac{1}{\delta x_1 \delta x_3}\left[(\delta y_3)_1(\delta y_2)_3 - (\delta y_3)_3(\delta y_2)_1\right] = \frac{1}{\delta x_1 \delta x_3} b_1^2$$

$$\beta_2^2 \approx \frac{1}{\delta x_1 \delta x_3}\left[(\delta y_1)_1(\delta y_3)_3 - (\delta y_1)_3(\delta y_3)_1\right] = \frac{1}{\delta x_1 \delta x_3} b_2^2 \qquad (2\text{-}30)$$

$$\beta_3^2 \approx \frac{1}{\delta x_1 \delta x_3}\left[(\delta y_1)_3(\delta y_2)_1 - (\delta y_1)_1(\delta y_2)_3\right] = \frac{1}{\delta x_1 \delta x_3} b_3^2$$

$$\beta_1^3 \approx \frac{1}{\delta x_1 \delta x_2}\left[(\delta y_2)_1(\delta y_3)_2 - (\delta y_2)_2(\delta y_3)_1\right] = \frac{1}{\delta x_1 \delta x_2} b_1^3$$

$$\beta_2^3 \approx \frac{1}{\delta x_1 \delta x_2}\left[(\delta y_1)_2(\delta y_3)_1 - (\delta y_1)_1(\delta y_3)_2\right] = \frac{1}{\delta x_1 \delta x_2} b_2^3$$

$$\beta_3^3 \approx \frac{1}{\delta x_1 \delta x_2}\left[(\delta y_1)_1(\delta y_2)_2 - (\delta y_1)_2(\delta y_2)_1\right] = \frac{1}{\delta x_1 \delta x_2} b_3^3$$

In correlations (2-30) δx_1, δx_2, δx_3 stand for the distance of the numerical notes along the curvilinear coordinate system (x_1, x_2, x_3).

Since equations (2-18), (2-25) and (2-26) are written in the general curvilinear coordinate system (x_1, x_2, x_3), they have to be integrated over the computational volume

$$dv = dx_1 \cdot dx_2 \cdot dx_3 \qquad (2\text{-}31)$$

It has to be noted that the volume of integration in the physical (Cartesian) space is given from:

$$dV = dy_1 \cdot dy_2 \cdot dy_3 = J \cdot dx_1 \cdot dx_2 \cdot dx_3 \Rightarrow \delta V = J \cdot \delta x_1 \cdot \delta x_2 \cdot \delta x_3 \tag{2-32}$$

2.2.3.1 Diffusion and convection terms

Initially, the continuity equation will be investigated. Integrating the first term of equation (2-18) over the control volume and using the Green theorem we obtain:

$$\int_{\delta v} \frac{\partial}{\partial x_1} U_1 \cdot dx_1 dx_2 dx_3 = \int_{\delta v} \frac{\partial}{\partial x_1} \left[\rho\left(u_1\beta_1^1 + u_2\beta_2^1 + u_3\beta_3^1\right)\right] \cdot dx_1 dx_2 dx_3 \approx$$

$$\left[\rho\left(u_1\beta_1^1 + u_2\beta_2^1 + u_3\beta_3^1\right) \cdot \delta x_2 \delta x_3\right]_w^e = \left[\rho\left(u_1 b_1^1 + u_2 b_2^1 + u_3 b_3^1\right)\right]_w^e = \tag{2-32}$$

$$\rho_e\left(u_1 b_1^1 + u_2 b_2^1 + u_3 b_3^1\right)_e - \rho_w\left(u_1 b_1^1 + u_2 b_2^1 + u_3 b_3^1\right)_w$$

where u_i is the relative velocity between the moving fluid and the numerical grid. Similar expressions can be derived for the following two terms which are finally transformed into differences of surface integrals between the 'n'-'s' and 'd'-'u' surfaces of the volume of integration. The values of the independent variables that appear in these equations and refer to the 'e'-'w'-'n'-'s'-'d'-'u' surfaces are usually estimated using linear interpolations between neighbouring nodes. For example, for any independent variable φ it can be taken:

$$\varphi_e = \varphi_P + \left(1 - f_{lP}\right)\left(\varphi_E - \varphi_P\right) \qquad \varphi_w = \varphi_W + \left(1 - f_{lW}\right)\left(\varphi_P - \varphi_W\right) \tag{2-33}$$

where the factor f can be calculated on the basis of the geometric distance between the corresponding nodes, for example as:

$$f_{lP} = \frac{\overline{Ee}}{\overline{Ee} + \overline{Pe}} \tag{2-34}$$

with similar expressions written for the other two directions. The source terms on the right hand side of the continuity equation are integrated as:

$$\int_{dv} Js_{mass} \cdot dx_1 dx_2 dx_3 \approx s_{massP} \cdot J \cdot \delta x_1 \delta x_2 \delta x_3 \approx s_{massP} \cdot \delta V_P \tag{2-35}$$

We can now proceed to the estimation of the diffusion terms. The derivative on any variable φ in a direction normal to any cell face of the control volume is estimated using central derivative:

$$\left(\frac{\partial\varphi}{\partial x_1}\right)_e \approx \frac{\varphi_E - \varphi_P}{\delta x_{1e}} \tag{2-36}$$

while the cross-derivative terms which are also required at each cell face are approximated as:

$$\left(\frac{\partial\varphi}{\partial x_2}\right)_e \approx \frac{(\varphi_n - \varphi_s)_e}{\delta x_{2e}} \qquad \left(\frac{\partial\varphi}{\partial x_3}\right)_e \approx \frac{(\varphi_d - \varphi_u)_e}{\delta x_{3e}} \tag{2-37}$$

where values of φ_{ne} are estimated using linear interpolations from their values on neigbouring nodes. With the above approximations the diffusion term of any scalar variable φ can be estimated as an integral using the derivatives with respect to x_1 of equations (2-18) and (2-25):

$$-\int_{\delta v}\frac{\partial}{\partial x_1}\left[\frac{\Gamma_{\varphi,eff}}{J}\left(\left(\beta_1^{1^2}+\beta_2^{1^2}+\beta_3^{1^2}\right)\frac{\partial\varphi}{\partial x_1}+\left(\beta_1^1\beta_1^2+\beta_2^1\beta_2^2+\beta_3^1\beta_3^2\right)\frac{\partial\varphi}{\partial x_2}+\left(\beta_1^1\beta_1^3+\beta_2^1\beta_2^3+\beta_3^1\beta_3^3\right)\frac{\partial\varphi}{\partial x_2}\right)\right]\cdot dx_1dx_2dx_1 \tag{2-38}$$

This integral can be expressed as the difference between two surface integrals over the 'e' and 'w' surfaces, for example for the 'e' surface the expression is:

$$-\int_{A_e}\left[\frac{\Gamma_{\varphi,eff}}{J}\left(\begin{array}{l}\left(\beta_1^{1^2}+\beta_2^{1^2}+\beta_3^{1^2}\right)\frac{\partial\varphi}{\partial x_1}+\left(\beta_1^1\beta_1^2+\beta_2^1\beta_2^2+\beta_3^1\beta_3^2\right)\frac{\partial\varphi}{\partial x_2}+\\ \left(\beta_1^1\beta_1^3+\beta_2^1\beta_2^3+\beta_3^1\beta_3^3\right)\frac{\partial\varphi}{\partial x_2}\end{array}\right)\right]\cdot$$

$$dx_2dx_1 = -\left(\frac{\Gamma_{\varphi,eff}}{\delta V}\right)_e\cdot\left(b_1^{1^2}+b_2^{1^2}+b_3^{1^2}\right)\cdot(\varphi_E-\varphi_P)- \tag{2-39}$$

$$\left(\frac{\Gamma_{\varphi,eff}}{\delta V}\right)_e\cdot\left[\begin{array}{l}\left(b_1^1b_1^2+b_2^1b_2^2+b_3^1b_3^2\right)\cdot(\varphi_n-\varphi_s)+\\ \left(b_1^1b_1^3+b_2^1b_2^3+b_3^1b_3^3\right)\cdot(\varphi_d-\varphi_u)\end{array}\right]_e = I_e^{DN}+I_e^{DCI}$$

In the above correlation, the first of the two terms refers to the diffusion terms in a direction normal to the direction of the variables on the transformed coordinate system while the second one refers to the cross-derivative direction. It can also be seen that the Jacobian of the transformation is absent from the final expressions (2-32), (2-38) and (2-39). The same is true for the coordinates on the transformed coordinate system. The only variable that appears is the volume of the computational cell which can be calculated from purely geometrical conditions.

2.2.3.2 Time derivatives, pressure and remaining source terms

In the general equation (2-18) appears the time derivative $\frac{\partial(J\rho\varphi)}{\partial t}$ which can be estimated using an implicit first order Euler numerical scheme as:

$$\frac{\partial(J\rho\varphi)}{\partial t}\cdot dx_1dx_2dx_3 \approx \frac{\rho\varphi\cdot\delta V-(\rho\varphi\cdot\delta V)^{old}}{\delta t} \tag{2-40}$$

where the volume of the computational cell in general is not the same between the two different time steps. The superscript 'old' expresses the values of all variables involved in the previous time step (which are known from the solution of the previous time step or from the initial conditions for the beginning of the calculations).

The pressure source term for the 'k' velocity component is estimated from the expression:

$$S_{\varphi press} = \int_{\delta v}\left(\frac{\partial p}{\partial x_1}\beta_k^1+\frac{\partial p}{\partial x_2}\beta_k^2+\frac{\partial p}{\partial x_3}\beta_k^3\right)\cdot dx_1dx_2dx_3 \approx \tag{2-41}$$
$$(p_e-p_w)\cdot b_{kP}^1+(p_n-p_s)\cdot b_{kP}^2+(p_d-p_u)\cdot b_{kP}^1$$

where the b coefficients are estimated on the geometrical centre P of the computational cell.

The rate of production of turbulent kinetic energy G is estimated from the expression:

$$G_P = (\frac{\mu_t}{\delta V^2})_P \{2[(\delta u_1)^1 b_1^1 + (\delta u_1)^2 b_1^2 + (\delta u_1)^3 b_1^3]^2 +$$

$$2[(\delta u_2)^1 b_2^1 + (\delta u_2)^2 b_2^2 + (\delta u_2)^3 b_2^3]^2 +$$

$$2[(\delta u_3)^1 b_3^1 + (\delta u_3)^2 b_3^2 + (\delta u_3)^3 b_3^3]^2 +$$

$$[(\delta u_1)^1 b_2^1 + (\delta u_1)^2 b_2^2 + (\delta u_1)^3 b_2^3 + (\delta u_2)^1 b_1^1 + (\delta u_2)^2 b_1^2 + (\delta u_2)^3 b_1^3]^2 +$$

$$[(\delta u_1)^1 b_3^1 + (\delta u_1)^2 b_3^2 + (\delta u_1)^3 b_3^3 + (\delta u_3)^1 b_1^1 + (\delta u_3)^2 b_1^2 + (\delta u_3)^3 b_1^3]^2 +$$

$$[(\delta u_2)^1 b_3^1 + (\delta u_2)^2 b_3^2 + (\delta u_2)^3 b_3^3 + (\delta u_3)^1 b_2^1 + (\delta u_3)^2 b_2^2 + (\delta u_3)^3 b_2^3]^2\}_P -$$

$$[\frac{2}{3}(\nabla \vec{u}) \cdot (\rho \cdot k + \mu_t \nabla \vec{u})]_P \qquad (2\text{-}42)$$

where δu are the velocity increments which are defined as:

$$\begin{aligned} (\delta u_i)_P^1 &= u_{ie} - u_{iw} \\ (\delta u_i)_P^2 &= u_{in} - u_{is} \\ (\delta u_i)_P^3 &= u_{id} - u_{iu} \end{aligned} \qquad (2\text{-}43)$$

Finally, the velocity gradient can be estimated by integrating over the computational volume as:

$$(\nabla \vec{u})_P = \frac{1}{\delta V_P} \cdot [(u_1 b_1^1 + u_2 b_2^1 + u_3 b_3^1)_e - (u_1 b_1^1 + u_2 b_2^1 + u_3 b_3^1)_w +$$

$$(u_1 b_1^2 + u_2 b_2^2 + u_3 b_3^2)_n - (u_1 b_1^2 + u_2 b_2^2 + u_3 b_3^2)_s + \qquad (2\text{-}44)$$

$$(u_1 b_1^3 + u_2 b_2^3 + u_3 b_3^3)_d - (u_1 b_1^3 + u_2 b_2^3 + u_3 b_3^3)_u]$$

2.2.4 Differentiation schemes

In the discretised form of the conservation equations the independent variables have to be estimated on the cell faces of the computational volumes. These values should be estimated as a function of their actual values calculated on the centre of the computational cell. In this way algebraic equations will appear which will correlate the values of the flow properties of neigbouring cells. To obtain this task a differentiation scheme has to be used; its selection is of major importance since it affects stability during the numerical solution and its accuracy. The differentiation scheme should also satisfy a few additional criteria:

a. in the absence of internal sources, the value of any tranported quantity φ resulting from the solution should be bounded from the values of this quantity at the boundaries of the computational domain.

b. in case there is a constant source of any variable φ in a flow field with uniform velocity and diffusivity, the shape of the iso-φ contours would be infuenced by the ratio of convection to diffusion (which is defined as the Peclet number). Failure of the descritised equation to satisfy this criterion will result to numerical diffusion and unrealistic results.

c. all internal fluxes should cancel in pairs on the cell fases; that will quarantee the overall (integral) conservation of any conservation quantities in the computational domain.

Up to now there are many different diferentiation schemes reported in the literature and details about them can be found in any textbook of computational fluid mechanics. In the present investigation the hybric scheme has been used which reduces to the central differentiation scheme at low Peclet numbers and behaves as a first order upwind differentiation scheme at high Peclet numbers. It is defined as:

$$\varphi_e = \begin{cases} \varphi_P & \text{, if } \quad Pe_e > \dfrac{1}{1-f_{lP}} \\ f_{lP}\varphi_P + (1-f_{lP})\varphi_E & \text{, if } -\dfrac{1}{f_{lP}} \le Pe_e \le \dfrac{1}{1-f_{lP}} \\ \varphi_E & \text{, if } -\dfrac{1}{f_{lP}} > Pe_e \end{cases} \qquad (2\text{-}45)$$

where φ_e is the value of the variable φ at point 'e' which lies between points 'E' and 'P' and the coefficient f is calculated on the basis of the geometrical distances between the three points, for example as $f_{lP} = \frac{\overline{Ee}}{\overline{Ee} + \overline{Pe}}$. The local Peclet number is thus defined as:

$$Pe_e = \frac{C_e}{I_e^{DN}} \tag{2-46}$$

where C_e is the convection term from volume P to volume E through surface 'e' and I_e^{DN} is the normal diffusion on the 'e' surface (as defined in equation (2-39)). This scheme is simple for implementation into numerical codes and although it may introduce numerical diffusion at high Peclet numbers, its overall accuracy justifies its use in the present study.

Following this differentiation scheme for the convection terms, the contribution of node E to node P can be estimated as:

$$A_E^C = \begin{cases} 0 & ,\text{if} \quad Pe_e > \dfrac{1}{1-f_{lP}} \\ (f_{lP}-1)C_e & ,\text{if} -\dfrac{1}{f_{lP}} \le Pe_e \le \dfrac{1}{1-f_{lP}} \\ 0 & ,\text{if} -\dfrac{1}{f_{lP}} > Pe_e \end{cases} \tag{2-47}$$

where C_e can be calculated as:

$$C_e = \rho_e\left(\left(u_1 - u_{g1}\right)b_1^l + \left(u_2 - u_{g2}\right)b_2^l + \left(u_3 - u_{g3}\right)b_3^l\right)_e \tag{2-48}$$

If for node Pthe contibution from all neigbouring cells in taken into account, then it can be found that:

$$C_e\varphi_e - C_w\varphi_w + C_n\varphi_n - C_s\varphi_s + C_d\varphi_d - C_u\varphi_u = A_P^C\varphi_P - \sum_n A_n^C\varphi_n \tag{2-49}$$

$$A_P^C = \sum_n A_n^C - S_m \quad , \quad S_m = C_e - C_w + C_n - C_s + C_d - C_u \quad , \quad n = E, W, N, S, D, U$$

We can now proceed to the discretisation in the diffusion terms. The term in equation (2-39) expressing normal diffution can be written as a function of the values of φ at the neigbouring nodes as:

$$I_e^{DN} = -\left(\frac{\Gamma_{\varphi,eff}}{\delta V}\right)_e \cdot \left(b_1^{12} + b_2^{12} + b_3^{12}\right) \cdot \left(\varphi_E - \varphi_P\right) \tag{2-50}$$

The contribution of node E to node P has the form:

$$A_E^{DN} = \left(\frac{\Gamma_{\varphi,eff}}{\delta V}\right)_e \cdot \left(b_1^{12} + b_2^{12} + b_3^{12}\right) \tag{2-51}$$

$$A_P^{DN} = \sum_n A_n^{DN} \quad , \quad n = E, W, N, S, D, U$$

and again the following correlation can be estimated similar to that of the convection terms:

$$I_e^{DN} - I_w^{DN} + I_n^{DN} - I_s^{DN} + I_d^{DN} - I_u^{DN} = A_P^{DN}\varphi_P - \sum_n A_n^{DN}\varphi_n \tag{2-52}$$

$$A_P^{DN} = \sum_n A_n^{DN} \quad , \quad n = E, W, N, S, D, U$$

The discretisation of the cross-derivative diffution terms of equation (2-39) is obtained through the following correlations:

$$I_e^{DC} - I_w^{DC} + I_n^{DC} - I_s^{DC} + I_d^{DC} - I_u^{DC} = A_P^{DC}\varphi_P - \sum_n A_n^{DC}\varphi_n \tag{2-53}$$

$$A_P^{DC} = \sum_n A_n^{DC} \ , \ n = E, W, N, S, D, U, DE, DW, DN, DS, UE, UW, UN, US, NE, NW, SE, SW$$

The final algebraic equation for node P has the form:

$$A_P\varphi_P = \sum_n \left(A_n^C + A_n^{DN}\right)\varphi_n + S_{\varphi u} + S_{\varphi p}\varphi_P + \sum_k I_k^{DC} + S_{\varphi press}$$

$$A_P = \sum_n \left(A_n^C + A_n^{DN}\right) + S_m \qquad s_\varphi \cdot \delta V_P = S_{\varphi u} + S_{\varphi p} \cdot \varphi_P \tag{2-54}$$

$S_m = C_e - C_w + C_n - C_s + C_d - C_u$, n = E, W, N, S, D, U , k = e, w, n, s, d, u

Using the described discretisation procedure, the differential conservation equations of any variable φ are transformed to a system of N algebraic equations, where N is equal to the number of the computational cells. In this system also appear N unkown variables (the values of φ at every computational cell) which allows this system of equations to be numerically solved. In the present investigation the TDMA method has been used; details can be found in any textbook of numerical analysis, for example see Pres et al. (1989).

For the safe convergence of the solution procedure, it is necessary to introduce underelaxation factors. These can be achieved by modifing the coefficients of equations (2-54) as:

$$A_P \rightarrow \frac{A_P}{U_{rf}} \qquad S_{\varphi u} \rightarrow S_{\varphi u} + \left(1 - U_{rf}\right) \cdot A_P \varphi_P^{old} \tag{2-55}$$

where U_{rf} is the underelaxation factor and the superscript 'old' denotes values of the variable φ as calculated in the previous iteration.

For the unsteady case, equation (2-40) can be discretised in the following form:

$$\frac{\rho\varphi \cdot \delta V - \left(\rho\varphi \cdot \delta V\right)^{old}}{\delta t} = \frac{\rho \cdot \delta V}{\delta t} \cdot \varphi - \frac{\left(\rho\varphi \cdot \delta V\right)^{old}}{\delta t} = S_{pt} \cdot \varphi + S_{ut}$$

$$S_{pt} = \frac{\rho \cdot \delta V}{\delta t} \qquad S_{ut} = -\frac{\left(\rho\varphi \cdot \delta V\right)^{old}}{\delta t} \tag{2-56}$$

where the terms S_{pt} and S_{ut} are added to the terms $S_{\varphi p}$ and $S_{\varphi u}$ of equation (2-54), respectively.

2.2.5 Pressure correction

During the iterative solution procedure, the values of the velocity components are initially estimated on the basis of an assumed (or estimated from the previous

iteration) pressure field. The pressure field is continuously updated in such a way that the mass conservation equation is satisfied at every computational cell. The stability of this iterative solution procedure relies, to a large extent, on the strong coupling between the velocity components and pressure gradients. This requirement has given rise to the widely used staggered arrangement of pressure and velocity. However, it is more attractive to use a collocated arrangement where all variables (pressure, velocity and any scalar) are calculated at the center of the numerical cells. In order to use this type of grid arrangement and at the same time to avoid pressure-velocity decoupling problems, an interpolation method initially proposed by Rhie and Chow (1982) is used which is extended to the 3-D problem in curvilinear non-orthogonal coordinate systems. The algebraic equation for the 'i' velocity component at node P is discretized as a function of pressure in the following way:

$$A_{iP}u_{iP} = \sum_n A_{in}u_{in} + S_i - \left(b^1_{iP}\cdot\left(p_e - p_w\right) + b^2_{iP}\cdot\left(p_n - p_s\right) + b^3_{iP}\cdot\left(p_d - p_u\right)\right) \Rightarrow$$
$$u_{iP} = \frac{H_{iP}}{A_{iP}} - \frac{1}{A_{iP}}\cdot\left(b^1_{iP}\cdot\left(p_e - p_w\right) + b^2_{iP}\cdot\left(p_n - p_s\right) + b^3_{iP}\cdot\left(p_d - p_u\right)\right) \tag{2-57}$$

where

$$H_{iP} = \sum_n A_{in}u_{in} + S_i \tag{2-58}$$

The key feature of this approximation is that the velocity used for the calculation of the corresponding convective flux term at the east 'e', for example, cell face is not estimated by linear interpolation but it is modified to be directly linked to the two adjacent pressure nodes (p_P and p_E for this cell face). Thus, the convection term on the 'e' cell face can be calculated from equations (2-39) and (2-57) as:

$$C_e = \rho_e\left(\left(u_1 - u_{g1}\right)b^1_1 + \left(u_2 - u_{g2}\right)b^1_2 + \left(u_3 - u_{g3}\right)b^1_3\right)_e =$$
$$\rho_e\left(\left(u_{1e} - u_{g1e}\right)b^1_{1e} + \left(u_{2e} - u_{g2e}\right)b^1_{2e} + \left(u_{3e} - u_{g3e}\right)b^1_{3e}\right) \tag{2-59}$$

$$u_{1e} = \left\{\left(u_{1P} + \frac{b^1_{1P}}{A_{1P}}(p_e - p_w)\right) + (1-f_{1P})\cdot\left[\left(u_{1E} + \frac{b^1_{1E}}{A_{1E}}(p_{Ee} - p_e)\right) - \left(u_{1P} + \frac{b^1_{1P}}{A_{1P}}(p_e - p_w)\right)\right]\right\} - \left[\frac{b^1_{1P}}{A_{1P}} + (1-f_{1P})\cdot\left(\frac{b^1_{1E}}{A_{1E}} - \frac{b^1_{1P}}{A_{1P}}\right)\right]\cdot(p_E - p_P)$$

$$u_{2e} = \left\{\left(u_{2P} + \frac{b^1_{2P}}{A_{2P}}(p_e - p_w)\right) + (1-f_{1P})\cdot\left[\left(u_{2E} + \frac{b^1_{2E}}{A_{2E}}(p_{Ee} - p_e)\right) - \left(u_{2P} + \frac{b^1_{2P}}{A_{2P}}(p_e - p_w)\right)\right]\right\} - \left[\frac{b^1_{2P}}{A_{2P}} + (1-f_{1P})\cdot\left(\frac{b^1_{2E}}{A_{2E}} - \frac{b^1_{2P}}{A_{2P}}\right)\right]\cdot(p_E - p_P)$$

$$u_{3e} = \left\{\left(u_{3P} + \frac{b^1_{3P}}{A_{3P}}(p_e - p_w)\right) + (1-f_{1P})\cdot\left[\left(u_{3E} + \frac{b^1_{3E}}{A_{3E}}(p_{Ee} - p_e)\right) - \left(u_{3P} + \frac{b^1_{3P}}{A_{3P}}(p_e - p_w)\right)\right]\right\} - \left[\frac{b^1_{3P}}{A_{3P}} + (1-f_{1P})\cdot\left(\frac{b^1_{3E}}{A_{3E}} - \frac{b^1_{3P}}{A_{3P}}\right)\right]\cdot(p_E - p_P)$$

Using this interpolation method, the correction of the convective term due to the pressure correction can be written as:

$$C'_e = \rho_e\left(u'_1 b^1_1 + u'_2 b^1_2 + u'_3 b^1_3\right)_e = \rho_e\left(u'_{1e} b^1_{1e} + u'_{2e} b^1_{2e} + u'_{3e} b^1_{3e}\right)$$

$$u'_{1e} = -\left[\frac{b^1_{1P}}{A_{1P}} + (1-f_{1P})\cdot\left(\frac{b^1_{1E}}{A_{1E}} - \frac{b^1_{1P}}{A_{1P}}\right)\right]\cdot(p'_E - p'_P)$$

$$u'_{2e} = -\left[\frac{b^1_{2P}}{A_{2P}} + (1-f_{1P})\cdot\left(\frac{b^1_{2E}}{A_{2E}} - \frac{b^1_{2P}}{A_{2P}}\right)\right]\cdot(p'_E - p'_P) \qquad (2\text{-}60)$$

$$u'_{3e} = -\left[\frac{b^1_{3P}}{A_{3P}} + (1-f_{1P})\cdot\left(\frac{b^1_{3E}}{A_{3E}} - \frac{b^1_{3P}}{A_{3P}}\right)\right]\cdot(p'_E - p'_P)$$

The mass conservation equation can be written in the following algebraic form to account for the pressure correction as:

$$A_P p'_P = \sum_n A_n p'_n + S_{mass} - (C_e - C_w + C_n - C_s + C_d - C_u)$$

(2-61)

$$A_P = \sum_n A_n \quad , \quad n = E, W, N, S, D, U$$

where , for example, the contribution of node E as results from the above equations (2-60) takes the following form:

$$A_E = \rho_e \cdot \left\{ b^1_{1e} \cdot \left[\frac{b^1_{1P}}{A_{1P}} + (1-f_{1P})\cdot\left(\frac{b^1_{1E}}{A_{1E}} - \frac{b^1_{1P}}{A_{1P}}\right)\right] + \right.$$

$$\left. b^1_{2e} \cdot \left[\frac{b^1_{2P}}{A_{2P}} + (1-f_{1P})\cdot\left(\frac{b^1_{2E}}{A_{2E}} - \frac{b^1_{2P}}{A_{2P}}\right)\right] + b^1_{3e} \cdot \left[\frac{b^1_{3P}}{A_{3P}} + (1-f_{1P})\cdot\left(\frac{b^1_{3E}}{A_{3E}} - \frac{b^1_{3P}}{A_{3P}}\right)\right]\right\}$$

(2-62)

The solution procedure, which resembles the well known SIMPLE method, can be summarised as follows:

1. a pressure field is initially assumed
2. the momentum equations are solved using this pressure field in order to obtain the three velocity components; these do not necessarily satisfy the mass conservation equation.
3. the residual mass is calculated at every computational cell where the pressure correction equation is solved
4. the pressure field is updated and the velocity components as well as the convection terms are corrected in such a way as to satisfy to a better degree the mass conservation equation.
5. the remaining scalar variables (temperature, turbulence, consentration e.t.c) of the flow field are estimated
6. steps 2 to 5 are repeated until the method converges

Before proceeding to the next iteration, the pressure field is updated by adding the calculated pressure correction to the pressure of each cell using the following relationship:

$$p = p_{old} + U_{rfp} \cdot \left(p' - p'_{ref}\right) \tag{2-63}$$

where again the use of the underelaxation factor is necessary. It should be mentioned that the pressure estimated from this numerical procedure is the relative pressure and not the absolute one.

The convection terms through each cell face are corrected according to:

$$C_n = C_n^{old} + C'_n \tag{2-64}$$

while the velocities are corrected according to:

$$\begin{aligned} u_i &= u_i^{old} + u'_i \\ u'_{iP} &= -\frac{1}{A_{iP}}\left(b^1_{iP} \cdot \left(p'_e - p'_w\right) + b^2_{iP} \cdot \left(p'_n - p'_s\right) + b^3_{iP} \cdot \left(p'_d - p'_u\right)\right) \end{aligned} \tag{2-65}$$

It should also be mentioned that in order to avoid any dependency of the underelaxation factors a method initially proposed by Miller and Majumdar (1988) has been used. Thus, here the final expresion for the convection term is presented, ie.

$$\begin{aligned} C_e = {} & \rho_e\left(\left(u_{1e} - u_{g1e}\right)b^1_{1e} + \left(u_{2e} - u_{g2e}\right)b^1_{2e} + \left(u_{3e} - u_{g3e}\right)b^1_{3e}\right) \\ & + \left(1 - U_{rf}\right) \cdot \left(C^*_e - C''_e\right) \end{aligned} \tag{2-66}$$

$$\begin{aligned} u_{ie} = {} & \left\{\left(u_{iP} + \frac{b^1_{iP}}{A_{iP}}\left(p_e - p_w\right)\right) + \right. \\ & \left. \left(1 - f_{1P}\right) \cdot \left[\left(u_{iE} + \frac{b^1_{iE}}{A_{iE}}\left(p_{Ee} - p_e\right)\right) - \left(u_{iP} + \frac{b^1_{iP}}{A_{iP}}\left(p_e - p_w\right)\right)\right]\right\} - \\ & \left[\frac{b^1_{iP}}{A_{iP}} + \left(1 - f_{1P}\right) \cdot \left(\frac{b^1_{iE}}{A_{iE}} - \frac{b^1_{i1P}}{A_{i1P}}\right)\right] \cdot \left(p_E - p_P\right) \end{aligned} \tag{2-67}$$

$$C''_e = \rho_e\left(\left(u''_{1e} - u_{g1e}\right)b^1_{1e} + \left(u''_{2e} - u_{g2e}\right)b^1_{2e} + \left(u''_{3e} - u_{g3e}\right)b^1_{3e}\right) \tag{2-68}$$

$$u''_{ie} = u''_{iP} + \left(1 - f_{1P}\right)\cdot\left(u''_{iE} - u''_{iP}\right) \tag{2-69}$$

2.2.6 Boundary and initial conditions

In this section the appropriate modifications required for the calculation of the flow at the boundary cells are described. These modifications are introduced in order to be able to estimate the wall friction without using an enormous large number of cells close to the boundaries and are usually called wall functions (Launder and Spalding (1974)).

The wall friction vector from the wall to the moving fluid can be expressed as a function of the parallel to the wall relative velocity component at the adjascent to the wall cells as:

$$\vec{\tau}_w = -\lambda_w \cdot \vec{u}_{pr} \tag{2-70}$$

where u_{pr} is the relative velocity component parallel to the wall and λ_W the friction coefficient which can be estimated as:

$$\lambda_w = \frac{\mu_l}{\delta n} \qquad \text{if} \quad y_P^+ < 11.6 \quad \text{(laminar boundary sublayer)} \tag{2-71}$$

$$\lambda_w = \frac{\rho \cdot C_\mu^{1/4} \cdot k_P^{1/2} \cdot \kappa}{\ln\left(E \cdot y_P^+\right)} \qquad \text{if} \quad y_P^+ \geq 11.6 \quad \text{(turbulent boundary layer)} \tag{2-72}$$

where the dimensionless length y^+_p is defined as:

$$y_P^+ = \frac{\rho \cdot C_\mu^{1/4} \cdot k_P^{1/2} \cdot \delta n}{\mu_l} \tag{2-73}$$

where δn is the distance between the wall and the centre of the computational cell (P), κ=0.4187 is the von-Karman constant and E is a constant whose value depends on the wall roughness (it is usually set equal to 9.7 for smooth walls). The friction force between the wall and the moving fluid is:

$$\vec{T}_w = \vec{\tau}_w \cdot A_w = -\lambda_w \cdot \vec{u}_{pr} \cdot A_w \tag{2-74}$$

where A_w is the area of the cell in contact with the rigid wall. The three Cartesian components of this vector can be geometrically estimated for every cell face in contact with the wall as:

$$\begin{aligned} T_{W1} &= -\lambda_w A_w \cdot \left[\left(1-n_1^2\right)\cdot u_{pr1} - n_1 n_2 \cdot u_{pr2} - n_1 n_3 \cdot u_{pr3}\right] \\ T_{W2} &= -\lambda_w A_w \cdot \left[-n_1 n_2 \cdot u_{pr1} + \left(1-n_2^2\right)\cdot u_{pr2} - n_2 n_3 \cdot u_{pr3}\right] \\ T_{W3} &= -\lambda_w A_w \cdot \left[-n_1 n_3 \cdot u_{pr1} - n_2 n_3 \cdot u_{pr2} + \left(1-n_3^2\right)\cdot u_{pr3}\right] \end{aligned} \tag{2-75}$$

where (n_1, n_2, n_3) are the three components in the Cartesian coordinate system of the normal to the wall unit vector. Thus, in the momentum equation the shear stresses terms for the cell face in contact with the wall are replaced with the above friction force. This term is incorporated as a source term in equation (2-54).

In addition to the momentum equation, the k-ε equations have to be modified. According to Launder and Spalding (1974) there is an equilibrium between production and dissipation of the turbulent kinetic energy within the turbulent boundary layer, from which the following correlations can be estimated for ε:

$$\begin{aligned} \varepsilon &= \frac{C_\mu^{3/4}\cdot k^{3/2}}{\kappa y_n} && \text{(laminar boundary sublayer)} \\ \varepsilon &= \frac{C_\mu^{3/4}\cdot k^{3/2}}{\kappa y_n}\cdot\left(1+\ln\left(\frac{y_n}{y_v}\right)\right) && \text{(turbulent boundary layer)} \end{aligned} \tag{2-76}$$

where $y_n=\delta n$, y_v is the thickness of the laminar boundary sublayer which can be estimated by solving equation (2-73) for δn setting $y_P^+ = 11.63$. The transport equation of ε does not have to be calculated for the boundary cells since its value for these cells can be calculated directly by setting the source terms of equations (2-54) equal to:

$$S_{cu} = L \cdot \frac{C_\mu^{3/4} \cdot k_P^{3/2}}{\kappa y_n} \cdot \left(1 + \max\left\{0, \ln\left(\frac{y_n}{y_v}\right)\right\}\right) \qquad S_{cp} = -L \tag{2-77}$$

where in this correlation k_p is the value of the turbulent kinetic energy of the boundary cell and $L=10^{30}$.

The source term for the equation of the turbulent kinetic energy for the boundary cells has the form:

$$S_k = s_k \cdot \delta V = \int_{\delta V} (G - \rho\varepsilon) \cdot \delta V = G \cdot \delta V_P - \int_{\delta V} \rho\varepsilon \cdot \delta V \tag{2-78}$$

$$\int_{\delta V} \rho\varepsilon \cdot \delta V \approx \frac{\rho \cdot C_\mu^{3/4} \cdot k_P^{1/2} \cdot u_P^+}{y_P} \cdot \delta V_P$$

$$u_P^+ = \begin{cases} y_P^+ & \text{if} \quad y_P^+ \le 11.6 \\ \dfrac{1}{\kappa} \cdot \ln(E \cdot y_P^+) & \text{if} \quad y_P^+ > 11.6 \end{cases} \tag{2-79}$$

The rate of production of turbulent kinetic energy can be estimated if the wall friction forces as given from equations (2-70) and (2-75) replace the shear stresses in equations (2-16) and (2-42):

$$\begin{aligned} G_P = (\frac{\mu_t}{\delta V^2})_P \{ & 2[(\delta u_1)^1 b_1^1 + (\delta u_1)^2 b_1^2 + (\delta u_1)^3 b_1^3]^2 + \\ & 2[(\delta u_2)^1 b_2^1 + (\delta u_2)^2 b_2^2 + (\delta u_2)^3 b_2^3]^2 + \\ & 2[(\delta u_3)^1 b_3^1 + (\delta u_3)^2 b_3^2 + (\delta u_3)^3 b_3^3]^2 + \\ & \frac{\tau_w^2}{\mu_\tau} [\frac{2}{3} (\nabla \vec{u}) \cdot (\rho \cdot k + \mu_t \nabla \vec{u})]_P \end{aligned} \tag{2-80}$$

Similar wall functions can be estimated for the other scalar quantities (such as temperature). The diffusion flux through a cell face on a wall is estimated as:

$$I_W^D = \begin{cases} \dfrac{\mu}{\sigma_\varphi}(\varphi_w - \varphi_P)\dfrac{A_w}{\delta n} & \text{if} \quad y_P^+ \le 11.6 \\ \dfrac{\rho \cdot C_\mu^{1/4} \cdot k_P^{1/2} \cdot c_P \cdot (\varphi_W - \varphi_P) \cdot A_W}{\varphi_P^+} & \text{if} \quad y_P^+ > 11.6 \end{cases} \tag{2-81}$$

where:

$$\varphi_P^+ = \sigma_{\varphi t} \cdot \left[u_P^+ + P\left(\frac{\sigma_{\varphi l}}{\sigma_{\varphi t}}\right)\right] \tag{2-82}$$

In the above correlations, $\sigma_{\varphi l}$ and $\sigma_{\varphi t}$ are the molecular and turbulent Prandl numbers, respectively, c_p is a constant (in the case of temperature is the specific heat under constant pressure) and P is an empirical constant which is calculated as a function of the values $\sigma_{\varphi l}$ and $\sigma_{\varphi t}$. For the case of temperature, it is given from the correlation:

$$P = 9.24 \cdot \left[\left(\frac{\sigma_{Tl}}{\sigma_{Tt}}\right)^{3/4} - 1\right] \cdot \left(1 + 0.28 \cdot e^{-0.007 \cdot \frac{\sigma_{Tl}}{\sigma_{Tt}}}\right) \tag{2-83}$$

where $\sigma_{Tl} = 0.728$, $\sigma_{Tt} = 1.0$ for air.

In the pressure correction equation, the first derivative is set equal to zero for the adjascent to the wall cells.

At the inlet boundaries of the computational domain, all variables should be known. Usually, the turbulence kinetic energy is assumed to be 5% of the total kinetic energy of the fluid while its dissipation rate is assumed to be proportional to:

$$\varepsilon \propto \frac{k^{3/2}}{l} \tag{2-84}$$

where l is the length scale of turbulence which can be estimated from the geometrical characteristics of the simulated geometry.

At the outlet boundaries the second derivative of all variables is set equal to zero in the normal to the exit boundary direction. This type of boundary conditions is meaningful only for fully developed flows.

2.3 Modeling of Diesel Fuel Injection Systems

2.3.1 Introduction - literature review

In this section a general description of diesel fuel injection systems is given, together with a literature review on previous simulation works in this field.

The fuel injection system of a diesel engine has to perform several functions: meter the quantity of fuel injected, accurately time the injection and mix the fuel with the air in the combustion chamber in the shortest possible time. The correct quantity of fuel must be injected to generate the required engine power and torque. The injection timing affects performance, smoke levels, noise and exhaust emissions. In addition, the fuel has to be atomized in order to vaporize and mix with the air in the combustion chamber. The function of the injection nozzle is to produce a finely atomized spray of fuel droplets that will mix readily with the air and ensure complete combustion in the time available. The nozzle outlet is controlled by a needle valve held against its seat by a mechanical or electronic mechanism, which determines the fuel pressure needed to lift the valve off its seat in order to initiate fuel injection.

The level of emissions in diesel engines is strongly affected by the fuel injection system characteristics. The NOx, particulate and unburned hydrocarbons usually found in the exhaust system of diesel engines depend on the performance of the fuel injection system i.e. on the shape of the fuel injection rate and on the injection timing. It is known that burning during combustion in a typical DI diesel engine has three distinguishable stages (Heywood (1988)): (i) premixed or rapid combustion phase (ii) mixing-controlled combustion phase and (iii) late combustion phase. These burning modes are preceded by an ignition delay period which is the time between the start of fuel injection into the combustion chamber and the start of combustion. During the premixed phase the fuel injected during the ignition delay period, which has mixed with air to within the flammability limits, burns rapidly in a few degrees of crank angle. There is a peak in the heat-release rate during this phase associated with the NOx levels. In the mixing-controlled combustion phase the burning rate is determined by the rate at which the mixture becomes available for burning and, as a result, it is mainly controlled by the fuel-air mixing process. The final or late combustion phase continues well into the expansion stroke due to unburned fuel, soot or fuel rich products in the combustion

chamber. The heat release rate is low during this phase and NOx is mainly formed in the high temperature burned gas regions. Soot is formed in the rich core of fuel sprays within the flame region and it then oxidizes when soot particles come in contact with oxygen and/or OH. Unburned hydrocarbons originate in regions where the flame quenches. The start of combustion is primarily determined by the start of injection. Retarded injection, for example, reduces emissions of oxides of nitrogen while over-retarded injection increases the emissions of hydrocarbons and particulates. Deviation of the start of injection from the nominal value by one degree of crank angle can increase the emissions of NOx or HC by approximately 15%. This high sensitivity implies that the start of injection must be precisely determined. Fuel injected into the combustion chamber after the main combustion phase may reach the exhaust system unburned and thus increase the hydrocarbon and particulate emissions. Increasing the injection rate increases NOx emissions but decreases particulate emissions.

There are many FIE systems which can perform the tasks of the fuel injection system, manufactured by a number of different companies (Bosch, Lucas, Stanadyne, Zexel and Nippodenso), and are based on distributor type pumps, in-line pumps, electronic pumps, e.t.c. Lately, high pressure common rail systems are under development by the industry incorporating different nozzle configurations. The pintle-type injector, the hole-type injector, high- and low-spring injectors, two-stage injection nozzles, the Stanadyne Pencil-type injector, unit injectors are examples of frequently used FIE. However, it is not the scope of the present investigation to describe in detail all the operating characteristics of the above injection systems. They all need a mechanical system (pump) to pressurize the fuel, usually through a cam-pumping mechanism. Then, depending on the type of the specific pump, the pressurized fuel is transferred to the injection nozzles through the high pressure pipes. The opening of the needle in the nozzles is determined either by a mechanical or by an electronic system. In paragraph (2.3.2) a method for computational 'reconstruction' of any FIE is proposed through the connection of a number of fluid elements.

The importance of fuel injection simulation in the development of fuel injection equipment and the improved understanding of combustion and pollutant formation has been recognized for some time and several computer models have already been developed. A computer simulation can be used to improve existing FIE systems as well as analyzing the injection characteristics of new innovative systems. Fuel injection

models can be used to examine variables not easily obtained by experimentation and to quantify the effect of new emerging parameters such as increasing injection pressures. They can also be used to expand the scope of existing diesel engine performance simulation codes and multi-dimensional computer models of diesel spray development, combustion and exhaust emissions.

To simulate a fuel injection system, the pressures and flow rates throughout the system must be calculated and the wave propagation between the pump and the nozzle must be adequately simulated. Thus, the core of any computer simulation involves solving the equations governing the fluid flow in pipes and the dynamics of the mechanical components. Validation of the developed models is usually performed on the basis of comparison between the line pressures, the needle lift, the fuel injection rate and the total fuel injection quantity.

Until now a number of publications have been reported, simulating various fuel injection systems. Becchi (1971) modeled a Fiat fuel injection system with accumulator, using an acoustic approximation. Wylie et al. (1975) modeled an American Bosch in-line pump with hole type nozzles using the method of characteristics and a Hamming's modified predictor-corrector method. Henein et. al (1975) modeled an N-50 Unit injector mounted on a 2 stroke Detroit Diesel Allison Division 2-53 engine using a 4th order Runge-Kutta method. Matsuoka et al. (1976) modeled a Bosch in-line pump with pintle nozzle, throttle nozzle and a hole-type nozzle using a finite difference scheme. Goyal (1978) modeled a Roosa Master distributor pump, in-line pump and Universal fuel injection system with hole-type nozzle using the method of characteristics and a 4th order Runge-Kutta method. Wannenwetsch and Egler (1985) modeled a Bosch in-line pump with hole-type nozzles using the method of characteristics and an implicit finite difference scheme. Marcic and Kovacic (1985) modeled a Friedmann & Maier company standard in-line pump and a hole-type nozzle using the Allevi theory of pressure wave propagation. Scullen and Hames (1978) modeled a GM Unit Injector, Gibson (1986) modeled a Caterpillar's 3115 engine pump-pipe-nozzle system using the method of characteristics and Lee (1993) and Russell and Lee (1996) modeled a Lucas pump connected to various devises such as single- and two-stage injection nozzles and pilot injection using a finite difference scheme and a model accounting for condensation in order to accurately model non-linear effects and cavitation. Many other studies have been reported both on the testing and modeling of fuel injection systems, for example

Bosch (1966), Adey et al. (1981), Yoniyama et al. (1981), Suzuki et al. (1982), Gavanagh (1984), Schweimer et al. (1987), Soteriou (1990), Bower et al. (1990, 1991), Smith et al. (1992), Spark et al. (1992), Bruni et al. (1993), Fairbrother (1994), Arcoumanis et al. (1992, 1993, 1995, 1996, 1997), Ishimata et al. (1994), Minami et.al. (1994, 1995), Miura et al. (1995), Keql (1995), Ofner et al. (1996), Chen et al. (1996), Potz et al. (1996) and others. It is thus clear from the above that although a number of different injection systems have been modeled, the methods of solution of the employed equations are similar. In the following section, details of the model developed during the present investigation are presented.

2.3.2 Model description

The developed model simulates the flow in hydraulic systems. It is one-dimensional (the flow direction coincides with the mean pressure variation along the fuel injection system) since in most FIE systems the length of the pipes is much longer than their diameter. This model is based on the mass and momentum conservation equations for the calculation of the flow in pipes, on the equilibrium of forces for the calculation of the displacement of the valves and on the mass conservation for the calculation of the pressure at the volumes of the system. The model has been developed in such a way that any combination of the simulated basic fluid elements can be selected. Appropriate boundary conditions at the connection points make this model easily applicable to any fuel injection system. For the simulation of the flow in fuel injection systems it is assumed that they consist of pipes, valves which are forced to move due to the fluid pressure acting upon them and volumes where no major flow direction is calculated inside them but only their mean pressure. Also, slots, ports, cam plates as well as chambers of given pressure (with the same liquid as the one flowing in the fuel injection system or with pressurized gas) are used for the simulation of the flow. Usually, a cam lift is the initial condition required for the generation of the fluid flow in the fuel injection system or if this information is not available, a measured line pressure can also be used. The flow passage areas of the slots, spill ports and valves are further geometrical characteristics required for the simulation. In addition, various flow phenomena such as cavitation, variable discharge coefficients, pressure losses (due to friction forces, pipe bending, kinetic energy losses at the pipe connections and filters

present in the system), variable fuel properties (depending on the pressure and temperature of the injected fuel), pipe wall flexibility and leakage are modeled. The elements assumed to comprise any fuel injection system are the following: (i) *Cam plate profile* (the cam lift as a function of the cam angle is usually used to generate the flow motion in the fuel injection system; details about cam designs are given by Chen (1982)), (ii) *Pressure profile* (used as input if no other information for pressure generation mechanism is available; usually it is the measured pressure signal at a point in the high pressure connecting pipe), (iii) *Pipe* (it is assumed to be a circular (or annular) cross section element with length much longer than its diameter. The flow in these elements is assumed to be one-dimensional and is calculated using the conservation of mass and momentum (Wallis (1969), Tullis (1989) and Betamio et al. (1992)), (iv) *Valve,* both single- and two-stage (any mechanical mass-spring-damp system whose displacement is calculated from the equilibrium of forces acting upon it), (v) *Volume* (a uniform pressure chamber where no special flow direction is considered but only the average pressure resulting from the mass balance equation), (vi) *Chamber* (the pressure profile of a pressurized gas (the only possible flow direction is from the fuel injection system to the chamber); the injection chamber or the engine cylinder are treated as 'chambers'), (vii) *Slots* (any flow passage where the open area is a geometric characteristic of the fuel injection system) (viii) *Spill ports* (any flow passage where the open area is a geometric characteristic of the system but depends on a calculated or input valve displacement or any other mechanical movement) and (ix) *Sac volume* (this is a specific area of specially machined geometry at the injector tip; the details of the flow in this area play an important role on the spray characteristics).

In the following paragraphs, the equations used for the simulation of the flow in the above elements are given in detail.

2.3.2.1 One-dimensional flow in pipes

Momentum equation in pipes:

$$\frac{\partial P}{\partial x}+\rho u\frac{\partial u}{\partial x}+\rho\frac{\partial u}{\partial t}+\frac{\rho f u|u|}{2D_{EFF}}=0 \qquad (2\text{-}85)$$

$$\begin{aligned} D_{EFF} &= D && \text{circular pipe} \\ D_{EFF} &= D_{ext} - D_{int} && \text{annular pipe} \end{aligned} \qquad (2\text{-}86)$$

where D is the diameter of the circular pipe, D_{ext} is the external diameter and D_{int} is the internal diameter of the annular pipe and f is the friction factor of the pipe. The value of f is a function of the Reynolds number and the roughness of the pipe and is given below. Also P is the pressure of the liquid in the pipe, u is the liquid velocity in the x-direction of the pipe length and t is the time.

Continuity equation:

$$\frac{\partial u}{\partial x} + \frac{1}{\rho \alpha^2} \frac{\partial P}{\partial t} = 0 \qquad (2\text{-}86)$$

where

$$\alpha = \sqrt{\rho\left(\frac{1}{K} + \frac{D(1-\mu^2)}{Ee}\right)}^{-1} \qquad (2\text{-}87)$$

is the speed of sound in the pipe as a function of the local density ρ, the compressibility of the liquid (bulk modules) which is defined as $K = \rho \frac{dP}{d\rho}$, the flexibility of the wall E, the diameter of the pipe D, the thickness of the wall e and the coefficient μ of the material of the pipe. For the numerical solution of the above mass and momentum conservation equations, the method of characteristics has been selected since its implementation is simple and the boundary conditions at the edges of each pipe can be easily modeled. If we let:

$$\frac{dx}{dt} = \frac{a^2}{\lambda} = \lambda \qquad (2\text{-}88)$$

the momentum equation can be written in the form:

$$\frac{A\lambda}{\rho a^2}\frac{\partial P}{\partial t}+\frac{\partial Q}{\partial t}+\frac{f}{2DA}Q|Q|=0 \tag{2-89}$$

The required conditions for λ is $\lambda = \pm a$ and the ordinary differential equation is valid in the independent variable space (x,t) only when the last equation is satisfied. This equation defines lines in the independent variable space (x,t) which are called characteristic lines. The line associated with $\lambda=+a$ is called the C-plus characteristic while that associated with $\lambda=-a$ is called the C-minus characteristic.

Along the C-plus characteristic defined by $\lambda=a$, we have

$$\frac{A\lambda}{\rho a^2}\frac{\partial p}{\partial t}+\frac{\partial Q}{\partial t}+\frac{f}{2DA}Q|Q|=0 \quad \text{and} \quad \frac{dx}{dt}=a \tag{2-90}$$

Along the C-minus characteristic defined by $\lambda=-a$, we have

$$-\frac{A\lambda}{\rho a^2}\frac{\partial P}{\partial t}+\frac{\partial Q}{\partial t}+\frac{f}{2DA}Q|Q|=0 \quad \text{and} \quad \frac{dx}{dt}=-a \tag{2-91}$$

These equations can be discretized into a finite-difference scheme if it is assumed that the relatively small frictional resistance term is constant over local regions in dx and dt. If we consider the independent variable space (x,t) associated with a length of pipe, we can consider discrete lengths along the pipe dx and discrete time steps dt. We can use the last two equations along with the C-plus characteristic lines and along the C-minus characteristic lines shown in the following Figure 2-2:

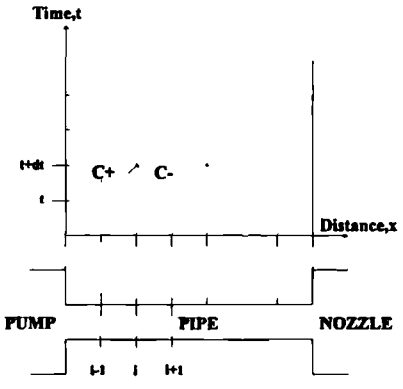

Figure 2-2 : Schematic representation of the method of characteristics

$$\text{along C - plus}: \; p_i(t+dt) = Cplus(t) - BQ_i(t+dt) \tag{2-92}$$

$$\text{where} \quad Cplus(t) = P_{i-1}(t) + BQ_{i-1}(t) - RQ_{i-1}(t)\left|Q_{i-1}(t)\right| \tag{2-93}$$

$$\text{along C - minus}: \; p_i(t+dt) = Cminus(t) + BQ_i(t+dt) \tag{2-94}$$

$$\text{where} \quad Cminus(t) = P_{i+1}(t) - BQ_{i+1}(t) + RQ_{i+1}(t)\left|Q_{i+1}(t)\right| \tag{2-95}$$

For numerical stability, $dx \geq a \cdot dt$ and $B = \dfrac{\rho \cdot \alpha}{A}$ and $R = \dfrac{f\,\rho\alpha}{2\,D\,A^2}\,dt$

Note that the Cplus and Cminus can be calculated from the boundary conditions at any time t. At any interior point *i*, the above equations can be solved simultaneously to obtain the pressure and flow at time t+dt. This yields:

$$P_i(t+dt) = \frac{Cplus(t) + Cminus(t)}{2}$$

$$Q_i(t+dt) = \frac{Cplus(t) - P_i(t+dt)}{B} \tag{2-96}$$

where the Cplus and Cminus depend only on the conditions existing at time *t*.

2.3.2.2 Valve movements

The equilibrium of forces acting on each valve is used for the calculation of its movement. This equation can be written in the form:

$$m_v \frac{d^2x}{dt^2} + c_v \frac{dx}{dt} + k_v x = F_{init} + \sum_{i}^{N_i} A_i P_i \tag{2-97}$$

where $x_{min} \leq x \leq x_{max}$

where k_v m_v and c_v are the effective spring rate, mass and damping coefficients of the valve, respectively, x is the valve lift, x_{max} and x_{min} are the minimum and maximum lifts due to the valve stops usually present, t is the time, F_{init} the initial force on the valve and A_i any area of the valve in the direction of its movement exposed to the pressure P_i.

2.3.2.3 Volumes

The continuity equation is used for the calculation of the pressure in any volume of the system. This equation can be written in the form:

$$\frac{dP(t)}{dt}\frac{V(t)}{K(P)} = \frac{dV(t)}{dt} + \sum (Q_{in}(t) - Q_{out}(t)) \qquad (2\text{-}98)$$

(usually $\frac{dV(t)}{dt} = A \cdot v(t)$) where P is the pressure of the volume, t is time, V stands for the volume, A is any area compressing or decompressing the fuel in the volume, Q is the flow rate (the subscript 'in' denotes fuel that flow into the volume while the subscript 'out' denotes fuel that flows out from the volume), v the velocity of area A and K the bulk module of the fuel.

2.3.2.4 Boundary conditions

In order to be able to select from the above basic fluid elements and connect them in the desired order, appropriate boundary conditions have to be introduced describing the pressures and flow rates at the connecting points. The most frequent boundary conditions that can be found in a typical fuel injection system (Tullis (1989), Betamio et.al. (1992)) are given below.

Volume or chamber at the first point of a pipe (Figure 2-3)

The pressure losses from the volume to the pipe can be written in the form:

$$\Delta P = \rho Q^2/(2A^2) + \varsigma\rho Q^2/(2A^2) = (1+\varsigma)\rho Q^2/(2A^2)$$

$$P_{pipe} = P_{ch} - \Delta P \tag{2-99}$$

where P_{ch} is the volume pressure, P_{pipe} is the pressure at the first point of the pipe, Q is the flow rate at the first point of the pipe, A is the area of the pipe and ζ is a discharge coefficient due to the geometry of the connection between the pipe and the volume. In this equation, the first term is due to the kinetic energy loss of the liquid flowing into the pipe.

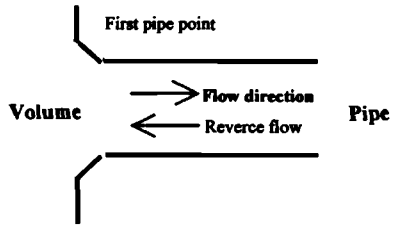

Figure 2-3 : Schematic representation of the boundary condition

Since $P_{pipe}=C_{mn}+B_{mn}Q$ where the C_{mn} and B_{mn} are calculated from the method of characteristics, combining these two equations, we obtain:

$$kQ^2 + B_{mn}Q - (P_{ch} - C_{mn}) = 0 \tag{2-100}$$

where $k = (1+\varsigma)\rho/(2A^2)$. From this equation, the flow rate at the first point of the pipe can be calculated as:

$$Q = \frac{-B_{mn} + \sqrt{B_{mn}^2 + 4k(P_{ch} - C_{mn})}}{2k} \tag{2-101}$$

and then the pressure can be calculated from equation (2-92). It should be mentioned that in the case of reverse flow, the pressure at the first point of the pipe is related to the volume pressure with the expression

$$P_{pipe} = P_{ch} + \rho Q^2/(2A^2) \tag{2-102}$$

(the term related to the pressure losses caused by the shape of the connection has been neglected here since in cases where fuel flows from a pipe to a chamber it is ζ=0). For that case, the flow rate is calculated from the correlation:

$$Q = \frac{B_{mn} - \sqrt{B_{mn}^2 - 4k(P_{ch} - C_{mn})}}{2k}, k = \rho/(2A^2) \qquad (2\text{-}103)$$

Volume or chamber at the last point of a pipe (Figure 2-4)

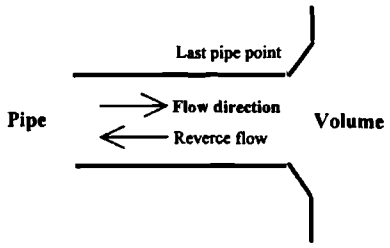

Figure 2-4 : Schematic representation of the boundary condition

The pressure losses are due to the kinetic energy losses of the liquid flowing into the volume and can be written in the form:

$$\Delta P = \rho Q^2/(2A^2) \ , \ P_{pipe} = P_{ch} + \Delta P \qquad (2\text{-}104)$$

Since $P_{pipe} = C_{pl} - B_{pl}Q$ where B_{pl} and C_{pl} are calculated from the method of characteristics, combining these two equations, we obtain:

$$kQ^2 + B_{pl}Q + (P_{ch} - C_{pl}) = 0 \ , \ k = \rho/(2A^2) \qquad (2\text{-}105)$$

from which the flow rate at the last point of the pipe can be calculated as:

$$Q = \frac{-B_{pl} + \sqrt{B_{pl}^2 - 4k(P_{ch} - C_{pl})}}{2k} \qquad (2\text{-}106)$$

and then the pressure P_{pipe} can be calculated from equation (2-105). In the case of reverse flow, the pressure losses become:

$$\Delta P = (1+\varsigma)\rho Q^2/(2A^2)\ ,\ P_{pipe} = P_{ch} - \Delta P \qquad (2\text{-}107)$$

and the flow rate is calculated from the expression:

$$Q = \frac{B_{pl} - \sqrt{B_{pl}^2 + 4k(P_{ch} - C_{pl})}}{2k} \qquad (2\text{-}108)$$

while the pressure at the last point of the pipe from equation (2-107).

Valve is located at the last point of a pipe (Figure 2-5)

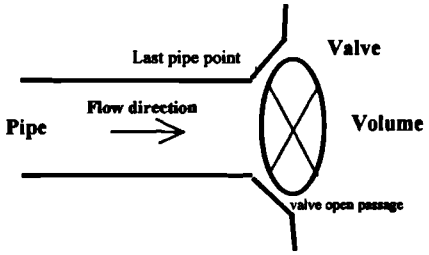

Figure 2-5 : Schematic representation of the boundary condition

In this case, the flow rate through the open passage of the valve can be calculated from the expression:

$$Q = C_d A_d \sqrt{2\frac{P - P_{ch}}{\rho}} \Rightarrow Q^2 = k(P - P_{ch})\ ,\ \ k = (C_d A_d)^2 2/\rho \qquad (2\text{-}109)$$

where P is the pressure at the last point of the pipe and P_{ch} is the pressure of the volume downstream of the valve, C_d is the discharge coefficient (function of the geometry of the open flow passage) and A_d is the cross sectional area of the open valve. Since $P = C_{pl} - B_{pl}Q$, from these two equations the flow rate through the valve passage can be calculated as:

$$Q = \frac{-B_{pl} + \sqrt{(kB_{pl})^2 - 4k(P_{ch} - C_{pl})}}{2} \qquad (2\text{-}110)$$

and then, the pressure is calculated from equation (2-109).

Valve at an interim point of a pipe (Figure 2-6)

In this case, the flow rate through the valve is calculated as:

$$Q = C_d A_d \sqrt{\frac{2(P_N - P_1)}{\rho}} \Rightarrow Q^2 = k(P_N - P_1) \ , \ k = (C_d A_d)^2 2/\rho \qquad (2\text{-}111)$$

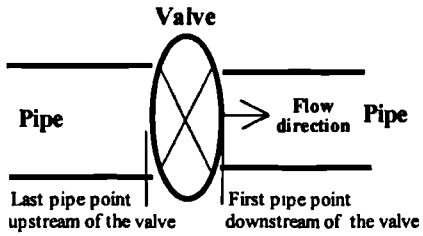

Figure 2-6 : Schematic representation of the boundary condition

where P_N is the pressure at the last point of the pipe upstream of the valve and P_1 is the pressure at the first point downstream of the valve. Also:

$$\begin{aligned} P_N &= C_{pl} - B_{pl} Q \\ P_1 &= C_{mn} + B_{mn} Q \end{aligned} \qquad (2\text{-}112)$$

Combining equation (2-111) and (2-112), we obtain:

$$Q = \frac{-k(B_{pl} + B_{mn}) + \sqrt{k^2 (B_{pl} + B_{mn})^2 + 4k(C_{pl} - C_{mn})}}{2} \qquad (2\text{-}113)$$

and the pressures at the last point of the pipe upstream the valve and the first point downstream the valve are calculated from equation (2-112).

Connection between pipes (Figure 2-7)

At the point of the connection, the continuity equation gives:

$$Q_N = \sum_{i=1}^{i=Np} Q_{li} \qquad (2\text{-}114)$$

where N_P is the number of the pipes that start from the last point of the main pipe, Q_N is the flow rate at the last point of the main pipe and Q_{1i} is the flow rate at the first point of the i-pipe. Also, from the boundary condition of the method of characteristics, we have:

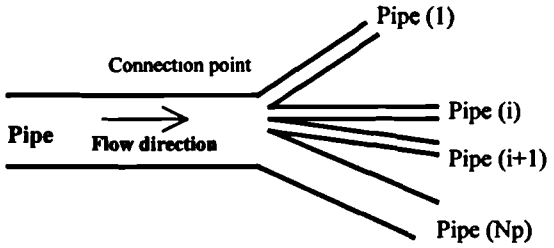

Figure 2-7 : Schematic representation of the boundary condition

$$Q_N = C_{pl} - B_{pl}P$$
$$Q_{1i} = C_{mn_i} + B_{pl_i}P \qquad (2\text{-}115)$$

where it has been assumed that the pressure at the last point of the main pipe equals the pressure at the first point of each of the other pipes, although a pressure loss term can be easily introduced. Combining these equations, the unknown pressure is calculated from the correlation:

$$P = \frac{C_{pl}/B_{pl} + \sum_{i=1}^{i=Np} C_{mn_i}/B_{mn_i}}{1/B_{pl} + \sum_{i=1}^{i=Np} 1/B_{mn_i}} \qquad (2\text{-}116)$$

and the flow rates are calculated from the boundary condition of each pipe (equations (2-115)).

2.3.2.5 Cavitation

Cavitation is an important phenomenon in fuel injection systems. It occurs when the local pressure in a pipe falls below the pressure of vaporization of the liquid (P_{CAV}). Many studies in the past have focused on the investigation of the effect of cavitation on the operation of fuel injection systems, on possible damages caused by the collapse of the cavitating bubbles and on possible ways of numerically treating cavitation in

simulation models; typical examples are those of Lush (1983), Watanabe et al. (1986), Takaishi et al. (1987), Lee (1994) and Minami (1994).

In the present investigation it is assumed that if the minimum pressure at any point of the pipe is equal to the critical cavitation pressure of the liquid ($P=P_{CAV}$), then, the volume of the cavity formed at this point can be calculated from the correlation $V_{CAV}=\Sigma(Q_{in}-Q_{out})dt$, where Q_{in} is the fuel rate flowing into the point where cavitation occurs and Q_{out} is the fuel rate flowing out of the cavitating point; the cavity collapses when $V_{cav}<0$. The flow rates Q_{in} and Q_{out} are calculated from the method of characteristics using the appropriate boundary conditions for the cases where P= constant at the end or at the beginning of the pipe.

2.3.2.6 Minor pressure losses (pipe bending, filters, friction forces)

At several points in the injection system extra pressure losses are caused from the geometrical characteristics of the system. These are due to bended pipes, presence of filters and friction and have been included into the simulation in the following way:

Pipe bending & filters

The bending of pipes is modeled by adding to the momentum equation an extra term which takes into account the pressure losses caused by bending. This term can be written in the form:

$$\Delta P = \varsigma \frac{\rho Q^2}{2A^2} \qquad (2\text{-}117)$$

where the coefficient ζ depends on the geometry of the pipe. Similarly, any filter present in the system can be considered as a resistance to the flow and can be described by the extra pressure losses attributed to the presence of the filter which are mathematically expressed from equation (2-117). The loss coefficient ζ can be calculated from the reduction of the flow area at the point of the filter; values of this coefficient can be found in fluid mechanics textbooks.

Friction

The friction coefficient f in the momentum equation can be calculated from the Moody diagram, given in many fluid mechanics textbooks (for example see White (1988)), by assuming that it is also valid for unsteady flows and is a function of the local Reynolds number and the roughness of the pipe, through the following correlation:

$$f = 64/Re \quad , Re < 2300 \qquad \text{(laminar flow)} \qquad (2\text{-}118)$$

$$f = \frac{1}{(-1.8\log(\frac{6.9}{Re} + (\frac{\varepsilon}{3.7 \cdot D})^{1.11}))^2} \quad , Re>2300 \text{ (turbulent flow)} \qquad (2\text{-}119)$$

where ε is the roughness of the pipe, D its diameter and Re the Reynolds number. For annular pipes, the same relationships can be used, with D calculated from the expression:

$$D=2(D_{ext}-D_{int})\zeta \qquad (2\text{-}120)$$

where

$$\zeta = \frac{(D_{ext} - D_{int})^2 (D_{ext}^2 - D_{int}^2)}{(D_{ext}^4 - D_{int}^4) - (D_{ext}^2 - D_{int}^2)^2 \ln \frac{D_{ext}}{D_{int}}} \qquad (2\text{-}121)$$

The calculation of the Reynolds number is based on the hydraulic area of the pipe, so that

$$Re = \frac{uD_h}{v}$$

where (2-122)

$$D = \frac{4A}{S}$$

where A is the cross sectional area and S is the wetted peripheral flow area.

2.3.2.7 Leakage

The calculation of leakage is based on the equation that describes laminar flows between passages, also known as Couete flow (details can be found, for example, in Schlichting (1979)).

The momentum equation that describes the flow in the annular clearance is

$$\rho\frac{\partial u}{\partial t}=-\frac{\partial P}{\partial x}+\mu\left(\frac{\partial^2 u}{\partial y^2}+\frac{\partial^2 u}{\partial x^2}\right) \tag{2-123}$$

where μ is the kinematic viscosity of the liquid, y is the direction normal to the flow and x is the flow direction. The flow rate calculated from this equation is:

$$Q_{leak}=c_{leak}\frac{\pi d_{pl}(P-P_{feed})}{12\mu l}y_{max}^3 \tag{2-124}$$

where $c_{leak}\approx 1.0$ (depending on various factors of the specific geometry).

2.3.3 One-dimensional injection hole flow model

This model determines the flow characteristics at the exit of the injection holes. For non-cavitating cases, the CFD model can be used. However, when cavitation takes place, existing CFD models cannot be used, since they do not account for two-phase cavitating flows. The physics involved in such flow processes (typical relevant publications are those of Knapp (1970), Hestroni (1982), Young (1989) and Brennen (1995)) are very complex and to solve the problem a simple phenomenological approach has to be used. In this approach, it is assumed that the pressure in the sac volume P_{SAC} is uniform and its value during the injection period is calculated from the FIE model. Then, the discharge coefficient of the injection holes is calculated from the following correlation (based on the work of Lefebvre (1989), Soteriou et al (1993, 1995), Berwick (1954) and Chaves et al. (1995)) as a function of the hole geometry, the Reynolds and

cavitation numbers, the hole position in the sac area relative to the needle, and the pressure difference between the sac volume pressure and the back (chamber) pressure, i.e.

$$Cd_{hole} = \frac{Cd_{CAV}}{0.85} \frac{1}{\frac{1}{Cd_{max}} + \frac{20}{Re}(1 + 2.25\frac{L_{hole}}{D_{hole}})}$$

where :

$Cd_{CAV} = 0.71$ if no cavitation occurs

or

$Cd_{CAV} = \min\{0.71, \frac{1}{2+CN} + 0.66\}$ if cavitation occurs

$$Cd_{max} = \frac{1}{\sqrt{1+Z_{loss}}} - 0.00875\frac{L_{hole}}{D_{hole}}$$

$$Z_{loss} = Z_{entr} + 0.3\cos\theta + 0.2\cos^2\theta$$

$$Z_{entr} = -0.3\frac{r_{entr}}{D_{hole}} + 0.5$$

(2-125)

In the above correlation Re is the Reynolds number based on the hole diameter and the mean injection velocity corresponding to the geometric hole area and CN is the cavitation number defined as:

$$CN = \frac{P_{SAC} - P_{CAV}}{P_{BACK} - P_{CAV}} \quad (2\text{-}126)$$

L_{hole} and D_{hole} are the hole length and hole diameter, respectively, P_{BACK} and P_{CAV} the back pressure and the cavitation pressure (below which cavitation bubbles are formed) respectively, r_{entr} the hole entrance radius of curvature and θ is the flow turning angle defined as the angle between the needle seat axis and the injection hole axis of symmetry. From the calculated hole discharge coefficient the fuel injected from each of the injection holes can then be estimated. To determine whether cavitation occurs or not, two assumptions are adopted: the inlet flow is laminar and flow separation occurs at the inlet. Due to the separation bubbles, the smallest effective cross section close to the inlet is $A_{CONTR} < A_{hole}$. The critical back pressure below which cavitation will occur in the

injection hole is given from the following correlation, derived from Bernoulli equation as applied between the hole entrance and the point of maximum contraction:

$$P_{BACK,CRIT} = \rho[C_{CONTR}u_{CONTR}^2 - (C_{EXIT} + 0.5\lambda(\frac{L_{hole}}{D_{hole}} - 2)u_{EXIT}^2)] \quad (2\text{-}127)$$

In this correlation, $C_{CONTR}= A_{CONTR}/A_{hole}$, $C_{EXIT}= A_{EXIT}/A_{hole}$, u_{CONTR} is the mean velocity at the point of maximum contraction (calculated from the continuity equation applied between the hole entrance and the point of maximum contraction) and u_{EXIT} is the mean exit velocity calculated on the basis of the effective hole area and not the geometric one. The area A_{CONTR} is given from the correlation $A_{CONTR}=A_{hole}\cdot Cd_{hole}/C_{flow}$, where C_{flow} is an empirical coefficient with a value of 1 for turbulent flows. The friction factor λ, which depends on the nozzle hole wall roughness k_{rough} and the Reynolds number, is determined from the expression:

$$\frac{1}{\sqrt{\lambda}} = -2\log[\frac{2.51}{Re\sqrt{\lambda}} + \frac{k_{rough}}{3.71D_{hole}}] \quad (2\text{-}128)$$

As already mentioned, cavitation occurs if the pressure in the flow becomes smaller than the critical cavitation pressure. For this case, two different possibilities exist: either the cavitation bubbles collapse in the injection holes or reach the hole exit. The criterion for which mechanism prevails is the value of C_{EXIT}. If C_{EXIT} <1, then the cavitating bubbles exit from the injection hole and the area of the hole at its exit occupied by liquid is calculated from one-dimensional considerations. Downstream of the point of maximum contraction, viscous losses are neglected. By applying the mass, momentum and Bernoulli equations between the point of maximum contraction and the exit of the hole, and assuming that the pressure at the point of maximum contraction equals the cavitation pressure while the pressure at the exit of the hole equals the back pressure, then the effective velocity at the exit of the hole can be calculated from the following correlation:

$$u_{EXIT} = [1 - \frac{A_{hole}}{A_{CONTR}}\frac{P_{BACK} - P_{CAV}}{P_{SAC} - P_{CAV}}]\sqrt{\frac{2(P_{SAC} - P_{BACK})}{\rho}} \quad (2\text{-}129)$$

If the above velocity equals the velocity based on the geometric hole area, then $C_{EXIT}=1$ and the cavitation bubbles collapse inside the hole. For the calculation of the unknown parameters u_{EXIT} and $P_{BACK,CRIT}$ a predictive-corrective method is used.

The fuel injection rate for each of the injection holes is calculated as a function of the geometric hole area, the hole discharge coefficient and the pressure difference, i.e.

$$R_{INJ} = Cd_{hole}A_{hole}\sqrt{\frac{2(P_{SAC}-P_{BACK})}{\rho_{LIQUID}}} \tag{2-130}$$

Another case verified experimentally is the case of hydraulic flip; that occurs when the recirculation zone formed at the hole entrance reaches the exit of the hole and a smooth jet is formed starting from the inlet edge of the injection hole rather than the hole exit. However, hydraulic flip does not usually occur under practical injection conditions. Since it is difficult to estimate the length of the recirculation zone from one-dimensional considerations, this case will not be considered here.

Another problem related to the flow in the injection holes is the calculation of the turbulent kinetic energy generated in the injection holes and its dissipation rate. A simple one-dimensional k-ε model is used for their estimation:

$$\begin{aligned} K_{TURB} &= \frac{u_{EXIT}^2}{8\frac{L_{hole}}{D_{hole}}}\left[\frac{1}{Cd_{hole}^2}-k_{form}\right] \\ \varepsilon_{DISS} &= \frac{C_e u_{EXIT}^3}{2L_{hole}}\left[\frac{1}{Cd_{hole}^2}-k_{form}\right] \end{aligned} \tag{2-131}$$

where k_{form} is the form loss coefficient (0.45 for practical cases) and $C_e=0.274$ is an experimentally determined coefficient.

2.4 Summary

In this chapter, the three-dimensional CFD model as well as the one-dimensional FIE model for predicting the sac volume flow motion or gas motion in the cases of

spray injection and the flow development in fuel injection systems, respectivelly, were presented.

For the CFD model, the time-averaged differential form of the governing conservation equations of mass, momentum and energy was given in a Cartesian non-orthogonal curvilinear coordinate system while the k-ε model of turbulence was employed in order to close the system of the flow equations. The discrete form of the above equations was also given together with the numerical solution procedure employed.

For the simulation of the flow in fuel injection systems a one-dimensional phenomenological model was presented; this model allows for any combination of elements, assumed to comprise the FIE, to be used. For each of the modeled elements the appropriate equations were given together with the boundary conditions expressing the pressure and flow rate distribution at the points of the connections. In addition, various flow phenomena that frequently occur in fuel injection systems, such as leakage, various pressure losses and cavitation were described. Emphasis was given to the modeling of hole cavitation and a mathematical model estimating the critical sac volume pressure above which cavitation occurs in the injection hole as well as the effective hole area was presented.

CHAPTER 3:

... we are not considering to know something if we haven't understand the basic principles and we haven't bring the analysis into the simplest of its elements. Therefor, it is clear that in the science of nature as well as in other areas, our first target is to define everything by determinig first its basic principles

Aristotle
(physica)

Model of Dispersed Phase

3.1 Introduction

During the last few years, a large number of studies have been performed aiming to understand the physics involved in the development of sprays injected from various types of injectors. This is due to the technological importance of sprays, since a lot of applications are related to this subject. Sprays are used in diesel and gasoline IC engines, gas turbines and turbomachines as well as in a lot of chemical, agricultural and other mechanical processes. In the present study the emphasis is on diesel engine sprays; typical operating conditions for these processes include injection of a diesel liquid fuel, usually from circular cross-section orifices, under high pressure (from 200 to 1500 bars) during a very short period of the order of 1 ms. The ambient conditions include pressures from a few bars to 100 bars and temperatures from 300 to 900 K for injection in a non-combusting environment. The primary problem in analyzing and modeling the spray development lies in the incomplete understanding of most of the physical processes and the limited number of relevant experimental data. These processes comprise cavitation in the nozzle, atomization, secondary break-up, droplet collisions and coalescence, inter-phase transfer of mass, momentum and energy, and spray-wall interactions. Many experimental and computational studies have been published up to now reporting the results of different techniques used to investigate the phenomena taking place during the spray injection. Photographic and laser techniques are usually employed in order to visualize the spray and to measure detailed characteristics of the droplet properties. Photographic techniques reveal the global spray characteristics, such as the spray tip penetration and the spray cone angle. Some of the most representative works in this field are those of Arai et al. (1984, 1994), Hiroyasu et al. (1989, 1990, 1991), Kuniyoshi et al. (1980), Fujimoto et al. (1981), Yule et al. (1985, 1989, 1992, 1995), Lefebvre (1989), Tabata et al. (1991, 1995), Xu et al. (1992), Ruff et al. (1989), Ahmadi-Befrui et al. (1991), Nakahira et al. (1992), Winklhofer et al. (1992), Hamady

et al. (1995), Huh (1991), Naber and Siebers (1996), Farrell et al. (1996), Cossali (1996) and many others. Many parameters have been identified to play a dominant role on the spray structure, such as the ambient gas pressure, temperature and density, the injection conditions (injection pressure, injection duration and injection quantity) the nozzle configuration and the fuel physical properties, such as its density, viscosity and surface tension. Throughout these studies, a qualitative understanding of the effect of the aforementioned parameters on the spray structure has been achieved. In addition, laser techniques have been extensively used to quantify the characteristics of diesel sprays. Amongst the various investigations are those at Imperial College of Arcoumanis et al. (1991, 1992, 1993, 1994 and 1995) for sprays injected from both single-hole and multi-hole one-spring or two-spring injectors and under a wide range of injection conditions, including injection under atmospheric conditions into both quiescent and cross-flowing environment, impinging sprays and engine sprays, Hardalupas et al. (1991, 1993, 1995) and others. Laser techniques are able to reveal the detailed spray structure, since they give quantitative information about the droplet size and velocity at specific points (or whole areas) selected for the measurements. Laser techniques also give information about the spray characteristics injected under real engine conditions, since special transparent engines have been manufactured for such purposes (Arcoumanis et al. (1995)). Also, fuel injection in high pressure constant-volume chambers has been extensively studied (Campanella et al. (1994), Hou et al. (1995), Naber and Siebers (1996), Payri et al. (1996) and others). Since the optical access for these cases is easier than in real engines, a lot of investigations have been performed in configurations simulating similar diesel engine conditions. Unfortunately, laser techniques can not be used in very dense spray regions, like in the area close to the nozzle.

Another set of experiments concerns the investigation of the dynamics of single droplets; the basic physical understanding of such processes is used in order to explain the global spray structure. Since nearly all of the spray-submodels are based on experiments of single droplets, a detailed review of these studies is given in section 3.3

On the computational side, phenomenological and more advanced CFD models are widely used. In phenomenological models (for example Hiroyasu et al. (1984; 1987; 1989; 1990; 1991), Lefebvre (1989), Faeth (1977; 1987; 1983; 1992-1995), Sirignano et al. (1985; 1993)), correlations giving global spray characteristics, such as the spray tip penetration, the spray cone angle and the mean droplet size, have been developed. A

summary of them is given by Lefebvre (1989) and Bayvel and Orzechowski (1993). However, these models do not accurately represent the different physical phenomena taking place during the spray injection; nevertheless, due to their simplicity, they have been extended to simulate the transient engine operation, such as for example by Borgnakke et al. (1981), Davis et al. (1982), Nishida and Hiroyasu (1989), Qiao (1992), Yoshizaki et al. (1993), Bazari et al. (1992, 1993, 1994) and many others, and they are widely used by the industry.

The CFD spray models are based on the numerical solution either of the Euler-Euler or Euler-Lagrange two-phase conservation equations expressing the local spray development and its interaction with the surrounding gas. Typical examples of relevant investigations are those of Reitz and Bracco (1982, 1985), Reitz and Diwakar (1986, 1987), O'Rourke and O'Rourke et al. (1980, 1987, 1989, 1993, 1996), Gosman et al. (1982, 1983), Watkins et al. (1985, 1994) and others. Most of the commercial or available in the public domain CFD codes, like KIVA, STAR-CD, FLUENT, SPEED, SPICE, FIRE and many other in-house university ones, have implemented diesel spray models and use a Eulerian-Lagrangian numerical approximation in order to solve numerically this kind of two-phase flow as long as the total volume of the droplets in a computational cell is small compared to the volume of the computational cell itself. These models have been extensively used in the past for the simulation of the flow in internal combustion engines, for example by O'Rourke and Amsden (1987), Frank and Schulze (1994), Kohnen et al. (1994), Khalighi et al. (1995), Ayoub and Reitz (1995), Hori et al. (1995), Strauss et al. (1995), Tanner and Boulouchos (1996), Jones et al. (1996), Lebreve et al. (1996), Bo et al. (1997) and others. Since the number of droplets in a typical diesel spray is enormously high for the existing computer power and storage capacity, stochastic statistical approximations have been adopted. Thus, the simulation of sprays is based on the discrete droplet model (DDM). These models are based on the Monte-Carlo method, according to which the properties of representative droplets are randomly chosen from calculated distribution functions. The spray is represented by a number of droplet parcels, each of which contains a large number of identical and non-interacting droplets. The droplet initial properties are determined by the flow conditions at the exit of the injection holes from which they are injected. Following their injection, various spray sub-models are used for the calculation of the liquid core primary break-

up, the droplet deceleration, the secondary break-up, the droplet collisions, the droplet evaporation, the droplet impingement and the droplet turbulent dispersion.

It has to be noted that all the spray processes mentioned above are based on the following general assumptions:

a. the interphase transport of mass, momentum and energy are quasi-steady, i.e. their rates are equal to the steady-state value under the same boundary conditions.

b. the transfer coefficients of mass, momentum and energy to and from the droplets are independent of the proximity of neighbouring droplets and can be represented by empirical correlations.

Details about the validity of the above general assumptions will be discussed in the following sections of this chapter. Section 3.2 gives the mathematical formulation of the spray model while section 3.3 describes the various submodels used to represent the various physical processes present in diesel sprays. Section 3.4 describes the inter-phase coupling terms and the last section 3.5 gives details about the numerical implementation of the developed Lagrangian spray model in the CFD code used in the present investigation.

3.2 Spray Model Formulation

For the calculation of the dispersed phase, it is required that the properties of particles of different size are known and their contribution to the interface mass, momentum and energy exchange can be estimated. A statistical description of the spray may be given by the distribution function $f(\vec{x},\vec{u},m,T,t)$, which gives at time t the probable number of particles per unit volume located in the spatial range $(\vec{x},\vec{x}+d\vec{x})$, with velocities in the range $(\vec{u},\vec{u}+d\vec{u})$, mass in the range (m,m+dm), and temperature in the range (T,T+dT). Here, $\vec{x}$ and $\vec{u}$ are the abbreviations for the three-dimensional elements of physical space and velocity space, respectively. It has also been assumed that all fluid elements have the same chemical composition (otherwise a similar distribution function f_j can be used to describe each of the j different chemical compositions). An equation describing the time rate of change of the distribution function f may be derived phenomenologically by using reasoning analogous to that used in the kinetic theory of gases. This equation expresses the conservation of the total number of particles in any volume of $(\vec{x},\vec{u},m,T)$ space moving with the particles. The

effect of fragmentation, coalescence and of all the other processes that could alter the number of particles can be added as a source term to the particle-number conservation equation (Travis et al. (1976), Williams (1985), Kuo (1986)):

$$\frac{d}{dt}\int_{\vec{x}}\int_{\vec{u}}\int_{m}\int_{T} f(\vec{x},\vec{u},m,t)\,d\vec{x}\,d\vec{u}\,dm\,dT = \dot{f}_{SOURCE}(\vec{x},\vec{u},m,T) \tag{3-1}$$

By means of the usual rules for differentiation of an integral and the condition that the volume of integration is arbitrary, the above equation can be transformed to the following equivalent Liouville equation:

$$\frac{\partial f}{\partial t} + \nabla_{\vec{x}}(f\cdot\vec{u}) + \nabla_{\vec{u}}(f\cdot\vec{a}) + \frac{\partial}{\partial T}(f\cdot\dot{T}) + \frac{\partial}{\partial m}(f\cdot\dot{m}) = \dot{f}_{SOURCE} \tag{3-2}$$

in which the total time derivatives are along the dynamically and kinematically allowable paths of the individual particles; thus:

$$\vec{u} = \frac{d\vec{x}}{dt} \quad \text{and} \quad \vec{a} = \frac{d\vec{u}}{dt} \tag{3-3}$$

where the force per unit mass (acceleration) on a particle $(\vec{x},\vec{u},m,T,t)$ is denoted by $\vec{a}$, the rate of change of the particle mass is defined as $\dot{m} = (dm/dt)$ and the rate of change of its temperature is defined as $\dot{T} = (dT/dt)$. Equation (3-2) is usually called the *spray equation* and describes the dynamics of the single-particle distribution function. No assumption has been adopted for the particle shape or for its state (solid or liquid), and thus, it is valid for any particulate flow. The term on the right hand side of equation (3-2) is the production source term and for the case of liquid droplets it can be approximated as:

$$\dot{f}_{SOURCE} = \dot{f}_{INJECTION} + \dot{f}_{ATOMIZATION} + \dot{f}_{BREAKUP} + \dot{f}_{COLLISION} + \dot{f}_{IMPINGEMENT} + \dot{f}_{TURBULENCE} \tag{3-4}$$

where the various terms on the right hand side of the above equation represent the variation of the liquid droplet size distribution function due to various physical

processes taking place during the droplet life time. The first term is due to the new fuel injected, the second term is due to the fluid particles formed from the disintegration of the liquid core jet emerging from the injection holes, the third term is due to distribution function variations occurring every time there is a droplet secondary breakup, the fourth term represents variation in the droplet size distribution due to collisions between the droplets, the next term is due to variations occurring at the time of impingement of a droplet on walls and the last term is due to changes in the particle distribution function attributed to the turbulence of the surrounding media. It is obvious that the spray equation (3-2) is valid for any gas-droplet flow. The void fraction at a specific point and time can be calculated as:

$$\theta = 1 - \int f(\vec{x},\vec{u},m,T,t)\cdot V_{PARTICLE}\cdot d\vec{x}\cdot d\vec{u}\cdot dm\cdot dT\cdot dt \qquad (3\text{-}5)$$

where $V_{PARTICLE}$ is the volume of the particle and the integral is to be performed with respect to all the velocities, masses and temperatures.

To solve for the above distribution function, several methods have been proposed. These can be generally divided into two categories: Eulerian continuum governing equations for all phases or a Lagrangian description for the particulate phase, and a Eulerian continuum description for the gas phase; for example see Drew (1983), Mostafa et al. (1985, 1986), Gidaspow (1986, 1994), Batchelor (1988), or a cloud-in-cell method (foe example see O'Rourke et al. (1993), Harlow and O'Rourke (1996)). Continuum models are more common for dense particulate flows and intuitively make sense, since common experience suggests that fluidized, dense-packed granules flow like fluids (Harris and Crighton (1994)). These continuum models readily allow the modeling of particle-particle stresses and particle viscous stresses using spatial gradients of phase volume fractions and velocities. However, the introduction of a particle size distribution greatly complicates the formulation and requires the introduction of equations to follow the movement of different particle sizes (Rizk (1993)). Thus, many separate continuity and momentum equations are required. An alternative formulation is to use a Lagrangian description for the particle phase and a Eulerian one for the underlying continuous gas phase (Harlow and Amsden (1975), Travis, Harlow and Amsden (1976), O'Rourke and Bracco (1981), Beshay, Gosman and Watkins (1986), Watkins (1987), Amsden, O'Rourke and Butler (1989) and many others). Trajectory and

momentum equations for individual particles are implicitly fully coupled with the gas phase. In such a Lagrangian approach, each particle can have different characteristics (size, density, shape, velocity, temperature), and the result is a truly multiphase flow model. If the particles have a distribution of velocities and masses, the Lagrangian method seeks to solve an equation for the particulate phase distribution function $f(\vec{x},\vec{u},m,T,t)$ and has at its root a stochastic formulation closely related to the recent development of the kinetic theory of granular flows (Gidaspow (1994)). This approach is limited to cases where the volume of the droplets in any computational cell is much smaller than the volume of the continuous phase. Since this condition is usually satisfied in diesel sprays and since, according to the previous investigations mentioned above, the Lagrangian approximation is simpler and more accurate than the Eulerian one, it has been adopted in the present investigation. The rest of this chapter focuses on the description of the various models required for the calculation of the distribution function $f(\vec{x},\vec{u},m,T,t)$.

3.2.1 The Lagrangian approximation

In this method of solution, the continuum distribution function $f(\vec{x},\vec{u},m,T,t)$ is approximated by a number of discrete particles each of which can has its own position, velocity, mass and temperature (Dukowicz (1980)). The spray equation (3-2) defines the behaviour of the droplet distribution function which is defined in such a way that:

$$dN = f(\vec{x},\vec{u},m,T,t)d\vec{x}\, d\vec{u}\, dm\, dT \tag{3-6}$$

is the average number of particles with mass m in the interval (m,m+dm), temperature T in the interval (T,T+dT), located at position $\dot{x}$ in the volume interval $(\vec{x},\vec{x}+d\vec{x})$ and with velocity $\vec{u}$ in the interval $(\vec{u},\vec{u}+d\vec{u})$, at time t. The number of particles in a small interval $\Delta m\,\Delta T\,\Delta\vec{x}\,\Delta\vec{u}$ can be expressed as

$$\Delta N = \int_{\Delta m,\Delta T,\Delta\vec{x},\Delta\vec{u}} \sum_{k} \delta(m-m_k)\,\delta(T-T_k)\,\delta(\vec{x}-\vec{x}_k)\,\delta(\vec{u}-\vec{u}_k)\,dm\,dT\,d\vec{x}\,d\vec{u} \tag{3-7}$$

where δ is the Dirac function. Taking an ensemble average, (3-7) becomes:

$$\Delta N = \int_{\Delta m,\Delta T,\Delta \vec{x},\Delta \vec{u}} < \sum_k \delta(m-m_k)\,\delta(T-T_k)\,\delta(\vec{x}-\vec{x}_k)\,\delta(\vec{u}-\vec{u}_k) > dm\,dT\,d\vec{x}\,d\vec{u} \qquad (3\text{-}8)$$

Since the ensemble average is expected to be essentially constant over the small interval $\Delta m, \Delta T, \Delta \vec{x}, \Delta \vec{u}$, it can be taken outside the integral, and then the following expression is obtained:

$$\begin{aligned}\Delta N =& < \sum_k \delta(m-m_k)\,\delta(T-T_k)\,\delta(\vec{x}-\vec{x}_k)\,\delta(\vec{u}-\vec{u}_k) > \int_{\Delta m,\Delta T,\Delta \vec{x},\Delta \vec{u}} dm\,dT\,d\vec{x}\,d\vec{u} = \\ & < \sum_k \delta(m-m_k)\,\delta(T-T_k)\,\delta(\vec{x}-\vec{x}_k)\,\delta(\vec{u}-\vec{u}_k) > \Delta m\,\Delta T\,\Delta \vec{x}\,\Delta \vec{u}\end{aligned} \qquad (3\text{-}9)$$

Comparing this with equation (3-6), it can be derived that for the infinitesimal volume $\Delta m, \Delta T, \Delta \vec{x}, \Delta \vec{u}$:

$$f(\vec{x},\vec{u},m,T,t) = < \sum_k \delta(\vec{x}-\vec{x})\,\delta(\vec{u}-\vec{u})\,\delta(m-m)\,\delta(T-T) > \qquad (3\text{-}10)$$

This defines the relationship between the continuum statistical description embodied in the spray equation and the discrete particle realization. For modeling purposes, it is not possible to deal with the large number of particles present in an actual physical system (a diesel spray for instance) so that a sampling technique must be employed in which each single computational parcel represents a characteristic group of droplets. This is equivalent to the following 'instantaneous' distribution function:

$$f(\vec{x},\vec{u},m,T,t) = \sum_k N_{pk}\,\delta(\vec{x}-\vec{x}_k)\,\delta(\vec{u}-\vec{u}_k)\,\delta(m-m_k)\,\delta(T-T_k) \qquad (3\text{-}11)$$

where N_{pk} is the number of identical droplets represented by particle k. The number N_{pk} is determined by initial-boundary conditions and by the constraint

$$\sum_k N_{pk} m_k = M_{TOTAL} \qquad (3\text{-}12)$$

where M_{TOTAL} is the total mass of the particles. It is assumed that particles of the same parcel do not interact between each other and follow exactly the same trajectory. That

introduces a stochastic Monte-Carlo approximation to the solved equations, since the various properties of the droplets of each parcel have to sampled randomly from distribution functions calculated for every physical process taking place in the particulate flow development. The number of parcels used should give statistically independent results. In the limiting case, the number of parcels equals to the number of droplets. In the present investigation, a Cartesian (x,y,z) coordinate system is used for the representation of the droplet positions at every time, while Cartesian velocity components are used to describe the parcel motion in the three-dimensional space.

To account for the particle properties, the various terms in equation (3-2) have to be determined.The term $\nabla_{\vec{x}}(f \cdot \vec{u})$ accounts for the variation of f due to particle movement and thus it is equivalent to the particle trajectory equation. The term $\nabla_{\vec{u}}(f \cdot \vec{a})$ accounts for variations of the particle velocities due to their acceleration, and thus it is equivalent to the Newton's second law; these are evaluated in section (3.3.1). The following two terms $\frac{\partial}{\partial T}(f \cdot \dot{T})$ and $\frac{\partial}{\partial m}(f \cdot \dot{m})$ account for variations of f due to droplet temperature and mass changes, respectively, caused by the heat and mass transfer between the liquid and the surrounding media. These are estimated in section (3.3.2). Finally, the source terms, $\dot{f}_{INJECTION}$, $\dot{f}_{ATOMIZATION}$, $\dot{f}_{BREAKUP}$, $\dot{f}_{COLLISION}$, $\dot{f}_{IMPINGEMENT}$ and $\dot{f}_{TURBULENCE}$ of the right hand side of equation (3-2) have to be determined; these are discussed in sections (3.3.3) to (3.3.8).

3.3 Spray Sub-Models

In this section, the various spray sub-models are described. These include the forces acting on the moving droplets, droplet evaporation, liquid core atomization, droplet secondary break-up, droplet collisions, droplet turbulent dispersion and droplet-wall interactions.

3.3.1 Forces acting on a moving droplet

The forces exerted upon a droplet of a dispersion mixture, during its nonstationary rectilinear motion, may be predetermined in the form of a quasi-stationery force as:

$$F_{TOTAL} = F_{AEROD} + F_M + F_{BASSET} + F_A + F_G + F_{THERM} + F_{MAGNUS} + F_{SHAFMAN} + F_{PRES} + F_{CERT} \quad (3\text{-}13)$$

where the terms involved on the right hand side of the above equation have as follows: F_{AEROD} is the aerodynamic force (Stokes force for very low Reynolds number or drag force at higher Reynolds), F_M is the 'added mass' or 'virtual mass' force arising because the acceleration of the droplet requires acceleration of the surrounding fluid, F_{BASSET} is the 'Basset history integral' force in which past acceleration is included (arising from boundary layer unsteadiness of the flow around the droplet), F_A is the Archimides force arising from differences in the density between the droplets and the surrounding fluid, F_G is the gravitational force, F_{THERM} is the thermoforesis force arising from the temperature gradient of the surrounding fluid at the vicinity of the droplet, F_{MAGNUS} is the Magnus force arising from the circulation produced around rotating objects, $F_{SHAFMAN}$ is the Shafman force arising from the surrounding fluid velocity gradient in the vicinity of the moving droplet, F_{PRES} is the surrounding fluid pressure gradient force and F_{CENTR} are centrifugal forces acting if the droplet trajectories are not straight lines. Other external forces such as electrostatic effects e.t.c. have not been included since they are not present in diesel spray applications. The mathematical expressions of all the above forces are given below (they are also given by Clift, Grace and Weber (1978), Nigmatulin (1991) and other fluid mechanics publications) and their relative magnitude for diesel sprays is evaluated.

Added mass force

The virtual or added mass force is due to the inertia of the fluid displaced by the moving droplet, and can be expressed as:

$$\vec{F}_M = \Delta_{CREP,1} \frac{\rho_{liquid} V}{2} \frac{d\vec{u}_{rel}}{dt} \quad (3\text{-}14)$$

where V is the volume of the fluid particle and $\Delta_{CREP,1} \approx 1$ is a coefficient accounting for the differences from the creeping flow regime. This force can be neglected if the liquid

to gas density ratio is large; since in diesel spray applications this ratio is usually larger than 20, this force is neglected.

Basset force

The Basset force takes into account past droplet acceleration which arise from the unsteadiness of the boundary layers around the droplet. For spherical droplets it is given by the expression:

$$\vec{F}_{BASSET} = 6d^2\Delta_{CREP,2}\sqrt{\pi\rho_{liquid}\mu_{liquid}}\int_{-\infty}^{t}\frac{\partial}{\partial\tau}\frac{\vec{u}_{rel}}{\sqrt{t-\tau}}d\tau \qquad (3\text{-}15)$$

where $(t-\tau)$ is the time elapsed since the past acceleration and $\Delta_{CREP,2}$ another coefficient taking into account differences from the creeping flow; this force acts on the direction of the particle velocity. Ormancey and Martinon (1984) showed that this force can be neglected for low turbulence intensities and moderate departures from homogeneity. However, Hansell et al. (1992) showed that for movement in a highly turbulent flow a 25% error can result in the droplet acceleration if this force is neglected. For diesel sprays turbulence phenomena are small compared to other parameters. In addition, numerical implementation of this force demands large computer memory storage and, thus, it has been neglected in the present investigation.

Gravitational and Archimides forces

The Archimides force arises from the difference between the densities of the liquid droplets and the surrounding gas; it can be expressed as:

$$\vec{F}_A = -\rho_{gas}\,\vec{g}\cdot V \qquad (3\text{-}16)$$

while the gravity force is:

$$\vec{F}_G = \rho_{liquid}\,\vec{g}\cdot V \qquad (3\text{-}17)$$

Although they are quite small compared to the other major forces, they can be easily implemented into the simulation code.

Shaffman force

The Shaffman force (Shaffman(1966)) is induced by shear flow gradients, and it can be expressed as:

$$\vec{F}_{SHAFMAN} = 1.62\mu_{gas} d_{drop}^2 \left(\frac{1}{\nu}\frac{d\vec{u}_{gas}}{dx}\right)u_{rel} \tag{3-18}$$

Faeth (1983) showed that this force is at least an order of magnitude smaller than the drag force for distances larger than 10 hole diameters from the nozzle. However, in the near-wall region where strong fluid shear is induced, this force can become relatively important. Bai (1996) showed that this force is of the same order of magnitude as the drag force in the direction parallel to the wall and even bigger in the normal to the wall direction for distances within the boundary layer formed above the wall; as a result, this force has to be taken into account in the simulation of impinging sprays.

Thermoforesis

This is due to thermal gradients in the flow, and it can be written in the form:

$$\vec{F}_{THERM} = -\frac{12\pi\mu_{gas}\nu_{gas}r_{drop}C_s\left(\frac{k_g}{k_p} + C_t\frac{\lambda}{r_{drop}}\right)\frac{\nabla_x T}{T_{gas}}}{\left(1+3C_m\frac{\lambda}{r_{drop}}\right)\left(1+2\frac{k_g}{k_p}+2C_t\frac{\lambda}{r_{drop}}\right)} \tag{3-19}$$

$$\lambda = 2\mu_{gas}/(\rho_{gas}\bar{c}), \quad \bar{c} = \left(\frac{8R_{gas}T_{gas}}{\pi}\right)^{1/2}$$

where μ_{gas}, ν_{gas} and ρ_{gas} are the gas dynamic viscosity, gas kinematic viscosity and gas density respectively, ∇T is the thermal gradient of the surrounding gas at the vicinity of the particle, T_{gas} is the gas temperature, R_{gas} is the specific gas constant, k_g and k_p are the thermal conductivity of the gas and the particle respectively, r_{drop} is the radius of the particle (assumed to be spherical) and C_m=1.4, C_t=2.18 and C_s=0.75 are numerical

coefficients obtained from the kinetic theory. This force can become important only for very small droplets in regions where the thermal gradients in the flow are important, and thus they have been neglected in the present investigation; more details are given by Talbot, Cheng, Schefer and Willis (1980).

Magnus force

Magnus forces are associated with droplet rotation due to the non-uniform pressure distribution developing around rotating bodies; it is given by the expression:

$$\vec{F}_{MAGNUS} = 1.615\mu_{gas} d_{drop} \vec{u}_{rel} \sqrt{Re_\omega}$$

where (3-20)

$$Re_\omega = \frac{\rho_{gas} u_\omega d_{drop}}{\mu_{gas}}, \; u_\omega = \omega \frac{d}{2}$$

where ω is the annular velocity of the rotating droplet. This force acts on a direction normal to the axis of rotation of the fluid element. However, is has been assumed that the droplets do not rotate during their movement and since their value is quite small, as it has been shown by Faeth (1983), they have been neglected here.

Pressure gradient force

This force is due to the static pressure gradient in the flow and it is given as:

$$\vec{F}_{PRES} = V \cdot \nabla_x p \qquad (3\text{-}21)$$

where p is the pressure of the surrounding gas.

Centrifugal force

This force arises when droplets do not follow straight lines; the resulting force can be estimated from the expression:

$$\vec{F}_{CENTR} = \rho_{liquid} VR_{CERT} \omega_{CERT}^2 \tag{3-22}$$

and acts on a direction of the curvature radius. However, their magnitude is relatively small in diesel sprays where there is one main moving direction; in addition, their numerical evaluation is not very easy to be performed since that involves the estimation of the radius of curvature. As a result, they have been neglected in the present investigation.

Aerodynamic force

The aerodynamic force comprises skin friction and form drag; it has the form:

$$\vec{F}_{AEROD} = C_D \frac{\rho A}{2} \vec{u}_{rel} |u_{rel}| \tag{3-23}$$

where C_D is the aerodynamic drag coefficient and A is the cross sectional area of the particle exposed to the relative flow direction. The determination of this force involves the knowledge of the drag coefficient. Up to now, numerous investigations have dealt with this problem. For spherical solid particles several correlations have been reported for the calculation of the C_D as a function of the Reynolds number; Stokes (1901) found that C_D=24/Re. This law holds only for flows that are entirely dominated by viscous forces (creeping flows), that is, for flows characterized by low Reynolds numbers. For higher Reynolds numbers, the inertial forces become significant and the drag force may be increased due to the formation of a wake and possible detachment of energy-consuming vortices. Another departure from Stoke's law is caused by the presence of a boundary layer, since the actual volume moving through the fluid consists of the sphere together with its boundary layer. These considerations have led to various theoretical correlation factors for Stokes' drag law, but most of the correlations for droplet drag coefficient in common use are based on the analysis of experimental data.

In diesel engines the droplets usually experience a drag that differs from that of spherical solid particles, since the flow pattern around the droplet is considerably different. The main factors creating further complications in the estimation of the drag coefficient of the droplets in a diesel spray are the following:

a. the effect of relative flow unsteadiness: Briffa (1981) examined experimentally the unsteady relative motion effect on droplet drag, using a water spray decelerating in an air-stream. His results showed that the drag coefficients were quite different from the standard curve of solid spheres. Choi and Lee (1992) provided further observation that the droplet drag coefficient is much lower than the standard one during a severe droplet deceleration; however, no attempt has been made to incorporate a parameter, characterizing the droplet/gas relative unsteadiness into the correlation of the drag coefficient.

b. Effect of droplet-droplet interaction: In dense spray regions, the flow pattern around the droplets is affected from the presence of neighbouring droplets and as a result, the drag coefficient is also affected. Recently, this effect has been studied by a few investigators (Rowe and Henwood (1961), Raju and Sirignano (1990), O'Rourke (1981), Mulholand et al. (1988), Choi and Lee (1992)) and various correlations have been proposed; one of them (O'Rourke (1981)) has been incorporated in the present investigation.

c. Effect of droplet deformation: when a liquid droplet moves in a gas with a relatively high velocity, it performs deformation, which, as it will be discussed in section 3.3.5, leads to droplet break-up. During the period of droplet deformation, the drag coefficient changes considerably from that of a spherical droplet, as it has been reported by many investigators (Ranger and Nicholls (1969), Hinze, (1955), Hsiang and Faeth (1992), Klee and Treybal (1956), Greene et al (1993)). In addition, according to Liu et al. (1993), it is important to model the dynamic change of droplet drag coefficient with the droplet deformation. In his numerical study has been shown that although the spray tip penetration does not changes considerably if the dynamic drag coefficient is not taken into account, the detailed spray characteristics (such as droplet size and velocity distributions) can be differ considerably. In the present investigation, the effect of variable discharge coefficient due to droplet deformation is taken into account through correlations reported by Hsiang and Faeth (1992).

d. effect of droplet evaporation: Yuen and Chen (1976) found that evaporation affects droplet drag in two different ways; firstly, the temperature and concentration gradients between the droplet surface and the ambient gas cause substantial reductions in the viscosity of the gas which reduces drag coefficient. Secondly, the mass transfer associated with droplet evaporation induces the so called 'blowing' effect, which

reduces friction drag and increases form drag. These effects can be taken into the calculation of the drag coefficient through empirical correlations, for example those reported by Lefebvre (1989).

e. Effect of wall: Faxen (1923) noticed that the presence of a wall increases the drag coefficient of a sphere in the near wall region as compared to that in the case of unbounded flow. Faxen (1923), Brenner (1961), Maude (1961) and Dahneke (1974) have proposed correction factors on the calculation of the drag coefficient which take into account the presence of a wall. However, it seems that this subject requires further research and no modification has been introduced into the calculation of the drag coefficient in the presence of a wall in the present investigation.

As it is clear from the above description, there are many empirically determined functions that approximate the experimental data obtained by different investigators. Some of these are summarized by Lefebvre (1989), and Nguyen et. al. (1991). Since there is no single expression for droplet drag coefficient that applies to all conditions, the following correlation is usually adopted for a spherical undistorted droplet moving in a low temperature environment:

$$\begin{aligned} C_D &= \frac{24}{Re} && Re < 1 \\ C_D &= \frac{24}{Re}\left(1+\frac{1}{6}Re^{2/3}\right) && 1 \le Re < 1000 \\ C_D &= 0.44 && Re \ge 1000 \end{aligned} \qquad (3\text{-}24)$$

For movement in an evaporating environment:

$$C_{D,evap} = \frac{C_D}{1+B} \qquad (3\text{-}25)$$

where B is the Spalding mass transfer number (defined in section (3.3.2)). In case of movement in the presence of other droplets (O'Rourke (1980)):

$$C_D = \frac{24}{Re}\left(\theta^{-2.65} + \frac{1}{6}Re^{2/3}\cdot\theta^{-1.78}\right) \qquad (3\text{-}26)$$

where θ is the gas volume fraction (the limiting case θ=1 gives equation (3-24)). For deformed droplets the following correlation proposed by Hsiang et al.(1992) is used:

$$C_{D\,distorted} = C_{D\,sphere}(0.4 + 0.6\frac{D_{distorted}}{D_{drop}}) \tag{3-27}$$

where the parameters involved in the above correlation are given in section (3.3.5).

Droplet momentum equation

Having estimated the total force acting on a moving droplet, the rate of change of the droplet momentum can be written as:

$$\frac{d(m\vec{u})}{dt} = \vec{F}_{TOTAL} \tag{3-28}$$

from which the droplet velocity at every time step can be estimated.

3.3.2 Droplet evaporation

The evaporation of droplets in a spray involves simultaneous heat and mass transfer processes in which the heat for evaporation is transferred to the droplet surface by conduction, convection and radiation from the surrounding hot gas and vapour is transferred by convection and diffusion back into the gas steam. The overall rate of evaporation depends on the pressure, temperature and transport properties of the gas, the temperature, volatility and diameter of the droplets in the spray and the velocity of the droplets relative to that of the surrounding gas. As heat transfer takes place the droplets heat up (usually the injected fuel has lower temperature than the surrounding gas) and, at the same time, loose part of their mass by vapourization and diffusion into the surrounding air or gas. The rates of heat and mass transfer are markedly affected by the droplet Reynolds number. In a spray where a certain size distribution of droplets is present, the smaller droplets evaporate faster and in a typical diesel spray, where the smaller droplets are at the periphery of the spray, the autoignition sites appear in these regions of higher evaporation rates.

Many studies (Daidzic et al. (1995), Suresg et al. (1987), Delplanaue et al. (1993), Jia et al. (1993), Curtis and Farrell (1992) and others) have been performed on the single droplet evaporation rate. Most of them, assume spherical pure liquid droplets and neglect the radiation heat transfer. Steady state conditions are usually tested. Since convective unsteady effects have been found not to affect significantly the heat transfer to the droplet most models assume quasi-steady conditions around the droplet and use empirical correlations for the heat and mass transfer coefficients (Frossling (1938), Ranz and Marsall (1952), Faeth (1977, 1983, 1986).

Evaporation strongly affects the droplet size distribution in a diesel spray. That involves the effects of the different evaporation rates of droplets of different sizes, and thus, no general conclusions can be drawn on how the droplet size distribution changes. Significant differences through the injection period have been reported in the past; some of them are discussed by Lefebvre (1989).

Up to now, many studies have been reported on the modeling of droplet evaporation. Faeth (1983, 1987) and Sheares et al. (1979), Mehta et al. (1985), Chein (1989), Mostafa et al. (1985, 1987), Abramzon and Sirignano (1989), and Daidzic et al. (1995) are typical examples of relevant applications. In addition, a number of publications deals with the evaporation of multi-component fuels. For this type of modeling, internal droplet circulation effects, temperature variation in the droplet, diffusion effects between the different compounds and solubility effects need to be considered. The publications of Suresh and Aggarwal (1987), Wong et al. (1992), Jia and Gogos (1993), Kneer et al. (1993), Delplanque and Sirignano (1993), Hohmann et al. (1996) and Varnavas and Assanis (1996) are some typical examples of investigations in this area. However, it should be noted, that all the above investigations assume spherical droplets. No model has been reported accounting for the above described effects in distorted droplets, since for this approach the detailed fluid dynamics of the distorted droplet are required. However, since for most of their life time the droplets in a typical diesel spray are highly distorted, correlations have to be developed accounting for these effects.

In the present investigation three different approaches to model droplet evaporation have been examined. The widely used model of spherical droplets with uniform temperature is initially described, followed by a model accounting for the possible effects of droplet deformation on droplet-gas interphase surface area. Finally, a

model accounting for the temperature variation within the droplet is described. It should be mentioned that high pressure (solubility) effects as well as superheating effects at the critical point (Curtis and Farrell (1992)) are not considered here.

3.3.2.1 Spherical droplet with uniform temperature

The model used for the calculation of the droplet evaporation rate is based on the assumption that the droplet temperature is uniform (the droplet heating time is assumed to be small compared to its life time). It is also assumed that evaporation takes place under constant pressure and the vapour pressure of the evaporated mass equals the partial pressure at the droplet surface. Radiation and conduction are neglected; heat and mass transfer between the liquid droplet and the surrounding gas is governed by turbulent convection. Gravity, Dufour energy flux and mass diffusion due to pressure and temperature gradients are neglected. Under these assumptions, the energy balance equation can be written in the form:

$$\frac{d}{dt}(m \cdot c_l \cdot T) + \dot{Q}_{EVAP} = A_{CONV}\dot{Q} \tag{3-29}$$

where m is the droplet mass, T is the droplet temperature, c_l is the specific heat at constant pressure, L is the latent heat of vapourization, A_{CONV} is the area of the droplet in contact with the surrounding gas and is $\dot{Q}$ the rate of heat convection to the droplet surface per unit area. The first term on the left hand side of this equation represents the amount of energy used in order to increase the temperature of the droplet, the second term is the amount of energy used for the evaporation of the droplet and the term on the right hand side is the total energy flux. Equation (3-29) has to be solved to allow the droplet temperature T to be determined. The following correlations are used:

$$\dot{Q}_{EVAP} = L(T,P)\frac{dm}{dt} \tag{3-30}$$

$$A_{CONV} = 4\pi r_{DROP}^2$$
$$m = \frac{4}{3}\pi\rho_{LIQUID}r_{DROP}^3 \qquad (3\text{-}31)$$
$$\frac{dm}{dt} = 4\pi\rho_{LIQUID}r_{DROP}^2\frac{dr_{DROP}}{dt}$$

Derivation of the droplet vapourization rate equation is usually pursued by neglecting thermal diffusion and assuming that the driving force for species is a concentration gradient in the direction of the diffusion path. The expression for dm/dt is given by (Faeth (1977), Goldsmith and Penner (1954), Spalding (1955) and Williams (1985, 1990)):

$$\frac{dm}{dt} = -2\pi\frac{D_{GAS}Sh_D P_{GAS}}{R_{GAS}T_{GAS}}\ln\left(\frac{P_{GAS}-P_{v,\infty}}{P_{GAS}-P_{v,S}}\right) \qquad (3\text{-}32)$$

where Sh_D is the Sherwood number for mass transfer which is calculated from the correlation (Ranz and Marsall (1952)):

$$Sh_D = (2.0+0.6Re^{1/2}Sc^{1/3})\frac{\ln(1+B)}{B} \qquad (3\text{-}33)$$

where Re is the Reynolds number, Sc is the Schmidt number and B is the Spalding number. These are calculated as:

$$Re = \frac{2\rho_{GAS}r_{DROP}u_{REL}}{\mu_{GAS}(\hat{T})}$$
$$Sc = \frac{\mu_{GAS}(\hat{T})}{(\rho D)_{GAS}(\hat{T})} \qquad (3\text{-}34)$$
$$B = \frac{Y_1^* - Y}{1-Y_1^*}$$

where Y^*_1 is the fuel vapour mass fraction at the droplet's surface, $Y=\rho_{LIQUID}/\rho_{GAS}$ and $D_{GAS}(\hat{T})$ is the fuel vapour diffusivity in air. P_{GAS} is the pressure around the droplet, $P_{v,\infty}$ is the partial pressure of the fuel vapour away from the droplet, $P_{v,S}$ is the partial vapour pressure of the fuel vapour at the droplet surface and μ_{GAS} is the kinematic

viscosity of the surrounding gas calculated on the basis of the same mean temperature on droplet surface as $\mu_1\hat{T}^{3/2}/(\mu_2+\hat{T})$, with μ_1=1.457e-6 and μ_2=100 being empirical constants. The vapour diffusivity and the fuel vapour mass fraction are calculated as:

$$D_{GAS}(\hat{T}) = D_1\hat{T}^{D_2} \tag{3-35}$$

$$Y_1^* = \frac{MW_{ALL}}{MW_{ALL} + MW_{GAS}(\frac{P_{GAS}}{P_{min}} - 1)} \tag{3-36}$$

$$P_{min} = \min\{P_{GAS}, P_{v,S}\}$$

where D_1=1.0 and D_2=0.6 are empirical constants, MW_{ALL} is the molecular weight of the gas including the fuel vapour, MW_{GAS} is the molecular weight of all species of the gas excluding fuel vapour. In all the above correlations, $\hat{T}$ is a mean gas-liquid temperature calculated as:

$$\hat{T} = \frac{T_{GAS} + 2T}{3} \tag{3-37}$$

To calculate the latent heat of vapourization, it is assumed that the liquid density is constant and that its internal energy is a function of its temperature only. Thus, the liquid enthalpy will have a small pressure dependence:

$$h(T,P) = I(T) + \frac{P}{\rho_{LIQUID}} \tag{3-38}$$

where h is the liquid enthalpy and I the liquid internal energy. Since the latent heat of vapourization L is the energy required to convert a unit mass of liquid to vapour at constant pressure equal to the equilibrium vapour pressure, the liquid and vapour enthalpy, the internal energy and the latent heat of vapourization are related with the expression:

$$L(T) = h(T,P) - h(T,P_{v,\infty}(T))$$

or (3-39)

$$L(T) = I_{GAS}(T) + \frac{R_{GAS}T}{MW_{ALL}} - (I(T) + \frac{P_{v,\infty}(T)}{\rho_{LIQUID}})$$

The total heat flux in equation (3-29) is assumed to be equal to the convective heat flux which can be calculated from expression (El Wakil et al. (1954)):

$$\dot{Q}_{CONV} = A_{CONV} \cdot h \frac{z}{e^z - 1}(T_{GAS} - T)$$

$$z = -\frac{c_l \frac{dm}{dt}}{2 \cdot \pi \cdot r_{DROP} \cdot k_m \cdot Nu_D} \quad (3\text{-}40)$$

$$Nu = \frac{2 \cdot h \cdot r_{DROP}}{k_m}$$

where k_m is the fuel thermal conductivity, $z/(e^z-1)$ is a correction factor due to the fuel evaporated and Nu_D is the Nusselt number calculated as (Ranz and Marshall (1952)):

$$Nu_D = (2.0 + 0.6 Re^{1/2} Pr^{1/3}) \frac{\ln(1+B)}{B} \quad (3\text{-}41)$$

which takes into account the effect of neighbouring droplets though the correction factor $\ln(1+B)/B$. In the above correlation Pr is the Prandl number calculated as:

$$Pr = \frac{\mu_{GAS}(\hat{T}) c_l(\hat{T})}{K_{GAS}(\hat{T})} \quad (3\text{-}42)$$

and

$$K_{GAS}(\hat{T}) = \frac{K_1 \hat{T}^{3/2}}{K_2 + \hat{T}} \quad (3\text{-}43)$$

where K_1=252.e-5 and K_2=200.0 are empirical constants.

3.3.2.2 Non-spherical droplet with uniform temperature

Experimental and computational results have revealed that during their life time the droplets are deformed. Thus, the area of the droplet in contact with the gas is larger than that of a spherical droplet and, thus, it is expected that this will affect the heat flux. Correlations accounting for deformation effects on the calculation of the A_{CONV}, dm/dt and $\dot{Q}_{CONV}$ have to be introduced. It is assumed that A_{CONV} is equal to the area of a spheroid, where its maximum and minimum diameters are equal to those calculated from the break-up model (section (3.3.5)):

$$A_{CONV} = 4 \cdot \pi \cdot r_{DROP}^2 \left(\frac{D_{max}}{D_{min}}\right)^2 \tag{3-44}$$

For the calculation of dm/dt, it is assumed that correlations (3-31) and (3-32) are valid, where now r_{DROP} represents the equivalent droplet radius (the model accounts for the mass evaporation rate by calculating the rate of change of an equivalent droplet radius). However, the Sherwood and Nusselt numbers (correlations (3-33) and (3-41), respectively) are calculated from correlations derived from heat transfer studies on spheroids:

$$Sh_D = (2 + 0.085 \cdot Sc^{1/3} \cdot Re^{0.804}) \frac{\ln(1+B)}{B}$$

$$Nu_D = (2 + 0.085 \cdot Pr^{1/3} \cdot Re^{0.804}) \frac{\ln(1+B)}{B} \tag{3-45}$$

The same numerical procedure is then used for the calculation of the equivalent droplet radius and its new temperature, as the one used for the spherical droplet.

3.3.2.3 Spherical droplet with non-uniform temperature

Recent studies on droplet evaporation have revealed that the temperature variation within the droplet can be an important factor affecting the evaporation rate. To account for this temperature, heat conduction equations should be used in order to solve

for the temperature profile within the droplet. These equations can be of practical use only under the assumption of spherical droplets and have as follows:

$$\text{Energy equation :} \quad -A_{CONV}\frac{\partial T(r=r_{DROP},t)}{\partial t} = \dot{Q}_{CONV} - \dot{Q}_{EVAP} \tag{3-46}$$

Heat conduction equation within the droplet assuming spherical symmetry:

$$\frac{1}{r^2}\cdot\frac{\partial}{\partial r}\left[k_{DIFF}\cdot r\cdot\frac{\partial T(r,t)}{\partial r}\right] = \rho_{LIQUID}\cdot c_l\cdot\frac{\partial T(r,t)}{\partial t} \tag{3-47}$$

Initial and boundary conditions:

$$\frac{\partial T(r=0,t)}{\partial r} = 0$$
$$T(r,0) = T_{INJ} \tag{3-48}$$

where T_{INJ} is the temperature of the fuel in the fuel injection system. For the calculation of the terms on the right hand side of equation (3-47), the correlations described in the previous section (3.3.2.1) are used where in all of them the average droplet temperature has to be replaced with the droplet temperature at its surface. In order to solve for the temperature variation within the droplet, the above equations can be solved either analytically or numerically, as described, for example, by Kakac (1993). However, this type of solution demands large computer memory capacity; in addition the computational time required for such a solution can be extremely large when a very large number of droplets are simulated in a diesel spray. Thus, a third alternative method is used. According to Clerides (1997), the profile method can be used to describe the variation of the droplet temperature under diesel engine conditions (where the gas temperature is always higher than the temperature of the droplet surface). The temperature variation along the droplet radius is assumed to have the form:

$$T(r,t) = C_1 + C_2T(r,t) + C_3T^2(r,t) \tag{3-49}$$

where the coefficients C_1, C_2 and C_3 are determined from equations (3-46), (3-47) and (3-48) at every computational time step. Their final expressions are:

$$C_1(t) = T_{INJ} + \frac{\dot{Q}_{EVAP}}{\dot{Q}_{CONV}} - r_{DROP} \cdot C_3(t)\left(\frac{2 \cdot k_{DIFF}}{h \cdot f} + r_{DROP}\right)$$

$$C_2(t) = 0$$

$$C_3(t) = C_4 \exp\left(-\frac{\frac{3k_{DIFF}}{\rho_{LIQUID} \cdot c_l}}{\frac{r_{DROP}^2}{3} + \frac{k_{DIFF} \cdot r_{DROP}}{h \cdot f}} t\right)$$

$$C_4 = \frac{T(r_{DROP},0) - T_{INJ} - \frac{\dot{Q}_{EVAP}}{\dot{Q}_{CONV}}}{-\frac{2 \cdot k_{DIFF} \cdot r_{DROP}}{h \cdot f} - \frac{2 \cdot r_{DROP}^2}{3}} \qquad (3\text{-}50)$$

$$f = \frac{z}{e^z - 1}$$

In the above correlations k is the thermal diffusivity which can be calculated from the following expression as a function of the liquid temperature T:

$$k_{DIFF} = \frac{A(1 - T_r)^{0.38}}{T_r^{1/6}}$$

$$T_r = T / T_{CRIT} \qquad (3\text{-}51)$$

$$A = \frac{A^* \cdot T_b^{a1}}{MW^{a2} \cdot T_{CRIT}^{a3}}$$

In this empirical correlation, A^*, a1, a2 and a3 are empirical constants which are given in section 3.5, T_{CRIT} is the critical temperature of the liquid and T_b the normal boiling point.

Many investigators have suggested the use of the effective thermal conductivity in order to take into account the faster heating of the droplet resulting from the flow

motion created inside the droplet. According to Abramzon and Sirignano (1989), the factor multiplying the thermal conductivity is given from the empirical correlation:

$$\chi = 1.86 + 0.86 \cdot \tanh[2.245 \cdot \log_{10} \frac{Pe_L}{30}] \qquad (3\text{-}52)$$

where $Pe_L = Re_L \cdot Pr_L$ is the Peclet number and Re_L and Pr_L are the Reynolds and Prandl numbers, respectively, calculated on the basis of the droplet diameter and the physical properties of the liquid; this factor varies between 1 and 2.72.

3.3.3 Fuel injection (initial conditions)

The Lagrangian approximation adopted for the numerical approximation of the spray equation (3-2) requires that the initial droplet characteristics are known variables. This is mathematically expressed through the source term $\dot{f}_{INJECTION}(\vec{x},\vec{u},m,T,t)$ of equation (3-4). Generally, most of the spray models implemented in CFD codes require as input to the model the experimentally estimated fuel injection rate (or the line pressure which is assumed to proportional to the actual injection pressure during the injection period). However, as it will be clear in the next section, the knowledge of the fuel injection rate is not the only information required for the spray calculation, especially under cavitating hole flow conditions. This is mainly due to the increased injection velocity (due to the volume occupied by the cavitation bubbles) and to the variable hole discharge coefficient which affects both fuel injection rate and hole turbulence characteristics; thus the percentage of the hole exit cross-sectional area occupied by cavitation bubbles is an additional parameter which has to be known. In the present investigation, all flow characteristics at the exit of the injection holes are given as a function of time from the solution of the flow in the fuel injection system and the injection holes. The mass of the injected fuel is calculated from the equation giving the fuel injection rate from each individual injection hole while the injection velocity is assumed to be uniform along the injection hole cross sectional area and equal to the effective injection velocity; the effects of non-uniformity of the velocity profile at the hole exit are considered in the liquid core atomization model only for non-cavitating hole flow conditions and only if the 3-D flow field at the sac volume and the injection

holes is known. The droplet parcel injection rate is not taken to remain constant during the injection period, as it is the case in most of the other spray models reported up to now; it is assumed that it is proportional to the fuel injection rate. To account for the number of particles injected at each computational time step, it is assumed that their initial diameter equals the effective hole diameter (calculated from the one-dimensional flow model in the sac volume area and usually varying during the injection period). Then, a droplet parcel is injected assuming that it consists of only one droplet. The number of parcels injected at every time step is adjusted according to the total fuel injected (for example, for a typical diesel spray, approximately 1500-3000 parcels are injected from each of the injection holes over the injection period). This approach leads to a better representation of the droplet number density calculation as it will be more clear in chapter 4. The position of the injected parcels, forming initially the liquid core, is assumed to be the (x,y,z) coordinate of the injection hole exit from which they are injected. Their direction of movement coincides with the hole axis which is the same as the spray axis. Thus, the three (u,v,w) Cartesian velocity components of the injected parcels are calculated from the magnitude of the injection velocity and the hole orientation in the three-dimensional space. The initial droplet deformation is assumed to be zero. The temperature of the injected fuel is set equal to the temperature of the fuel in the FIE (possible thermal heating effects at the sac volume region are neglected). It has to be noted that the present model allows for the calculation of spray-to-spray variations of multihole inclined injection nozzles, since different injection conditions are calculated for individual injection holes from the FIE model. This is not the case in most of the other reported spray models where the calculations are performed by either assuming average flow conditions for all injection holes or by scaling the fuel injected per hole on the basis of experimental data for the spray tip penetration of each spray (Bo et al. (1997)).

3.3.4 Liquid jet atomization

3.3.4.1 General approach - literature review

Liquid atomization is an important phenomenon occurring in cases of injection of a liquid in a surrounding gas or even in vacuum. The term *atomization* expresses the

physical process by which the continuous liquid jet gradually disintegrates into a large number of small droplets and ligaments. These phenomenon is of major importance in combustion (and other mechanical and chemical applications), where a big number of droplets is required in order to improve the combustion characteristics or in general, to increase the performance of the system. Up to now, a lot of different ways of liquid atomizers have been developed, for example jet atomizers, swirl atomizers, rotary atomizers, air-blast and others. In the present investigation, the atomization of sprays injected from circular cross section orifices is examined.

It is generally accepted that the nozzle flow strongly affects the atomization process of a liquid injected from a nozzle. However, the experimental works tending to identify the flow characteristics within the injection holes are very limited. Also, CFD models cannot predict transient cavitating flows. In what follows the most significant research works on this field are described and the most important conclusions are presented.

Most of the works in this area have revealed that under practical diesel injection pressures (200 to 1500 bars), the flow in the injection holes is a two-phase cavitating flow. Based on this fact, most of the experimental techniques applied in order to identify the characteristics of that kind of flow are basically photographic techniques. As a consequence, only qualitatively characteristics of the flow have been identified. Also, due to the complexity of the geometry of real injectors, most of these works refer to simplified single hole nozzle geometries. Having also in mind that the dimensions of the real size injectors are of the order of 0.2 mm in hole or even smaller and that the pressure in the sac volume can be as high as 1500 bars, most of the relevant experimental works have been conducted in large scale models under steady-state conditions. Laser techniques have also been applied in simplified nozzle geometries, but these works have been used only in conditions were no cavitation occurs. From the above, it is clear that further investigation is required about the flow characteristics in the sac volume and injection holes area.

It is generally accepted that the atomization processes can be characterized from the relative magnitude of three dimensionless groups; these are the Reynolds, the Weber and the cavitation numbers which are defined as :

$$\text{Reynolds number : } \mathrm{Re} = \frac{U_{INJ} D_{HOLE}}{\nu} \qquad (3\text{-}53)$$

$$\text{Weber number : } We = \frac{\rho_{GAS} \cdot D_{HOLE} \cdot U_{INJ}^2}{\sigma} \tag{3-54}$$

$$\text{Cavitation number : } CN = \frac{P_{INJ} - P_{BACK}}{P_{BACK} - P_{CAV}} \tag{3-55}$$

were U_{INJ} is the mean injection velocity, D_{HOLE} is the diameter of the injection hole, ν is the kinematic viscosity of the injected fluid, ρ_{GAS} is the density of the surrounding gas, σ is the liquid surface tension, P_{INJ} is the injection pressure, P_{BACK} is the pressure of the injection chamber (i.e. the engine pressure under engine operating conditions) and P_{CAV} the fuel vapour pressure at a given temperature. The Weber number expresses the ratio of inertial over the surface tension forces. Although in an absolute sense its influence on atomization is no greater than that of surface tension, its importance stems from the fact that it affects not only the droplet size distributions in a spray but also the nozzle flow and spray pattern. An increase in viscosity lowers the Reynolds number and also hinders the development of any instabilities in the jet. The combined effect is to delay disintegration and increase the size of droplets in a spray. Usually, the Ohnesorge number (or viscosity group) is used to account for the effects of viscosity. This is defined as:

$$\text{Ohnesorge number } On = \frac{\mu_{LIQUID}}{(\rho_{LIQUID} D_{HOLE} \sigma)^{1/2}} \tag{3-56}$$

where μ_{LIQUID} and ρ_{LIQUID} are the kinematic viscosity and density of the liquid respectively. Cavitation number is an important parameter whose value depends on the design of the nozzle and the operating conditions.

In what follows, a literature survey is given for the various subjects related to the atomization processes. These can be divided into the following two categories: (i) nozzle and injection holes flow characteristics and (ii) effect of nozzle configuration on spray characteristics.

(i) Nozzle and injection holes flow characteristics

Experimental studies

One of the earliest works on the nozzle flow characteristics has been reported by Bergwerk (1959). In this study, single hole perspex nozzles were constructed, covering a range of hole diameters between 0.2 and 2.5 mm. Steady state flow conditions were tested, covering Reynolds number from 1000 to 20000, typical for the operating conditions of real nozzles. The flow pattern in the injection holes was photographed as a function of the cavitation number. It was revealed that there is a critical cavitation number (i.e. a critical sac volume pressure) above which cavitation occurs in the injection hole. This was found to be a function of the L/D of the nozzle as well as of the Reynolds number. The spray pattern injected from the above nozzles was also photographed and changes of the spray shape depending on the level of cavitation in the injection hole were identified. Hole cavitation was found to enhance atomization. Moreover, the so called 'hydraulic flip' hole flow pattern was identified to occur in cases were the resirculation zone formed in the hole entrance, was reaching the exit of the injection hole. Another interesting point was that for different operating conditions, covering a wide range of cavitation and Reynolds numbers and for different ratios of L/D of the injection holes, the discharge coefficient Cd of the hole was estimated and presented in a map, taking values from 0.6 to 0.8.

Not much attention was given to this area until 1989. One of the latest works has been conducted within the framework of the IDEA project by Chaves et al. (1989, 1995). In this work, real size transparent single hole nozzles (with hole diameter from 0.2 to 0.4 mm and L/D ratios from 2.5 to 8) were manufactured and operated under steady state flow conditions. Similar to Bergwerk's results, cavitation was found to occur above a critical injection pressure. Significant changes on the spray formation (spray cone angle, spray tip penetration and spray structure) from that of non-cavitating conditions were also observed. Two different types of cavitating flows were reported: cavitation were the formed bubbles were collapsing in the injection hole and super-cavitating caseswherethe bubbles were transported by the liquid velocity flow field and exit from the injection hole. In the former case, the level of turbulence in the injection hole was increased while in the latter one, a significant increment in the velocity at the

hole exit (injection velocity) was identified. This observation of the higher injection velocity due to the volume occupied by the cavitation bubbles has been also verified by other studies on droplet PDA measurements at the spray centerline close to the injector (Arcoumanis and Chang (1993)). Another contribution of this work was a development of an one-dimensional phenomenological model which calculates the effective injection velocity of the emerging liquid jet.

Another important work in this area has been reported from a Lucas research group (Soteriou et al. (1993, 1995)). In this work, different transparent enlarged injectors were constructed; single hole nozzles as well as real VCO nozzles were tested. Again, cavitation was found to be one of the major factors affecting the spray characteristics. Cavitation was again initializing when the cavitation number was bigger than a critical number for a certain geometric hole arrangement. By increasing the cavitation number, foam was formed in the injection hole. Further increment of the cavitation number was leading to hydraulic flip. This was identified to occur when the resirculation zone was extended over the injection hole; boundary layer theory was applied in order to explain the flow behaviour, the onset of cavitation and the hydraulic flip. The discharge coefficient (Cd) of the nozzles was measured and it was found to depend more on the cavitation number rather than on the Reynolds number. Also, above a cavitation number, the Cd was found to remain constant. Values from 0.65 for cavitating holes to 0.85 for non-cavitating holes were reported. In addition, for the real size VCO nozzle, completely different spray patterns injected from different holes were photographed; these differences were attributed to the needle eccentricity and the cavitation level in each of the holes, i.e. depending on the characteristics of the nozzle flow field. It was also proposed that under real operating condition, only the case of super-cavitating flow occurs, and as a consequence, this was believed to be the main mechanism causing atomization. Unlikely from the single hole nozzles, hydraulic flip was not observed in the multihole VCO nozzle.

Park and Lee (1994) have reported a very interesting work on the flash atomization mechanism. The idea of this work was to use large scale transparent rectangular shaped single hole nozzles operating under steady state conditions with preheated liquid in order to create boiling flow in the nozzle. The level of gas concentration in the flow could be adjusted as desired. In this way, different two phase flow regimes, the so called bubbly, slug and annular were generated. The associated

effect on the injected sprays were quantified by measuring the droplet sizes using a Malvern particle sizer and by measuring the spray cone angle. Completely different spray shapes were observed for the different two-phase flow regimes in the injection hole. For the same flow pattern in the injection hole, completely different spray structures were observed depending on the temperature of the injected fuel and revealing the dependency of the processes on thermodynamic effects as well as on physical properties of the mixture. Information for the droplet size was given, showing smaller droplets for higher level of bubble concentration in the injection holes and for higher injection temperature. Also, similar trends were measured for the spray cone angle: the higher the level of the bubbles concentration, the higher the spray cone angle. For the same internal flow conditions, the L/D of the injection holes was found not to affect significantly the spray characteristics. Similar spray characteristics were observed for sprays injected from circular nozzles, with the same internal flow characteristics.

A Nippondenso research group (Date et al. (1993, 1996)) has visualized the flow in the injection hole of an enlarged transparent nozzle using a particle tracking technique. Two different sac volume geometries, close to that of real injectors, were tested under steady conditions. Due to the method used for the flow visualization, only non cavitating conditions were investigated. The recirculation zones at the hole entrance were observed and information about the pressure drop in the injection holes and the needle seat areas for different needle lifts and flow rates was given.

In another work by Zhen et al. (1994), a similar approach of large scale nozzle models were used in order to identify the pressure characteristics in the injection hole. Single hole orifices were used with 1.5 mm diameter and L/D ratios 2, 4 and 10. In this work, a static pressure tap was incorporated in the injection hole, close to the wall. Using a mercury manometer, the pressure characteristics inside the hole were evaluated. From these measurements, a typical pressure distribution in the injection hole was estimated for the cavitating and the hydraulic flip cases. Significant effects of the nozzle flow on the spray characteristics were identified by measuring the spray cone angle as well as the droplet Sauter mean diameter of the spray formed at the hole exit.

Attempts using laser techniques have also been performed in order to identify the flow characteristics in the nozzle. Arcoumanis et al. (1992), used a refractive index matching technique in order to measure the velocity flow field in the gallery and in the nozzle pipe of an enlarge transparent model of an injector. The results, for different flow

rates and different valve lifts, confirmed that the flow before the needle seat passage was a well developed turbulent pipe flow (i.e. the three-dimensional flow field in the nozzle gallery has small effect on the flow conditions just before the sac volume). This information is useful for the modeling of the flow in fuel injection systems, since several assumption should be adopted both for one-dimensional or three-dimensional sac volume CFD models. This work was not extended to the sac volume and injection holes areas.

Finally, in another work by Knox-kelecy and Farrell et al. (1993), the turbulence characteristics of the flow in the injection hole were measured by using a PDPA laser technique. Different L/D ratios (from 1.3 to 7.7) of single hole nozzles with different entrance shapes (r/D from 0.0 to 0.3) operating under a typical Reynolds number of 10.000 (corresponding to an equivalent injection pressure of 670 bars) were tested. The main aim of this work was to identify the spectral characteristics of the turbulence in the injection hole as a function of the hole geometry. However, it is not clear if these results can be extended to real shape nozzles operating under transient and usually cavitating conditions.

Computational studies

Due to the limited physical knowledge of the flow characteristics in the injection holes, the computational studies trying to predict the flow field in this area are very limited. Theoretical approaches should be divided in two major categories: one-dimensional and three-dimensional models.

The three-dimensional models solve for the full Navier-Stokes equations describing the flow field of any fluid in motion. Until now, all of the developed models use similar discretization schemes and pressure correction methods in order to simulate the flow field in the sac volume area. However, it should be mentioned from the beginning that the models used have not been fully validated since no experimental information is available about the detailed velocity flow field in the sac volume and the injection holes. Also, most of these works refer to steady state non-cavitating conditions. This is due to the fact that the flow characteristics during the injection period just before the needle seat can not be measured. As a consequence, this information which is required by that kind of models is usually not available. One-dimensional

models describing the pressure wave propagation in the fuel injection system can provide this information, but such an attempt has not been performed until now. In addition, the equations describing the physical details about the onset of cavitation and the development of the resulting two-phase flow can not be easily applied due to the complexity of the geometry; thus, several assumptions have to be made. Due to the absence of such information, these models usually simulate only the steady non-cavitating flow through the injection holes. The main contribution of such models is that they give a qualitatively information of the effect of small changes of the sac volume geometry on the flow field and the corresponding discharge coefficient, for example Ohrm et al. (1991), Okajima et al. (1991), Oishi et al. (1992) and others.

A series of CFD studies of the flow field in the sac volume and the injection holes comes from Nippondenso Co. (Date et al.(1992, 1993, 1996), Okazima et al. (1991)). The Navier-Stokes equations were numerically solved by applying a first order upwind differential method, the standard k-ε model for the simulation of the turbulence and the SIMPLE method for the pressure correction procedure. Different sac volume geometries were tested covering standard sac volume and VCO nozzles and various hole inclination angles. The flow rates from each hole was calculated, as well as the spatial distribution of the pressure and velocity flow field in the sac volume and the injection holes. Parametric studies were performed giving information about the flow characteristics under different needle lift positions and operating conditions. The validation of the model was based on the measured and the calculated discharge coefficient of the simulated geometries. The results were correlated with experimental spray data injected from nozzles of the simulated geometries and it was attempted to correlate basic spray characteristics, such as the spray tip penetration, with the internal nozzle flow field.

A similar work was performed at Nissan Diesel Motor Co. (Oishi et at. (1992)), who predicted the flow field through a five-hole sac-type nozzle using the commercial CFD code STAR-CD. The results were again compared with the measured discharge coefficient of each individual hole, showing a very good agreement. Information was given about the velocity profile at the hole exit. The results showed that the injection velocities are different from hole to hole, depending on the hole inclination angle relative to the needle seat axis. Also, the velocity profile across the hole diameter was found to reassemble to a turbulent pipe flow velocity. As a consequence, the maximum

value of the velocity profile in the injection hole was very close to the value of the mean injection velocity.

Finally, another CFD work by Bruni et al. (1993), gave information about the flow field in a VCO nozzle. Differences in the flow rate amongst the injection holes were identified and attributed to the asymmetry of the injection hole position relative to the needle seat axis. The same group has reported another work on the effect of the sac volume geometry on the measured characteristics of the sprays which will be described later on. The measured spray tip penetration was correlated with the flow characteristics of the individual holes of the VCO nozzle.

On the other hand, the one-dimensional models usually use the available experimental data for the discharge coefficient of real size nozzles (for example Bergwerk (1959), Solomon and Faeth (1985), Lefebvre (1989, 1991), Soteriou et al. (1993, 1995), Karasawa et al. (1994) and others) in order to calculate the mass flow rate through the injection holes under transient cavitating or non-cavitating conditions of real multihole nozzles. That makes these models widely used in industry. The injection pressure (sac volume pressure) should be also known, and its value is usually predicted by fuel injection simulation models. A series of parametric studies of the effect of different sac volume shapes on the predicted flow rate is given by Dreeben et al. (1992); another work has been reported by Kano et al. (1990).

(ii) Effect of nozzle configuration on spray characteristics

Except for the investigations revealing the dependency of the spray structure on the internal nozzle flow (Bergwerk (1959), Chaves et al. (1995), Soteriou et al. (1993, 1995), Park et al. (1994)), a number of other investigations have also been reported verifying that different sac volume or injection hole geometries affect the characteristics of the injected sprays. All of these works are experimental ones, and they can be divided into two categories. In the first one, the primary break-up of usually steady sprays is investigated. In the second one, the spray characteristics are measured far away from the spray liquid core, for different nozzles geometries. In that way, the effect of the sac volume shape, or the hole to hole spray variations of multihole injectors can be identified; however, only qualitative conclusions can derive about the effect of the nozzle configuration on the spray characteristics.

Near nozzle spray structure

A lot of studies have been performed until now on the primary break-up of liquid jets emerging from circular holes, initially expressed mathematically by Rayleigh (1878). Also, various theoretical phenomenological models have been developed trying to predict the droplet sizes formed during the primary break-up of liquid jets. An analytical description of all of the developed models is given in the following sections. Representative works on this field are following described.

An extensive review of the different steady state spray structures produced by holes with different L/D ratios, different hole entrance shapes and different turbulence levels has been reported by McCarthy and Molloy et al. (1974) for non-cavitating hole flow conditions. Information about how the nozzle design affects the characteristics of the emerging jet was given. Furthermore, simple theories trying to predict the behaviour of that kind of jets were summarized. It is important at this point to present Figure 3-1 which summarizing the generally accepted dependence of the liquid core break-up length on the injection velocity. The initial dashed part of this curve below point A corresponds to drip flow. Point A denotes the lower critical velocity at which the drip flow changes to jet flow. From A to B the break-up length increases linearly with velocity. This part of the curve corresponds to disintegration of the jet due to surface forces as studied by Rayleigh (1878) and Weber (1931). Point B on the stability curve corresponds to the change in the break-up mechanism from varicose to sinuous (the term 'varicose' is usually used to describe jet deformation without the influence of air). It is not clear why the break-up length decreases in the transition region (between points B and C). This is usually attributed to turbulence generation within the liquid jet. For even higher injection velocities, where fully turbulent conditions have been obtained in the nozzle, the break-up length increases with injection velocity, regardless of the detailed mechanisms causing atomization. However, it is uncertain what happens to the shape of this curve if the jet velocity is increased indefinitely. Beyond point D, the fully atomization regime occurs, usually caused by the onset of cavitation in the injection hole.

Many other investigations, for example, Castman (1932), Phinney (1973), Hiroyasu et al. (1982), Chehroudi et al. (1985), Oza and Sinnamon (1983), Chigier et al. (1993), Yule and Salters (1995), Zeigerson-Katz et al. (1996), have shown that the

liquid jet requires a finite distance to fully atomize. This distance is usually referred to as 'break-up length' and in some cases may be comparable to the distance between the hole exit and the point of impingement (as evidenced of Yule and Filipovic (1992)).

Similar works, although not as extensive as the previous one, has been reported by Hiroyasu et al. (1991), Hosoya and Obokata (1993) and Xu et al. (1993). Again, the same conclusions about the break-up length of a steady state liquid jet were reported. Lefebvre (1989) summarizes most of the reported correlations on the break-up length and time.

A work in the same area has been reported by Faeth et al. (1995). The effect of initial flow conditions on primary break-up of non-turbulent and turbulent liquid jets emerging from large scale pressure atomizers was studied; it was revealed that the jet exit conditions, particularly the presence of vorticity due to turbulence or due to variations of mean velocity from viscous effects in boundary layers along the injector passage, play a dominant role in primary break-up along the surfaces of liquid jets. Non-turbulent flows with boundary layers at the jet exit undergo non-turbulent primary break-up and yield drop sizes that correlate with the thickness of boundary layers at the passage walls near the jet exit. More disturbed conditions at the inlet increase the range of conditions where turbulent primary break-up can be observed, depending on the L/D of the hole, the hole entrance shape and the Reynolds number. Also, the drop sizes as well as the location of the onset of turbulent primary break-up were estimated and correlations for these magnitudes were proposed, valid only for cases where the aerodynamic effects are small.

Koo and Martin (1995) studied similar to the previous investigation near nozzle jet characteristics but for transient fuel sprays and for a wider range of gas ambient conditions. The spray characteristics were found to depend on the level of turbulence in the injection hole. The latter was calculated to be a function of the needle lift position. The effect of the density of the surrounding gas was also found to play an important role on the rms fluctuating velocity at the near nozzle region. It was also revealed by microphotographs that the spray angle was time dependent, even for injection into near vacuum conditions,whereatomization occurred even in the absence of ambient gas.

A completely different investigation has been published by Santangelo et al. (1995). They studied the near nozzle spray structure of an effervescent atomizer produced spray, by holographic imaging. In this investigation, air was injected together

with the liquid. The studies showed that increasing the air-liquid ratio resulted in a complex evolutionary break-up process. At air-liquid mass ratios of less than 2%, the break-up process was governed by individual bubble expansion. A cylinder of liquid was observed exiting the final orifice and then exploding into ligaments and drops due to rapidly expanding bubbles. At air-liquid ratios greater than 5%, the length of the cylinder of liquid was substantially reduced and sometimes even eliminated. Portions of the liquid were replaced by a ring of limbs, which formed a 'tree'. As the air-liquid ratio was increased, the liquid cylinder decreased in length and the ring of limbs evolved from a small number of large limbs to a higher number of thinner limbs and branches. The holograms also showed that an increase in viscosity increases the diameters of the fluid structures, although the effect was minimal at low viscosities. In addition, a decreasing surface tension was observed to decrease the diameter of the fluid structures.

Global spray characteristics

Another area of research concerns the effect of different nozzle shape configurations on the spray characteristics (spray tip penetration, spray cone angle, droplet size) far from the near-nozzle area. Single-hole special shaped nozzles or real geometry multihole nozzles operating under steady of unsteady conditions have been examined. However, except the injector geometry, a lot of other factors, such as the liquid properties and the operating condition affect the spray development. Also, only representative nozzle shapes can be tested which implies that only quantitative knowledge on how the nozzle geometry affects the spray structure. In what follows, the conclusions of some representative works in this area are summarized.

Dodge et al. (1992) studied the effect of 12 different hole shapes on the spray droplet size and spray cone angle. All hole shapes were circular in cross-section with minimum diameters of 0.4 mm and included converging and diverging hole shapes. Overall hole lengths were constant at 2.5 mm (giving a ratio L/D=6.2). The ambient gas temperature was 300°C, while the gas density was about one-half of the density of a typical diesel engine at the time of injection; only steady state injection conditions were tested. As an overall conclusion from this work, no special hole shape was found to produce dramatically enhanced mixing rates or better atomization quality. Also, the

spray angle was not found to depend dramatically on the hole shape. The droplet sizes were found to depend more on the injection pressure rather than on the hole geometry.

In another work by Hosoya et al. (1993), again steady state sprays were tested for different sac volume geometries, varying from single-hole to real multihole nozzles. The droplet size and droplet velocities were measured with a PDA system. Typical diesel engine injection conditions were applied in the injection system, while the spray was injected under atmospheric conditions. The results showed that the sprays injected from multihole injectors have different droplet velocities and droplet sizes from these injected from single hole injectors, although no explanation was given.

A more interesting work has been published by Campanella et al. (1994). In these studies, two five-hole VCO nozzles were used. The geometrical differences between the two nozzles were concentrated in the needle diameter. An analysis was carried out examining how the injection quantity was altered with the running time of the nozzles as well as with the injection pressure. The main aim of this investigation was the identification of the variations of the spray characteristics injected from each of the five holes. Differences in the spray tip penetration and the spray cone angle were observed as well as in the images of the five sprays. These were attributed to the location of the injection holes relative to the needle seat. These differences were smaller for higher injection pressures. By comparing the spray characteristics of the two different nozzles, it was found that big differences were present, which implied that the needle shape is of great importance in the designing of VCO nozzles. In a similar study by Giorgio et al. (1995), SMD values of the spray droplets at various times from the start of injection as well as at different locations from the injection holes showed big differences, as a function of the needle shape, the injection pressure, the injection duration and the hole position relative to the needle. All these investigations confirm that the spray characteristics are affected by a lot of different and very often, contradicting factors.

Another work by Hiroyasu et al. (1991) showed that the spray characteristics are affected by the shape of the hole entrance. Different hole entrance shapes can induce hole cavitation. Also, big asymmetries of the droplet distribution within the spray cone angle relative to the spray axis were measured, caused by asymmetries of the shape of the hole entrance. Another work by Williams (1978) showed big differences of the droplet size distribution of sprays injected from nozzles with different sac volume

geometries; similar conclusions were proposed by Synder and Reitz (1996) who examined the effect of hole size on the atomization process.

Arcoumanis et al. (1993) reported a different investigation on the effect of different nozzle configurations on the measured spray characteristics. Two Stanadyne pencil-type nozzles were used, with the same sac volume and injection holes configuration, the same nozzle opening pressure but with different needle specification. The first was an single-stage injector while the other was a two-stage injector. It was revealed how the spray characteristics, measured by a PDA system were altered from the single- to the two-stage injector. This was a further evidence that the spray characteristics depend on the internal nozzle flow, which depends on the needle movement.

3.3.4.2 Liquid core atomization modeling

In this section a more detailed approach on the atomization mechanism of a liquid jet is performed. The parameters leading the liquid jet to disintegrate have been identified in the past to include the liquid physical properties (surface tension and viscosity), the ambient gas conditions, the velocity profile at the exit of the injection hole, and especially, the type of the atomizer. It is already clear from the previous section that, for diesel spray atomizers, the mechanisms causing a liquid jet to disintegrate is usually the presence of cavitation in the injection holes. Also, the internal jet turbulence plays an important role. Aerodynamic effects are present but not important if cavitation occurs in the injection holes as it will be demonstrated latter on in this section.

The atomization processes can be divided into laminar, turbulent and cavitating cases depending on the type of flow in the injection hole. Usually, the aerodynamic effects are present in laminar and coexist in turbulent jet atomization regimes. When cavitation occurs in the injection hole, experimental studies confirm that it is usually the dominant factor inducing atomization. Theories describing the disintegration of laminar steady state jets are now well developed. These theories can take into account the effect of gas compressibility or the evaporation of the liquid jet present at injection in a hot environment. However, for atomization cases dominated by the turbulence of the injected liquid, only phenomenological models have been developed. For more

complicated cases such as unsteady turbulent or cavitating jets, further investigation is required. The unsteady cases are usually treated as quasi-steady, since the internal flow field in the emerging liquid jets is not modeled by any of the developed theories. It is usually assumed that the variations of the injection velocity during the injection period do not affect the disintegration of the liquid already injected or to be injected (i.e. at every time step it is assumed that the liquid jet disintegrates with the same manner as if it was injected with constant injection velocity). Following, a description of the relevant publications is given.

(i) Aerodynamic-induced atomization

The earliest investigations into jet flow phenomena appear to have been carried out by Bidone (1829) and Savart (1833). Bidone's research was concerned with the geometric forms of jets produced by nozzles of non-circular cross section, while Savart supplied the first quantitative data related to jet disintegration.

An early mathematical investigation on the primary break-up of liquid jets emerging from circular orifices has been performed by Rayleigh (1878). In this work, the size of the droplets created at a distance from the nozzle (usually referred to as break-up length) was calculated, by employing the method of small disturbances. This work, although fundamental, was limited to laminar steady jets

A more general theory for disintegration for low viscosity liquids was developed by Weber (1931), who extended Rayleigh's analysis to include viscous liquids. He assumed that any disturbance causes rotationally symmetrical oscillations of the jet. If the wavelength of the initial disturbance is smaller than a critical value, the surface forces tend to damp out the disturbance. In the opposite case, the surface tension forces tend to increase the disturbance, which eventually leads to disintegration of the jet. There is, however, one particular wavelength that is most favorable for drop formation. Weber also considered the case where the air motion induces wave formation and showed that this can occur only at relative velocities above a certain minimum value.

The most commonly quoted criteria for classifying jet disintegration are those proposed by Ohnesorge (1936). From photographic records of jet disintegration, Ohnesorge classified the images according to the relative importance of gravitational, gas inertial, surface tension and viscous forces. He used dimensionless analysis to show

that the break-up mechanism of a jet could be expressed in three stages, each stage characterized by the magnitudes of Reynolds and Ohnesorge numbers. A map showing the various atomization regimes was constructed and it is given in Figure 3-2. The left hand side of this chart corresponds to the Rayleigh atomization regime (low Reynolds numbers); surface tension forces induce instability of the axisymmetric jet surface perturbations whose wavelengths are greater than the jet periphery. The amplitude of these perturbations becomes unstable many diameters below the hole while the size of the formed droplets is almost double of the size of the nozzle. As the injection velocity increases, the perturbations on the surface of the liquid jet grow and finally cause the disintegration of the jet. This regime is usually called wind-induced atomization regime, while the surface waves are usually referred to as Kelvin-Helmholtz instabilities. Usually, a wide range of droplet sizes is produced. For even higher injection velocities, the surface disintegrates in an unpredictable way. The average droplet size formed is much smaller than the hole diameter. For even higher injection velocities, the disintegration starts almost immediately at the hole exit; this is usually referred to as the atomization regime.

Transition conditions between the atomization regimes are necessary for the purpose of theoretical modeling of the atomization process. Some of the commonly accepted criteria declare that the transition from the drip flow happens at We=4. The transition boundary from the Rayleigh to wind-induced regime is associated with a combination of the Weber and Laplace numbers while no criterion has been proposed for the transition from the first to the second wind-induced primary break-up regime. Many subsequent studies have been performed in this area, all of them trying to predict the break-up length, the break-up time and the size of the droplets formed under conditions of practical interest and most of them are based on experimental data. Empirical correlations have derived giving the break-up time and length and the droplet size as a function of the injection velocity, injection hole diameter, pressure and density of the ambient gas (for example Hiroyasu et al. (1982)). A summary of these correlations is given by Lefebvre (1989) while Anno (1977) gives the mathematical formulation of the mechanics of liquid jets while Bayrel and Orzechowski (1993) give a similar mathematical formulation.

In another study by Reitz and Bracco (1982) it was assumed that the break-up of the liquid jet was induced by a surface wave growing on the liquid jet surface (Kelvin-

Helmoltz instability), originated by the relative motion between the liquid and the surrounding gas. The break-up time and the size of the formed droplets were calculated as a function of the relative velocity between the jet and the gas, the densities of the jet and the surrounding gas and the diameter of the injection hole. From the analysis it was revealed that the phenomena occurred in such conditions can be described by a group of dimensionless parameters: the Weber, the Ohnesorge and the Reynolds numbers.

Based on previous analysis, Lian and Reitz (1993), examined the effect of gas compressibility and jet vapourization on the atomization of a liquid jet. It was found that the growing of the surface waves depends on the vapourization level of the surface. The growth rate was accelerated in the Rayleigh regime while it was decelerated in the atomization regime. The gas compressibility was found to have a destabilizing effect on the surface deformation and also to be important only for Mach numbers (calculated with the relative velocity between the liquid and the gas) greater that 0.3.

In a similar work by Xianguo Li (1995), a complete mathematical analysis on the development of the surface waves of liquid jets injected from a circular orifice was presented. Viscous effects as well as three-dimensional phenomena were taken into account. The analysis gave the same results for the jet stability in the Rayleigh regime, where the three-dimensional phenomena were relatively unimportant for low Weber numbers. However, for large Weber numbers, the surface wave growth rate becomes almost identical to that of varicose waves. In particular, sinus waves can become the most unstable waves under certain flow conditions within the wind-induced break-up regime. As the Weber number is increased, more and more three-dimensional disturbances become unstable and significant, and hence, the jet break-up process becomes more and more complicated. The results of this theory were found to agree well with experimental observations. It should be noted that all of the described theories assume constant injection velocity. However, as it is discussed by Lefebvre (1989), the variable injection velocity present in most cases of practical interest is another factor affecting atomization.

(ii) Jet turbulence-induced atomization

As it has already been discussed in previous sections, jet turbulence is an important factor affecting atomization. For fully turbulent conditions in the injection

hole, the radial velocity component in the jet soon leads to disruption of the surface film followed by general disintegration of the jet. It should be noted that when the issuing jet is fully turbulent, no aerodynamic forces are needed for break-up. Even when injected into a vacuum, the jet will disintegrate solely under the influence of its own turbulence.

Several experimental studies have been published showing the effect of jet turbulence on jet disintegration. However, no theory has been developed able to represent the phenomena occurring under these injection conditions. Only phenomenological correlations or models exist. These are based on experimental observations, which denotes that experimental coefficients are required to make model predictions comparable to the experimental data. It should be also mentioned that due to the small scales and poor optical accessibility under diesel engine injection conditions, no adequate experimental information exist for that type of atomization. Usually, the models are validated against measurements of consequential features, such as the spray angle and peripheral droplet size.

Among the research works on the turbulence-induced atomization, investigations by Wu et al. (1993, 1995) have shown how jet turbulence induces atomization. The effect of boundary layers formed along the walls of the injection hole was found to be an important factor. The size of the formed droplets was correlated with the boundary layer thickness. Also merged primary and secondary break-up was taking place when the Rayleigh break-up times of ligaments formed by turbulent fluctuations were longer than the secondary break-up time of similar sized droplets. Phenomenological analysis based on the experimental observations yielded reasonable correlations for the break-up length and the droplet size for the enhanced aerodynamic break-up regime.

A phenomenological model of diesel spray turbulence-induced atomization has been reported by Huh et al. (1991). As it has already been described, gas inertia has been invoked to explain atomization via the mechanism of the surface wave growth. However, in this analyses it was assumed that the surface instability occurs at the most unstable wavelength. The latter was independent of the initial surface perturbations. At this model, it was postulated that turbulent fluctuations within the liquid emerging from the injection nozzle were the producers of the initial surface perturbations, which occur predominantly at a certain characteristic wavelength, proportional to the integral turbulence scale. A connection was thereby established, for the turbulence structure at

the nozzle exit. From this, the break-up time, the size of the secondary droplets and the spray cone angle were calculated using phenomenological integral relationships.

(iii) Cavitation-induced atomization

When cavitation initializes in the injection hole, dramatically changes occur in the spray structure. Experimental results by Bergwerk (1959), Soteriou et al. (1993) and (1995), Chaves et al. (1995), Park et al. (1994) and Zhen et al. (1994) verify the above statement. However, theoretical investigations on the cavitation induced atomization are very limited.

Oza and Sinnamon et al. (1983) published a theoretical investigation on the bubble growth originated by preheating the fuel flowing through a nozzle. A thermodynamic approach was combined with equations describing the bubble dynamics in two phase bubbly flows and the results were found to explain the measured increment of the velocity at the nozzle exit, and also the faster spray tip deceleration. The bubble number density was modeled and found to improve atomization as it was also supported by photographic investigations on the spray structure. Higher spray cone angles were observed for higher bubble number densities in the two-phase mixture. The calculated bubble radius and time scales of the phenomenon were found to be in agreement with the experimental observations.

Another study by Fujimoto et al. (1991) and Senda et al. (1994) on the modeling of atomization processes in flash boiling sprays was applied to injection systems of gasoline engines. The main features of this model were the process of bubble nucleation inside the nozzle, the fuel vapourization due to the growth of the cavitation bubbles and the break-up of the fuel film at the exit of the injector (note that a non-cylindrical nozzle was modeled in this investigation, which is not the case for diesel nozzles). A fairly quantitative estimation of the droplet diameter and the vapour mass fraction was obtained as a function of the back pressure. The calculation results were found to agree with the experimental ones, although experimental information about the nucleation process was necessary for the estimation of the experimental coefficients of the model.

During the present investigation, three different atomization models were tested in order to examine how well or not they predict the available experimental data. These are a model accounting for the aerodynamic-induced atomization, a model accounting

for the jet-turbulence induced atomization and a newly developed model accounting for the cavitation-induced atomization. In what follows, their mathematical formulation is given and described in detail.

3.3.4.3 Model for the aerodynamic-induced atomization

The analysis considers the stability of infinitesimal waves on an axially symmetric jet surface of infinite length. The flow is assumed to be incompressible and a cylindrical coordinate system is chosen which moves with the jet. Under these assumptions the linearized Navier-Stokes equations can be written in the form:

$$\frac{\partial u_i}{\partial z}+\frac{1}{r}\frac{\partial}{\partial r}(r v_i)=0 ,$$

$$\frac{\partial u_i}{\partial t}+U_i(r)\frac{\partial u_i}{\partial z}+v_i\frac{dU_i}{dr}=-\frac{1}{\rho_i}\frac{\partial p_i}{\partial z}+\frac{\mu_i}{\rho_i}\left[\frac{\partial^2 u_i}{\partial z^2}+\frac{1}{r}\frac{\partial}{\partial r}(r\frac{\partial u_i}{\partial r})\right] \qquad (3\text{-}57)$$

$$\frac{\partial v_i}{\partial t}+U_i(r)\frac{\partial v_i}{\partial z}=-\frac{1}{\rho_i}\frac{\partial p_i}{\partial r}+\frac{\mu_i}{\rho_i}\left[\frac{\partial^2 v_i}{\partial z^2}+\frac{\partial}{\partial r}[\frac{1}{r}\frac{\partial (r v_i)}{\partial r}]\right]$$

where the subscript i={JET,GAS} denotes liquid and gas phase, respectively, U_{JET}=0 while U_{GAS} (r) is a specific axial velocity profile in the gas. Hence, u,v and p are the velocity and pressure perturbations about the mean motion in the gas and liquid flows. With the assumption that the surface wave elevation $n<<r_{JET}$, the kinematic, tangential and normal stress interface conditions at $r= r_{JET}$ are to first order:

$$v_i=\frac{\partial \eta}{\partial t}+U_i\frac{\partial \eta}{\partial z} \qquad (3\text{-}58)$$

$$\frac{\partial u_{JET}}{\partial r}=-\frac{\partial v_{JET}}{\partial z} \qquad (3\text{-}59)$$

$$-p_{JET}+2\mu_{JET}\frac{\partial u_{JET}}{\partial z}-\frac{\sigma}{r_{JET}^2}(\eta+r_{JET}^2\frac{\partial^2 \eta}{\partial z^2})+p_{GAS}=0 \qquad (3\text{-}60)$$

where μ is the liquid kinematic viscosity (the gas phase has been assumed to be inviscid) and σ is the surface tension. Further boundary conditions are symmetry at

the jet axis (r=0) and u_{JET}, v_{JET} and $p_{JET} \rightarrow \infty$ for $r \rightarrow \infty$. Equations (3-57) can be solved by introducing a velocity potential , and a stream function of the form:

$$\phi_{JET} = \Phi_{JET}(r)e^{ikz+\omega t} \ , \Psi_{JET} = \Psi_{JET}(r)e^{ikz+\omega t} \ ,$$
$$\Psi_{GAS} = [U_{GAS}(r) - i(\omega/k)]\eta\, \phi(r) \qquad (3\text{-}61)$$

where $\eta = \eta_0 e^{ikz+wt}$ (η_0 is the initial wave amplitude), k is the wavenumber, and R(ω) is the wave growth rate. Substituting these definitions into equation (3-57) for the liquid flow yields the solution:

$$\Phi_{JET} = c_1 I_0(kr) \ , \ \Psi_{JET} = c_2 r I_1(lr) \qquad (3\text{-}62)$$

where I_n is the n^{th} order modified Bessel function of the first kind, c_1 and c_2 are arbitrary constants and $l^2 = k^2 + \omega/\nu_{JET}$. For the gas phase similar analysis leads to an Orr-Sommerfeld equation for f(r), and under the assumption that $U_{GAS}(r)=U_{JET}$, equation (3-58) may be solved to give the gas pressure:

$$p_{GAS} = -\rho_{GAS}\,(U_{JET} - i\frac{\omega}{k})^2\, k\, \frac{K_0(k \cdot r_{JET})}{K_1(k \cdot r_{JET})}\eta_0\, e^{ikz+\omega t} \qquad (3\text{-}63)$$

where K_n are Bessel functions of the second kind. Finally, equations (3-57) and (3-58) can be used to relate the constants c_1, c_2 and η_0 in equations (3-62) and (3-63), and with the relation $p_{JET} = -\rho_{JET}\frac{\partial \phi_{JET}}{\partial t}$ equation (3-59) yields the dispersion relationship:

$$\omega^2 + 2\nu_{JET} k^2\, \omega[\frac{I_1'(k \cdot r_{JET})}{I_0(k \cdot r_{JET})} - \frac{2kl}{k^2+l^2}\frac{I_1(k \cdot r_{JET})}{I_0(k \cdot r_{JET})}\frac{I_1'(k \cdot r_{JET})}{I_1(k \cdot r_{JET})}] =$$

$$\frac{\sigma k}{\rho_{JET} r_{JET}^2}(1 - r_{JET}^2 k^2)\frac{l^2-k^2}{l^2+k^2}\frac{I_1(k \cdot r_{JET})}{I_0(k \cdot r_{JET})} + \qquad (3\text{-}64)$$

$$\frac{\rho_{GAS}}{\rho_{JET}}(U_{JET} - \frac{i\omega}{k})^2 k^2 \frac{l^2-k^2}{l^2+k^2}\frac{I_1(k \cdot r_{JET})}{I_0(k \cdot r_{JET})}\frac{K_0(k \cdot r_{JET})}{K_1(k \cdot r_{JET})}$$

where the prime indicates differentiation. Equation (3-64) relates the wave growth rate ω to its wavelength k, but its solution is complicated by the fact that the parameter l is still a function of ω. Various limiting forms of equation (3-64) have been studied, particularly for low speed jets. This equation includes the results of previous investigations as special cases. Thus, for example, with $p_{GAS}=\mu_{JET}=U_{JET}=0$, equation (3-64) reduces to

$$\omega^2 = \frac{\sigma}{\rho_{JET}\, r_{JET}^2} k(1 - r_{JET}^2 k^2) \frac{I_1(kr_{JET})}{I_0(kr_{JET})} \tag{3-65}$$

This is the result of Rayleigh for low-speed inviscid jets which predicts that longer wavelength surface waves are responsible for the break-up of the jet and droplets are produced with diameters larger than the jet diameter.

The limiting case of interest for jet atomization is $kr \to \infty$ since the droplet sizes are much smaller than the jet diameter. This limit of equation (3-65) should be distinguished from the limit kr~1 which was considered by Weber, where the droplet sizes are still of the order of the jet diameter. Indeed, replacing the Bessel function in equation (3-64) by their asymptotic values for $kr \to \infty$ yields the result:

$$\begin{aligned}(\omega + 2k^2)^2 + \sigma k^3/\rho_{JET} - 4\nu_{JET}^2 k^3 (k^2 + \omega/\nu_{JET})^{1/2} \\ + (\omega + iU_{JET}k)^2 (\rho_{GAS}/\rho_{JET}) = 0\end{aligned} \tag{3-66}$$

in which it is seen that the wave growth rate is now independent of the jet diameter. For numerical studies, the maximum growth rate and its corresponding wave length are given by the equations:

$$\begin{aligned}\frac{\Lambda}{r_{JET}} &= 9.02 \frac{(1+0.45Z^{0.45})(1+0.4T^{0.2})}{(1+0.87We_{GAS}^{1.67})^{0.6}} \\ \Omega\left[\frac{\rho_{JET}\, r_{JET}^3}{\sigma}\right]^{0.5} &= \frac{(0.34+0.38We_{GAS}^{1.5})}{(1+Z)(1+1.47T^{0.6})}\end{aligned} \tag{3-67}$$

where Λ and Ω characterize the fastest growing (or most probable) wave on the liquid surface. In these correlations $Z = We_{JET}^{0.5}/Re_{JET}$ and $T = Z \cdot We_{GAS}^{0.5}$. Reitz and Bracco (1982) modeled the liquid atomization by postulating that new drops with radius r are formed from the liquid jet (with radius r_{JET}) with

$$\begin{aligned} &r = B_0 L \qquad \text{if } B_0 \cdot \Lambda \le r_{JET} \\ &\text{or} \\ &r = \min\{[\frac{3\pi \cdot r_{JET}^2 \cdot U_{JET}}{2 \cdot \Omega}]^{0.33}, [\frac{3 r_{JET}^2 \cdot L}{4}]^{0.33}\} \quad \text{if } B_0 \cdot \Lambda > r_{JET} \end{aligned} \tag{3-68}$$

where B_0 is a constant taken equal to 0.61. In the above equation it is assumed that small droplets are formed with droplet size proportional to the wave length of the fastest growing or most probable unstable surface wave. The rate of change of droplet radius in a liquid element emerging from the nozzle was described using the expressions:

$$\begin{aligned} &\frac{dr}{dt} = -\frac{r_{JET} - r}{\tau} \quad (r \le r_{JET}) \\ &\tau = 3.726 \frac{B_1 r_{JET}}{\Lambda \Omega} \end{aligned} \tag{3-69}$$

where $r(t=t_0) = r_{JET}$ in the initial droplet (jet radius) and $B_1 = 10$. The spray cone angle is calculated from the correlation

$$\tan\frac{\theta_{SPRAY}}{2} = A \cdot \Lambda \cdot \Omega / U_{JET} \tag{3-70}$$

where A is a constant depending on the nozzle design, and usually taking values between 4 and 8.

3.3.4.4 Jet turbulence-induced atomization

This model has been developed at Imperial College by Huh and Gosman (1991). It considers both the turbulence fluctuations at the exit of the injection hole and the jet surface wave growth mechanisms caused by the Kelvin-Helmholtz instabilities. From

the injection hole flow analysis, the emerging liquid jet turbulence time and length scales can be estimated at the hole exit as a function of the turbulence kinetic energy and its dissipation rate as:

$$L_{TURB} = C_{\mu} \frac{K_{TURB}^{3/2}}{\varepsilon_{DISS}}$$
$$\tau_{TURB} = C_{\mu} \frac{K_{TURB}}{\varepsilon_{DISS}} \qquad (3\text{-}71)$$

where C_{μ}=0.09 is a constant given by the k-ε model. Initially, perturbations on the jet surface are induced by the jet turbulence. Once these fluctuations have reached a certain level, they grow exponentially according to the Kelvin-Helmholtz instability mechanism until they detach from the liquid core and form droplets.

It is assumed that the length scale of turbulence is the dominant scale of atomization, so that:

$$L_{ATOM} = C_1 L_{TURB} = C_2 L_{WAVE} \qquad (3\text{-}72)$$

where L_{ATOM} is the length scale of atomization and L_{WAVE} is the wavelength of the jet surface perturbations. The time scale of atomization is expressed as a linear sum of the turbulence and wave growth time scales:

$$\tau_{ATOM} = C_3 \tau_{TURB} + C_4 \tau_{WAVE} = \tau_{spn} + \tau_{exp} \qquad (3\text{-}73)$$

where the turbulence time scale determines the initial growth time and the wave growth time scale τ_{WAVE} determines the exponential growth time. The latter is determined for an inviscid liquid from the Kelvin-Helmholtz instability theory as:

$$\tau_{WAVE} = \frac{1}{\left[\frac{\rho_{fluid}\rho_{gas}}{(\rho_{fluid}+\rho_{gas})}\left(\frac{u_{EXIT}}{L_{WAVE}}\right)^2 - \frac{\sigma}{(\rho_{fluid}+\rho_{gas})L_{WAVE}^3}\right]^{0.5}} \qquad (3\text{-}74)$$

The equation giving the atomization time scale guarantees that atomization does not occur in vacuum or with a laminar jet flow since the turbulence time scale is infinite for

laminar jets and the wave growth time scale is infinite for injection in a vacuum. The atomization constant C_1 is determined from the assumption that the secondary droplet diameter equals to the dominant eddy diameter, which is twice the integral length scale of turbulence (C_1=2). In addition, C_2=0.5 assuming that half of the surface wave area is detached from the jet forming a droplet, while C_3=1.0 and C_4=1.5. Once the length and time scale of atomization have been determined, the spray cone angle and the atomization break-up rate are calculated from the correlations:

$$\tan\frac{\theta_{SPRAY}}{2} = \frac{L_{ATOM}/\tau_{ATOM}}{u_{EXIT}}$$

$$\frac{dD}{dt} = 2\frac{L_{ATOM}}{\tau_{ATOM}} \qquad (3\text{-}75)$$

The break-up rate equation is applied to the atomization break-up regime only. The transition criterion for this regime is arbitrarily chosen as $\tau_{spn} = \tau_{exp}$ which means that after the pass of time τ_{spn} the internal turbulence of the jet has decayed to such a level that does not affect atomization any longer. This decay can be calculated on the basis of the k-ε model. Assuming isotropic turbulence and realizing that there is no turbulence generation term, the resulting length and time scale of turbulence are given as a function of time from the following formulas:

$$L_{TURB}(t) = L_{TURB}(0)\cdot[1+(C_5-1)\frac{t}{\tau_{TURB}(0)}]^n$$

$$\tau_{TURB}(t) = \tau_{TURB}(0)+(C_5-1)t \qquad (3\text{-}76)$$

$$\text{where}\quad n = 1-\frac{1}{2(C_5-1)}$$

The constant C_5 is set equal to 1.92 according to the k-ε model. Time t measures from the time of the injection of each individual fluid element emerging from the injection hole.

The size of secondary droplets detached from the liquid jet are sampled randomly from a calculated probability distribution function. This can be determined if

the following assumptions are adopted: (i) the number of droplets with size d is inversely proportional to the atomization time scale τ_{ATOM} (d), (ii) the number of droplets with size d is proportional to the surface area ratio $(D_{JET}/d)^2$, (iii) the number of droplets with size d is proportional to the turbulence energy spectrum $\Phi(d)$ and (iv) the number of droplets with size d per unit interval of d is proportional to 1/d, which represents a logarithmic distribution of the probability density function with respect to the droplet size variation. Combining the above assumptions, the probability distribution density function is given from the correlation:

$$pdf(d) = C\frac{\Phi(d)}{\tau_{ATOM}(d)} \tag{3-77}$$

where C is the normalization constant. The turbulence energy spectrum is given from:

$$\Phi(d) = C\frac{(k/k_e)^2}{[1+(k/k_e)^2]^{11/6}} \tag{3-78}$$

where the wave number k is the inverse of d and the k_e is obtained from $k_e=1/L_e$, $L_e=\Lambda/0.75$, where Λ is an integral length scale interpreted as the average size of the energy-containing eddies. Realizing that the pdf(d) is defined as the volume fraction of droplets with size d per unit interval of d around d:

$$pdf(d) = \frac{1}{V}\frac{\partial V}{\partial d} \tag{3-79}$$

$$\text{and thus} \quad \int_0^{dmax} pdf(d)dd = 1 \tag{3-80}$$

the droplet size is then randomly selected from this distribution function.

3.3.4.5 Cavitation-induced atomization

This model has been developed during the present investigation; this has been considered necessary since the previous two atomization models were found not to predict satisfactorily the experimental data as it will be shown in chapter 5.

The model considers the effect of cavitation on the disintegration of the liquid jet. It is assumed that the liquid jet emerging from the injection hole atomizes due to the collapsing of the cavitation bubbles exiting from the injection hole together with the liquid. Since the surrounding pressure is much higher than the pressure inside the bubbles (which is equal to cavitation pressure) the bubbles will gradually collapse. In addition, it is expected that the bubbles interact with the turbulence flow in the liquid jet; it is thus possible that they may burst on the surface of the liquid jet before their total collapse. For both cases, a characteristic time is calculated and the minimum of the two is assumed to determine the time scale of the atomization process. Also, a length scale of the perturbations caused on the jet surface by these effects can be calculated. Since the actual number of bubbles is an unknown parameter, the dynamic cavitation number is introduced in order to account for their effect on the disintegration process. This is defined as:

$$CN_{dyn} = \frac{P_{SAC} - P_{BACK}}{\frac{1}{2}\rho_{JET} u_{JET}^2} \tag{3-81}$$

From the model calculating the effective injection velocity due to the onset of cavitation, the total area at the exit of the injection hole occupied by bubbles can be determined and then the radius of an equivalent bubble having the same area as all the cavitating bubbles can be derived as:

$$R_{CAV,EFF} = \sqrt{r_{hole}^2 - r_{EFF}^2} \quad , \quad r_{EFF}=(A_{EFF} / \pi)^{0.5} \tag{3-82}$$

where A_{EFF} is the effective hole area.

Also, from the correlations giving the turbulent kinetic energy inside the injection hole, a turbulent liquid velocity can be estimated as:

$$u_{TURB} = \sqrt{\frac{2}{3} K_{TURB}} \tag{3-83}$$

assuming isotropic turbulence. The bubble collapse time for a bubble with radius R_{CAV} can be estimated from the Rayleigh theory of bubble dynamics as:

$$\tau_{COLLAPSE} = 0.9145 R_{CAV} \sqrt{\frac{\rho_{JET}}{P_{GAS}}} \tag{3-84}$$

while an average time required for a bubble of radius R_{CAV} to reach the periphery of the jet, can be estimated from the following correlation assuming that the bubbles move radially within the liquid jet with liquid turbulent velocity:

$$\tau_{BURST} = \frac{r_{hole} - R_{CAV}}{u_{TURB}} \tag{3-85}$$

The characteristic time scale of atomization is assumed to be the smaller of the collapse time and the bursting time:

$$\tau_{ATOM} = \min\{\tau_{COLLAPSE}, \tau_{BURST}\} \tag{3-86}$$

It has to be noted that the cavitation bubbles in reality are not spherical since experimental images show that they are regions of cavitation extended from the hole entrance up to the hole exit. It is thus expected that correlation (3-84) does not represent the actual collapsing time since its derivation requires spherical bubbles. However, the introduction of experimental coefficient to the working correlations of the model are assumed to balance all possible uncertainties. It is also interesting to see that the bubble collapse time is smaller than the bursting time if the effective bubble radius is smaller than a critical value which is a function of the back pressure. For injection under atmospheric conditions, where it is expected that the effective hole area is of the order of 65% of the geometric one, the bursting time is expected to control the atomization process. However, there is a critical back pressure for a given geometric hole arrangement and a given level of cavitation above which the collapse time becomes the

smaller time scale and thus determines the time scale of atomization. It is also interesting to examine the case at the onset of cavitation, where very small bubbles reach the hole exit. As can be seen, the bubble collapse time is smaller for smaller bubbles, and thus if R_{CAV} is close to zero then the collapse time will become the smaller characteristic time of the phenomenon. However, by introducing the parameter L_{ATOM} which is a characteristic length scale of the perturbations of the jet surface caused by the collapsing of the cavitation bubbles, as:

$$L_{ATOM} = 2\pi R_{CAV,EFF} \tag{3-87}$$

it can be seen that this also goes to zero for small bubbles. The overall contribution will give no final disintegration of the jet at the limiting case at which the effective bubble radius tends to zero as it will be demonstrated further in this section. From the time and length scales as introduced here, the force acting on the jet surface every time of collapsing or bursting of a bubble with radius R_{CAV} can be estimated as

$$F_{TOTAL} = C \cdot CN_{dyn} \cdot M_{JET} \frac{L_{ATOM}}{\tau_{ATOM}^2} \tag{3-88}$$

where C is an empirical constant whose value is determined from the comparison between the model predictions with the experimental data and M_{JET} the mass of the liquid jet element to be atomized. Assuming that the surface tension forces oppose the atomization of the jet, the maximum stable diameter of a droplet is calculated from the condition:

$$F_{TOTAL} = F_{SURFACE} \tag{3-89}$$

where

$$F_{SURFACE} = 2\pi r_{JET}\sigma . \tag{3-90}$$

It can be seen that the calculated droplet size goes to zero for zero effective bubble radius which denotes that the liquid jet does not atomizes due to cavitation as it should

be expected. More details about the maximum stable droplet diameter as it is estimated from correlation (3-89) will be given in chapter 5.

To account for the droplet size distribution of the droplets formed due to the disintegration of the liquid jet it is assumed that the possibility of formation of a droplet with radius d_i (and mass m_i) is the same for all possible droplet sizes, from the minimum to the maximum stable diameter calculated above. Although in reality this would strongly depend on the bubble sizes exiting the injection hole, no other detailed approximations can be done since a three-dimensional solution of the coupled problem of bubble growth rate and liquid disintegration would be required.

The spray cone angle is calculated as:

$$\tan\frac{\theta_{SPRAY}}{2} = \frac{L_{ATOM}}{\tau_{ATOM}\, u_{JET}} \tag{3-91}$$

The droplets formed from the disintegration of the liquid jet are not distributed uniformly in the spray cone angle, in agreement with many experimental data which show that the larger droplets are found on the spray axis and the smaller ones at the spray edge. Since it is not possible to account for the detailed physics of the droplets dispersion in the radial direction, it is assumed that the possibility of finding a droplet at a certain angle off the spray axis is inversely proportional to the droplet mass, i.e. it is assumed that the radial distribution of the droplets is mainly a function of their inertia, which is proportional to their mass. The expression used for the distribution of the droplets in the spray cone angle is:

$$\theta_i = C_{PROFILE} \cdot \theta_{SPRAY}\left(1 - \frac{m_i}{m_{max}}\right) \tag{3-92}$$

where θ_{SPRAY} is the half spray cone angle, m_i is the mass of the i^{th} droplet formed during the atomization process (selected from the calculated distribution), m_{max} is the mass of the droplet with the maximum possible size and $C_{PROFILE}$ is a coefficient depending on the exit velocity profile. According to Hiroyasu et al. (1991) and Su and Farrell (1996), asymmetries in the distribution of the liquid mass relative to the spray axis are attributed to the non-uniform injection-hole flow. Variations in the fuel mass distribution

depending on the injection velocity profile are taken into account through the coefficient $C_{PROFILE}$, calculated as:

$$C_{PROFILE} = XX\frac{Q(\theta_i)}{Q_{total}} \tag{3-93}$$

where XX is a random number uniformly distributed in the range (0,1), $Q(\theta_i)$ is the flow rate at the angle θ_i and Q_{total} the total flow rate. If a uniform velocity profile is used, then $C_{PROFILE}$=XX, which means that the droplets are distributed independently of the velocity profile.

3.3.5 Droplet secondary aerodynamic-induced break-up

3.3.5.1 General approach - literature review

After the disintegration of the liquid jet emerging from the injection nozzle, the formed droplets may further break-up as they move into the surrounding gas. The liquid droplets undergo deformation due to the non-uniform pressure distribution developing around them resulting from the relative velocity between the droplets and the gas and the enhanced motion within the droplet. Development of these processes leads to droplet deformation and finally to break-up into small droplets. The process of this break-up is very intricate and is determined by the relationship between forces of surface tension, viscosity and inertia. For various relative velocities and various physical parameters of both the gas and the droplet, the patterns of their fragmentation process may be significantly different. The break-up of the dispersed droplets has an important bearing upon the interface exchange in multiphase systems, as it has been realized in many applications. Up to now, a large number of both experimental and theoretical publications have been concerned with the investigation of the mechanism of droplet break-up of both single droplets and droplet systems in various conditions of their interaction with gas flow. Based on these studies, correlations giving various important parameters, such as the break-up time and the size of the smaller droplets have been developed. However, detailed numerical studies solving the complex fluid dynamics in the distorted droplet are very limited and in any case not of practical use in spray CFD

numerical codes due to not only to the enormous big computational time required for such a solution but also to the complex flow phenomena related to these processes.

Following, some of the most important publications on the relevant area are briefly described.

Ranger and Nichols (1969) studied the mechanism of the stripping break-up of a droplet deforming under shock wave conditions. From this study, experimental data were given for the droplet deformation and the break-up time. Typical values for the dimensionless break-up time (which is defined later on in this section) were found to be approximately 5.5 for the studied range of Weber and Mach numbers. Also, an analysis was presented on the calculation of the mass flux leaving the breaking droplet due to the stripping mechanism. This analysis considers that this mass flux is due to the boundary layers developed inside the droplet; a useful correlation was established.

Krzeczkowski (1980) reported a set of experimental data on the various mechanism of droplet break-up occurring in various Weber numbers. The aim of this investigation was focused on the classification of types of droplet deformation, on the kinematics of deformation and on the duration of disintegration. The bag, bag-jet, transition and stripping break-up mechanisms were identified as the Weber number increases. Data for the maximum droplet deformation were given for all of the examined cases, taking values six time larger than the initial droplet diameter. Also, data for the break-up time for all categories were plotted for several liquid. The results of this study have been verified from other following studies.

A similar study has been reported by Pilch and Erdman (1987). The vibrational bag, bag-and-stamen, stripping, wave crest stripping and the catastrophic break-up were identified as different modes of fragmentation as a function of the Weber number. Clear limits between the various regimes were established and for all of these break-up regimes, correlations for the break-up time were reported as a function of the Weber and the Ohnesorge numbers. The break-up time data were for both the initiation time and the total break-up time. Finally an estimation of the maximum droplet diameter was given.

Kitscha et al. (1989) developed a simple break-up model based on the combination of Kelvin-Helmholtz and Rayleigh-Taylor instability theory to describe the break-up of freely rising or falling fluid particles (i.e. bubbles and droplets). According to this model, break-up is predicted to occur if the growth rate of interfacial waves on the leading front is faster than the rate at which waves propagate around the interface to

the side of the particle. Based on this model and available experimental data, simple correlations were developed predicting the maximum size a fluid particle can reach.

Wierzba (1990) determined experimentally values of the critical Weber number between different break-up regimes. For Weber number in the range 11 to 14 five different break-up regimes were identified; the deformation and break-up process of a liquid droplet in a gas stream was found to be very sensitive to very small fluctuations of the flow conditions.

In another study by Arcoumanis et al. (1994) the break-up of droplets of both Newtonian and non-Newtonian fluids was investigated by a high-speed camera and differences were identified between the different types of fluids investigated.

A series of papers on the deformation and break-up of droplets have been reported by Faeth et al. (1995) and Hsiang et al. (1992, 1993). Correlations giving the break-up time, droplet size, droplet velocity, droplet drag coefficient and droplet deformation have been derived as a function of the Weber and Ohnesorge numbers based on the experimental observations.

A few number of studies have been reported on the calculation of the detailed break-up mechanism of liquid droplets. In these calculations multi-dimensional techniques describing the dynamics of laminar flows were applied in order to predict the droplet deformation. Although promising, they are not applicable to practical cases. Some of the reported studies are those of Rallison (1984), Stone (1994) and others.

Summary

In what follows, an analysis based on previous works on droplet secondary break-up is given and finally the break-up models used in the present investigation are described in detail.

With the predetermined law of a flow past a liquid droplet, the process of break-up is defined by the following principal physical characteristics in the original state: gas and liquid densities (ρ_{gas} ,ρ_{liquid}), gas and liquid viscosities (μ_{gas} ,μ_{liquid}), surface tension σ, speed of sound v_{sound} , droplet diameter d, relative velocity and acceleration between the gas and the droplet (u_{rel}, du_{rel} /dt) and time t. These parameters yield five independent dimensionless criteria: the Weber number We, the Laplace number Lp (Ohnesorge number $On=1/Lp^2$), the Bond number Bo, the Mach number M, and the

Strouhal number St, and in addition they yield ratios of the phase densities and viscosities. Analysis of experimental data shows that six major mechanisms of droplet breaking modes may be singled-out in gas flows; these modes are realized in various ranges of variation of the above indicated parameters and are the following:

1. A mode of the original droplet fragmentation into several (generally 2 to 4) almost identical droplets. This is the so-called vibrational mode of break-up. This mode is generally realized at near to critical Weber numbers.

2. A mode of droplet fragmentation preceded by a tore-like ballooning ('parachute'-type breaking). It is realized at Weber numbers slightly exceeding the critical values, sufficient external flow time, and large Laplace numbers (low viscosity liquids). This type of fragmentation is initiated by the film disintegrating into a multitude of small droplets followed by fracture of the liquid torus, thereby forming significantly larger droplets.

3. A mode of deformation with the formation of a bag-like balloon with a tiny streamer. Unlike mode 2, it is realized in the entire range of investigated Laplace numbers, and, generally, at somewhat higher Weber numbers. The internal tiny streamer usually breaks down a little later than the balloon; the droplets are of the same size as the droplets obtained from the balloon fracture.

4. Transitional mode of irregular or chaotic fragmentation occurring when up to a certain stage of deformation, the droplet breaks down due to both ballooning and breaking of stretched (along the flow) filaments resulting from the liquid surface layer ripping. At some stage of the fragmentation process, the droplet is so much deformed and shapeless that it simply breaks into a number of fragments.

5. A mode of continuous ripping of the surface layer when, up to a certain stage of deformation, breaking takes place only to stripping, from the droplet surface, the boundary layer of liquid in the form of a film or a multitype of filaments. As in mode 4, when reaching some level of critical deformation, the droplet that was a unit prior to that point in time break into several smaller fragments.

6. A mode of explosive fragmentation that is realized at considerably large Weber numbers, and often observed in sufficient strong shock waves. In this case, when the flow strongly affects the droplet, no ripping is practically observed: the original droplet abruptly breaks down into a great number of smaller droplets.

In modes 2-5, the fracture begins when the droplet deforms into a flattened ellipsoid or disc of thickness 0.2d and a maximum size of 6d to 12 d (where d stands for the droplet diameter). For modes 1 and 6, the disc formation is not characteristic feature of the process. Of all the defining criteria, the strongest impact on both the mode and intensity of droplet break-up is exerted by We; the effect of Lp becomes noticeable only at Lp<10. The ρ_{gas}/ρ_{liquid} criterion significantly affects the intensity and characteristic time of break-up. As to the μ_{gas}/μ_{liquid} criterion in the studied range of liquid viscosities, it exhibited no discernible effects. The direct effects of Mach numbers has not been extensively studied either; in addition, it is beyond the scope of the present investigation. Each of the six above indicated break-up mechanisms is realized in its own range of Weber numbers, which is limited by some critical numbers We that generally depend on the Laplace number of the liquid. Apparently, six adequate ranges for the Weber numbers may be indicated:

$$
\begin{aligned}
&1.\ We \approx We_{CR,1} \\
&2.\ We_{CR,1} < We < We_{CR,2} \\
&3.\ We_{CR,2} < We < We_{CR,3} \\
&4.\ We_{CR,3} < We < We_{CR,4} \\
&5.\ We_{CR,4} < We < We_{CR,5} \\
&6.\ We_{CR,5} < We
\end{aligned}
\qquad (3\text{-}94)
$$

The critical values $We_{CR,i}$ (i=1-5) depend on the laws of external flow. Various values have been proposed by different investigators which have performed experiments under different basic flow categories related to droplet break-up mechanism. Various correlations have been proposed, based on experimental data; these will be given in a following section.

Another problem concerns with the upper limit of the catastrophic mode. The explosion-type mode 6 is usually associated with the Rayleigh-Taylor instability which develops on the upstream side of the droplet. Therefore, the above-discussed Bond criterion Bo is used as the criterion of explosive fracture. As it is stated by Nigmatulin (1991), the critical values Bo are in the range 1000-5000. However, it is more convenient to use the We numbers as characteristic of this and other modes. Because the inherent acceleration of a droplet induced by the gas flow is $du_{rel}/dt \approx C_D \cdot \rho_{gas}/\rho_{liquid}$

where C_D is the droplet drag coefficient, then at sufficiently great Reynolds numbers (characteristic for this case of fragmentation), the drag is approximately constant and Bo number is approximately equal to Weber number. Thus, it is generally accepted that $We_{CR,5}$ =1000.

The inherent times of fragmentation for a number of applied analyses and predictions are of great importance. The droplet fragmentation is not an instantaneous process. It becomes noticeable upon some induction time t_{b1} , and comes to an end in time t_{b2} after the beginning of the gas flow effects. The inherent fragmentation time t^* is generally taken as :

$$t^* = \frac{d_0}{\nu_{liquid}} \left(\frac{\rho_{liquid}}{\rho_{gas}}\right)^{0.5} \tag{3-95}$$

This time characterizes the rate of the perturbation amplitude growth on the surface as a consequence of the Rayleigh-Taylor instability development. The dimensionless times $\frac{t_{b1}}{t^*}$ and $\frac{t_{b2}}{t^*}$ should depend on the defining criteria and the break-up mode.

Analysis of the experimental data leads to some conclusions about the order of inherent induction times and time of complete break-up, and also to conclusions about critical (maximum) deformation of a droplet and the spectrum of secondary droplets. In the fragmentation mode 1, the droplet breaks into 2-4 fragments, and to the maximum point in time t^* (which equals 2-3), the droplet deformation reaches d_{max}/d_0, and at this particular time the droplet generally divides in two. The fragmentation time almost equals t^* plus the period of the droplet natural oscillations. In the balloon-type fragmentation modes 1 and 2 to the time t/t^* =1-2, the maximum lateral deformation d_{max}/d_0=3-6 is reached, and the balloon inflation begins. The film fracture takes place at t/t^* =2-3, the torus fracture at t/t^* =2-4, and the fragmentation is completed at t/t^* =5. The film breaks into droplets whose size is of the order of $0.1d_0$; the size of the droplets formed in the torus fragmentation are several times larger. About 70%-80% of the secondary droplets (by their mass) are of the larger size. In the process of fragmentation, the droplet has sufficient time to undergo a displacement by a distance about $10d_0$. During the fragmentation in mode 4 of chaotic structure, or mode 5 of stripping, the fragmentation initiates approximately at a time close to the point of attaining the

maximum deformation d_{max}/d_0=2-3 at t/t^*=1-2, and ends at t/t^*=3-5. In the mode of stripping, the original droplet may break not only due to the stall of the boundary layer, but also to the disc perforation caused by the instability development. The tiny droplets of $d=0.1d_0$ begin to prevail, and their amount grows with the increase of the Weber number. In mode 6 of explosive fragmentation, the maximum deformation may not be reached; the overwhelming majority of the secondary droplets are generally of a size significantly smaller than the original size of the droplet.

A various number of correlations for predicting the inherent induction time and droplet fracture may be found in the literature, and they often differ from one another. Here, some of these correlation implemented in the CFD code are given. These are the models of Reitz and Diwakar (1986, 1987), Pilch and Erdman (1987), Hsiang et al. (1992) and O'Rourke and Amsden (1987). The proposed model which has been found to give better results against the experimental data combines correlations from all the above literature findings.

3.3.5.2 TAB model

The Taylor Analogy Break-up model (TAB) for diesel sprays was proposed by O'Rourke and Amsden (1987). According to this model, the droplet surface is assumed to oscillate as a mass-spring system while the external force on the mass is supplied by the gas aerodynamic forces. Damping is supplied by liquid viscosity and the surface tension forces are assumed to represent the spring forces. The model assumes that droplet break-up occurs if and only if its deformation exids a certain value, usually taken equal to the droplet radius. The equation for a damped, forced harmonic oscillator is:

$$\ddot{y} = \frac{C_f}{C_d}\frac{\rho_{liquid}}{\rho_{gas}}\frac{u_{rel}^2}{r_{drop}} - \frac{C_k\sigma}{\rho_{liquid}r_{drop}^3}y - \frac{C_d\mu_{liquid}}{\rho_{liquid}r_{drop}^2}\dot{y}$$

where (3-96)

$$y = \frac{x}{C_b r_{drop}}$$

In the above equation, x is the displacement of the equator of the droplet from its equilibrium position and C_k=8, C_d=5, C_f =1/3, C_b=1/2 are empirical coefficients introduced to match the experimental data with predictions.

Break-up is calculated if y>1 which is equivalent to $We>We_{CRIT}$. The critical Weber number We_{CRIT} is assumed to be 6. Also, the droplet life time should be bigger than the critical break-up time, which is calculated from the correlation:

$$t_{break} = \sqrt{\frac{3\rho_{liquid}}{\rho_{gas}}} \frac{r_{drop}}{u_{rel}} \tag{3-97}$$

To predict the droplet sizes after break-up, an analysis based on energy conservation was carried out. In this analysis, the energy of the parent droplet before break-up is set equal to the combined energies of the product droplets after break-up. Before break-up, the energy of the parent droplet in its own frame of reference is the sum of its minimum surface energy and the energy of oscillation and distortion. After break-up, it is assumed that the product droplets are not oscillated or distorted. Thus, the energy after break-up is the sum of the minimum surface energies of the product droplets and the kinetic energy the product droplets have due to their motion normal to the path of the parent droplet. Under these assumptions, the Sauter mean diameter of the droplets after break-up can be written as:

$$SMD = \frac{6r_{drop}\sigma}{6\sigma + \rho_{liquid} r_{drop}^3 \omega^2 y^2 - \rho_{liquid} r_{drop}^3 \dot{y}^2 (1 - C_v^2 C_b^2)} \tag{3-98}$$

The size of the newly formed droplets is randomly selected from an χ^2 distribution function. The velocity of the droplets in a direction normal to the velocity of the breaking droplet is calculated from the correlation:

$$u_{NORMAL} = c_b \cdot dy/dt \tag{3-99}$$

In a study by Assanis et al. (1993), it was proposed that $C_v C_b = 1$. In the above correlation, ω is the oscillation frequency calculated from the correlation:

$$\omega^2 = C_k \frac{\sigma}{\rho_{liquid} r_{drop}^3} \tag{3-100}$$

The number of the droplets per parcel is calculated from the mass balance equation after the size of the new droplets in the parcel has been selected and under the assumption that no extra parcels are formed.

3.3.5.3 Reitz and Diwakar model

In this model, two regimes, the bag break-up and the stripping break-up are considered. The criteria used are the following:

$$\begin{aligned} &We > C_{bag} && \text{Bag break - up} \\ &We/Re^{1/2} > C_{strip} && \text{Stripping break - up} \end{aligned} \tag{3-101}$$

where C_{bag}=6 and C_{strip}=0.5. Having determined the break-up regime, the maximum stable diameter is calculated (diameter below which break-up does not occur) as:

$$D_{stable,bag} = 2C_{bag}\frac{\sigma}{\rho_{liquid}u_{rel}^2}$$

or (3-102)

$$D_{stable,strip} = 4C_{strip}^2\frac{\sigma^2}{\rho_{liquid}u_{rel}^3\mu_{liquid}}$$

If both criteria are satisfied, then the rate of change of the droplet diameter is calculated from the correlation:

$$\frac{dD_d}{dt} = -\frac{D_d - D_{stable}}{\tau_{break}} \tag{3-103}$$

where τ_{break} is the break-up time assumed to be the minimum of the τ_{bag} and τ_{strip} defined as:

$$\tau_{bag} = C_b D_d \sqrt{\frac{\rho_{liquid} D_d}{\sigma}}$$

and (3-104)

$$\tau_{strip} = \frac{C_b D_d}{u_{rel}} \sqrt{\frac{\rho_{liquid}}{\rho_{gas}}}$$

where C_b is an empirical coefficient used to much the experimental data. Different values have been proposed by various researchers. Reitz and Diwakar (1987) used C_b=10, Nicholls (1972) gave C_b=4 and O'Rourke and Amsden (1987) suggested $C_b=3^{0.5}/2$.

The velocity of the new droplets is assumed to be the same as the velocity of the old parcel (although that corrections have been proposed by several authors and can be easily implemented). The number of the droplets per parcel is calculated from the mass balance equation after the size of the new droplets in the parcel has been selected and under the assumption that no extra parcels are formed.

Although this model is the standard break-up model in the CFD codes KIVA-II and KIVA-III and also implemented in other codes (like the SPEED code), it was found to be to simplistic too describe the droplets behaviour during break-up. The liquid viscosity does not play any effect, the break-up time is similar for all different break-up regimes, only one droplet size is calculated and no information is given about the droplet distortion and drag coefficient.

3.3.5.4 Pilch-Erdman model

This droplet break-up model is based on the correlations obtained from measured data collected in a literature survey by Pilch and Erdman (1987). They found correlations for the critical Weber number and the break-up time. Their analysis includes data on the droplet velocity history and droplet sizes which enabled them to propose a concept of the maximum stable diameter below which break-up is not calculated.

Droplet break-up occurs if the droplet Weber number is greater than the critical Weber number We_{CRIT}.This critical Weber number is given as:

$$We_{CRIT} = 12(1+1.077Oh^{1.6}) \quad (3\text{-}105)$$

where $On = \frac{\mu_{liquid}}{(\rho_{liquid}\sigma \cdot D)^{0.5}}$. is the Ohnesorge number accounting for viscosity effects. In the model five break-up regimes are distinguished: bag break-up, bag-and-stamen break-up, sheet stripping break-up, wave crest stripping break-up and catastrophic break-up.

The actual break-up time is calculated through correlations giving this dimensionless break-up time. This is defined as:

$$\tau = t\frac{u_{rel}}{D_d}\left(\frac{\rho_{liquid}}{\rho_{gas}}\right)^{0.5} \tag{3-106}$$

Two different break-up times are considered. The time required to initiate break-up $\tau_{break,start}$ and the total break-up time $\tau_{break,end}$. The first one is given from the correlation:

$$\tau_{break,start} = 1.9(We-12)^{-0.25}(1+2.2On^{1.6}) \tag{3-107}$$

Five regimes are considered for the total break-up time as a function of the Weber number of the droplet, corresponding to five break-up regimes:

$$\begin{aligned}
\tau_{break,end} &= 6(We-12)^{-0.25} && 12 \le We \le 18 \\
\tau_{break,end} &= 2.45(We-12)^{0.25} && 18 < We \le 45 \\
\tau_{break,end} &= 14.1(We-12)^{-0.25} && 45 < We \le 351 \\
\tau_{break,end} &= 0.766(We-12)^{0.25} && 351 < We \le 2670 \\
\tau_{break,end} &= 5.5 && 2670 < We
\end{aligned} \tag{3-108}$$

After the pass of time $\tau_{break,end}$, the droplet is assumed to break-up, forming new smaller droplets. The maximum stable diameter of these droplets is calculated from the correlation:

$$D_{stable} = We_{CRIT}\frac{\sigma}{\rho_{liquid}u_{rel}}\left(1-\frac{V_s}{u_{rel}}\right)^{-2} \tag{3-109}$$

where V_s is the velocity of the fragment cloud when all break-up processes cease. This is calculated as:

$$V_s = u_{rel}(\frac{\rho_{liquid}}{\rho_{gas}})^{0.5}(B_1\tau_{break,end} + B_2\tau^2_{break,end}) \quad (3\text{-}110)$$

where B_1=0.375 and B_2=0.236 are empirical constants chosen to fit the experimental data. The size on the new droplet is set equal to the maximum stable diameter and the number of the droplets formed is calculated from the mass balance equation assuming that no extra parcel is formed.

3.3.5.5 Hsiang and Faeth et al. corellations

A number of publications Hsiang et al. (1992, 1993), Wu et al. (1993, 1995) and Faeth et al. (1995) discuss the droplet break-up and correlations are given in order to calculate various parameters during the droplet break-up. These are the break-up time (both time of initiation of break-up and total break-up time), the Sauter Mean Diameter of the formed droplets, the droplet drag coefficient during the disintegration process and the droplet deformation. Thus, this model gives information not available from the previous models. An extensive analysis is given in these publications; here, only the correlations used in the present study are presented.

The proposed correlations are valid for all different break-up regimes and are the following. For the total break-up time:

$$t_{break,end} = \tau\frac{u_{rel}}{D_d}\sqrt{\frac{\rho_{liquid}}{\rho_{gas}}} \quad (3\text{-}111)$$

where

$$\tau = \tau_{break,end} = 5/(1-On/7) \quad , We < 1000 \quad (3\text{-}112)$$

The maximum droplet deformation can be derived from the data presented which can be fitted to the correlation:

$$D_{max}/D_d = 1+0.19We^{0.5} \quad ,On < 0.1 \tag{3-113}$$

During the break-up time, the droplet deformation varies from the initial undistorted frame to the maximum deformation according to:

$$\frac{D_{distorted}-D_d}{D_{max}-D_d} = 0.8\frac{t}{\tau_{break,end}} \tag{3-114}$$

The droplet drag coefficient during that time can be estimated from the correlation:

$$C_{Ddistorted} = C_{Dsphere}[0.4+0.6\frac{D_{distorted}}{D_d}] \tag{3-115}$$

where $C_{Dsphere}$ is the drag coefficient of a spherical droplet. The Sauter mean diameter (SMD) of the formed droplets is given by:

$$\frac{\rho_{gas}\cdot SMD\cdot u_{rel}^2}{\sigma} = C\cdot(\frac{\rho_{liquid}}{\rho_{gas}})^{1/4}\cdot(\frac{\mu_{liquid}}{\rho_{liquid}D_d u_{rel}})^{1/2}\cdot We \tag{3-116}$$

where C=6.2 is an empirical coefficient introduced to fit the experimental data.

Another important correlation was given for the velocities of the formed droplets as a function of their size. This correlation is:

$$\frac{u_{rel}}{u_{break}}-1 = 2.7[(\frac{\rho_{gas}}{\rho_{liquid}})^{1/2}D_d/d_{break}]^{2/3} \tag{3-117}$$

where u_{break} is the relative velocity of the newly formed droplets and the surrounding gas and d_{break} is their size. As far as it concerns the droplet size distribution, it is proposed that MMD/SMD=1.2 (where MMD stands for the median mean diameter) for all of the break-up regimes except the stripping mode. However, for the latter case, this correlation is valid if the primary droplet is excluded. The droplet size distribution is assumed to follow that proposed by Simmons (1977).

3.3.5.6 Proposed model

During the present investigation, it was found that various proposed empirical correlations can be combined in order to predict the properties of the droplets formed during the droplet secondary break-up. The model predicts the Sauter mean diameter of the formed droplets, their velocities, their deformation and the maximum possible size of the distribution of the new droplets. Then, the droplet diameter and the number of computational parcels used are randomly sampled from a calculated distribution function. Seven different break-up regimes were distinguished (Nigmatulin (1991) and Pilch and Erdman (1987)): vibrational, bag, bag-and-stamen, chaotic, sheet stripping, wave crest stripping and catastrophic break-up. The criterion for these regimes was the Weber number. The following criteria were adopted:

1. $We \leq 12$	Vibrational	
2. $12 < We \leq 18$	Bag	
3. $18 < We \leq 45$	Bag - and - steamen	
4. $45 < We \leq 100$	Chaotic	(3-118)
5. $100 < We \leq 350$	Sheet stripping	
6. $350 < We \leq 1000$	Wave crest stripping	
7. $1000 < We$	Catastrophic	

The break-up time for each of these regimes was calculated from the following expressions:

$$\tau_{break,end} = 0.25\pi\left[\frac{\sigma}{\rho_{liquid} d_0^3} - 6.25\frac{\mu_{liquid}}{\rho_{liquid} d_0^2}\right]^{-1/2} \qquad We < 12$$

$$\tau_{break,end} = 6(We-12)^{-0.25} \qquad 12 \leq We \leq 18$$

$$\tau_{break,end} = 2.45(We-12)^{0.25} \qquad 18 < We \leq 45 \qquad (3\text{-}119)$$

$$\tau_{break,end} = 14.1(We-12)^{-0.25} \qquad 45 < We \leq 351$$

$$\tau_{break,end} = 0.766(We-12)^{0.25} \qquad 351 < We \leq 2670$$

$$\tau_{break,end} = 5.5 \qquad 2670 < We$$

and in order to include viscosity effects:

$$\tau_{break,end} = \tau_{break,end}/(1-On/7) \quad ,We < 1000 \tag{3-120}$$

These are combination of various break-up times reported in the literature (O'Rourke (1987), Pilch and Erdman (1987), Nigmatulin (1991), Faeth et al. (1992, 1993, 1995)). During that time, the droplet was assumed to be distorted. The droplet deformation is calculated from correlations (3-113) and (3-114) and the calculation of the droplet drag coefficient is based on correlation (3-115). After the pass of the total break-up time, the size of the formed droplets is calculated. Three different cases are considered. In the vibrational, bag and bag-and-stamen modes (We<45), the SMD of the formed droplets is given by:

$$SMD = \frac{4d_0}{4+0.5(1+f(On)We^{1/2})} \tag{3-121}$$

where f(On) is generally function of the Ohnesorge number On. In the present study it was assumed to be constant and equal to 0.19. For these regimes, the maximum possible droplet size required for the calculation of the droplet size distribution (described in section (3.3.5.8)) is assumed to be equal to the initial droplet size. For the chaotic and catastrophic regimes, correlation (3-116) is used. The maximum possible droplet size is assumed to be equal to the initial droplet size for the chaotic regime, and equal to the maximum stable diameter for the catastrophic break-up regime. This is calculated from correlation (3-109).

A different approximation is introduced for the calculation of the droplet size in the stripping regime(10^2<We<100^3).The mass flux leaving the droplet is calculated from the correlation:

$$\frac{dm_{strip}}{dt} = C\rho_{liquid}(\rho_{gas}/\rho_{liquid})^{1/3}(\mu_{gas}/\mu_{liquid})^{1/6}\mu_{liquid}^{1/2}u_{rel}^{1/2}d_0^{3/2} \tag{3-122}$$

where C is an empirical constant between 12-18. This correlation derives from a boundary layer analysis in the droplet and the assumption that the droplet size formed under the stripping mechanism is proportional to the thickness of this layer. Details can be found in Ranger and Nichols (1969).

The critical feature of this approximation is that allows for bimodal distribution modeling, since the size of the primary droplet is calculated from the above correlation, while the size of the small droplets is sampled randomly after the droplet size distribution function has been calculated according to the maximum entropy formalism model which is described in section (3.3.5.8). It has been assumed that for the small droplet, $d_{30}=0.1d_0$, according to Nigmatulin (1991). The maximum possible droplet size for this regime is calculated from the mass balance in the breaking droplet and by the assumption that only one droplet is formed from the calculated mass flux.

Having identified the Sauter mean diameter and the maximum possible droplet size of the formed droplets, the maximum entropy formalism model (section (3.3.5.8)) is used for the calculation of the droplet size distribution from which the droplet size is sampled randomly. The initial parcel is replaced with new parcels. The number of the new parcels formed is assumed to be proportional to the number of the formed droplets which can be estimated as D_{DROP}/D_{30} for all modes except the stripping where the number of droplets is D_{NEW}/D_{30}. Having identify the droplet size d_{break}, then its velocity is calculated from correlation (3-110). The associated loss of droplet kinetic energy is assumed to be dissipated within the droplet during its deformation; since this represents only a very small fraction of the total droplet kinetic energy (of the order of 0.5% in the most extreme cases), it is not added as source term to the energy exchange between the liquid and gas phases.

3.3.5.7 Droplet size distribution

Another problem related to spray applications concerns the calculation of the droplet size distribution derived from the different physical processes taking place during the spray development. It is clear from the above mathematical models of droplet secondary break-up and liquid jet atomization that the experimental correlations usually used, predict only the maximum droplet stable diameter or the Sauter mean diameter. However, measurements of the droplet sizes in sprays reveal that a range of droplet sizes is usually found. In the absence of any fundamental mechanism or model on which to build a theory of droplet size distributions, a number of mathematical functions have been proposed, based on either probability or purely empirical considerations, that allow the mathematical representation of measured droplet size distributions. Those in general

use include normal, χ^2 , log-normal, Nukiyama-Tanasawa, Rosin-Rammler, upper-limit, hyperbolic and log-hyperbolic distributions. No single distribution can represent all droplet size data at different injection conditions or even at different positions within the same spray. It is usually necessary to test several distribution functions to find the best fit to any given set of experimental data. A mathematical presentation of the droplet size distributions used can be found in Simmons (1977), Bhatia et al. (1988), Domnick et al. (1992), Long et al. (1994), Quoc et al. (1994), Xu et al. (1992, 1993, 1994), Lefebvre (1989), Bayvel and Orzechowski (1993) and many others.

Whatever the droplet size distribution in a spray is, and independent of the physical mechanisms leading to these distributions, it is convenient in many calculations to work only with mean or average diameters. Thus, most of the experimental data for the droplet size in sprays are usually given in terms of a mean droplet size. The definition of some of the most common mean diameters is given below.

$D_{10} = \frac{\int D(dN/dD)dD}{\int (dN/dD)dD}$: Mean diameter (linear average value of all droplets in the spray)

$D_{20} = [\frac{\int D^2(dN/dD)dD}{\int (dN/dD)dD}]^{1/2}$: Surface mean diameter

$D_{30} = [\frac{\int D^3(dN/dD)dD}{\int (dN/dD)dD}]^{1/3}$: Volume mean diameter (the diameter of a droplet whose volume, if multiplied by the number of droplets, equals the total volume of the spray)

$D_{32} = SMD = \frac{\int D^3(dN/dD)dD}{\int D^2(dN/dD)dD}$: Sauter mean diameter (the diameter of a droplet whose ratio of volume to surface is the same as that of the entire spray)

Also, some other representative diameters can be defined, such as the MMD (Mass Median Diameter: droplet diameter such that 50% of total liquid volume is in droplets of smaller diameter) e.t.c.

From the above analysis it has become obvious that a fundamental model is required for the calculation of the droplet size distribution in a spray. The mathematical

functions used in the past have no physical meaning and are not applicable in the absence of experimental data. Also, the various droplet break-up and jet atomization models usually account for the one of the previously defined mean diameters. In this direction, a series of investigations have been published. All of them use the so-called 'maximum entropy formalism' in order to calculate the droplet size distribution. This can be achieved by applying the mass, momentum and energy conservation equations in the spray process. In addition, a fourth condition derived from thermodynamics is used. Since there is an infinite set of probability functions that would satisfy the above conservation equations, it is assumed that the most probable distribution is the one that maximizes the Shannon entropy. The definition of this entropy has the same form as the statistical thermodynamic definition of entropy proposed by Boltzmann. This method has been applied to a number of different mechanical, chemical, dynamic and biological systems. In sprays, all the modifications of this theory have been applied in phenomenological approximations where no detailed models are used for the spray development. Some of the relevant publications are those of Sellens et al. (1985, 1993), Li et al. (1989, 1991) Sankagiri et al. (1993), Van Der Geld et al. (1994) and Ahmadi et al. (1993). In the present investigation, a similar model was developed accounting for the droplet size distribution at every time step of a droplet break-up; this model is described below.

3.3.5.8 Maximum entropy formalism model

This model accounts for the most probable probability distribution function describing the droplet sizes after the break-up of the original droplet. It is assumed that the droplet sizes follow a distribution function pdf(d) giving for any value of the droplet diameter d the number of droplets with size in the range dd around d. Usually, a joint velocity-size pdf(u,d) distribution function is necessary to describe the outcome of a break-up process. However, it is difficult to describe the energy and momentum loss associated with these processes. Since an empirical correlation exists for the calculation of the droplet velocities formed during the breaking processes as a function of their size, only the pdf(d) is considered. Before and after the droplet break-up, the mass balance can be written in the form:

$$\int_{D\,min}^{D\,max} pdf(D)D^3 dD = 1 \tag{3-123}$$

where $D=d/d_{30}$. Here, d is the droplet size and d_{30} is the volume mean diameter. $D_{max}=d_{max}/d_{30}$ is the maximum possible droplet size in the distribution, calculated by the break-up model, and $D_{min}=d_{min}/d_{30}$ is the minimum droplet size, calculated according to the Taylor theory as:

$$d_{min} = 2\pi \frac{(\rho_{liquid} + \rho_{gas})\sigma}{\rho_{liquid}\rho_{gas}u_{rel}^2} \tag{3-124}$$

Also, the normalization constrain for the pdf(D) is:

$$\int_{D\,min}^{D\,max} pdf(D)dD = 1 \tag{3-125}$$

To select for a specific probability distribution function from the infinite number of functions that satisfy these two correlations, a mathematical constrain is required. It is assumed that the pdf(D) maximizes the Shannon entropy. This is given as:

$$S = -\int_{D\,min}^{D\,max} pdf(D)\cdot \ln[pdf(D)]dD \tag{3-126}$$

Using the method of Lagrance multipliers, the function that maximizes the above correlation and at the same time satisfies the mass balance equation and the normalization constrain, can be written in the form:

$$pdf(D) = 3D^2 \exp[-a_1 - a_2 D^3] \tag{3-127}$$

where a_1 and a_2 are coefficients to be determined. These are functions of the d_{max} and d_{30} and play an important role on the shape of the calculated pdf(D). Since there is no analytical solution, a numerical technique is used for their calculation. Initially, two

values for these coefficients are assumed, for example $a_1^0 = -1$ and $a_2^0 = -1$. Then, the following functions are calculated:

$$G_1(a_1, a_2) = \sum_i pdf(D_i) D_i^3$$
$$G_2(a_1, a_2) = \sum_i pdf(D_i) \qquad (3\text{-}128)$$

Then, the new coefficients are calculated using a Newton-Rampson method extended to a system of algebraic equations, as:

$$a_1^n = a_1^{n-1} + da_1^n$$
$$a_2^n = a_2^{n-1} + da_2^n \qquad (3\text{-}129)$$

where the da_1 and da_2 are given from the solution of the linear system:

$$da_1 \frac{\partial G_1(a_1, a_2)}{\partial a_1} + da_2 \frac{\partial G_1(a_1, a_2)}{\partial a_2} = -G_1$$
$$da_1 \frac{\partial G_2(a_1, a_2)}{\partial a_1} + da_2 \frac{\partial G_2(a_1, a_2)}{\partial a_2} = -G_2 \qquad (3\text{-}130)$$

The procedure is terminated when both da_1 and da_2 become smaller than a certain value.

It should be noted that this model requires as inputs (calculated from the break-up model) the maximum droplet size d_{max} and the volume mean diameter d_{30}. However, the various break-up models usually calculate the Sauter mean diameter rather than the d_{30}. Thus, an external loop is required for the calculation of the d_{30} of the calculated distribution. Starting from an assumed value for the d_{30}, the $SMD_{a1,a2} = \frac{\sum_i pdf(D_i) D_i^3}{\sum_i pdf(D_i) D_i^2}$ is calculated after the calculation of a_1 and a_2, and it is compared with the SMD value of the break-up model. The calculation terminates when their difference becomes smaller than a certain value (for example 0.1 microns). The D_{30} required for the estimation of

the number of the droplets formed is calculated after the two unknown coefficients have been determined as $D_{30} = [\frac{\sum pdf(D_i)D_i^3}{\sum_i pdf(D_i)}]^{1/3}$.

3.3.6 Droplet collisions

3.3.6.1 General approach - literature review

Droplet collisions occur in various spray applications, such as climatic chambers, agriculture sprayers and engines. Thus, the physics involved in such procedures is an important aspect in spray modeling. Collisions between droplets are caused by differences in their velocities. The differences in velocities arise particularly from the interaction of droplets from opposite streams or overlapping spray regimes (for example it is shown in the present study that collisions occur during the spray impingement close to the wall since the incoming and the outcoming droplets are moving in almost the opposite direction). Also, collisions may arise due to differences in response to a flow field by droplets of different size and mass, flow field shear and turbulence, waves and flow instabilities. It has been shown that collisions play an important role at the regions with high droplet number density, such the regions close to the spray axis of a diesel spray (O'Rourke and Bracco (1980)). Another reason leading to droplet collision arises from the differences in the injection velocity during the injection period. Droplets injected with high injection velocity may catch-up earlier injected droplet with smaller velocity. The lamella formed in the front of a liquid jet is attributed to this regulation in the injection velocity and the collision between the fluid elements (Chaves et. al. (1996)).

Up to now, no fundamental theory exists to describe in detail the flow dynamics during the collisions of two or more droplets. Usually, simple mechanistic models are used to describe these processes. Several types of interaction are possible (Ashgriz & Givi (1987): (i) the droplets may bounce apart (bouncing collision), (ii) they may bounce but contact of the two surfaces being prevented by the intervening air film (grazing collision), (iii) they may coalesce and remain permanently united (permanent coalescence), (iv) they may coalesce temporarily, with the subsequent separation accompanied by satellite droplets or (v) with very high collision energy, shattering may occur, in which tiny droplets are expelled radially from the periphery of the interacting

droplets (shattering collision). The type of interaction depends upon the sizes of droplets, their velocities, the angular momentum and other parameters such as the liquid and gas properties.

A large number of investigations have been performed on the understanding and modeling of droplet collisions. The evolution of droplet size distribution in spatially homogeneous droplet clouds involving coalescence has been studied extensively (Pzuppacher and Klett (1978), Pearson et al. (1984, 1985)). Kinetic equations were derived describing the change with time of a droplet size probability density function. The expression for droplet collision rates in these kinetic equations incorporates a collection kernel, which is calculated from the expected droplet relative velocity and the impaction efficiency in collision. Collection kernels have been suggested for Brownian and turbulent coagulation, gravitational sedimentation, thermophoresis and diffusiophoresis. Gillespie (1975) rigorously derived a Monte-Carlo procedure for modeling the stochastic coalescence process, employing such collection kernels. Numerous numerical simulations have been performed, yielding results in agreement with experimental observations. The kinetic equations of numerical methods for the calculation of droplet size distribution in homogeneous clouds, taking into account the droplet break-up and rebound in collisions, as well as coagulation, were also developed (Gillespie and List (1979)). Brown (1985) proposed a finite difference scheme for solving coalescence-break-up equations for rain droplets in the atmosphere, where the droplets were assigned terminal falling velocity. Inhomogeneous gas-droplet flows have received considerable attention (Faeth (1983), Mostafa and Elgobashi (1985) and Mostafa and Mongia (1986, 1987)) have solved a system of coupled conservation equations governing the flow in a turbulent jet with vapourizing droplets. They employed a Lagrangian approach to describe droplet motion in a turbulent velocity field and used expressions for the droplet diffusivity in gas. O'Rourke (1980) has thoroughly analyzed the vapourization of fuel droplets in a turbulent jet, taking into account collisions between droplets, particularly droplet coagulation. The relevant mass, momentum and energy conservation equations were solved numerically. The method treats droplet collisions though a Monte-Carlo procedure.

Kitron et al. (1991) suggested a stochastic model based on the Boltzmann kinetic equation in order to describe the droplet size and spatial distribution in a dense spray. The Monte-Carlo method was again used. This model was valid only if the inertia of the

droplets is very high and the dynamic coupling with the gas is low. The results showed that droplet collisions strongly affect the droplet size and spatial distribution in the testing area (reactor). This was found to have a profound effect on the fuel evaporation rate. The collision-induced break-up was found to significantly affect the flow pattern. Another study by Nguyen et al. (1991) was concerned with the investigation of the interaction effects in a stream of single droplets and small groups of droplets. In particular, the effect of neighbouring droplets on droplet drag coefficient was examined, using both an experimental and numerical analysis. A summary and evaluation of different drag and evaporation models was presented.

In a more recent study by Jiang et al. (1992), the collision dynamics of water droplets and hydrocarbon droplets was examined. The results show that in the investigated range of Weber numbers, the behaviour of hydrocarbon droplets is significantly more complex than that of water droplets. For head-on collisions, while the permanent coalescence always results for water droplets, the outcome is quite non-monotonic for the hydrocarbon droplets in that, with increasing Weber number, the collision can result in permanent coalescence, bouncing, permanent coalescence again, and coalescence followed by separation with or without production of satellite droplets. Similar complexities were found to exist for off-center collisions. Phenomenological explanations were offered based on the fluid properties, the relative influences of the normal and shearing aspects of the collision, and the nature and extent of energy dissipation due to droplet deformation during collision.

Another fundamental study has been reported by Silverman and Sirignano (1994), on the modeling of dense sprays. In the statistical approach used for the simulation of the fuel cloud, correlations were used for the effects of interactions between neighbouring droplets on various parameters such as the drag coefficient, Nusselt number and Sherwood number. The correction factors introduced enable the calculation of the drag coefficient, evaporation and heat transfer of a droplet in a cloud based on models for a single droplet. It was found that the interaction effects are important during a large fraction of the droplet lifetime as the droplet size decreases. The multi-droplet interactions cause the drag coefficient of a droplet in a dense spray to be lower - and hence its velocity higher - than that of an isolated droplet. This was found to have a profound effect on fuel evaporation rate. Many other studies have demonstrated the importance of droplet collisions in Diesel sprays (Bracco (1985),

Tambour et al. (1985), Nguyen et al. (1991), Oeserle et al. (1991), Gavaises et al. (1996)).

In the present study, a model developed by O'Rourke (1980) and used by O'Rourke and Bracco (1981) for the modeling of dense sprays has been implemented in the CFD code. This model is the standard collision model in most of the commercial CFD codes. Following the mathematical formulation of this model is given.

3.3.6.2 Collision model

Collisions are modeled using a statistical approach rather than a deterministic one. Three types of collision outcomes are taken into account: permanent coalescence, separation and bouncing. During their collision, droplets can exchange mass, momentum and energy. Collisions are allowed only between droplets of different parcels (in consistence with the droplet-parcel discretization method adopted in the present investigation).

Initially, it has to be decided when collision between two parcels occurs. This criterion can not be based only on the geometric condition for collision between two parcels (i.e. when the distance between their centers becomes smaller than the sum of their radius) since only a small fraction of parcels is used compared to the actual number of droplets in a diesel spray. To solve that problem, different assumptions have been made by several authors. Most of them (for example KIVA and SPEED codes), assume that two parcels may collide if and only if lie in the same computational cell. However, this assumption is a bit dubious because collision between two spatially very close parcels which reside in different computational cells is a priori excluded, in contrast to a pair of possibly far distant parcels in the same computational cell. Under this assumption, the collision model is strongly depended on the computational mesh used. To resolve this problem, it is assumed that two parcels may collide if their distance is smaller than a critical value, which depends on the number of droplets in both of the two parcels. This critical distance is calculated as $R_{CRIT} = r_1 N_1 + r_2 N_2$, where r_i is the droplet radius, N_i the number of droplets in the parcel and the subscripts i=1,2 refer to the two parcels under examination (it is obvious that in the limiting case of $N_1 = N_2 = 1$, this criterion coincides to the pure geometric condition for collision). If the condition:

$$D_{1,2} = \sqrt{\left|(x_1 - x_2)^2 + (y_1 - y_2)^2 + (z_1 - z_2)^2\right|} \le R_{CR} \tag{3-131}$$

is satisfied, then it is possible collision between the two parcels to occur. Figure 3-3 shows a schematic representation of this criterion.

To decide if collision will occur, the collision frequency is calculated as:

$$f_{COLL} = \frac{\pi}{2}(r_1 + r_2)^2 |u_{rel}| E_{1,2} \frac{N_1 + N_2}{V_{COLL}} \tag{3-132}$$

The term $(N_1 + N_2)/V_{COLL}$ represents the droplet number density in the examined volume, since $V_{COLL} = \frac{4}{3}\pi R_{CR}^3$ is the volume of a spherical area with radius R_{CR} in which collisions between the two parcels are allowed. The above equation comes from the kinetic theory of gases, but because of the differences between droplet and molecular collisions, the collision efficiency $E_{1,2}$ is introduced to allow for these effects (these differences are the following: the droplet motion is influenced by the gas, so the collision cross-section will differ from that calculated assuming straight-line trajectories. Also, collisions between droplets can result in a greater number of outcomes than those between molecules). This is defined as the ratio of the effective collision cross-section to that obtained by assuming straight-line trajectories of droplets, and it is evaluated as:

$$E_{1,2} = \left(1 + \frac{3}{4}\ln\frac{2W}{W - 1.214}\right)^{-2} \qquad W > 1.214$$
$$E = 0.0 \qquad W \le 1.214 \tag{3-133}$$

where

$$W = \frac{\rho_{liquid} |u_{rel}| r_2^2}{9\mu_{liquid} r_1}$$

where is has been assumed that $r_2 > r_1$.

The probability that the larger droplet (collector) undergoes n collisions with the droplets during a time interval dt, is assumed to follow a Poisson distribution with mean value $\bar{n} = f_{COLL} dt$:

$$P_n = \frac{(\bar{n})^n}{n!} e^{-\bar{n}} \qquad (3\text{-}134)$$

The case n=0 gives the probability of no collisions $P_0 = e^{-\bar{n}}$. To determine whether collisions take place between the droplets in the considered parcels, a random number Y_1 in the interval (0,1) is selected. If $Y_1 < P_0$, no collision occurs. It should be noted that the time step dt should be smaller that the characteristic time scale of the collision, which is assumed to be $1/f_{COLL}$.

In the case that a collision occurs between the droplets of the two parcels under consideration, three possible outcomes are considered: coalescence, bouncing and separation. However, the criteria used in order to determine which of the three occurs are arbitrary rather than deterministic one, in the absence of further physical information.

Initially, another random number Y_2 in the same range (0,1) is selected. If $Y_2 > E_{COAL}$, then separation occurs. In the opposite case, if $Y_2 > E_{BOUNCE}$, then bouncing occurs while coalescence is calculated for all other values of Y_2. E_{COAL} and E_{BOUNCE} are the coalescence efficiency and bouncing efficiency respectively, and are calculated as follows.

Separation

Brazier-Smith et al. (1972) studied the criterion for the separation type of collisions from the coalescence type. Their experiments showed that when the collision involves the droplets of nearly equal size and the impact parameter exceeds some critical value, the droplets will separate. Often two or three smaller satellite droplets are produced in this process. However, these are not taken into account by introducing new computational parcels. In the theoretical part of their study, they found that in order for separation to occur, the rotational energy must exceed the additional surface energy required to form the initial droplets from the coalescence drop-pair. In mathematical terms, this condition reads:

$$E \geq E_{COAL} \qquad (3\text{-}135)$$

where E and E_{COAL} are the coalescence efficiency and its critical value, respectively, defined as:

$$E = \left(\frac{D_{1,2}}{(r_1 + r_2)} \right)^2$$

$$E_{COAL} = \min\left(\frac{2.4f(g)}{We_2}, 1 \right)$$

$$f(g) = g^3 - 2.4g^2 + 2.7g \qquad (3\text{-}136)$$

$$g = \frac{r_1}{r_2}$$

$$We_2 = \frac{\rho_{liquid} u_{rel}^2 r_2}{\sigma}$$

Note that the condition $Y_2 > E_{COAL}$ is equivalent to $X > D_c$, where $D_c = (r_1 + r_2)E_{COAL}^{1/2}$ is the critical inter-droplet distance when separation is still possible, and X is the randomly chosen distance given by $X = (r_1 + r_2)Y_2^{1/2}$.

O'Rourke (1980) derived the droplet parcel velocities from the conservation of the linear and angular momentum and energy under the assumption that the droplets retain their initial size. The following expressions were obtained:

$$u_i = \frac{1}{m_1 + m_2}[(mu)_1 + (mu)_2 + m_j(u_i - u_j)f_u]$$

$$f_u = \frac{X - D_c}{(r_1 + r_2) - D_c} = \frac{Y_2^{1/2} - E_{COAL}^{1/2}}{1 - E_{COAL}^{1/2}} \qquad (3\text{-}137)$$

where

$i = 1,2$

Coalescence

In the case that separation does not occur, then permanent coalescence or bouncing may be the outcome of the collision. If the droplets kinetic energy is high enough to overcome the resistance of the air film trapped between them, the outcome of the collision will be coalescence. Then, the $Y_2 < E_{BOUNCE}$ is satisfied, where:

$$E_{BOUNCE} = \left(\frac{We_2}{2.4f(g)} \right)^{1/3} \tag{3-138}$$

Only a specific number of droplet is assumed to collide (and not all the droplets in the two parcels under consideration). The number of droplets N which take part in the coalescence with each collector droplet is determined by:

$$\sum_{i=0}^{i=N-1} P_i < Y_2 < \sum_{i=0}^{i=N} P_i \tag{3-139}$$

The new properties of the collector (the larger of the two droplets) are estimated from the conservation of mass, momentum and energy, assuming that the properties (velocity and temperature) of all the other droplets remain the same:

$$\begin{aligned} m_1^n &= m_1 + m_2 N \\ (mu)_1^n &= (mu)_1 + (mu)_2 N \\ (mT)_1^n &= (mT)_1 + (mT)_2 N \end{aligned} \tag{3-140}$$

The number of droplets in the collector is assumed to remain unchanged while N droplets are removed from the other parcel (until its complete depletion).

Bouncing

The bouncing type of collision occurs at low droplet velocities and it is accompanied by the deformation of each of the approaching droplet pair approximately into the shape of an oblate spheroid due to the film of air trapped between them. The threshold condition for bouncing is $Y_2 \geq E_{BOUNCE}$. As the droplets involved in bouncing do not touch each other, they retain their size and internal energy, and exchange only momentum. Their velocities are determined as in the case of separation. However, the value of coefficient f_u is given for this case from the expression:

$$f_u = \frac{Y_2^{1/2} - E_{BOUNCE}^{1/2}}{1 - E_{BOUNCE}^{1/2}} \tag{3-141}$$

It should be noted that the calculation of collisions strongly slows down the calculations and if the number of computational parcels used is more than approximately $2 \cdot 10^4$, it is almost impossible to be used. An alternatively way is to take into account only the changes of the droplet velocities during collisions and neglect any possible coalescence. Then, according to Andrews and O'Rourke (1996), the corresponding force can be calculated as a function of the void fraction (which represents the density of the spray at the droplet position) as:

$$\vec{F}_{COLLISION} = \frac{1}{\theta} \nabla_x \tau \tag{3-142}$$

where θ is the liquid void fraction and according to Harris and Grighton (1994)

$$\tau = P_S \frac{\theta}{\theta_{CP} - \theta} \tag{3-143}$$

where P_S is a constant with units of pressure and θ_{CP} is the void fraction at close packing. This force can be taken into account during the calculation of the droplet velocity from equation (3-28).

3.3.7 Effect of gas turbulence on droplet motion

Gas turbulence affects the dispersion of the moving droplets. Most of the studies on particle-turbulence interactions, concern solid particles, since break-up and other phenomena related to the liquid droplets significantly complicate the investigation of such effects on liquid droplets. It is generally assumed that the droplet have a similar behaviour as the solid particles as far as it concerns their interaction with the turbulence characteristics of the continuum phase. Experimental studies of turbulent two-phase flows (Modarress, Wuerer and Elgobashi (1982, 1984) and Modarress, Tan and Elgobashi (1983)), show that the particles dispersion is higher than in laminar flows. They also reveal that turbulence levels depend on the loading and are usually smaller than those of single-phase turbulence levels. However, a mechanism of turbulence production is due to very high relative velocity between the droplets and the gas close to

the injection nozzle. This turbulence production has a reverse effect on the droplets dispersion. Turbulence kinetic energy and its dissipation rate are affected by the loading (which is equivalent to the number of droplets in an eddy with length $l_{eddy} = c_\mu^{3/4} k^{2/3} / \varepsilon$). For dilute sprays, turbulence effects can be modeled using linear approximations for the calculation of the coupling terms added to the k-ε turbulence model of the gas phase (Modarress, Tan and Elgobashi (1983)). These terms are a function of the relative velocity between the droplets and the gas, the size of the particles, the drag coefficient, the kinematic viscosity of the gas phase, the density ratio and k and ε. Their calculation is also based on the particle response to the gas-phase turbulence spectrum. However, for dense sprays, like the cases close to the injection holes, although these approximation might not be valid, no further investigation has been performed. It is usually assumed that atomization and collision effects in these regions play the dominant role on determing the spray characteristics (O'Rourke (1980) and O'Rourke and Bracco (1980)).

Hinze (1972) showed that if the response time of the particles on the turbulence perturbations is smaller than the Kolmogorov time scale, then, the particles follow the smaller eddies. He also showed that the particles response time depends on the eddy life time and scale, the droplet size and the density ratio between the particles and the gas. In flow fields with low frequency turbulence levels, the particles do not follow the gas phase turbulence perturbations. Their response time depends on the Stokes number defined as $St = \frac{\nu}{\omega d^2}$ where v is the gas kinematic viscosity, d is the diameter of the particle and ω is the frequency of turbulent perturbations.

Choi and Chung (1983) showed that small particles decrease the turbulence fluctuations and increase the dissipation rate of turbulence kinetic energy. These results indicate that friction at the particle surface plays an important role in determining k and ε.

Ahmadi and Goldshmidt (1969) studied the diffusion (dispersion) of particles in random fields simulated by the superposition of randomly distributed vortices accounting for kinematic effects only; they showed that the relative mass diffusivity first increases and ultimately decreases to zero as the particle size is increased.

It is generally accepted that the turbulence effects on the particle motion can be modeled under the assumption that the gas velocity is the sum of an average velocity and a fluctuating velocity:

$$\vec{u} = \vec{u}_{MEAN} + \vec{u}' \tag{3-144}$$

where the fluctuating velocity term can be estimated as a function of the turbulence kinetic energy and its dissipation rate calculated from the gas-phase turbulence model. If the above hypothesis for the velocity that the particle 'sees' is adopted, then, the distribution function $f(\vec{x},\vec{u},m,T,t)$ can be written as $f(\vec{x},\vec{u},\vec{u}',m,T,t)$ where

$$f(\vec{x},\vec{u},\vec{u}',m,T,t) = (\frac{4}{3}\pi k)\exp[\frac{-3|\vec{u}'|^2}{4k}]f'(\vec{x},\vec{u},m,T,t) \tag{3-145}$$

where k is the turbulence kinetic energy at the particle position and f' can be obtained from f by integrating over all values of $\vec{u}'$. Under these assumptions, the spray equation (3-2) can be written as:

$$\frac{\partial f}{\partial t} + \nabla_{\vec{x}}(f\cdot\vec{u}) + \nabla_{\vec{u}}(f\cdot\vec{a}) + \frac{\partial}{\partial T}(f\cdot\dot{T}) + \frac{\partial}{\partial m}(f\cdot\dot{m}) + \nabla_{\vec{u}'}(f\frac{\partial\vec{u}'}{\partial t}) = \dot{f}_{SOURCE} \tag{3-146}$$

where the last term is equal to the turbulence production term:

$$\dot{f}_{TURBULENCE} = \nabla_{\vec{u}'}(f\frac{\partial\vec{u}'}{\partial t}) \tag{3-147}$$

Turbulence effects on the motion of particles in two phase flows are modeled according to Dukowicz (1980) and O'Rourke (1989). Gosman and Ioannides (1983) have proposed similar ideas for the modeling of the calculations on the fluctuating velocity.

In this model, isotropic turbulence is assumed. It is also assumed that every single component of the fluctuating velocity $\vec{u}'$ follows a Gaussian distribution with standard deviation $s = \sqrt{2k/3}$. Then the $\vec{u}'$ is randomly selected from the distribution:

$$G(\vec{u}') = \frac{1}{\sqrt{2\pi}\, s} \exp\left(-\frac{\vec{u}'^2}{2s^2} \right) \tag{3-148}$$

The $\vec{u}'$ is selected after the pass of the so-called turbulence correlation time, defined as the minimum of the eddy life time and the time required for the particle to traverse this eddy, thus:

$$t_{TURB} = \min\{t_{EDDY}, t_{TRAV}\}$$

where (3-149)

$$t_{EDDY} = k/\varepsilon \text{ and } t_{TRAV} = C_{ps} \frac{k^{3/2}}{\varepsilon} \frac{1}{|u_{rel}|}$$

where it has been assumed that the characteristic eddy size equals to the dissipation length scale given as $l_{eddy} = c_{\mu}^{3/4} k^{2/3} / \varepsilon$ and C_{ps}=0.145 is an empirical constant.

O'Rourke (1989) proposed a model of numerical implementation of the above physical considerations in three-dimensional CFD codes in cases where the time step of the particle tracking is larger than the turbulence correlation time; this model has been used in the present investigation.

3.3.8 Droplet-Wall interactions

3.3.8.1 General approach - literature review

Spray impingement on a wall is an important phenomenon occurring in many application, among them in the piston bowl of small passenger car DI diesel engines or in the valve stem during the port injection of gasoline engines. The importance of the phenomenon is revealed throughout a lot of observations. First of all, the spray characteristics significantly change during its impaction (droplet size and spray dispersion). A lot of emission studies on diesel engines show that a significant amount of the unburned hydrocarbons is due to the fuel film formed on the piston walls during the spray impingement. The heat transfer between the spray and the hot walls of the engine usually affects the evaporation rate of the fuel, and as a result, the engine

performance. Other studies show that a better fuel atomization and a faster mixing can be achieved in cases of spray impingement.

A lot of experimental and computational investigations have been reported studding the spray-wall interactions; these can be divided in two basic categories: single droplet impingement cases where the main aim is the understanding of the basic physics of the phenomenon, and spray impingement cases revealing the global spray characteristics during impingement. The wall conditions (roughness, temperature and presence of liquid film) are important factors affecting the phenomenon. In order to achieve good optical access to the impingement area, most of the experiments have studied impingement of single droplets or sprays on flat surfaces. Photographic as well as laser techniques have been used in order to obtain information about the droplet characteristics before and after impingement. On the contrary, studies on the associated with the impingement process wall film formation and development are very limited. In the simulation side, most of the studies are based on phenomenological models rather than on multidimensional ones solving for the detailed fluid dynamics during the impingement of every single droplet, since the former ones can be easily implemented in CFD spray codes, All of these phenomenological droplet-wall interaction models use empirical correlations derived from the single droplet impingement investigations; the whole impinging spray dispersion is then predicted as a function of the dispersion of every single droplet in the spray. In what follows, a review of the most important investigations in this area is given.

(i) Experiments - single droplet impingement

Single droplet impingement cases are fundamental, since they reveal the basic physics of the phenomenon. Different impinging conditions have been studied, examining the effect of droplet size and velocity, the liquid physical properties, the angle of impaction and the wall conditions on the characteristics of the droplet(s) ejecting from the wall; studies on droplets impinging on a wetted surface (or in a pool) have also been published.

An early study by Jayaratne and Mason (1964) was focused on the investigation of the rebounding process of water droplets impinging on water pool. The size of the impinging droplets was varying from 60 to 200 microns, while the impinging velocity

was of the order of 1 m/s. The pool temperature was kept constant (290K). Relations were established between the droplet radius and the critical values of impinging velocity and angle of impaction at which coalescence between the liquid pool and the impinging droplet occurs. In the case of droplet rebounding, the contact time between the droplet and the water surface was estimated, together with the kinetic energy loss of the impinging droplets.

A fundamental study, reference in most of the simulation models, has been published by Wachters and Westerling (1966). They studied the heat transfer between an impinging water droplet and a heated polished flat surface. The droplet diameter was in the order of 2 mm, the wall surface temperature was 400° C and the temperature of the impinging droplets was 300°C. A wide range of injection velocities was examined, giving a droplet Weber number between 0 to 140. Photographs of the deformation process of the droplets during their impingement were taken, showing that different hydrodynamics regimes can occur: the rebounding, the splashing, the break-up and the sticking regimes were identified as possible outcomes of the process. The first one was observed for low Weber numbers and the following two for Weber numbers between 40 and 80. For Weber numbers higher than 80, the droplets were found to stick on the wall forming a liquid film. The heat transfer between the droplet and the heated wall was also examined, for different wall temperatures, using heat flow meters. The vapour formed between the impinging droplet and the wall was found to play an important role in the rebounding process as well in the heat transfer process. An important result from this investigation was the presentation of a map, showing a relationship between the Weber number of the impinging and the rebounding droplets.

Another fundamental study on the behaviour of a single droplet impinging on a hot surface has been published by Takeuchi et al. (1982). The results showed, that for wall temperatures between 200 to 400 °C, the break-up behaviour of the impinging droplets could be divided into six categories, depending on the vapour formation in the solid-liquid interface and the droplet Weber number. Also, the results showed that the mean diameter of the droplets formed during the break-up process, could be described as a function of the thickness of the radial film and the Weber number for all of the different cases identified. The hydrodynamic regimes observed by photographing the deformation process of the impinging droplets, were classified as follows: in the case of low impinging velocity the droplet was initially spreading in the surface forming a radial

film independently of the examined range of wall temperature. Since its momentum was not enough to break-up the droplet, it was thereafter shrink and rebounded from the surface without breaking up. For higher impinging velocities, when the disturbances in the shrinking process of the radial film were becoming larger, rebounding with break-up was the outcome. For higher wall temperature, the radial film was breaking up due to the vapour blowing in the center of the film. (thus, no shrinking process was occurring). Small droplets were observed to blown upward with vapour, while most of the mass of the droplet was remaining on the surface in separated forms. For even higher impinging velocities, a widen number of small droplets was formed, occurring by both the blowing process and the breaking up of the radial film. This was happening because the momentum of the film was high enough to overcome the surface tension forces opposing to the film disintegration. For even higher wall temperatures, the blowing effect of the vapour formed in the solid-liquid interface was becoming the dominant factor of the droplet disintegration. No radial film was formed on the surface, which was becoming dry after a very sort time. For higher impinging velocities and hot wall, the vapour film at the bottom of the droplet was blown in the radial direction. Thereafter, as the diameter of the film was further increasing, it was broken up into droplets. Small droplets were formed with dispersion velocity in the radial direction higher than the film velocity.

Senda et al. (1988) presented a similar work on the heat transfer characteristics of small droplets impinging upon a hot surface. The break-up behaviour was related to the surface temperature at the point of the maximum evaporation rate (Leidenfrost point). Heat transfer measurements were taken and heat transfer coefficients were estimated.

An exceptional work in this field has been reported by Chandra and Avedisian (1991, 1992). In this study, the primary parameter was the surface temperature, while the droplet Weber number was kept constant in the value of 43. The droplet diameter was of the order of 1.5 mm and the ambient pressure was 1 bar. The surface temperature was varied from 24°C to above the Leidenfrost temperature of the liquid. Experiments were also performed on a droplet impacting a surface on which liquid film created by deposition of a prior droplet was present. A flash photographic method was used in order to visualize the deformation process during the droplet impingement. The evolution of the wetted area and the spreading rate of a droplet impinging either on a

stainless steel surface or spreading over a thin liquid film, were found to be independent of the surface temperature at the early period of impact. A single bubble was observed to form within the droplet during impact at low temperatures. As surface temperature was increased the population of bubbles within the droplet also increased because of progressive activation of nucleation sites on the stainless steel surface. At surface temperatures near to the boiling point of the fuel, a spoke-like cellular structure in the liquid was created during the spreading process by coalescence of a rig of bubbles that had formed within the droplet. At higher temperatures, but below the Leidenfrost point, numerous bubbles appeared within the droplet. A model, calculating the maximum spreading ratio of the droplet during its impingement and the impact time was presented, showing good agreement with the experimental data.

More recently, a work by Naber et al. (1993) was published on the hydrodynamics of impinging droplets on heated surfaces. Different hydrodynamic regimes were again observed, named wetting, transition and non-wetting, associated with the specific impingement conditions (droplet size, velocity, surface temperature, and ambient pressure). Images from selected impingement conditions were analyzed to quantify the atomization resulting from the impingement. In the wetting hydrodynamic regime on dry and liquid coated surfaces, atomization resulting from the impingement did not occur for Weber<130. For Weber>130, atomization was resulting from the splashing of the droplet. In the transition hydrodynamic regime significant atomization was resulting due to the rapid formation of vapour bubbles in the liquid film on the surface. In the non-wetting regime, atomization increased with increasing Weber number. As the impinging Weber number increased from 20 to 120 for a normal impingement, the Weber number calculated on the basis of the mean normal to the wall droplet ejection velocity was decreased while the Weber number estimated on the basis of the mean droplet tangential to the wall velocity component was increased from 0 to 80. It was also identified that in cases where the ambient pressure was greater than the critical pressure of the liquid (such as in DI diesel engines), for surface temperatures between 150°-300°C, the wetting regime occurs. In these cases, fuel film formation was unavoidable.

Mundo et al. (1995) published results of an extensive investigation on the behaviour of single droplet impingement on cold surfaces. The impinging droplet diameters were between 60 and 150 microns, the normal to the wall velocities between

12 and 18 m/s, impingement angles between 4 and 65°, viscosities between 1.0 and 2.9 mPa and surface tensions between 22 and 72 mN/m. Cases with different surface roughness relative to the size of the impinging droplets (from 0.03 to 0.86) were also tested. The different physical processes taking place during the impingement on smooth or rough surfaces were revealed. One major result from the visualization was a correlation for the deposition-splashing boundary in terms of the Reynolds and Ohnesorge numbers. For the case of a splashing droplet, a two-component PDA was used to characterize the size and velocity of the secondary droplets. The obtained droplet size distributions and correlations between droplet size and velocity around the point of impingement were also presented, giving unique information about the splashing mechanism. In another paper from the same authors (1995), a numerical model was proposed, based on the experimental data of this investigation.

Karl et al. (1995) published an investigation on the disintegration process of droplets (water and ethanol) impinging on a surface with temperature above the Leidenfrost temperature of the liquid droplet. The droplet diameter was varying from 70 to 260 microns and the Weber number from 0 to 2500. From the experimental data it was revealed that a new mode of disintegration different from the droplet splashing: satellite formation can occur during the droplet impingement if the impinging velocity is much smaller that the one required for splashing. A correlation between the capillarity number (defined as Ka=We/Re) and the dimensionless viscosity length (defined as $L=Re^{3/2}/We \cdot Str^{1/2}$ with Str=f·D/Vn being the Strouhal number (f is the frequency that droplets impinge on the wall), was identified, giving the conditions for satellite formation or droplet splashing.

(ii) Experiments - impingement of diesel sprays

A number of experiments has been conducted until now, investigating the characteristics of the whole spray impinging on flat surfaces. During these experiments, droplets with different sizes and different velocities impinge almost simultaneously on the surface. However, the results show that the phenomena occurring are more complicated than those taking place during the single droplet impingement. Factors such as the gas motion induced by the spray, which is usually referred to as head vortex, the droplet-droplet interactions and the impingement on wetted surfaces of variable film

thickness and usually in relative motion with the wall, complicate the phenomenon. Thus, the structure of impinging sprays cannot be explained only with the information derived from single droplet experiments. Both photographic and laser investigations have been carried out over the last few years; the most important of them are summarized below.

Choi et al. (1987), examined the mechanisms of film boiling heat transfer of normally impacting sprays. The fuel injection system used was able to produce uniform droplets, with independent variables of droplet size, velocity and liquid flow rate. The heated target was placed either horizontally or vertically (in the direction of gravity), so the secondary droplets were 'removed' from the area under examination. It was found that the film boiling heat transfer was mainly controlled by the liquid mass flux impinging on the wall, and it was increased when the liquid mass flux was increased. In the film boiling region, a vertically impacting spray was found to have higher heat transfer than a horizontal impacting spray, due to the secondary contacts of splattered droplets. The opposite was found to be the case in the transition boiling region.

Another study, widely used until now for the validation of phenomenological impingement models implemented in CFD codes, has been reported by Katsura et al. (1989). A diesel spray was injected into a high pressure chamber in which compressed air or CO_2 at room temperature was charged. The growth of the spray was photographed with both transient and scattered light. The temporal and spatial distribution of the droplets density in the impinging spray was estimated The effect of the ambient gas density on the spray dispersion was revealed together with the effect of the distance between the injector and the impinging wall. Also, experimental correlations for the wall spray radius and the wall spray height were proposed.

Zurlo et al. (1991) studied the dynamics of a diesel impinging spray, using photographic techniques as well as a modified polarization-ratio-particle sizer. Cases with the wall placed in different position relative to the injector, from 10 to 70 mm (and thus, different impinging velocities) were tested. The injection pressure was kept constant and equal to 480 bar. Still photographs taken through the bottom of the plate (made by quartz to allow optical access), showed the presence of several different zones. The impaction region was centered on the spray centerline. Surrounding the impaction zone was a liquid build-up region. Ligaments pointing radially outward were found at the edge of the liquid build-up region. At the leading edge of the impinging spray,

droplets were observed. Droplet size measurements showed that smaller droplets were close to the spray rather than away from it. Ligament formation rather than droplet shattering, was found to be the dominant re-atomization mechanism for this high speed diesel spray, revealing that the liquid film dynamics is an important factor.

Hardalupas et al. (1992) studied the droplet characteristics of a spray impinging on a plate using a PDA system. Different impaction angles (0, 20 and 45) were tested, trying to simulate the geometry of the valve in the inlet port of gasoline engines. Information about the droplet re-atomization was given. It was found that the size of the droplets generated by re-atomization as well as the droplet flux were depended on the angle of impingement.

Booth et al. (1994) examined the geometry of the fuel cloud created by impingement of a diesel jet onto a small heated target. A Lucas CAV injector system was used to inject the spray in a high pressure and temperature bomb. The radial penetration of the impinging spray was measured by a laser interrupt method, as a function of nozzle size, impingement distance, ambient density and target diameter. The droplet cloud penetration and height at discrete time steps was measured by high speed movies. The images taken revealed the spray development. Finally, heat transfer measurements were also used to determine the total amount of thermal energy transferred into the spray from the heated target.

An investigation on the droplet sizes occurring during spray impaction has been performed by Ozdemir and Whitelaw (1993). The results of this work revealed how differently the dynamics of an impinging spray could be relative to the impingement of a single droplet. Phase-Doppler velocimetry as well as a laser diffraction technique were used to quantify the droplet velocities and size during the impaction process. Two mechanisms of secondary atomization were identified. The first one did not involve direct wall contact and was due to the strain acting on the droplets by the continuous phase within the impingement region. This was enhanced by thermal effects from the wall to cause break-up. The approaching velocity of the inflowing droplets to the plate was important to this process so the higher velocities increased the rate of strain within the impingement region and, consequently, the wall temperature promoting the secondary atomization shifted towards lower values. The second mechanism required direct wall contact and involved atomization of the film deposited on the wall by the impingement of the spray. With the penetration of high-speed inflowing droplets into

the film, liquid mass was raised into the two-phase medium due to splashing from the film so that a new size class with larger droplets was generated. The resulting large droplets tended to stay close to the wall within the impingement region with small vertical velocities. Another interesting result of this investigation was based on the film dynamics between subsequent injection. In between them, the suspended droplet field above the film oscillated normal to the plate as a cloud so that the impact of large droplets on the film resulted in coalescence with the film and the ejection of smaller numbers of small droplets. The unsteady wall jet flow, caused by the arrival of the spray at the plate, swept the vertically oscillating droplet cloud radially outwards so that the resulting radial transport caused the dynamics of the unsteady film to be correlated with the size characteristics of the unsteady wall jet. Based on this phenomenological description, a radial droplet transport equation was derived.

Finally, another set of investigations has been published by Arcoumanis and Chang (1993, 1994), and Arcoumanis and Cutter (1995). A PDA system was used to characterize the velocity and the size of the droplets of a diesel spray injected from a Stanadyne multihole injector. Measurements were performed in the absence of the wall, so the spray structure without impingement was fully quantified. Following, similar PDA measurements reveal the spray structure when impaction was taking place. The flat wall was placed 30 mm from the injector, which is a distance where the atomization process of the liquid core has been completed. Measurements were performed with cold or heated plate in a quiescent of in an cross flowing gas, applied to represent the swirl velocity present in the bowl of a diesel engine. Also, extensive heat transfer measurements were performed, using fast response thermocouples instrumented in the impinging plate. Different injection conditions were tested as well as different cross flow velocities and wall temperatures. A correlation for the heat transfer characteristics during the spray impingement was derived. Many other similar studies have been performed showing similar results as these aforementioned.

Summary

Droplet impingement dynamics is a flow process involving all three phases (gas, liquid and wall). At the early stages of impact the wetting dynamics is negligible compared to the inertial effects since the droplet experiences rapid spreading and

deformation owing to the rapid pressure increase inside the droplet at the point of impingement. This pressure is relieved by the motion of the liquid along the surface principally through the formation of a jet at the base of the droplet. Meanwhile, the impinging droplet is typically subject to the following forces: (a) adhesion force (b) contact pressure and wall shear stress (c) long-range forces due to the presence of ultra-thin liquid zones close to the contact line and (d) thermally-induced forces resulting from the heat transfer between the wall and the droplet. The outcome of the impingement is determined by the conditions concerning whether or not the spreading process is stable. The case of stable flow leads to either droplet rebound if the incident kinetic energy is larger than the sum of the dissipation and adhesion energies. Otherwise the droplet spreads forming a liquid film. In the unstable case, the liquid film may disintegrate causing the ejection of secondary droplets as well as the deposition of a portion of liquid mass on the wall. Major sources of flow instability are the high impact energy, the surface roughness and a temperature gradient across the spreading liquid film in situations involving heated walls. Thermal instability for larger droplets is of the Rayleigh-Taylor type of the liquid-vapour interphase and the dynamics of the bubbles resulting from the periodic instability of the interphase. The complexity of the thermal instability makes the shattering of the droplets on a hot wall to exhibit a variety of patterns.

This discussion makes clear that there are many parameters affecting the dynamics of single droplets. These are usually assumed to be the liquid physical properties (density, viscosity and surface tension), the droplet size, the droplet velocity and the wall conditions (wall roughness, temperature, presence of wall film and curvature). Following, a discussion on the effect of various parameters on the single droplet dynamics as reported up to now in the open literature is given. The analysis considers the impingement only of spherical droplets and not ligaments.

(a) Liquid physical properties: these are the liquid density, surface tension and molecular viscosity. Liquid density affects the impact pressure between the droplet and the target wall (the latter is proportional to the liquid density) and thus, contributes to the deformation and spreading process. Surface tension resists to any additional surface area, and as a result it is an important parameter during the droplet deformation process. Viscosity enhances energy dissipation during the spreading ratio and also hinders the

development of natural instabilities of the spreading liquid film. The combined effect is to delay disintegration upon impingement.

(b) Droplet size: droplet kinetic energy, which is as important parameter during impingement, is proportional to the volume of the droplet. Also droplet size has a direct influence on the deformation and film spreading due to the fact that the duration of peak impact pressure decreases with droplet size (due to the proximity of the free surface of the droplet to the center of the impact, Brunton and Rochester (1979)). The film spreading process plays an important role on the splashing outcome, i.e. to the number and to the sizes of the formed droplets. According to Stow and Stainer (1977), the number of the formed droplets is proportional to the droplet size. Another regime has been realized for droplets with size of the order of $1\mu m$. In such cases electrostatic and Van der Waals forces exert an influence compared to that of other factors (Gillespie and Rideal (1955), Jordan (1954).

(c) Droplet incidence velocity: impact velocity determines directly the deformation and radial flow of the impinging droplet since the impact pressure inside the droplet is proportional to the square power of the normal to the wall droplet velocity component. In addition, droplet velocity together with droplet diameter determine the time scale of the impingement process. Levin and Hobbs (1971) found that the maximum diameter of the liquid sheet and the height of the jet crown formed during splashing increase for higher impact velocity. This results to the formation of smaller droplets.

(d) Wall roughness: few investigations (Levin and Hobbs (1971), Mutchler (1970), Stow and Stainer (1977)) have shown that surface roughness is a parameter that significantly affects the droplet impingement dynamics. For the same incident conditions, a droplet can spread on a smooth wall while it splashes on a rough one. More secondary droplets are produced and spread in a wider area in cases of impingement on a rough wall (Stow and Hadfield (1981)). Another effect of the surface roughness is that it alters the actual local incidence angle of the impinging droplet, especially for droplets with sizes comparable to the wall roughness. Due to the complicated structure of the roughness, the effect on the incidence angle can be described as a stochastic process (Chandra and Avedisian (1992), Sommerfeld et al. (1992)).

(e) Wall temperature: from the investigations on single droplet impinging on a heated wall, it is clear that a lot of different droplet hydrodynamic regimes can occur. Various

characteristic wall temperatures have been identified as adequate criteria for the transition from one regime to another. These characteristic temperatures are summarized by Bai and Gosman (1995): $T_B < T_{PA} < T_N < T_{PR} < T_{Leid}$. T_B is the liquid boiling temperature, T_{PA} is the pure adhesion temperature, T_N is the Nakayama temperature, or the temperature at which the droplet reaches its maximum evaporation temperature, T_{PR} is the pure rebound temperature and T_{Leid} is the Leidenfrost temperature or the minimum evaporation rate temperature. Details about their estimation, especially for the Leidenfrost point are discussed by Spiegler at al. (1963), Baumeister and Simon (1973), Whalley (1987), Avedisian and Koplic (1987) and Nguyen and Avedisian (1987). In another study by Naber and Farrell (1993), the hydrodynamics of the liquid droplet impingement process were directly linked with the heat transfer regimes of the liquid/solid system. These were typically categorized as film evaporation, vapourization-boiling, transition and spheroidal evaporation (Leidenfrost).

In the film evaporation and vaporization-boiling regimes, the liquid is in contact with the surface and the hydrodynamic impingement process is categorized as the wetting regime. In the transition heat transfer regime, the liquid is in contact with the solid surface only intermittently while for the rest of the time is separated from the surface by a vapour layer formed due to liquid vapourization. Finally, in the Leidenfrost heat transfer regime the liquid is completely separated from the wall due to liquid vapour trapped in between. This regime is called the non-wetting regime.

What is the droplet deformation process when a droplet impinges on a hot wall? In the vapourization boiling regime, Chandra and Avedisian (1991) took photographs revealing the droplet deformation process. For wall temperature close to the liquid boiling temperature, a cellular structure in the liquid was created during the spreading process by coalescence of a ring of bubbles that had formed within the droplet. At higher temperatures, in the transition regime, numerous bubbles appeared within the droplet due to nucleate boiling of the liquid in contact with the wall. If the pressure of the vapour escaping below drop was increased enough to levitate the droplet, then the bulk mass makes only intermittent contact with the surface. Numerous bubbles are inside the droplet. However, if the temperature increases above the Leidenfrost point, no bubbles are present because there is no longer liquid-solid contact. For that wall temperatures, the droplet shape is similar to what occurs at lower temperatures, particularly in the early stages of impact.

(f) Droplet impact angle: the effect of impact angle are presumably associated to the asymmetry of spreading liquid sheet resulting from oblique impact. Such asymmetries induce additional instabilities during the spreading period. Jayarantne and Mason (1964) observed that a water droplet impacting on a liquid surface with low collision energy would either bounce or coalesce with the water pool depending on the impact angle. In cases of impingement on a liquid film, a part or all of the droplet mass could coalesce with the liquid on the wall, depending on the incidence angle (Glushkov (1975)). Yao and Cai (1985) found that droplet tangential velocity component contributes to destabilize the spreading film. In addition, they found that incident angle can affect the Leidenfrost temperature in case of impingement on hot wall.

(g) Presence of liquid film: its presence can alter the characteristics of the secondary droplets formed during splashing as it has been reported by many investigators (Mutchler (1970), Ghadiri (1978), Macklin and Hobbs (1969), Gregory et al. (1959). The results have shown that the number of secondary droplets decreases as the depth of liquid layer increases. In addition, the time scale of he splashing is much longer with the presence of a liquid film. Furthermore, the size distribution of the ejecting from the wall droplets is different when a droplet impinges on a wet wall; usually larger droplets are formed and sometimes the carrying mass is larger than that of the impinging droplet (Ozdemir (1992)).

From the above description of previous investigations on the spray-wall interaction, it was revealed that a lot of parameters affect the hydrodynamics of a droplet impinging on a wall. Following dimensionless analysis and the Buckingham II theorem, the number of the independent parameters can be reduced by a number of fundamental dimensions which can be summarized as follows :

Reynolds number : $Re = \frac{\rho_{LIQUID} \cdot D_{DROP} \cdot U_{NORMAL}}{\mu_{LIQUID}}$ expressing the ratio of inertial forces over viscous forces

Weber number : $We = \frac{\rho_{LIQUID} \cdot D_{DROP} \cdot U^2_{NORMAL}}{\sigma}$ expressing the ratio of impact forces (which cause the droplet disintegration) over surface tension forces which tend to keep

the droplet in the spherical shape. Usually, the Ohnesorge number (or viscosity group) and the Laplace number are used. These are defined as : $On = (We/Re^2)^{0.5}$, $Lp = Re^2/We = 1/On^2$. These numbers measure the relative importance of surface tension forces and viscous forces acting on a surface. Note that their definition is based on the normal to the wall droplet velocity component.

Relative wall roughness : $S_t = R_t / d_{drop}$

Relative wall film thickness : $S_{film} = H_{film} / d_{drop}$

Wall temperature : no dimensionless group has been introduced.

A complete theory on the droplet impingement should describe the hydrodynamic regimes occurring during the spray impingement as a function of the above parameters (in other worlds, to introduce mathematical criteria that distinguish between the various regimes). Following the identification of the hydrodynamic regime occurring during the droplet impingement, correlations giving the post impingement droplet characteristics i.e. droplet velocities, the droplet sizes, the total mass of the droplets that is carried by the rebounding droplets or the droplet mass stick on the wall, the number of droplets formed and their temperature should be estimated. Also, for the liquid mass remains on the wall (liquid film), the wall film thickness and the spreading ratio should be calculated. The hydrodynamic regimes that have been experimentally identified to occur on single droplet impingement on a flat wall according to Bai (1996) can be summarized as follows:

(a) Stick: the droplet remains on the wall in nearly spherical form. This occurs when the impact energy is very low and the wall temperature is below adhesive temperature (Xiong and Yuen (1991)). The spreading dynamics is driven by Laplace pressure (Diez et al. (1994)).

(b) Spread: the droplet spreads and forms a liquid film on the surface (Xiong and Yuen (1991), Chandra and Avedisian (1991, 1992), Yao and Cai (1985), Gukhman et al. (1985), Naber and Farrell (1993), Seki et al. (1978)). Lately, studies on the behaviour and modeling of the liquid film have been reported, for example, Bai and Gosman (1996), Bourke and Evers (1994), Ladomatos (1993), Ahmadi-Befrui et al. (1996).

(c) Rebound: the droplet bounces after impaction; this has been observed in cases of impingement on dry and hot wall where the hot surface is prevented by the intervening vapour film resulting in bounce (Wachters and Westerling (1966), Moureau et al. (1979), Yao and Cai (1985), Chandra and Avedisian (1991, 1992)) or on impingement on a wetted wall, when the impact energy is low and the air film trapped in between the droplet and the liquid film causes low energy consumption and results in bouncing (Jayarante and Mason (1964), Zhbankova and Kolpakov (1991), Ching et al. (1984)).

(d) Rebound with break-up: that occurs when the droplet impinges on a hot wall and bounces forming two to three smaller droplets (Watchers and Westerling (1966, Moureau and Giot (1979), Yao and Cai (1985), Chandra and Avedisian (1991, 1992), Araki and Moriyama (1982), Xiong and Yuen (1991), Takeuchi et al. (1982)).

(e) Boiling-induced break-up: the droplet, even at very low collision energy, disintegrates due to rapid liquid film boiling on a hot wall whose temperature lies near the Nakayama temperature (Seki et al. (1978), Inada (1988), Nichio and Hirata (1978), Naber and Farrel (1993), Makino and Michiyoshi (1984), Xiong and Yuen (1991)).

(f) Break-up: the droplet first undergoes a large deformation to form a radial film on the hot wall, then the thermo-induced instability within the film causes the fragmentation of liquid film in a random manner (Araki and Moriyama (1982), Gukhman et al. (1985), Xiong and Yuen (1991), Takeuchi et al. (1982), Watchers and Westerling (1966), Naber and Farrel (1993))

(g) Splash: following the collision of a droplet with the surface at very high impact energy, a crown is formed, jets develop on the periphery of the crown, become unstable and break-up into many fragments (Worthington (1877), Mutchler (1967), Levin and Hobbs (1971), Stow and Stainer (1977), Heymann (1969), Hobbs and Osheroff (1967), Yarin and Weiss (1995)).

As far as it concerns the criteria distinguishing between the various hydrodynamic regimes, there is no generally accepted theory applied to all possible outcomes. Various researchers have proposed different criteria. Most of them are described in the following section 3.3.8.2 where the modeling of impingement processes is analyzed in detail.

3.3.8.2 Modeling of droplet-wall interactions

Over the last years, most of the CFD codes predicting the spray development in diesel engines, have implemented phenomenological models describing the spray impingement. All of them are based on empirical correlations deriving from studies on the dynamics of the impingement of single droplets. Usually, the comparison between the computational and the experimental results is based on the wall spray radius and the wall spray height, and on spray images under various conditions. Simple cases of impingement on flat plates are usually simulated, since most of the available experimental data refer to cases like these. Only lately studies have been published on the validation of impingement models on the basis of detailed droplet characteristics, such as their velocity and size. At this point it should be emphasized that the validation of impingement models is very complicated since a lot of parameters related to the prediction of the spray characteristics before the impingement affect the results. If the predicted free spray characteristics are not in agreement with the experimental ones, then any study on the prediction of the spray characteristics after its impingement is meaningless, since 'different' cases would be compared. However, not much attention has been given to that point until now. Another area of modeling is the wall film formation and movement, and its influence on the impinging droplets (wet wall cases) and the heat transfer between the impinging spray and a hot wall. Lately, models have been published attempting to model this complex physical procedure (Bai (1996), Stanton et al. (1996)); however, these processes are not examined here. Following, most of the published works in the modeling of droplet impingement are summarized, while the mathematical formulation of those used in the present investigation is given in the next sections.

Naber and Reitz (1988) reported results of an impingement model that they implemented in the KIVA-II code. In this study, three droplet hydrodynamic regimes were considered, based on the Weber number of the impinging droplets: the sticking regime, where the impinging droplets were assumed to form a film on the wall and simply evaporate afterwards, the reflecting regime, where the impinging droplets were assumed to reflect from the wall without any loss of kinetic energy and finally, the so called 'Jet model', where it was assumed that the droplet was leaving the wall with unchanged magnitude of tangential velocity but in a different direction, calculated on

the basis of a continuous jet impinging on a surface and mass and momentum balance. The normal to the wall droplet velocity component was kept unchanged. The results were compared with experimental values for the wall spray radius and wall spray height, for a number of ambient gas pressures, angles of impaction and impaction distances, showing surpassingly good agreement. However, in another study by Naber et. al. (1988), in order to predict the spray development, the normal to the wall droplet velocity component was arbitrary chosen in the range of 0 to 34% of the its value before impaction. Together with other modifications in the KIVA-II code used in this investigation, no model was able to predict satisfactory the spray development. It is now well known that the deformation process of an impinging droplet cannot be represented by these simplistic approximations. Also, no differentiation between low-temperature or high-temperature wall cases was distinguished. The same simplistic approximations were adopted for dry or wetted wall cases.

Another impaction model was published by Wang and Watkins (1993). The initially proposed model, based on the experimental observations of Watchers and Westerling (1966), had to be modified since there was no satisfactory agreement between the computational and the experimental results. The proposed model was trying to model the wet wall cases, and it was based on a droplet collision model of O'Rourke and Bracco (1980). Different regimes for the outcome of a droplet impingement were taken account, based on the Weber number of the incoming droplet. It was assumed that for Weber number greater than 80, the droplets were sticking on the wall. For smaller values, correlations were given for the calculation of the velocity of the rebounding droplet. Different test cases were examined, including normal of angled impaction, different gas ambient pressures and different cross flow velocities. However, the results were found to underestimate the experimental ones, for most of the cases examined.

Two papers on this area were reported by Senda (1994) and Senda et al. (1994). In the model presented, correlations were proposed for the impingement on unheated or heated surfaces. The fuel film formation, and its break-up due to the impinging droplets was taken into account. Different correlations for the dry or the wet wall cases were proposed, giving the mass, size and velocity of the rebounding droplets. The heat transfer between the impinging droplets and the hot wall was also considered. For the case of high-temperature wall, different hydrodynamic regimes were taken into account, based on the correlation between the droplet Weber number before and after the droplet

impingement as it was proposed by Wachters et al. (1966). Also, cases of droplet break-up for high Weber numbers were taken into account. Results, again for the wall spray radius and the wall spray height, were compared with experimental ones and also with results of previous models. This model was found to predict the experimental data better than the other models examined.

Naitoh et al. (1994) reported a new model on the deformation process and the subsequent re-atomization of a droplet during its impingement. A non-linear ordinary differential equation was developed for the droplet deformation calculating the droplet size distribution after break-up, while the amount of fuel remaining on the wall, and the number of droplets formed were calculated from the mass and energy conservation laws. Comparisons with fundamental experimental data confirmed that this model was effective for droplets with velocities in a range between 2 and 40 m/s and for diameters smaller than 300 μm.

Nagaoka et al. (1994) published a paper for spray impingement on hot surfaces applied to gasoline engines port injection. Heat transfer was also considered. In this model, the calculation of the size of the splashing droplets was based on the size of the formed liquid film. This was a function of the impinging Weber number. The droplet velocities were calculated from correlations giving the Weber number of the rebounding droplets as a function of the Weber number of the impinging droplets. A new correlation was proposed applicable for inclined injection. A value of 80 for the Weber number was assumed as a limit between the adhesion region and the splashing region. The heat transfer between the liquid film and the heated walls was performed assuming that the film reassembles to a lens shape geometry.

A model by Eckhause and Reitz (1995) was reported on the heat transfer between an impinging transient diesel spray and a heated wall. For the droplet impingement, the previous model of Naber and Reitz (1988) implemented in the CFD code KIVA-II was used. The heat transfer model depended on the wall conditions; flooded and non-flooded regimes were considered. The heat transfer between the spray and the heated wall was measured for three different test cases, and it was compared with the calculations; generally good agreement was achieved. However, the question that still remains from this work, is how a simplified impingement model (which does not represent accurately the film formation and impingement mechanisms) gives good agreement for even more complicated cases, such as the heat transfer between the

impinging spray and the hot wall, where boiling phenomena dominate both the characteristics of the rebounding droplets and the fuel film characteristics.

A model on spray impingement for both heated and unheated surfaces was developed by Bai and Gosman (1995). Both wet wall or dry wall cases were considered. In this model, criteria for the different hydrodynamic regimes occurring during the spray impingement were established. The rebounding, splashing, sticking, spreading and break-up regimes were considered. Correlations for the velocity and the size of the droplets after impingement were proposed, taking into account the formation of liquid film on the wall surface. The computational results were compared with experimental results, showing a good agreement. These included the wall spray radius, the wall spray height and the droplet velocities. Also, the spray pattern was compared with photographs of sprays impinging either on a flat plate or in the piston wall, showing a relatively good behaviour of the model.

Work by Watkins et al. (1996) was also reported in this area. A wall impaction model was presented and the results were compared with the experimental data of Arcoumanis et al. (1994). However no models for the spray atomization were incorporated in this work; thus, the pre-impinging spray characteristics were expected not to be in agreement with the experimental ones. The predictions were not in a very good agreement with the experimental data, probably due to the different spray characteristics predicted before the spray impingement. Many other studies have also been reported, for example Shih and Assanis (1991), Wright (1986), Gavaises et al. (1996) and others.

Although the modeling of impingement is based on the dynamics of each droplet, only integral (and usually arbitrary) assumptions are used to represent the physics involved in the phenomenon. However, recently a few investigation have been published, attempting to represent the deformation process of the droplet during its impaction by solving the Navier-Stokes equations with appropriate boundary conditions. These works (representative examples are those of Tsurutani et al. (1994), Zhang et al. (1994), Mundo et al. (1995)) are a new approximation to that problem. However, until now, they have been applied only in cases where deformation without break-up takes place, and without boiling heat transfer (two-phase flow within the droplet) between the droplet and the wall. Also, the enormous time that would required to solve numerically

the Navier-Stokes equations for every single droplet impinging on a wall, makes this approximation not applicable to diesel sprays simulation.

Few of the numerous numerical models on spray-wall interaction that have been reported over the last years have been implemented in the CFD code developed during the present investigation, in order to examine how well on not predict the impinging spray characteristics. Following their mathematical formulation is given.

3.3.8.3 Naber and Reitz model

In this model, neither the wall temperature nor wall wetting were considered. Three different cases were analysed:

Stick model : The impinging droplet sticks to the wall at the position of impingement. No film formation was calculated.

Reflect model : The impinging droplet is reflected without energy losses and with unchanged droplet size

Jet model : The magnitude of the tangential and normal velocity components are kept unchanged. However, a turning angle ψ is calculated, simulating the spreading of the spray occurring during its impingement. Its calculation is based on a theory of a liquid jet impinging on an inclined wall. In this consideration, the jet was transformed into sheet flowing outward along the wall. The sheet thickness $H(\psi)$ calculation was based on an empirical correlation. The introduced experimental coefficient β was calculated from the mass and momentum conservation laws. In the case of a droplet impingement, the function $H(\psi)$ was assumed to interpret the probability that a droplet leaves in a direction between $d\psi$ around ψ. The stochastic nature of the phenomenon was taken into account by using a random number in the calculation of this angle. The turning angle ψ was calculated from the correlation :

$$\psi = -\frac{\pi}{\beta} \ln[1 - p(1-e^{-\beta})] \qquad (3\text{-}150)$$

where p is a random number uniformly distributed in the range (0,1) and β the aforementioned coefficient which is calculated from the relationship :

$$\sin \alpha = \left[\frac{e^{\beta} + 1}{e^{\beta} - 1}\right] \frac{1}{1 + (\pi / \beta)^2} \qquad (3\text{-}151)$$

where α is the angle of impaction relative to the normal direction of the wall.

In a modification of this model suggested by Naber, Enright and Farrel (1988), the normal to the wall droplet velocity component was calculated as:

$$Vn_{out} = -p_1 \, Vn_{in} \qquad (3\text{-}152)$$

where p_1 is a random number in the range (0, 0.34), Vn the normal to the wall velocity component and the subscripts 'in' and 'out' denote incoming and outgoing droplets, respectively. The tangential to the wall droplet velocity component was kept unchanged. The droplet size was arbitrary assumed to be the 1/5 of the size of the impinging droplet.

3.3.8.4 Senda, Kobayashi, Iwashita and Fujimoto model

Two different conditions were considered: impingement on a low-temperature wall and impingement on a high-temperature wall. In both cases, a fuel film formation model was used. However, both of them consider normal impingement on flat walls.

Spray impingement on low - temperature wall :

The spray impingement model for the low temperature wall considers the fuel film formation on the wall, its break-up process due to the droplet impingement and the dispersion process of the newly formed droplets.

Fuel film formation model:. In the case of droplets impinging on a wall with temperature below the liquid saturation temperature T_{sat}, the impinging droplet just spreads as a radial film flow ; the film remains on the surface without rebound or break-up due to boiling phenomena. Since the surface changes from dry in the initial stage to

the wetted condition owing to the liquid film formation a time of pool formation τ_{lf} after the spray arrival on the wall is calculated. Thereafter the break-up of the film is considered due to the succeeding droplets impinging on the fuel film.

The time required for the pool formation on the wall surface τ_{lf} is assessed as follows: it is assumed that the impinging droplets with diameter D_{in} are homogeneously distributed in the spray cone angle and after their impaction they spread as a film having a diameter of $b \cdot D_{in}$. No interference between the impinging droplet and the subsequent film formation with the adjacent film flow (calculated from the impingement of droplets already impinged on the wall) is considered. Accordingly, the wetted area A (surface covered with the film in the impingement region), is given by the following equation:

$$A = \tau \frac{\pi}{4} \sum N_i \, (b \, D_{in})^2 \tag{3-153}$$

where τ is the elapsed time after the spray impingement, D_{in} the diameter of the impinging droplet, b the spreading ratio of the impinging droplet on the wall (thus, $b \cdot D_{in}$ is the maximum diameter of the film) and N_i the number of impinging droplets with a certain diameter range per unit time. The area S of the spray impingement region on the wall is also given as $S = \pi \cdot (Z_{imp} \cdot \tan \theta_{spray})^2$, where Z_{imp} is the impinging distance from the nozzle and $2\theta_{spray}$ the spray angle. The ratio ξ at which the film flow covers the surface of area S, is expressed as:

$$\xi = \frac{A}{S} = \frac{\tau \, \frac{\pi}{4} \sum N_i \, (b \, D_{in})^2}{\pi \, (Z_{imp} \tan \theta_{spray})^2} \tag{3-154}$$

from which the completion time τ_{lf} is assessed at $\xi = 1$:

$$\tau_{lf} = \frac{4 (Z_{imp} \tan \theta)^2}{b^2 \sum N_i \, D_{in}^2} \tag{3-155}$$

The spreading ratio b was taken equal to 5 as it was revealed from some experimental observations.

Fuel film break-up model: When the droplet impinges on a liquid film which is relatively thick or on a liquid pool, the dispersing splash, which result in the formation of small droplets, is known as 'milk-crown'. Also, it has been indicated that the film or the impinging droplet breaks up into small 'splashing' droplets, even if the droplet impinges an a thin liquid film with a thickness less than the droplet diameter. In this analysis, the break-up of the film or of the impinging droplet is classified into three types based on the Weber number of the impinging droplet:

$$
\begin{aligned}
&We < 80 : && D_{10}/D_{in} = \text{-} \text{ (no break-up)} \\
& && V_{break}/V_{in} = 0 \text{ (no rebound)} \\
&80 < We < 600 : && D_{10}/D_{in} = 0.3 \\
& && V_{break}/V_{in} = 0.3 \\
&We > 600 && D_{10}/D_{in} = 0.1 \\
& && V_{break}/V_{in} = 0.5
\end{aligned}
\qquad (3\text{-}156)
$$

where D_{10} is the arithmetical mean diameter of the formed droplets and V_{break} is their total volume. The difference in the droplet mass is considered to be absorbed into the film. For both break-up regimes (We > 80), the delay period required for the break-up of the film and the droplet formation (the residence time of the impinging droplet in the film) is not considered.

Dispersion model for the newly formed droplets: It is assumed that the energy of the impinging droplet is conserved during the break-up process of the liquid film. Then, the dispersing velocity of the formed droplets is set equal to the impinging droplet velocity. The reflecting angle θ from the film is assessed by the following expression: $\theta = \pi \cdot \exp(-C \cdot p)$, where p is a random number uniformly distributed in the range (0, 1) and C is a constant. Therefore, the vertical component W_{out} is given as:

$$W_{out} = -\sin\theta \cdot (U_{in}^2 + V_{in}^2 + W_{in}^2)^{0.5} \qquad (3\text{-}157)$$

The dispersing angle ψ in the circumferential direction is estimated by the wall Jet model of Naber and Reitz (1988). Then, the velocity components U_{out} and V_{out} are calculated from the relations :

$$U_{out} = \cos\psi \cdot (U_{in}^2 + V_{in}^2 + W_{in}^2 - W_{out}^2)^{0.5}$$
$$V_{out} = \sin\psi \cdot (U_{in}^2 + V_{in}^2 + W_{in}^2 - W_{out}^2)^{0.5} \quad (3\text{-}158)$$

3.3.8.5 Bai and Gosman model

This model uses data deriving from experimental observations on the different hydrodynamic regimes occurring during the single droplet impingement under various Weber numbers and wall temperatures. Conditions for wet or dry wall are also taken into account. The hydrodynamic regimes that have been observed during single droplet impaction can be summarized as following:

'Stick' : the impinging droplet adheres to the wall in nearly spherical form. This occurs when the impact velocity is very low and the wall temperature T_W is below a characteristic value T_{PA}, which is called 'pure adhesion temperature' (below which adhesion occurs).

'Spread' : the droplet impacts with a moderate velocity onto a dry or wetted wall and spreads out to form a wall film for a dry wall, or merges with the pre-existing liquid film for a wetted wall.

'Rebound' : the impinging droplet bounces off the wall after impact. This regime is observed for two cases: (i) on a dry wall when $T_W > T_{PR}$, another characteristic temperature in which contact between the liquid droplet and the hot surface is prevented by the intervening vapour film (called 'pure rebound temperature') (ii) on a wetted wall, when the impact energy is low, and the air film trapped between the droplet and the liquid film causes low energy loss and results in bouncing.

'Rebound with break-up' : where the droplet bounces off a hot surface ($T_W < T_{PR}$), accompanied by break-up into two or three droplets

'Boiling-induced break-up' : the droplet, even at very low collision energy, disintegrates due to rapid liquid boiling on a hot wall whose temperature lies near the Nakayama temperature T_N (temperature at which the droplet reaches its maximum evaporation temperature).

'Break-up' : the droplet first undergoes a large deformation to form a radial film on the hot surface ($T_W > T_{PA}$), then the thermo-induced instability within the film causes the fragmentation of the liquid film in a random manner.

'Splash' : following the collision of a droplet with a surface at a very high impact energy, a crown is formed, jets develop on the periphery of the crown and the jets become unstable and break-up into many fragments.

It should be noted that $T_B < T_{PA} < T_N < T_{PR} < T_{Leid}$ (T_B is the liquid boiling temperature, T_N is the Nakayama temperature and T_{Leid} is the Leidenfrost temperature or the minimum evaporation rate temperature)).

Although that a general description of the hydrodynamics regimes occurring during a droplet impingement can be made, no quantitative information is available for transition criteria between the above regimes. For this reason, not all of them were considered in this model. Actually the following cases were modeled :

(a) Dry wall : Stick - Spread - Splash

(b) Wetted wall : Rebound - Spread - Splash

The transition criteria between these regimes were modeled as following :

(a) Dry wall :

Adhesion-Splash : $We_c = A \cdot La^{-0.18}$ (3-159)

where A is a coefficient depending on the surface roughness r_S.

(b) Wetted wall:

Rebound - Spread $We_c \approx 5$ (3-160)

Spread - Splash $We_c = 1320 \cdot La^{-0.18}$ (3-161)

The droplet post-impingement characteristics for the above hydrodynamic regimes considered, are as follows:

(i) *Adhesion (stick or spread)* :the impinging droplets are assumed to form a local film

(ii) *Rebound* : the following relations developed for a solid particle bouncing an a solid wall were used to determine the rebound velocity components:

$Vt_{out} = 5/7 \cdot Vt_{in}$ (3-162)

$Vn_{out} = -e \cdot Vn_{in}$ (3-163)

The quantity e is the 'restriction coefficient', calculated from the correlation:

$$e = 0.993 - 1.76\,\alpha + 1.56\,\alpha^2 - 0.49\,\alpha^3 \qquad (3\text{-}164)$$

where α is the incident angle. The possible rotation effects have been neglected, as in all other investigations.

(iii) *Splash* : For this regime, the total secondary to incident droplet mass ratio, the sizes, the velocity magnitudes and the ejection angles of the secondary droplets are determined as following:

mass ratio m_{out} / m_{in}

$$m_{out} / m_{in} = 0.2 + 0.6\,p \qquad \text{for dry wall} \qquad (3\text{-}165)$$

$$m_{out} / m_{in} = 0.2 + 0.9\,p \qquad \text{for wetted wall} \qquad (3\text{-}166)$$

where p is a random number in the range (0, 1). It should be noted that in reality the mass ratio m_{out} / m_{in} is a function of all the aforementioned dimensionless parameters, but no experimental data exist to give a mathematical correlation.

Secondary droplet size : it is assumed that an impinging parcel is divided in to two. If N_1 and N_2 are the number of droplets with sizes D_1 and D_2 (corresponding to the droplets of each newly formed parcel), then the $N_1 + N_2 = N$, where N is the total number of secondary droplets per splash given from the correlation:

$$N = 5\left(\frac{We}{We_c} - 1\right) \qquad (3\text{-}167)$$

The N_1 is selected randomly. Then, assuming that the two parcels have the same mass, the size of the droplets in the parcel are calculated from the mass conservation:

$$\begin{aligned} N_1 D_1^3 &= 0.5\, m_{out} / m_{in} D_{in}^3 \\ N_2 D_2^3 &= 0.5\, m_{out} / m_{in} D_{in}^3 \end{aligned} \qquad (3\text{-}168)$$

Secondary droplets velocity components : These are determined in three steps. First, overall energy conservation requires:

$$\frac{1}{4}m_{out}(U_1^2 + U_2^2) + \pi\sigma(N_1D_1^2 + N_2D_2^2) = E_{k,s} \tag{3-169}$$

in which $E_{k,s} = E_k - E_{k,c}$ is the splashing energy, E_k is the kinetic energy of the incident droplet and $E_{k,c}$ is the critical energy below which no splashing occurs. The latter can be evaluated from the critical Weber number as:

$$E_{k,c} = \frac{We_c}{12}\pi\sigma D_{in}^2 \tag{3-170}$$

Next, from experimental data on secondary droplet characteristics, it is deduced that:

$$\frac{U_1}{U_2} \approx \ln(\frac{D_1}{D_{in}}) / \ln(\frac{D_2}{D_{in}}) \tag{3-171}$$

The main implication of this relation is that the larger the size of the secondary droplets, the smaller the magnitude of their velocities. Finally, application of the tangential momentum conservation law produces:

$$\frac{m_{out}}{2}U_1\cos(\theta_1) + \frac{m_{out}}{2}U_2\cos(\theta_2) = c_f m_{in}U_{in}\cos(\alpha) \tag{3-172}$$

where c_f is the wall friction coefficient (between 0.6 and 0.8). θ_1 and θ_2 are the ejection angles of the two parcels. One of the two is selected randomly to lie somewhere in the ejection cone, and then the other one is calculated from the last relationship.

3.3.8.6 Mundo, Sommerfeld and Tropea model

In this model three different outcomes of a single droplet impact are possible: (i) droplet deposition and liquid film formation, (ii) for higher energetic conditions, atomization of the impinging droplet may occur, leading to a cloud of smaller droplets around the point of impingement (iii) for special surface conditions the droplet may be

completely reflected, for instance on very hot surfaces above the Leidenfrost temperature.

The outcome of an impact of a single droplet depends not only on the kinetic parameters and on the fluid properties, but also upon the surface conditions, e.g. the presence of a liquid film or the roughness structure of the surface. Applying the Buckingham II theorem to this problem a set of four independent numbers describing the phenomena may be formulated as follows: Weber number, Reynolds number, surface roughness height relative to the droplet size and liquid film thickness relative to the droplet size. From detailed experimental studies performed with visualization techniques, a correlation was found which describes the splashing/deposition limit of individual droplets impacting on a surface with surface roughness height:

$$K = \sqrt{We\sqrt{Re}}$$
$$K < 57.7 \quad \text{Deposition} \qquad (3\text{-}173)$$
$$K \geq 57.7 \quad \text{Incipient splashing}$$

The following correlations give the outcome of an impinging droplet (size, velocity, number of droplets and ejection angle):

Smooth surface (relative roughness = relative film thickness ≈ 0.03):

tangential velocity component :	$Vt_{out} = 1.088 \cdot Vt_{in} \sin\alpha$	
Ejection angle :	$\theta = 0.249\alpha + 66.704$	(3-174)
Diameter	$D_{out} = 8.719\ K^{-0.0281}\ D_{in}$	
Number of droplets	$N_{out} = 2.44 \cdot 10^{-14} \cdot K^{6.642}$	

Rough surface (relative roughness ≈ 0.8):

tangential velocity component :	$Vt_{out} = 1.047 \cdot Vt_{in} \sin\alpha$	
Ejection angle :	$\theta = 0.080\alpha + 59.369$	(3-175)
Diameter	$D_{out} = 0.376\ K^{-0.0062}\ D_{in}$	
Number of droplets	$N_{out} = 2.13 \cdot 10^{-14} \cdot K^{6.421}$	

The mass of the impinging droplet remaining on the wall is calculated form the mass balance between the incoming and the outcoming droplets.

3.3.8.7 Leidenfrost temperature

In this paragraph, correlations previously proposed for the calculation of the Leidenfrost temperature are given.

Spiegler et al. (1963) have identified the wall temperature at which film boiling begins - the Leidenfrost temperature - with the thermodynamic limit of superheat. This temperature is the maximum temperature that a liquid can sustain at a given pressure below the thermodynamic point without undergoing a phase transition (Avedisian, (1985)). The thermodynamic limit of superheat of a single component is defined by $(\partial P / \partial V)_T = 0$, which for the van der Waals equation of state is:

$$T_{Leid} = \frac{27}{32} T_C \tag{3-176}$$

where T_C is the critical temperature.

Baumeister and Simon (1973) added an empirical correction to the previous equation which accounts for the effect of surface cooling caused by the impact of the droplet:

$$T_{Leid} = (\frac{27}{32} T_C - T_L) / [\exp(0.00175 \cdot k) \cdot \mathrm{erfc}(0.042 \cdot \sqrt{k})] + T_L, \qquad k = 1 / (K \rho c)_{surface} \quad (s \cdot cm^4 \cdot {}^{\circ}C^2 \cdot cal^{-2}). \tag{3-177}$$

where c is the heat capacity, ρ the liquid density, σ the surface tension, K the thermal conductivity and T_L the temperature of the liquid.

In another study by Whalley (1987), the Leidenfrost phenomenon was studied by considering the stability of the vapour film formed between the liquid and the wall. The result is usually quoted in terms of the minimum heat flux Φ_{min} which maintains film boiling. The result is in the form:

$$-\Phi_{min} = C \lambda \rho_{gas} [\frac{\sigma g (\rho_{liq} - \rho_{gas})}{(\rho_{liq} + \rho_{gas})^2}]^{1/4} \tag{3-178}$$

where C is a non-dimensional constant lying between 0.09 and 0.18, λ is the latent heat of vapourization and ρ the density of the gas or the liquid as denoted. Usually, the physical properties in the above relation are calculated at the saturation temperature. The value of ΔT_{min} (which corresponds to the Leidenfrost temperature) at Φ_{min} can be calculated from a film-boiling equation:

$$h=\Phi_{min}/\Delta T_{min} \tag{3-179}$$

where

$$h = 0.62\left[\frac{\rho_{gas}(\rho_{liq}-\rho_{gas})g\lambda k_{gas}^3}{\mu_{gas}\Delta T_{min} l}\right]^{1/4},\ l = 2\pi\left[\frac{\sigma}{g(\rho_{liq}-\rho_{gas})}\right]^{1/2} \tag{3-180}$$

where μ_{gas} is the gas viscosity and k_{gas} the gas vapour thermal conductivity. It should be noted that the calculated value of ΔT_{min} is the temperature difference between the Leidenfrost temperature and the saturation temperature (boiling temperature).

In a more detailed experimental and analytical study by Gottfried et al. (1967), the Leidenfrost temperature and the droplet evaporation rate were determined. The model was based on the Navier-Stokes equation, which under the assumptions adopted, were simplified in order to have analytical solution. However, when introducing heat transfer correlations, the analysis was complicated, and thus is non presented here. The computational data were found to agree with 20% accuracy with the experimental ones. It was found that radiative heat flux cannot be neglected at temperatures beyond the Leidenfrost point. This was found to be 100-105°C. above the saturation temperature for all organic liquids. It was also found independent of the droplet size.

Two more studies have been published by Avedisian and Koplic (1987) and Avedisian and Nguyen (1987). In both studies, the heat and mass transfer between the droplet and the heated wall, the Navier - Stokes equations were solved numerically under appropriate assumptions. In the solution, vapour flows outward from the droplet, and the corresponding streamlines bend due to the presence of the wall. A pressure field is thus created, and the component of this field normal to the surface lifts the droplet off the wall. From the solution (which is too complex to be presented here), the velocity and temperature field, the levitation height and the droplet diameter were determined.

3.4 Inter-phase Coupling Terms

To account for the effects of the particles motion on the surrounding continuum media, source terms should be added to the Navier-Stokes equations. These coupling terms express the mass, momentum and energy exchange between the two phases. The mathematical expression of these terms is very complicated for the general case (Nigmatulin (1991)). However, for particulate flows where the particles are assumed to be almost spherical and a Lagrangian approximation is used for the calculation of the distribution function $f(\vec{x},\vec{u},m,T,t)$, simpler expressions can be derived. These can be found in a number of studies (Ramos (1989), Amsden et al. (1989), Travis et al. (1976) and many others).

The general form of the spray source term added to the gas phase equations is:

$$S_{\Phi} = \frac{d\Phi}{dt} \tag{3-181}$$

where $\Phi^{mass}=f\cdot m$ is the mass of the liquid, $\Phi^{momentum}=f\cdot m\cdot u$ is the momentum of the liquid phase and $\Phi^{energy}=f\cdot(m\cdot u/2+m\cdot I)$ is the liquid phase total energy.

Accounting for the variation of the droplet mass due to evaporation and integrating over all droplets, we take the mass source term as:

$$\dot{S}_{MASS} = \int f(\vec{x},\vec{u},m,T,t)\frac{dm}{dt}d\vec{x}d\vec{u}dmdT \tag{3-182}$$

where the term dm/dt is the fuel evaporation rate, determined from the evaporation model.

Variation of the relative momentum between the two phases can result either from the variation of the relative velocity or from variation of the mass of the particulate phase due to its evaporation. During collisions, mass, momentum and droplet kinetic energy are conserved, and thus, these processes do not contribute to the momentum coupling. Accounting for these variations, the corresponding coupling term is (for each of the three x,y,z directions):

$$\dot{S}_{MOMENTUM} = \int f(\vec{x},\vec{u},m,T,t)[m\frac{d\vec{u}_{rel}}{dt} + \vec{u}_{rel}\frac{dm}{dt}]d\vec{x}d\vec{u}dmdT \qquad (3\text{-}183)$$

To account for the energy coupling term, we have to account for both the heat flux between the two phases and for the kinetic energy variations. It is assumed that the kinetic energy variation of the droplets due to their deceleration is transferred to the kinetic energy of the gas. One could account for any other kinetic energy losses, for example these during the break-up of the droplets; these are not considered here. Assuming that for the liquid is $I_l = c_{liquid}T$ where I_l is the internal energy and c_{liquid} the liquid specific heat, the energy coupling term can be expressed as:

$$\begin{aligned}\dot{S}_{ENERGY} = \int f(\vec{x},\vec{u},m,T)[&\frac{dm}{dt}(\frac{u_{rel}^2}{2} + c_{liquid}T) \\ &+ m(\left|u_{rel}\frac{du_{rel}}{dt}\right| + c_{liquid}\frac{dT}{dt})]d\vec{x}d\vec{u}dmdT\end{aligned} \qquad (3\text{-}184)$$

Many studies (for example, Amsden, O'Rourke and Buttler (1987), Ikonomou (1996), Kraji (1995), Bai (1996)) take also an extra coupling term to the turbulence kinetic energy of the gas phase. It is generally accepted that the effect of the droplets on the gas fluctuating velocity field is to decrease the turbulence kinetic energy and to increase its dissipation rate due to the friction between the droplets and the gas. However, its contribution plays only a minor role in the dissipation of the turbulence kinetic energy, as shown by Kraji (1995) and it has been neglected in the present investigation.

3.5 Liquid Physical Properties

Fuel properties are important factors affecting the calculations in all spray submodels. Thus, is was considered necessary to implement the physical properties of various hydrocarbon fuels in a form of block data creating libraries of fuels that can be used from the user of the program. The following data have been taken from various handbooks of liquid physical properties, for example, Reid et al. (1987). In the developed code, the liquid fuels listed in Table 3-1 have been modeled. For each of these fuels, the molecular weight, density, surface tension, vapour pressure, thermal

diffusivity, kinematic viscosity and latent heat of vapourization have been inputted into data blocks as a function of the liquid temperature while it has been assumed that the pressure does not affect their properties. This is valid for the chamber pressure variation during the injection period under diesel engine conditions. Linear interpolations are used in order to calculate the above properties in intermediate values. Table 3-1 and Figure 3-4 summarizes the aforementioned properties of the fuels implemented into the simulation program, while the latent heat of vapourization is calculated from correlation (3-39) for the various fuels, and it is presented in Figure 3-5 together with the internal energy of the liquid and the evaporated fuel as well as with the specific heat of the liquid. The thermal diffusivity can be estimated from correlation (3-51) where the various coefficients involved can be taken as:
A^*=0.0035 for fuels 3,4,5, 6, 8 and 9, A^*=0.0346 for fuel 7, A^*=0.031 for fuels 1 and 2, a1=1.2, a3=0.167 and a2=0.5 for fuels 3,4,5,6 and 1.0 for all other fuels. Typical values for the thermal diffusivity are between 0.1-0.17 W/(m·K).

3.6 Numerical Implementation of the Spray Model

In this section the discretized form of the spray model equations is given together with the solution procedure used for the calculation of the dispersed phase.

3.6.1 Numerical solution procedure

Figure 3-6 shows the flow diagram summarizing the solution procedure. Initially new parcels are injected according to the fuel injection rate. It is assumed that a new parcel is formed when its mass is equal to the mass of droplet having a diameter equal to the effective hole diameter. Then, the trajectory equation 3-3 is solved for all parcels present in the calculation in order to determine their new position in the computational domain. At this point the local properties of the flow field (velocity, pressure, density, temperature, composition and flow field gradients) at the point of each droplet are specified, since these are required for all following calculations. In addition, it is checked whether or not the parcels impinge on the walls. In case they do, the impingement process is calculated; for the other case, the various physical processes present in the spray development are taken into account in the following sequence:

liquid atomization, secondary break-up, droplet collisions, droplet turbulent dispersion and droplet evaporation. Finally, the droplet momentum equation is solved at the end in order to account for their new velocity.

Two topics require special attention at this point. The first one is related to the iterative prediction-correction procedure of the coupled gas-liquid phases. As can be seen in Figure 3-6, the time step used for the numerical implementation of the gas phase equations is usually much larger than that employed to the spray processes. Since the latter ones require a very small time step in order to represent physically the spray development, it is not possible to solve the gas phase equation with the same time step due to the enormous time required for such a solution. Thus, many spray subcycles correspond to one time step of the gas phase. The spray coupling terms are summed during this time period. At the end on the spray subcycles the results have to be saved, update the flow field are redo the calculation until the difference in the results between two subsequent subcycles are smaller than a given limit. The smaller the number of spray subcycles corresponding to one gas-phase time step, the smaller the internal prediction-correction procedures required. It has been found that if the time step of both the droplets and the gas are quite small, only one correction is enough; thus, this has been used in the present investigation and proposed for any further work since the CPU time becomes the minimum possible for this type of solution. It has to be pointed that the error introduced with this approximation seems to be much smaller than that introduced by other numerical approximation, such as the grid resolution or the number of the injected parcels.

The second point that demands special attention is related to the number of parcels used for the calculation. During the liquid core atomization and the droplet secondary break-up and in impinging cases during splashing, more than one parcels are formed and introduced into the calculation. Since the individual models predict the size distribution from which the properties of the representative parcels are sampled, the average number of droplets can be estimated. In the limiting case where there is enough computer memory storage and power, the number of the parcels used can be set equal to the number of the droplets. However, for practical cases, approximately 10 to 20 parcels are allowed to be formed from the disintegration of each droplet emerging from the nozzle while 2 to 3 new parcels are formed during the secondary break-up. For middle speed and load conditions such as those examined in the present investigation, these

numbers will give approximately $1 \cdot 10^5$-$5 \cdot 10^5$ parcels at the end of injection; the larger one corresponds to approximately to 1/10 of the total number of droplets present in the spray and it is big enough to give statistically independent results. The advantage of this procedure of parcels formation during the spray development enables for bimodal distributions to be easily taken into account, since parcels can be sampled from that kind of distributions. In addition, it is expected that this procedure will represent more accurately the droplet number density variation during the spray development. However, special attention has to be given to the position of the newly formed parcels, since if their position is assumed to be the same as that of the parent parcel, then this could result to predictions of unrealistic collisions. Thus, collisions have to be calculated only for droplets which at the current time step have not been formed from the fragmentation of the same parcel.

3.6.2 Discretized form of the spray equations

In this section the discretized form of the working correlations is given. These include the droplet trajectory equation, the droplet momentum equation and the mass, momentum and energy coupling terms between the two phases.

Droplet trajectory equation:

$$\vec{x}_{(n+1)\,\Delta t} = \vec{u}_{n\,\Delta t} \cdot \Delta t + \vec{x}_{n\,\Delta t} \tag{3-185}$$

Droplet momentum equation:

$$\frac{\vec{u}_{(n+1)\,\Delta t} - \vec{u}_{n\,\Delta t}}{\Delta t} + \frac{1}{m_{n\cdot\Delta t}} \frac{m_{(n+1)\,\Delta t} - m_{n\,\Delta t}}{\Delta t} = \left(1 + \frac{\rho_{gas}}{\rho_{liquid}}\right)\vec{g} + D_D(\vec{u}^{GAS}_{(n+1)\cdot\Delta t} + \vec{u}'_{(n+1)\cdot\Delta t} - \vec{u}_{n\cdot\Delta t}) + \frac{3}{4}\frac{\vec{F}_{SHAFMAN}}{\rho_{liquid} \cdot r^3_{n\,\Delta t}} - \frac{1}{\rho_{gas}} \frac{P^{GAS}_{(n+1)\,\Delta t} - P^{GAS}_{n\,\Delta t}}{\Delta \vec{x}_{GAS}} \tag{3-186}$$

Source term in mass conservation equation:

$$S_{MASS}^{(I,J,K)} = \sum_{t}^{t+\Delta t_{GAS}} [\sum_{(I,J,K)} N_P \frac{4}{3}\pi\rho_{liquid}(r_{(n+1)\cdot\Delta t}^3 - r_{n\cdot\Delta t}^3)] \tag{3-187}$$

Source term in momentum conservation equation:

$$S_{MOMENTUM}^{(I,J,K)} = \sum_{t}^{t+\Delta t_{GAS}} [\sum_{(I,J,K)} N_P \frac{4}{3}\pi\rho_{liquid}[(r_{(n+1)\cdot\Delta t}^3 - r_{n\,\Delta t}^3)\vec{u}_{n\cdot\Delta t}^{rel} + (\vec{u}_{(n+1)\cdot\Delta t}^{rel} - \vec{u}_{n\cdot\Delta t}^{rel})r_{n\cdot\Delta t}^3]] \tag{3-188}$$

Source term in energy conservation equation:

$$S_{ENERGY}^{(I,J,K)} = \sum_{t}^{t+\Delta t_{GAS}} [\sum_{(I,J,K)} N_P \rho_{liquid}(S_1 + S_2)]$$

where:

$$S_1 = \frac{1}{2}\frac{4}{3}\pi[(r_{(n+1)\cdot\Delta t}^3 - r_{n\cdot\Delta t}^3)(u_{(n+1)\,\Delta t}^{rel})^2 + r_{n\,\Delta t}^3((u_{(n+1)\cdot\Delta t}^{rel})^2 - (u_{n\cdot\Delta t}^{rel})^2)] \tag{3-189}$$

$$S_2 = \frac{4}{3}\pi c_{liquid}[T_{n\cdot\Delta t}(r_{(n+1)\cdot\Delta t}^3 - r_{n\cdot\Delta t}^3) + r_{n\cdot\Delta t}^3(T_{(n+1)\cdot\Delta t} - T_{n\,\Delta t})]$$

In all of the above correlations, the subscript n represents the previous time step where all variables are known while (n+1) the current time step for which the numerical solution has to be performed. Δt is the time step employed for the particle motion and Δt_{GAS} is the time step of the gas phase. In addition, N_P is the number of droplets per parcel and the summation of the source terms is performed for all parcels present in the cell (I,J,K) at the current time step. In addition, m, ρ_{liquid} and ρ_{gas} represent the droplet mass and the liquid and gas densities, respectively, P^{GAS} is the gas pressure, u, u^{GAS} and u' the droplet velocity, the gas phase velocity and the turbulent velocity that the droplet 'sees', respectively, while u^{rel} is the relative velocity between the droplet and the gas; r and T represent the droplet radious and the droplet surface temperature, respectively, g is the gravitational acceleration and x and x_{GAS} represent the droplet position and the gas phase cell phase coordinates in the three dimensional space, respectively. The term D_D involved in equation (3-186) is due to droplet drag force and it is estimated from the following correlations:

$$D_D = \frac{3}{8}\frac{\rho_{gas}}{\rho_{liquid}}\frac{\left|u^{GAS}_{n\cdot\Delta t} + u'_{n\cdot\Delta t} - u_{n\cdot\Delta t}\right|}{r} C_D \qquad (3\text{-}190)$$

where C_D is the droplet drag coefficient given from correlations (3-115). Finally, $F_{SHAFMAN}$ is the Shafman force given from correlation (3-18).

3.7 Summary

In this chapter the physical processes taking place during the development of diesel sprays were described and various mathematical models for their prediction were given.

The three-dimensional CFD model presented in Chapter 2 was modified in order to account for two-phase particulate flows with liquid droplets. An Eulerian-Lagrangian approximation was employed in which a number of liquid parcels was considered representative of the liquid phase while appropriate coupling terms were added, accounting for the mass, momentum and energy exchange between the two phases.

The various processes occurring during the development of diesel sprays were implemented as individual sub-models into the developed code; these included fuel injection, liquid core atomization, droplet secondary break-up, droplet evaporation, droplet collisions, droplet turbulent dispersion, droplet-wall interactions and droplet decelerations. Various models reported in the open literature, representing different physical approximations, have been implemented into the code. In addition, the development of new spray submodels was presented which included the cavitation-induced atomization model and the droplet secondary break-up model.

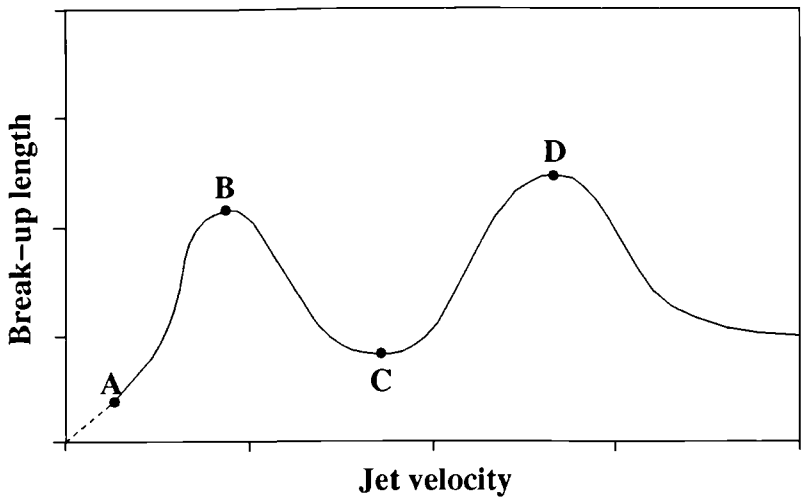

Figure 3–1 : Variation of break–up length with injection velocity: (a) –A: dripping flow, (ii) A–B: laminar flow regime flow (iii) B–C: transition regime flow, (iv) C–D: turbulent flow regime and (v) D–: fully atomization regime (from Lefebvre (1989)).

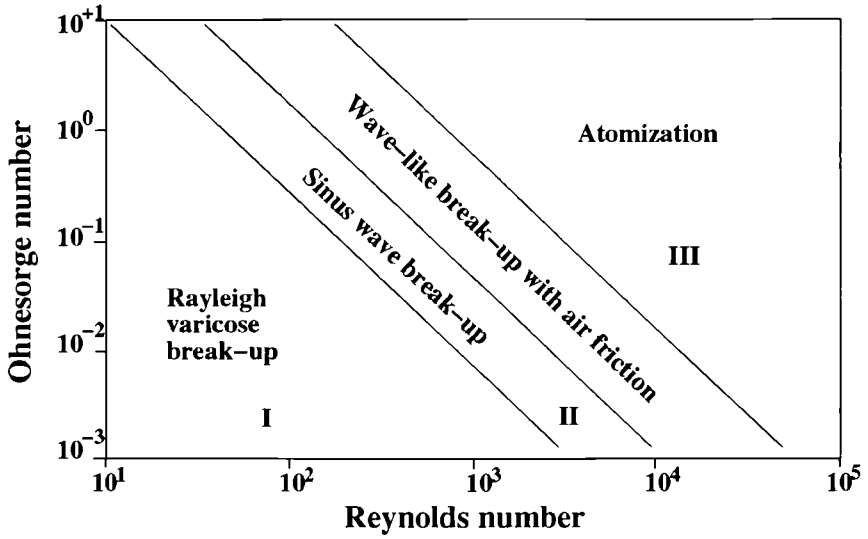

Figure 3–2 : Ohnesorge atomization map (1936)

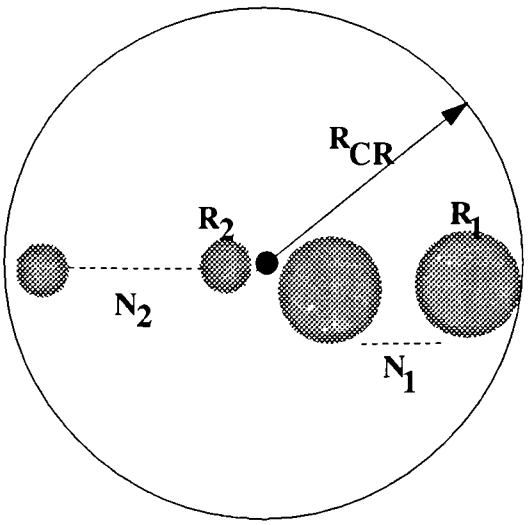

Figure 3–3 : Schematic representation of the criterion used to allow collisions between parcels

	Fuel type		Molecular weigth (kg/kmole)	Critical temp. (K)	Enthalpy of formation (J/mole)	Density (kg/m^3)	Normal boiling point (K)
1	n–heptane	C_7H_{14}	100.205	540.16	–144.557e+3	676.5	371.58
2	n–octane	C_8H_{18}	114.232	569.35	–159.828e+3	698.3	398.66
3	n–dodecane	$C_{12}H_{26}$	170.340	659.00	–220.789e+3	744.3	489.47
4	n–tridecane	$C_{13}H_{28}$	184.367	677.00	–236.081e+3	749.1	526.47
5	n–tetradecane	$C_{14}H_{30}$	198.394	695.15	–251.291e+3	758.8	526.59
6	n–hexadecane	$C_{16}H_{34}$	226.448	725.00	–281.792e+3	769.4	560.05
7	benzene	C_6H_6	78.114	562.60	+100.416e+3	868.1	353.10
8	light diesel	df2	170.340	725.00	–220.789e+3	826.0	540.00
9	light diesel	di	179.327	736.00	–41.112e+3	840.0	551.00

Table 3–1 : List of physical properties of the fuels modeled

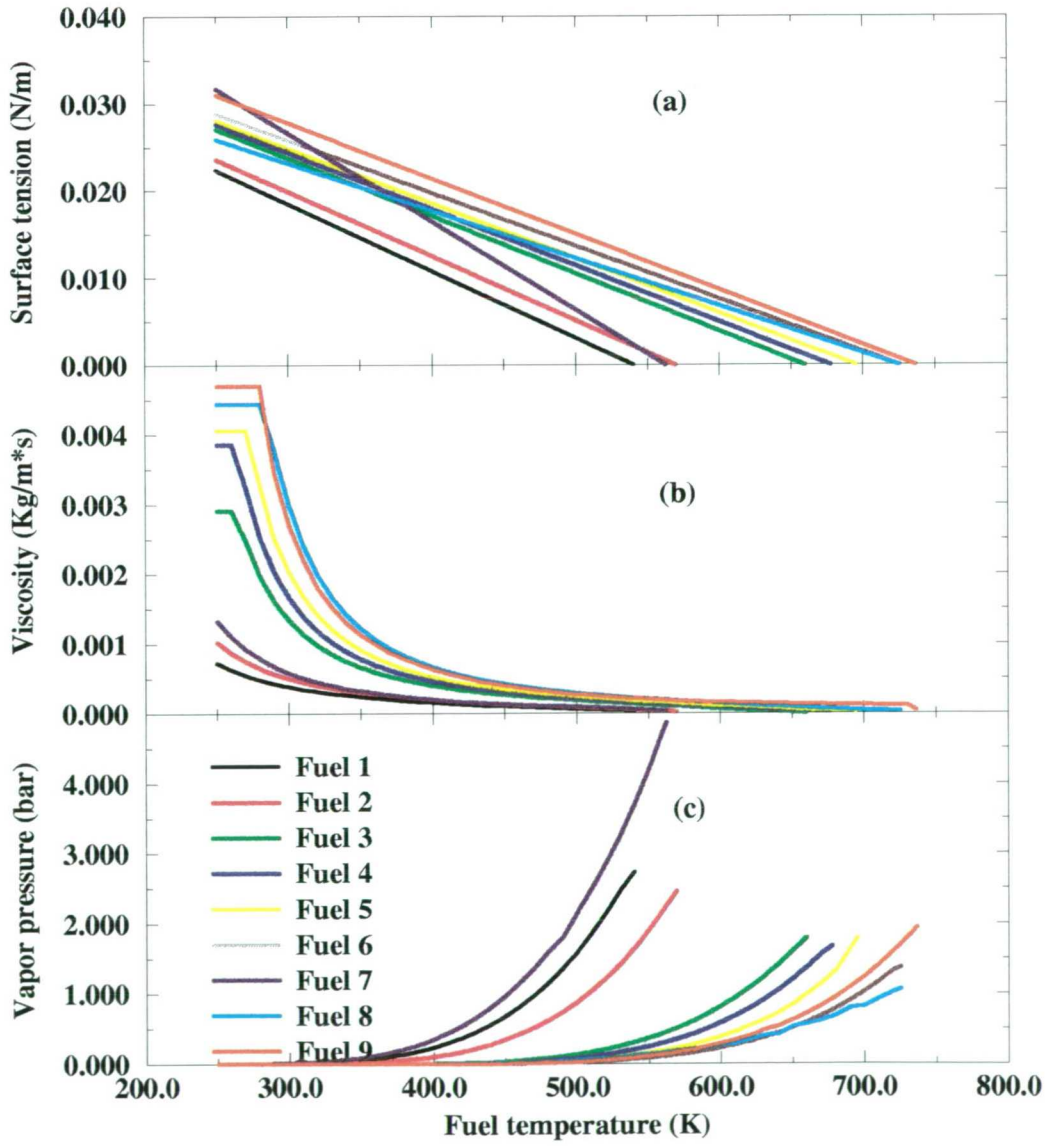

Figure 3–4 : Variation of (a) surface tension (b) kinematic viscosity and (c) vapor pressure of the various fuels modeled as a function of temperature

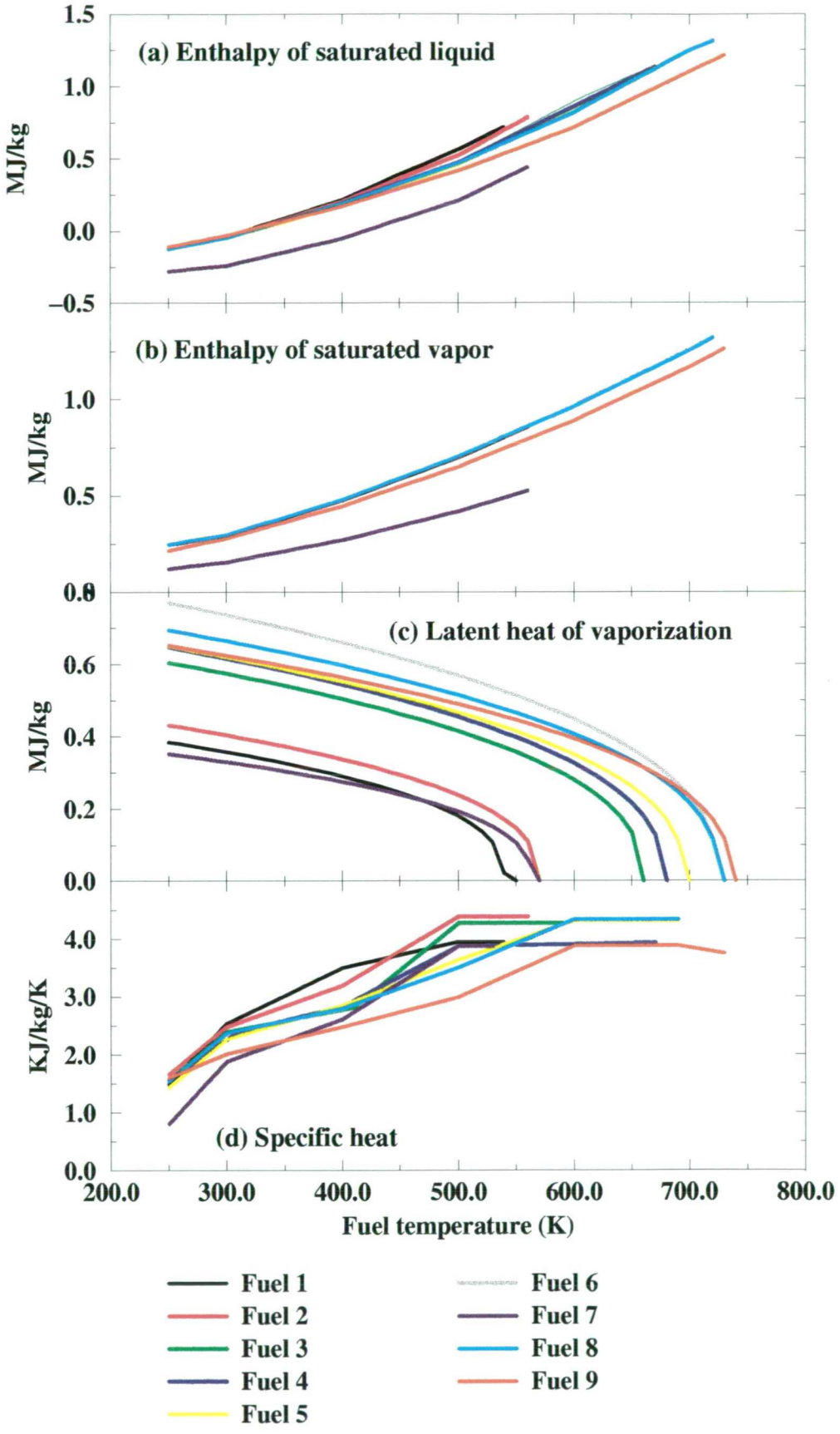

Figure 3–5 : Physical properties of the modeled liquids (a) enthalpy of saturated liquid (b) enthalpy of saturated vapor (c) latent heat of vaporization and (d) specific heat

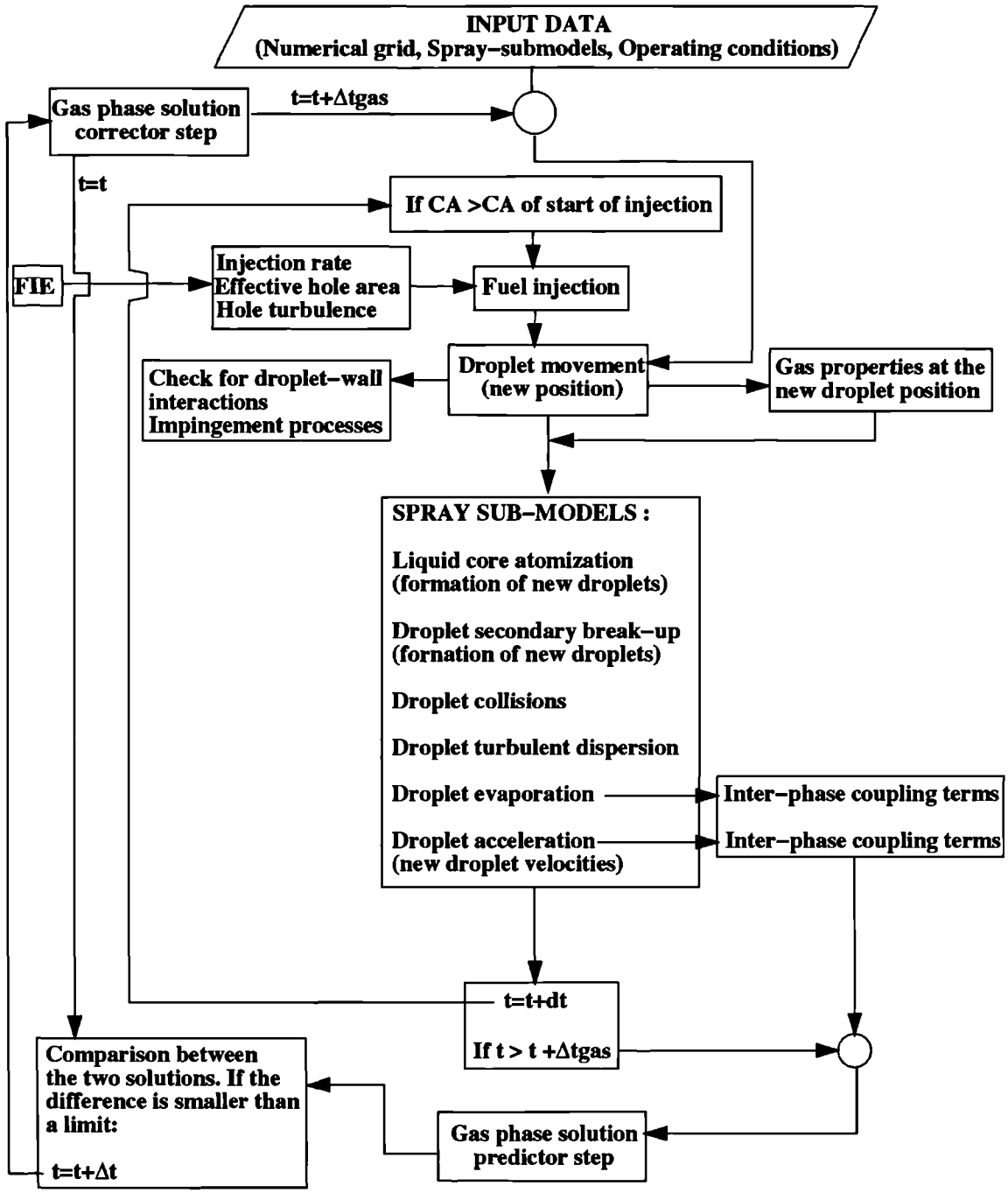

Figure 3–6 : Schematic representation of the solution procedure

CHAPTER 4

What ever the mathematical formulation that describes the universal principles of turbulence is, we ought to explain why these considerations should be applicable to every turbulent motion. This question will be answered inevitably on the basis of both random processes (such as the tide flow or the shape of canals) and universal principles (such as the laws of fluid motion and the properties of fluids) which again have to be explained from first principles.

Steven Wienberg
(Dreams for a final theory)

Results: FIE Flow Processes

4.0 Introduction

In this chapter the results obtained with the simulation model for the fuel flow processes inside the fuel injection system are described. These are divided into three sections. The first one examines the one-dimensional flow in conventional fuel injection systems for DI Diesel engines while the second one investigates the flow in the sac volume and the injection holes under non-cavitating hole flow conditions using the 3-D CFD model for both steady and unsteady conditions. In the third section the effective hole area model is used after the onset of cavitation in order to predict the hole exit characteristics.

4.1 Fuel Injection System Simulation

4.1.1 Pump operation and geometric characteristics of the system

Two different fuel injection systems have been used for the validation of the developed model. Both of them consist of a Bosch VE distributor-type pump connected to four Stanadyne pencil-type injection nozzles. The first of them has been designed to work on a naturally-aspirated DI diesel engine while the second for a turbocharged engine. Figure 4-1 shows selected photographs of the cross-sectioned pump as well as of the rollers, the cam plate and the plunger. Figure 4-2a shows a schematic representation of the injection pump and Figure 4-2b shows a more detailed view where all the parameters required for the modeling of its operation are defined; Figure 4-6 shows a schematic representation of the high pressure pipe and the pump.

In what follows a description of the operation of the pump is given. As the cam plate rotates on the rolls, fuel fills the pumping chamber from the feed chamber. At a specific cam angle the inlet slot closes and, at the cam angle at which the cam lift starts

to increase, the moving plunger compresses the fuel in the pumping chamber which is supplied to the injection system through the outlet port to the delivery pipe. The compression of the fuel is completed when the spill port opens; the cam angle at which this port opens is determined from the control spool position and it is a function of the pump speed and lever position. Its value is determined from the mechanical governor installed in the pump and shown in Figure 4-2a. The control spool position at which the spill port opens determines the 'plunger effective travel'. After the spill port opens, the pressure falls to the pressure of the feed chamber and the cycle is repeated (four times for a four cylinder engine completing a full 360 deg. revolution of the cam plate). Figure 4-3 shows a schematic representation of the various phases during pumping. During the compression stroke of the pump, the high pressure wave generated in the pumping chamber travels with the speed of sound in the delivery pipe, and after the opening of the delivery valve, into the high pressure pipe until the nozzle. The needle in the nozzle opens when the pressure in the nozzle chamber reaches the value of the nozzle opening pressure, which is determined from the spring preload and the dimensions of the nozzle chamber. Injection starts at the time of the needle opening and it is terminated when the pressure in the nozzle chamber falls below the nozzle opening pressure. In order to model the operation of the pump itself, its dimensions were estimated by cross sectioning it since relevant information was not available from the pump manufacturers. The estimated characteristics included the cam plate profile, the dimensions of the rollers, the plunger effective travel, the pumping chamber volume, the plunger diameter and the flow area of the spill, feed and outlet slots. Figure 4-5a shows the measured cam lift as a function of the cam angle as well as the estimated actual plunger movement which differs from that of the cam lift; Figure 4-4 describes the method employed in order to estimate the actual plunger movement. Figure 4-5b shows the experimentally estimated plunger effective travel as a function of the pump speed and lever position for the naturally-aspirated injection system. Finally, Figure 4-5c shows the estimated variation of the feed, spill and outlet port areas as a function of the cam angle for a pump speed of 1000 rpm and a lever position of 50%; similar curves could be estimated for all the other operating points. In addition, the estimated geometric characteristics of the delivery pipe, the delivery valve, the delivery chamber and the delivery volume chamber are given in Table 4-1 while Figure 4-5d shows the delivery valve flow area as a function of its lift.

Tables 4-2 and 4-3 present the geometric characteristics of the high pressure pipe and the injection nozzles of the two injection systems investigated. The estimated nozzle opening pressure is 230 bars. In order to estimate the details of the geometry of the sac volume and the injection holes, the nozzle tip was cross-sectioned and the magnified photographic images are presented in Figures 4-7 and 4-8. Figure 4-7 shows a 100x magnification of the sac volume with the needle placed at its seat. From this picture the sac volume as well as the area of the needle inside the sac volume were estimated; these values are given in Tables 4-4 and 4-5 for the two different nozzles examined. Figure 4-8 shows a 500x magnification of the injection holes. It is important to note that the hole entrance shape, defined in Figure 4-9, is quite sharp giving an estimate of $r/D \approx 0$. In addition, the hole inclination angle, defined in Figure 4-9, was estimated for all different injection holes. As can be seen, three different groups of holes can be identified in the specific inclined nozzle; holes 1 and 5 are the more restricted ones while hole 3 allows for the flow to turn easier from the needle seat to the hole; holes 2 and 4 are in between the two extremes. As it will become clear later on, this specific design has an important effect on the discharge coefficient of the individual injection holes.

4.1.2 Experimental system

For the validation of the model, the FIE system was instrumented and several parameters were measured; these are presented in Figure 4-10. They include the pumping chamber pressure, the line pressure (at the pump end), the needle lift and the injection rate for the first FIE and the line pressure (both at the pump end and the nozzle end), the needle lift and the injection rate for the second FIE investigated. Details about the measuring techniques and instrumentation used can be found in the Ph.D. Thesis of Fairbrother (1994). The operating conditions tested are listed in Table 4-6; they cover pump speeds from 500 to 2000 rpm and lever positions from 20 to 100%. In addition to the above the total fuel injection quantity was collected in a burette tube over 1000 successive injections. The corresponding reading (averaged per cycle) is presented in Figures 4-11a and 4-11b for the two fuel injection systems, respectively. On these speed-load fuel quantity maps, the points denoted with an asterisk represent the points of measurements of the aforementioned signals during the injection period. It can also be seen that, for the first fuel injection system, the total fuel injection quantity does not

vary significantly for lever positions higher than 50%. This is due to the plunger effective travel, which, as the measured values presented in Figure 4-4b indicate, it is almost constant, independent of the lever position. However, the case is different for the second FIE (which as already mentioned is used in a turbocharged DI diesel engine), where the total fuel injection quantity varies significantly for lever positions between 50 and 100%.

4.1.3 Simulation model

Having identified the geometry of the system it is now possible to describe the application of the developed 1-D model on this specific FIE system. Figure 4-12a shows a more detailed schematic representation of the pump, the high pressure pipe and the nozzle together with the definition of the various flow elements used to represent its operation. As can be seen, the pumping chamber, the delivery chamber, the delivery valve chamber and the nozzle chamber have been represented by the element 'volume', the delivery pipe, the high pressure pipe and the annular nozzle pipe have been represented by the element 'pipe' and the delivery valve and needle have been represented from the element 'valve'. In addition, the plunger movement has been represented by the element 'cam' which is required as the initial condition for generating the pressure in the system while the feed and back pressures are required as boundary conditions and have been represented by the element 'chamber'. The three 'slots' represent the variation with time of the feed, spill and outlet ports. Figure 4-12b shows the link between the various components and gives in detail the connections between the various elements.

The compression of the first volume of the system, resulting from the presence of element 1, is needed for the calculation of its pressure. Furthermore, this specific volume has three flow passages, those related to elements 2,3 and 5 (spill, feed and outlet slots, respectively). Element 16, which is the feed pressure, is required for the estimation of the flow rate through the feed and spill port flow passages. The first point of the delivery pipe is used for the estimation of the flow rate through slot 5.

Element 7 (second volume of the system), which represents the delivery chamber, has two flow passages. The first one is the last point of the delivery pipe while the second one is the flow passage through the delivery valve flow area. In addition, this

volume is compressed (or decompressed) as the delivery valve moves during the injection period. A similar situation occurs for the third volume of the system (element 9) which represents the delivery valve chamber. Again two flow passages are present, the first being the delivery valve open area and the second being the first point of the high pressure pipe. As already mentioned, the delivery valve is located between volumes 2 and 3 whose pressure acts upon it and force it to move; pressure from element 7 forces the valve to open while pressure from element 9 acts on the opposite direction which is the same as that of its spring.

Element 11 is the last volume of the system and represents the nozzle chamber which is connected between the high pressure pipe and the annular nozzle pipe (elements 10 and 13, respectively). In addition, the motion of the needle affects the calculation of its pressure since the needle area in the nozzle gallery either decompresses or compresses the fluid in this volume. The needle (element 12) is forced to move by the pressures in elements 11, 13 (last point of annular nozzle pipe) and 14 (sac volume pressure). The back pressure is represented by element 16 and it is required in order to calculate the flow pattern in the sac volume and injection holes as well as the fuel injection rate.

As it has become clear already, elements 6, 10 and 13 are the pipes of the system and they are located between elements 4 and 7 for the delivery pipe, 9 and 11 for the high pressure pipe and 13 and 14 for the nozzle pipe.

In order to identify possible uncertainties resulting from the modeling of the pumping chamber pressure, another simulation case included the use of the measured pumping chamber pressure as the initial condition for the simulation. Its value was assumed to be identical to the value of the pressure at the first point of the delivery pipe; as a result, elements 1-5 where replaced by a 'pressure' element.

The above description represents the connections used to model the flow in the naturally-aspirated FIE. However, for the second fuel injection system investigated, the details of the geometry of the pump were unknown. Thus, elements 1-9 were deleted from the connectivity file and instead, a 'pressure' element was used as the initial condition, representing the measured value of the line pressure either at the pump end or at the nozzle end point.

Figure 4-13 shows a typical result of the pressure and flow rate distributions within the FIE, as calculated from the simulation model, at three different cam angles

during the pumping period for a pump speed of 1000 rpm and lever position 50%. Figure 4-13a corresponds to the cam angle of the needle opening when the pressure in the nozzle chamber equals the nozzle opening pressure. As can be seen, the pressure in the pumping chamber is approximately 600 bars. The pressure in the connecting pipe decreases gradually from the pump to the nozzle inlet. The flow rate distribution implies that most of the fuel has not been delivered to the rest of the system. Figure 4-13b shows the pressure and flow rate distribution at the cam angle corresponding to the maximum injection pressure (sac volume pressure) which is approximately 550 bars for the specific injection condition presented. As can be seen, at this time the spill port has already opened and the pressure in the pumping chamber has gradually fallen to the value of the supply pressure. However, although the delivery valve has returned back to its seat, the fuel remains pressurized in the high pressure pipe and the nozzle while the needle has reached its maximum stop position. Figure 4-13c, which corresponds to the time of the needle closing, shows the reversed flow in the system generated by the reflected pressure waves traveling through the fuel injection system. As can be seen, the pressure in the delivery valve chamber has again started to increase with its value reaching levels as high as 300 bars. The residual pressure in the high pressure pipe is due to this pressurized fuel trapped within the system after the end of injection, and it is a function of the operating conditions and the design of the system itself. In order to calculate this pressure, the simulation has to be repeated for about four cycles.

4.1.4 Model validation

Figures 4-14 to 4-19 show the comparison between the computational and the experimental results for the first fuel injection system investigated and the test cases listed in Table 4-6. As already mentioned, the experimental data include the pumping chamber pressure, the line pressure, the needle lift and the injection rate. Two sets of computational results are presented. In the first one, results obtained using as input to the simulation model the cam profile and the geometry of the pump are presented. In order to identify possible errors resulting from the modeling of the pumping chamber pressure, its measured value was used in order to predict the flow in the rest of the fuel injection system. As can be seen, the computational results are in satisfactory agreement with the experimental ones. Possible differences between the two different inputs to the

model are small and they mainly occur for cam angles after the spill port opening which requires accurate determination of the discharge coefficient of the spill port. Since the simulation model calculates accurately the pumping chamber pressure prior to the opening of the spill port, it is evident that the timing of the start of injection is predicted as accurately as that calculated using as input the measured pumping chamber pressure. The good agreement between the maximum calculated pressure and the experimental one implies that the mean line pressure and the total fuel injection quantity should be similar to each other in the cases of the two inputs. Similar results can be drawn out from the simulation of the second fuel injection system. For this particular system, the experimental signals of the line pressure have been used for the prediction of the flow in the high pressure pipe downstream of the measurement point and in the injection nozzle. The results for this system are presented in Figures 4-20 to 4-24 for the operating conditions listed in Table 4-6. Again, the needle lift and the injection rate are reasonably well predicted, implying that the injection timing as well as the total fuel injection quantity are also reasonably well simulated.

The comparison between the computational and the experimental results for the total fuel injection quantity and the start of injection is shown in Figure 4-25 for both systems and for all the different test cases. The total fuel injection quantity is presented as the percentage difference from the burette reading. In addition to the simulation values, two more bars are plotted; these represent the difference between the integrated injection rate signal measured without and with a 4 kHz filter which was used to suppress the fluctuations in the unfiltered injection rate signal (Figures 4-14 to 4-19). It is evident that for both fuel injection systems, the calculated difference between the predicted injection quantity and the burette value is of the same order as that resulting from the integration of the measured injection rate signal.

Finally, for the estimation of the start of injection, two methods have been considered and the results are also presented in Figure 4-25. It should be mentioned that the filter used to reduce the fluctuations present on the unliftered fuel injection rate signal has a strong effect on the start of injection which implies that for its estimation the unfiltered signal should be used. In the first method the point of the first increment of the injection rate signal is used to estimate the start of injection, while in the second the time corresponding to the 10% of the maximum needle lift has been plotted. Overall, the start of injection can be estimated with an uncertainty of 0.6 deg. of cam angle;

simulation values fall between the experimental readings and almost coincide with the values based on the unfiltered injection rate signal.

4.1.5 Parametric studies

Having extensively validated the model, a set of parametric studies has been performed in order to identify the geometric parameters that have a strong effect on the nozzle exit characteristics, which include the start of injection, the injection duration and the total fuel injection quantity. These studies can be divided in two sets; the geometric characteristics of the high pressure pipe and the nozzle are included in the first one while the pump design parameters are examined in the other.

Figure 4-26 presents the effect of the high pressure pipe length and diameter, nozzle chamber area, needle preload, needle diameter and injection hole diameter on the shape of the fuel injection rate while Figure 4-27 summarizes the effect of a percentage variation from their nominal values of the above parameters on the start of injection, injection duration and total fuel injection quantity, respectively, for the typical case of pump speed of 1000 rpm and lever position 50%. The effect of all the aforementioned parameters on the nozzle exit characteristics can be summarised as follows:

High pressure pipe: Figure 4-27a shows that for a larger high pressure pipe length, the start of injection is delayed. This happens because the pressure wave needs more time in order to travel through the pipe to the nozzle chamber, so the needle opens later. However, the duration of injection is not affected as much as the start of injection. As a consequence, the total fuel injection quantity remains relatively constant with pipe length variation; in any case, its variation would not be higher than 2%. At this point it should be mentioned that for a multi-cylinder engine the length of the high pressure pipes should be the same for all cylinders since the injection may not start at the same crank angle (relative to the top dead centre (TDC) for each cylinder).

High pressure pipe diameter: Decreasing the high pressure pipe diameter, the pressure losses in the pipe become higher. As a result, it takes more time until the pressure reaches the nozzle opening pressure. This is illustrated in Figure 4-27 where it can be seen that the start of injection is delayed, the injection duration is smaller and the total fuel injection quantity is reduced for smaller pipe diameters. For example, a 10%

reduction in the high pressure pipe diameter, can lead to a 4% reduction in the total fuel injection quantity.

Needle preload: The initial force on the nozzle valve is an important parameter, since its value determines the nozzle opening pressure. Increasing the initial nozzle valve force, increases the nozzle opening pressure which delays the start of injection. Also, the needle will close earlier and the total fuel injection quantity will be reduced. The initial nozzle valve force is one of the most important parameters affecting the start of injection and the injection duration. A 10% increase of this force will delay the start of injection by approximately 0.6° CA and will reduce the injection duration by 0.75° CA. The variation of the total fuel injection quantity is not so severe as the other two parameters, and in any case it want exceed 3.5%.

Nozzle chamber volume: Variations in the nozzle chamber volume affect only the start of injection, since for larger nozzle chamber volumes the time needed until the pressure reaches the nozzle opening pressure is larger. The effect on injection duration and on the total fuel injection quantity is very small.

Nozzle chamber area: This is defined as the area of the nozzle chamber where the pressure acts upon in order to open the needle. So its value determines the nozzle opening pressure and, as a result, the effect of its variation on the start of injection is important. Increasing the nozzle chamber area, the start of injection is advanced; for example, for +10% variation the injection will start earlier by approximately 0.4° CA. The variation in injection duration is even higher, about 0.8° CA for that variation. Also, there is a strong effect on the total fuel injection quantity, which is approximately 5% larger than its actual value.

Injection hole diameter: The nozzle orifice diameter affects the injection pressure but not the nozzle opening pressure. So its variation has no effect on the start of injection and on injection duration but it has a strong effect on the total fuel injection quantity. For smaller hole diameters, the area from which the fuel is injected to the engine is smaller and as a result, less fuel can pass through it. A 10% reduction of the nozzle orifice diameter reduces the total fuel injection quantity by approximately 10%.

Needle diameter: The needle diameter determines the effective area of the nozzle (i.e. the passage from which the fuel flows from the nozzle chamber to the sac volume). For smaller needle diameters, the effective area is increased and a larger amount of fuel can be injected. Also, the value of the needle diameter determines the area where the

force of the pressurized fuel in the sac volume acts upon. As a consequence, decreasing the needle diameter, reduces injection duration and the start of injection is delayed since the total volume in the nozzle pipe would be larger and, as a result, the time needed until the pressure reaches the nozzle opening pressure in the nozzle chamber will be larger.

It should also be mentioned that variations in the nozzle valve mass and the nozzle spring rate have a negligible effect on the start of injection, on injection duration and on the total fuel injection quantity. This happens because the pressure forces acting upon the nozzle valve (from the pressurized fuel in the nozzle chamber and in the sac volume) are significantly higher than the inertia and spring forces.

As far as it concerns the effect of pump design parameters on the nozzle exit characteristics, a set of calculations has been performed revealing the relative effect of the control spool position, the cam plate profile and the delivery valve design. These parameters were selected since their design is strongly affecting the nozzle exit characteristics.

Cam plate profile: The cam lift geometry determines the rate of increment of the pumping chamber pressure for a given pump speed, since the plunger displacement is the parameter responsible for the generation of the high pressure in the injection system. To examine its effect relative to the standard cam plate profile its geometry was varied by simply multiplying the cam lift by a factor of 1.2, which corresponds to a more abrupt cam plate profile. It should be mentioned that it is the spill port opening that determines the end of fuel compression in the pumping chamber rather than the maximum cam lift independent of the pump operating condition.

Two different ways of controlling the end of injection have been examined. The first is to keep unchanged the cam angle at which the spill port opens; this implies that the end of injection should remain nearly constant for the two different cam plates. In the second approach, the plunger effective travel has been kept constant. These three different cases are schematically presented in Figure 4-28 by means of three (black, red and green) solid circles. As can be seen in Figure 4-28a, the effect of the increased cam lift is to increase the pumping chamber pressure thus keeping unchanged the end of injection. However, the start of injection is advanced since the pressure reaches earlier the nozzle opening pressure. According to Figure 4-28b, the actual injection pressure is significantly increased and, as a result, the total fuel injection quantity which is the area under the injection rate curve increases significantly with increasing cam lift.

The second way of controlling injection is to keep unchanged the plunger effective travel. In this case, both the start and the end of injection are affected but their difference (the duration of injection) remains unchanged, thus maintaining similar total fuel injection quantity.

Control spool position: The control spool position (i.e. the lever position) defines the plunger effective travel which, for a given cam plate profile, determines the angle at which the spill port opens. Following the opening of the spill port, the pressure drops from its maximum value to the pressure of the feed chamber. Therefore, the plunger effective travel is an important parameter since its value determines the injection duration and the peak injection rate (peak pumping chamber pressure). From Figures 4-28a,b and c it can be seen that, for a given cam lift, a higher plunger effective travel delays the spill port opening; its effect on the pumping chamber pressure and injection pressure is also significant. Although the increment of the pumping chamber pressure remains unchanged, the compression of the fuel in the pumping chamber continues which affects significantly the injection duration and, as a result, the total fuel injection quantity.

Leakage: another important factor determining the value of the pumping chamber pressure and, as a result the injection characteristics, is the hydraulic efficiency of the pump; this is associated with possible leakage of the fuel. For the particular pump investigated, leakage may take place between the plunger and the body of the pump. Two different values of equivalent clearances have been examined, corresponding to 10 μm and 15 μm, respectively. As can be seen in Figure 4-28, the value of the leakage passage strongly affects the value of the pumping chamber pressure, the injection pressure and the total fuel injection quantity. The particular injection pump examined here has a hydraulic efficiency (defined as the ratio between the actual fuel injected and the volume of the pumping chamber displaced by the plunger during its effective travel) of the order of 40%.

Delivery valve design: the use of the delivery valve is standard in all existing pump-based diesel fuel injection systems. As already clear from Figure 4-13, the delivery valve prevents any damage and noise resulting from the pressure waves traveling within the fuel injection system after the start of injection since it isolates the pump from the rest of the fuel injection system. In order to investigate its role on the performance of the system, three different designs were simulated. The first one

corresponds to the nominal geometric characteristics of the examined FIE, the second has a similar design but a much smaller delivery valve chamber and in the third the delivery valve has been completely removed. As can be seen in Figure 4-29, when the delivery valve chamber volume is reduced, the pressure in this volume increases significantly. The result from the reflected pressure wave is secondary injection since the value of the pressure in the nozzle chamber can become higher than the value of the nozzle opening pressure. Removing the delivery valve, the pumping chamber pressure becomes smaller and injection is advanced. However, the fluctuations present in the delivery valve chamber pressure imply that this design will give higher noise.

4.2 Three-Dimensional Sac Volume Flow

Over the last few years many studies have concentrated on the investigation of the flow characteristics inside the sac volume and the injection holes of diesel injectors due to their significant influence on the atomization process of the emerging liquid jet. Since flow measurements in real size diesel injectors are difficult due to their very small size and the relatively high injection pressures, large scale transparent nozzles have been used instead, to allow flow visualization; dynamic flow similarity can then be employed to extrapolate the conclusions of the investigation in the large scale models to the real size injectors. Despite this fact, up to now limited quantitative information exists about the details of the flow in the sac volume and the injection holes since most of the studies in the open literature have mainly concentrated on photographic investigations of either cavitating or non-cavitating flow conditions. However, laser techniques are available and can be used to provide quantitative information about the mean flow and the turbulence intensity in non-cavitating cases. In the present investigation, the refractive index matching technique was employed which is based on the fact that if the refractive index of the transparent acrylic large-scale model is the same to that of the working fluid, which is a mixture of hydrocarbons, the laser beams of a laser Doppler velocimeter (LDV) can propagate into the liquid inside the transparent material without distortion. The velocity flow field can then be measured from the Doppler frequency shift in the scattered light.

Since quantitative experimental information is rather limited, CFD models have been widely used over the last few years in order to predict the flow pattern inside diesel injectors. However, no detailed validation of these models has been performed up

to now for such complicated geometries as those of multihole injection nozzles. In the present investigation, an existing CFD model, described in chapter 2, was used in order to predict the flow in the transparent large-scale nozzle used for the LDV measurements, thus allowing a detailed validation of the model. In the next section, the details of the experimental technique are briefly described followed by the presentation of the results.

4.2.1 Experimental set-up

Figure 4-30 shows a photograph of the transparent nozzle from two different views as well as a photograph of the adaptor used to collect the fuel from the individual injection holes; the body of the nozzle, the needle and the adaptor were manufactured from an acrylic material with a refractive index of 1.49. The dimensions of the nozzle and the needle represent a 20x magnification of a Bosch six-hole vertical diesel injection nozzle; the hole diameter of the model is 3.44 mm which corresponds to a hole size of about 0.17 mm in the real injector. The details of the nominal geometry can be seen in Figure 4-32. Measurements were performed for two different needle lifts, 1.75 and 6.0 mm, respectively; the latter one corresponds to the maximum lift (0.3 mm) of the real size injector.

Figure 4-31 shows two photographs and a schematic representation of the experimental rig. There are four pipes delivering the flow in the nozzle gallery which was designed in such a way as to ensure that the mixing of the flow in this area results in a uniformly distributed flow at the needle seat. The length of the nozzle pipe was600 mm, which was considered long enough to create turbulent flow conditions just upstream of the transparent nozzle. The working fluid was a mixture of 31.8% by volume of 1,2,3,4-tetrahydronapthalene (tetraline) and 68.2% oil of turpentine with a density and kinematic viscosity of 0.893 kg/m^3 and 1.64×10^{-6} m^2/s at 25°C. The mixture was maintained at a temperature of 25±0.2°C by a temperature controller, using a heater and a cooler installed within the storage tank, and a platinum resistance sensor near the pump outlet, to maintain the fluid refractive index at a level of 1.49 which is identical to that of the cast acrylic. The flow rate of the mixture was controlled by a valve in the pipe downstream of the pump and measured by an orifice plate, calibrated to be accurate within 3%. In order to identify possible differences in the flow rate exiting from individual injection holes, the fuel flowing through each of them was collected in a

burette tube; the differences identified were of the order of ±5% from the mean value and were attributed to small differences in the size of the injection holes as well as to their surface roughness resulting from the manufacturing process.

The laser Doppler velocimeter comprised a Helium-Neon laser operating at a wavelength and power of 632.8 nm and 60 mW, respectively, a diffraction-grating arrangement to divide the laser beam into two of equal intensity and to provide frequency shifts up to 12MHz, collimating and focusing lenses to bring the two beams to an intersection volume, a photomultiplier (Dantec 55x34) and a frequency counter (TSI model 1990) interfaced to a microcomputer using a DMA board (Dostek 1400). The intersection volume was approximately 1120 μm in length and 79 μm in diameter, with a fringe spacing of 3.03 μm. The signals from the photomultiplier were processed by the counter to form ensemble averages from more than 4000 individual velocities. The overall maximum uncertainty in the measurement of the mean and rms velocities in the region of steep velocity gradients is expected to be not more than 5% and 10%, respectively.

Figure 4-33 shows the experimentally estimated flow rate through the system as a function of the needle lift; in addition, the total discharge coefficient of the nozzle (needle seat and injection holes) is presented together with the Reynolds number calculated on the basis of the hole diameter and the mean injection velocity. As can be seen, for needle lifts higher than 1.5 mm, the Reynolds number remains almost constant at around $2 \cdot 10^4$, which ensures fully turbulent flow within the nozzle. The mean injection velocity is around 10 m/s which corresponds to an injection velocity in the real size injector of the order of 250-300 m/s, depending on the viscosity of the diesel fuel. The discharge coefficient at the maximum needle lift is around 0.8; since for this needle lift the main pressure drop through the nozzle occurs at the entrance of the injection holes (as it will become evident in the following section), this value represents the discharge coefficient of the holes under non-cavitating conditions.

4.2.2 Simulation model

Figure 4-34 shows the numerical grid consisting of 50052 computational cells which are non-uniformly distributed in the simulated geometry. In the injection holes region, 8×8 grid notes were placed along the cross-section of each hole and 27 planes

along the length of the holes. In this figure, different views of the numerical grid are presented; the cross section A-A shows the internal grid structure at the sac volume and the injection holes area for both needle lifts investigated. Furthermore, the cutting planes selected for the presentation of the results are shown; three different groups of planes have been selected. Cutting plane 1 is a vertical plane passing through the axis of two injection holes while cutting planes 2a, 2b, 2c and 2d have the same inclination angle as that of the injection hole and they are located at 0.5, 1.0, 1.5 and 2.5 mm below the top side of the injection hole. Finally, cutting planes 3a, 3b, 3c and 3d are vertical to the hole axis and they are located at 0.0, 1.0, 4.0 and 12.0 mm, respectively, from the entrance plane of the injection hole.

Prior to the validation of the simulation model, results obtained with the model will be presented describing the detailed flow characteristics in the sac volume and the injection holes. Figure 4-35 shows the velocity flow field, pressure and turbulent kinetic energy distributions on cutting plane 1 with the needle placed at 6.0 mm. Three different views have been selected for presentation; the first one (left column) gives the flow in the whole computational domain. As it is evident, the pressure is uniform in the needle seat and the sac volume regions. The pressure drop across the nozzle is around 0.85 bars, which agrees with the measured value. The uniform turbulent kinetic energy distribution corresponds to a turbulent velocity of the order of 5-10% of the mean inlet velocity. However, a pressure drop does occur at the hole inlet as can be clearly seen in the middle and right columns of Figure 4-35. Looking at the velocity flow field, there is a recirculation zone formed at the entrance of the injection hole; if the pressure in this region becomes lower than the critical cavitation pressure of the liquid, cavitation bubbles may be formed. Downstream of the point of flow reattachment, which is at around 1/3 of the total hole length, pressure recovers and becomes equal to the back pressure. Looking at the turbulent kinetic energy distribution, one can see that there is a high turbulence region just before the entrance of the hole which is due to the recirculation zone formed close to the needle seat. The highest turbulence levels are found inside the injection hole just after the reattachment of the flow on the wall. Another point that should be mentioned is related to the velocity distribution at the hole exit; as can be seen, the flow is non-uniformly distributed. This distribution is a function of the geometric details of the hole itself (i.e. inclination angle, entrance shape, L/D) as

well as of the needle position in the sac volume and it will be investigated in detail in a following section.

Figure 4-36 presents the velocity flow field (left column) and the pressure distribution (right column) along cutting planes 2a, b, c and d. As can be seen, the velocity distribution exhibits two peaks after the point of flow reattachment; this results from the fact that the flow turns in a direction tangential to the normal cross section of the hole. This can become more clear by concentrating on Figure 4-37 which shows the pressure, velocity and turbulent kinetic energy distributions inside the injection hole along cutting planes 3a, b, c and d. As it is clear, inside the recirculation zone the flow is directed from the bottom to the top while after the flow reattaches, the liquid fills the empty space giving rise to the aforementioned double-peak velocity profile. It can also be seen that although the pressure distribution at the exit of the hole is uniform and equal to the back pressure, the turbulent kinetic energy has a strong peak almost at the center of the injection hole. This point results from the flow development after the point of reattachment. Figure 4-38 shows the predicted flow field, pressure and turbulent kinetic energy distributions along cutting plane 1 for the 1.75 mm needle lift case. It can be seen that a similar flow pattern is calculated. However, the pressure drop across the needle seat is now important and represents an approximately 40% of the total pressure drop across the nozzle. As a result, the recirculation zone inside the hole is much weaker and the calculated turbulent kinetic energy levels are much smaller. Figure 4-39 shows the calculated velocity flow field and pressure distributions along cutting planes 2a, b, c and d. The double-peak velocity distribution is still present downstream of the regime where the flow reattaches; however this occurs only at the upper part of the injection hole and it represents lower values due to the smaller extension of the low pressure region formed at the hole entrance.

4.2.3 Model validation

In this section the LDV measurements are described and compared with the results obtained with the simulation model. The velocity flow field was measured at different points on a vertical plane passing through the geometric axis of two of the six injection holes (cutting plane 1). The flow rate from these holes corresponded to the minimum (plane 1) and maximum (plane 2) values as measured with the burette tube.

The points of measurement were mainly concentrated at the entrance of the injection holes in the sac volume as well as inside the holes. However, in order to identify possible asymmetries in the flow at the nozzle pipe, measurements were also obtained above the needle seat as well as in the needle seat area.

Figure 4-40 shows the velocity measurements obtained at three different planes located at 80, 60 and 26 mm above the lowest point of the sac volume. For the first two planes, the axial (U) and the radial (V) velocity components were measured. As can be seen, the flow resembles a plug turbulent flow profile which is reasonably well predicted by the computer model. At the 60 mm plane, there is a small recirculation zone formed just above the step present in the specific design. However, this geometry has a small effect on the flow downstream since, as can be seen at the 26 mm plane, the flow becomes almost uniform. At this axial position the measured velocity component was on a plane having an inclination angle of 15 deg. which is identical to the inclination of the needle. The much larger velocities present in the 1.75 mm needle lift case compared to the 6.0 mm are due to the much narrower flow passage available for the liquid to flow through it. Another point that should be mentioned is that the velocity distribution along planes 1 and 2 seems to be the same, which means that any experimentally identified differences in the flow injected per hole are not due to the inlet flow but are created by the details of the geometry of the individual injection holes. In addition, the swirl velocity component that was measured in all the above locations was found to be zero. Having verified that the flow just upstream of the sac volume is uniform, turbulent and non-swirling, we proceed to the presentation of the results obtained in the sac volume and injection holes.

Figure 4-41 shows the velocity measurements obtained at four different horizontal planes placed at 14.5, 12.7, 11.2 and 9.0 mm above the lowest point of the nozzle which is the geometric center of the sac volume. The first of these points corresponds to the upper level of the entrance to the injection holes, the second approximately to the middle of the hole, the third to the lower entrance level of the holes while the last one passes through the lowest point of the needle tip. Measurements were obtained at both planes 1 and 2, as also shown schematically in Figure 4-41. Both the axial (U) and the radial (V) velocity components, normalized by the mean injection velocity, are presented; these are also defined in the schematic shown on the same page which presents the details of the sac volume as well as the relative position of the

measurement points. Positive values of the axial velocity are directed from larger to smaller z-coordinates while positive radial velocities are directed from the inlet to the exit of the injection holes which also corresponds to the trend from smaller to larger x-coordinates.

Two different sets of computational results have been selected for presentation. In the first set (referred to as 'case 1'), the geometry of the nozzle was identical to that having the nominal geometric characteristics. Since this geometry would predict the same flow rate through all of the injection holes, a second numerical grid was constructed matching holes of different sizes in such a way that the same flow rate as that measured from the individual holes could be predicted. For the second type of calculation, referred to as 'case 2', the results for both planes 1 and 2 are presented. As can be seen, the main pattern in both measured and calculated flows shows that the flow mainly turns inside the injection holes. The relative magnitude of the U and V velocity components presented in the graphs indicates that the highest velocities are present at the upper level of the injection holes. Predictions of 'case 2' are in better agreement with measurements compared to those of 'case 1' and they also exhibit the same trend in terms of the measured differences of the velocity in the two planes 1 and 2. Concerning the flow pattern inside the sac volume, as can be seen from both the experimental and the computational results, due to the differences in the size of the injection holes, the liquid flowing along plane 1 can not be delivered through the injection hole at the same plane and flows inside the sac volume below the needle towards the hole at the opposite side. However, at the lower entrance level of the hole in plane 2, a recirculation zone is formed which interacts with the liquid coming from the sac volume; the overall result is a complex flow pattern which, as will be seen in the next figure gives rise to high turbulent levels at the entrance of this specific hole. The vector plots also presented in Figure 4-41 are those predicted by the simulation model for 'case 2' and provide details of the flow in the sac volume and the entrance of the injection holes.

Figure 4-42 shows the experimental as well as the computational results in three different vertical planes located at 6.2, 7.0 and 8.5 mm from the axis of symmetry of the nozzle. The plane at 8.5 mm is located just at the entrance of the injection holes; the corresponding z-coordinates extend from z=9.0 mm up to z=15.0 mm which covers the whole length of the hole entrance; again, results on both planes 1 and 2 are presented. As can be seen, the relative values of the V velocity components become relatively

higher at the entrance to the hole; the V velocity profile at the 8.5 mm position gives the flow distribution at the entrance of the injection holes. The measured axial velocity component shows that there is a recirculation zone formed close to the needle (6.2 mm distance), which is stronger for plane 2 due to the flow distribution within the sac region presented in the previous figure 4-41. Predictions are in relatively good agreement with the experimental values with the largest differences present in the extent of the recirculation zone close to the needle; however, the predicted flow pattern at the hole entrance is in good agreement with the measured values. In the same figure, the calculated pressure distribution in plane 1 and the turbulent kinetic energy have been plotted. It can be seen that the pressure distribution in the sac volume is almost uniform, but there is a sudden pressure drop at the entrance to the hole. The lowest pressure regions are located at the upper part just after the hole entrance inside the injection holes; it is at this region that cavitation was observed to start at slightly higher flow rates. Moving inside the injection holes, the pressure recovers after the reattachment of the recirculation zone and becomes equal to the back pressure, which was atmospheric in the present investigation. The turbulent kinetic energy distribution shows that there is a highly turbulent zone at the entrance to the injection hole which corresponds to the area of the recirculation zone close to the needle. Relatively higher levels of turbulence were predicted for plane 2 due to the mixing of the flow from the sac region moving towards the hole inlet on plane 2. As the flow turns inside the injection hole, the regions with the highest turbulence levels are located around the area of the flow reattachment.

Having investigated the flow characteristics inside the sac volume, measurements were performed inside the injection hole along plane 1 at different distances from the hole inlet. These measurements were obtained at two different planes; the first plane, which is referred to as 'hole plane a' in Figure 4-43, is a vertical plane passing through the axis of the injection hole. The second plane, which is referred to as 'hole plane b' is vertical to the previous one and it has the same inclination angle as that of the injection hole. The velocity component plotted is almost parallel to the direction of the injection hole. The measurement positions correspond to vertical planes located 9.5, 10.5, 13.5 and 16.5 mm from the nozzle axis of symmetry for hole plane 1 and to horizontal planes located at 8.5, 9.5, 13.5 and 16.5 mm for hole plane b. The predicted flow distribution on these two planes is also shown in Figure 4-43. As can be seen, there is a recirculation zone formed just after the hole entrance. The disagreement

between the computational and the experimental results at this flow region is attributed to both the relatively coarse mesh and the model of turbulence used. However, both measurements and predictions show that the recirculation zone extends up to approximately 1/3 of the hole length and although the flow reattaches from that point downwards, the velocity distribution at the hole exit seems to be strongly influenced by the formation of the recirculation at the hole entrance. Measurements and predictions on hole plane b show that the velocity profile on this plane is again strongly affected by the recirculation zone. The flow distribution on hole plane b shows that the velocity profile exhibits two peaks along the hole diameter which is due to the reattachment of the recirculation zone and the corresponding tangential, relative to the hole cross-sectional area, flow direction at this region. Predictions have been plotted for two different planes, named as b1 and b2 which correspond to a slightly different position inside the injection hole in order to demonstrate that the accurate prediction of the measured values is not only a function of the turbulence model used but also of the uncertainty in the actual point of measurement since the relative size of the control volume of the laser beams is comparable to the dimensions of the numerical grid and of the hole itself. In the same graphs, the measured rms values representing turbulence are also plotted. As can be seen, the highest rms values are present at the areas of flow reattachment, as already stated. These can be as high as 0.3 to 0.5 of the mean injection velocity, which implies that the jet emerging from the injection holes is turbulent and this would have a significant affect on the atomization mechanism of the liquid jet.

Figure 4-44 shows the experimental as well as the computational results at four horizontal planes located at 14.5, 12.7, 9.0 and 4.5 mm above the sac volume centre point for the lower needle lift case. At this specific needle position, the 4.5 mm plane passes through the lowest point of the needle inside the sac. Although similar conclusions can be drawn for the highest needle position, it can be seen that the recirculation zone close to the needle is weaker compared to that present at the 6.0 mm needle lift case. Also, since the needle is deep inside the sac region, it becomes difficult for the flow to turn from plane 2 to plane 1. Another point worth mentioning is related to the prediction of the velocity distribution at the hole exit. It is evident that the velocity profiles on planes 1 and 2 are different with the velocity on plane 2 more uniformly distributed. It can also be seen that predictions using the non-uniform numerical grid are again in better agreement with the experimental data.

Figure 4-45 shows the comparison between the computational and the experimental results for the same points as those presented in Figure 4-42 but for the 1.75 mm needle lift case. Again similar conclusions can be drawn, since the major point of interest is the flow turning from the needle seat towards the injection hole. However, the recirculation zone close to the needle extends less this time since the flow turns more directly from the needle seat towards the injection holes. Finally, Figure 4-46 shows the comparison between the computational and the experimental results inside the injection hole for the 1.75 mm needle lift case. It can be seen that the hole recirculation zone is smaller compared to that of the higher needle lift case. However, the simulation model fails this time to predict the actual flow distribution just at the hole entrance probably due to the model of turbulence employed in the CFD code.

4.2.4 Parametric studies

Having validated the simulation model, we can now proceed to a set of parametric studies examining the effect of some important geometric characteristics of the nozzle on the detailed flow distribution. Since small differences in the size of the injection holes have been already investigated, emphasis is now given to the effect of hole inclination angle and the effect of needle eccentricity on the calculated flow field. Figure 4-47 shows details of the test cases simulated; in all of them, the needle lift was set at 6.0 mm and the flow rate was kept the same as that used in all previous studies.

Figure 4-48 shows the effect of the hole inclination angle on the velocity flow field and the pressure distribution. As can be seen, the larger the flow turning angle (72.5 deg angle) is, the easier becomes for the flow to turn inside the injection hole; as a result, lower pressures are required to inject the same amount of fuel, which is equivalent to larger values of the hole discharge coefficient. Also, a more uniform velocity profile at the exit of the hole is calculated. The low pressure region inside the hole entrance is weaker, which means that cavitation will be initiated at higher flow rates. Overall, the hole inclination angle is an important factor affecting the detailed flow characteristics inside the injection hole. This is of major importance in inclined nozzles, which are widely used in two-valve diesel engines, as will be discussed later in this chapter.

Figures 4-49 to 4-54 present the effect of the needle eccentricity on the flow distribution in the sac volume and the injection holes. Figure 4-49 shows the details of the simulated geometry and presents results for the velocity flow field, pressure and turbulent kinetic energy distributions on two different vertical planes named 1a and 1b which pass through the geometric axis of two different groups of injection holes. As can be seen, there are four holes expected to exhibit different flow pattern for this specific needle position which are referred as to holes 1,2,3 and 4.

Results on cutting plane 1 reveal that there is a strong motion inside the sac volume directed from hole 2 towards hole 1. This motion results in a much more uniform flow distribution in hole 1 compared to hole 2. Also, the turbulent kinetic energy levels close to the entrance of hole 1 are much higher than those calculated for hole 2 due to the very intense recirculation zone formed close to the needle. The calculated differences between holes 3 and 4 are smaller since the needle eccentricity does not restrict the flow passage in these two holes as much as in the other two.

Another interesting point is related to the swirling motion created inside the sac volume due to the needle eccentricity. Figure 4-50 shows the velocity flow field on seven horizontal planes covering a distance from the upper point of the injection holes up to the lowest point of the needle inside the sac volume. As can be seen, there is a swirling motion directed from hole 1 towards holes 3 and 4; as a result, the flow distribution at the inlet of these two holes is not uniform and this can have a significant effect on the flow pattern at the hole exit. This swirling motion seems stronger in planes a and b rather than in the other planes located closer to the bottom of the injection holes. Figure 4-51 shows the pressure and turbulent kinetic energy distributions at three planes. It is evident that the lowest pressure region is located at hole 2 while in holes 3 and 4 the swirling motion at their inlet creates a low pressure region asymmetrically located relative to the hole axis. These conclusions about the effect of the flow inside the sac volume on the flow characteristics in the injection holes become more clear in the following Figures 4-52, 4-53 and 4-54.

Figure 4-52 shows the velocity flow field on four vertical planes defined by the notation j=1, j=4, j=5 and j=6 on the same figure. The j=1 plane is located at the hole entrance, the j=4 plane is located at 1/4 of the total hole length, the j=5 plane is located at the middle of the hole while the j=6 plane is located at the hole exit. It is clear that the flow distribution in holes 3 and 4 is strongly affected by the swirling motion in the sac

volume. As can be seen, there is a swirl velocity component, which is stronger for hole 3, and this swirl reaches the hole exit. Experimental studies (Soteriou et al. (1995)) on the spray characteristics have revealed that when there is a swirl motion in the injection hole, the corresponding centrifugal forces tend to create a hollow cone spray. Figure 4-53 shows the pressure distribution in the same four holes, but at this time on planes j=1, j=2, j=3 and j=4. As already mentioned the lowest pressure region occurs at the entrance to hole 2 while for holes 3 and 4 this region is inclined relative to the hole axis. This is also important since the onset of cavitation at this low pressure region will cause further non-uniformities at the hole exit characteristics. Finally, Figure 4-54 shows the predicted turbulent kinetic energy distribution at the same injection holes. As can be seen, the centrifugal forces present in the swirling flow in holes 3 and 4 cause high friction between the fluid and the walls; as a result, the highest turbulent levels are located close the walls of the hole, implying further complications for the atomization mechanism of the emerging liquid.

4.2.5 Inclined injector

The previous model validation study was performed in the large scale transparent nozzle. However, since the injector used in the FIE model is a Stanadyne inclined one and since the same injector was used for the measurements of the spray characteristics, it was considered necessary to investigate the flow characteristics of this particular injector under transient but still non-cavitating flow conditions.

Figure 4-55 shows the numerical grid constructed to represent the geometry of this particular 5-hole nozzle. The hole diameter is 0.18 mm and the inclination angle of each hole is given in Table 4-4. In order to investigate the transient flow characteristics, the needle lift and the flow rate through the nozzle were input into the model and they are presented in Figure 4-56 as a function of time; their values are those predicted by the FIE model for a pump speed of 1000 rpm and a lever position of 15%. The back pressure was kept constant and equal to 30 bars. For this particular injection condition the lowest pressure calculated by the model was almost zero which implies that this is the limiting case for the onset of cavitation. The black dots superimposed on the curves of this figure denote the time steps selected for the flow visualization. As can be seen,

they correspond to 0.16, 0.26, 0.30, 0.40, 0.50 and 0.60 ms after the start of injection while the total fuel injection quantity was around 3 mm^3.

Figure 4-57 shows the predicted pressure distribution at two cutting planes passing through the axis of two holes having different inclination angles. The selected holes have the lowest and the highest inclination angle which also correspond to the overfuelling and the underfuelling injection holes as will become clear later in this chapter. As can be seen, during the injection period the pressure in the sac volume is mainly uniform and equal to that calculated by either the FIE or the CFD model. The pressure drops at the hole entrance and recirculation zones are formed with the lowest pressure approaching close by the cavitation pressure of the liquid. The pressure at the exit of the holes is uniform and equal to the back pressure. The maximum pressure calculated by the model corresponds to a time step just after the maximum needle lift and it is due not only to the highest flow rate through the nozzle but also to the compression of the liquid inside the sac volume.

Figure 4-58 shows a more detailed view of the velocity flow field and the pressure distribution inside the sac volume and the injection holes area. As can be seen, more fuel is delivered through the hole with the higher flow turning angle where a much more uniform velocity profile is calculated compared to that of the other hole. The lowest pressure region occurs in the underfuelling hole implying that cavitation will first initiate in this hole.

Overall, it can be said that the flow distribution in inclined nozzles is non-uniform between the various holes and strongly depends on the hole inclination angle relative to the needle seat axis. These differences have a significant effect on the spray characteristics and this will be verified in the next chapter.

4.3 Hole Cavitation Model

Although the analysis of the 3-D single-phase flow field in the sac volume and the injection holes is very useful, it not applicable in the presence of cavitation. For cavitating flow cases, only phenomenological approximations can be used at present which are capable of predicting the fuel injected between the differently oriented injection holes and calculating the effective hole area. Resent experimental data have revealed that when the pressure in the sac volume for a given injection hole and

chamber back pressure becomes larger than a critical value, the pressure in the injection hole may fall locally below the critical cavitation pressure of the liquid. Cavitating bubbles are then formed within the recirculation zones at the entrance to holes having a narrow angle to the flow direction and/or a sharp entrance shape which are convected by the liquid downstream towards the exit of the injection holes. To account for the detailed dynamics of the resulting two-phase flow, models are needed which should be capable of calculating the accurate position of the bubble formation, their mass, their growth rate, their shape and the effects of their motion and eventual collapse on the liquid phase. However such an approach is very complicated and it is beyond the scope of the present investigation, although certain aspects of this type of pressure-driven flow and its effect on the two-phase flow characteristics at the exit of the injection holes can be taken into account using a phenomenological one-dimensional approach. As the three-dimensional analysis of the flow in the sac volume reveals, the pressure in the sac volume (P_{SAC}) can be considered uniform and equal to the mean pressure calculated by the FIE model (Figure 4-59). The discharge coefficient of the injection holes is then calculated as a function of the hole geometry, the Reynolds and cavitation numbers, the hole position in the sac volume relative to the needle seat axis and the pressure difference between the sac volume pressure and the back chamber pressure (for the pressure distribution see Figure 4-59). Figure 4-60 shows a schematic representation of the 1-D flow pattern in the injection hole and the pressure variation along the hole length for both the cavitating and non-cavitating cases. Figure 4-61 shows the effect of the various geometric parameters mentioned above on the discharge coefficient of the injection hole. In particular, Figure 4-61a shows the effect of the hole inclination angle, Figure 4-61b the effect of the hole entrance radious of curvature r/D and Figure 4-61c the effect of the hole length L/D on the hole discharge coefficient. The smaller the flow turning angle, the sharper the hole entrance shape or the higher the L/D, the smaller the value of the discharge coefficient. The effect of cavitation on the amount of fuel injected per hole is presented in Figure 4-62a which shows the variation of the hole discharge coefficient as a function of the cavitation number for different values of the Cd_{max} which depends on the hole geometric characteristics rather than on the operating conditions. The value of Cd_{hole} decreases with increasing cavitation number and reaches asymptotically a minimum value. It is important to note that during the injection period the cavitation number changes significantly and thus the discharge coefficient also

changes. From the calculated hole discharge coefficient, the fuel injected from each hole of multihole injectors can thus be estimated. Figure 4-62b shows the critical back pressure below which cavitation occurs in the injection hole as a function of the sac volume pressure for different hole discharge coefficients (which correspond to holes with different geometric characteristics); as can be seen, its value strongly depends on the value of the discharge coefficient, which, as already mentioned, varies during the injection period. The area of the injection hole at its exit occupied by liquid can be calculated from one dimensional considerations. Figure 4-62c shows how the effective flow area changes as a function of the cavitation number for holes with different discharge coefficients; the latter has been kept constant for this particular calculation. As cavitation number increases, the more cavitating the flow becomes and the smaller the value of the effective hole area is. Furthermore, holes with a smaller discharge coefficient, i.e. holes with a smaller flow turning angle or holes with a sharper entrance shape are expected to cavitate earlier and to exhibit a smaller effective area. It should also be noted that the effective hole area is affected by the hole size; the smaller the hole diameter, the smaller the hole effective area. From Figure 4-62c it becomes obvious that during the injection period when both the operating conditions and the hole discharge coefficient change dramatically, the hole effective area also changes. Thus, as it will become more clear in the following chapter, its calculation strongly affects the calculation of the spray characteristics at the nozzle exit and further downstream.

In order to identify the effect of the injection hole orientation on the amount of fuel injected per hole, a specially designed adaptor was fitted at the exit of the nozzle tip. Holes with the same axis as the actual injection holes were drilled on the body of the adaptor to allow the fuel injected per hole to be estimated by the burette reading tube. The results of these measurements expressed as percentage variation from the mean value are presented in Figure 4-63a for a wide range of pump operating conditions, covering pump speeds from 300 to 2000 rpm and lever positions from 0% to 100%; considerable differences in the amount of fuel injected from individual injection holes were identified. For the particular injector tested, three different hole orientations existed; two holes were found to consistently inject approximately 10% less fuel than the mean value, the other two were injecting approximately 3% to 4% more fuel than the mean and the fifth hole was over-fueling by approximately 10%. The orientation of the low-fueling holes corresponds to holes having a smaller flow turning angle, which

gives rise to a smaller discharge coefficient; this is also consistent for the other two groups of holes. Figure 4-63b shows the computational results for the fuel injected from the five individual injection holes for all test cases. It is evident that the experimental trend is correctly predicted which implies that the correlations used for the calculation of the discharge coefficient of the injection holes are valid since they are in good agreement with the experimental observations. According to Figure 4-63b, two of the holes inject approximately 8% less fuel than the calculated mean value, two holes inject approximately 3% more fuel than the mean value and the last hole injects approximately 9% more fuel. Thus, it can be concluded that although the simulation model represents in a rather simplistic way the flow pattern in the sac volume, it provides reasonable estimates of the mass distribution in the differently orientated injection holes. It should also be noted that these results account for a wide range of pump speeds and lever positions, or in terms of injection pressures, they correspond to pressures from almost equal to the back pressure (at very low needle lift) to as high as 900 bars. This is an important conclusion since this model is expected to predict the observed differences in diesel engine sprays emerging from multi-hole injectors under realistic operating conditions.

Having identified the fuel injected from each of the injection holes, the injection velocity was then calculated under cavitating flow conditions. It is expected that when cavitation occurs in the injection holes, the actual injection velocity is higher than that calculated on the basis of the geometric hole area and the volumetric flow rate, due to the volume occupied by the cavitating bubbles. Since direct measurement of the injection velocity is very difficult, due to the very high injection pressures and the very small injection hole diameter, an indirect way was selected for its estimation. Figures 4-64a and 4-64b compare the injection velocity estimated form the experimental fuel injection rate and the geometric hole area with the measured droplet velocities using a PDA system at a position as close as possible to the nozzle exit (10 mm) for a pump speed of 600 rpm and 1200 rpm, respectively. It is clear that the experimentally estimated injection velocity underestimates the measured droplet velocities at the time of the peak injection rate by approximately 30%. It is thus expected that the differences between the calculated and the actual injection velocity would be even larger due to droplet deceleration and to atomization and break-up effects within the distance of the 10 mm between the hole exit and the measurement point. The effective flow area model

calculates a 35% to 40% higher injection velocity at the hole exit, and, as it is indicated in Figure 4-64, this velocity is much closer to the measured droplet velocities; as it will become more clear later on, its value allows for a reasonable prediction of the spray characteristics close to the injector. This confirms that hole cavitation has a significant effect on the actual injection velocity and the subsequent spray development.

Furthermore, it was considered useful to obtain estimates of the effective hole area as calculated by the simulation model. Three different test cases have been selected for presentation, corresponding to three different injection conditions (Figure 4-65). Peak injection pressures are approximately 900 bars for the case of Figure 4-65a, 500 bars for the case of Figure 4-65b and 250 bars for the case of Figure 4-65c while the back pressure was kept constant at 30 bars for all three cases. In each figure, three different curves are plotted, corresponding to the calculation of the effective hole area for the three different groups of injection holes. As can be seen, the effective hole area is a function not only of the sac pressure, which varies during the injection period, but also a function of the hole orientation. Holes with a smaller flow turning angle are expected to cavitate more than holes with a larger flow turning angle due to the smaller value of their discharge coefficient; in these cases the calculated effective area is a smaller percentage of the geometric hole area. It should also be noted that although the actual injection velocity is calculated on the basis of the calculated effective hole area, this is not necessarily higher in the more cavitating holes, since the amount of fuel injected from these holes is smaller than the fuel injected from the rest.

4.4 Conclusions

Summarizing the most important conclusions of the analysis of the flow in the fuel injection system and the sac volume, it can be argued that for the accurate estimation of the flow characteristics and the fuel injection rate of individual injection holes, which is required as input to the spray model, a detailed analysis of the flow in the sac volume area and the injection holes, such as the one presented here, becomes a prerequisite. The results showed that the uncertainties in the fuel injected per hole are of the order of 10% from the mean value averaged over all holes, which gives a 20% difference in the peak fuel injection rate per hole from the mean value. The injection velocity based on the geometric hole area can be 35% to 40% lower than the actual

injection velocity if the effect of hole cavitation is not considered and, in addition, the uncertainty in the estimation of the start and end of injection when injecting in a diesel engine is of the order of 1-2 deg. CA. These values can be reasonably well estimated from the FIE-sac volume flow model during the injection period and used as inputs to the spray model.

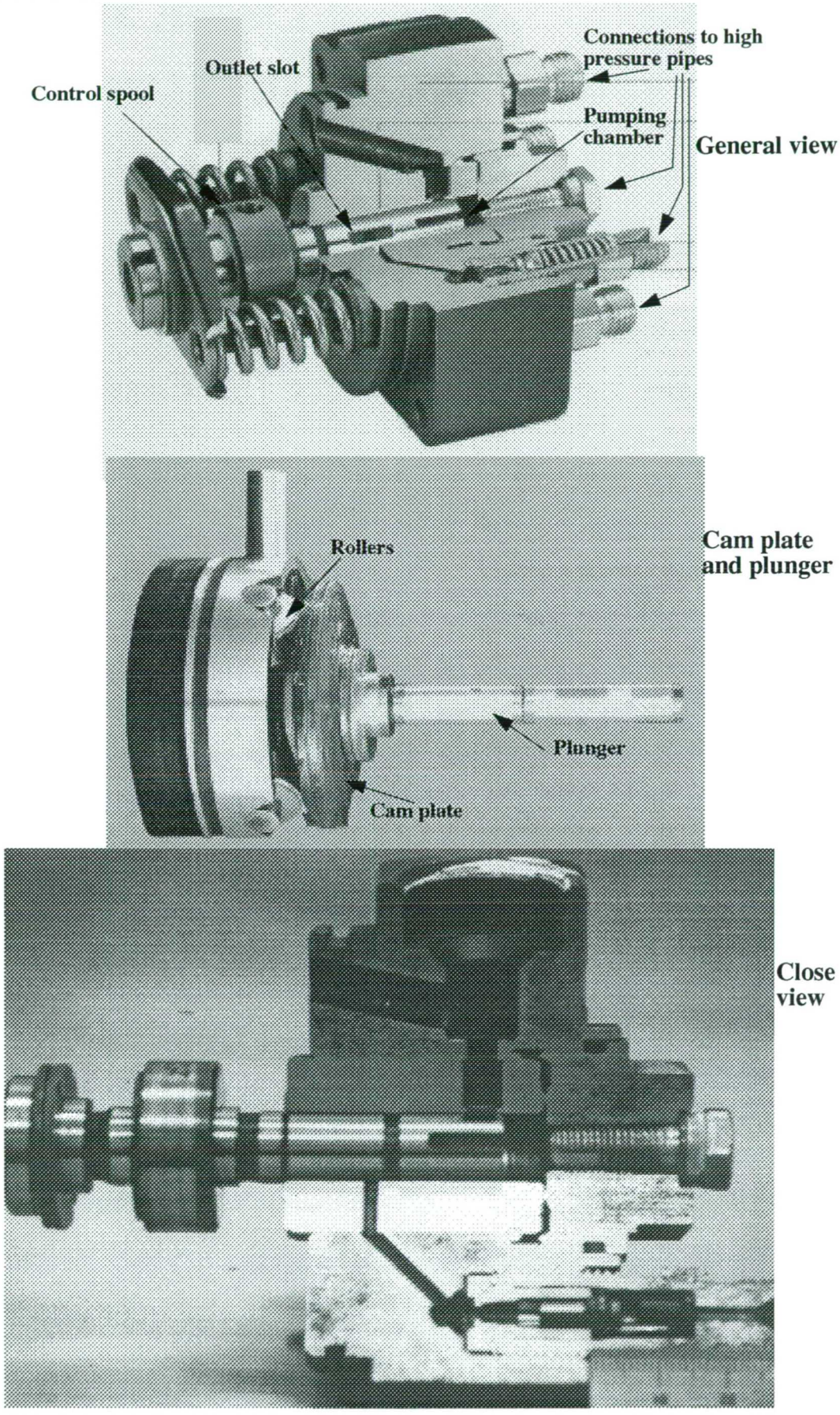

Figure 4–1 : Photograph of the cross sectioned Bosch VE distributor–type pump

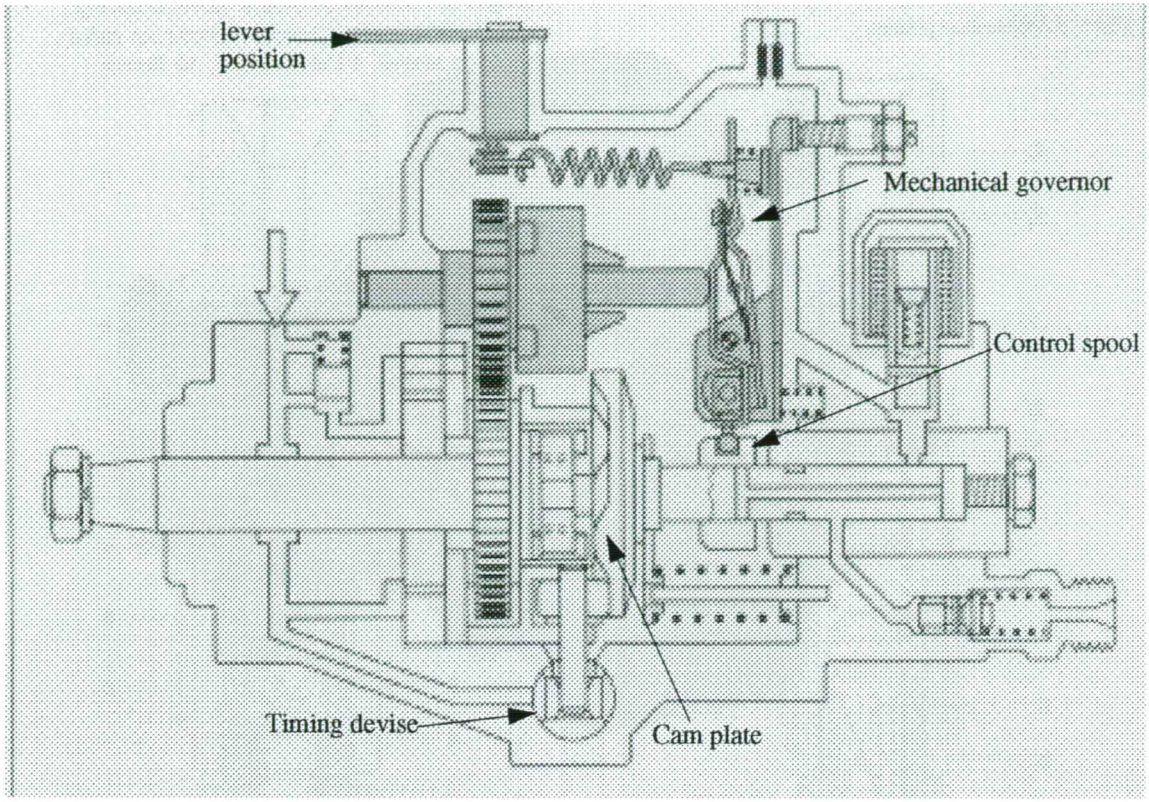

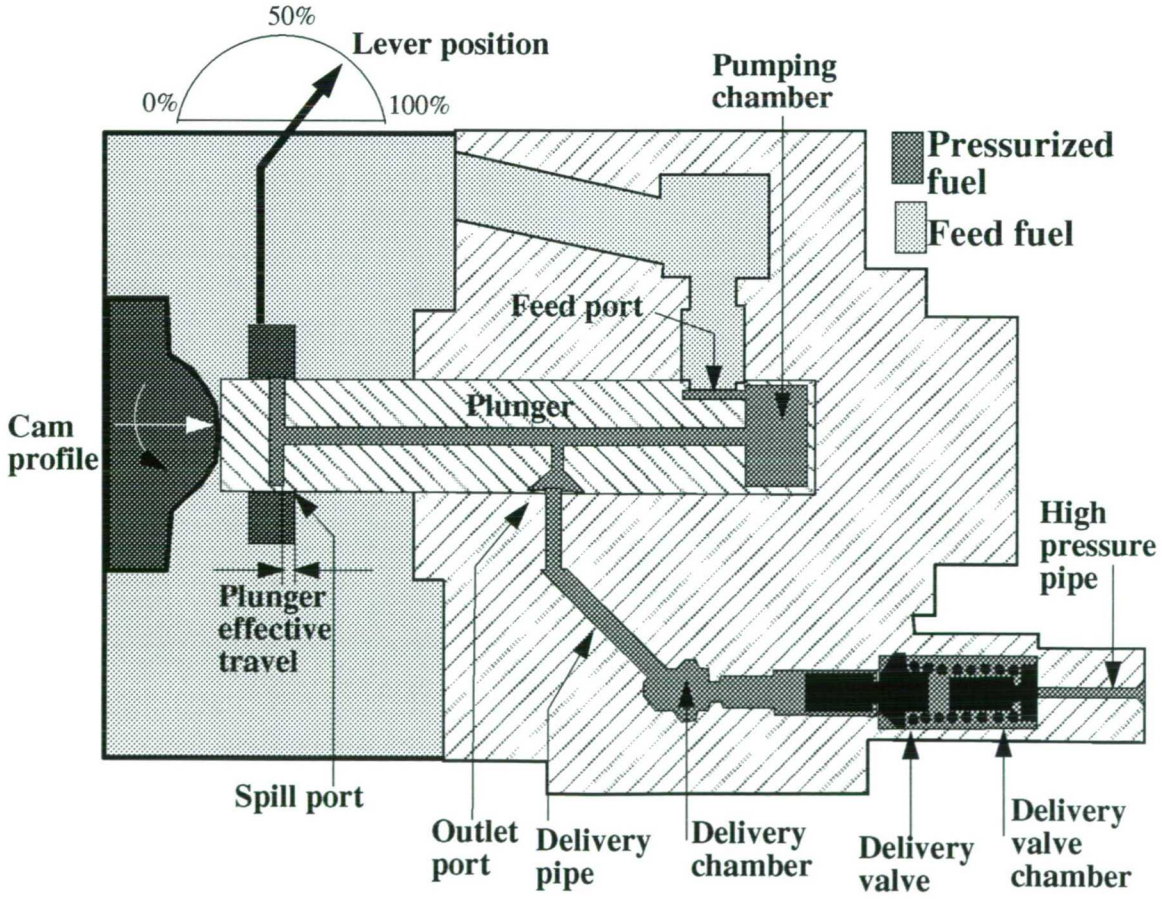

Figure 4–2 : Schematic representation of the VE–type pump and definition of the various parameters

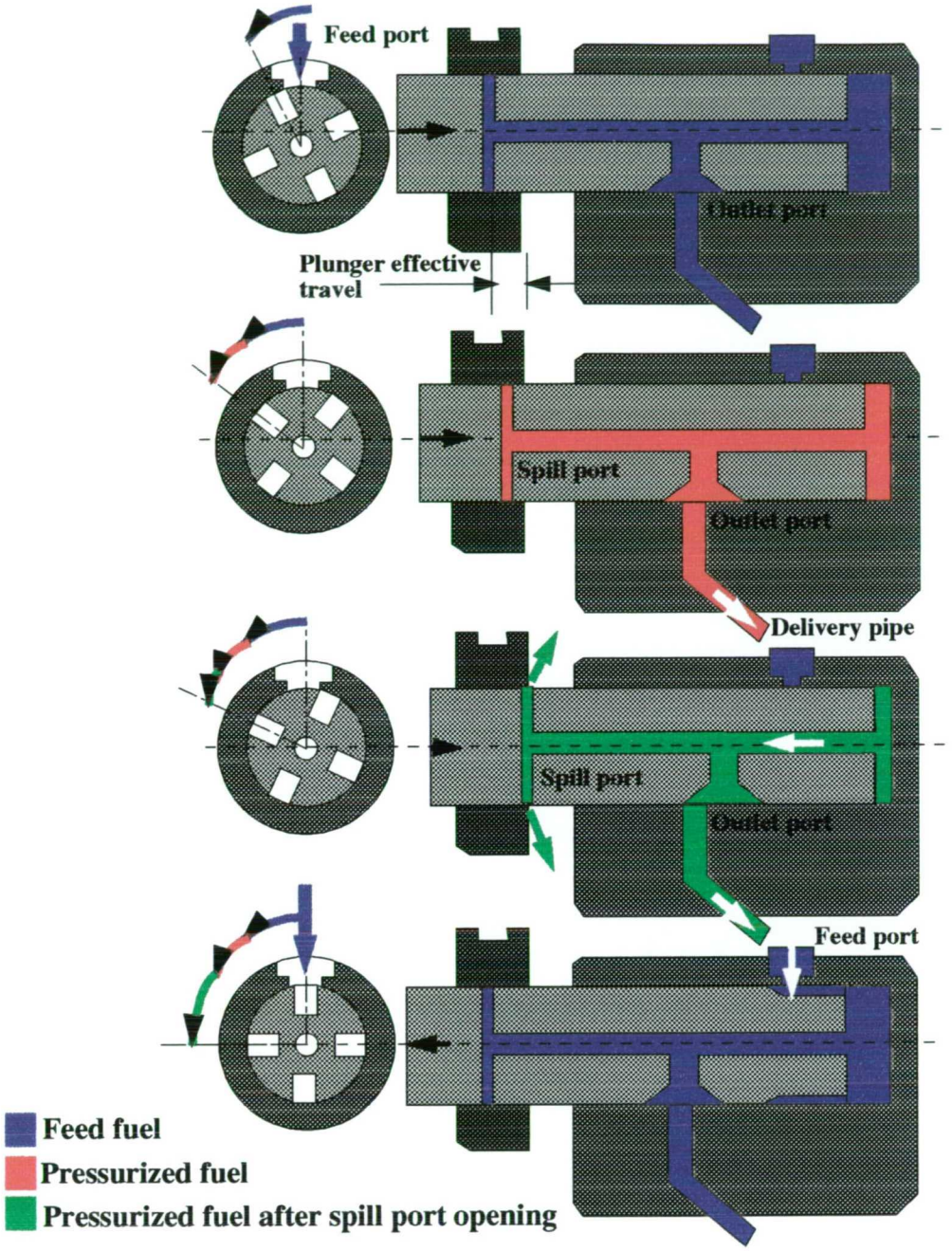

Figure 4–3 : Schematic representation of the pump operation

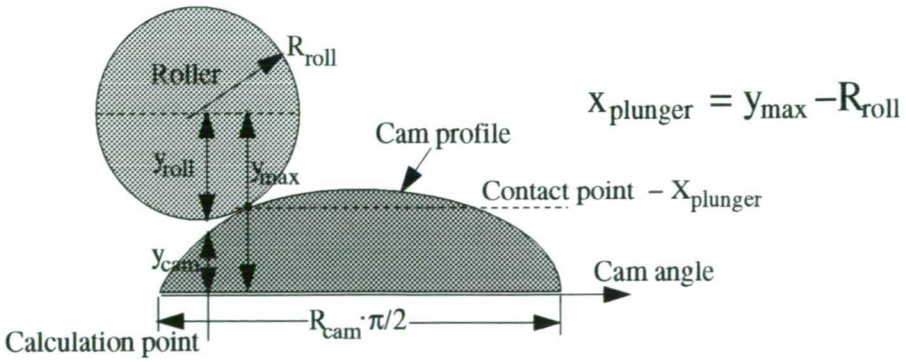

Figure 4–4 : Schematic representation of the geometric method employed for the estimation of the actual plunger movement as a function of the cam plate profile and the dimensions of the rollers

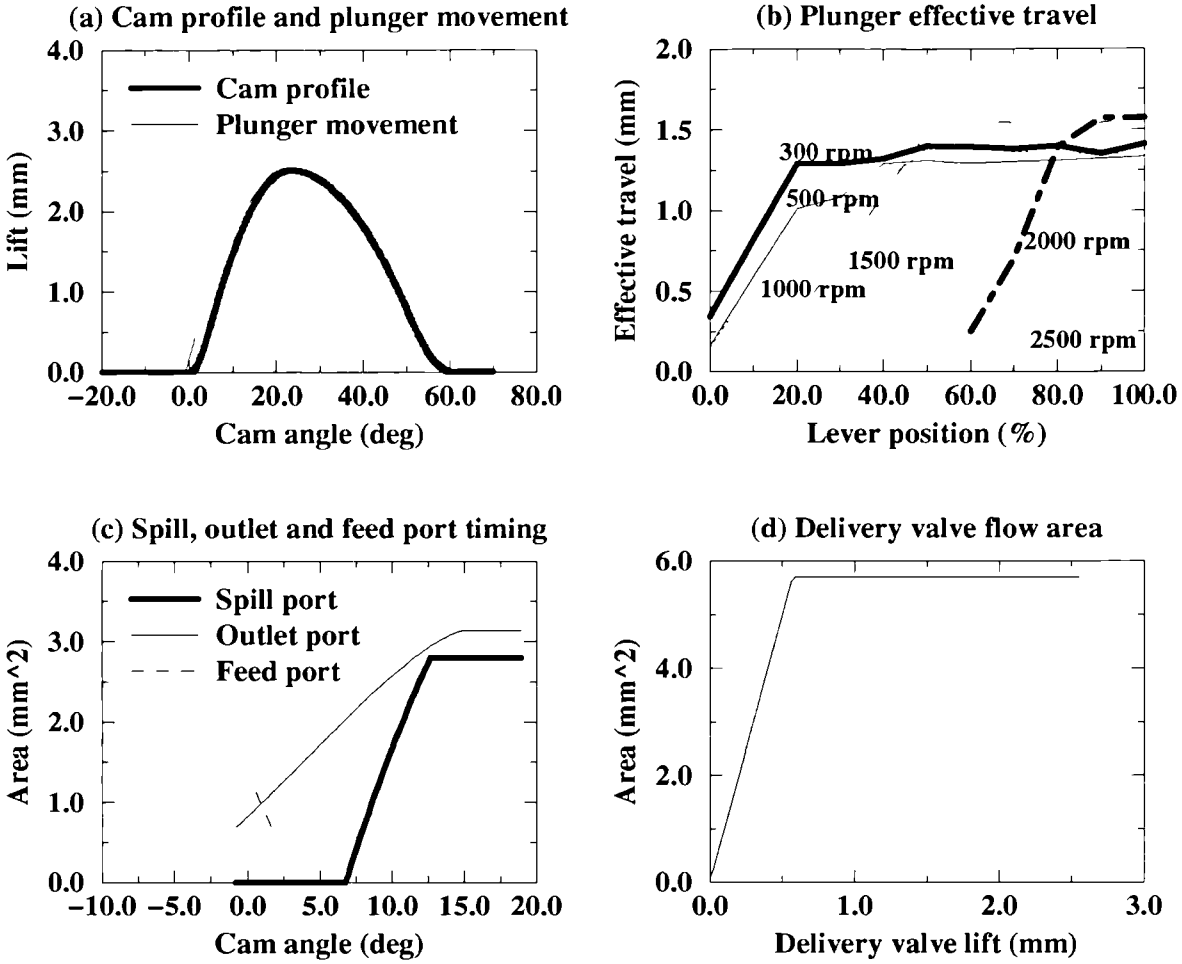

Figure 4–5 : Estimated pump geometric–operating characteristics

Pumping chamber	Delivery pipe	Delivery chamber	Delivery valve chamber	Delivery valve
Volume (mm^3):	Lenght (mm)	Volume (mm^3):	Volume (mm^3):	Mass : 0.0018 kg
$932-A \cdot x_{plunger}$	25.0	$180+A \cdot x_{valve}$	$450-A \cdot x_{valve}$	Spring rate : 7350 N/m
Plunger cross section area:	Diameter (mm)	Delivery valve cross section area:	Delivery valve cross section area:	Damping : 0.0064 Ns/m
A=84.45 mm^2	2.0	A=38.5 mm^2	A=19.6 mm^2	Preload : 29.4 N
				Max. lift : 2.5 mm

Table 4–1: Estimated nominal geometric characteristics of the pump

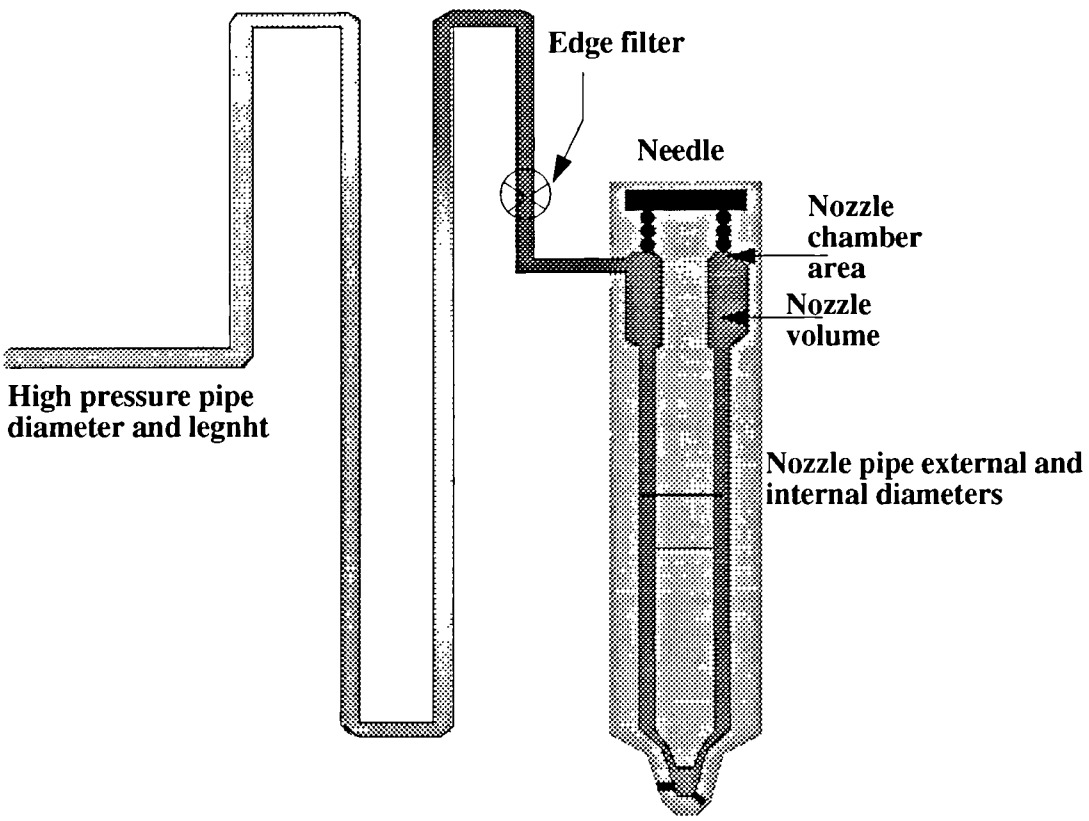

Figure 4–6 : Schematic representation of the high pressure pipe and the nozzle

High pressure pipe	Annular nozzle pipe	Nozzle chamber	Needle	Filter
Lenght (mm)	Lenght (mm)	Volume (mm^3):	Mass : 0.005 kg	Effective flow area
350.0	80.0	$365+A \cdot x_{valve}$	Spring rate : 149200 N/m	A=2.26 mm^2
	Diameter (mm)	Valve area:	Damping : 50.0 Ns/m	
1.2	External 2.65 Internal 2.184	A=6.68 mm^2	Preload : 160. N Max. lift : 0.32 mm	

Table 4–2: Estimated nominal geometric characteristics of the first fuel injection system (for natural–aspirated DI diesel engine)

High pressure pipe	Annular nozzle pipe	Nozzle chamber	Needle	Filter
Lenght (mm)	Lenght (mm)	Volume (mm^3):	Mass : 0.00626 kg	Effective flow area
370.0	43.0 and 29.8	$90.8+A\ x_{valve}$	Spring rate : 50245. N/m	A=2.26 mm^2
	Diameter (mm)	Valve area:	Damping : 100.0 Ns/m	
1.7	External 2.71 and 3.0 Internal 2.17 for both	A=6.29 mm^2	Preload : 171.5 N Max. lift : 0.34 mm	

Table 4–3: Estimated nominal geometric characteristics of the second fuel injection system (for turbocharged DI diesel engine)

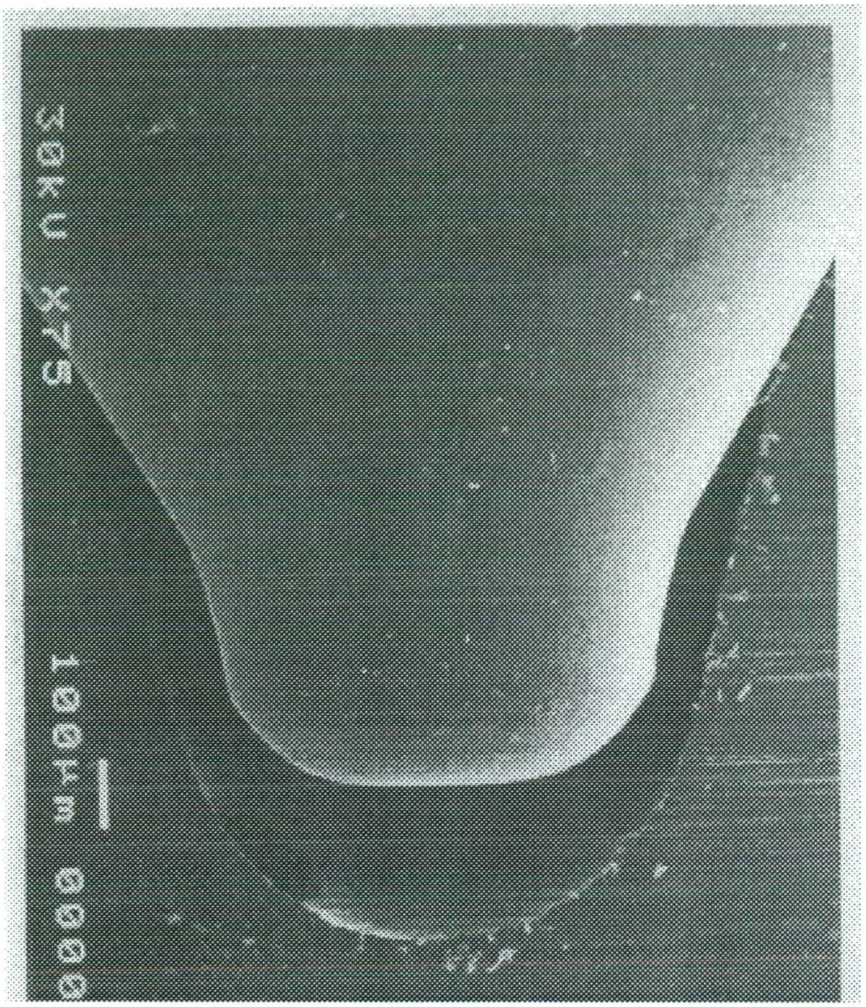

Figure 4–7 : Photograph of the cross sectioned sac volume with the needle placed at its closed position taken with a microscope (100x magnification)

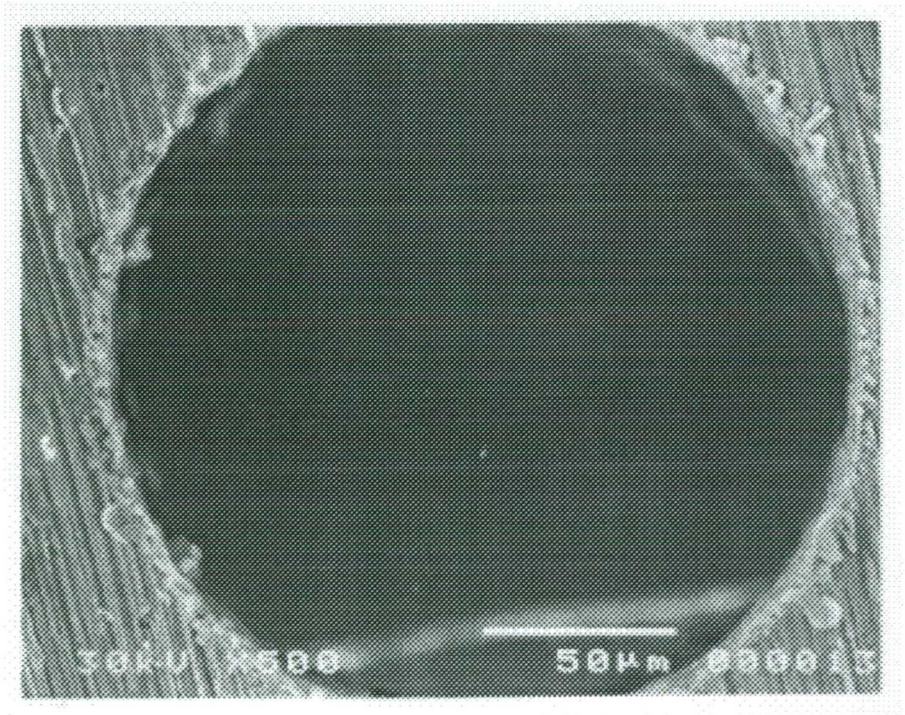

Figure 4–8 : Photograph of the cross sectioned injection hole taken with a microscope (500x magnification)

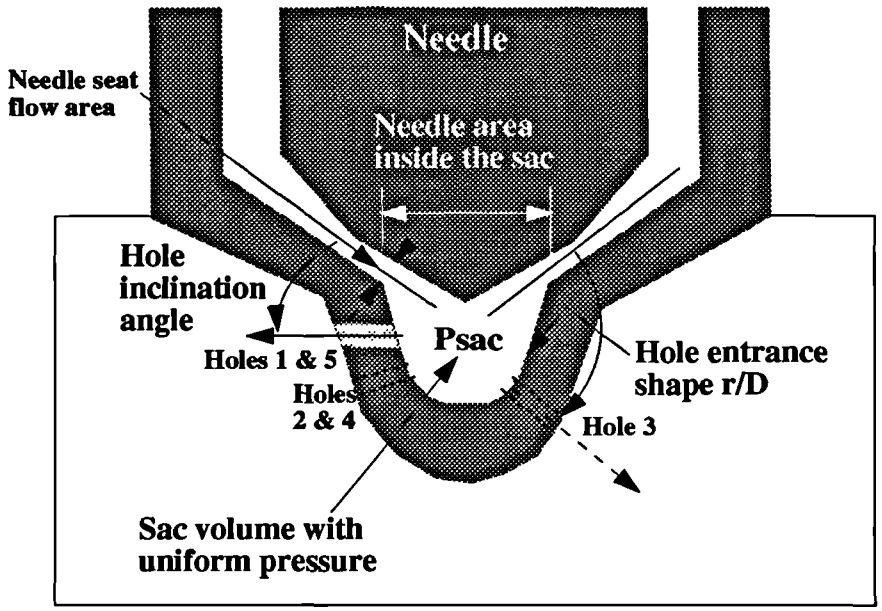

Figure 4–9: Schematic representation of the sac volume and the injection holes with the definition of the various geometric parameters estimated

Needle seat	Sac volume		Hole 1	Hole 2	Hole 3	Hole 4	Hole 5
Needle area inside the sac A=0.503 mm² 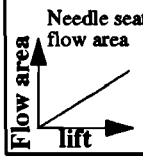	Volume (mm^3): $0.3+A \cdot x_{valve}$ Valve area: A=0.503 mm²	Lenght (mm)	0.6	0.6	0.6	0.6	0.6
		Diameter (mm)	0.18	0.18	0.18	0.18	0.18
		Inclination angle (deg)	60.0	90.0	120.0	90.0	60.0
		r/D	0.0	0.0	0.0	0.0	0.0

Table 4–4: Estimated geometric characteristics of the sac volume and the injection holes of the Stanadyne Pencil–type injector of the first FIE investigated (system I)

Needle seat	Sac volume		Hole 1	Hole 2	Hole 3	Hole 4	Hole 5
Needle area inside the sac A=0.718 mm² 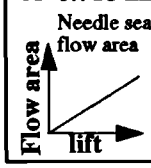	Volume (mm^3): $0.16+A \cdot x_{valve}$ Valve area: A=0.718 mm²	Lenght (mm)	0.7	0.7	0.7	0.7	0.7
		Diameter (mm)	0.2	0.2	0.2	0.2	0.2
		Inclination angle (deg)	63.0	87.0	99.0	87.0	63.0
		r/D	0.0	0.0	0.0	0.0	0.0

Table 4–5: Estimated geometric characteristics of the sac volume and the injection holes of the Stanadyne Pencil–type injector of the second FIE investigated (system II)

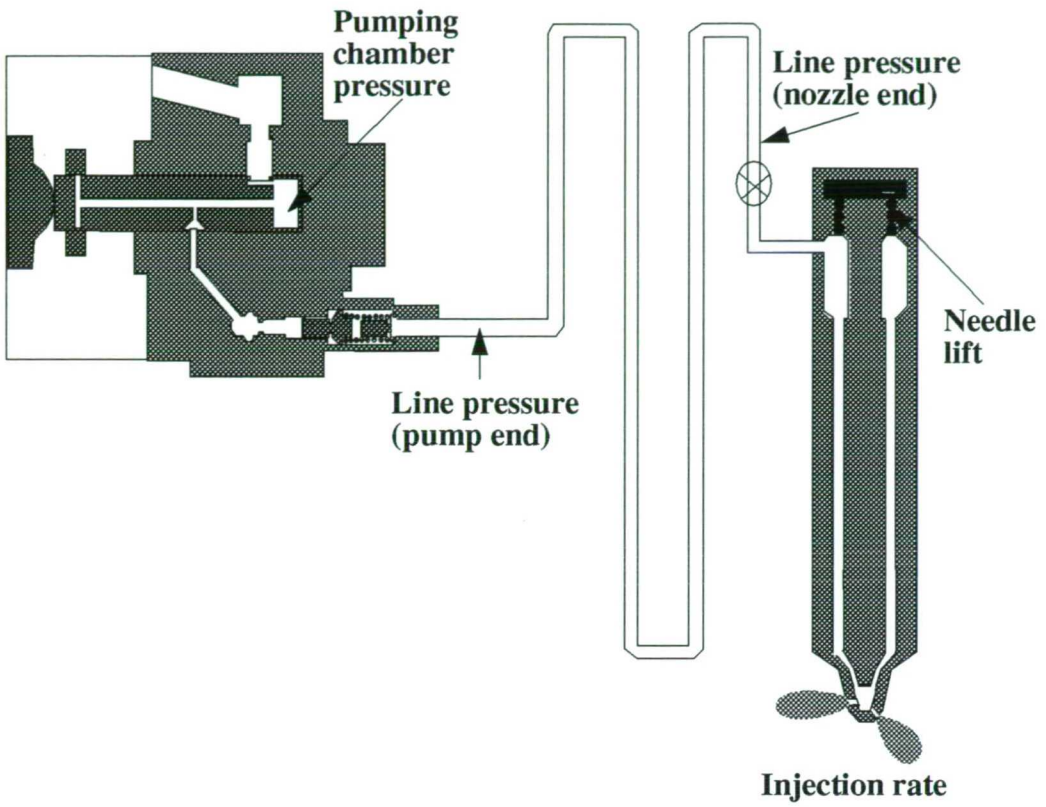

Figure 4–10 : Instrumented FIE and definition of the measured parameters

System I:
naturally–aspirated

Measured parameters:
Pumping chamber pressure
Line pressure (nozzle end)
Needle lift
Injection rate

Systen II:
turbocharged

Measured parameters:
Line pressure (pump end)
Line pressure (nozzle end)
Needle lift
Injection rate

System	Pump speed (rpm)	Lever position (%)
I	2000	100
I	1500	100
I	1000	100
I	1000	20
I	500	50
I	500	20
II	2000	100
II	1500	40
II	1000	50
II	1000	15
II	500	20

Tab1e 4–6 : List of experimental conditions and measured parameters for both FIE systems

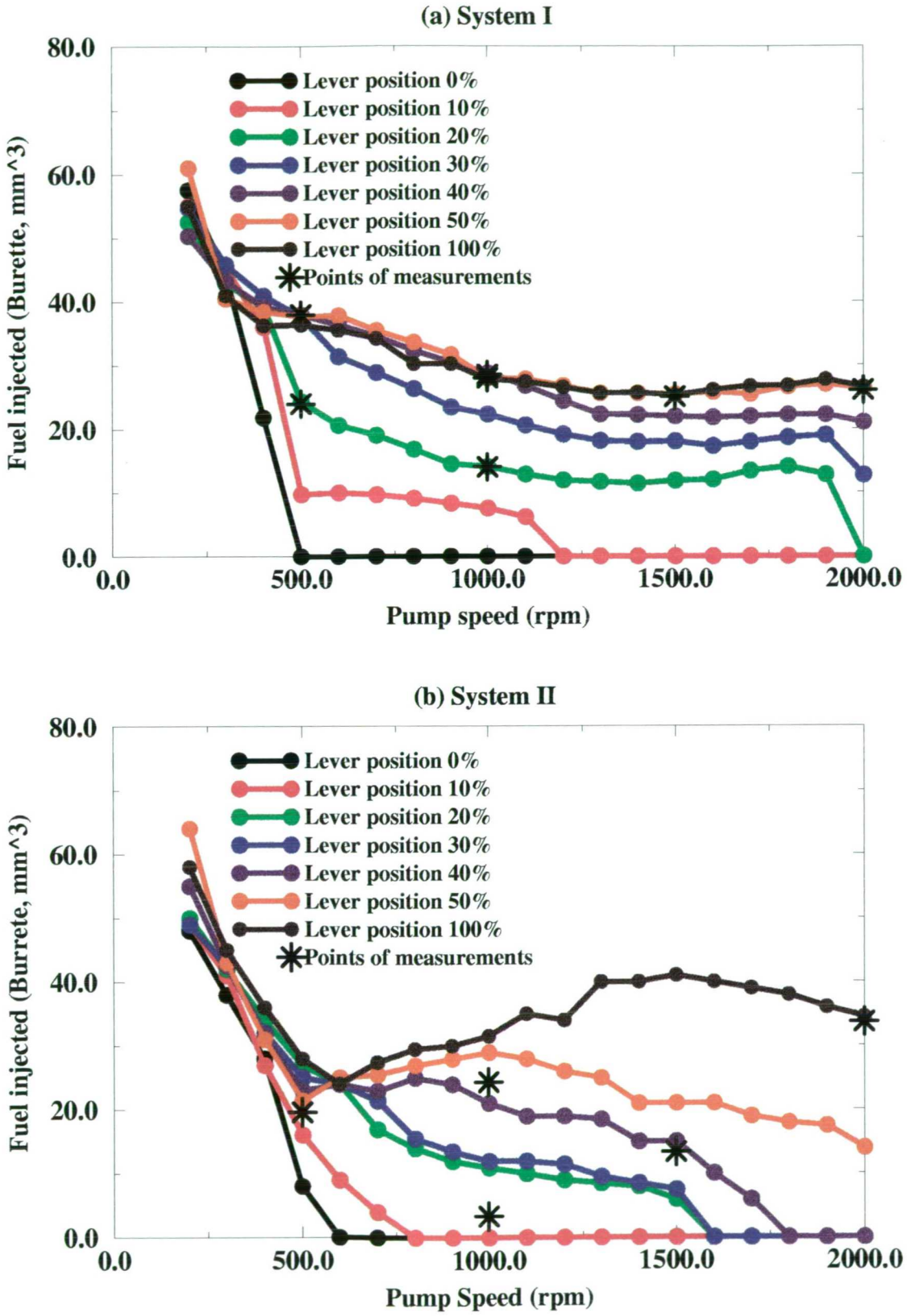

Figure 4–11: Burette reading of the total fuel injection quantity for the two fuel injection systems investigated as a function of pump speed and load. The operating points of the measurements of the various parameters are also shown

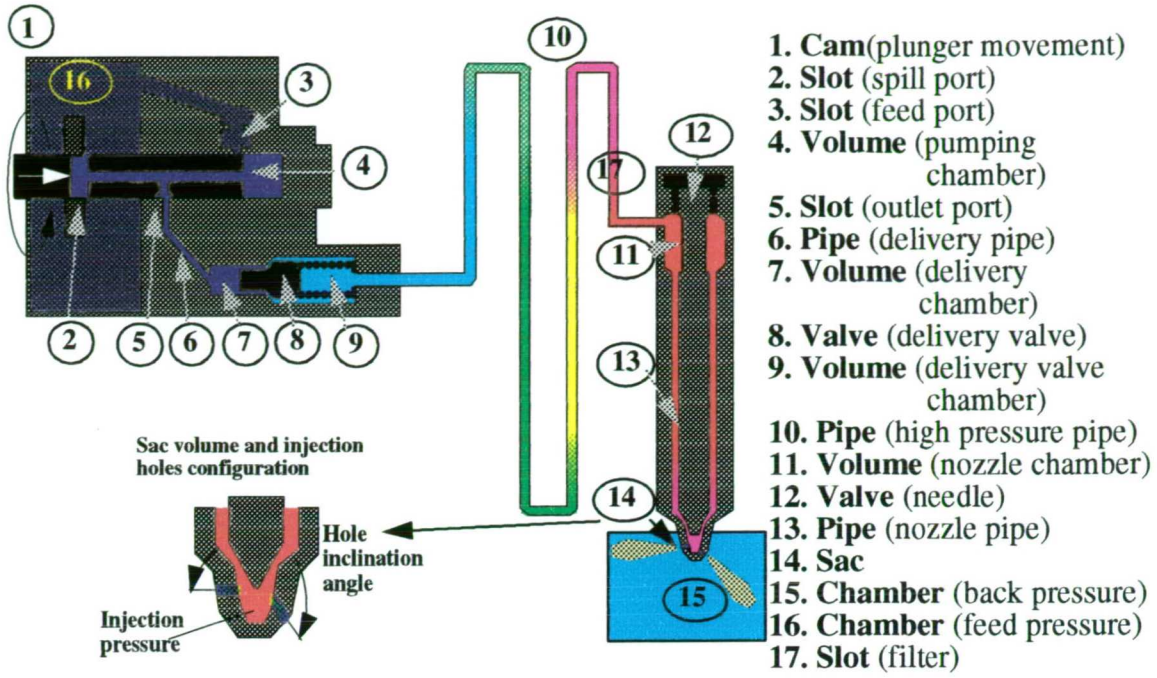

(a) FIE simulated

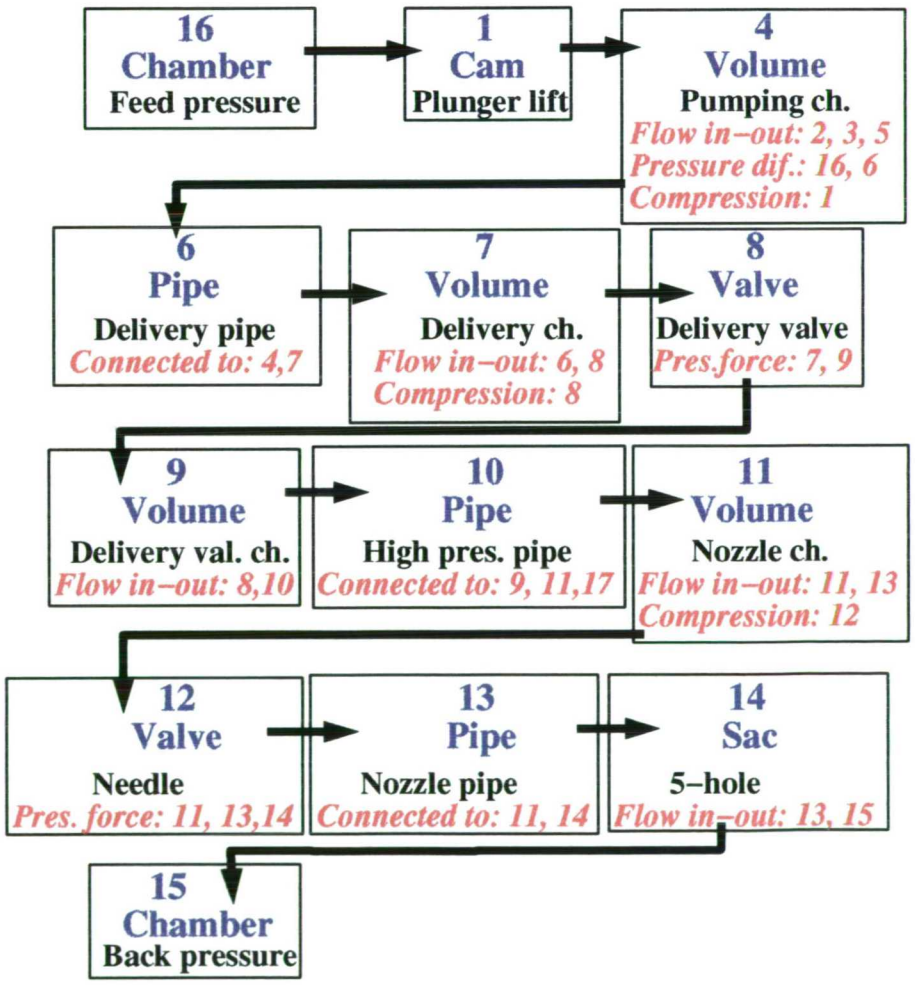

(b) link between components

Figure 4–12: Schematic representation of the simulated fuel injection system and the link between the various elements assumed to consist it

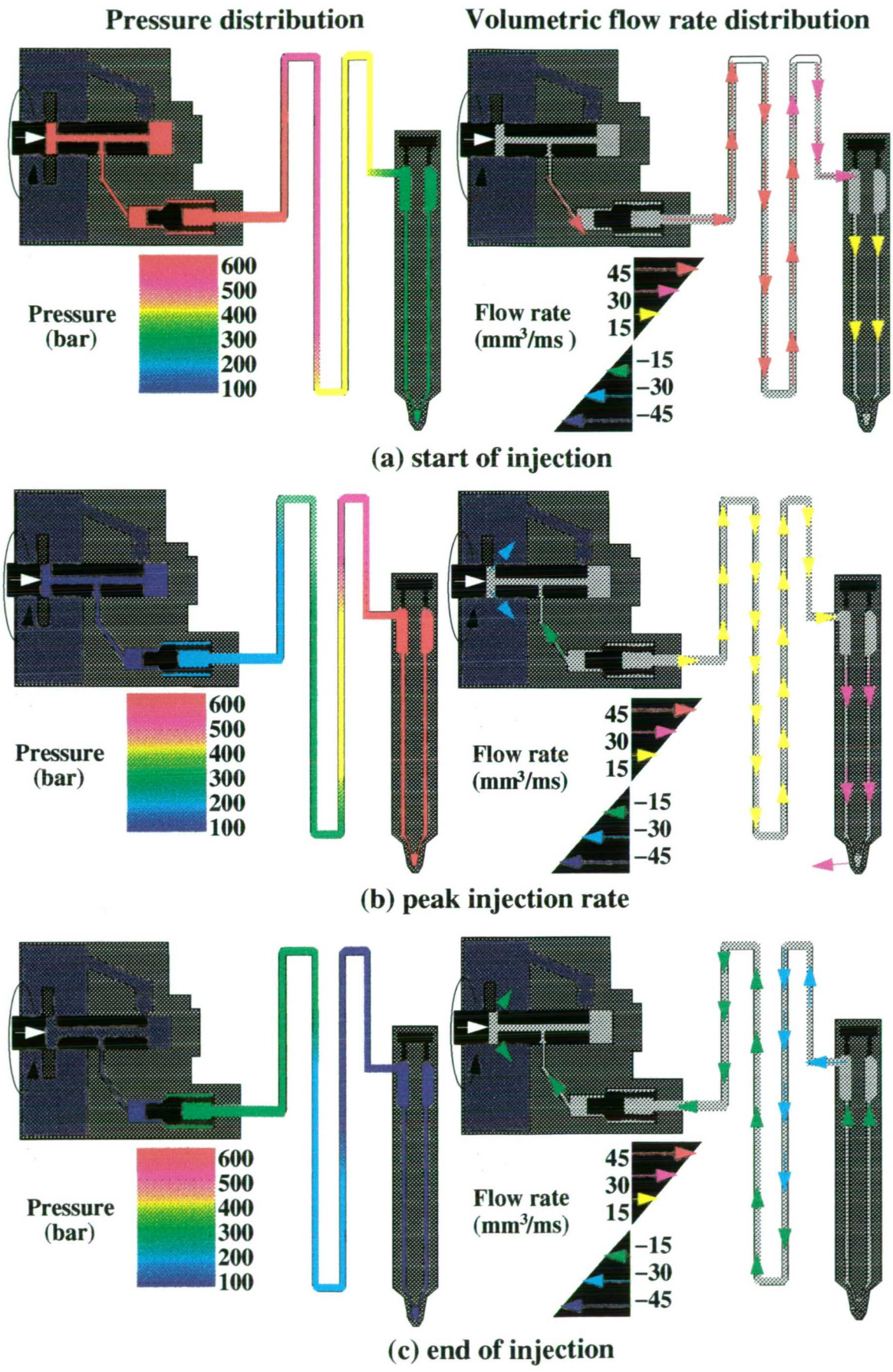

Figure 4–13: Calculated pressure and volumetric flow rate distributions within the fuel injection system at three different time steps (a) start of injection (b) peak injection rate and (c) end of injection

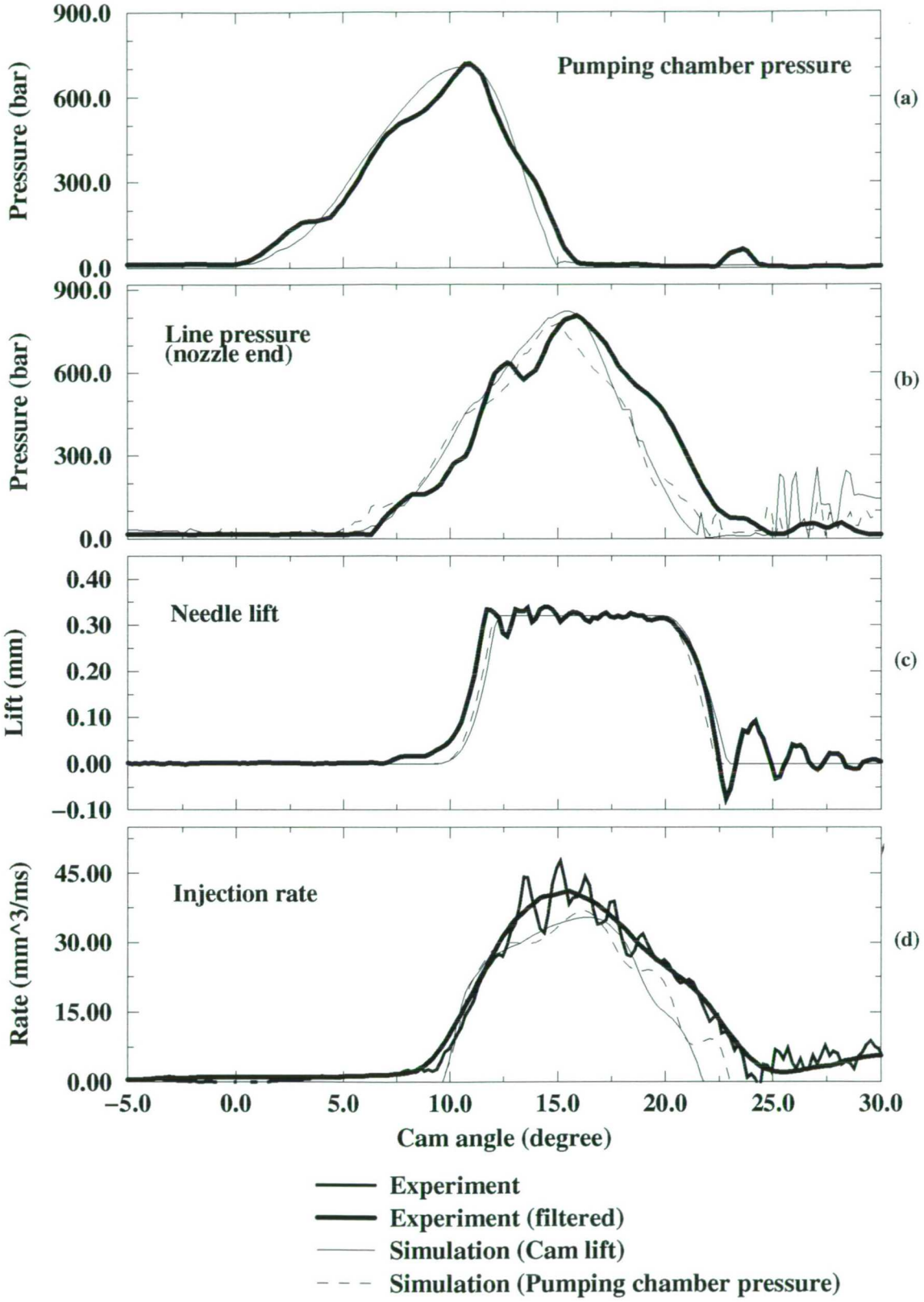

Figure 4–14 : Comparison between the computational and the experimental results for (a) Pumping chamber pressure (b) Line pressure (nozzle end) (c) Needle lift and (d) Injection rate [Pump speed 2000 rpm, lever position 100% – System I]

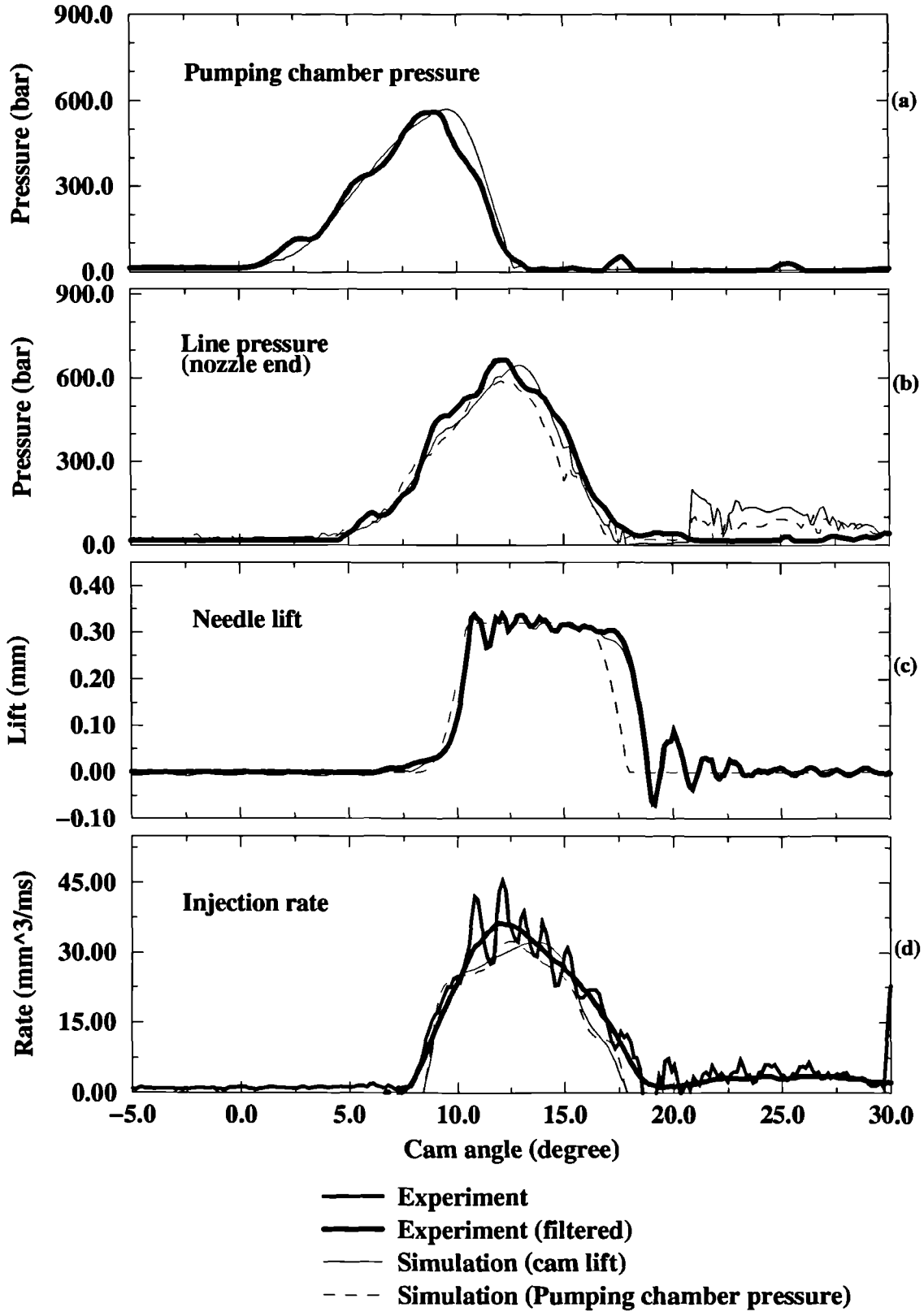

Figure 4–15 : Comparison between the computational and the experimental results for (a) Pumping chamber pressure (b) Line pressure (nozzle end) (c) Needle lift and (d) Injection rate [Pump speed 1500 rpm, lever position 100% – System I]

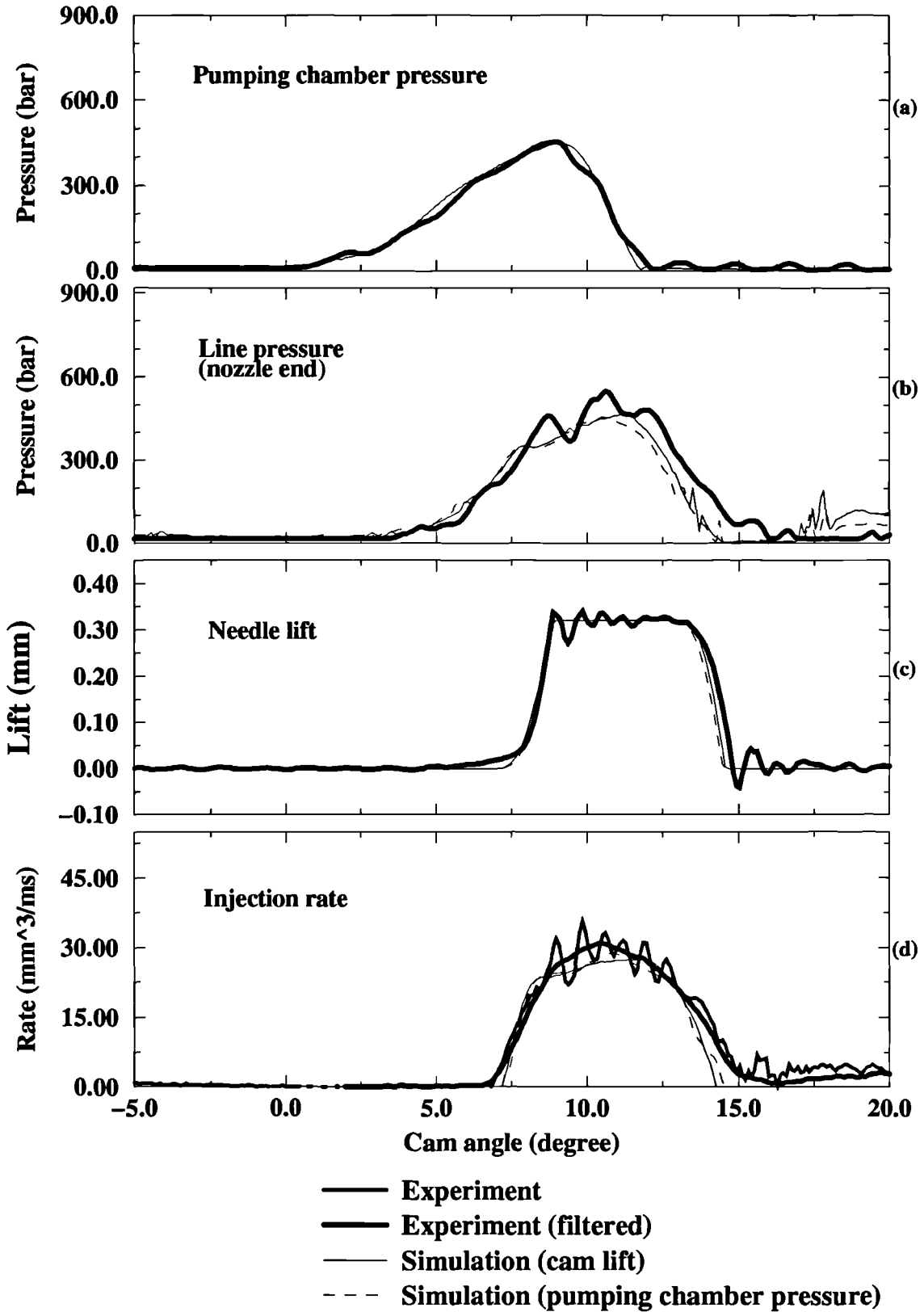

Figure 4–16 : Comparison between the computational and the experimental results for (a) Pumping chamber pressure (b) Line pressure (nozzle end) (c) Needle lift and (d) Injection rate [Pump speed 1000 rpm, lever position 100% – System I]

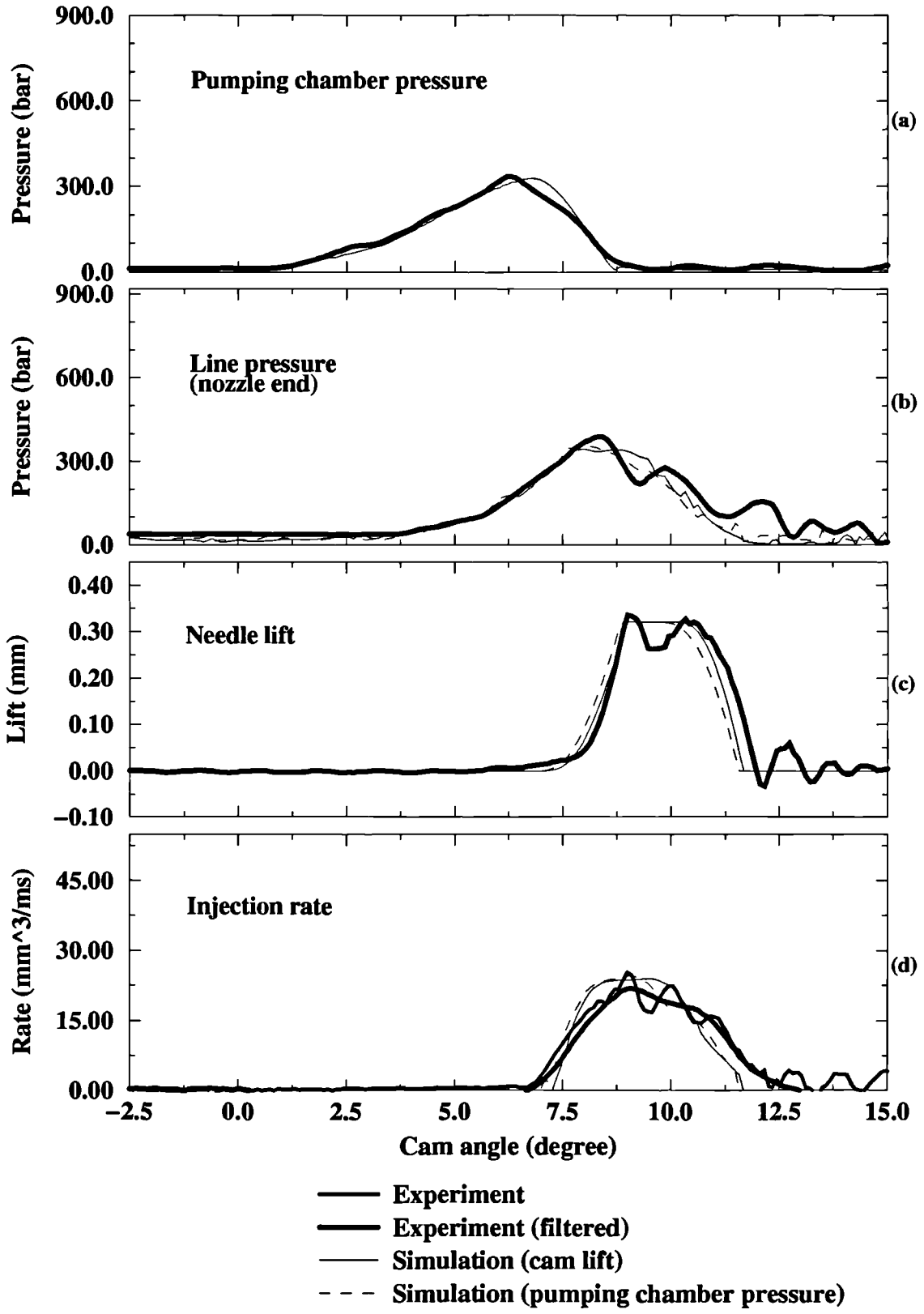

Figure 4–17 : Comparison between the computational and the experimental results for (a) Pumping chamber pressure (b) Line pressure (nozzle end) (c) Needle lift and (d) Injection rate [Pump speed 1000 rpm, lever position 20% – System I]

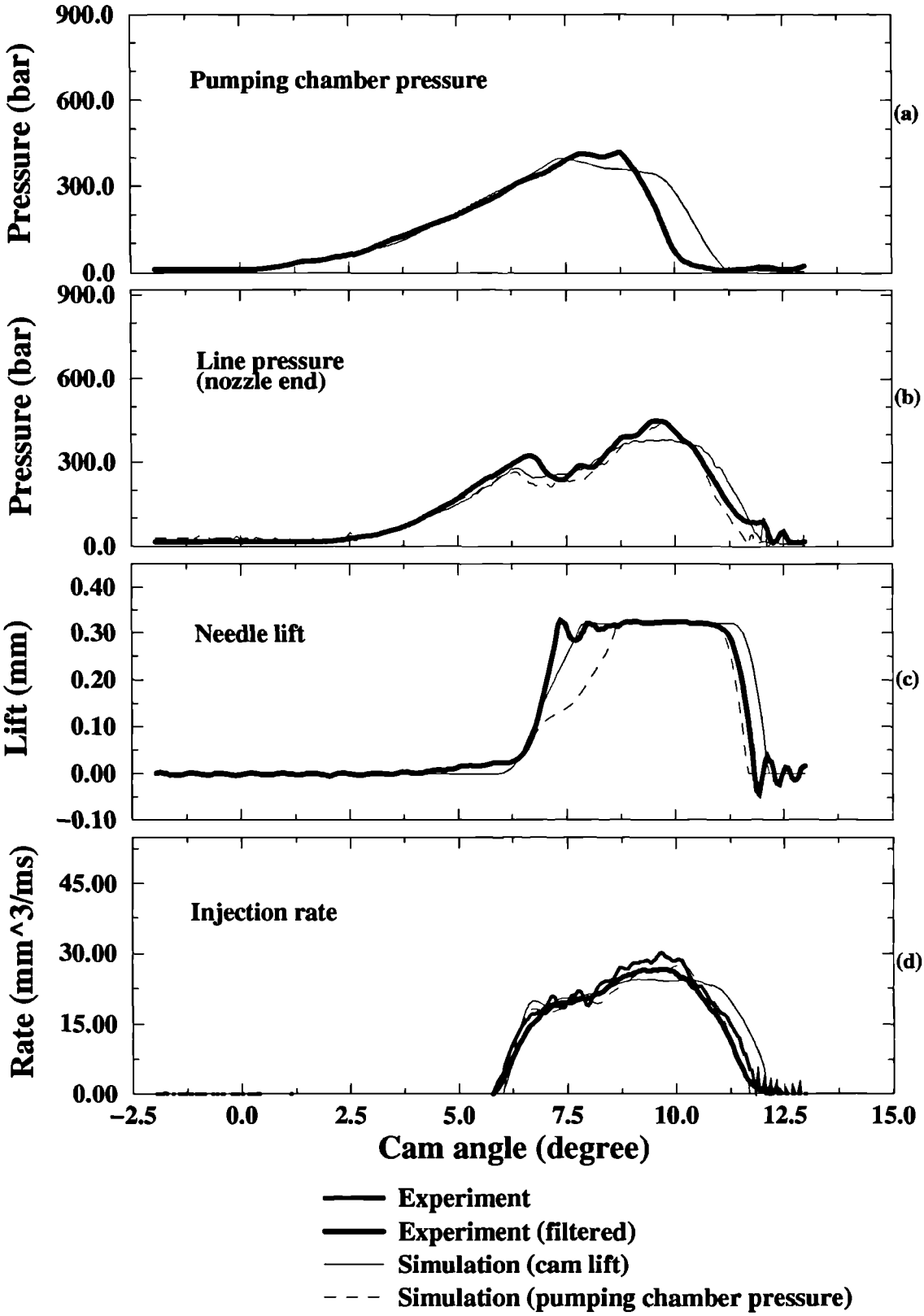

Figure 4–18 : Comparison between the computational and the experimental results for (a) Pumping chamber pressure (b) Line pressure (nozzle end) (c) Needle lift and (d) Injection rate [Pump speed 500 rpm, lever position 50% – System I]

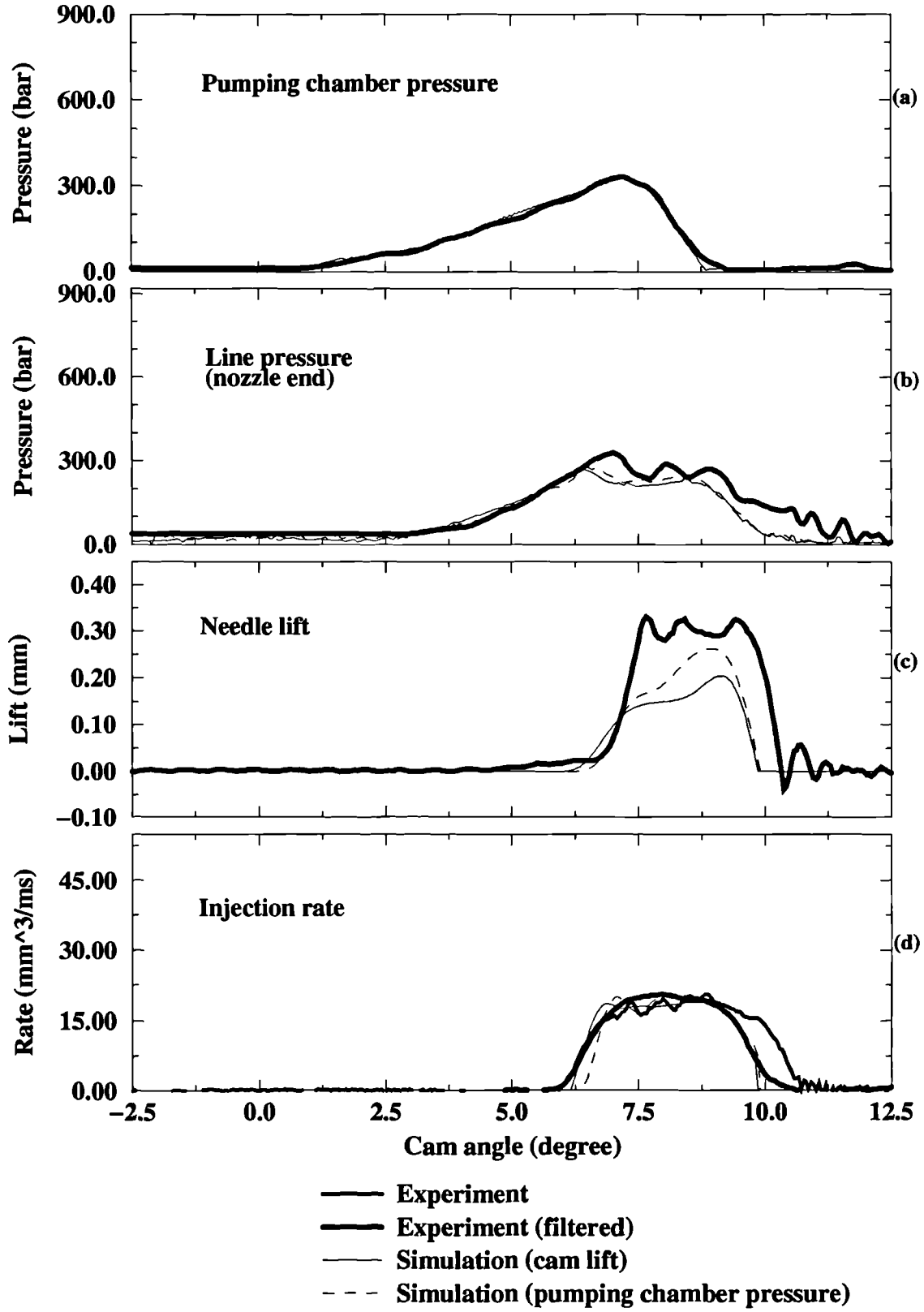

Figure 4–19 : Comparison between the computational and the experimental results for (a) Pumping chamber pressure (b) Line pressure (nozzle end) (c) Needle lift and (d) Injection rate [Pump speed 500 rpm, lever position 20% – System I]

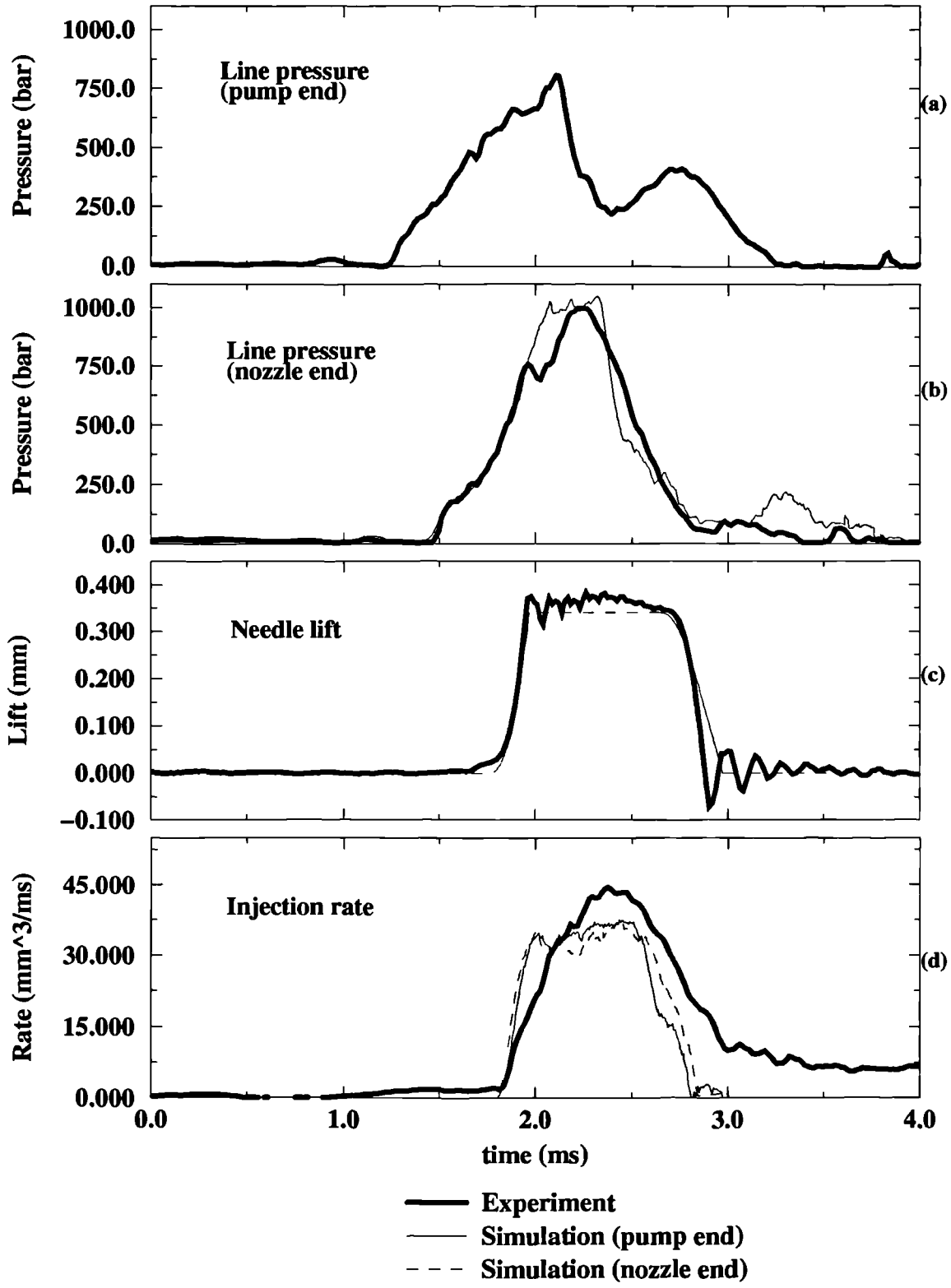

Figure 4–20 : Comparison between the computational and the experimental results for (a) Line pressure (pump end) (b) Line pressure (nozzle end) (c) Needle lift and (d) Injection rate [Pump speed 2000 rpm, lever position 100%– System II]

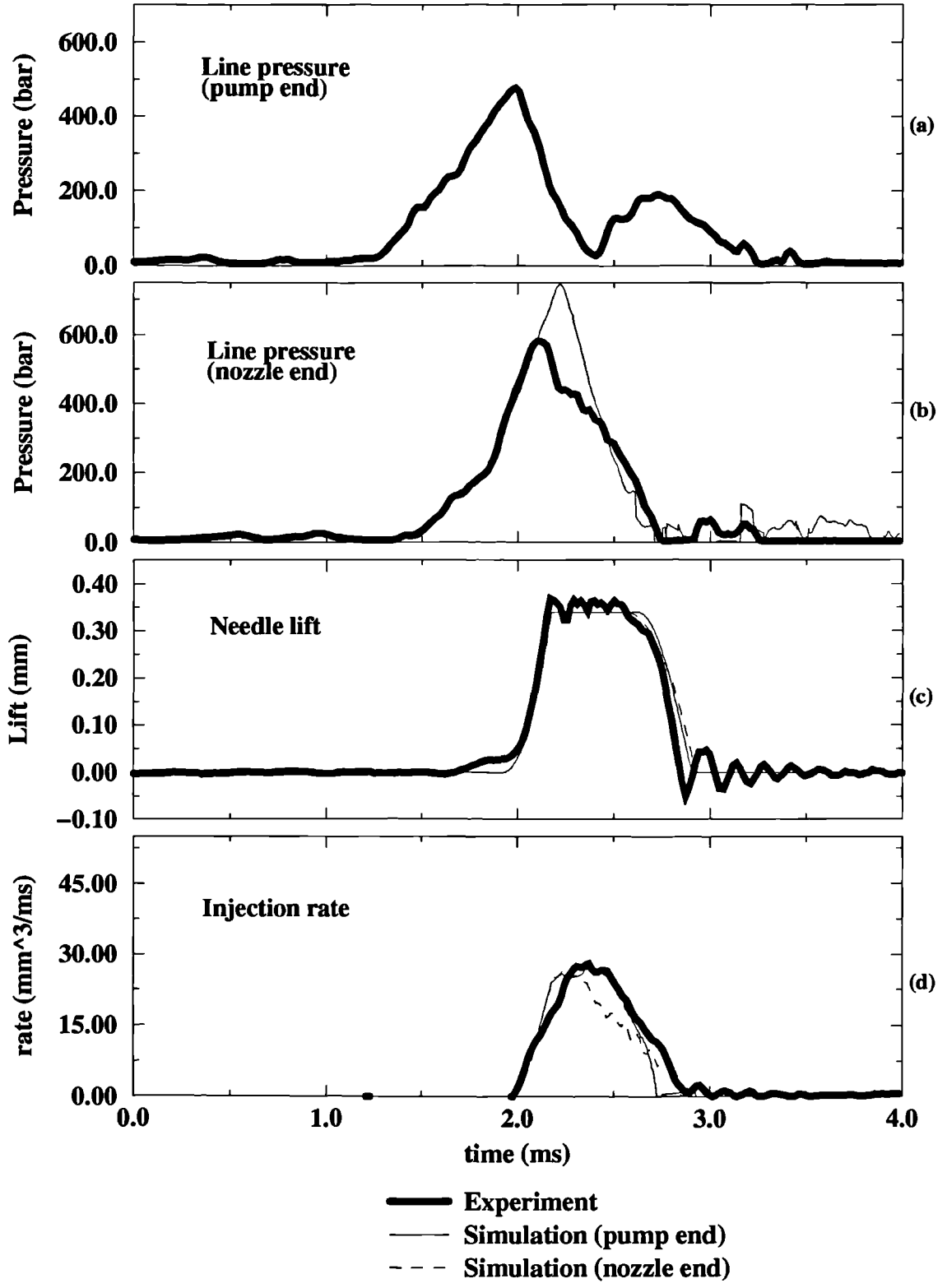

Figure 4–21 : Comparison between the computational and the experimental results for (a) Line pressure (pump end (b) Line pressure (nozzle end) (c) Needle lift and (d) Injection rate [Pump speed 1500 rpm, lever position 40%–System II]

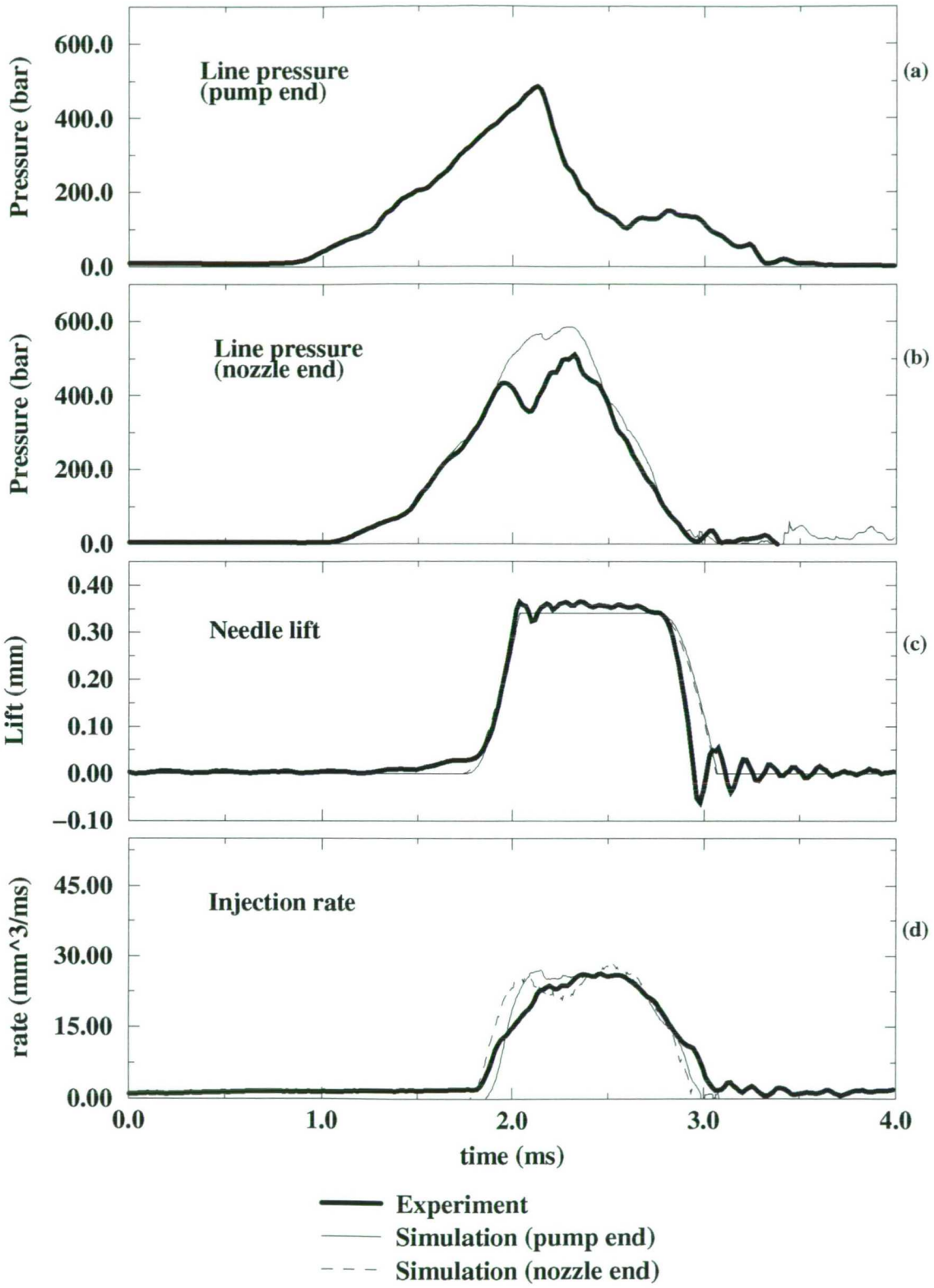

Figure 4–22 : Comparison between the computational and the experimental results for (a) Line pressure (pump end (b) Line pressure (nozzle end) (c) Needle lift and (d) Injection rate [Pump speed 1000 rpm, lever position 50%–System II]

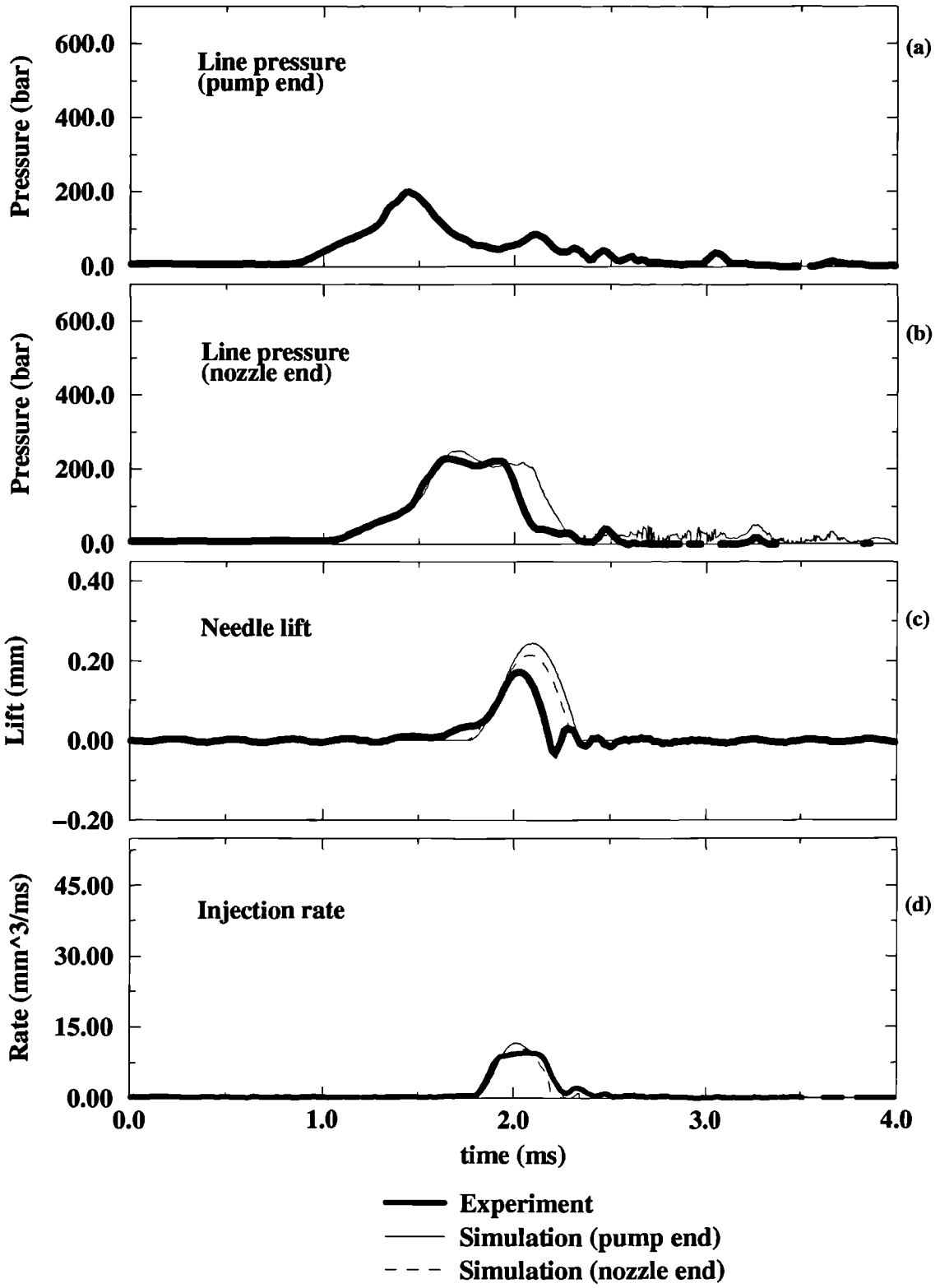

Figure 4–23 : Comparison between the computational and the experimental results for (a) Line pressure (pump end (b) Line pressure (nozzle end) (c) Needle lift and (d) Injection rate [Pump speed 1000 rpm, lever position 20%–System II]

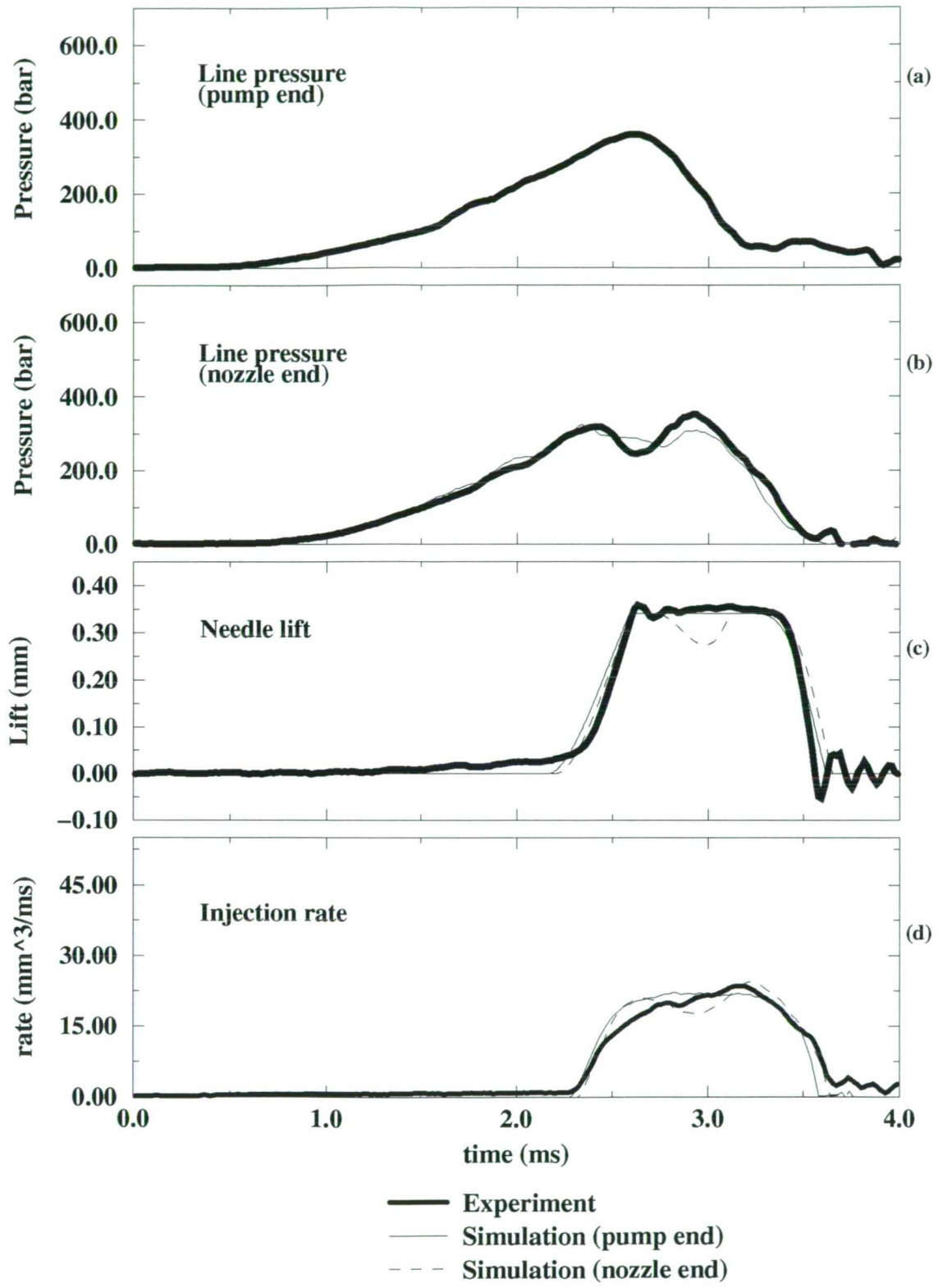

Figure 4–24 : Comparison between the computational and the experimental results for (a) Line pressure (pump end (b) Line pressure (nozzle end) (c) Needle lift and (d) Injection rate [Pump speed 500 rpm, lever position 20%–System II]

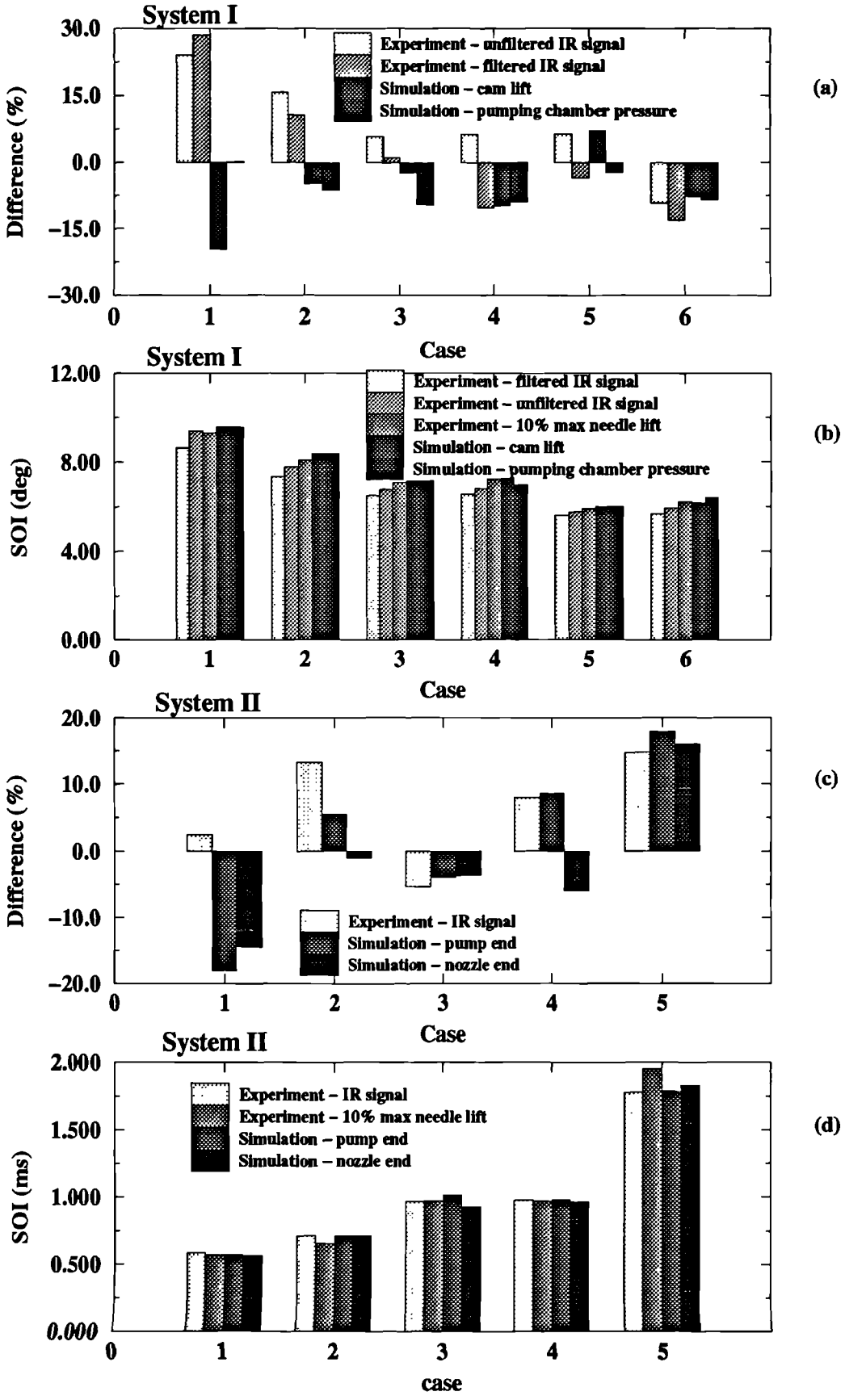

Figure 4–25 : Comparison between the computational and the experimental results for the total fuel injection quantity (expressed as the percentage difference from the burette reading) and the start of injection for all test cases and for both injection systems

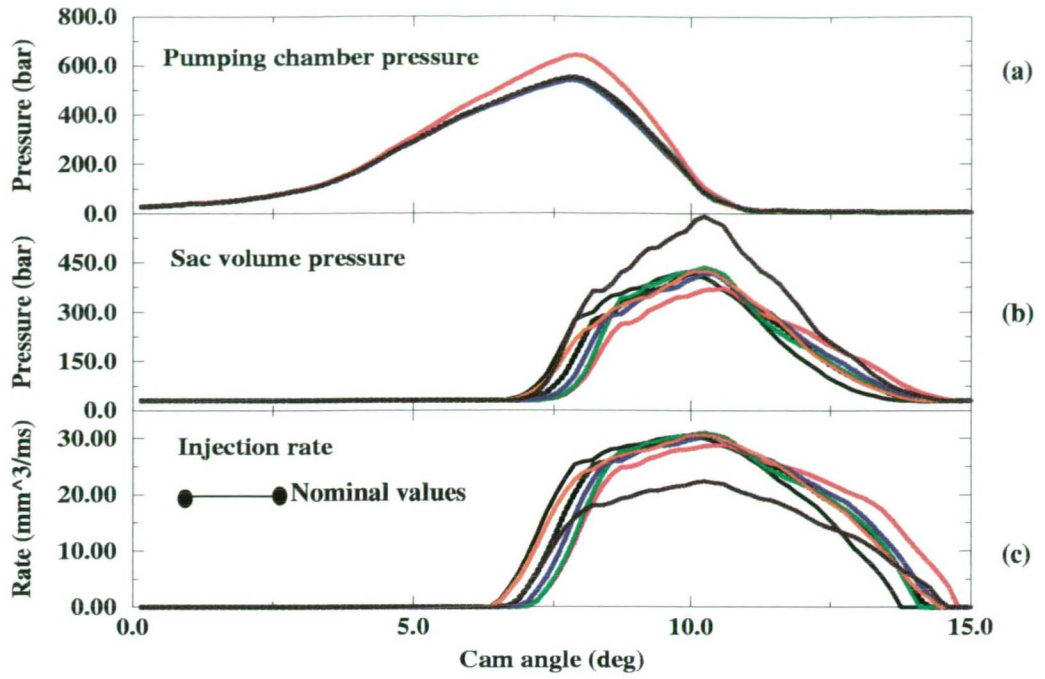

Figure 4–26 : Effect of –20% variation of various geometric parameters of the high pressure pipe and the nozzle on (a) pumping chamber pressure, (b) sac volume (injection) pressure and (c) fuel injection rate [Pump speed 1000 rpm, lever position 50%]

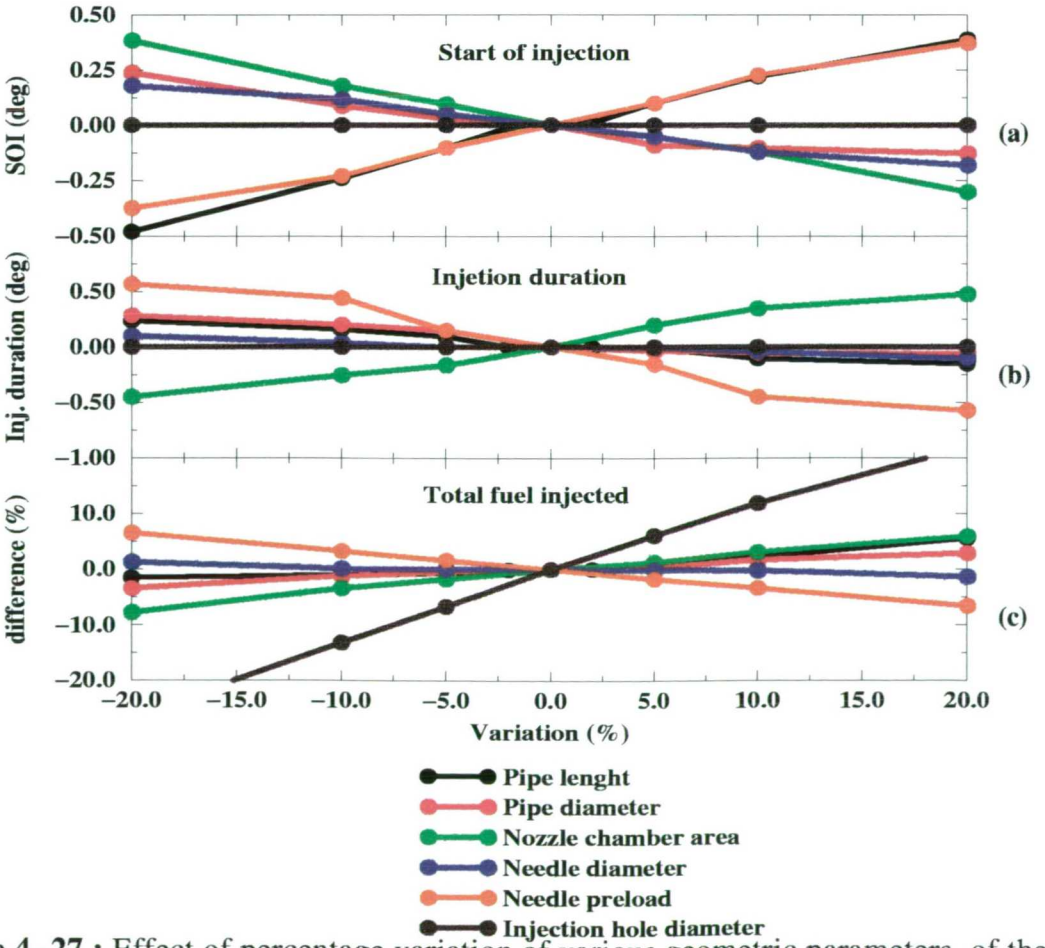

Figure 4–27 : Effect of percentage variation of various geometric parameters of the high pressure pipe and the nozzle on (a) start of injection (b) injection duration and (c) total fuel injected [Pump speed 1000 rpm, lever position 50%]

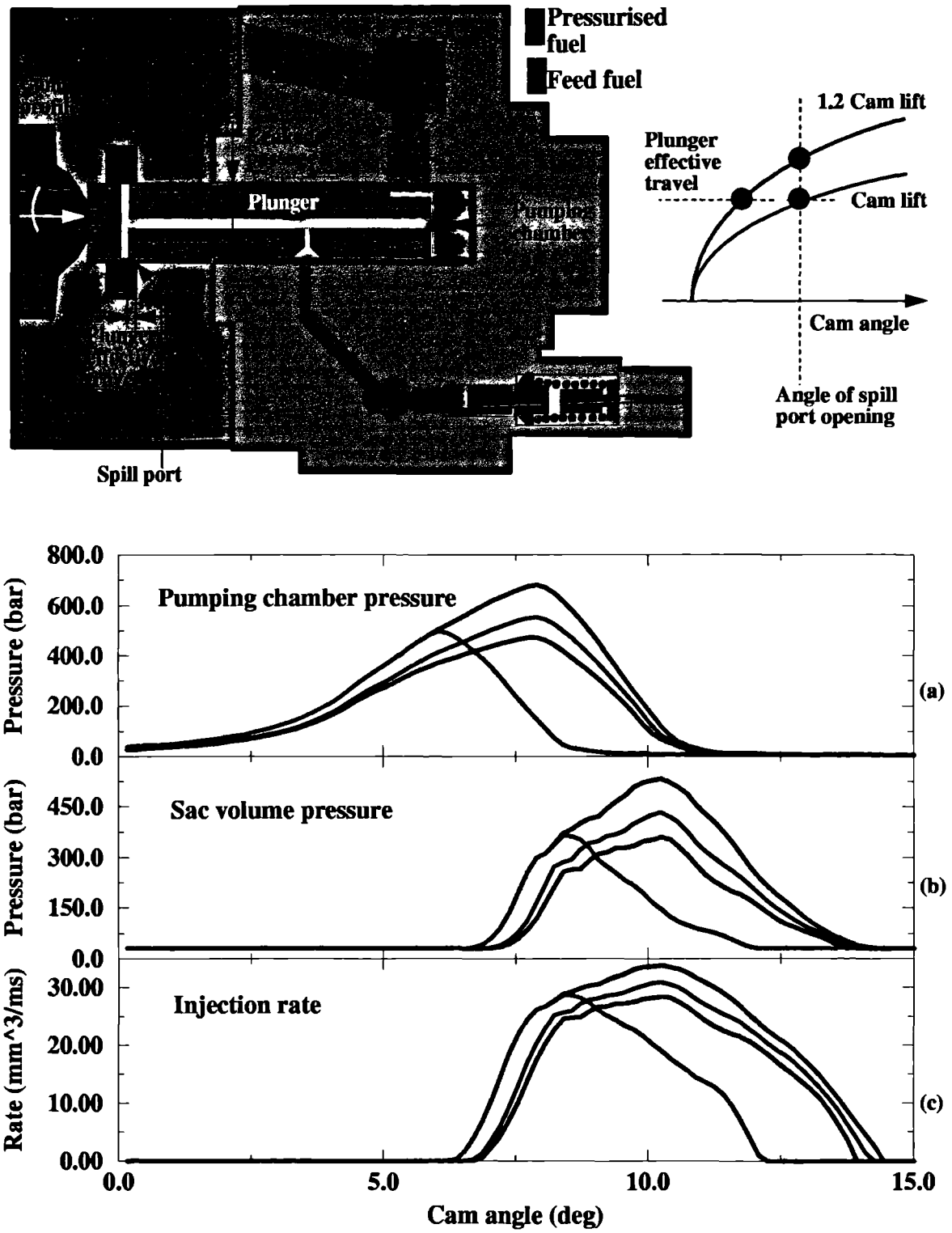

Figure 4–28: Effect of pump design parameters on (a) pumping chamber pressure, (b) sac volume (injection) pressure and (c) fuel injection rate [Pump speed 1000 rpm]

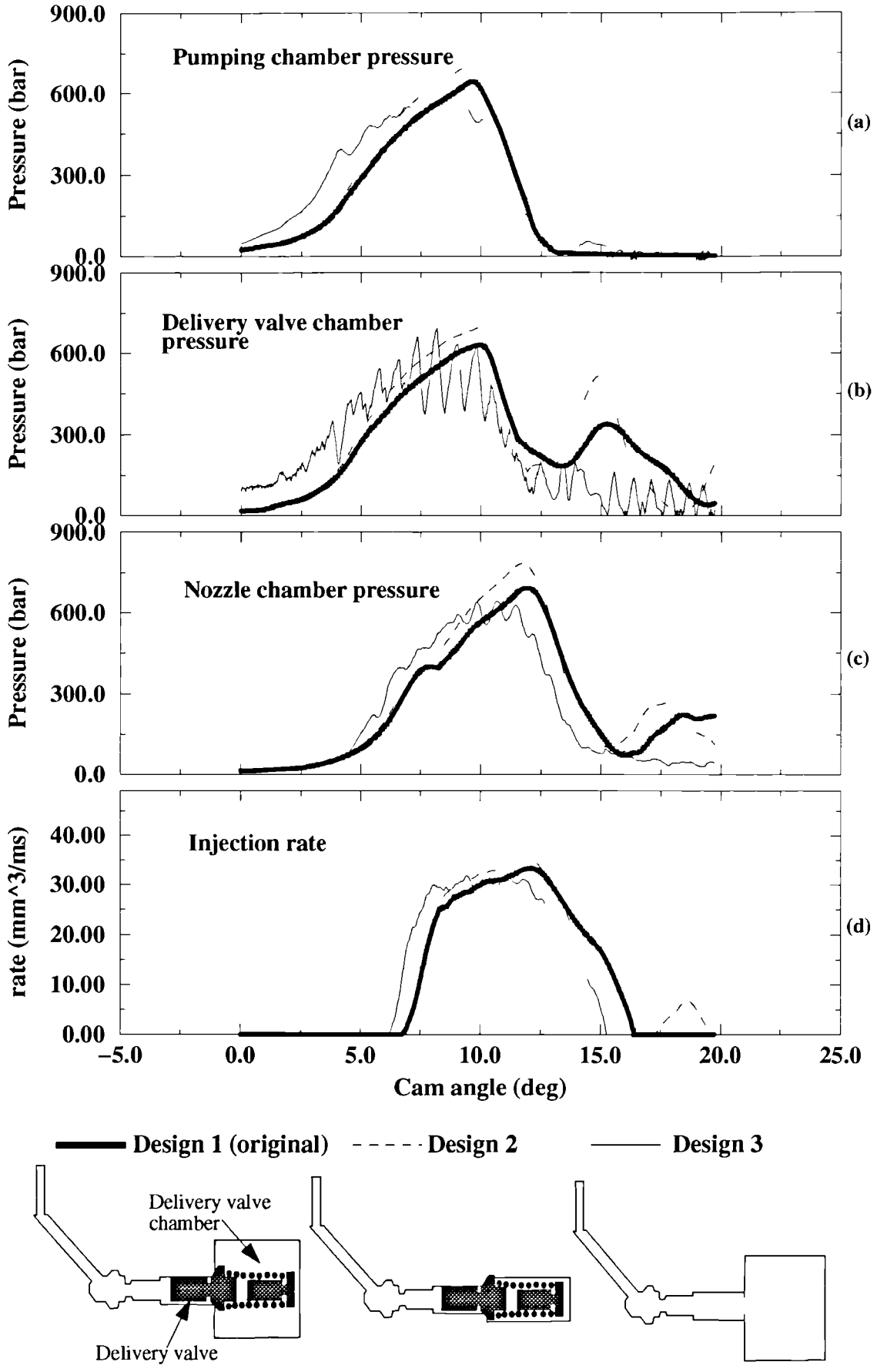

Figure 4–29 : Effect of various delivery valve designs on (a) pumping chamber pressure (b) delivery valve chamber pressure (c) nozzle chamber pressure and (d) fuel injection rate

Bottom view

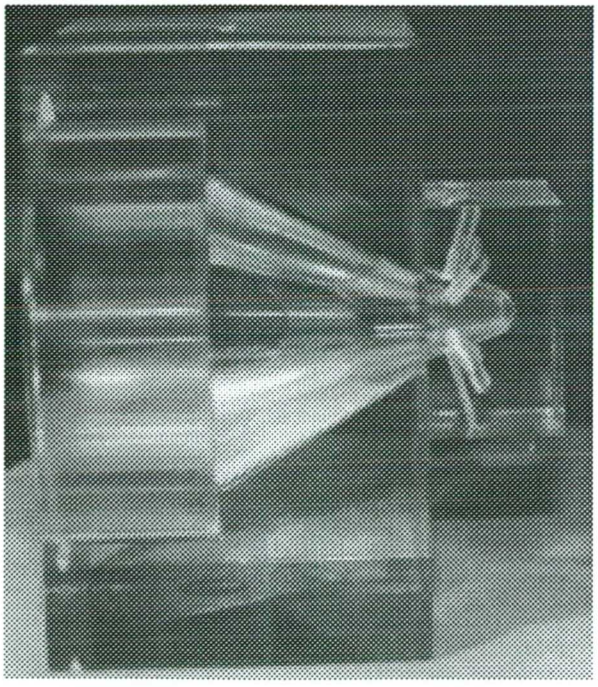

Side view

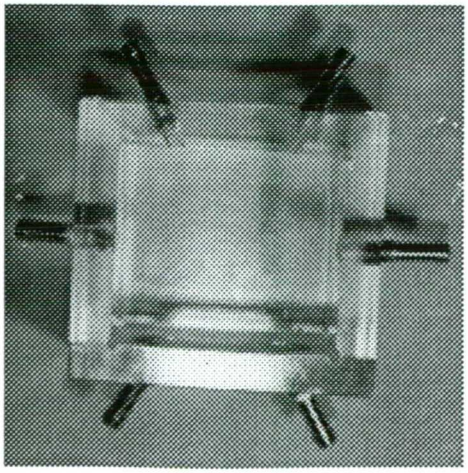

Adaptor for collecting the fuel from the holes

Figure 4–30 : Photograph of the transparent nozzle from different views

(a)

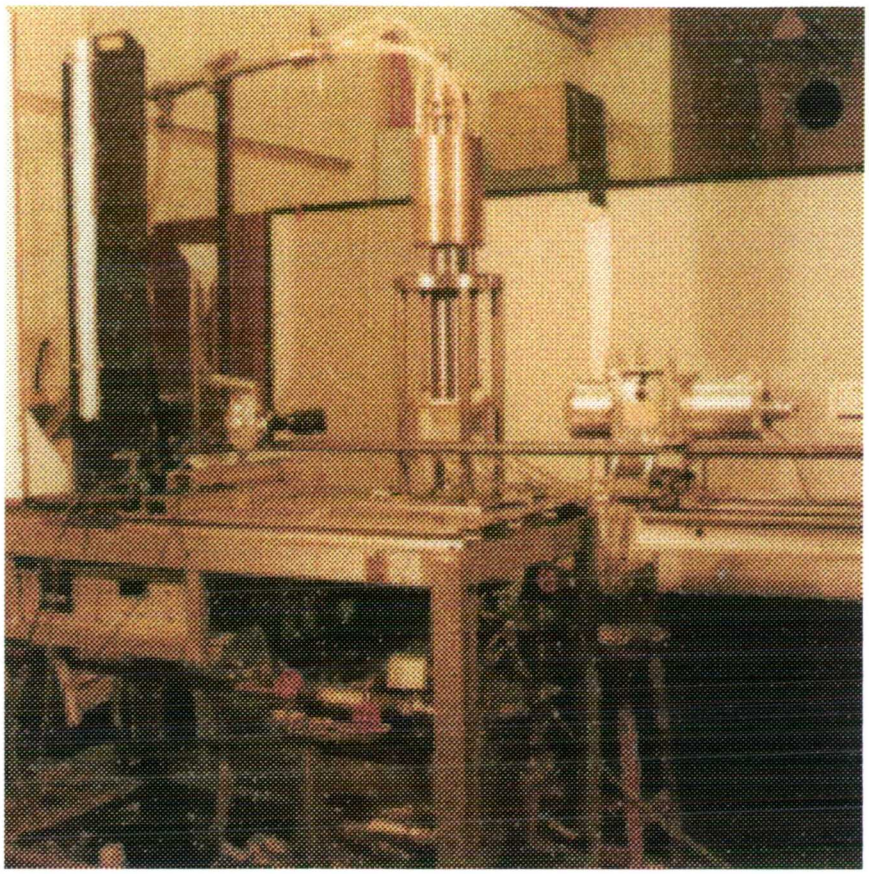

(b)

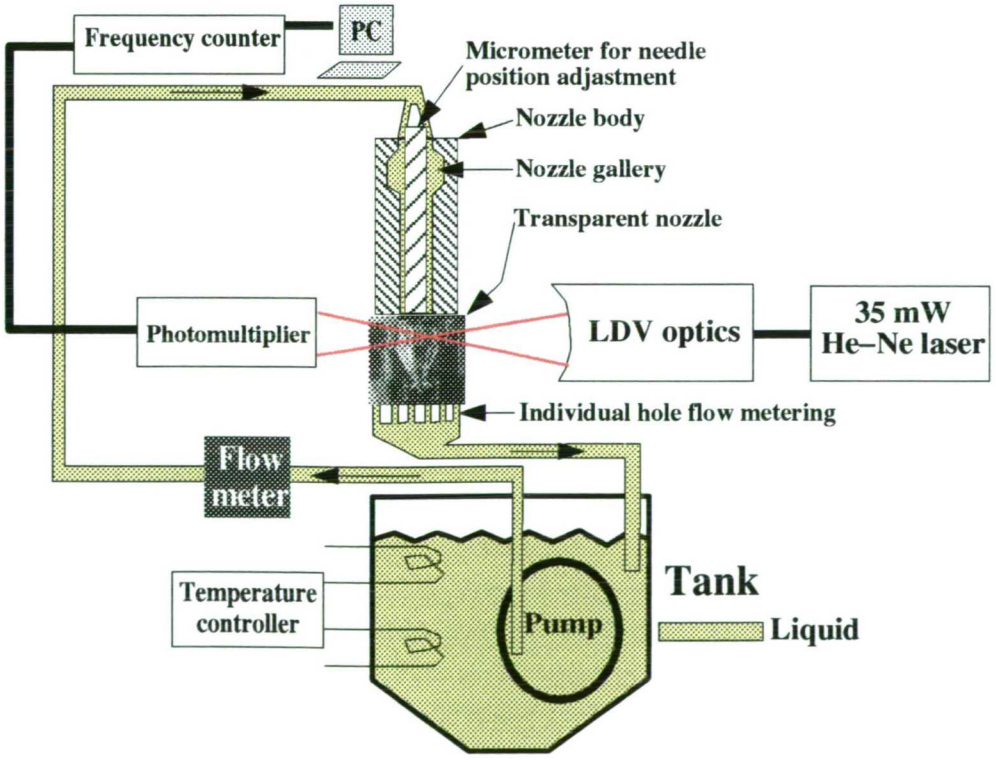

Figure 4–31 : (a) Photograph and (b) schematic representation of the refractive index rig used for the LDV measurement of the flow in the sac volume and the injection holes

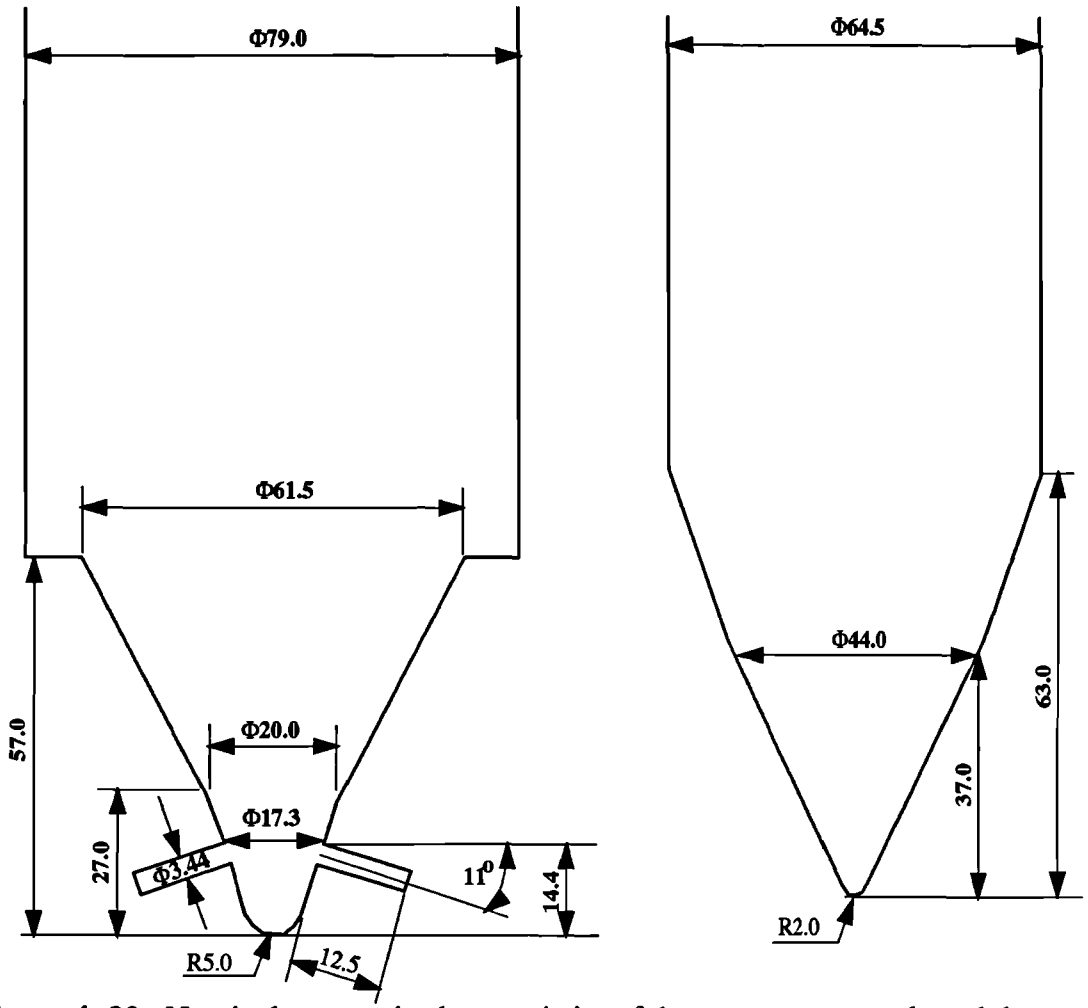

Figure 4–32 : Nominal geometric characteristics of the transparent nozzle and the needle

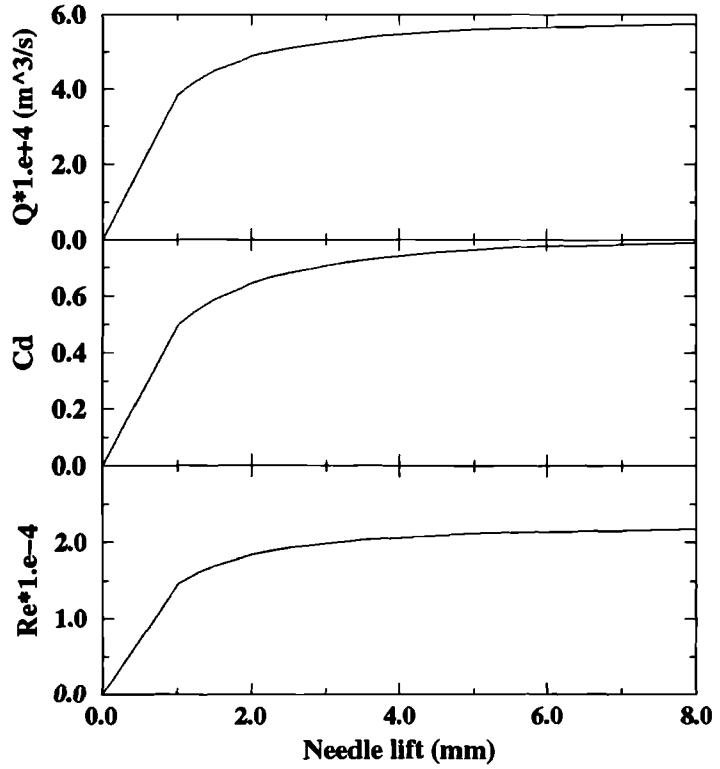

Figure 4–33: Experimental estimated volumetric flow rate, discharge coefficient and Reynolds number of the transparent nozzle as a function of the needle lift

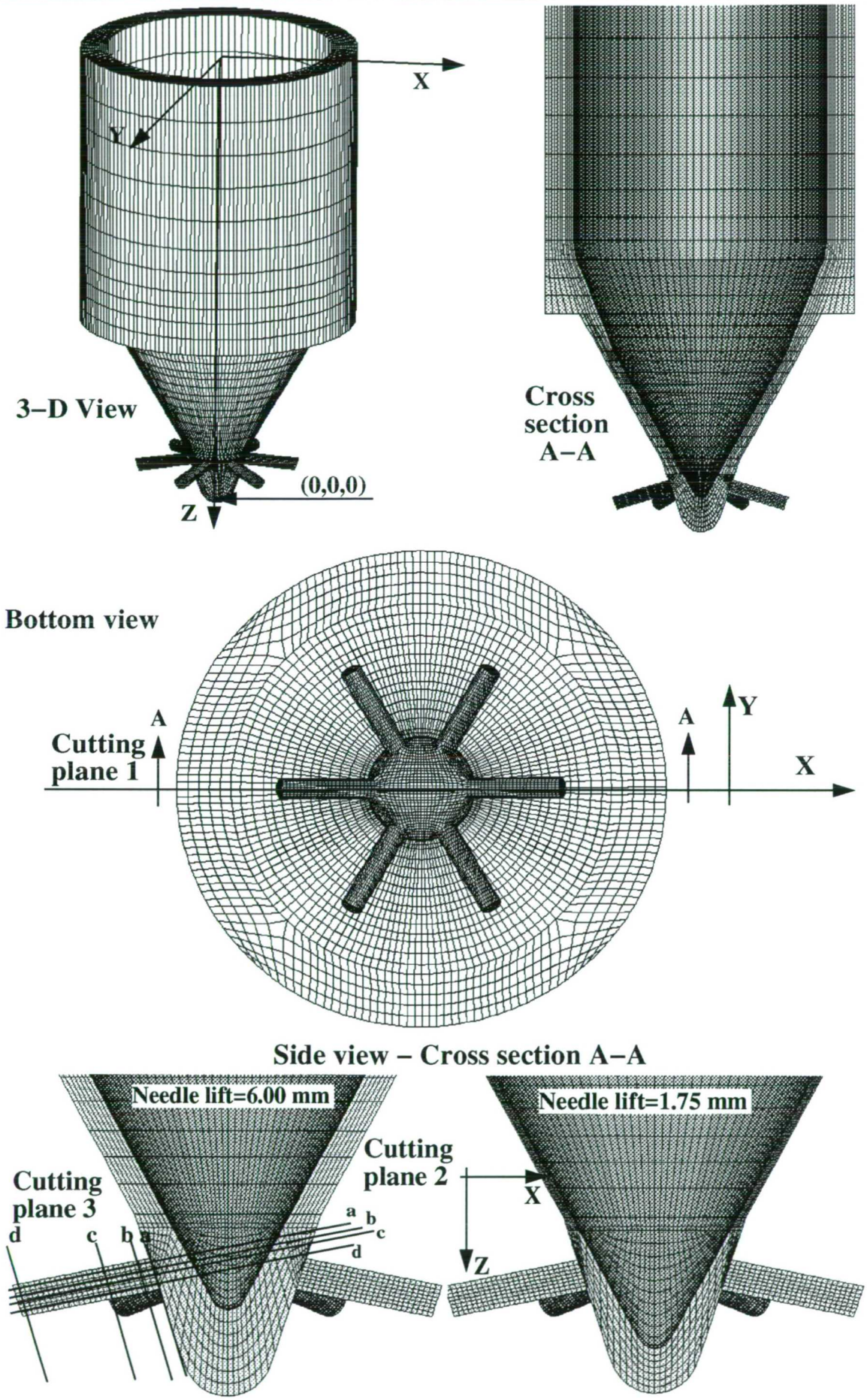

Figure 4–34: Numerical grid of the examined nozzle; the cutting planes selected for the flow visualization are also shown

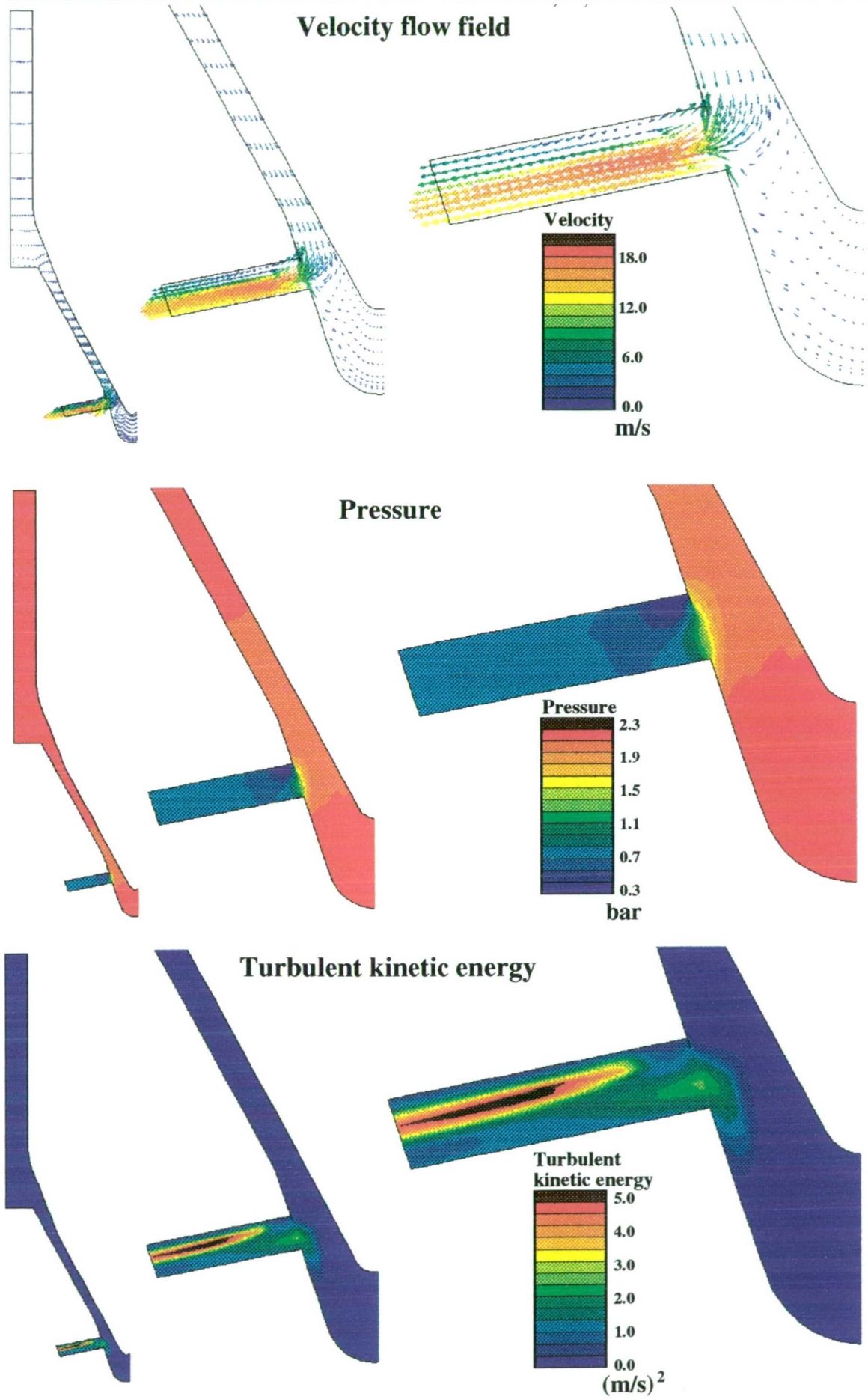

Figure 4–35 : Calculated flow field, pressure and turbulent kinetic energy distributions on cutting plane 1 [Needle lift 6.00 mm, nominal geometric characteristics]

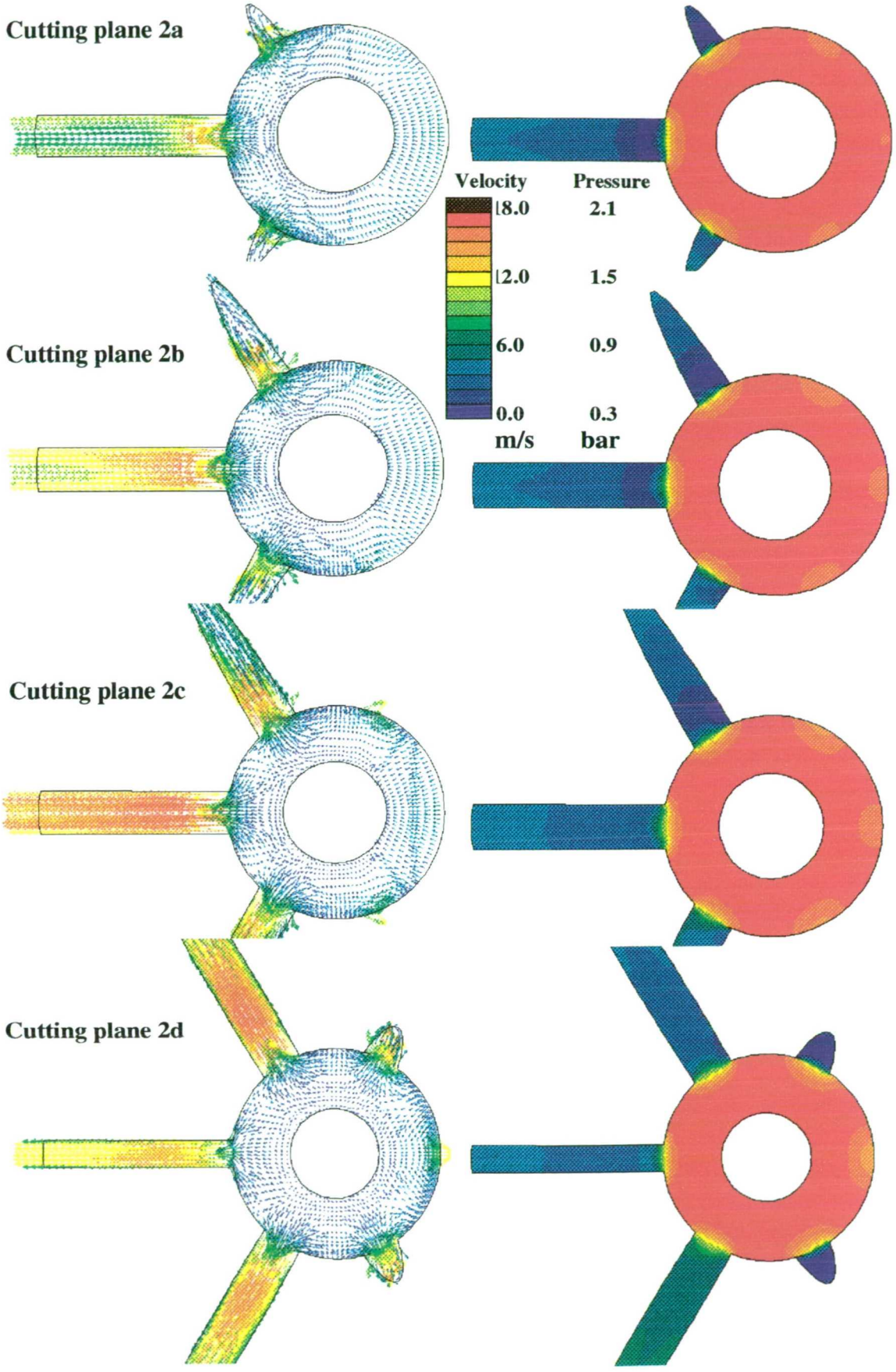

Figure 4–36 : Calculated velocity and pressure distribution on cutting planes 2a, 2b, 2c and 2d [Needle lift 6.00 mm, nominal geometric characteristics]

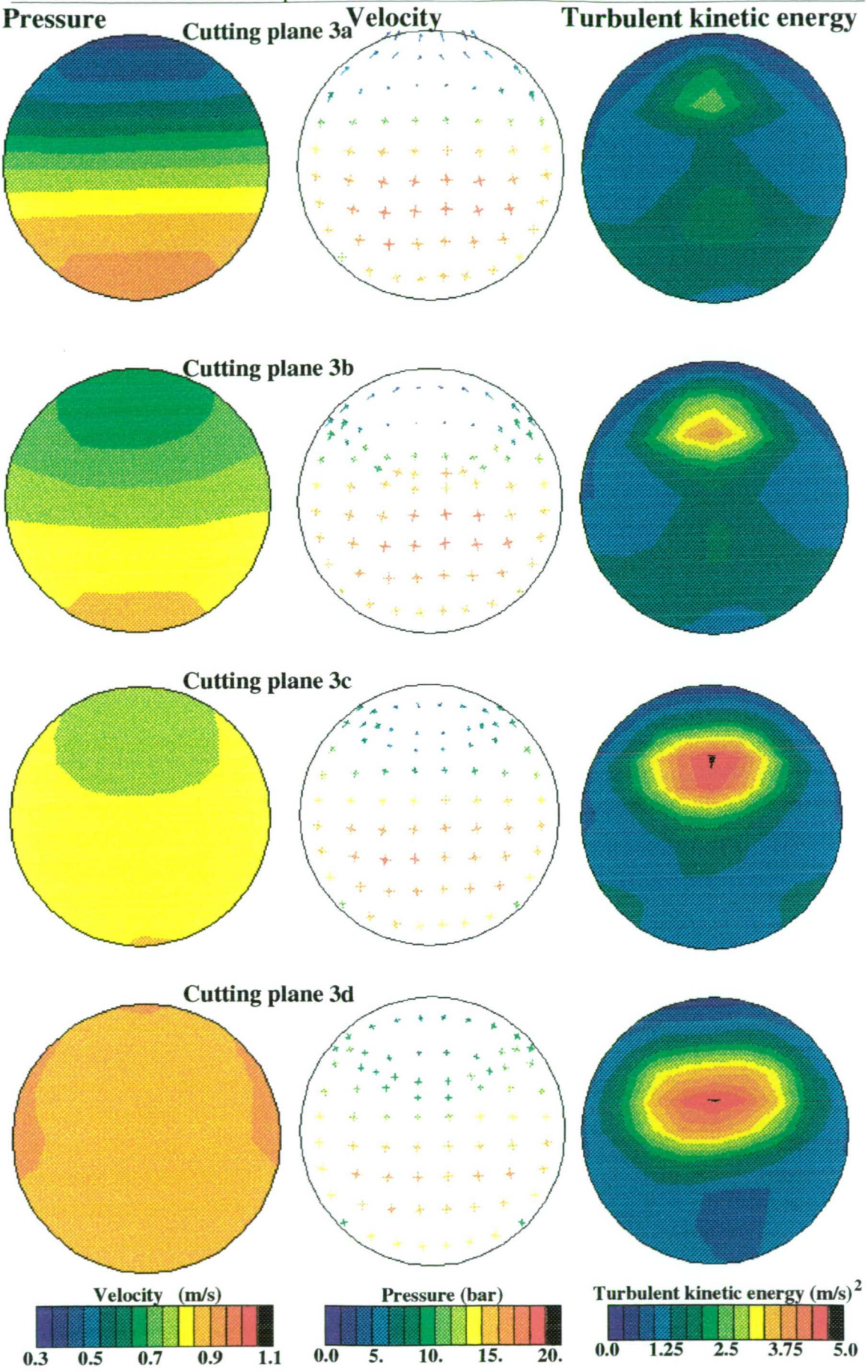

Figure 4–37 : Calculated velocity flow field, pressure and turbulent kinetic energy distributions on cutting planes 3a, 3b, 3c and 3d [Needle lift 6.00 mm [nominal geometric characteristics]

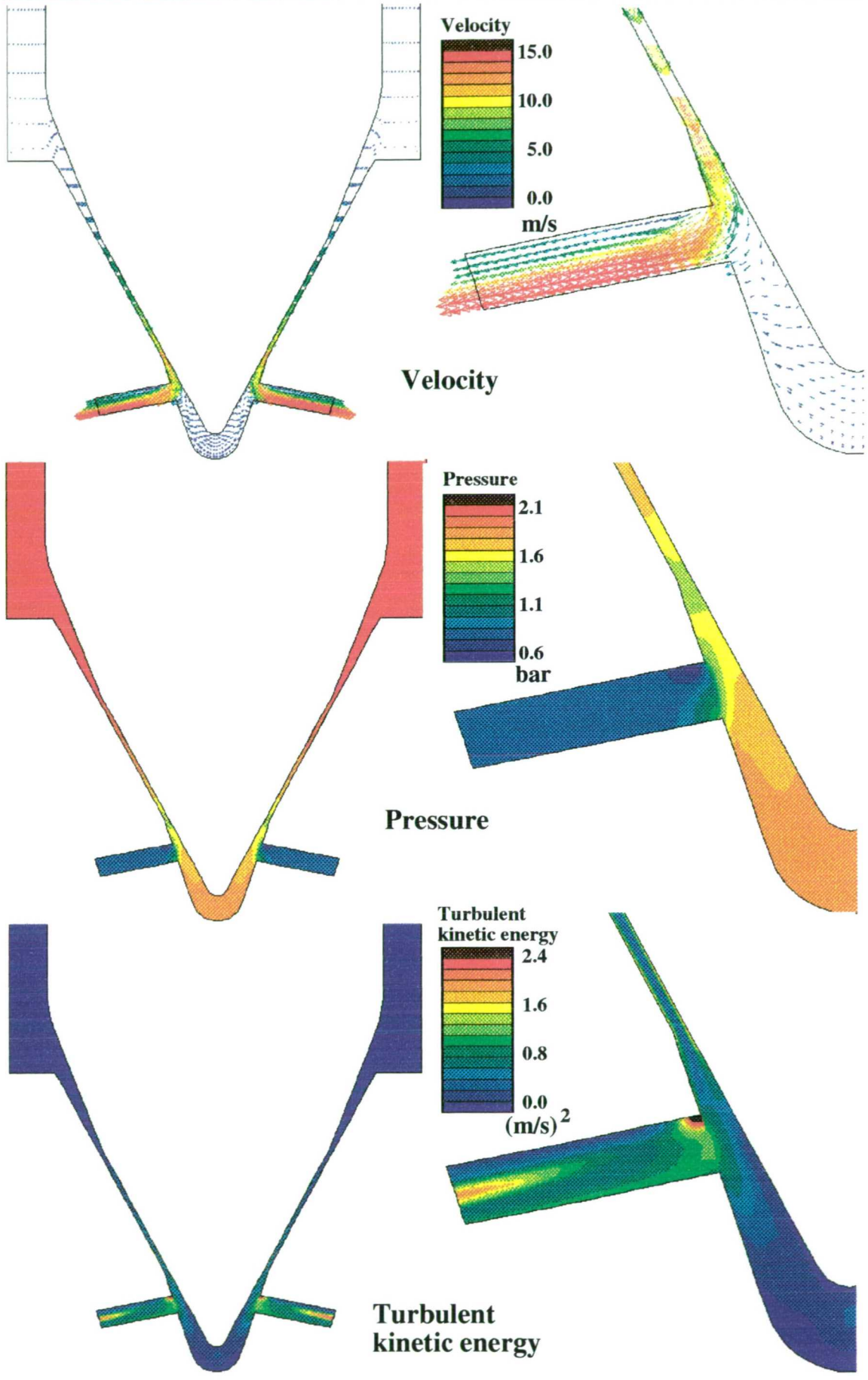

Figure 4–38 : Calculated velocity flow field, pressure and turbulent kinetic energy distributions on cutting plane 1 [Needle lift 1.75 mm, nominal geometric characteristics]

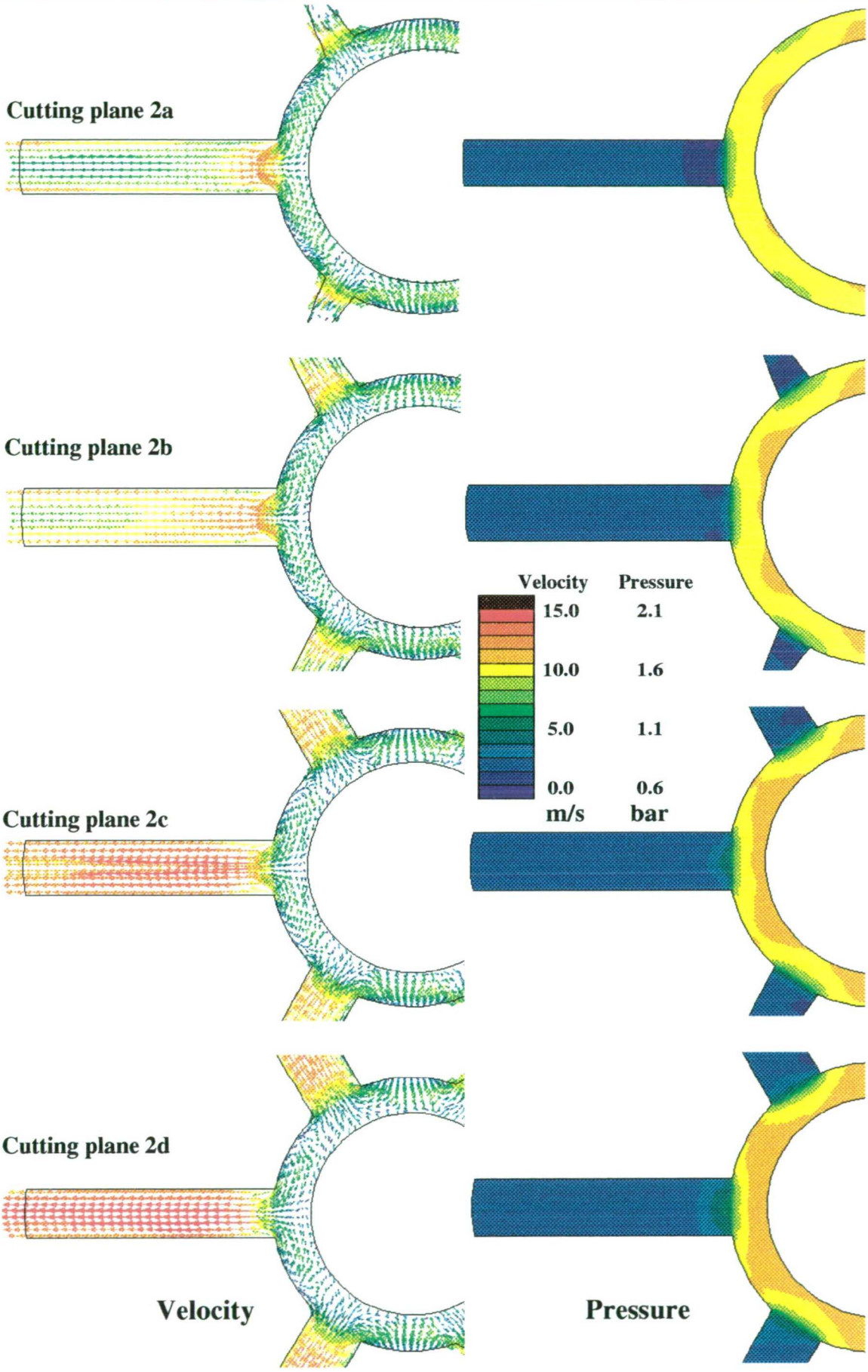

Figure 4–39 : Calculated velocity flow field and pressure distribution on cutting planes 2a, b, c and d [Needle lift 1.75 mm, nominal geometric characteristics]

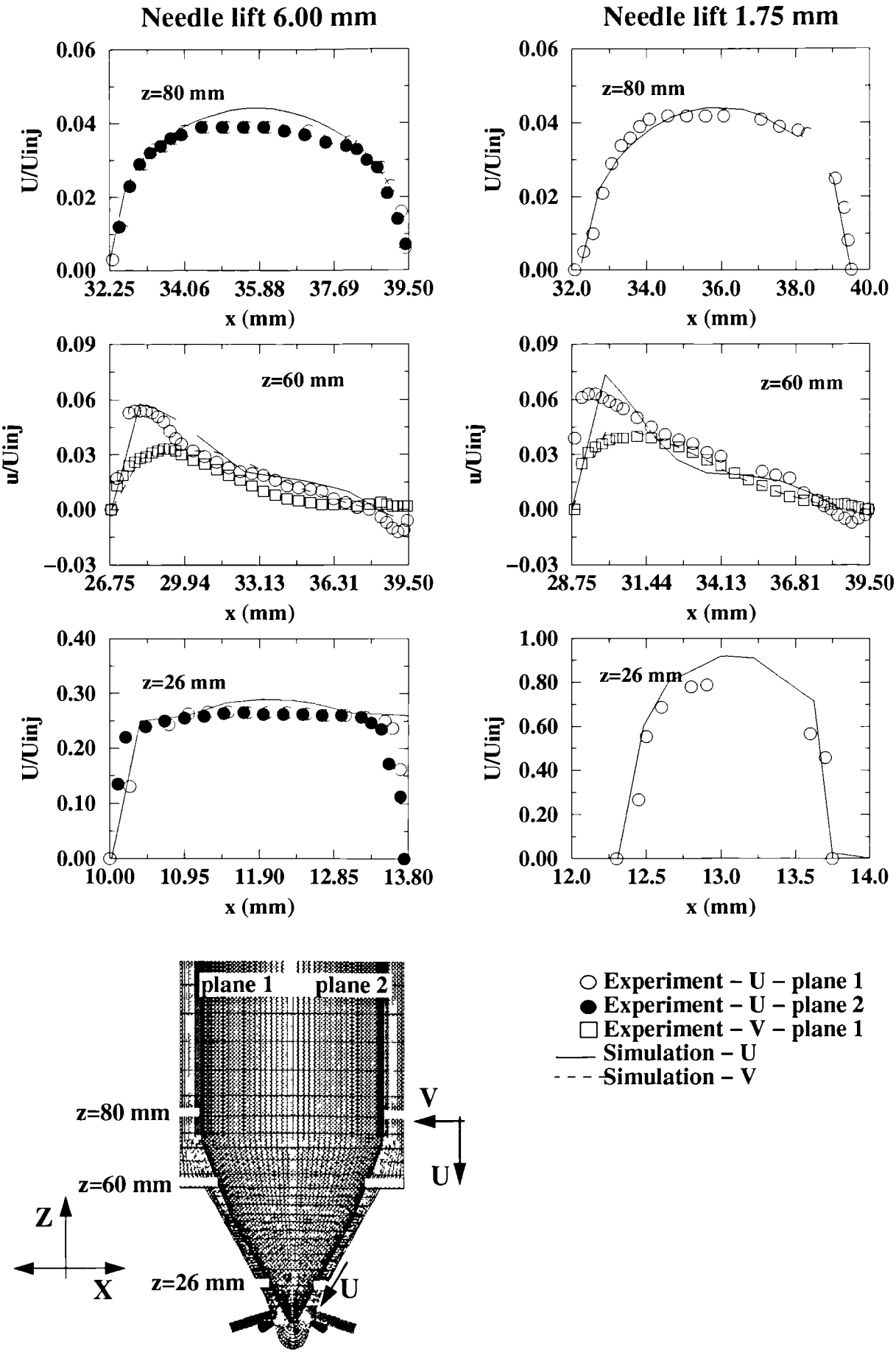

Figure 4–40: Comparison between the computational and experimental results on planes z=80, 60 and 26 mm [Needle lifts 6.00 mm and 1.75 mm]

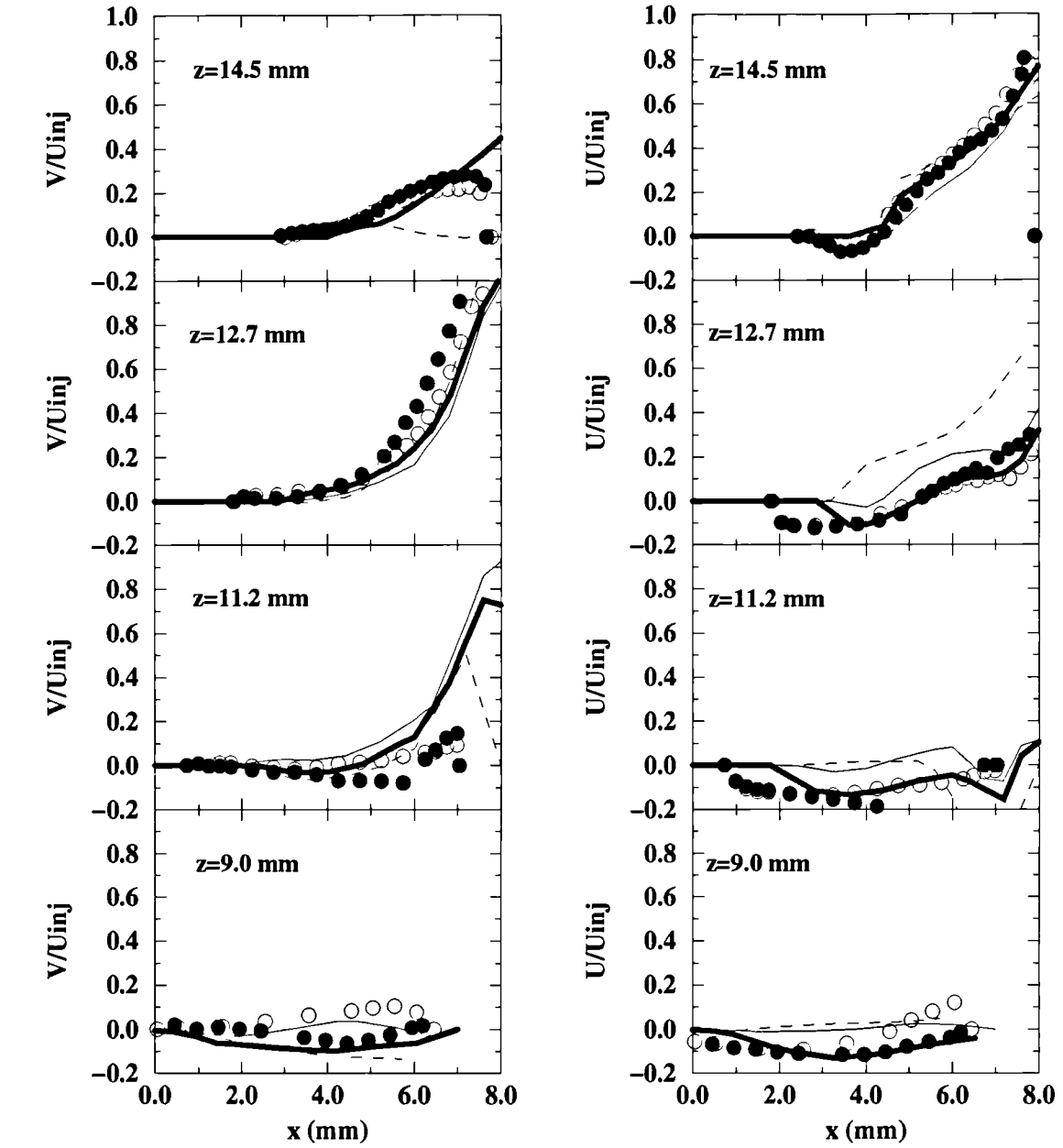

Figure 4–41: Comparison between the computational and the experimental results on horizontal planes z=14.5, 12.7, 11.9 and 9.0 mm [Needle lift 6.0 mm]

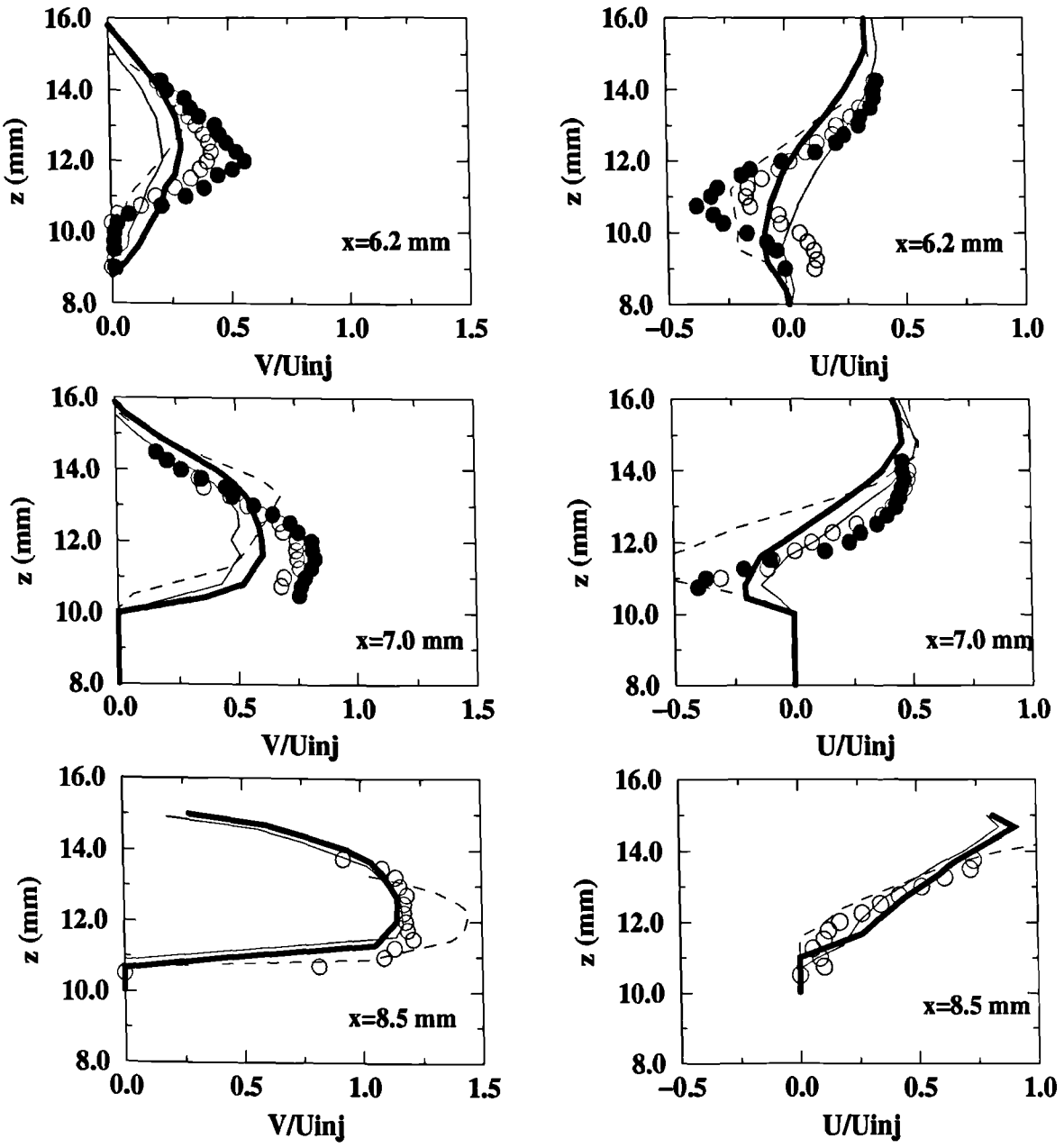

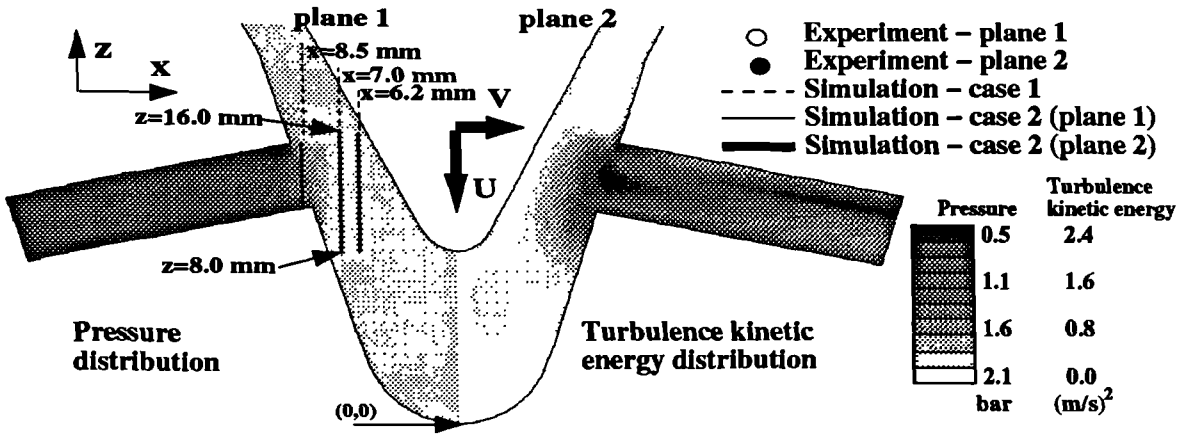

Figure 4–42 : Comparison between the computational and the experimental results on vertical planes x=6.2 mm, x=7.0 mm and x=8.5 mm [Needle lift 6.0 mm]

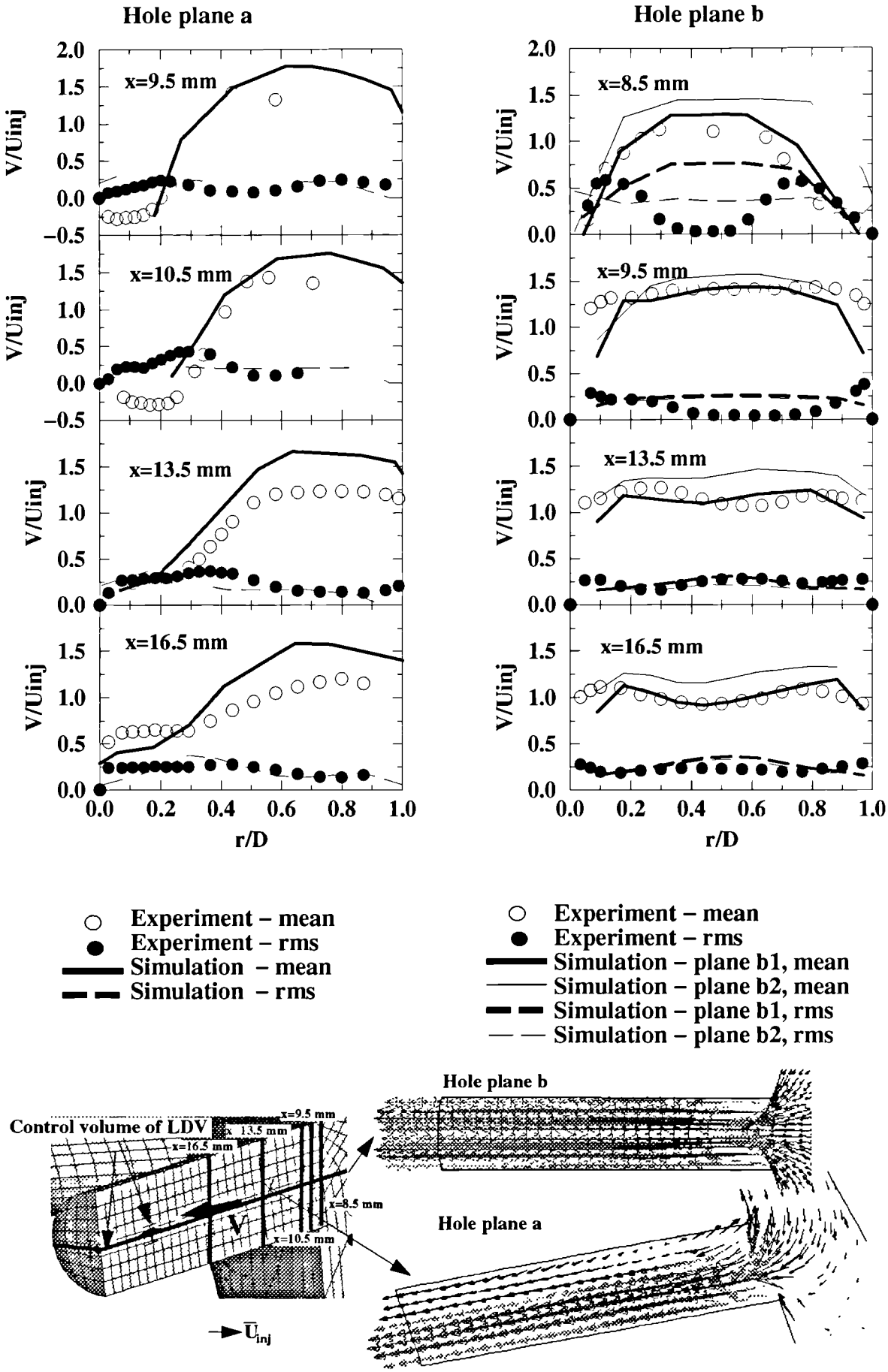

Figure 4–43 : Comparison between the computational and the experimental results on planes x=8.5, 9.5, 10.5, 13.5 and 16.5 mm inside the injection hole [Needle lift 6.00 mm]

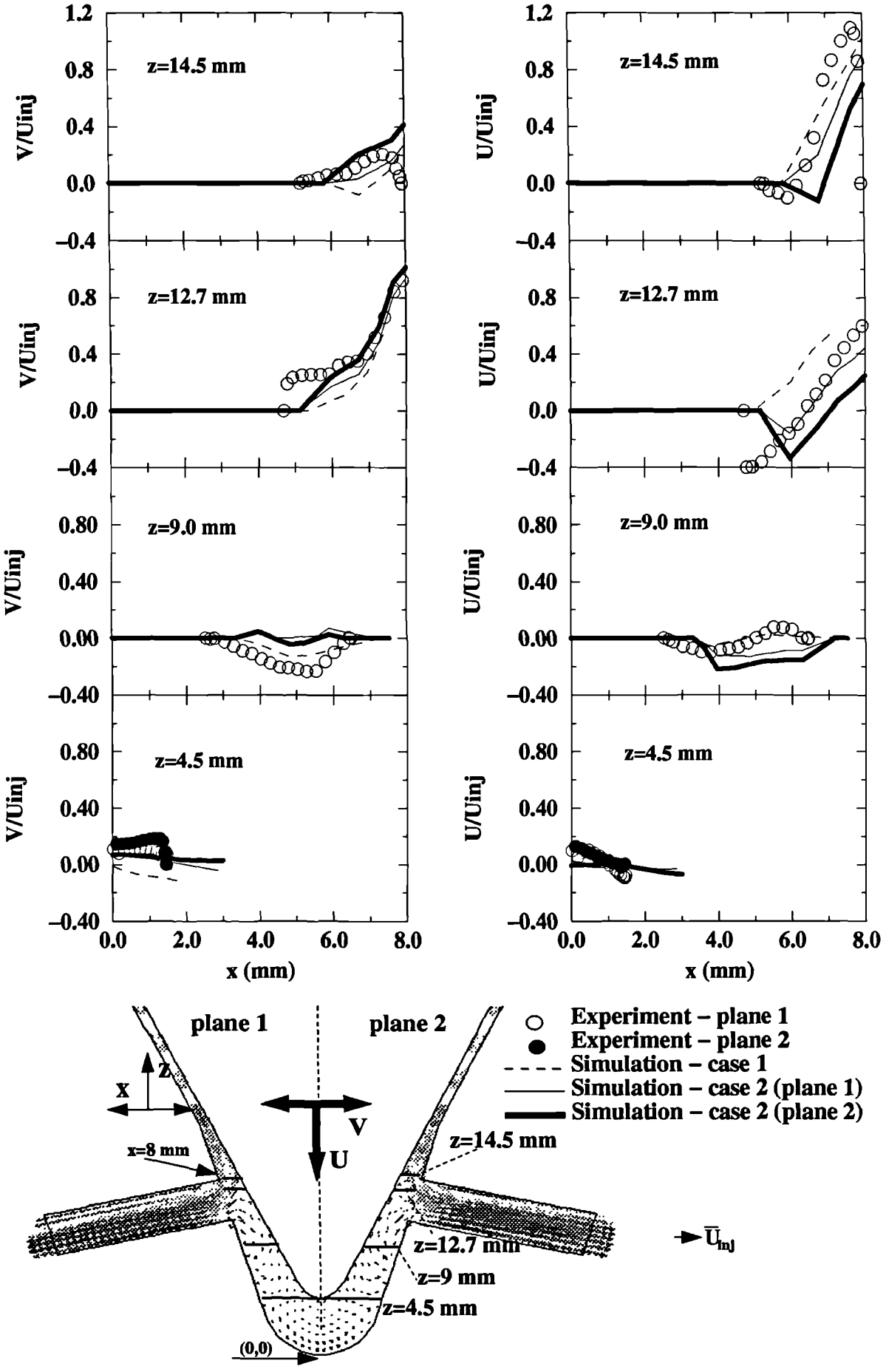

Figure 4–44 : Comparison between the computational and experimental results on planes z=14.5, z=12.7, z=9.0 and z=4.5 mm [Needle lift 1.75 mm]

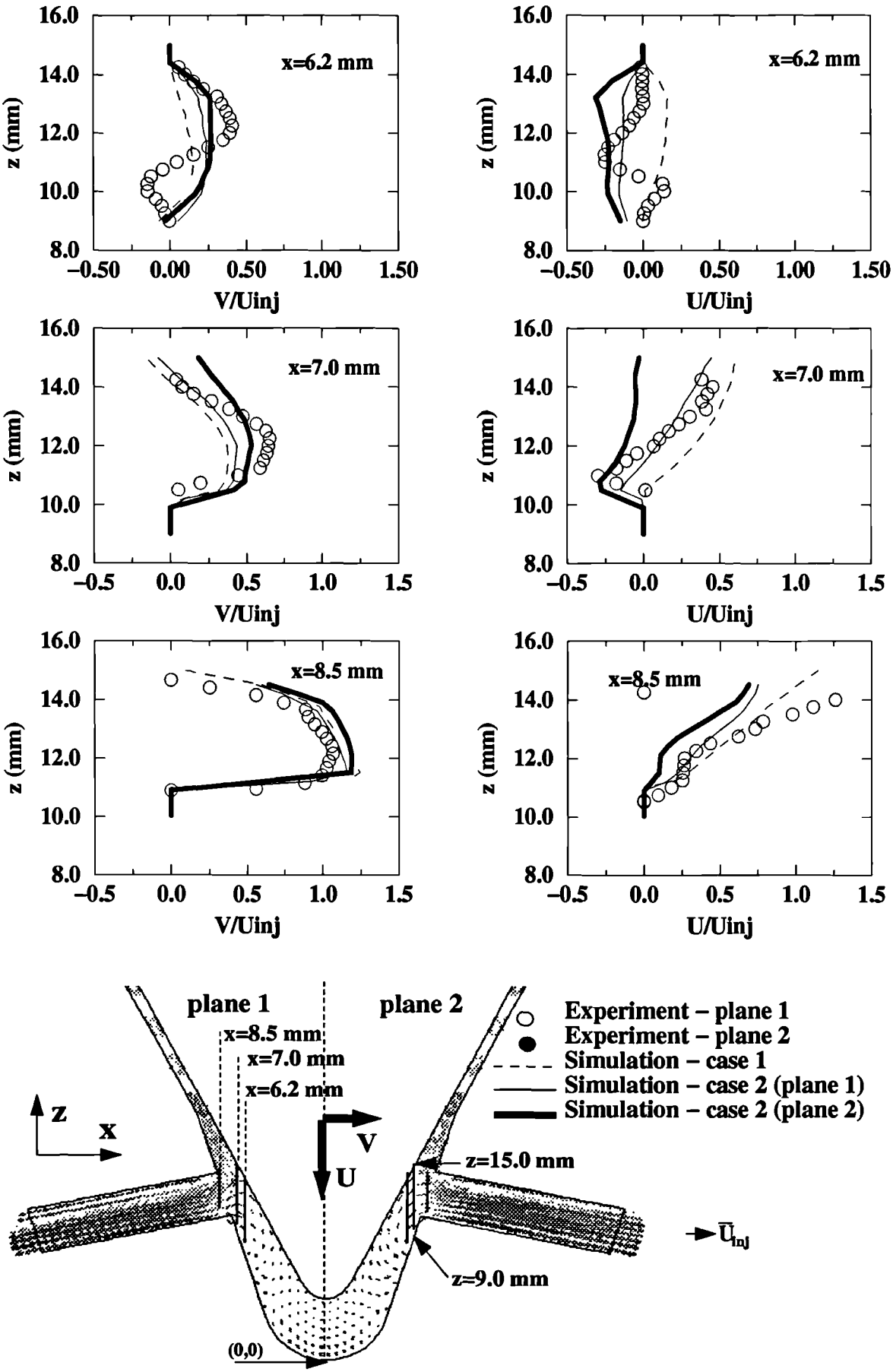

Figure 4–45 : Comparison between the computational and experimental results on planes x=6.2 mm, x=7.0 mm and x=8.5 mm [Needle lift 1.75 mm]

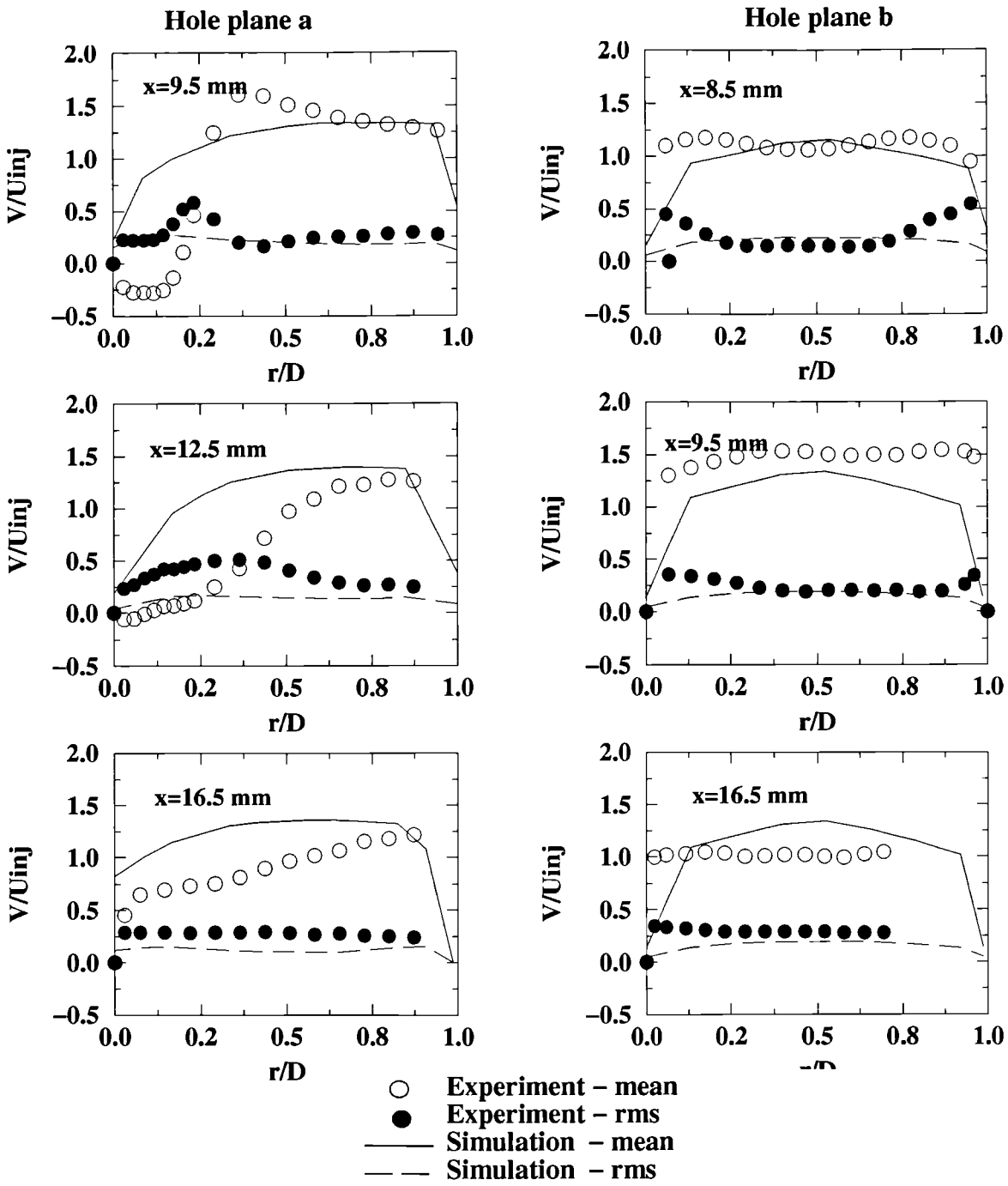

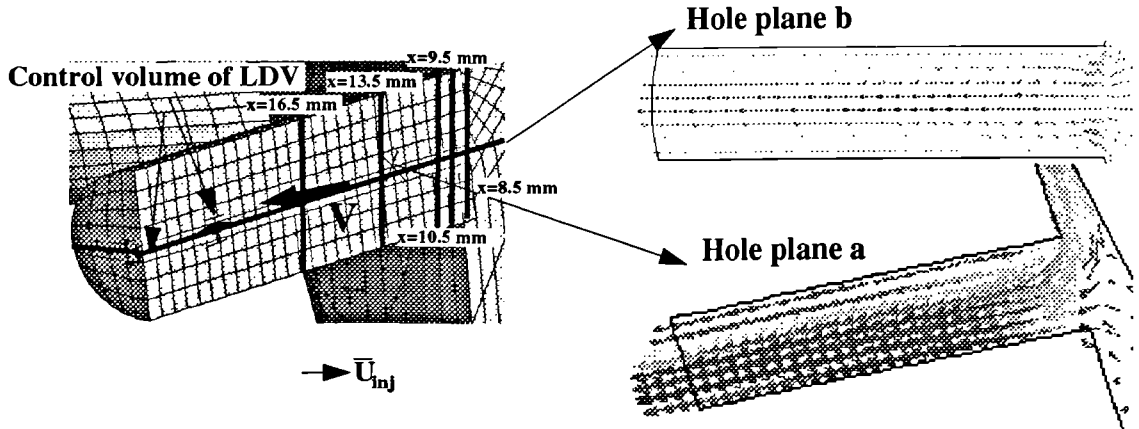

Figure 4–46 : Comparison between the computational and experimental results on planes x=8.5, 9.5, 12.5 and 16.5 mm [Needle lift 1.75mm]

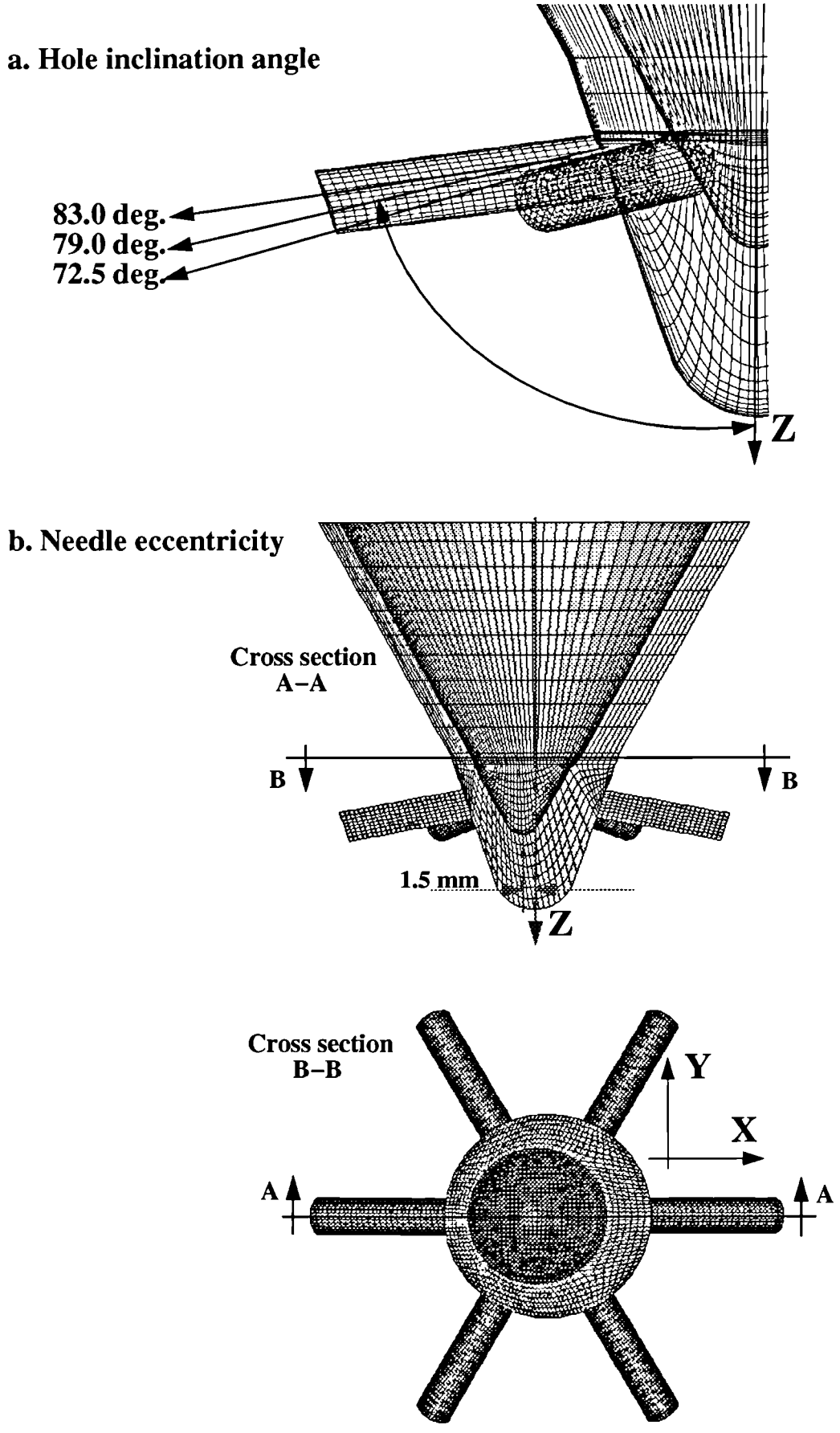

Figure 4–47 : Definition of the parameters investigated

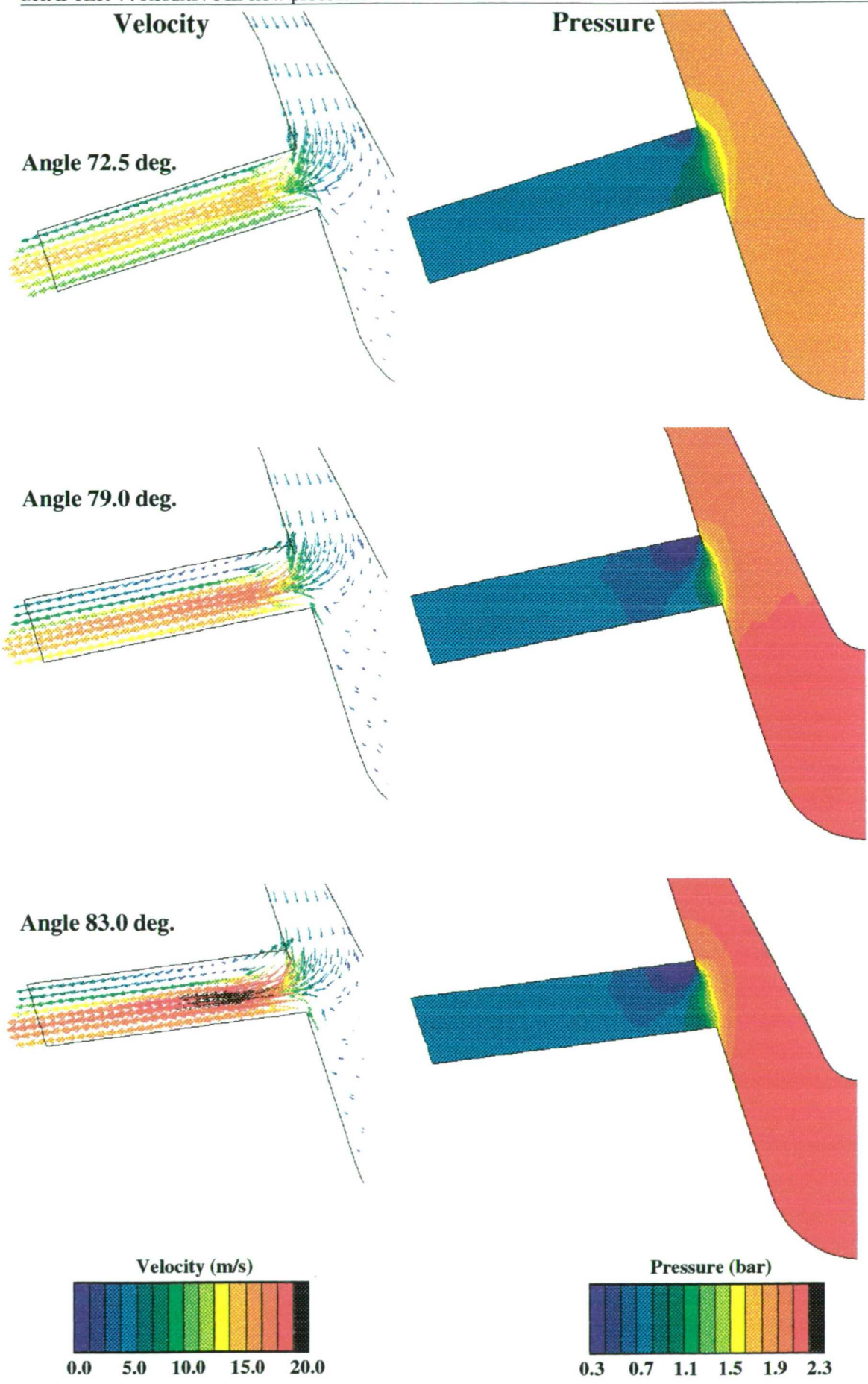

Figure 4–48 : Effect of hole inclination angle on calculated velocity flow field and pressure distribution along an injection hole for the same flow rate.

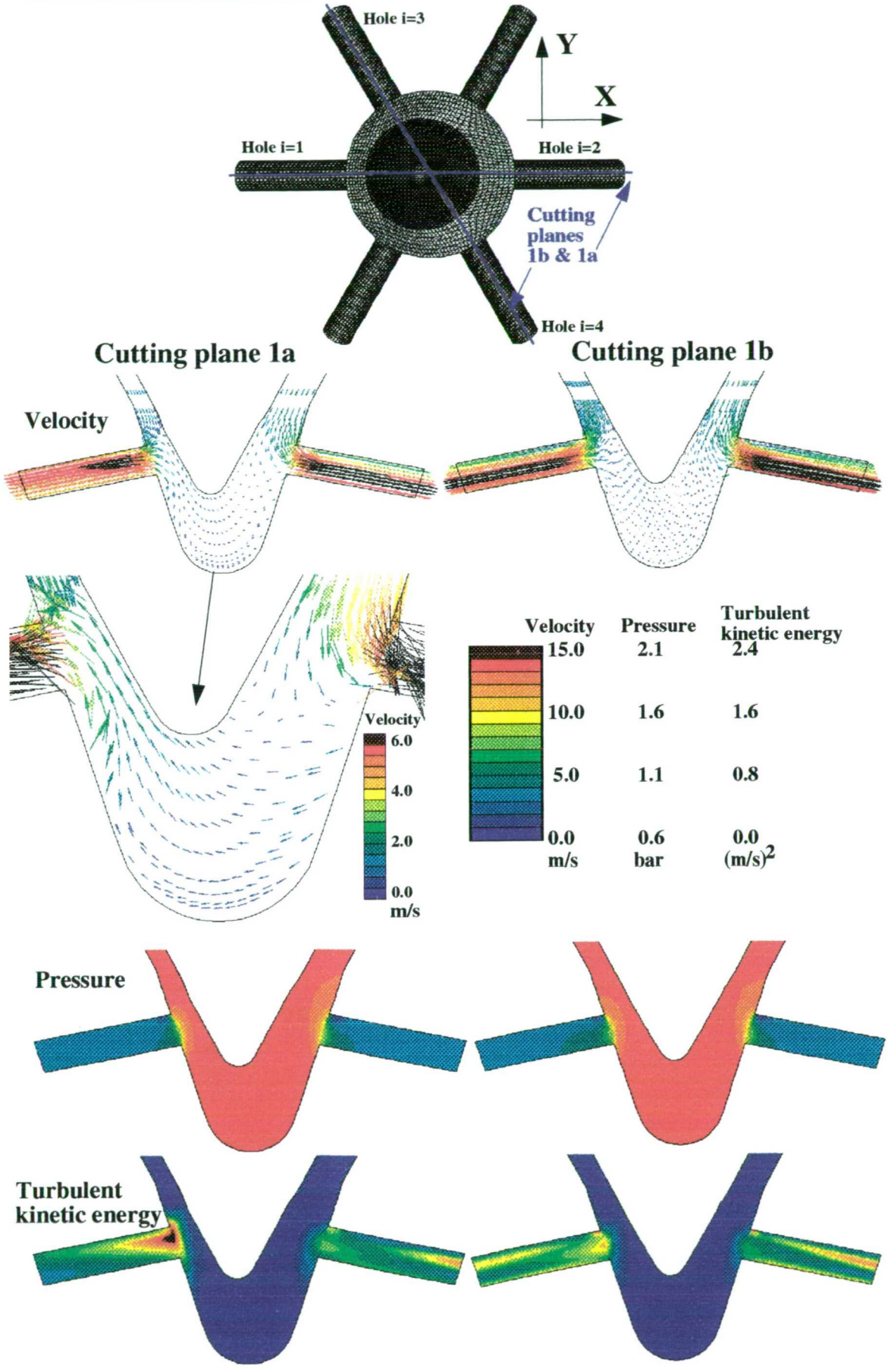

Figure 4–49 : Effect of needle eccentricity on calculated velocity flow field, pressure and turbulent kinetic energy on planes 1a and 1b. [Needle lift 6.0 mm]

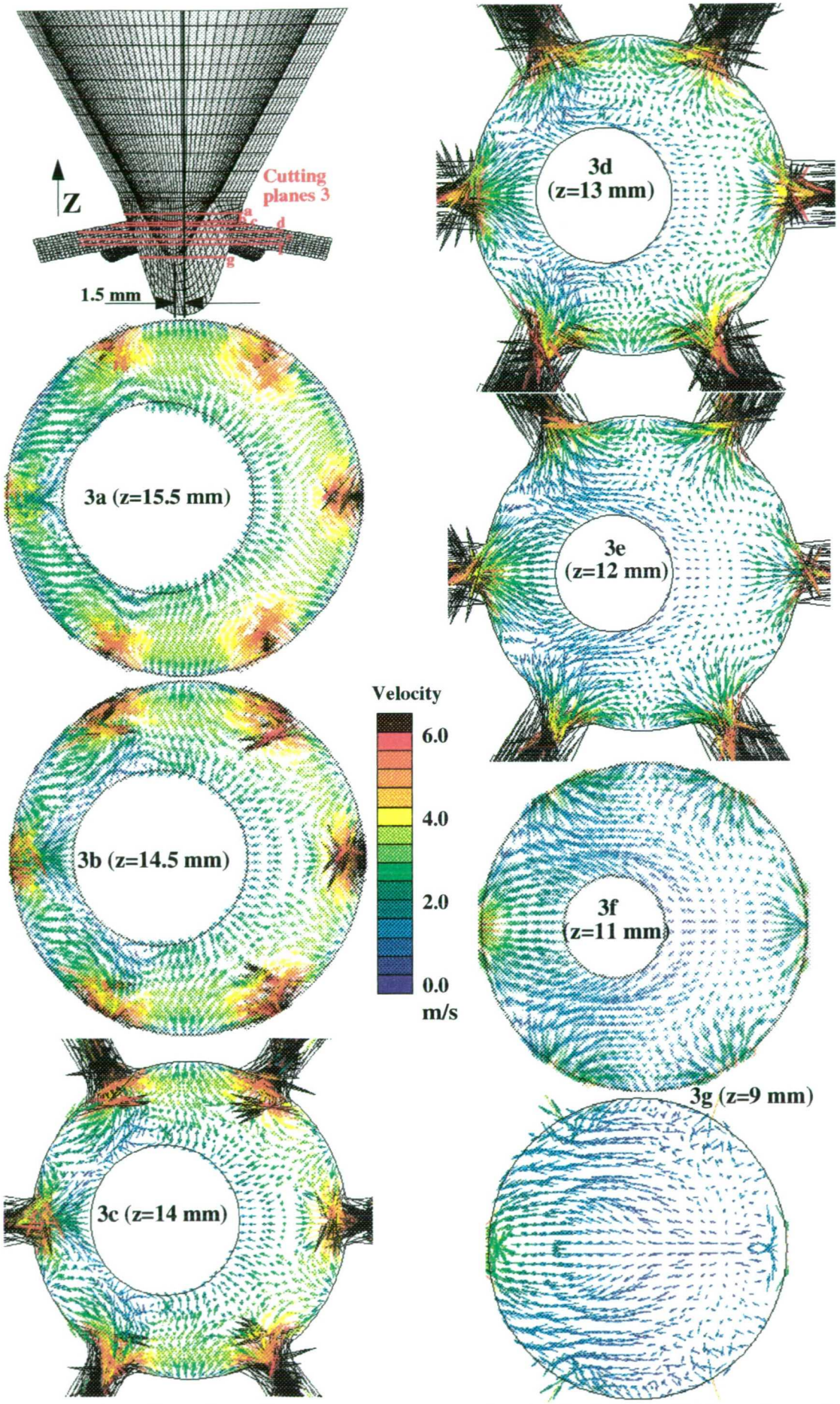

Figure 4–50 : Effect of needle eccentricity on calculated velocity flow field on planes 3a, 3b, 3c, 3d, 3e, 3f and 3g [Needle lift 6.00 mm]

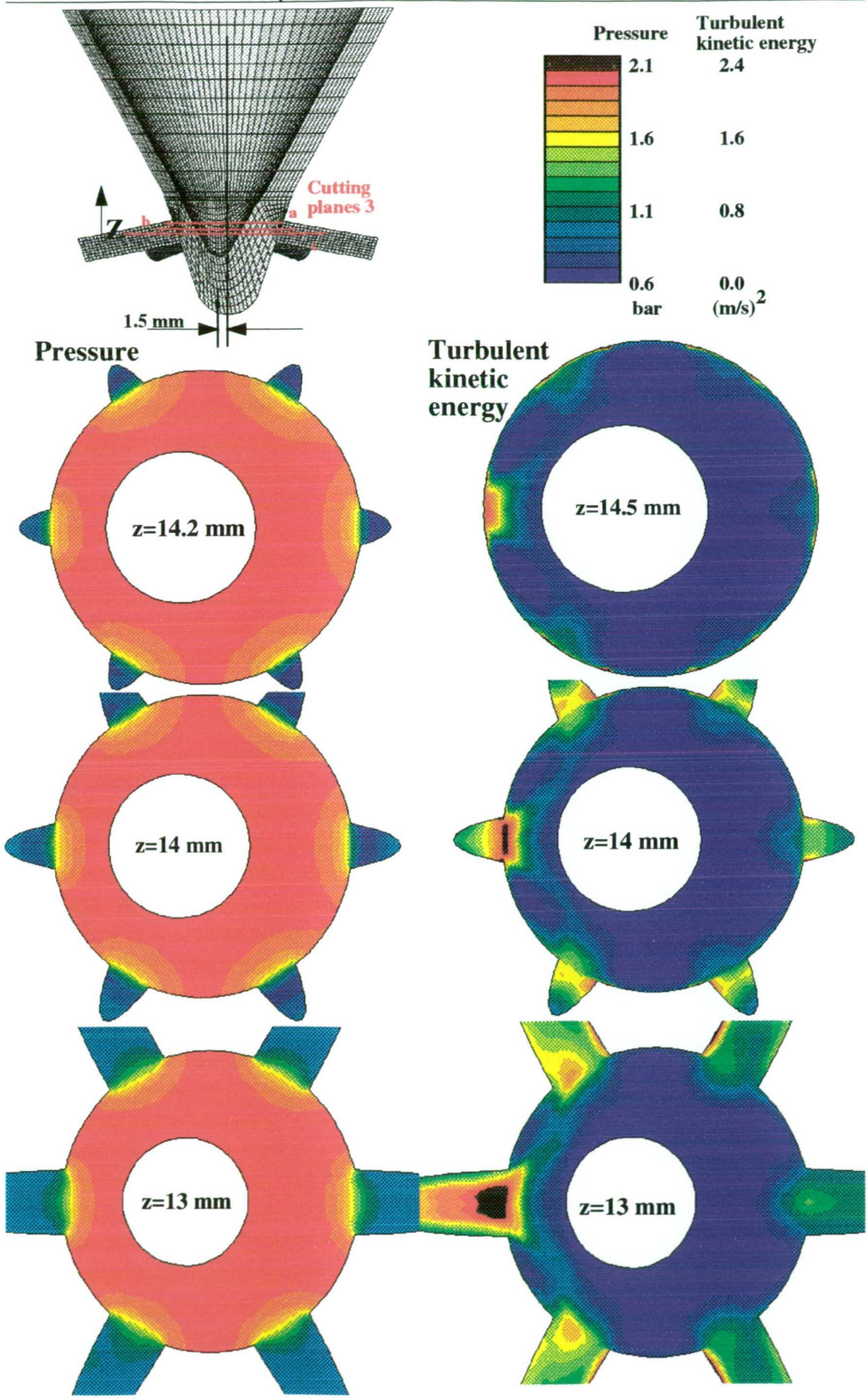

Figure 4–51 : Effect of needle eccentricity on calculated pressure and turbulent kinetic energy distributions on planes 3a, 3b, 3c and 3d [Needle lift 6.00 mm]

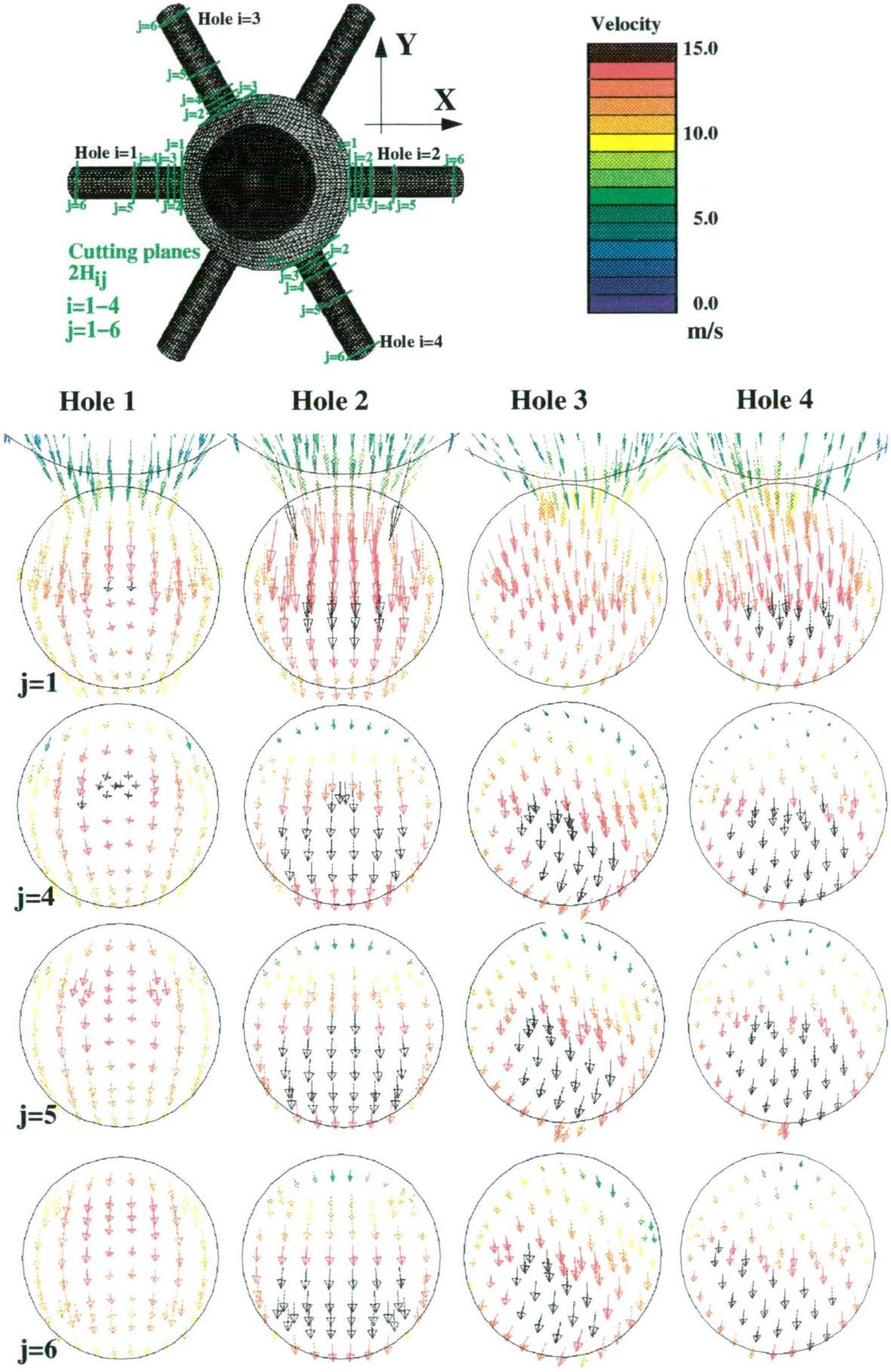

Figure 4–52: Effect of needle eccentricity on calculated velocity flow field in the injection holes on planes j=1, j=4, j=5 and j=6 [Needle lift 6.00 mm]

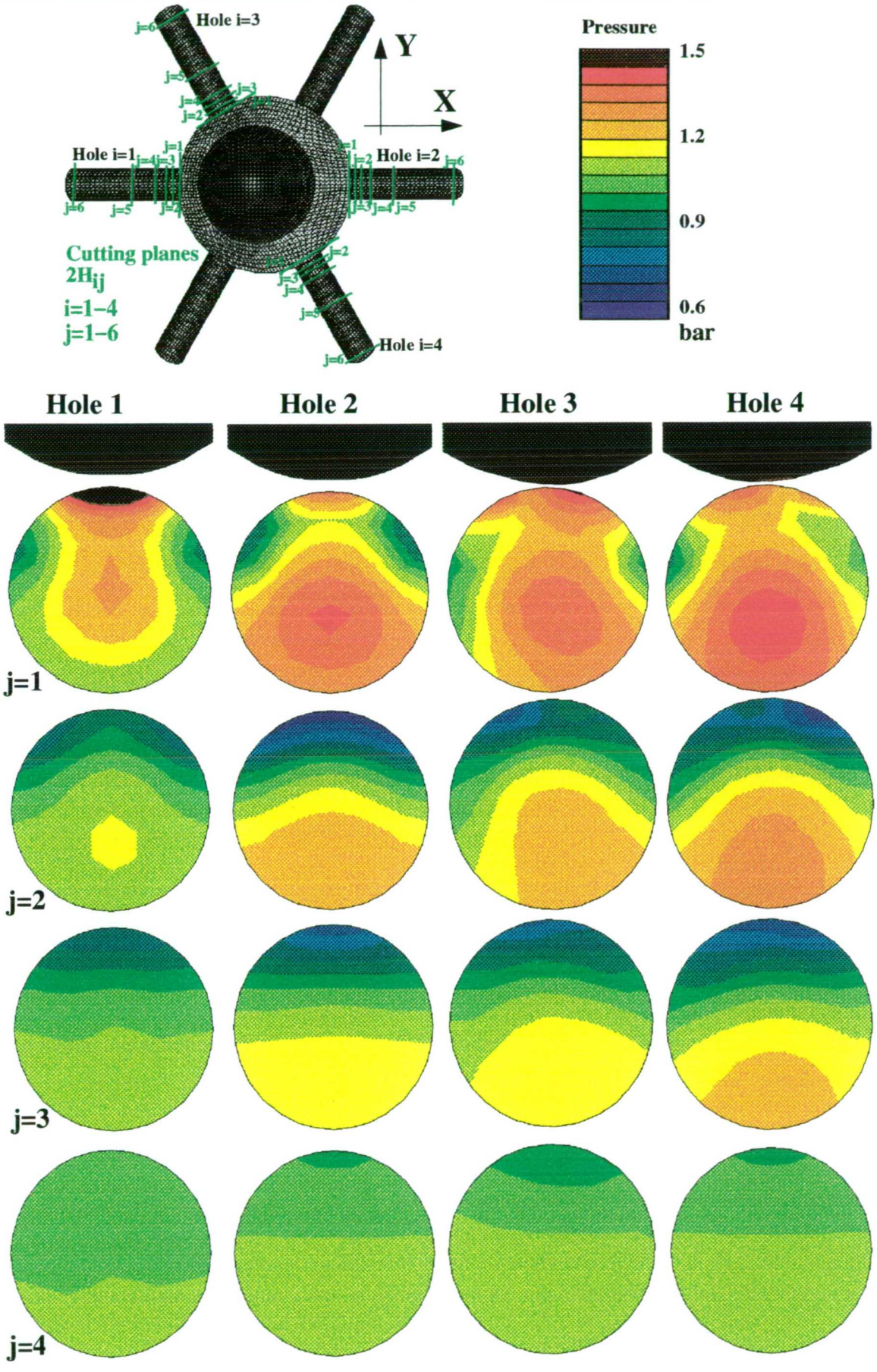

Figure 4–53 : Effect of needle eccentricity on calculated pressure distribution in the injection holes on planes j=1, j=2, j=3 and j=6 [Needle lift 6.00 mm]

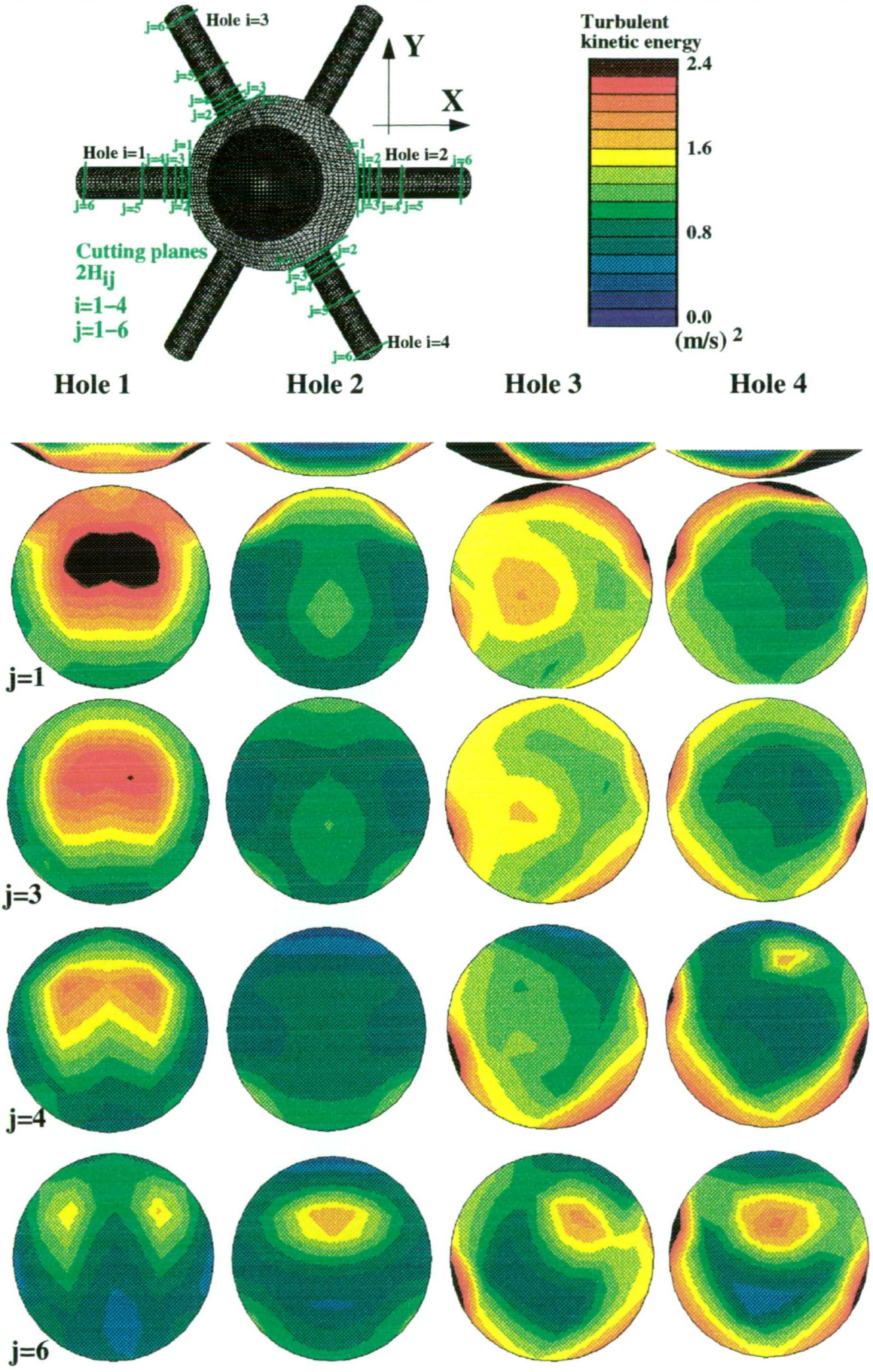

Figure 4–54 : Effect of needle eccentricity on calculated turbulent kinetic energy distribution inside the injection holes on planes j=1, j=3, j=4 and j=6 [Needle lift 6.00 mm]

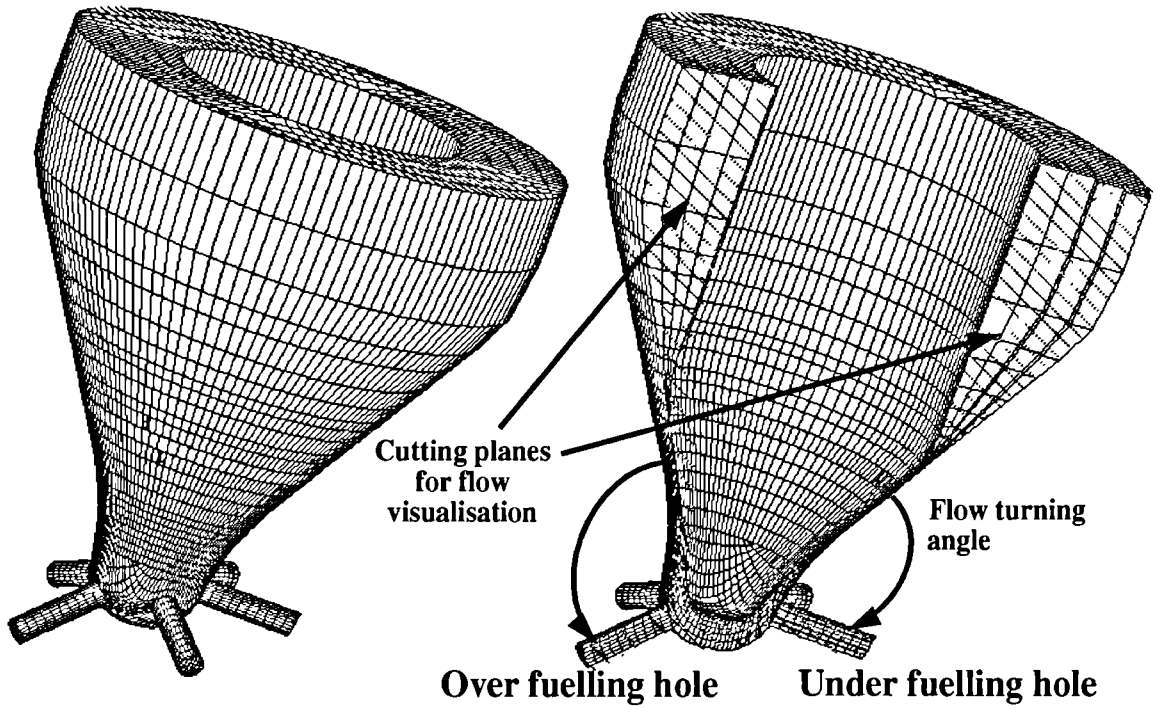

Figure 4–55 : Numerical grid of the 5–hole inclined injector. The cutting planes selected for the flow visualization are shown.

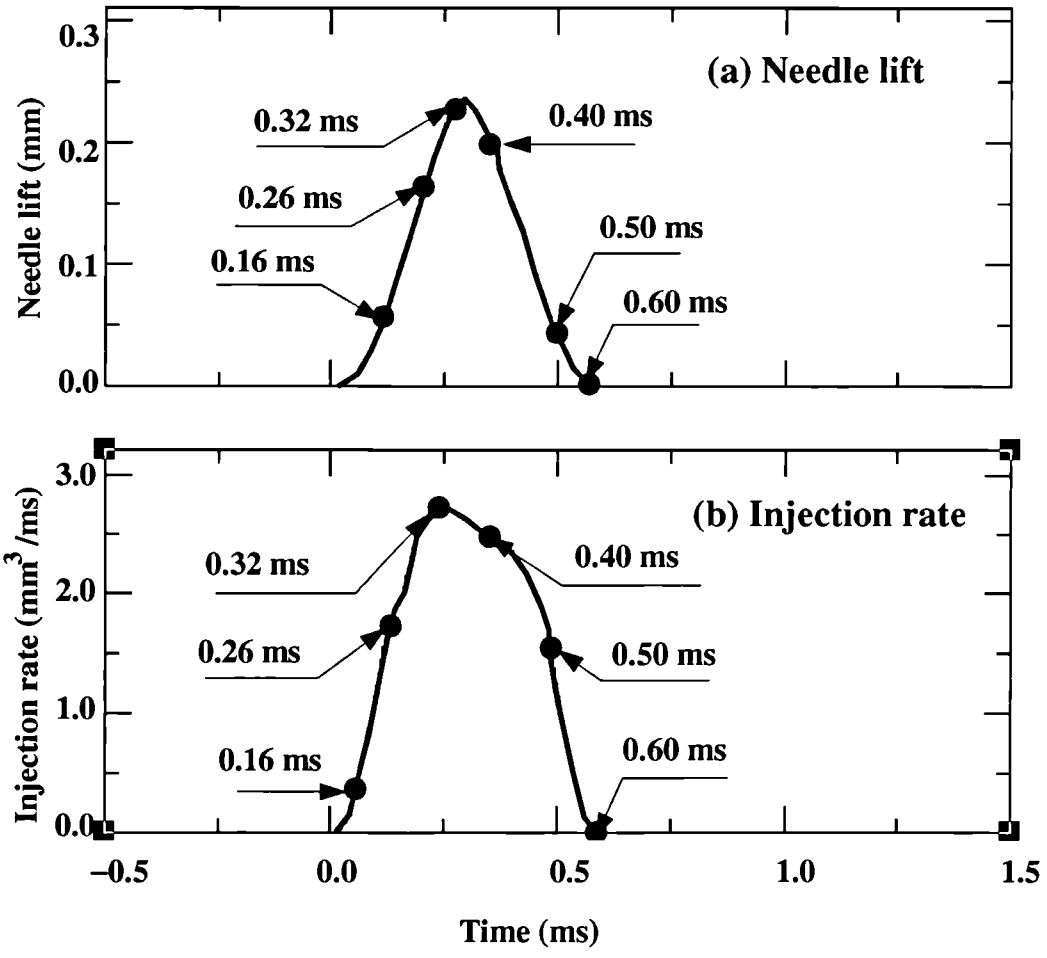

Figure 4–56 : Needle lift and flow rate inputted to the CFD model for the prediction of the transient flow inside the sac volume and the injection holes

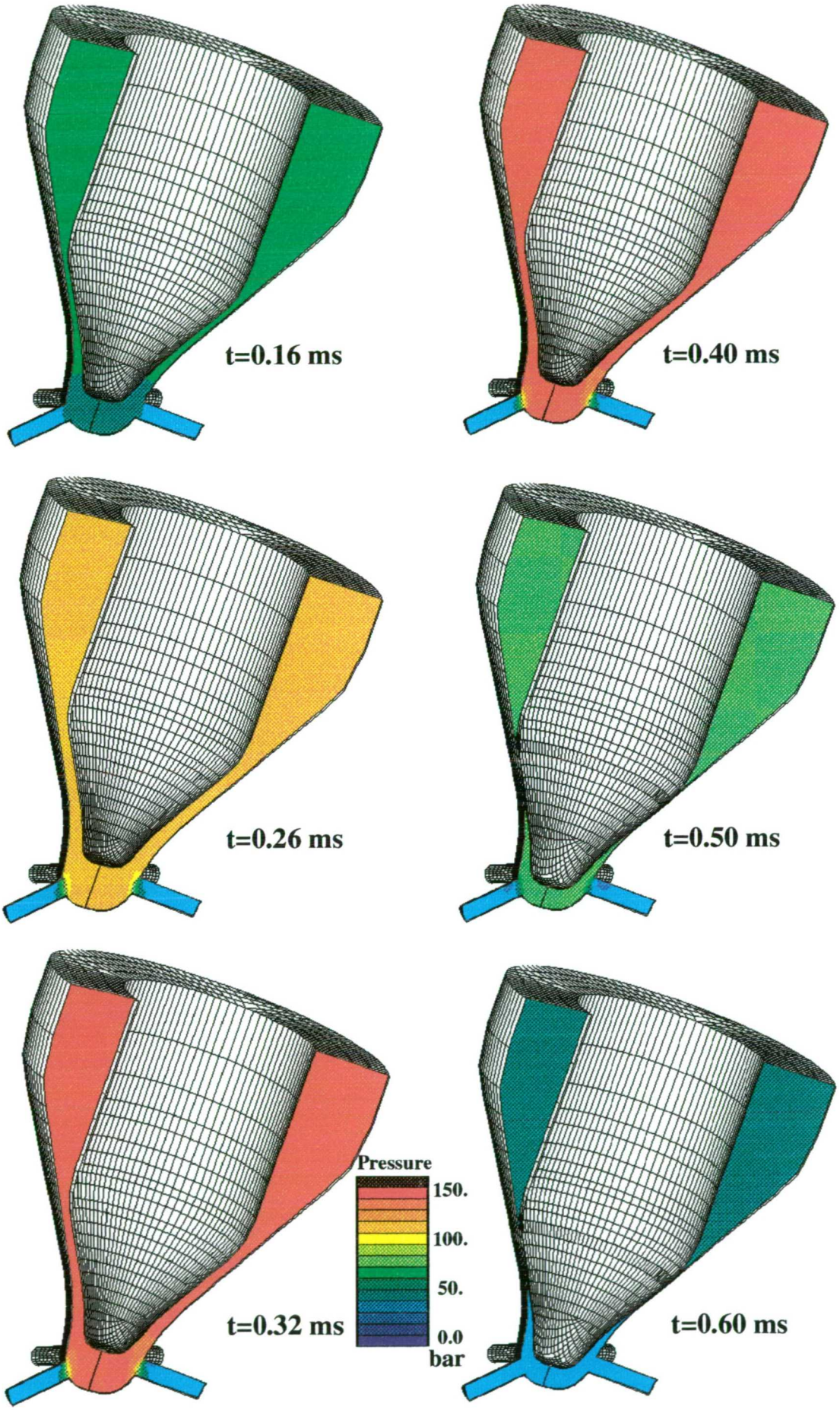

Figure 4–57 : Calculated pressure distribution at t=0.16, 0.26, 0.32, 0.40, 0.50 and 0.60 ms after the needle opening time on the two cutting planes

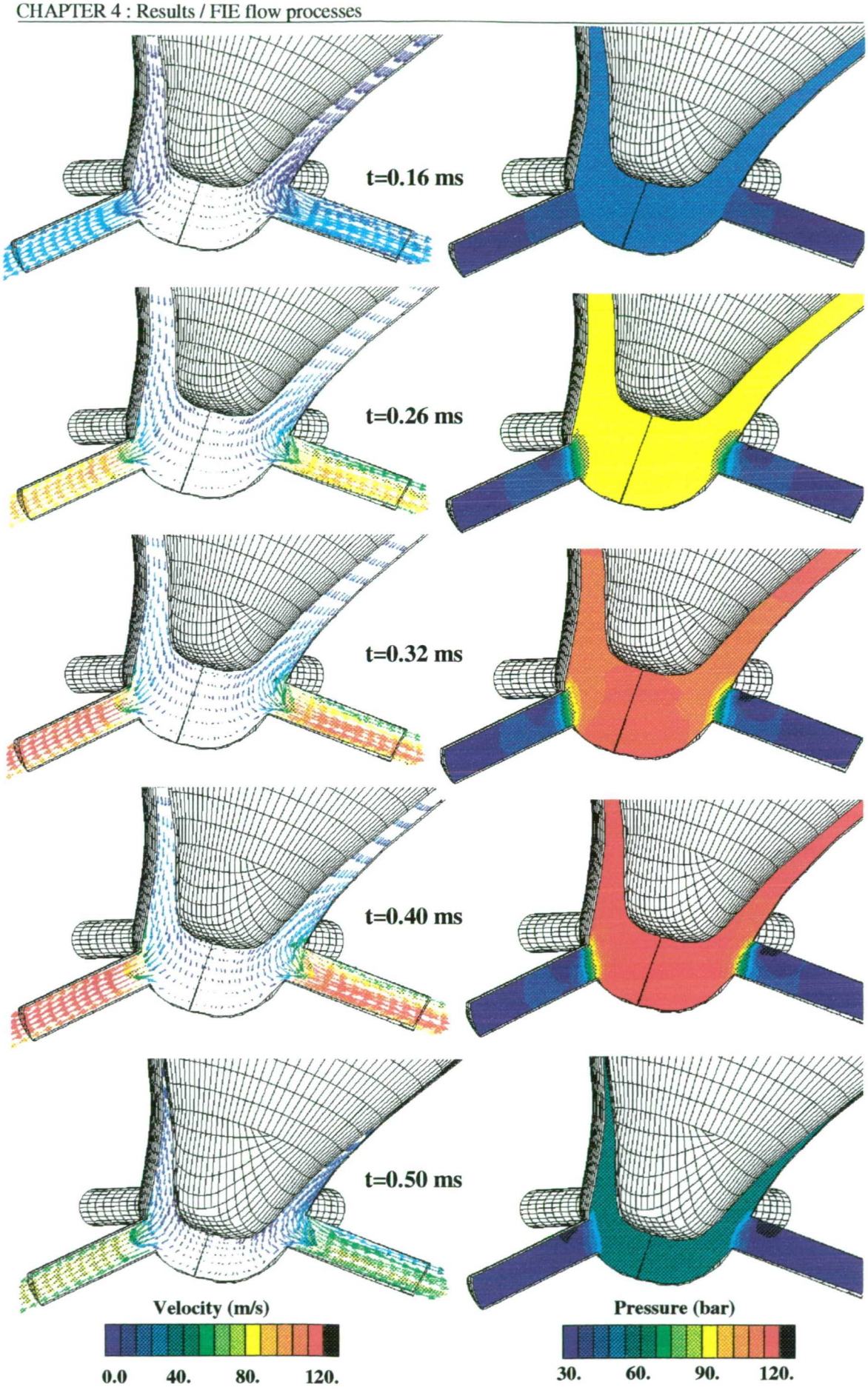

Figure 4–58 : Calculated velocity flow field and pressure distribution at t=0.16, 0.26, 0.32, 0.40 and 0.50 ms after the needle opening time on the two cutting planes

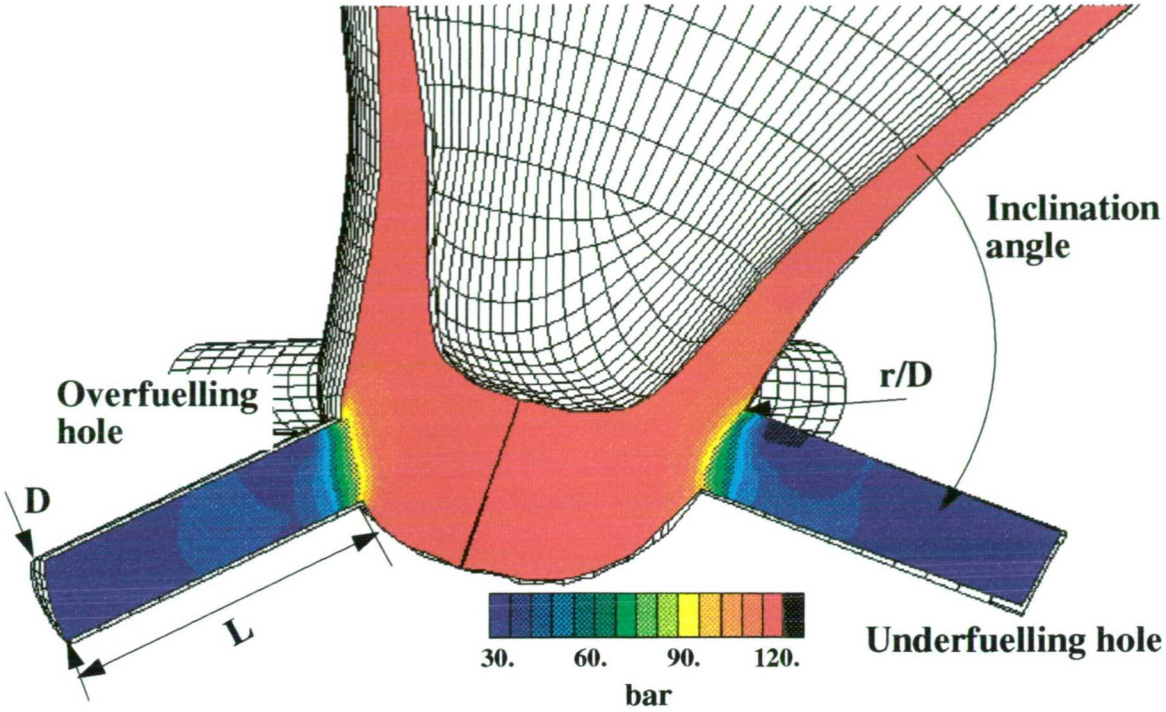

Figure 4–59 : Calculated pressure distribution inside the sac volume and the injection holes at the time of the onset of hole cavitation

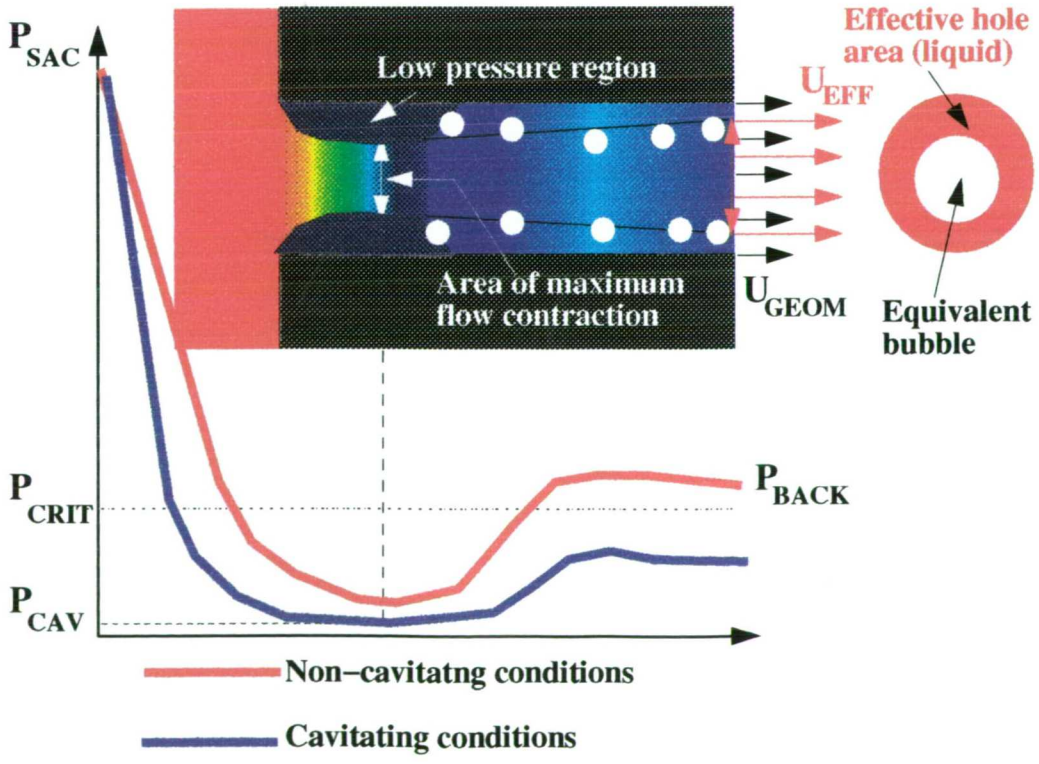

Figure 4–60 : Schematic representation of the 1–D hole flow model under cavitating flow conditions

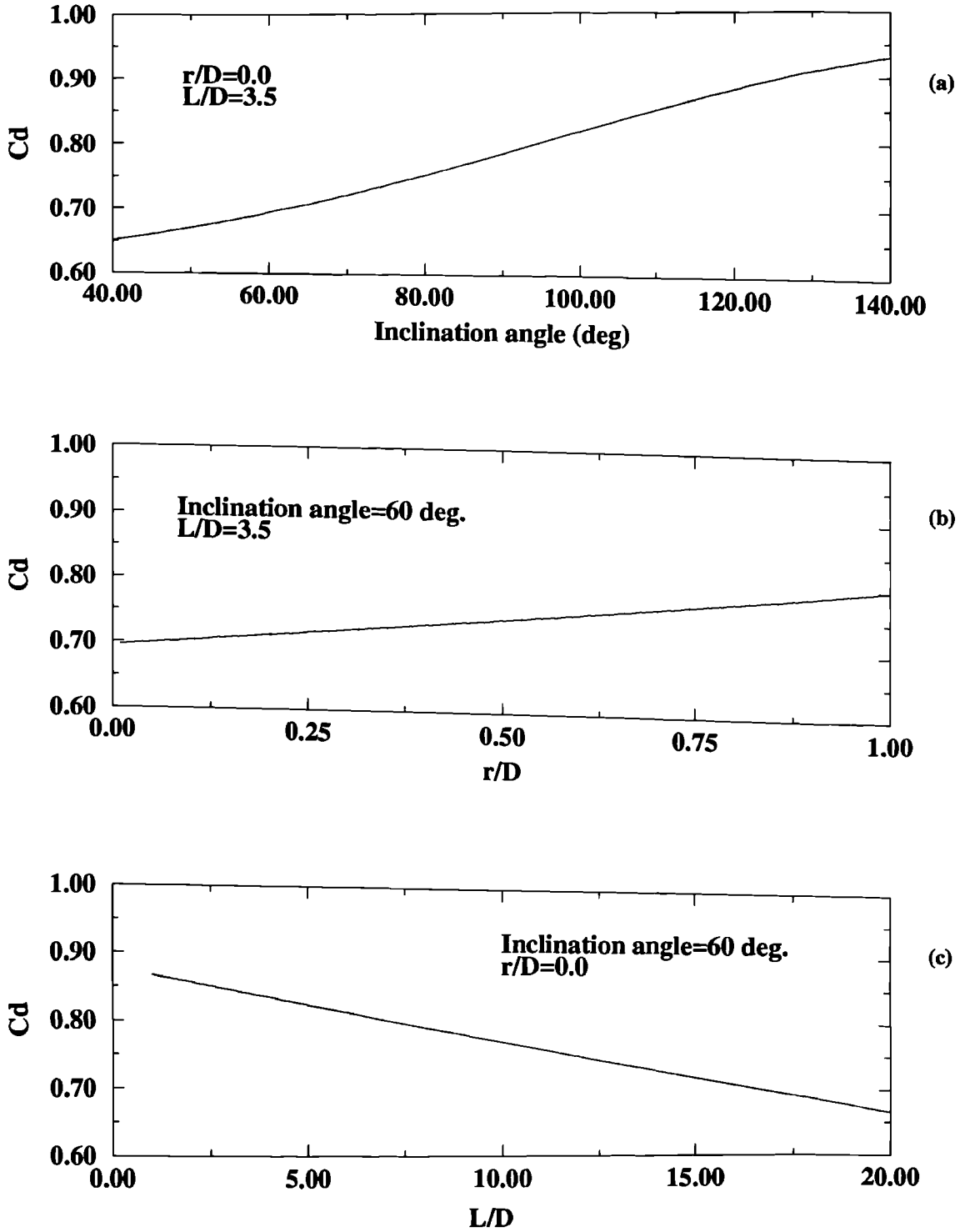

Figure 4–61 : Variation of hole discharge coefficient as a function of (a) hole inclination angle (b) hole entrance shape (r/D ratio) and (c) L/D ratio

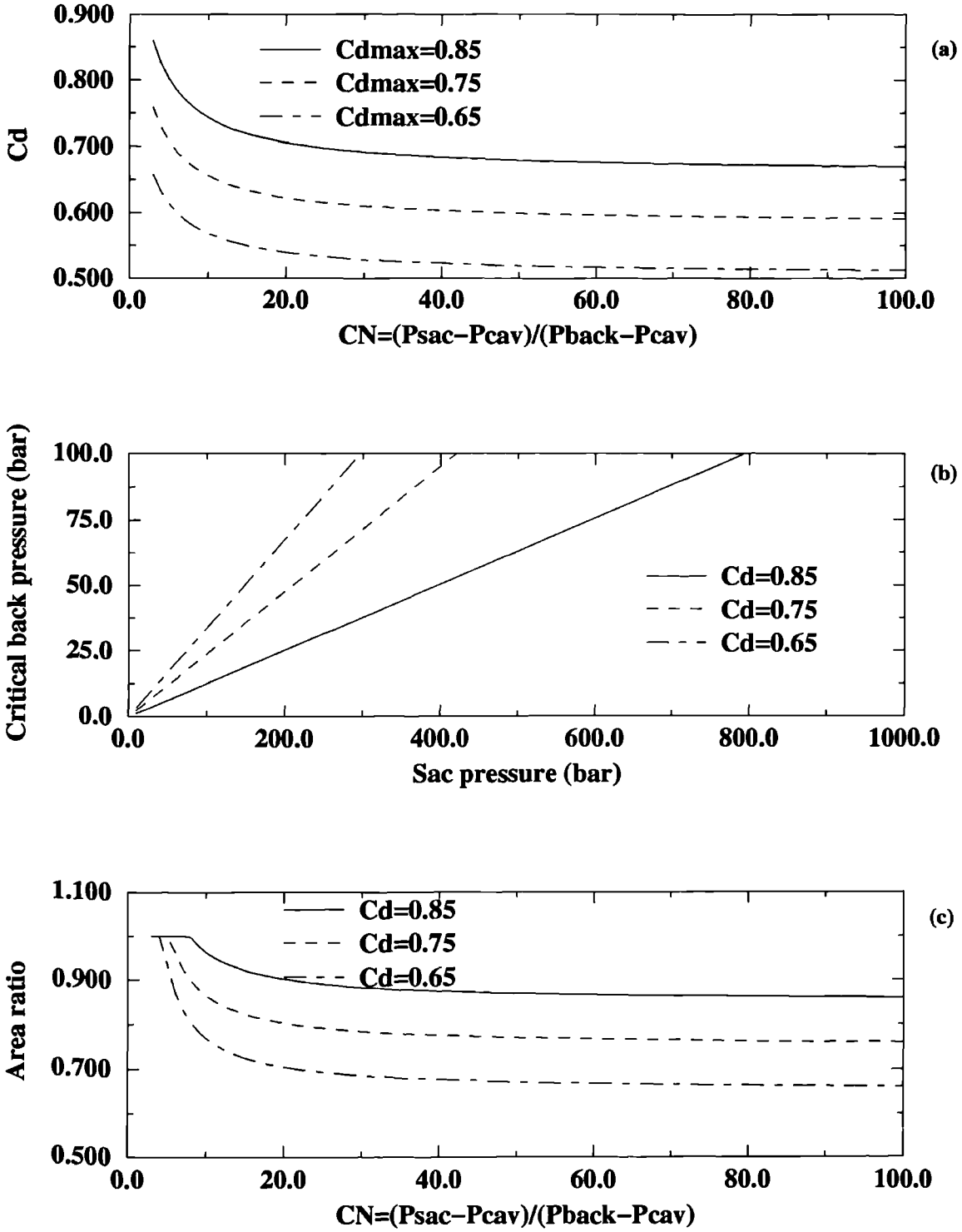

Figure 4–62 : (a) Variation of hole discharge coefficient with cavitation number (b) Critical cavitation pressure (c) variation of hole effective area as a function of cavitation number

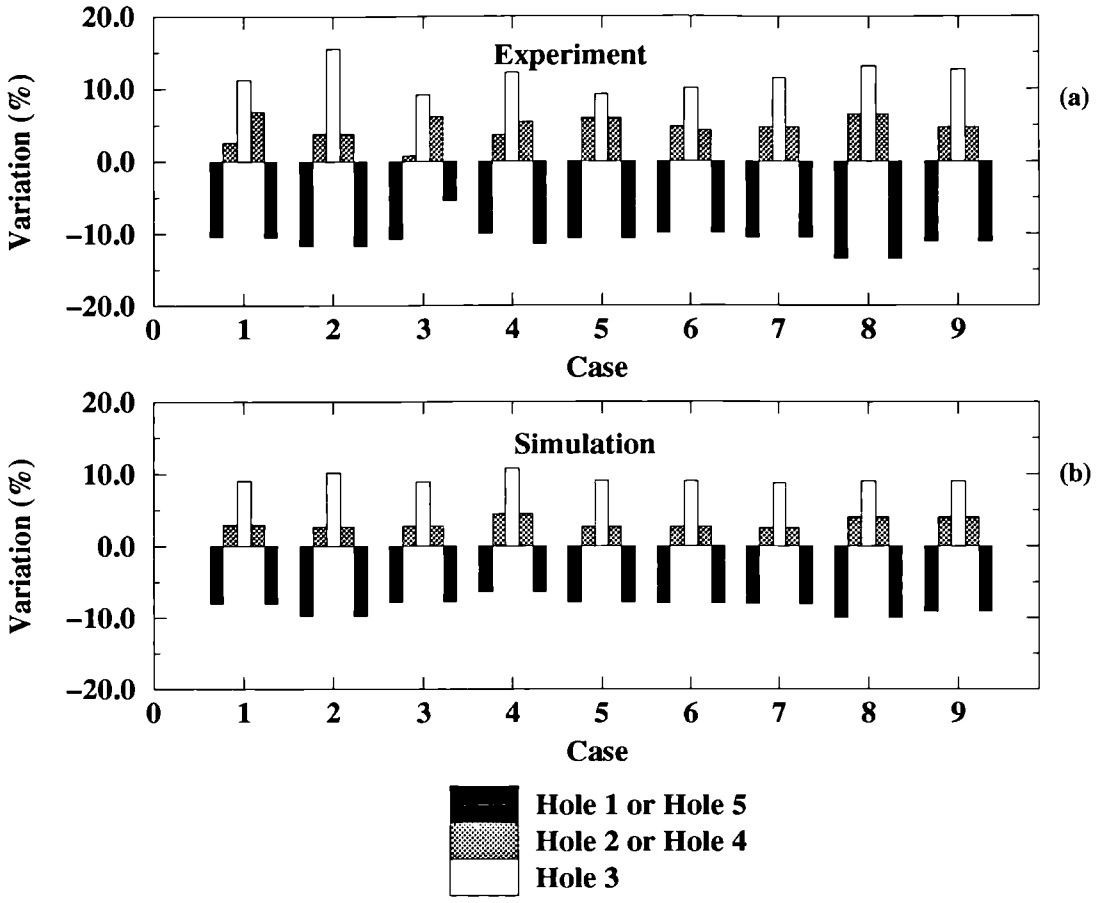

Case 1 : Pump speed 300 rpm, Lever position 0%
Case 2 : Pump speed 500 rpm, Lever position 20%
Case 3 : Pump speed 750 rpm, Lever position 15%
Case 4 : Pump speed 750 rpm, Lever position 50%
Case 5 : Pump speed 500 rpm, Lever position 50%
Case 6 : Pump speed 1000 rpm, Lever position 20%
Case 7 : Pump speed 1000 rpm, Lever position 50%
Case 8 : Pump speed 1500 rpm, Lever position 50%
Case 9 : Pump speed 2000 rpm, Lever position 100%

Figure 4–63 : Comparison between computational and experimental results for the total fuel injected from each of the injection holes. Pump speed from 300 to 2000 rpm and lever positions from 0% to 100%. (a) Experimental results (b) Calculations

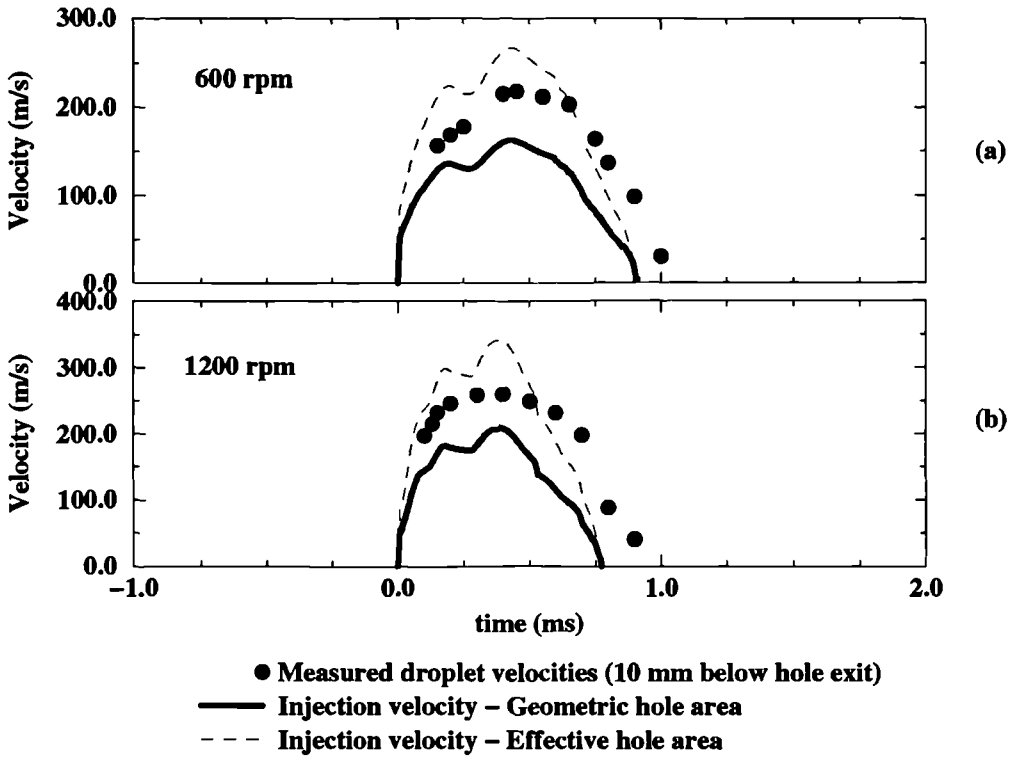

Figure 4–64 : Comparison between the measured droplet velocities 10 mm below the injection hole and the injection velocity based on both the geometric hole area and the effective hole area (a) Pump speed 600 rpm (b) Pump speed 1200 rpm

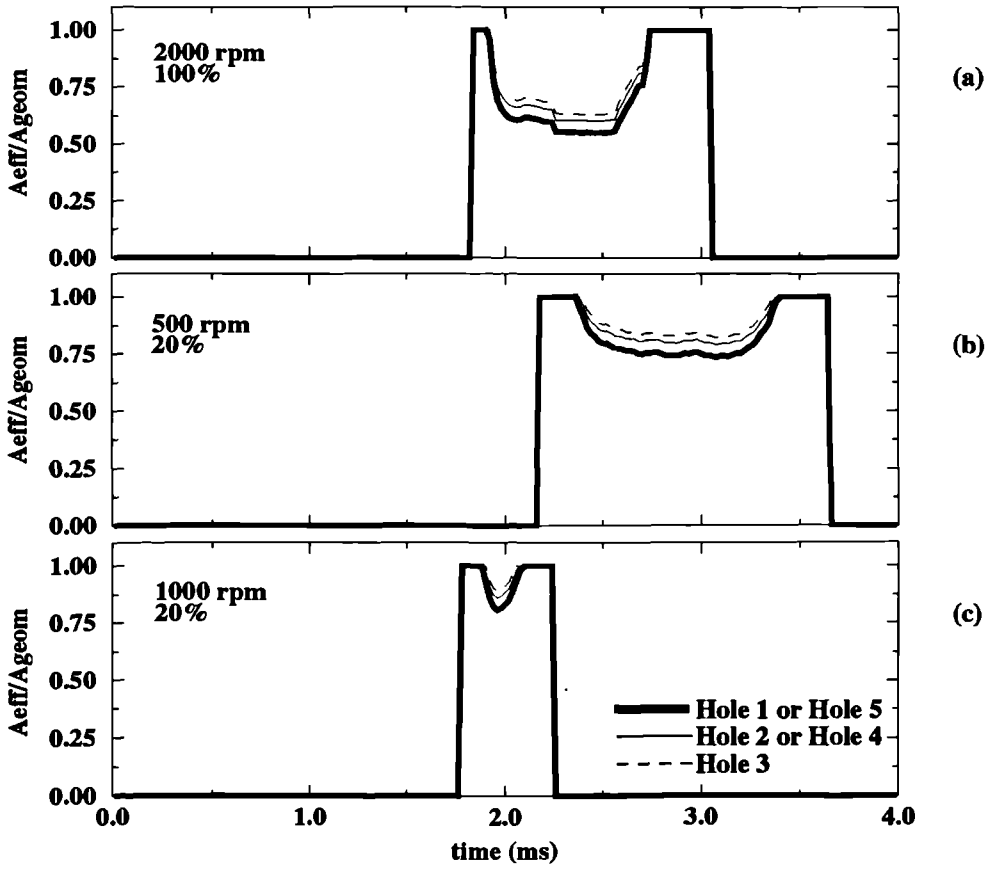

Figure 4–65: Calculation of the effective hole area for three different injection conditions and the three differently oriented injection holes (back pressure 30 bars) (a) Pump speed 2000 rpm, level position 100% (b) Pump speed 500 rpm, lever position 20% (c) Pump speed 1000 rpm, lever position 15%

CHAPTER 5

One has to pay a colossal amount of attention to accidental results because that's the way one often finds the right solution

B. Brecht

Results: Diesel Spray Processes

5.0 Introduction

This chapter describes the results obtained with the computer model simulating the development of diesel sprays; Table 5-1 summarizes the test cases examined which can be divided into three groups: free atmospheric diesel sprays, impinging atmospheric diesel sprays and in-cylinder diesel sprays. Figure 5-1 shows a schematic representation of the various test cases. The fuel injection system consists of a Bosch VE distributor-type pump, connected to Stanadyne pencil-type nozzles (5×0.22 mm in hole diameter) for the investigation of atmospheric sprays and to Bosch multihole inclined injectors (5×0.21 mm hole diameter) for the engine sprays investigation. On the same graph, the pressure distribution inside the FIE is shown (corresponding to the cam angle of the peak injection pressure), in order to illustrate the solution procedure. The injection conditions (flow rate per injection hole for inclined multihole injectors, effective hole area, hole turbulent kinetic energy and its dissipation rate, volume of cavitation bubbles) are the inputs required by the spray model which were provided by the FIE model presented in chapter 4. The test cases considered here, most of which have not been used previously for validation of other spray models, have allowed detailed validation of the model over a wide range of injection and surrounding gas conditions. In addition, they have allowed for the estimation of the relative importance of the various physical processes taking place during the spray development.

This chapter is divided into three sections. The first one investigates the development of free atmospheric sprays under both quiescent and cross flowing gas conditions, the second examines the diesel spray impingement process and the last one focuses on the development of diesel sprays injected from a multihole inclined nozzle inside the piston bowl of a DI diesel engine.

5.1 Free Atmospheric Diesel Sprays

5.1.1 Injection conditions - simulated geometry

Extensive experimental investigations have been reported in the open literature on the characteristics of free sprays injected either in quiescent or cross flowing environment under atmospheric conditions. Experiments at Imperial College by Chang (1993) and Cutter (1996) have provided information about the temporal and spatial droplet velocity and size distributions, as obtained with a phase Doppler anemometer (PDA). Comparison between computational and experimental results is performed here for injection conditions corresponding to pump speeds of 600 and 1200 rpm and lever position 50%. The fueling is approximately 4 mm^3 per hole, while the injection duration is approximately 0.8 ms. The hole orientation angle relative to the needle seat for all five holes has been given in Table 4-4; the calculated percentage difference from the above mean fueling value of the fuel injected from each hole has been described in the previous chapter (Figures 4-63 and 4-64). The specific spray examined here was injected from hole 4 which together with hole 3 represent the low fueling holes. The injection conditions, as calculated by the FIE model using as input the cam plate profile and the characteristics of the pump, the high pressure pipe and the nozzle, are given in Figure 5-2. In this figure the sac volume pressure, as calculated by the model, is also presented. As can be seen, the actual peak injection pressure is nearly 350 bars for the low speed case and 550 bars for the high speed case. The fuel injection rate is shown in Figure 5-2b for both test cases. The injection velocity based on both the geometric hole area and the calculated effective hole area is also plotted. As can be seen, the injection velocity based on the effective hole area can be 35% higher than its value calculated on the basis of the geometric hole area.

For these operating conditions detailed measurements for the spray characteristics were available. For quiescent gas conditions, comparison between the computational and the experimental results was made for the temporal variation of the centerline droplet SMD and the mean and rms axial velocity, at 10, 20, 30, 40, 50 and 60 mm below the injection hole as shown schematically on Figure 5-1. Also, the measured spatial distribution of the droplet mean axial velocity, droplet SMD and the number of droplets at the distance of 30 mm below the injection hole at 0.4, 0.7 and 1.0

ms after the start of injection were used for further validation of the model. Cross flowing conditions simulating the effect that the swirling motion present in the piston bowl of DI engines has on the spray development were also examined. The cross stream was introduced in the testing area from a 30 mm square shaped nozzle located 30 mm from the nozzle tip (figure 5-1). Injection took place on the plane of symmetry of the cross stream within the turbulent diffusion regime of the cross-stream. Two different cross-stream velocities, corresponding to 13.5 m/s and 22.5 m/s have been examined. In these two cases comparison between the computational and the experimental results was made in terms of the radial distribution of the droplet SMD and the droplet mean axial velocity at a distance of 30 mm below the injection hole.

In order to simulate the gas motion induced by the injected spray and by the cross air stream (or the in-cylinder flow field), the Navier-Stokes equations were numerically solved along the grids shown in Figure 5-3; these grids were used in the quiescent and cross flowing test cases investigated. For the quiescent gas conditions the grid consisted of 40×40×60 numerical notes non-uniformly distributed in the computational domain and occupying a volume of 60×60×180 mm^3 in the x,y,z directions, respectively, with the injection direction coinciding with the z-direction. The grid lines are dense in the area where injection takes place with a line spacing of 0.5 mm in all three directions. For the cases of cross flowing air, the numerical grid has been extended in the x-direction of the cross stream and the total volume occupied by the numerical grid is in this case 180×60×180 mm^3. The same grid spacing as for the quiescent conditions was used at the injection region. Before the start of injection, the steady-state gas motion of the diffusing cross stream was simulated. For all cases presented, entrainment boundary conditions have been used at the boundary cells.

The length of the control volume of the PDA system used to measure the droplet characteristics of the atmospheric sprays was 0.274 mm and the time window during which the droplets passing through the control volume were counted was 25μs; identical values have been used in the computational investigation. The experimental uncertainty in determining the start of injection (and as a result the spray characteristics) is of the order of 50μs and it is attributed to the response time of the Bosch injection rate meter used to measure the fuel injection rate.

As already mentioned, the number of parcels injected in the calculation is determined from the fuel injection rate per injection hole and the effective hole

diameter. However, during the injection period, the number of droplets becomes significantly large due to the liquid core atomization, the droplet secondary break-up and the impingement processes. To obtain statistically independent results, the total number of parcels is of the order of 1×10^5-2×10^5.

The liquid fuel used was a Shell calibration oil (4113) with density, surface tension and kinematic viscosity of 825 Kg/m^3, 20 mN/m and 2.46 mm^2/s, respectively at 25°C.

5.1.2 Simulation results

Having examined the injection conditions, we proceed to the description of the results obtained with the simulation model. The first physical process that strongly affects the spray characteristics is related to the atomization of the liquid jet emerging from the injection hole. As already described in chapter 3, three different mechanisms can be taken into account: the aerodynamic-induced atomization, the jet turbulence induced atomization and finally, the newly developed model for the cavitation-induced atomization; these are described schematically in Figure 5-4. At this stage it was considered important to compare the magnitude of the cavitation-induced atomization force relative to that of other forces responsible for the jet disintegration in the aerodynamic and jet turbulence-induced atomization cases. The following forces per fuel effective area acting on a cross section at the exit of the injection hole can be estimated from the following correlations:

F_{AERO}	=	aerodynamic (or gas inertia) force	$\rho_{GAS}U^2_{INJ}$
F_{TURB}	=	turbulent stress in the liquid jet	$\rho_{LIQUID}U^2_{TURB}$
F_{CAV}	=	cavitation-induced force	F_{TOTAL}/A_{EFF}

where ρ_{GAS} and ρ_{LIQUID} are the gas and liquid densities, respectively, U_{INJ} and U_{TURB} are the mean and turbulent injection velocities, A_{EFF} is the effective hole area and F_{TOTAL} is the cavitation-induced atomization force given from correlation (3-89) . Other smaller forces present in the disintegration process, such as liquid jet inertia, turbulent and viscous stresses in the gas and viscous stresses in the liquid jet are very small compared to the above forces and have been neglected. Assuming injection against a

back pressure and density of 30 bars and 11.0 kg/m^3, respectively, the above forces have been estimated as a function of the injection pressure and their values are presented in Figure 5-5a for a typical hole size and discharge coefficient of 0.2 mm and 0.75, respectively. As can be seen, for low injection velocities the aerodynamic force is the most important and co-exist with the turbulent stress force when the flow in the injection hole becomes turbulent. The latter force is relatively high even when cavitation is present in the injection hole; this is due to the increased level of turbulence in the injection hole which is taken into account through the correlation estimating the average hole turbulent kinetic energy as a function of the effective injection velocity. However, the cavitation-induced deformation force, as introduced here, seems to attain values much higher than the other two forces, and thus, it is expected to control the jet disintegration process under cavitating hole flow conditions.

Figure 5-5b shows the calculated from the cavitation-induced atomization model maximum droplet diameter as a function of the sac volume pressure for different chamber back pressures (1, 10, 30 and 50 bars) and a typical hole of 0.2 mm in diameter with a Cd_{max}=0.75. As can be seen, for injection pressures between the critical cavitation pressure and 1000 bars, the model predicts reasonable droplet sizes; this will be further clarified in the following section. For higher back pressures, the calculated maximum droplet size increases due to the smaller value of the cavitation number and, thus, the higher value of the hole effective area. In addition, the droplet size seems to become nearly constant for very large injection pressures which correspond to high values of the cavitation number and, thus, to nearly constant values of the hole effective area. It should be mentioned, however, that the value of the calculated maximum droplet size strongly depends on the hole diameter; for small holes, where cavitation initializes earlier and the effective hole area exhibits smaller values, relatively smaller droplets are expected to be formed than in larger holes.

For the specific injection conditions examined in this investigation (Figure 5-2), during the injection period and depending on the injection pressure, different flow regimes were numerically identified to occur in the injection hole. For injection velocities less than approximately 40 m/s the flow in the injection hole was non-cavitating and for this regime the liquid core disintegrates as a turbulent jet. The time until the injection velocity reaches this value corresponds to only a small fraction of the total injection period i.e. at the very early and the latest stages of injection. For most of

the injection period, cavitation is likely to occur in the injection hole; it should be reminded that injection takes place here under atmospheric conditions when the onset of cavitation occurs much earlier than in the case of injection into a diesel engine. Thus, it is expected that the cavitation-induced atomization represents the dominant factor determining the disintegration of the liquid jet emerging from the nozzle for both test cases examined in the present investigation.

Prior to the comparison of the computational and experimental results, it is useful to present information about the global spray structure as calculated using two different spray sub-models. In the first case, the spray sub-model accounts for the effects of hole cavitation on both the injection velocity and the droplet size. Results are also presented for the case when cavitation effects are neglected; the injection velocity in this case is based on the geometric hole area and the turbulence-induced atomization model was used with the droplets uniformly distributed within the spray cone independent of their size.

Figure 5-6 shows the spray development at three different times from the start of injection (0.4, 0.7 and 1.0 ms) for a pump speed of 600 rpm; the color of the droplets is representative of their size while the size of the spheres plotted to represent the droplet parcels, gives also an indication of their size. In Figure 5-6a the structure of the cavitating spray is shown and in Figure 5-6b the non-cavitating one. As can be seen for the cavitating sprays, larger droplets are found close to the injector and as the spray develops downstream larger droplets are concentrated close to the spray axis with much smaller droplets present at the periphery of the spray. Close to the injection hole the droplets have an average size of about 80 microns which is less than half the effective hole diameter; this results from the cavitation-induced atomization model. It is clear that the break-up length, as calculated by this model, is less than 1 mm when cavitation occurs, which means that the liquid core disintegrates immediately after its exit from the hole. The droplet size distribution within the spray cone angle is a result of the radial distribution model employed; according to this model, the possibility of finding a droplet away from the spray axis is inversely proportional to its mass. Thus, larger droplets are usually concentrated close to the spray axis which has an effect on the calculated droplet velocities. However, the non-cavitating sprays exhibit a completely different structure with much lower penetration, larger droplet sizes and droplets with no preferential position within the spray cone angle.

Figure 5-7 provides more detailed information about the spray structure as calculated using the cavitation-induced atomization model. In this figure, four different groups of results can be seen, each of them presenting the time development of the plotted quantity at 0.4, 0.7 and 1.0 ms after the start of injection for the low pump speed case: Figure 5-7a gives the mean droplet velocity, Figure 5-7b presents the droplet deformation, Figure 5-7c refers to the droplet mass density distribution and finally Figure 5-7d shows the droplet number density distribution. The mean droplet velocities are higher close to the spray axis and decrease at the periphery of the spray; this is attributed to two different factors: the first one is related to the fact that the larger droplets are found close to the spray axis and the second is due to the fact that the induced by the spray injection gas velocity, shown in Figure 5-8, is much higher at the spray axis rather than at the periphery of the jet. As a result, droplets located at the center of spray exhibit lower drag and also travel faster due to their larger inertia.

The color of the spheres plotted of Figure 5-7b corresponds to the droplet deformation as calculated by the droplet secondary break-up model (correlation (3-114) . It can be seen that the droplets close to the nozzle are highly distorted, exhibiting values up to 12; these droplets break-up in the catastrophic break-up regime. In the center of the spray, the average droplet deformation becomes slightly smaller, mainly due to the reduced relative velocity between the droplets and the gas. Less distorted droplets are found at the periphery of the spray where, as already mentioned, the smaller droplets are present. In this area, the break-up mechanism is the vibrational one while in the center of the spray the bag and the stripping break-up modes are the dominant. It can be also seen that at the time of 0.7 ms highly distorted droplets are found in groups clearly separated between each other, which, as will be seen later on, has an important effect on the predicted spray structure when a large number of parcels is used. Finally, at 1.0 ms after the start of injection, the droplets have smaller sizes, and their shape is close to the spherical as the small values of their deformation indicate.

Two more points, not usually examined in the past, require special attention. These are related to the droplet mass density and droplet number density distributions during the spray development. As can be seen in Figures 5-7c and d, spray is much more dense close to the spray axis and becomes dilute at the periphery of the spray. The contours of the droplet number density distributions are affected not only by the modulation in the injection velocity profile, but also from the break-up mechanism of

the moving droplets. As can be seen, the number of droplets is very small close to the injector and increases gradually downstream the injection hole.

Figure 5-8a shows the induced by the spray injection gas velocity field while Figure 5-8b shows the mean relative velocity between the liquid and the gas phase. It can be seen that the higher differences exist at the central spray region while at the periphery of the spray, a special vortex structure is formed. It should be remained that individual droplets, would 'see' different gas velocities than this mean value plotted, depending on their velocity; however, this figure shows how the air entrainment develops at the periphery of the spray. Many authors in the past have attributed to this structure of the air entrainment the 'Christmas tree' structure of the sprays experimentally identified in numerous investigations. However, as it will be demonstrated in the following paragraph, phenomena related to the disintegration and break-up of the moving droplets have been found to have a stronger influence on this specific spray structure. Figure 5-8c shows the turbulence kinetic energy distribution; the higher gas turbulent kinetic energy values are found on the spray axis, which implies that droplets located at this area will be affected by the turbulent flow field, through the turbulent dispersion model, and they will eventually 'see' a relatively higher gas velocity. However, droplets at the periphery of the spray are not expected to be influenced by the gas turbulence.

In order to examine in detail the effect of the secondary break-up mechanism of the droplets on the spray structure the following analysis is performed. As already described in chapter 3, six different modes of droplet secondary break-up are taken into account; these are schematically shown in Figure 5-9. In this model, the break-up time, droplet deformation and droplet drag coefficient during the deformation process for all six break-up regimes are calculated with the aim of satisfying experimental relationships given in chapter 3. This model allows more than one parcel to be formed after the break-up time of each droplet; thus, bimodal distributions resulting during the stripping break-up process can be represented. This model is combined with another model calculating the droplet size distribution of the formed droplets based on a maximum entropy formalism. Having determined the SMD of the formed droplets, their size was randomly selected from the calculated distribution function; the latter depends on the local droplet Weber number and the maximum stable diameter of the formed droplets. Figure 5-10 shows a typical result of the calculated distribution function for four different Weber

numbers, which correspond to four different break-up regimes (vibrational, bag, stripping and catastrophic). The calculated size distribution is qualitatively in agreement with most of the reported experimental observations on single droplet break-up. In the vibrational break-up regime, approximately two droplets of similar size are formed while five to six droplets with significant differences in their size can be formed in the bag regime. For the case of stripping break-up, the size of the parent droplet has been excluded from the calculated distribution. The curve shown represents the size distribution only of the small droplets generated from the liquid stripping from the boundary layers formed in the parent droplet. Finally, in the case of catastrophic break-up the model calculates a large number of droplets with size of the order of 0.1 to 0.2 of the initial droplet size. In order to identify how important the effect of the bimodal distribution occurring during the stripping break-up mechanism is, the number of break-up types occurring during the spray development was calculated. The results are presented on Figure 5-11 for injection into both quiescent air under atmospheric conditions and engine conditions. At two different times from the start of injection, approximately 50-60% of the droplets break-up according to the stripping break-up regime if the cavitation-induced or the jet turbulence-induced break-up models are employed. Thus, it is expected that the differences in mass, size and velocity distribution between the formed and the parent droplet could result in non-uniform droplet number distribution within the spray. This is due to two factors: since the velocities of the formed droplets depend on the their size (smaller droplets have lower velocities), a large number of small droplets will remain behind the large droplet. Also, the larger droplets present on the spray axis will penetrate faster than the droplets present at the edges of the spray. Figure 5-12 shows the combined effect of the injection process and the modeling of bimodal droplet size distribution on the predicted spray structure. In the first set of calculations referred as [model 1], the number of droplet parcels injected every time step was kept constant during the injection period and, in addition, bimodal distribution resulting during the droplet secondary break-up was not taken into account. In the second set of calculations referred as [model 2], the number of injected parcels was considered to be proportional to the fuel injection rate and a bimodal distribution was assumed. As can be seen, a spray structure resembling the frequently observed 'Christmas tree' structure could be predicted when the combined bimodal distribution model and injection rate variation model were used. It is also interesting to note the

effect of the modulation of the injection rate profile. According to Figure 5-2, the injection velocity exhibits two peaks which are attributed to the pressure waves developing within the injection system; the first is at 0.3 ms after the start of injection and the second at 0.6 ms. Looking at the spray structure of Figure 5-12b at the time of 0.6 and 0.9 ms two different groups of droplets can be identified with a narrower region between them; a resent study by Chaves et.al. (1996) has showed evidence of similar spray structure. For the specific calculation of the spray structure, approximately 5×10^5 droplet parcels were used. This huge number of droplet parcels used also implies that the results obtained with the simulation model strongly depend on the number of the droplet parcels used. This becomes clear by comparing the spray structure of figure 5-12 and 5-6a; in the latter one only 10000 droplet parcels have been used which is approximately 50 times smaller than in those of figure 5-12. Calculations have been also found to depend on the grid resolution. However, it has to be reminded that the Eulerian-Lagrangian method employed collapses when one computational cell is completely filled with liquid (which is also equivalent to void fraction values equal to zero), which is also a function of the total fuel injection quantity; the problem can become significant at very high loads and for injection under high back pressures were the spray tip penetration significantly decreases compared to the that of atmospheric sprays. Thus, special attention has to be given to that point during the solution procedure. Usually, a compromise for the smaller possible grid size to be used has to be taken. Results presented by other numerical investigations on diesel sprays (Kraji (1995), Clerides (1997)) have come to similar conclusions.

5.1.3 Model validation

Having identify the basic spray characteristics and the effect of cavitation and droplet secondary break-up on the general spray structure, we can now proceed to a more detailed spray investigation by comparing calculations with available point measurements. For the comparison between the computational and the experimental results all three aforementioned liquid jet atomization models have been used in order to examine how well or not they predict the experimental data. In all of them, the effective injection velocity has been used since the velocity based on the geometric hole area is much smaller (approximately 100 m/s at the peak injection rate) than the measured

droplet velocities close to the nozzle exit; calculations using the velocity based on the geometric hole area can give unrealistic predictions for the droplet velocities near the injector and further downstream.

Figure 5-13 shows the comparison between the computational and experimental results for the droplet mean and rms axial velocities at various distances from the hole exit plane along the spray centerline for the low pump speed test case. The closer to the nozzle exit measurement point is at 10 mm; the comparison between measurements and predictions at this location has been used for the evaluation of the various atomization models, since up to that distance atomization is the dominant physical process determining the droplet size. As can be seen, close to the injection hole the mean droplet velocities are very well predicted; this implies that the calculated effective injection velocity is close to the actual mean injection velocity. All atomization models give similar results up to that distance of the 10 mm, since the gas density effects are very small for injection under atmospheric conditions. Thus, any differences on the predicted droplet sizes do not have any significant effect on droplet deceleration. Moving further downstream, the predictions are still close to the measurements although some differences between the various models can be identified. Calculations using the aerodynamic-induced atomization model seem to give larger velocities; this results from the larger droplet sizes calculated by this model. Another interesting result is the magnitude of the droplet rms velocity; this is approximately 10-15% of the mean droplet velocity, implying that even very small droplets formed during the spray development period can still have large velocities. Also, turbulence effects do not seem to be dominant in this type of flow mixing environment; the spray momentum and its exchange with the surrounding gas play the dominant role on the spray dispersion under atmospheric conditions. Figure 5-14 shows the comparison between the computational and the experimental droplet velocities for the test case of the high pump speed. Similar conclusions to the lower pump speed case can be drawn.

Figure 5-15 shows the prediction of the droplet SMD at the same distances from the injection hole as in Figures 5-13 and 5-14; here the effect of cavitation on the jet disintegration process becomes more clear. Classical atomization theories taking into account the aerodynamic-induced atomization (or Weber number effects) fail to predict the liquid core disintegration mechanism since these theories calculate a break-up length of approximately 15 mm for the given injection conditions. Thus, they cannot predict

the much smaller droplet sizes measured at 10 mm from the injection hole. Even further downstream, very large droplets are found on the spray axis which implies that the various secondary break-up models cannot capture the spatial and temporal spray structure even at large distances from the injection hole, as long as the initial jet atomization process is not accurately estimated. The turbulence-induced atomization mechanism gives much smaller droplets than the previous model; also the calculated break-up length is much smaller. However, the calculated droplet sizes remain almost double the measured ones. Much better results can be achieved if the cavitation-induced atomization model is employed. As can be seen, at the closer to the nozzle distance at which measurements are available the calculated values are close to the experimental ones. This is also reflected at the other measurement points where predictions are in satisfactory agreement with the experimental data. The droplet size decreases with distance from the injection hole which is attributed to secondary droplet break-up effects.

Special emphasis should be given to the shape of the temporal profile of the droplet SMD during the injection period. Focusing at the 10 mm distance from the nozzle, it can be argued that the maximum of the droplet SMD corresponds to the maximum of the droplet mean axial velocity and then, as the droplet velocities decrease (corresponding to the lower injection velocities), the droplet SMD also decreases. This seems to be in disagreement with the usually adopted hypothesis relating the higher injection velocities with the formation of smaller droplets (due to higher Weber numbers). A possible explanation for this can be given by means of the cavitation-induced atomization mechanism. The higher the degree of cavitation in the injection hole, the more severe is the collapsing of the bubbles and the larger the spray angle. This means that the smaller droplets are deflected further away from the spray axis (due to their smaller inertia) leaving the larger droplets in the center. The time of the maximum velocity occurs approximately at 0.35 ms after the start of injection. From that point onwards, smaller droplets seem to pass through the measurement volume, and at the latest stages of injection smaller droplet sizes are calculated in agreement with the experimental data; it should be noted, however, that these droplets have been formed earlier during the injection period. The smaller droplets decelerate very quickly compared to the larger ones and pass through the control volume after a considerable time. Thus, the temporal profile of the SMD does not actually relate smaller droplets to

smaller injection velocities. It is mainly the combined effect of a time delay (affected by both the calculated droplet size and the air entrainment) and the bubble collapsing mechanism together with the radial distribution of the droplets in the spray cone angle. It is also interesting to note that for the case of the higher pump speed (Figure 5-16), the turbulence-induced atomization model gives results close to the cavitation-induced atomization model. As can be seen in Figure 5-2, the difference in the injection velocity calculated on the basis of the effective hole area and the geometric hole area is larger for the case of the higher pump speed. Although the injection velocity for this case is approximately 80m/s bigger than the injection velocity at the lower pump speed, the measured droplet centerline SMD is approximately 20 μm larger at 10 mm from the hole exit. This is predicted by the cavitation-induced atomization model and it is attributed to the disintegration mechanism of the liquid jet. It is possible that for higher levels of cavitation, the smaller droplets are deflected away from the spray axis leaving behind them the larger ones. However, due to higher injection velocity in this case, the turbulence-induced atomization predicts smaller droplet sizes than in the previous case. This conclusion confirms that the predictions based on both aerodynamic and jet turbulence-induced atomization models can not represent the jet disintegration mechanism under cavitating hole flow conditions.

Figures 5-17 and 5-18 show the estimated average droplet size obtained with a Malvern particle sizer for the low and high pump speed test cases, respectively; this technique gives an average droplet size of all the droplets passing through the control volume, which is a 9 mm diameter cylindrical area extended through the whole spray cone. It is interesting to note that at the distance of 30 mm from the injection hole, all three different sets of calculations give similar predictions. The value of the average droplet SMD is approximately 7-15 μm mainly due to the effect of the secondary aerodynamic-induced droplet break-up. The critical Weber number below which no break-up seems to occur is usually accepted to be 6-12 (depending on the liquid physical properties). For the given injection and surrounding gas conditions, this value corresponds to the above droplet sizes of 7-15 μm as experimentally and computationally verified. Thus, it can be argued that independent of the details of the atomization process and gas entrainment effects, the model predicts well the average droplet size. This is also the basis of most of the existing phenomenological spray models which simply use correlations for the droplet SMD, ignoring the aforementioned

effects; however, at distances closer to the injection hole, these effects play an important role in the calculated droplet size. Since spray penetration distances of practical interest are less than 25-30 mm from the injection hole (this is a typical distance at which wall impingement occurs in a passenger car DI diesel engine), the accurate calculation of the droplet size close to the injection hole is of considerable importance for the estimation not only of the deceleration and evaporation rates but also of the pre-impingement droplet characteristics upon which the predictions of impingement models depend.

Figure 5-19 shows the comparison between the computational and the experimental results for the radial distribution of the droplet SMD, the droplet axial mean velocity and the number of droplets 30 mm below the injection hole. These data are used for the validation of the model of the droplet radial distribution within the calculated spray cone angle resulting from the atomization process. Existing models usually distribute uniformly the droplets in the spray cone angle, independently of their size. Calculations with this model have been made in order to identify how closely they predict the experimental data. Figure 5-19a shows the comparison between computational and experimental data for the mean axial droplet velocity at three different time steps from the start of injection (0.4 ms, 0.7 ms and 1.0 ms), while Figure 5-19b shows the prediction for the droplet SMD at the same points. As can be seen, the experimental data confirm that the larger droplets are found close to the spray axis and this droplet size distribution has an important effect on the droplet velocities since smaller droplets decelerate faster than larger ones and, thus, droplets with larger velocities are located on the spray axis and with smaller at the spray periphery. This is also due to the much higher induced gas velocities present on the spray axis, which is a results of the spray mass and momentum distribution within the spray cone angle. Predictions with the model distributing uniformly the droplets within the spray cone angle has failed to predict the experimentally identified spray structure. In order to capture these effects, it has been assumed that the possibility to find a droplet close to the spray axis is proportional to its mass (thus, this mechanism is represented in a stochastic form in agreement with the statistical approach used for the spray simulation). This type of distribution actually assumes that whatever the details of the atomization process are, the same force (resulting from the bubble collapsing) is acting on the formed droplets with a direction normal to the direction of injection. Thus, according to Newton's second law, the radial acceleration resulting from this force will be larger for

smaller droplets. As can be seen (Figure 5-19), this model gives much better predictions. The different size of the droplets at the three time steps at which experimental data are available, results from the differences in the injection velocity and the time required for the droplets to pass through the control volume. For example, at 1.0 ms after the start of injection, smaller droplets exist on average. This is due to the time required for these droplets, which were formed earlier in the injection period, to pass through these points since the larger of them have already passed through the control volume leaving behind them the smaller droplets. Figure 5-19c shows the comparison between the computational and the experimental estimated radial distribution of the number of droplets which confirms that most of the droplets are located in the center of the spray. It should also be mentioned that the three-dimensional details of the flow in the sac volume and the injection hole can affect the spray characteristics. Any asymmetries present in the measured radial distribution of the number of droplets, droplet size and droplet velocity are expected to be related to the details of the velocity profile at the exit of the injection hole.

Figure 5-20 shows the comparison between the computational and the experimental results for the radial distribution of the droplet SMD and the mean axial velocity at 30 mm below the injection hole and at 0.7 ms after the start of injection, for the two cross flowing cases investigated. It is clear that the effect of the cross flow is to sweep the smaller droplets in the direction of the cross stream leaving behind the larger ones. A more uniform distribution is now formed compared to the case of quiescent flow. Three different sets of computational results are presented in this figure. In all of the plots, the cavitation-induced atomization model has been used together with the radial droplet distribution model. However, different mechanisms representing the droplet secondary break-up were employed; first a model reported by Reitz and Diwakar (1987) was used which takes into account only the bag and stripping break-up while the droplet size after the secondary break-up is set equal to the maximum stable diameter (model 1). The same assumption was also adopted in the model reported by Pilch and Erdman where all six break-up regimes mentioned previously are taken into account; the break-up time and the maximum stable diameter are the parameters calculated for each break-up regime (model 2). The last mechanism considered here is the model developed during the present investigation and described in chapter 3. According to this model, the break-up time, the droplet deformation and the droplet drag coefficient during the

deformation process for all six break-up regimes are calculated with the aim of satisfying experimental relationships described in chapter 3. This model was combined with the model calculating the droplet size distribution of the formed droplets based on a maximum entropy formalism. As can be seen, predictions with this model seem to be closer to the experimental values for both cross flow velocities.

5.1.4 Evaporating diesel sprays

At this point it was considered useful to investigate the development of evaporating diesel sprays, since these are of the major practical interest. Injection was assumed to take place with injection conditions corresponding to that of the 600 rpm pump speed case into a chamber with pressure and temperature of 30 bars and 800 K, respectively; the temperature of the injected liquid was assumed to be 300K and its physical properties were assumed to be those of $C_{12}H_{26}$. In addition to the previous spray sub-models investigated, a droplet evaporation model was taken into account calculating the heat transfer from the hot gas to the liquid droplets and the mass transfer from the evaporated fuel to the surrounding gas. The specific model used for this particular case calculates a uniform droplet temperature; results from other evaporation models will be investigated in a following section of this chapter for injection into the piston bowl of a DI diesel engine.

Before investigating the effect of the surrounding conditions on the droplet characteristics, results on the heat and mass transfer between the two phases are presented in Figure 5-21. Figure 5-21a shows the temperature of the surrounding gas at 0.2, 0.4, 0.7 and 1.0 ms after the start of injection. As can be seen, the gas is gradually cooled with the lower temperatures at the central region of the spray; this is due to the fact that most of the liquid mass is concentrated in this region. Figure 5-21b shows the fuel vapor concentration expressed in terms of percentage of the total mass of the gaseous phase. As can be seen while the liquid is gradually evaporated, the fuel vapor is also convected by the motion of the gas resulting to a higher liquid vapor penetration compared to that of the liquid droplets. This can be seen by comparing the contours of previous figure to those of Figure 5-21c which shows the liquid mass distribution at the same time from the start of injection as for the other two figures 5-21 a and b. It is also interesting to note that the evaporated fuel occupies more space not only in the axial but

also in the radial direction resulting mainly from the turbulence mixing between the surrounding gas and the evaporated fuel.

In order to investigate the effect of the fuel properties, which are a function of its temperature liquid, on the droplet characteristics, Figures 5-22 and 5-23 have been selected for presentation. Among the other liquid physical properties, the surface tension is an important one, since its value strongly affects the Weber number of the moving droplets. As the droplets are heated, their surface tension becomes smaller and reaches zero values when the temperature of the liquid reaches the critical temperature which for the examined liquid is approximately 660 K. Figure 5-22 shows the droplet deformation of the representative parcels used in the calculation as a function of their temperature and their size (shown with color of the spheres plotted) at 0.2, 0.4, 0.7 and 1.0 ms after the start of injection. As can be seen, droplet deformation exhibits two peaks which correspond to two different type of droplets. Large droplets with temperatures equal to the injection temperature seem to be highly distorted which is due to their large injection velocities. On the other hand, it seems that there is a number of very small droplets which have temperatures close to the critical temperature of the liquid and which also exhibit very large deformation values. As explained above, for these droplets the Weber number increases due to the decrease of their surface tension, which gives rise to higher deformation values. From this set of plots it can be also seen how the number of droplets with higher temperatures increases during the injection period.

Figure 5-23 compares the deformation of the droplets of the evaporating spray relative to that of the atmospheric spray investigated in the previous section. This time, the droplet deformation of the representative parcels present in the calculation has been plotted as a function of their velocity with color representing again their size. It is evident that while in the non-evaporating spray the droplet deformation is a function of their velocity only and gradually decreases as the spray decelerates, in the evaporating spray the droplets seem to exhibit more deformation. It is also interesting to note that the droplet deceleration is much faster when injecting into the high pressure environment due to the increased drag force of the moving droplets. Also, as it should be expected from Figure 5-5b showing the size of the droplets resulting from the cavitation-induced atomization process, when injecting into higher back pressure, the flow in the injection hole becomes less cavitating and as a result relatively larger droplets are formed; however, these droplets gradually become small due to their evaporation. From this

investigation it has become evident that special attention has to be given to the deformation process of the droplets under evaporating conditions since that would affect not only their velocities but also the interface surface area between the droplets and the surrounding gas. Another point that was also investigated, reveals how important the small droplets are during the evaporation process. Figure 5-24a shows the fuel injection history of the injected spray together with the total fuel remaining in liquid form and the total fuel evaporated as a function of time. For this particular injection conditions, the probability density function of the droplets present in the calculation is plotted in Figure 5-24b. As can be seen, much more small droplets exist while their number decreases as the their size increases. Despite that, the total mass carried by these droplets follows the opposite trend; this is also plotted on the same figure and it due to the fact that the liquid mass is proportional to the 3rd power of the droplet diameter. However, Figure 5-24c indicates that although the large droplets carry most of the mass in liquid form, the fuel evaporated results not from these large but at the same time cold droplets, but from the smaller ones. As can be seen, the droplets that practically contribute to the fuel evaporation are those with size smaller that 5 μm.

5.2 Impinging Atmospheric Diesel Sprays

5.2.1 Injection conditions - simulated geometry

Following the investigation of the free spray characteristics, an impingement test case was examined. At the distance of the 30 mm below the injection hole, where the droplet size and velocity distributions were estimated for the free spray, a flat plate was introduced, in order to examine the characteristics of impinging sprays. The selected distance between the injection hole and the flat plate is typical of piston bowls in small DI diesel engines but it is also large enough for the liquid core to be fully atomized ensuring that only droplets and not ligaments impinge on the wall. Experimental results reported by Chang (1993) include the temporal variation of the droplet SMD and the tangential velocity component at several points in the region of the ejected from the wall droplets. The points selected for comparison between the computational and the experimental results, also shown in Figure 5-1, are at 0.5 mm and 5 mm above the flat plate and at 6 mm, 10 mm and 15 mm along the radial distance from the spray axis of

symmetry. Measurements on the 0.5 mm above the flat plate points are used for the validation of the impingement model itself, while droplet characteristics at the 5.0 mm from the wall measuring points are mainly affected by the head vortex formation and its development and interaction with the ejected from the wall droplets; the pump operating conditions are the same as for the low-speed free spray test case. The results that will be presented correspond to low temperature wall conditions for a spray injected into a quiescent environment.

The numerical grid, which is shown in Figure 5-25 consists of 60×60×40 grid nodes occupying a volume of 180×180×50 mm^3. The same grid spacing as for the free sprays was used at the injection region. The numerical lines are also non-uniformly distributed over the flat plate and the grid spacing is 0.3 mm for the grids close to the wall. The same fuel (Shell oil) as for the free spray investigation was used and the measurements were performed using the same PDA system having identical settings as for the free spray investigation.

5.2.2 Simulation results

For droplet impingement on a low temperature wall, three hydrodynamic regimes are more likely to occur, as described in chapter 3; these are the rebounding, the spreading and the splashing regimes and are shown schematically in Figure 5-26. The parameters influencing the outcome of a single droplet impingement are the wall conditions (dry or wet, relative wall roughness) and the impinging droplet characteristics which are expressed through the Weber number. In addition to the above factors which have been extensively discussed in chapter 3, when a spray impinges on a wall, the presence of the other droplets as well as the formation of a gas motion parallel to the wall, which is usually referred to as 'head vortex' are additional factors affecting the spray droplet characteristics.

Figure 5-27 shows the development of the spray impinging on the flat wall at three different time steps from the start of injection corresponding to 0.4, 0.7 and 1.0 ms; the injection conditions are those described in the previous section for the 600 rpm pump speed case and the cavitation-induced atomization model together with the secondary break-up model developed during the present investigation have been used. The colour of the representative droplet parcels plotted in Figure 5-27a is proportional

to their size. As can be seen, the size of the droplets after their ejection from the wall is generally smaller than the size of the droplets in the main spray. The smaller of them and also those with the lower velocities are carried by the head vortex and travel along the wall direction. This spray structure was also observed experimentally and it will be further discussed in the next section of this chapter.

Figure 5-27b shows the same droplet parcels as in previous figures, but this time the colour of the representative parcels plotted is proportional to their deformation. As can be seen, the more deformed droplets are present in the main spray region. Those convected by the head vortex also exhibit slightly higher deformation values and they are expected to further break-up due to the head vortex action. Thus, it can be said that the dynamics of the impinging spray has a secondary atomization effect on the ejecting from the wall droplets through the formation of the induced by the spray gas motion over the flat plate. This effect will be quantified in the next section. Figure 5-27c presents the velocity of the representative parcels used at the same time steps from the start of injection as for the droplets in Figures 5-27a and b. In addition, Figure 5-30 presents the induced by the spray velocity flow field at 0.7, 1.0 and 1.4 ms after the start of injection with the size of the vectors plotted representing only the velocity direction and not the actual magnitude which can be observed from the color scale attached. The head vortex development can be observed as well as the high gas velocities close to the wall. As can be seen by comparing these two groups of velocity plots, the droplets after their impingement follow to a large extend the induced gas velocity flow field.

Another point that can be observed is related to the droplet mass density and droplet number density within the impinging region. Figure 5-28a shows the droplet mass density on the plane of symmetry of the spray. It is clear that most of the fuel mass is located close to the wall and in particular close to the impinging area. At this location, there exist two different groups of droplets, those belonging to the main spray which have not impinge on the wall and those already ejected from the wall and travel in the opposite direction. It is obvious that in this region where most of the fuel mass is concentrated, the possibility of two droplets colliding is relatively high due to the opposite velocities of the two different groups of droplets. This mechanism which is again related to the dynamics of the impinging spray rather than to the hydrodynamics of the single droplet, gives rise to the droplet size through the coalescence process; quantitative results will be presented in the next section. Figure 5-28b shows the droplet

number density distribution where, as can be seen, a large number of droplets are formed during splashing and are convected by the head vortex. It is also clear that the positions of the maxima of the droplet mass density and the droplet number density do not coincide, implying that a large amount of fuel spreads on the wall forming a liquid film and also that the size of the droplets formed during splashing is smaller than the size of the droplets in the main spray region.

Another point that should also be mentioned concerns the deformation of the droplets at the time of their impingement. Figure 5-29 shows the mean droplet deformation distribution (of the non-impinged droplets only) on a plane located 30 mm below the injection hole, i.e. just before the location of impingement, at 0.4, 0.7 and 1.0 ms after the start of injection. As can be seen, the impinging droplets are highly distorted which is expected to contribute to the splashing rather than to the rebounding regime. This point is usually neglected from single droplet impingement models reported up to now and it requires further investigation.

Having the general picture of the phenomena taking place during the spray impingement on the flat wall, we proceed to the validation of the model.

5.2.3 Model validation

Figures 5-31 and 5-32 show the comparison between the computational and the experimental results for the droplet tangential (parallel to the wall) velocity component and droplet SMD, respectively. Results obtained for five different sets of calculations are presented using the models of Senda et al. (1994) which is referred as [model 1], Mundo et al. (1995) which is referred as [model 2] and Bai (1996) which is referred as [model 3]; these model have been discussed in detail in chapter 3. These models reveal the consequences of considering different criteria for distinguishing between the different droplet hydrodynamic regimes observed during the impingement of single droplets on flat surfaces and their post-impingement characteristics. Wall roughness and presence of wall film are factors affecting the calculations. As can be seen in Figure 5-32, the calculations obtained assuming a dry and smooth surface of impingement (model 1) overpredict the droplet size. When wall roughness was introduced, the calculated droplet size resulting from the splashing hydrodynamic regime was found to be much closer to the experimental data. Results obtained by taking into account the presence of

wall film (model 2) are relatively close to the experimental data. Finally, predictions obtained using model 3, proved to be quite realistic in terms of both the droplet tangential velocity and the droplet size. In addition to the correlations describing the post-impingement droplet characteristics, other factors have been found to play an important role in the dynamics of impinging sprays, as discussed in the previous section 5.2.2. Prediction of the droplet velocities at points located at 0.5 mm above the wall were in good agreement with the experimental data. The tangential droplet velocity was found to be strongly affected by the injection velocity profile. Especially at the closest to the spray axis measurement point, most of the droplets passing through the control volume were not impinging on the wall. At points further downstream into the impingement region, droplet velocities were still affected by the injection velocity but also by their ejection velocity from the wall. However, 5 mm above the flat plate, considerable differences could be observed in the droplet characteristics compared to those at the 0.5 mm distance. Interestingly, the tangential droplet velocities have negative values corresponding to droplets which are convected by the head vortex formed over the flat plate and are forced to move backwards. For the atmospheric gas conditions examined here, the induced flow field was strong enough to significantly change the characteristics of the ejected droplets, eliminating possible differences in their initial post-impingement values. As can be seen in Figure 5-27c, droplet velocities are larger close to the wall.

Two additional sets of calculations were performed, where in the first case the collisions between the droplets have been neglected thus allowing this effect between droplets impinging on the wall and droplets ejected from the wall to be estimated. It is clear that, if collisions are not taken into account, the droplet size seems to be underpredicted which implies that coalescences between droplets is likely to occur in the impinging region. To estimate the relative importance of droplet collisions during the injection period, six possible collision regimes were identified. Bouncing or coalescences between droplets of the free spray, bouncing or coalescence between droplets ejected from the wall, and finally, bouncing or coalescences between impinging and ejected droplets. Figure 5-33 shows the calculated number of collisions as a function of the distance between the injection hole and the wall at different time steps from the start of injection. Since the initiation of spray impingement, the dominant collision mechanism seems to be coalescence between a droplet moving towards the

wall and a droplet ejected from it. For time steps up to the end of injection, when most of the spray has impinged on the wall, collisions between droplets in the head vortex area become also frequent, due to their backwards motion within the head vortex which gives rise to droplets moving with opposite velocities. The collision effect has proved to be an important factor determining the characteristics of the impinging spray depending and it depends much less on the dynamics of impingement of the single droplet than on the dynamics of the impinging spray as a whole.

The last set of calculations for the impinging spray has revealed the effect of the head vortex on the size of the ejected droplets. The gas velocity component parallel to the wall was found to exhibit large values during the injection period which, for the atmospheric injection conditions investigated here, can be as high as 100 m/s. This velocity can have a considerable disintegration effect on the droplet size due to their secondary break-up. Figure 5-34 shows the effect of this secondary atomization mechanism on the SMD of the whole spray together with all the other aforementioned mechanisms represented in the various sub-models. On the same graph, the droplet size of the free spray obtained with a Malvern particle sizer at a distance of 30 mm below the injection hole is also presented in order to reveal the overall effect of the presence of the wall on the calculated average droplet size which is a function of several competing factors. Small droplets are produced during the splashing while the wall head vortex contributes to the secondary atomization process. On the other side, droplet coalescence in the impinging region is responsible for the generation of larger droplets; in addition, a considerable amount of small droplets spreads on the wall forming a wall film. The overall effect is the calculation of a larger droplet size during the main injection period in the presence of a wall. However, towards the end of injection, the calculated droplet size is almost the same for the free and impinging sprays for the specific injection conditions examined here.

From the above it is clear that factors related to the accurate estimation of the fuel mass spreading on the wall, the temporal variation of the wall film thickness and its effect on the characteristics of the ejected from the wall droplets, are the most important parameters for the simulation of impinging sprays. However, existing experimental data proved to be inadequate for a more detailed comparison between the computational and experimental results. The impingement models used predict that, for the examined

injection and atmospheric gas conditions, approximately 40% of the total fuel injected is expected to spread on the wall forming a liquid film.

5.3 DI Diesel Engine Sprays

5.3.1 Injection conditions - simulated geometry

Having examined the characteristics of atmospheric sprays, it is sensible to proceed to the investigation of sprays injected inside the piston bowl of a DI Diesel engine.

Nagwaney (1996) reported details about the characteristics of the sprays injected in a 1.9 l DI Diesel engine. A general view of the specific engine together with the fuel injection system is shown in Figure 5-35. The specific injector used is a Bosch inclined multihole one; three different groups of hole inclination angles exist on the specific injector which are also given in Figure 5-35. The details of the geometry of the engine simulated is given in Figure 5-36; four different views have been selected for presentation with the last one showing the details of the numerical grid in the piston bowl region which was constructed in order to allow for numerical simulation of the in-cylinder gas motion. The specific engine has an off-center re-entrant piston bowl and a compression ratio of 21. The numerical grid consists of a total of 40000 grid nodes at TDC. In order to account for the swirling motion inside the bowl of the combustion chamber, measurements of the gas flow field at 350 deg. reported by Nagwaney (1996), were considered as the initial flow field. The gas motion inside the engine was initially simulated until the time of the start of injection and then during the spray injection until the start of combustion.

Comparison between the computational and experimental results is made here for three different injection conditions listed in Table 5-1 (cases 6, 7 and 8); they correspond to an engine speed of 1000 rpm at a fueling level of 6 mm^3, idle, and to 2000 rpm for two different loads (9.6 mm^3 and 35.6 mm^3), which will referred to as low load and high load cases, respectively. Since the injector was inclined, the details of the flow inside the sac volume are considered responsible for the observed differences between the five injected sprays. Figure 5-37 shows the measured line pressure and needle lift used as inputs to the FIE model in order to estimate the injection conditions; these are

presented in Figure 5-38 which shows the calculated sac volume pressure for all three cases as well as the fuel injection rate, the injection velocity and the effective hole area for all three different groups of holes. As can be seen, the maximum injection pressure is around 250 bars for the 1000 rpm, idle case, goes up to 450 bars for the 2000 rpm low load case and becomes as high as 750 bars for the 2000 rpm, high load injection condition. Holes 3 and 4 are the low fueling holes, and also the more cavitating ones as can be seen on the graphs presenting the effective hole area, which varies significantly during the injection period; this is important for the prediction of the spray characteristics as it will become clear later on.

Comparison between the computational and experimental results was made for the spray tip penetration for all five sprays. Especially for spray 4, shown in Figure 5-1, the comparison was focused on the droplet velocity obtained with a laser Doppler velocimetry technique (LDV); measurements were obtained at three different distances from the injection hole with coordinates (r,z)= (7.4 mm , 4.0 mm), (r,z)= (9.2 mm, 4.5 mm) and (r,z)=(11.2 mm, 5.0 mm) which are also shown schematically in Figure 5-1. The measured velocity component is on the x-y plane along the injection direction; however, these points are approximately 2 mm off the spray axis. For this specific spray 4, comparison is taking place also for the droplet velocities under atmospheric conditions at points located 10 mm and 20 mm below the injection hole on the spray axis, with injection conditions corresponding to cases 6 and 7.

The fluid used for these particular engine simulation cases was a Light Diesel (83.3 C / 13.7 H) with density, surface tension and kinematic viscosity of 840 Kg/m^3, 26 mN/m and 4.2 mm^2/s, respectively, at 40°C (fuel 9 from table 3-1). It should be mentioned that these are assumed to be a function only of the liquid temperature, as described in chapter 3.

5.3.2 Model validation

A droplet evaporation model was added to all other sub-models identified previously to give realistic predictions under atmospheric conditions. Droplet evaporation was modeled assuming either uniform temperature distribution within the droplet or a temperature variation within the volume of the droplet. For the specific engine and injection system used, cycle to cycle variations were found (Nagwaney

Figure 5-43 shows the comparison between the computational and experimental results for the mean velocity of the droplets of spray 4, corresponding to the injection conditions of 1000 rpm, idle, and obtained at three points downstream of the injection nozzle using various drag coefficient and evaporation models. As can be seen, droplet velocities are much smaller than the injection velocity, due to the high gas pressure and density in the piston bowl at the time of injection. The model giving the best predictions relative to the measurements is that which accounts for the effects of droplet deformation on both the drag coefficient and on the evaporation of the moving droplets. In order to emphasize the importance of the in-cylinder gas conditions at the time of injection on the prediction of droplet velocities, comparison was also performed between the computational and experimental droplet velocities for injection under atmospheric gas conditions for the sprays injected under injection conditions corresponding to cases 6 and 7. As can be seen in Figure 5-44, for low back pressures, such as for injection into atmospheric air, cavitation occurs in the injection holes which strongly affects the injection velocity. This velocity increase is necessary in order to predict correctly the droplet velocities downstream. However, even if cavitation occurs for injection under engine chamber pressures, the in-cylinder droplet velocities are still much lower than their values under atmospheric conditions. It should be mentioned that in-cylinder measurements are approximately 2 mm away from the spray axis; the calculated droplet velocities at the same distance from the injector as the points presented in Figure 5-44 are approximately 80% higher.

5.4 Conclusions

A spray model was developed and used to evaluate the relative importance of the various physical processes occurring in diesel sprays injected from hole-type nozzles. The model is based on a Lagrangian-Eulerian approximation and incorporates sub-models for hole cavitation, liquid core atomization, droplet secondary break-up, droplet collisions, droplet-wall interactions, droplet turbulent dispersion and droplet evaporation. Calculation of the droplet drag coefficient was based on droplet deformation which was estimated by the break-up model. Comparison between the computational and experimental results was made for the temporal and spatial distribution of droplet SMD, droplet velocity, number of droplets, spray tip penetration

and global spray structure for test cases including free and impinging on a flat plate atmospheric sprays under both quiescent and cross flowing conditions as well as in-cylinder engine sprays.

From the comparison between computational and experimental results at the closest to the injection hole measurement point it can be concluded that hole cavitation strongly affects the injection velocity and droplet size. Injection velocity was calculated on the basis of an effective hole area, while a model accounting for the cavitation-induced atomization was found to predict more accurately the droplet sizes of the spray. A model distributing the droplets formed during the atomization process within the spray cone angle according to their inertia was able to predict satisfactorily the radial distribution of droplet SMD, droplet velocity and number of droplets.

Having determined the characteristics of the droplets resulting from the atomization process of the liquid core, secondary break-up effects were examined and found to strongly affect the overall spray structure. The bimodal distributions resulting from the stripping break-up mechanism were taken into account together with a maximum entropy formalism-based model calculating the size distribution of the formed droplets for a range of different secondary break-up modes reported in the open literature. The frequently observed experimentally 'Christmas tree' spray structure was identified to be related to the bimodal droplet size distribution in addition to modulations in the injection velocity caused by the wave dynamics in the fuel injection system.

Investigation on the dynamics of impinging sprays has revealed that despite the differences between the models calculating the post-impingement droplet characteristics, coalescence between the impinging and the ejected from the wall droplets gives rise to larger droplet sizes. Droplets formed according to the splashing hydrodynamic regime were found to be affected by the wall roughness, and to have sizes much smaller than the size of the impinging droplets. Secondary droplet break-up effects caused by the formation of the head vortex and its convection over the flat plate have further contributed to the secondary atomization process.

Having investigated the characteristics of free and impinging atmospheric sprays, results were presented for in-cylinder engine sprays. Differences between the sprays injected from an inclined five-hole nozzle were attributed to differences in the injection velocity and the level of cavitation in the various holes. Strongly cavitating

holes produced better atomized sprays which penetrate less in the combustion chamber; evaporation of these sprays was found to be faster compared to the evaporation of the other sprays. Droplet evaporation was also found to be affected by the droplet deformation; the latter was estimated for all five sprays and considered to significantly affect the interphase area between the droplets and the hot gas. The drag force calculation was also based on droplet deformation and it was found to have a significant effect on droplet deceleration as a function of their size.

CASE	Gas conditions	Pump speed	Fuelling	Flat plate dist.	SOI
1	Quiescent (atm)	600 rpm	4.0 mm^3	–	0.0 ms
2	Quiescent (atm)	1200 rpm	4.0 mm^3	–	0.0 ms
3	Cross flow 13.5 m/s	600 rpm	4.0 mm^3	–	0.0 ms
4	Cross flow 22.5 m/s	600 rpm	4.0 mm^3	–	0.0 ms
5	Quiescent (atm)	600 rpm	4.0 mm^3	30.0 mm	0.0 ms
6	Engine	500 rpm	6.0 mm^3	bowl	357.68°CA
7	Engine	1000 rpm	9.6 mm^3	bowl	351.82°CA
8	Engine	1000 rpm	36.0 mm^3	bowl	351.97°CA

Table 5–1 : List of test cases investigated for the spray model validation

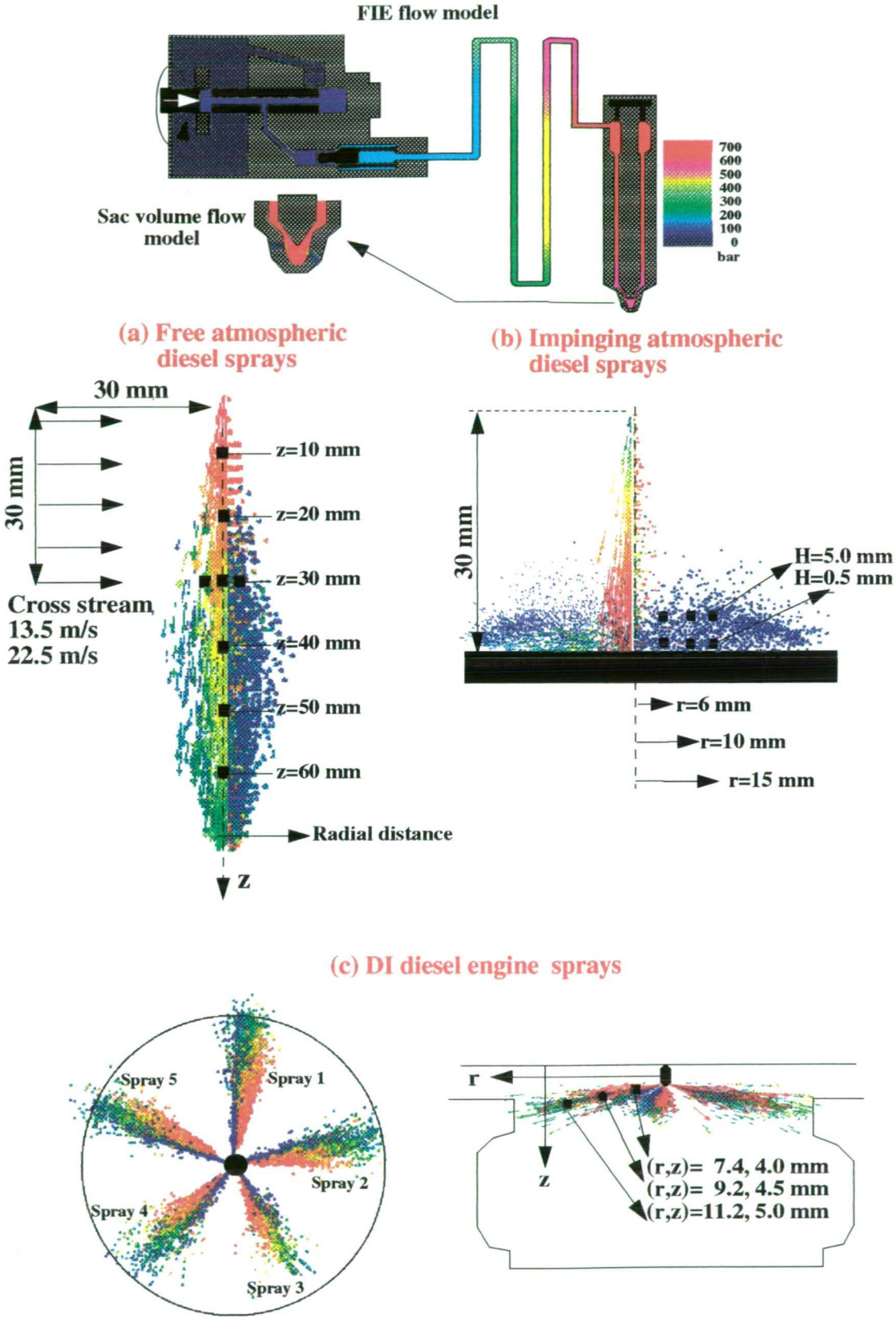

Figure 5–1 : Schematic representation of the test cases simulated: (a) free atmospheric sprays (quiescent and cross flowing conditions) (b) impinging atmospheric sprays (low wall temperature – quiescent conditions) and (c) engine sprays. The points of measurements used for the validation of the model are also shown.

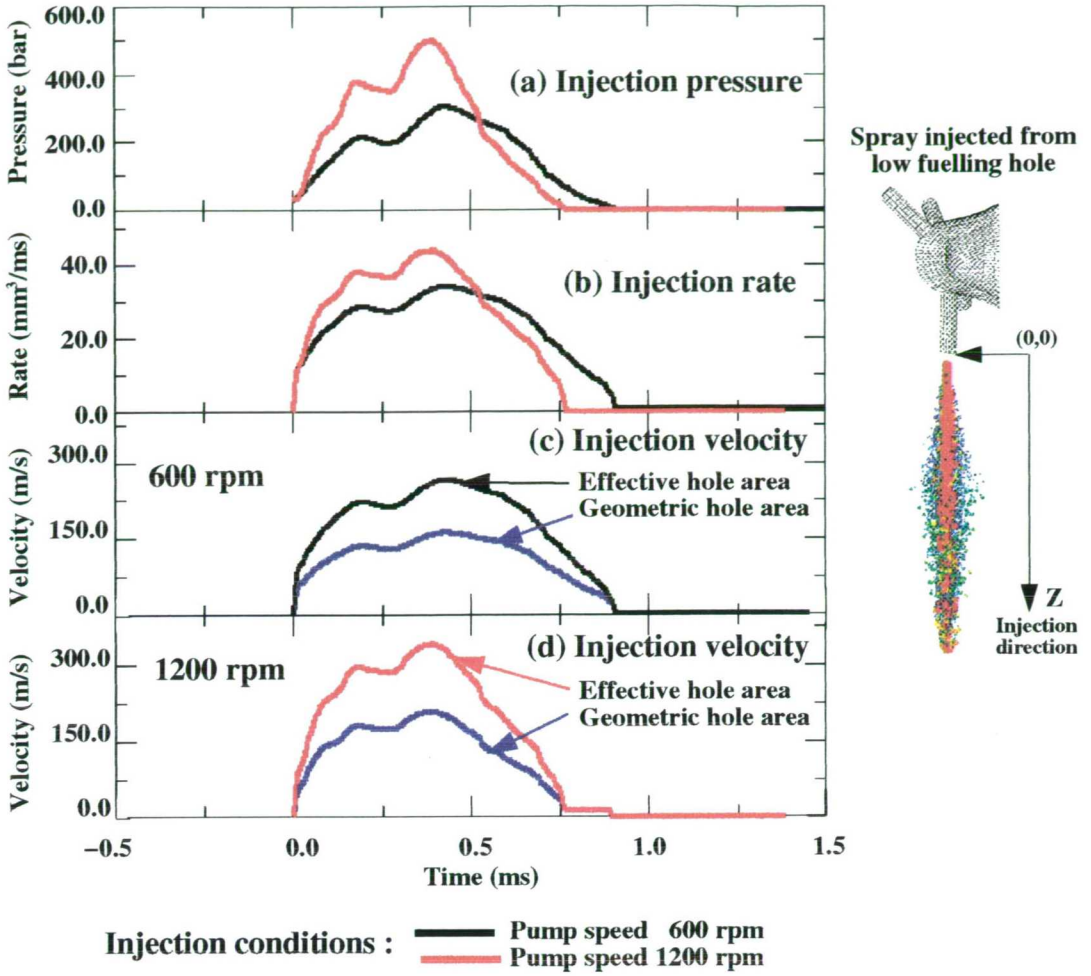

Figure 5–2 : Calculated from the FIE model injection conditions for the atmospheric sprays test cases (a) Injection (sac volume) pressure (b) Injection rate (c) injection velocity (pump speed 600 rpm) and (d) injection velocity (pump speed 1200 rpm)

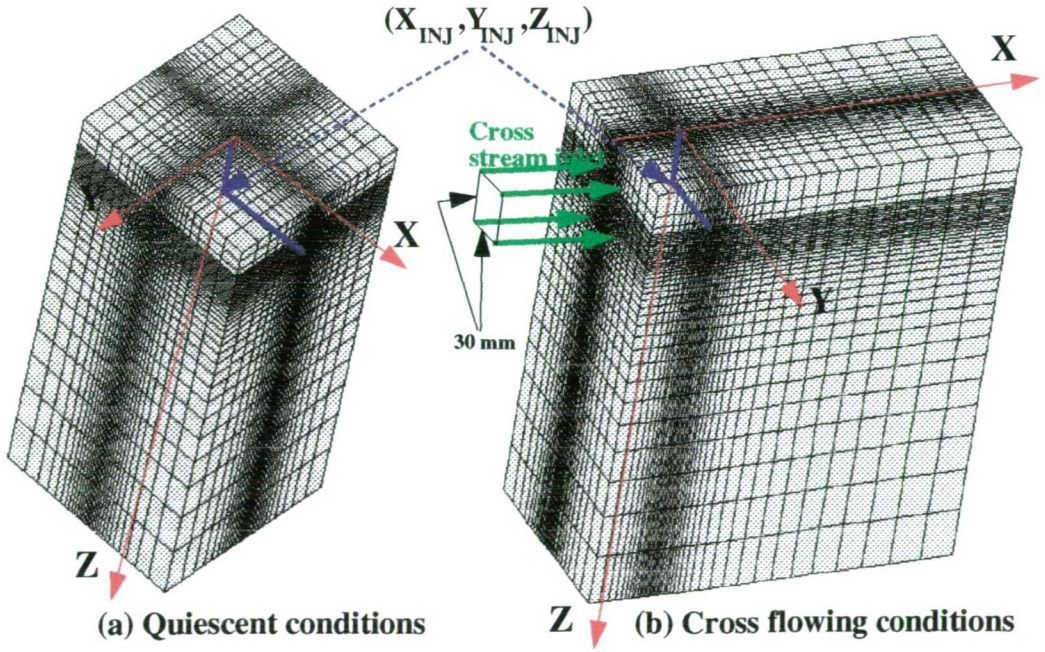

Figure 5–3 : Numerical grid constructed for the simulation of the free sprays under (a) quiescent conditions and (b) cross flowing conditions

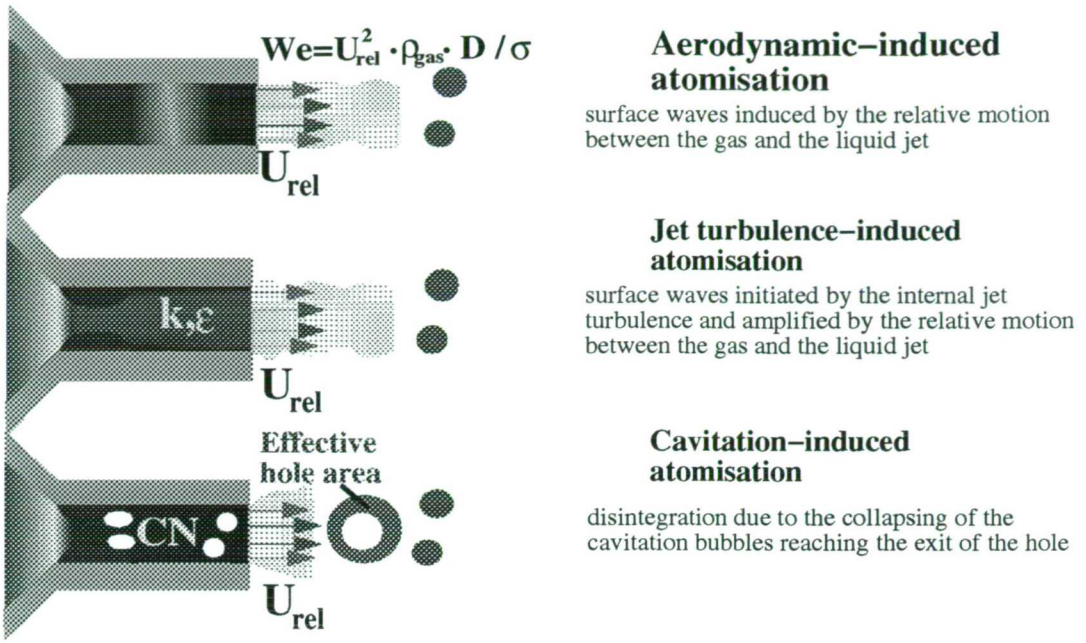

Figure 5–4 : Schematic representation of the atomization mechanisms considered

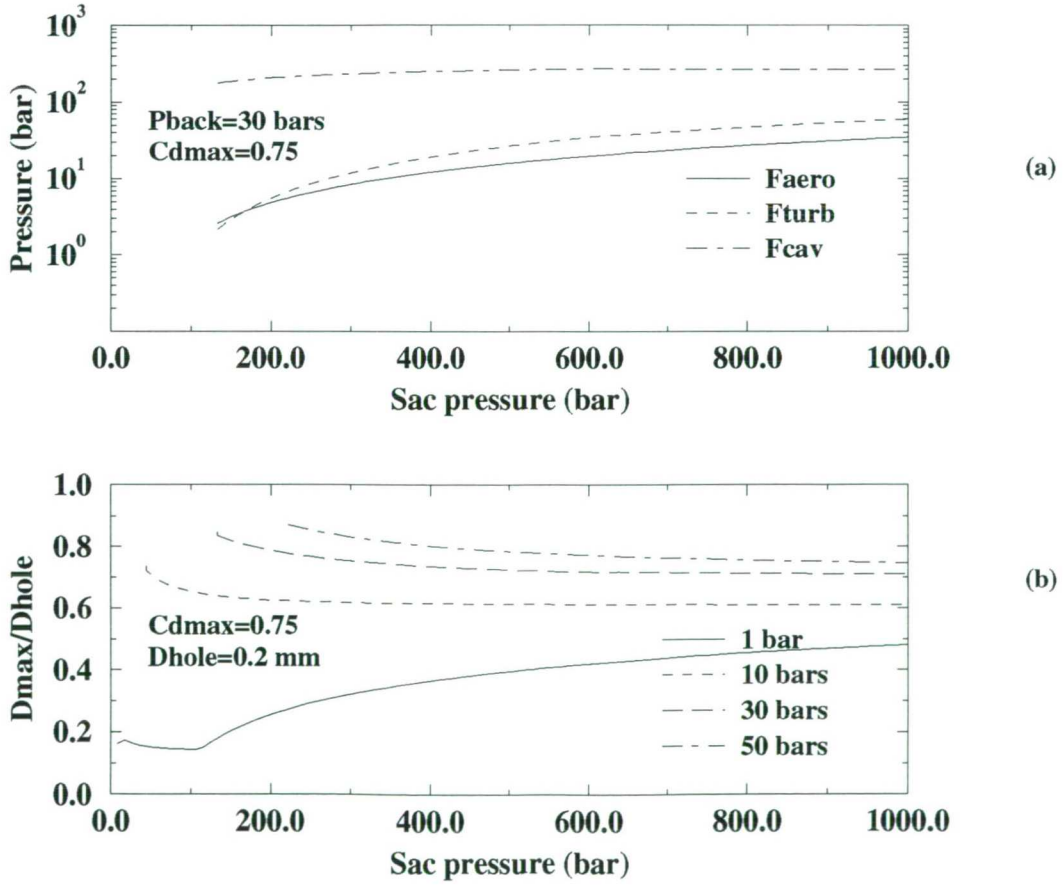

Figure 5–5 : (a) Calculated forces per effective hole area present during the liquid jet atomization process as a function of injection pressure (back pressure 30 bars, hole discharge coefficient 0.65). (b) Calculated maximum droplet size from the cavitation–induced atomization model as a function of the injection pressure under different back conditions (hole diameter 0.2 mm, maximum hole discharge coefficient 0.75)

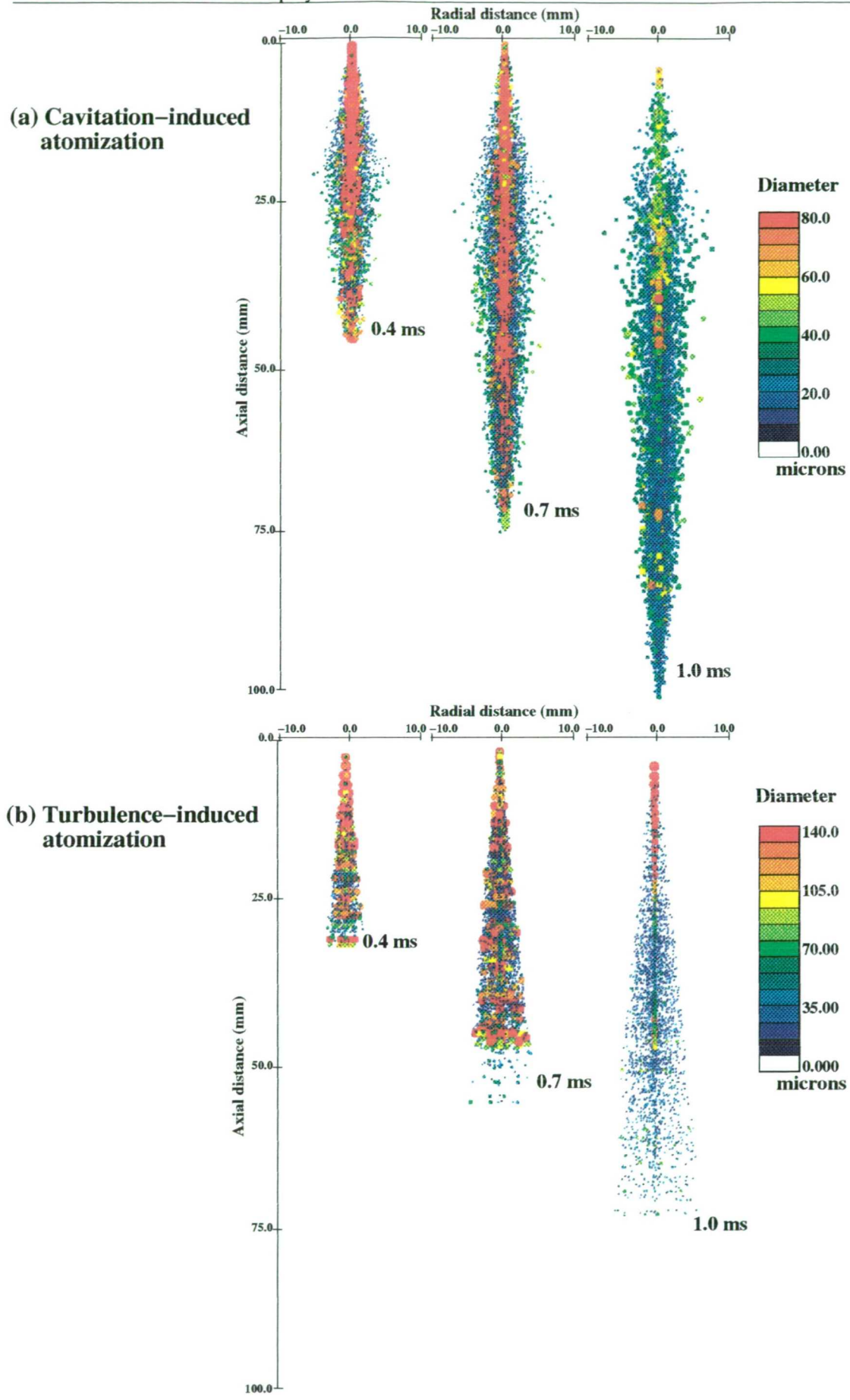

Figure 5–6 : Calculated spray development using two liquid core atomization models at 0.4, 0.7 and 1.0 ms after the start of injection. The size of the spheres plotted is proportional to droplet size.

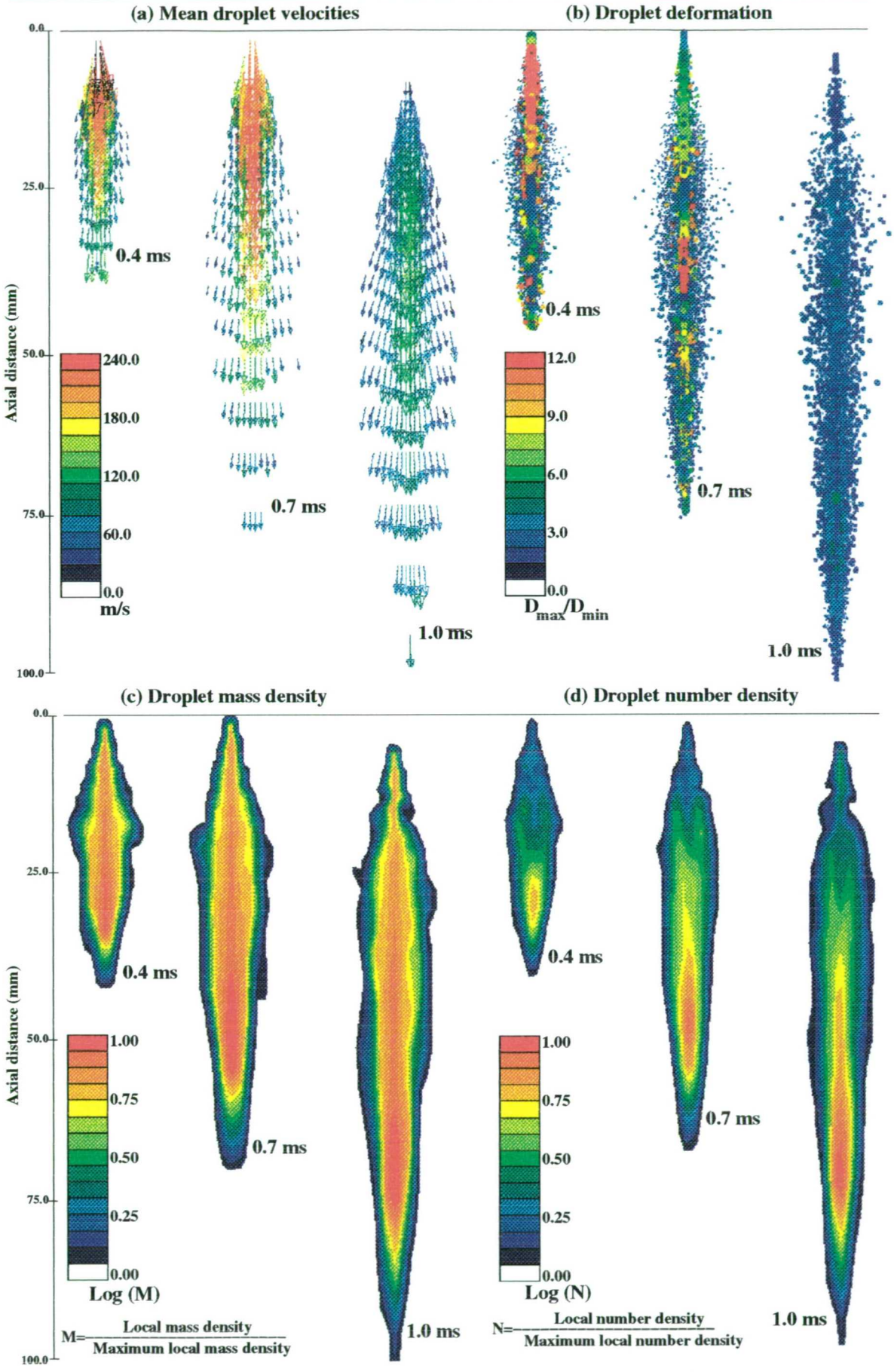

Figure 5–7 : Calculated (a) mean droplet velocity (b) droplet deformation (c) droplet mass density distribution and (d) droplet number density distribution at 0.4, 0.7, and 1.0 ms after the start of injection using the cavitation–induced atomization model (pump speed 600 rpm)

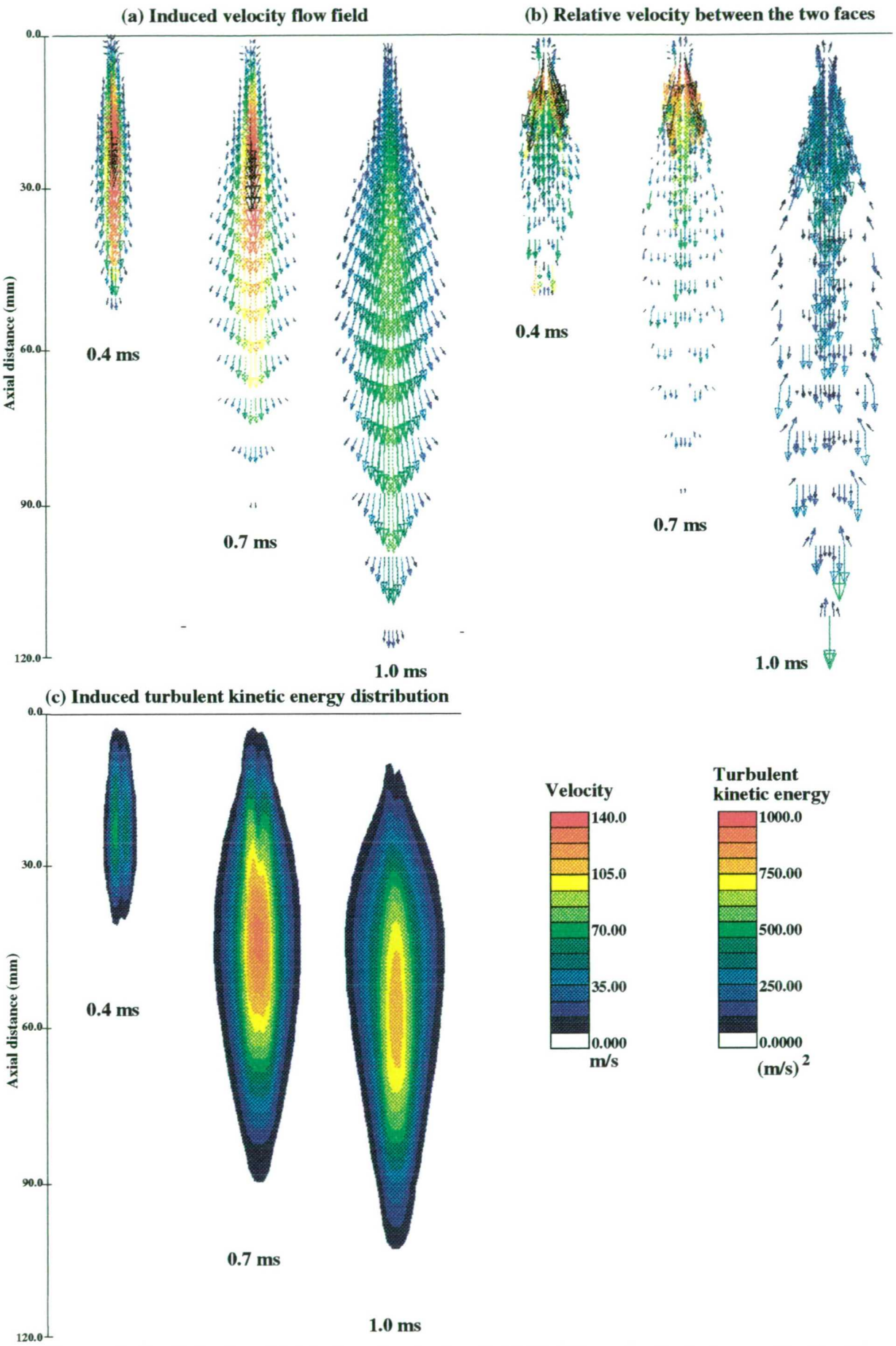

Figure 5–8 : Calculated (a) induced velocity field (b) Slip velocity between the liquid and gas phase and (c) turbulent kinetic energy distribution at 0.4, 0.7 and 1.0 ms after the start of injection (pump speed 600 rpm)

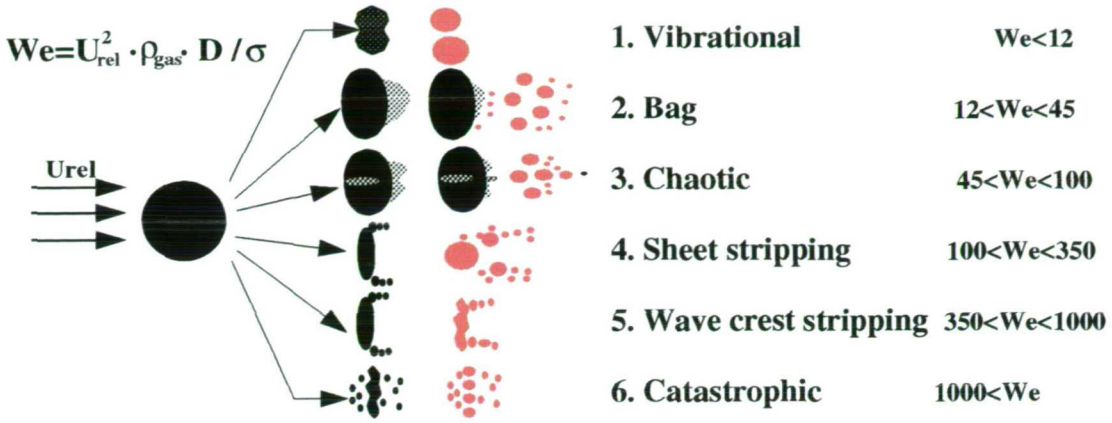

Figure 5–9 : Schematic representation of the various break–up regimes considered

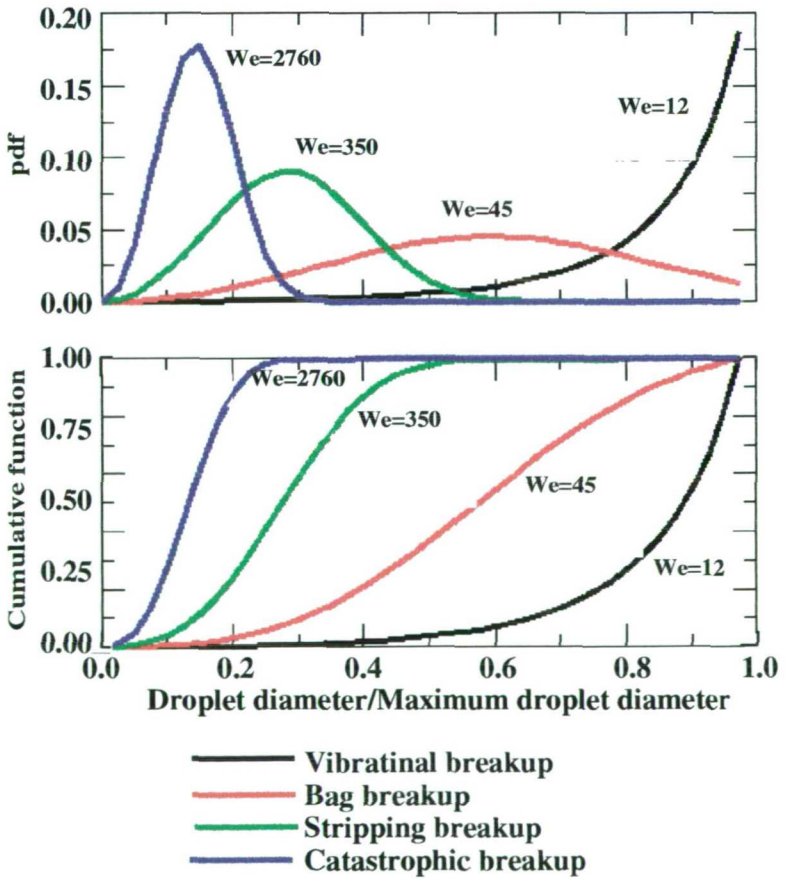

Figure 5–10: Calculated droplet size distribution using the maximum entropy formalism model

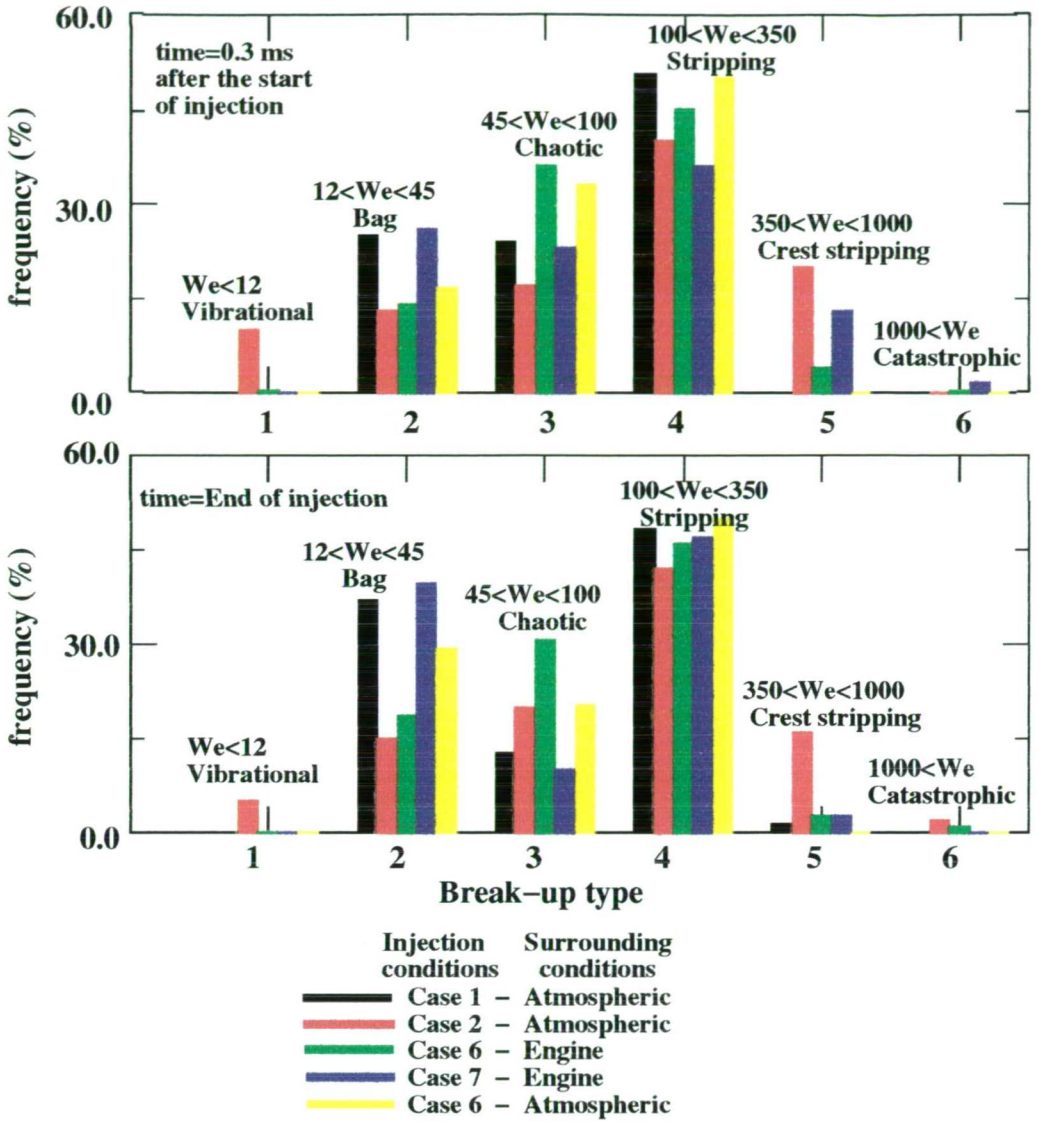

Figure 5–11 : Calculated breakup frequency for different injection conditions and back pressures

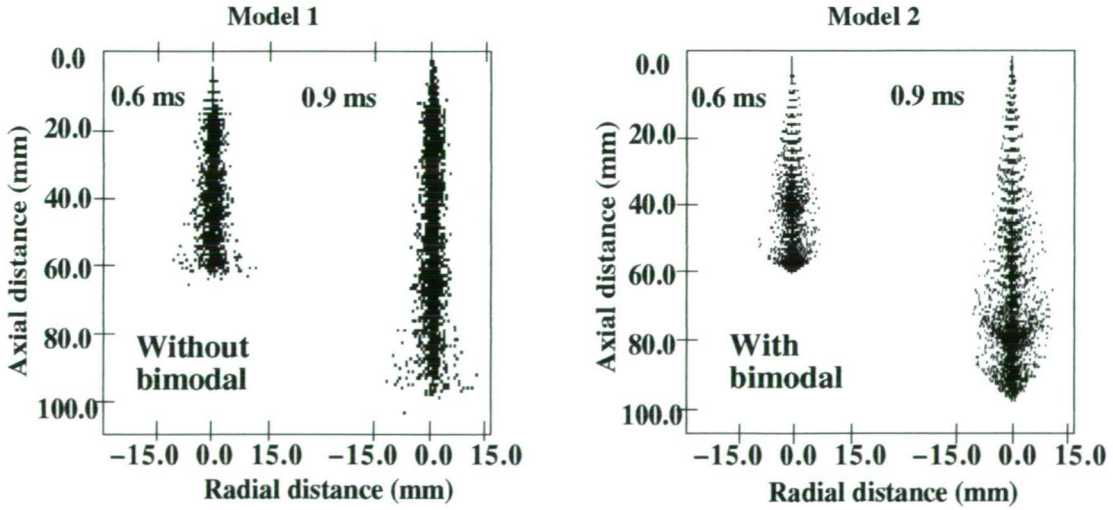

Figure 5–12 : Effect of bimodal distribution modeling on calculated spray structure at 0.6 and 0.9 ms after the start of injection (pump speed 600 rpm)

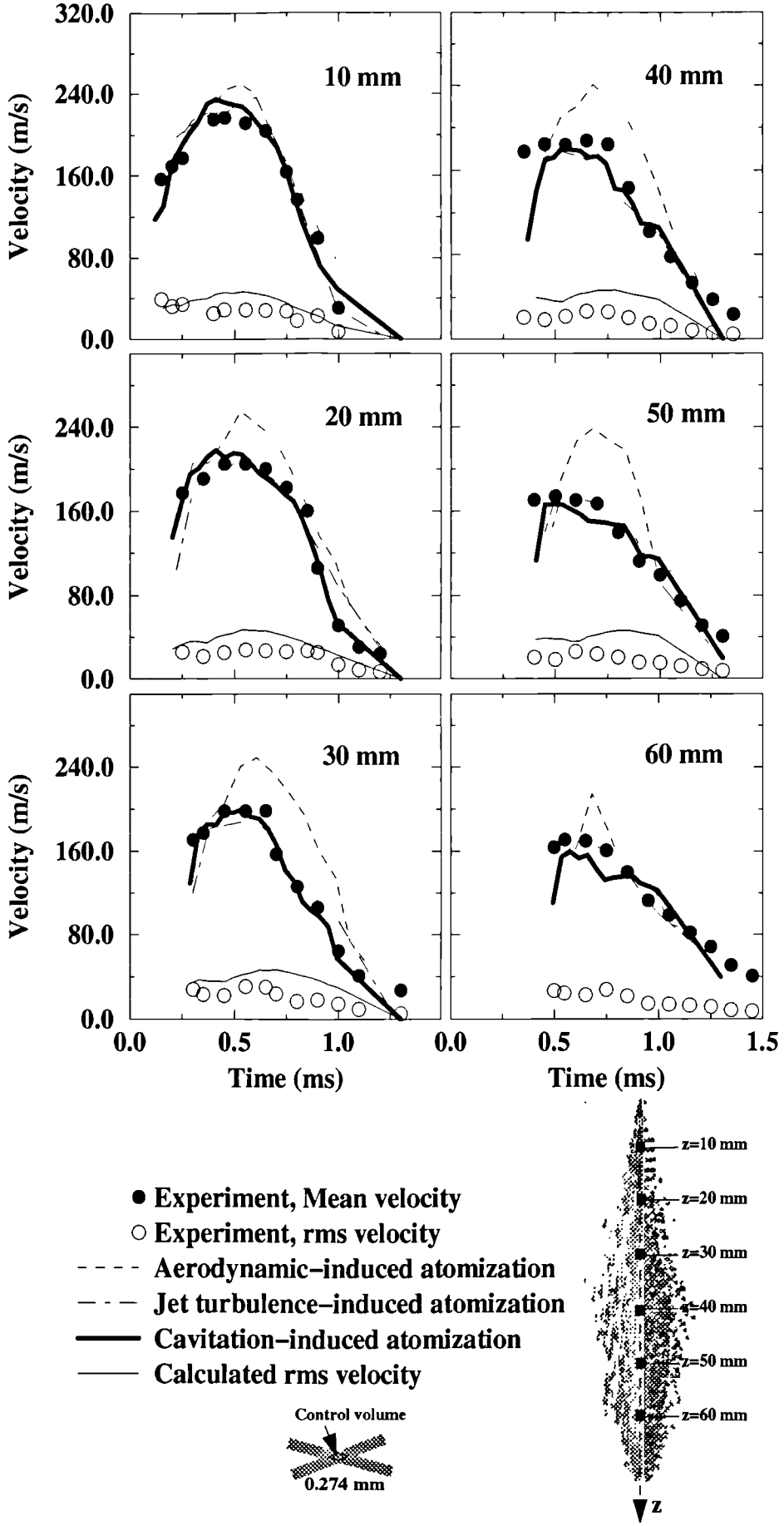

Figure 5–13 : Comparison between the computational and the experimental results for the centerline droplet mean axial velocity at 10, 20, 30, 40, 50 and 60 mm from the injection hole (pump speed 600 rpm)

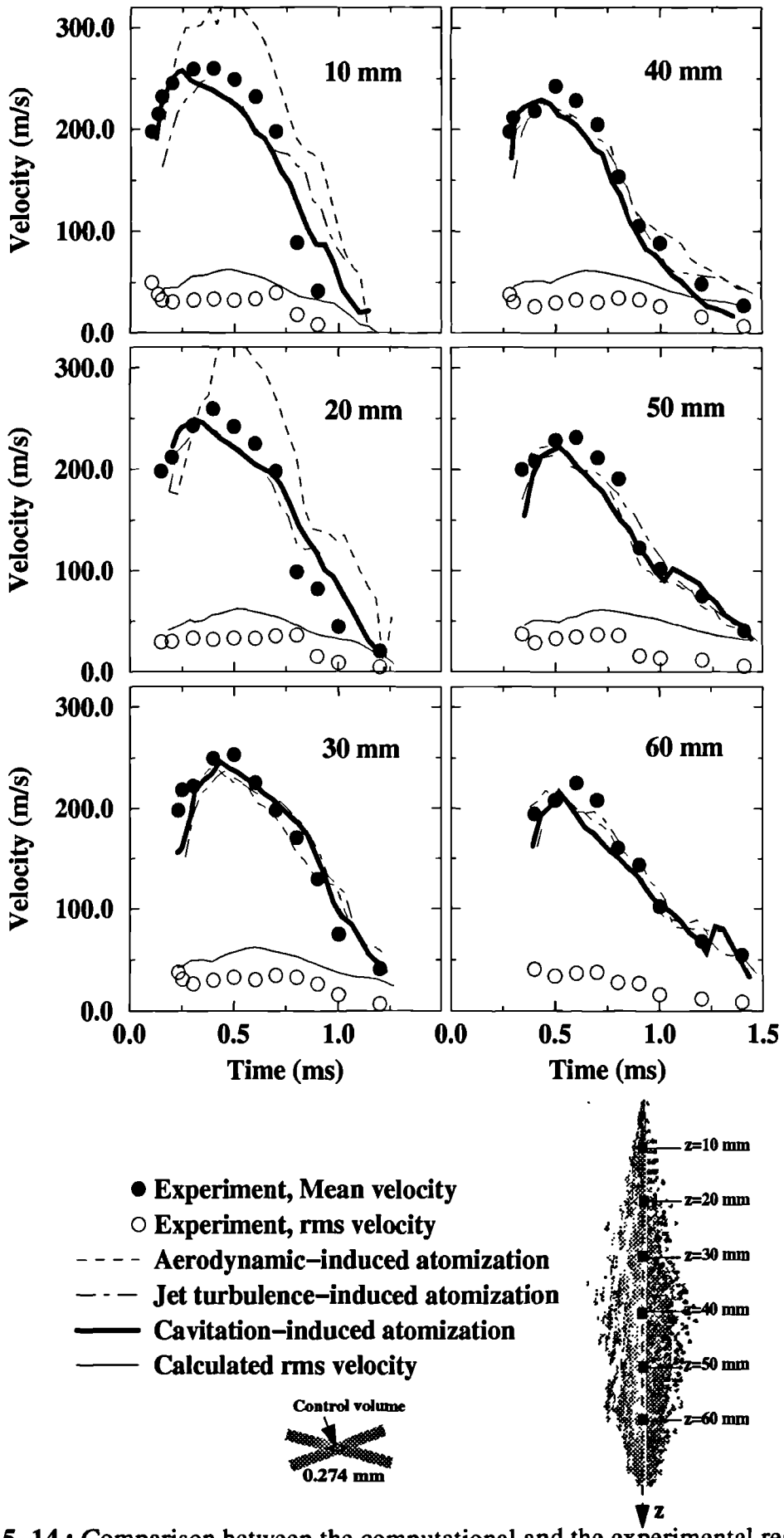

Figure 5–14 : Comparison between the computational and the experimental results for the centerline droplet mean axial velocity at 10, 20, 30, 40, 50 and 60 mm from the injection hole (pump speed 1200 rpm)

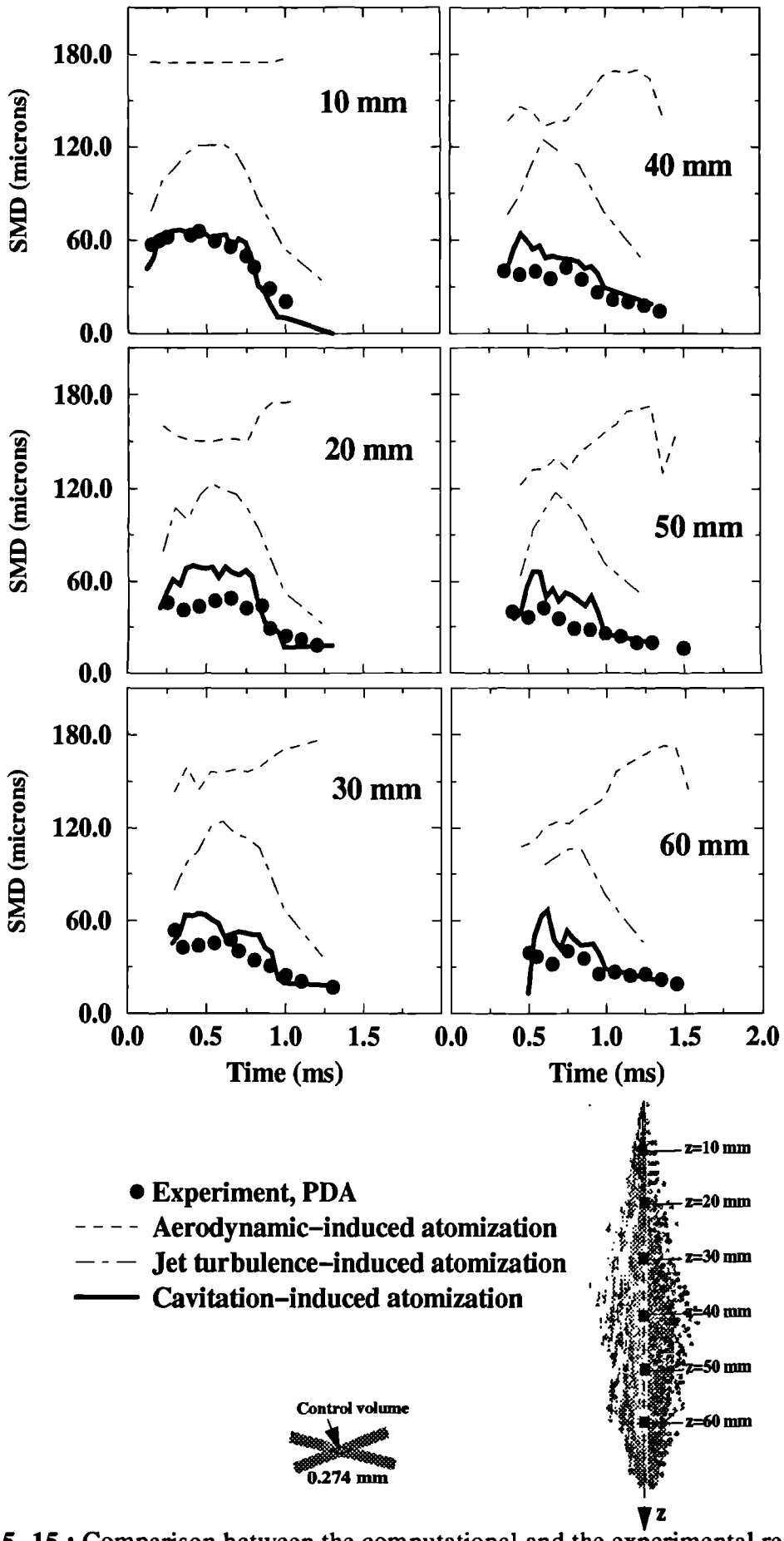

Figure 5–15 : Comparison between the computational and the experimental results for the centerline SMD at 10, 20, 30, 40, 50 and 60 mm from the injection hole (pump speed 600 rpm)

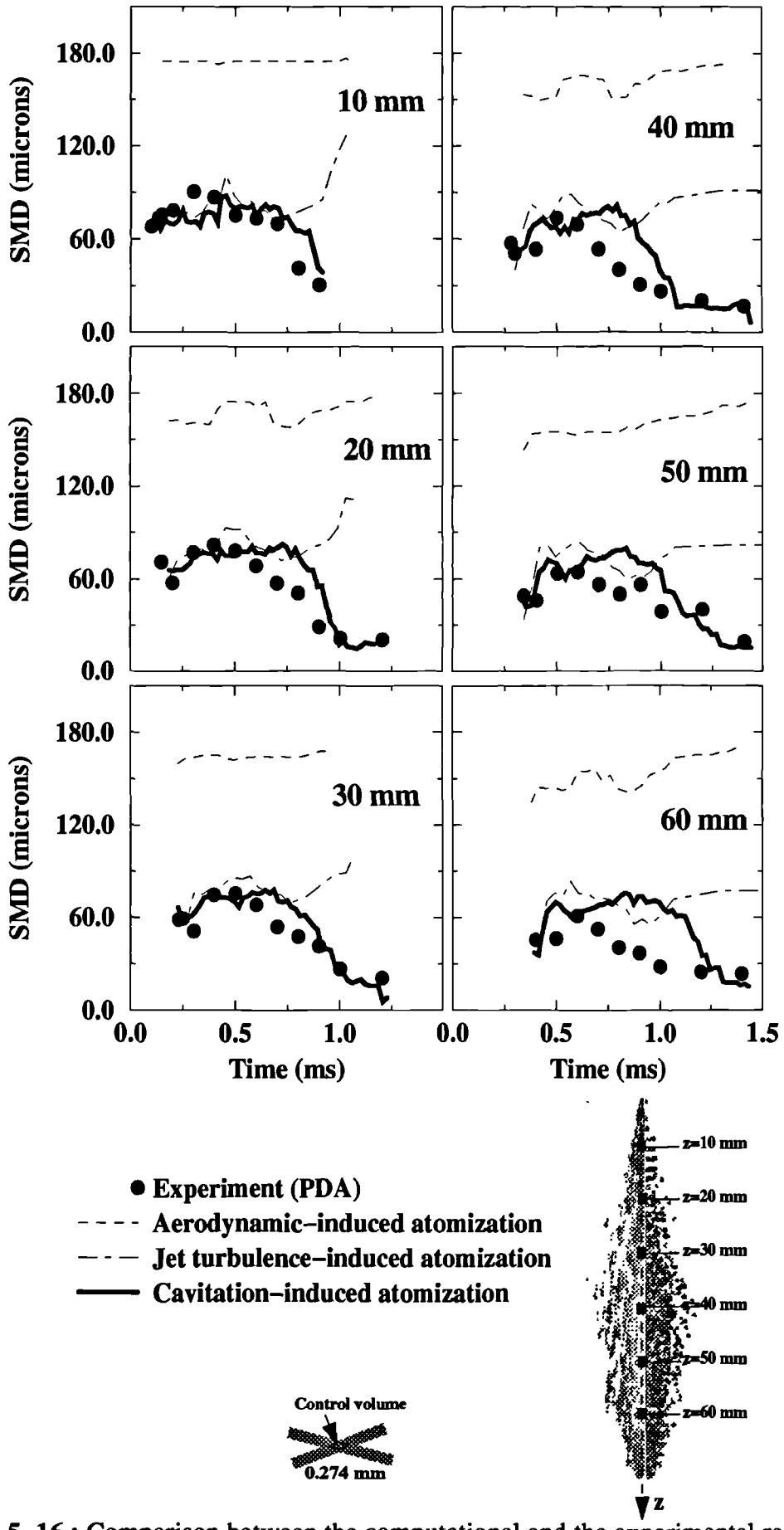

Figure 5–16 : Comparison between the computational and the experimental results for the centerline SMD at 10, 20, 30, 40, 50 and 60 mm from the injection hole (pump speed 1200 rpm)

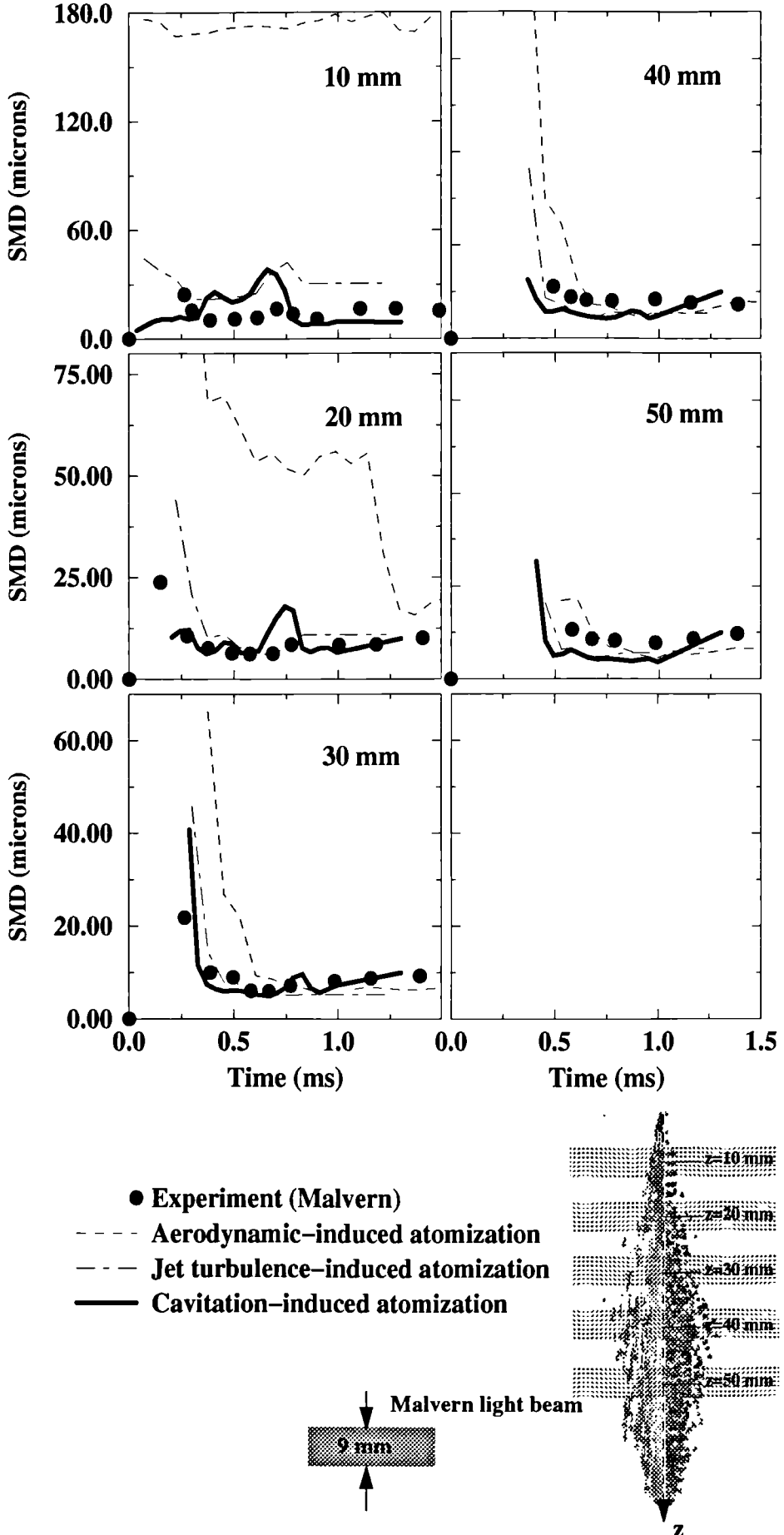

Figure 5–17 : Comparison between the computational and the experimental results for the average (Malvern) droplet SMD at 10, 20, 30, 40 and 50 mm from the injection hole (pump speed 600 rpm)

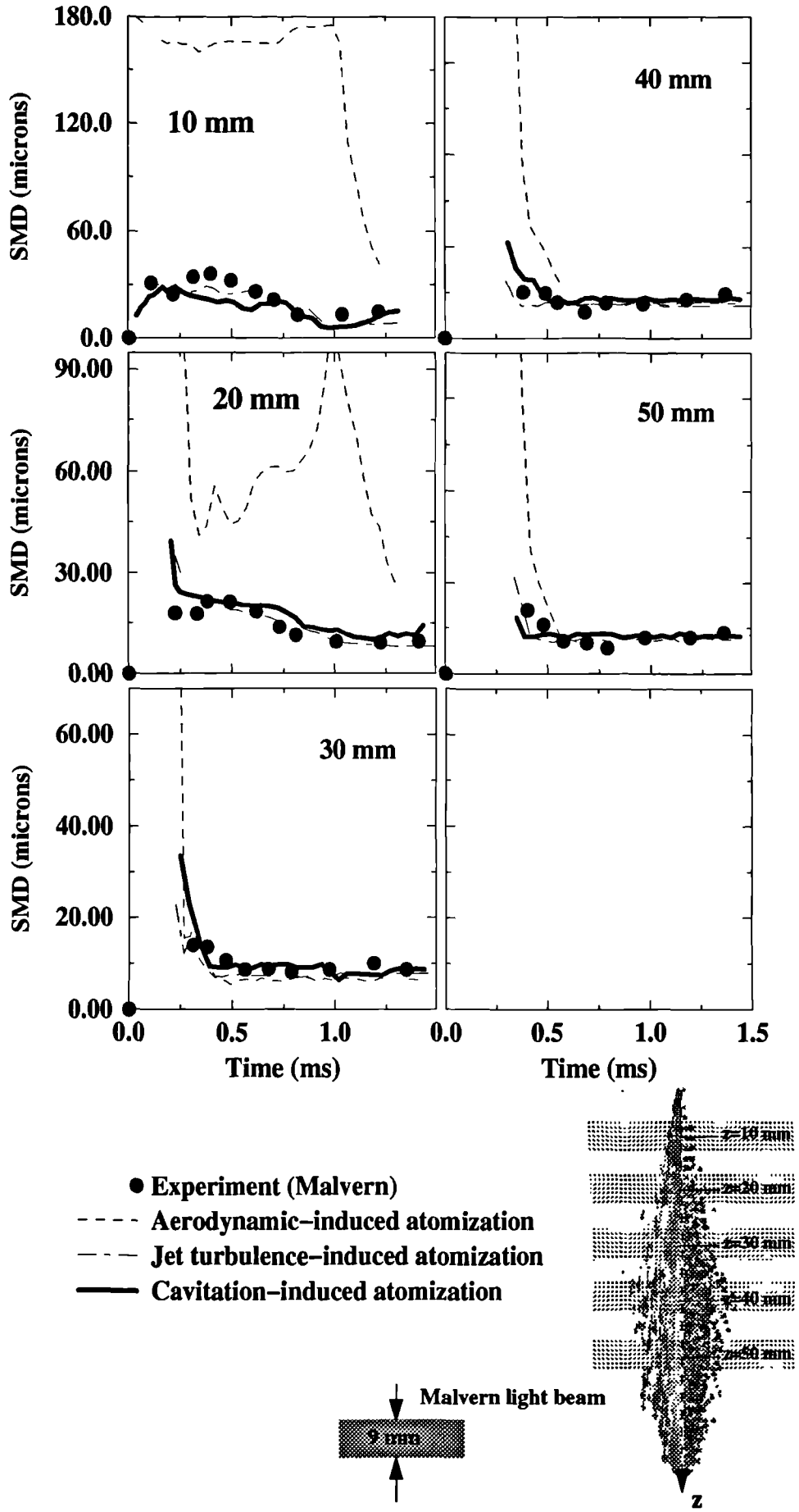

Figure 5–18 : Comparison between the computational and the experimental results for the average (Malvern) droplet SMD at 10, 20, 30, 40 and 50 mm from the injection hole (pump speed 1200 rpm)

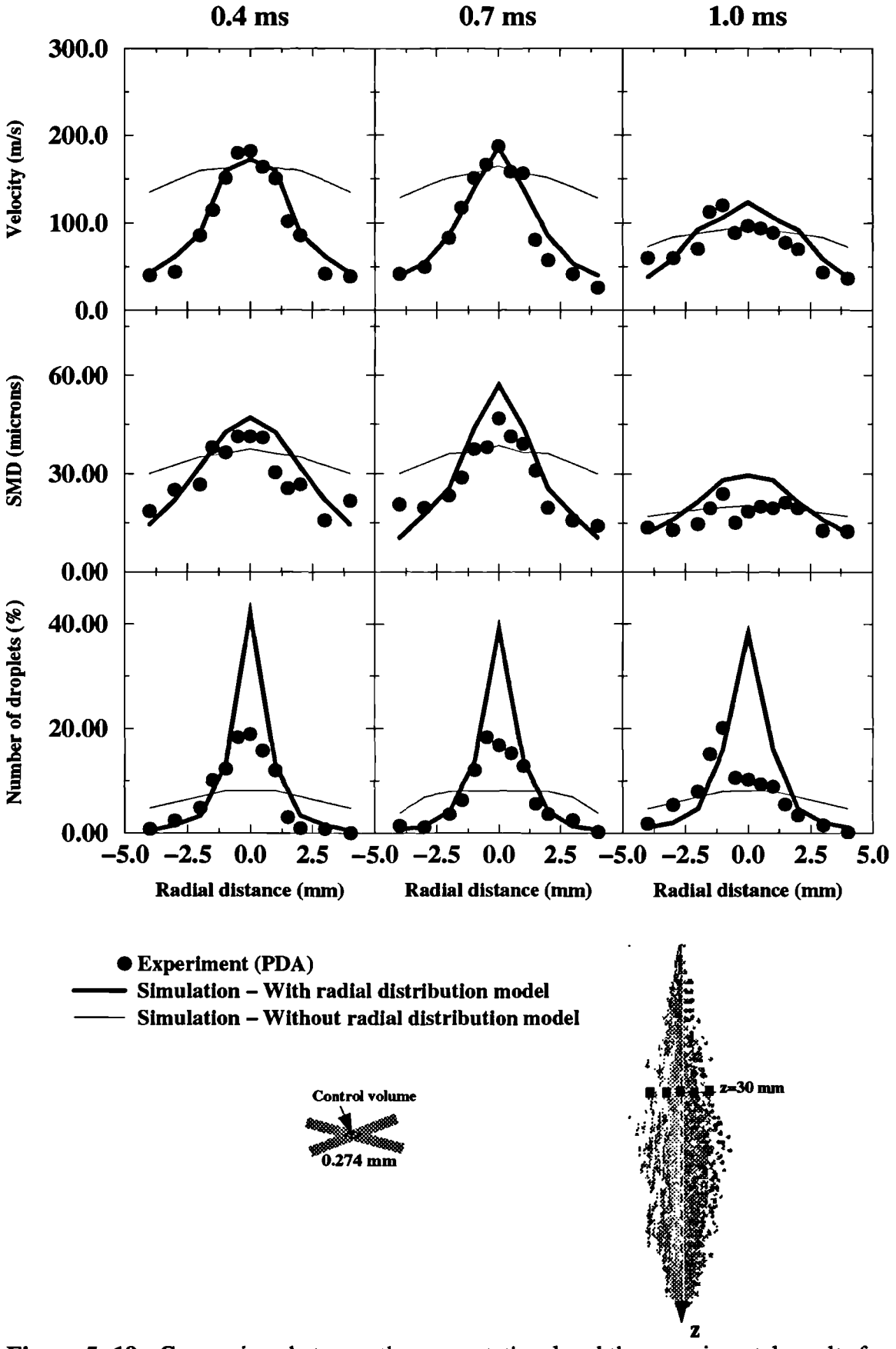

Figure 5–19 : Comparison between the computational and the experimental results for the radial distribution of droplet mean axial velocity, droplet SMD and number of droplets 30 mm below the injection hole at t=0.4 , 0.7 and 1.0 ms after the start of injection using two radial distribution models (pump speed 600 rpm).

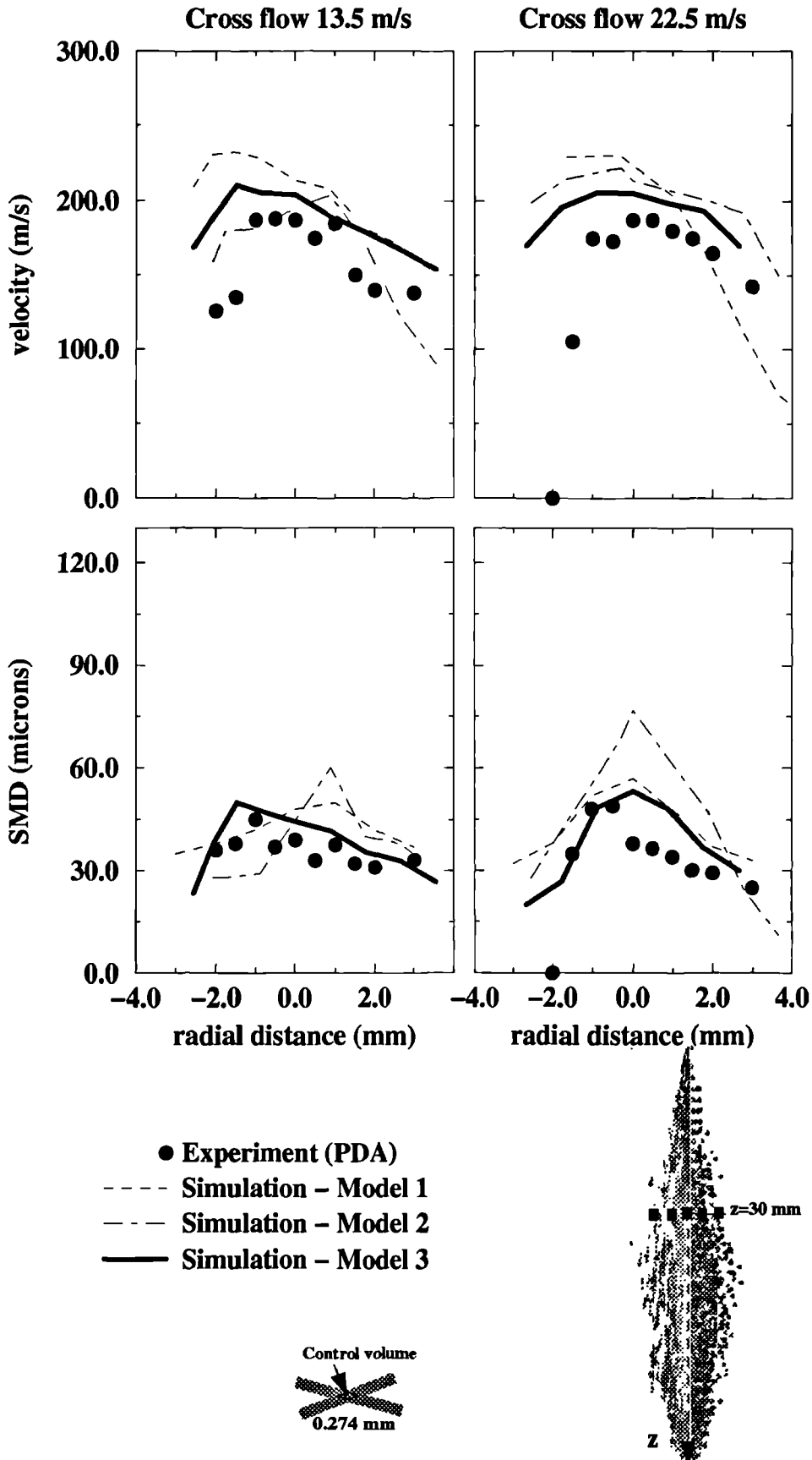

Figure 5–20 : Comparison between the computational and the experimental results for the radial distribution of droplet mean axial velocity and droplet SMD 30 mm below the injection hole at 0.7 ms after the start of injection for cross flowing conditions using different droplet secondary break–up models (pump speed 600 rpm). Model 1: Reitz & Diwakar (1987), Model 2: Pilch & Erdman (1987), Model 3: present

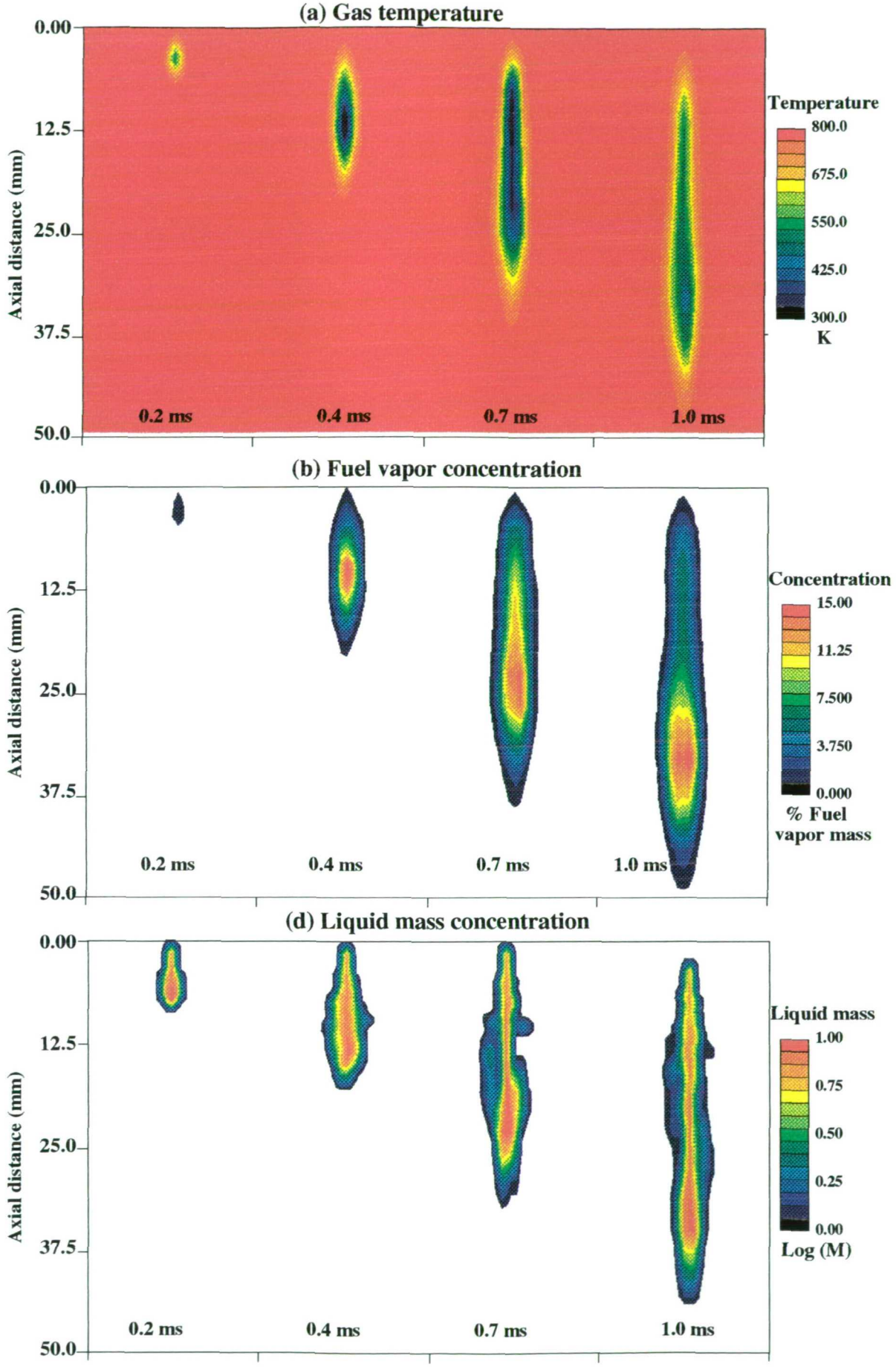

Figure 5–21 : Calculated gas chamber temperature, fuel vapor concentration and liquid mass distribution of an evaporating diesel spray at 0.2, 0.4, 0.7 and 1.0 ms after the start of injection (pump speed 600 rpm)

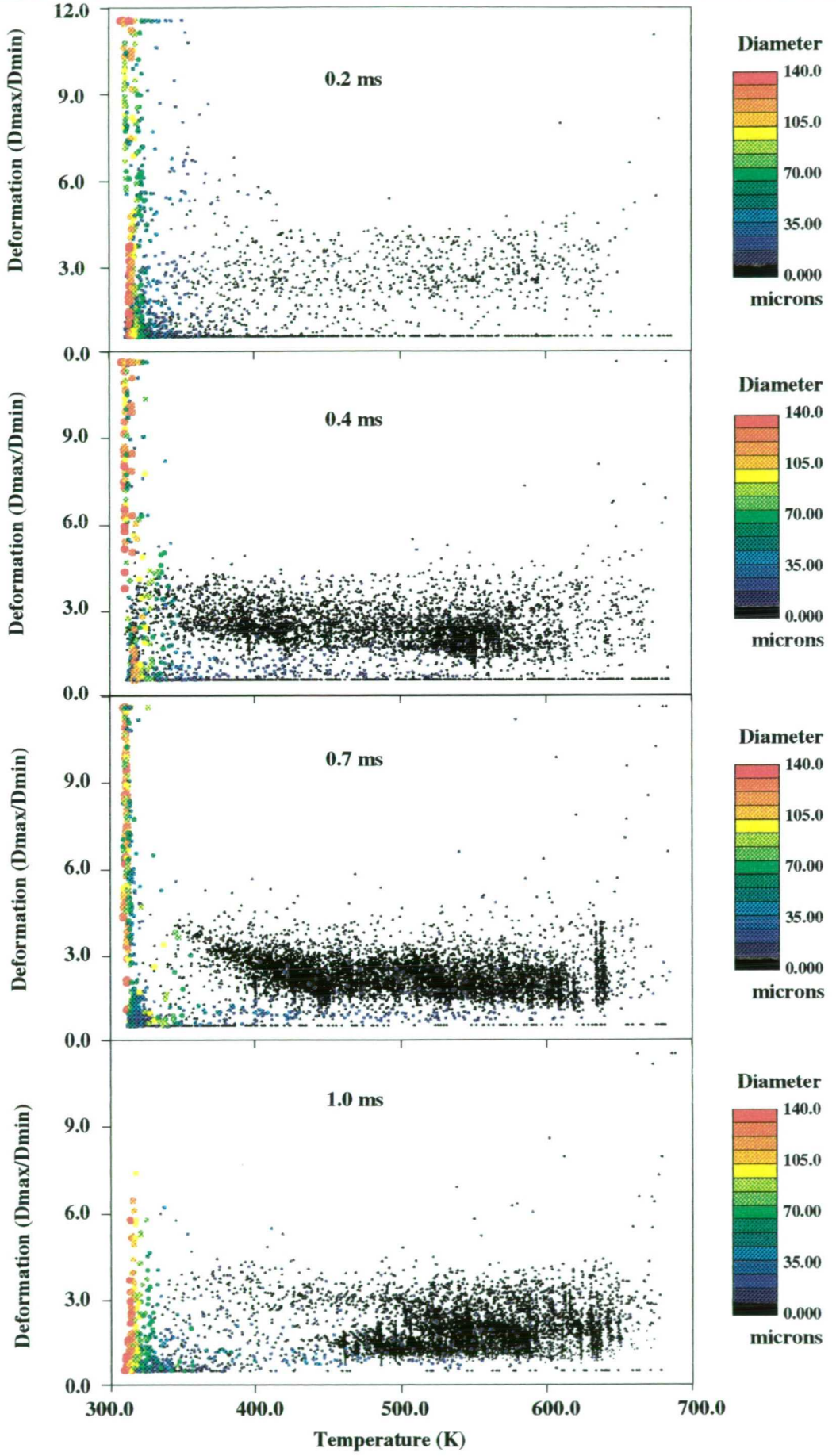

Figure 5–22 : Calculated droplet deformation of an evaporating spray as a function of droplet temperature and size at 0.2, 0.4, 0.7 and 1.0 ms after the start of injection (pump speed 600 rpm)

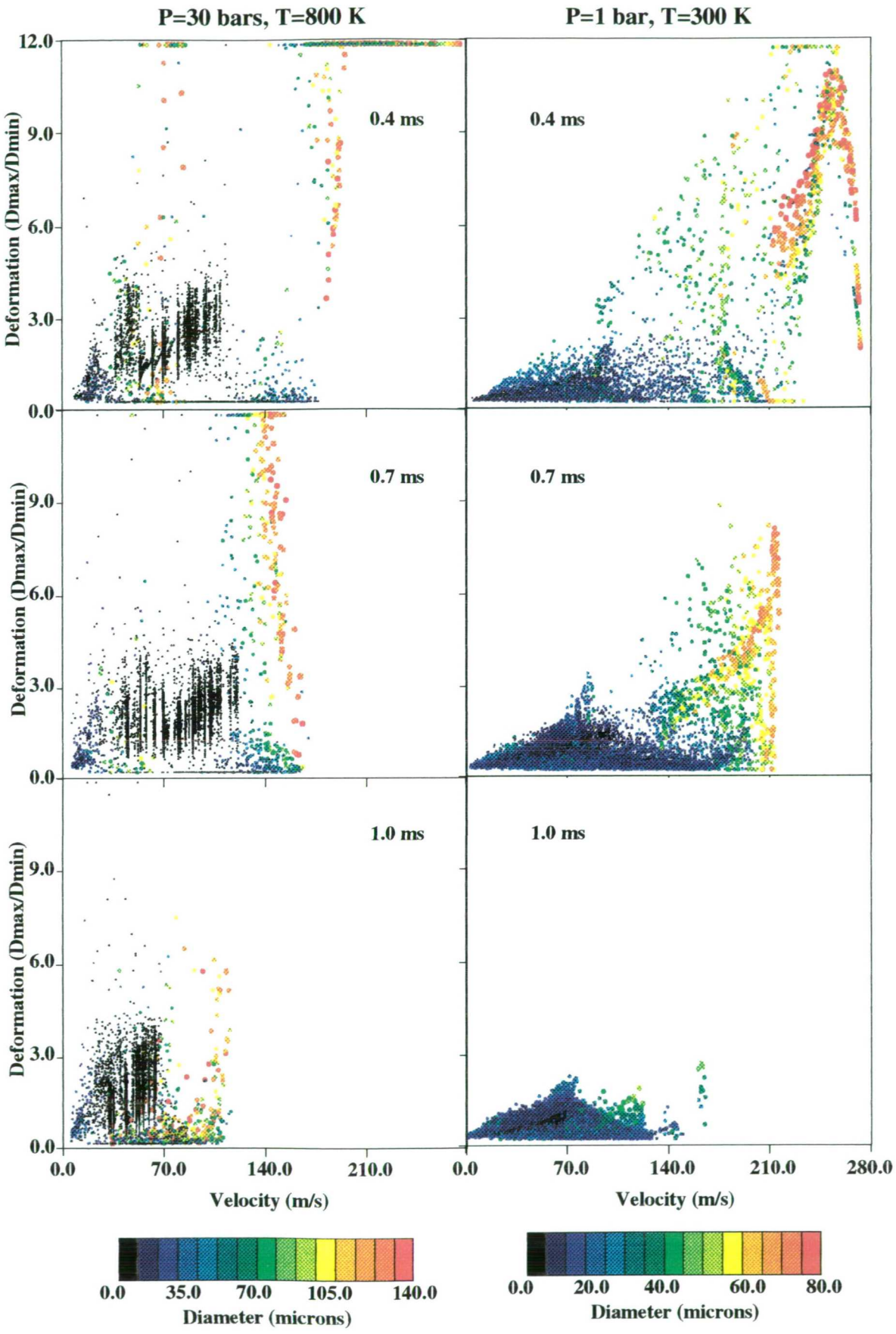

Figure 5–23 : Calculated droplet deformation as a function of droplet velocity and size for an evaporating and a non–evaporating diesel spray at 0.4, 0.7 and 1.0 ms after the start of injection (pump speed 600 rpm)

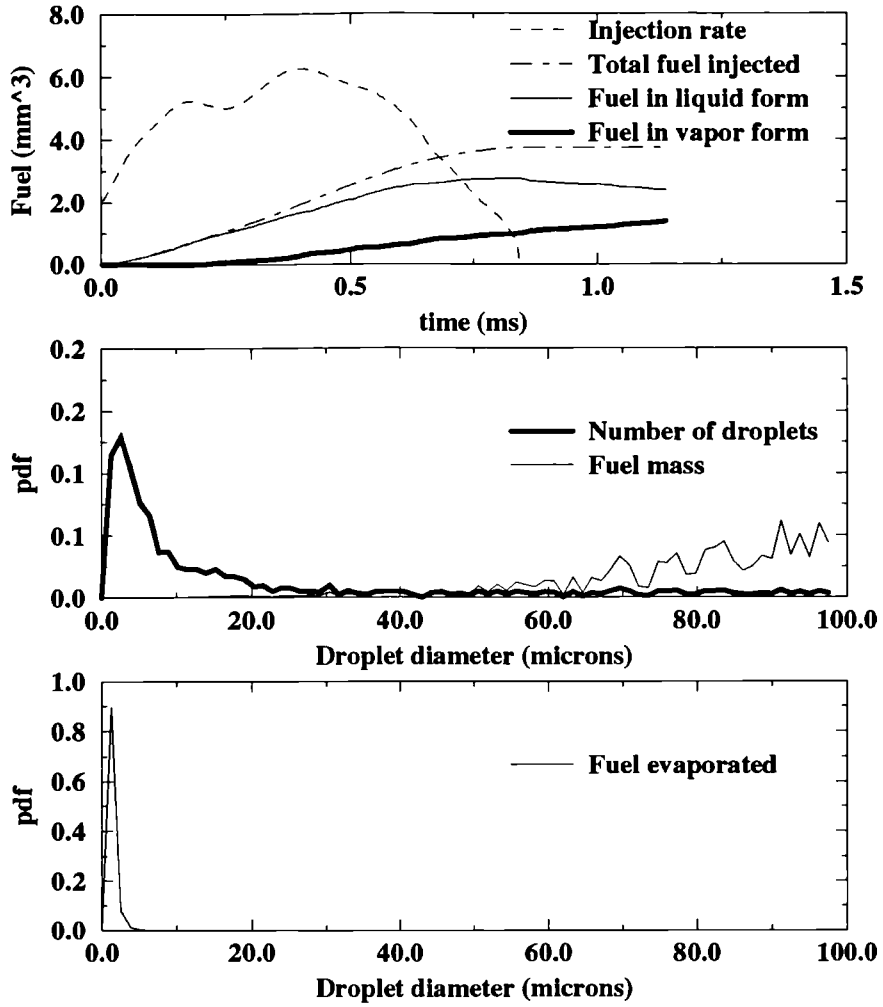

Figure 5–24 : (a) fuel injection rate, total fuel injection quantity, fuel remaining in liquid form and total fuel evaporated (b) Droplet size distribution and liquid mass distribution as a function of droplet size at 1.0 ms after the start of injection (c) Fuel evaporated as a function of droplet size distribution at 1.0 ms after the start of injection. (pump speed 600 rpm)

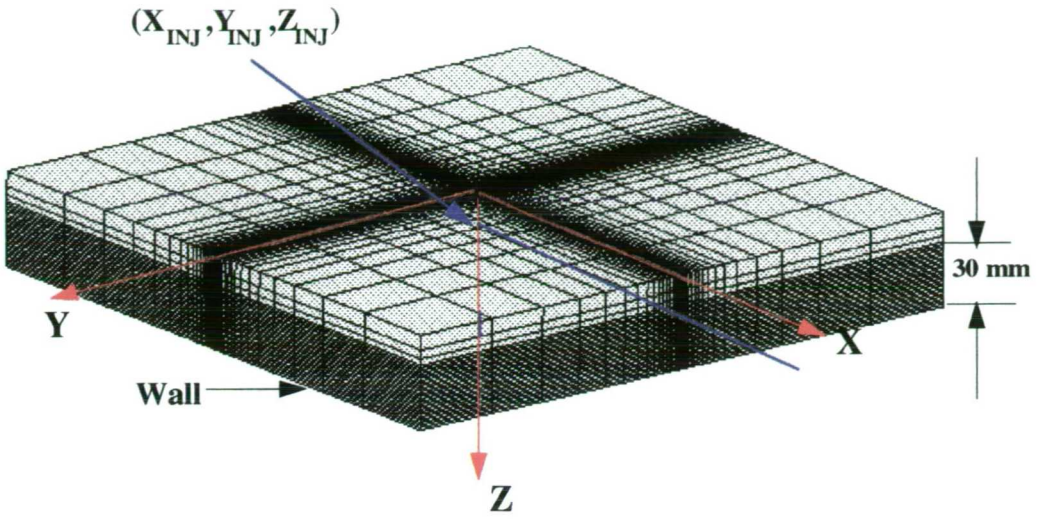

Figure 5–25 : Outline of the numerical grid used for the simulation of the impinging spray

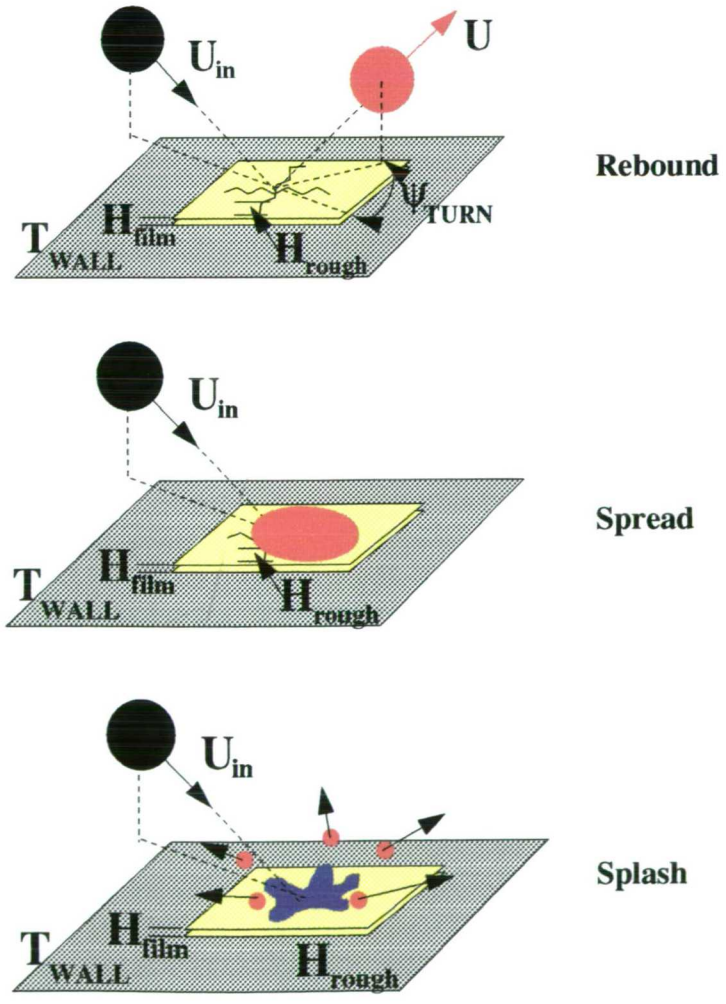

Figure 5–26 : Schematic representation of the hydrodynamic regimes taken into account for droplets impinging on a cold wall.

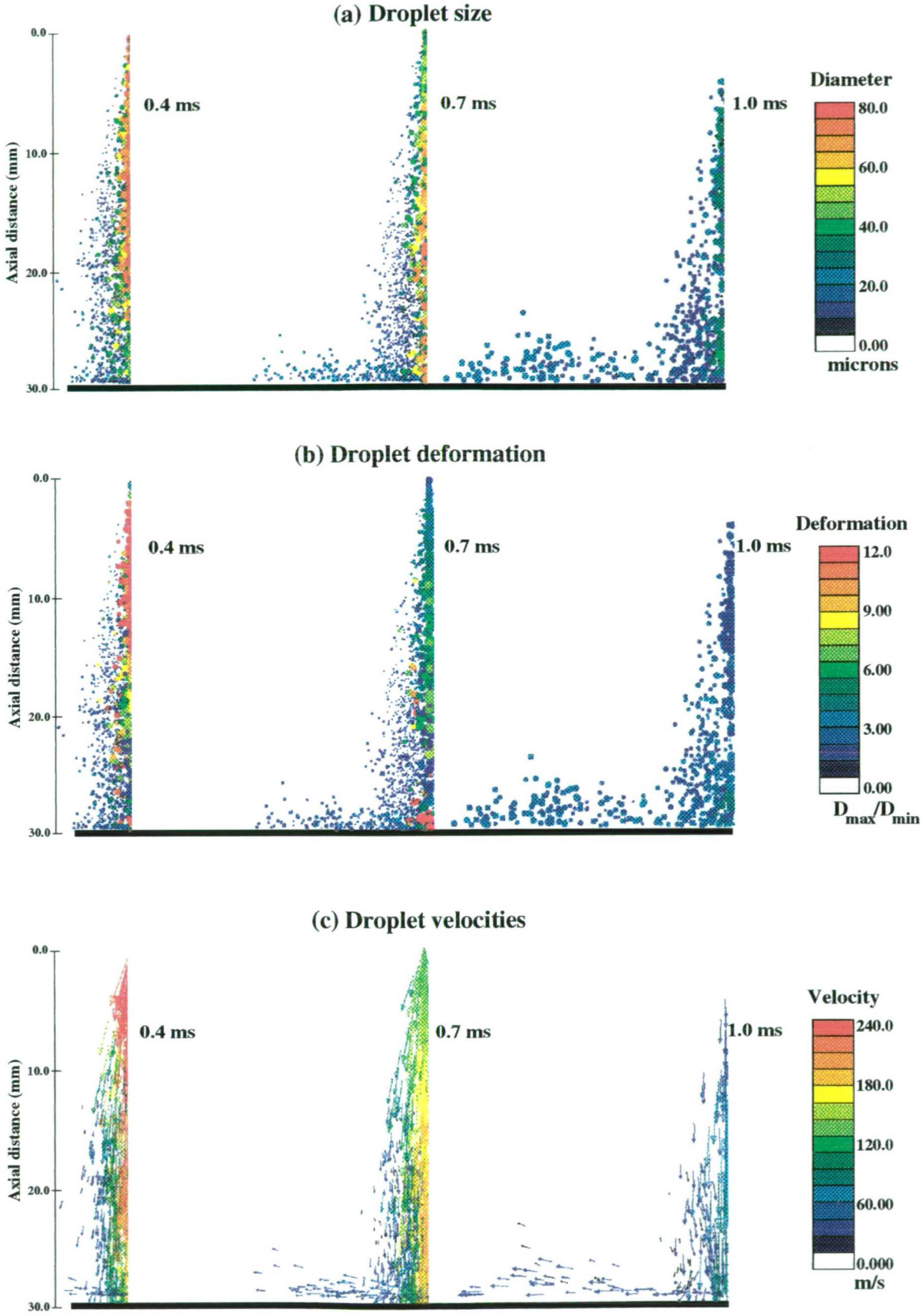

Figure 5–27 : Development of impinging diesel spray at 0.4, 0.7 and 1.0 ms after the start of injection under atmospheric quiescent conditions and low wall temperature (a) droplet size (b) droplet deformation and (c) droplet velocities (pump speed 600 rpm)

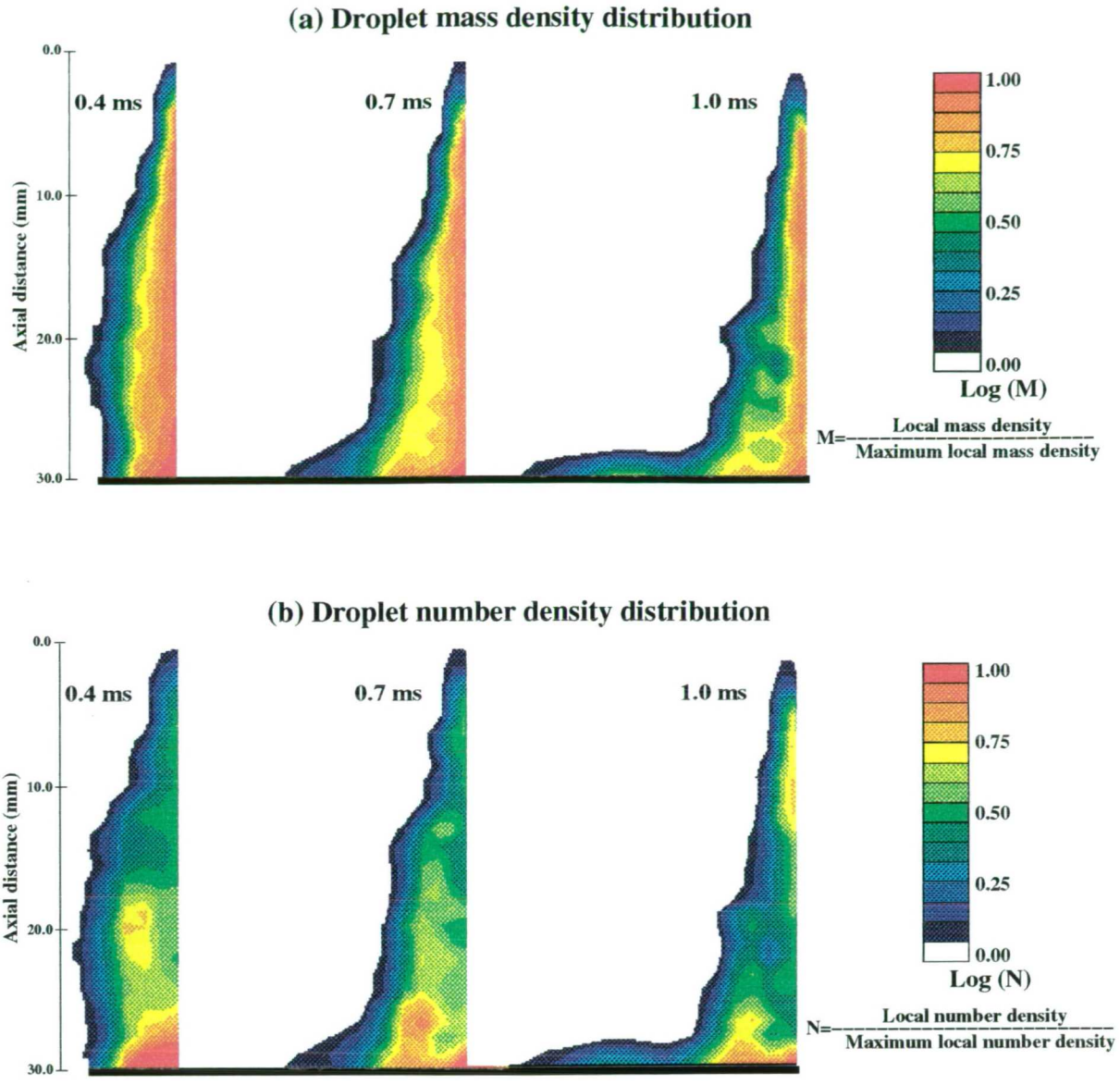

Figure 5–28 : Calculated droplet mass density and droplet number density distributions at 0.4, 0.7 and 1.0 ms after the start of injection for the impinging spray (pump speed 600 rpm)

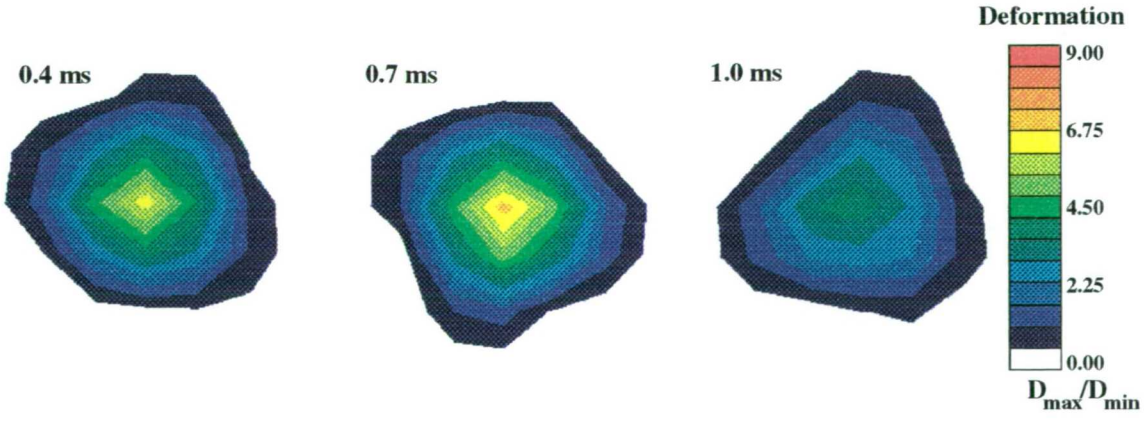

Figure 5–29: Calculated mean deformation of the non–impinging droplets on a horizontal plane 30 mm below the injection hole at 0.4, 0.7 and 1.0 ms after the start of injection (pump speed 600 rpm)

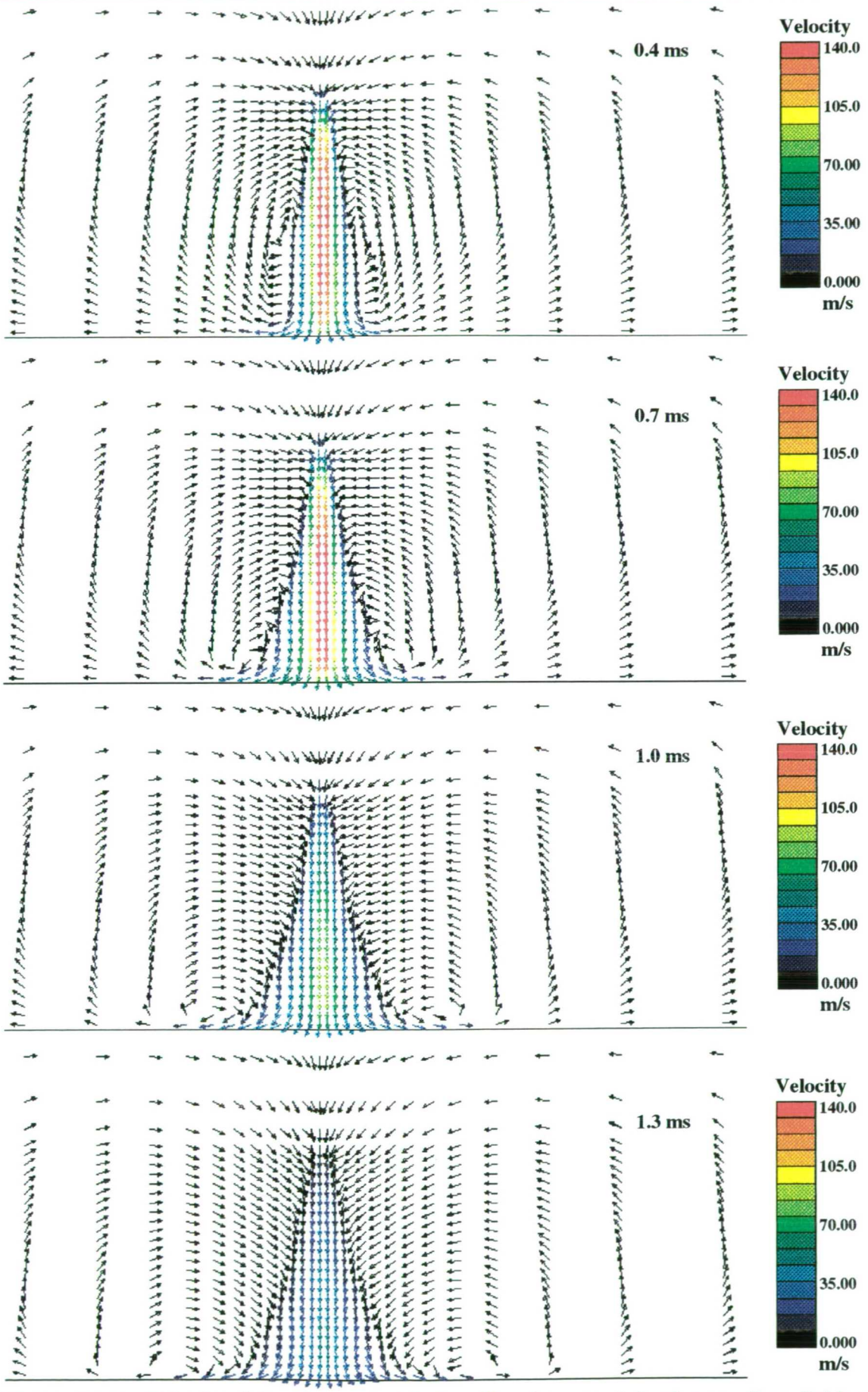

Figure 5–30 : Calculated development of induced by the spray injection gas flow field at 0.4, 0.7, 1.0 and 1.3 ms after the start of injection. The size of the vectors plotted indicates only flow direction (pump speed 600 rpm)

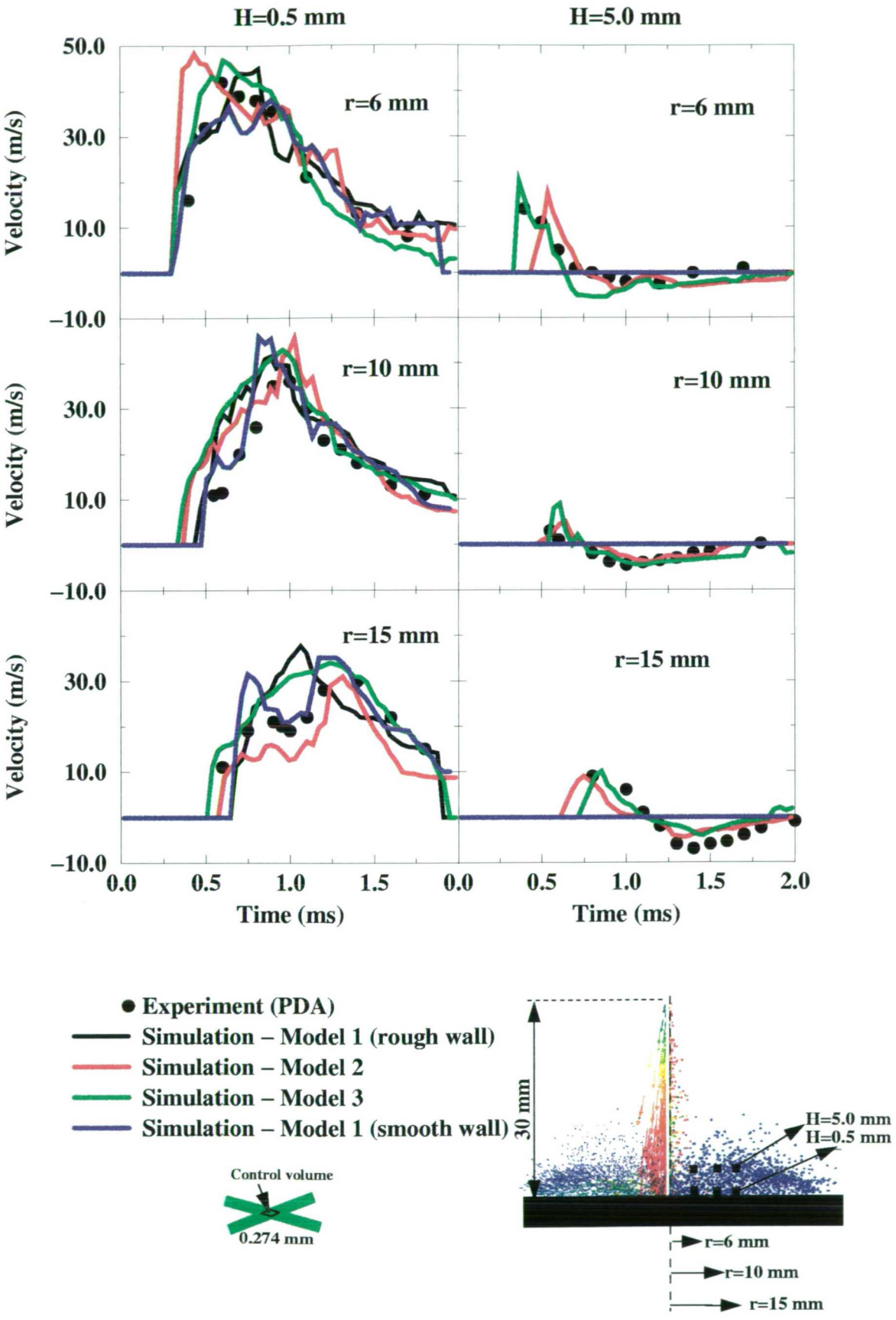

Figure 5–31 : Comparison between the computational and the experimental results for the droplet mean tangential velocity using various impingement models (pump speed 600 rpm). Model 1: Mundo et.al.(1995), Model 2: Senda et. al. (1994), Model 3: Bai (1996)

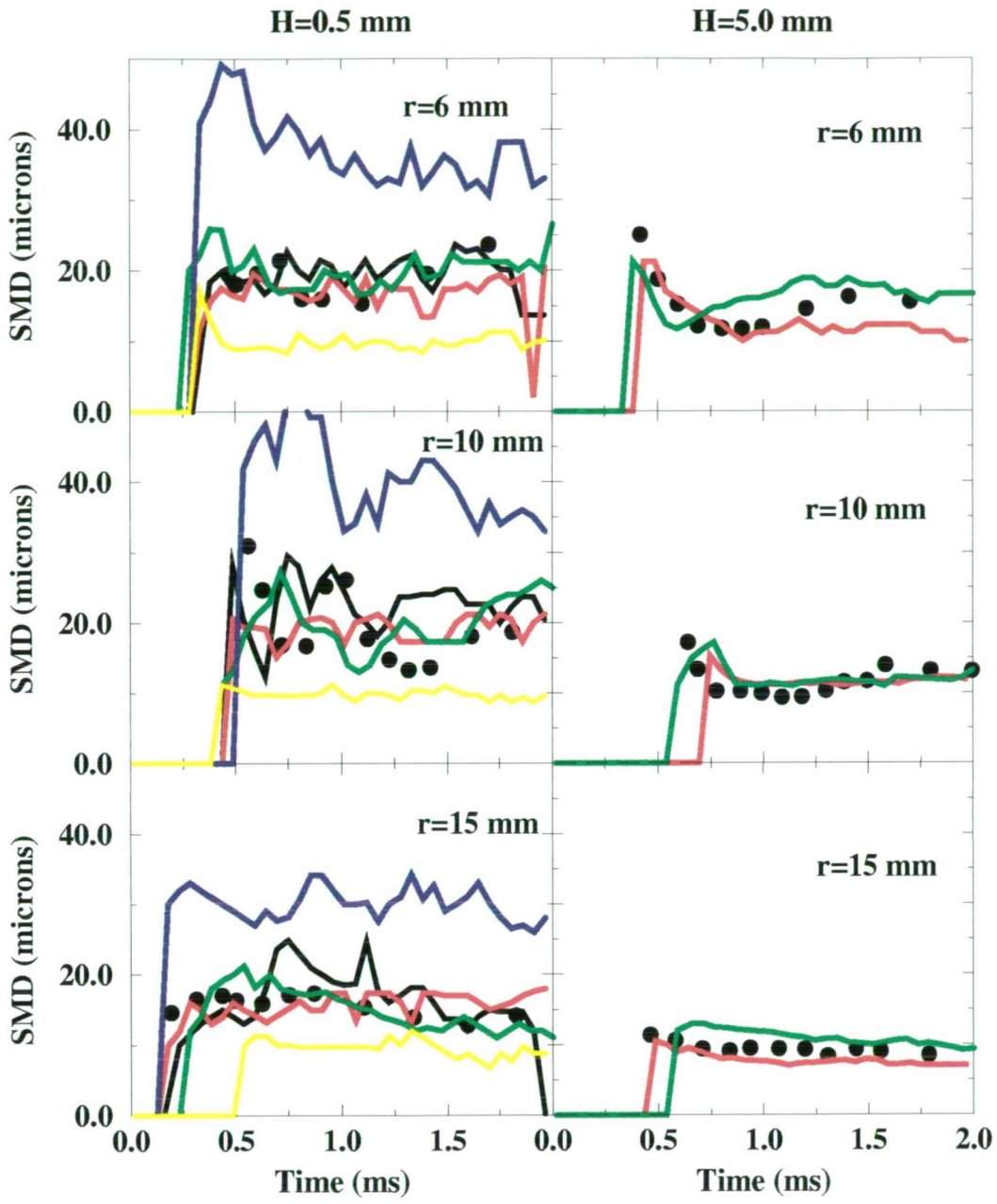

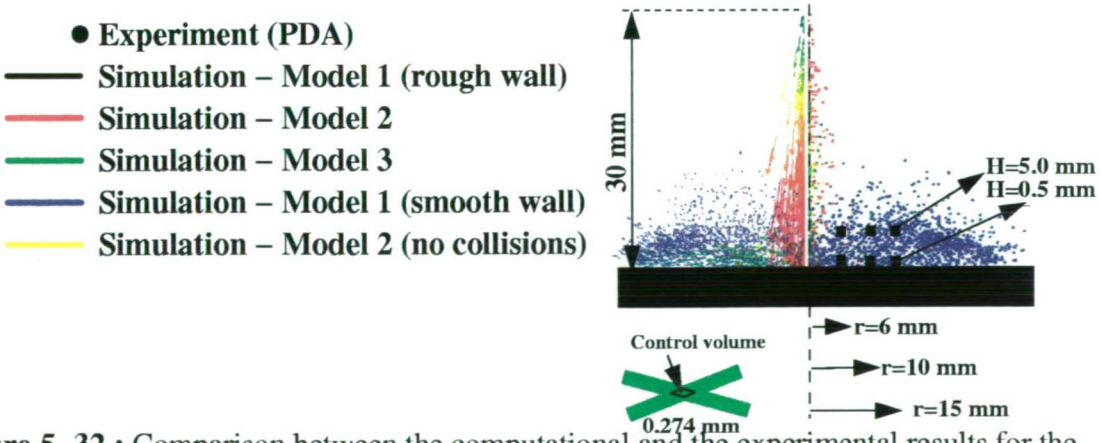

Figure 5–32 : Comparison between the computational and the experimental results for the droplet SMD using various impingement models (pump speed 600 rpm) Model 1: Mundo et.al.(1995), Model 2: Senda et.al. (1994), Model 3: Bai (1996)

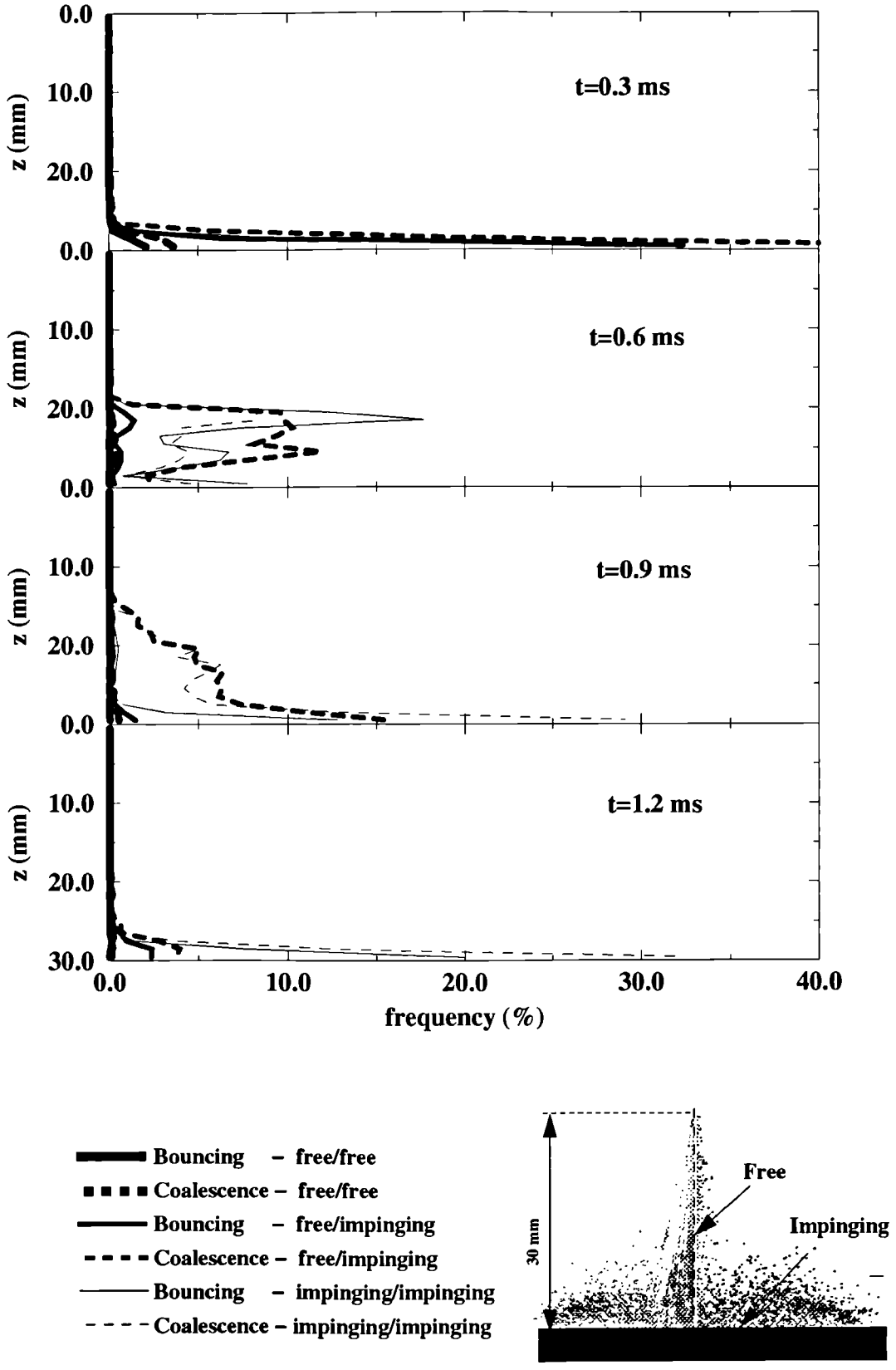

Figure 5–33 : Calculated collision frequency at four time steps from the start of injection as a function of the distance from the wall; six types of collisions between droplets are considered

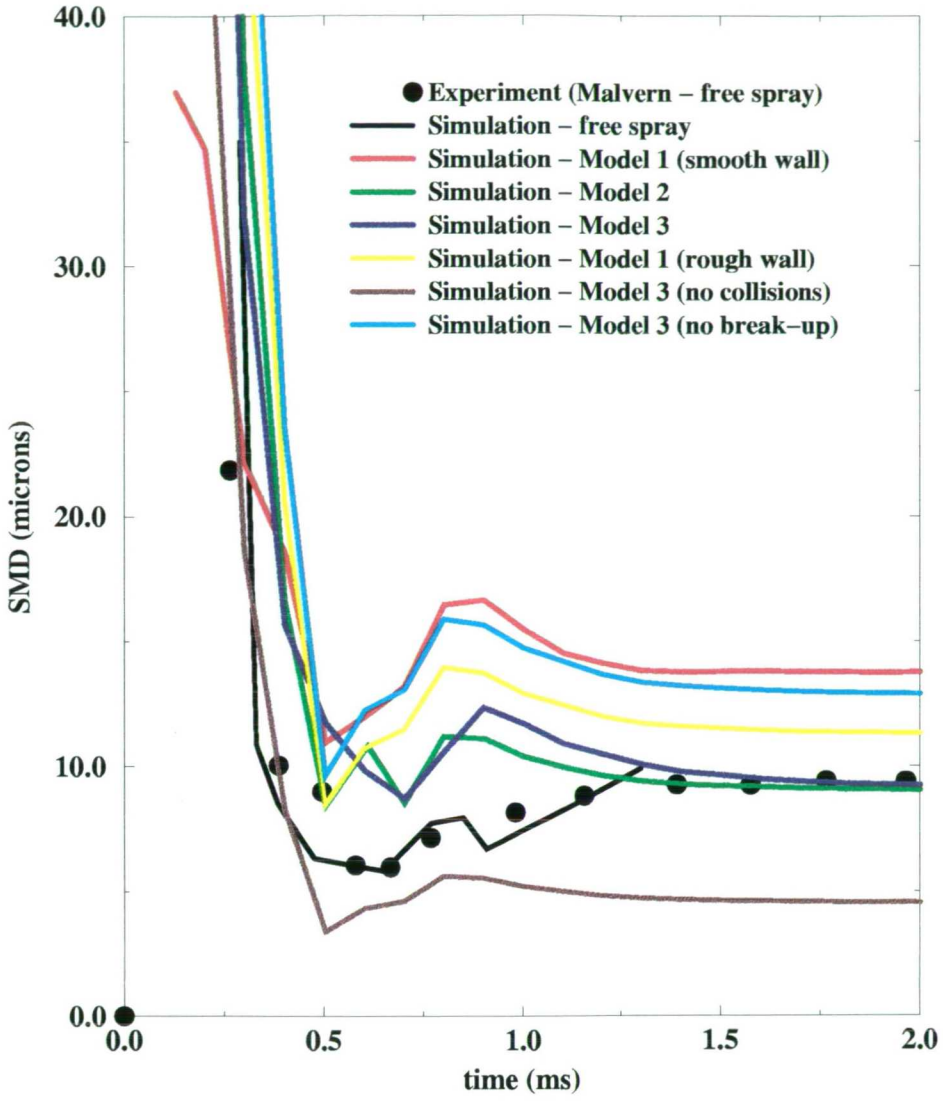

Figure 5–34 : Comparison between the droplet size obtained with a Malvern particle sizer 30 mm below the injection hole and the size of an impinging spray as calculated using different impingement models (pump speed 600 rpm) Model 1: Mundo et.al. (1995), Model 2 : Senda et.al. (1994), Model 3: Bai (1996)

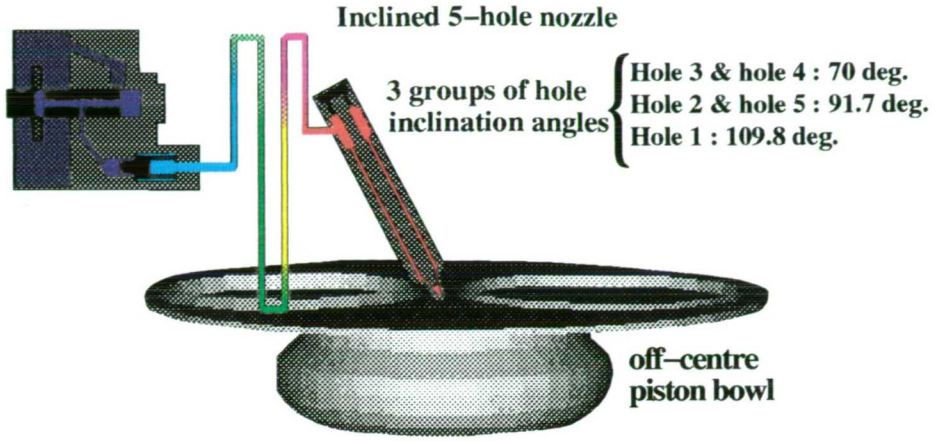

Figure 5–35 : Schematic representation of the fuel injection system and the DI Diesel engine simulated

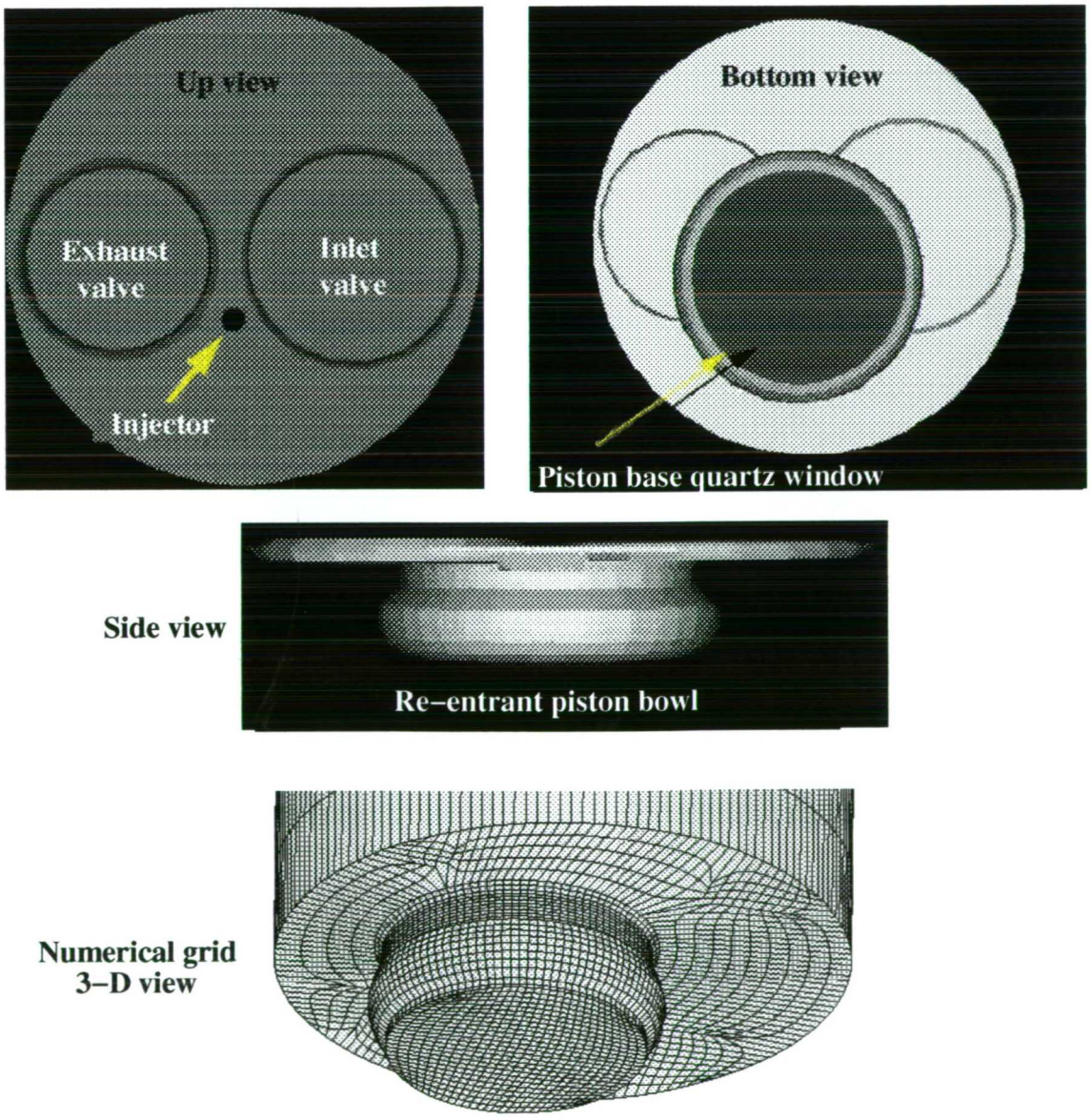

Figure 5–36 : Geometry of the 1.9 l DI Diesel engine and 3–D view of the numerical grid

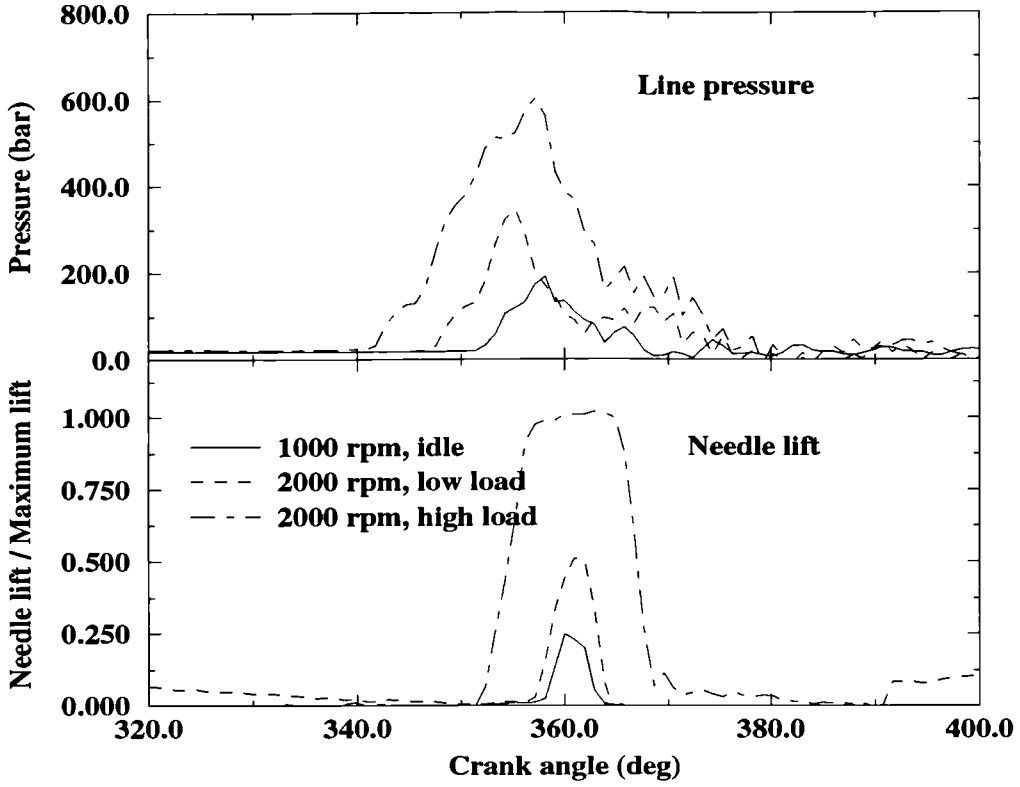

Figure 5–37 : Line pressure and needle lift for the three conditions examined

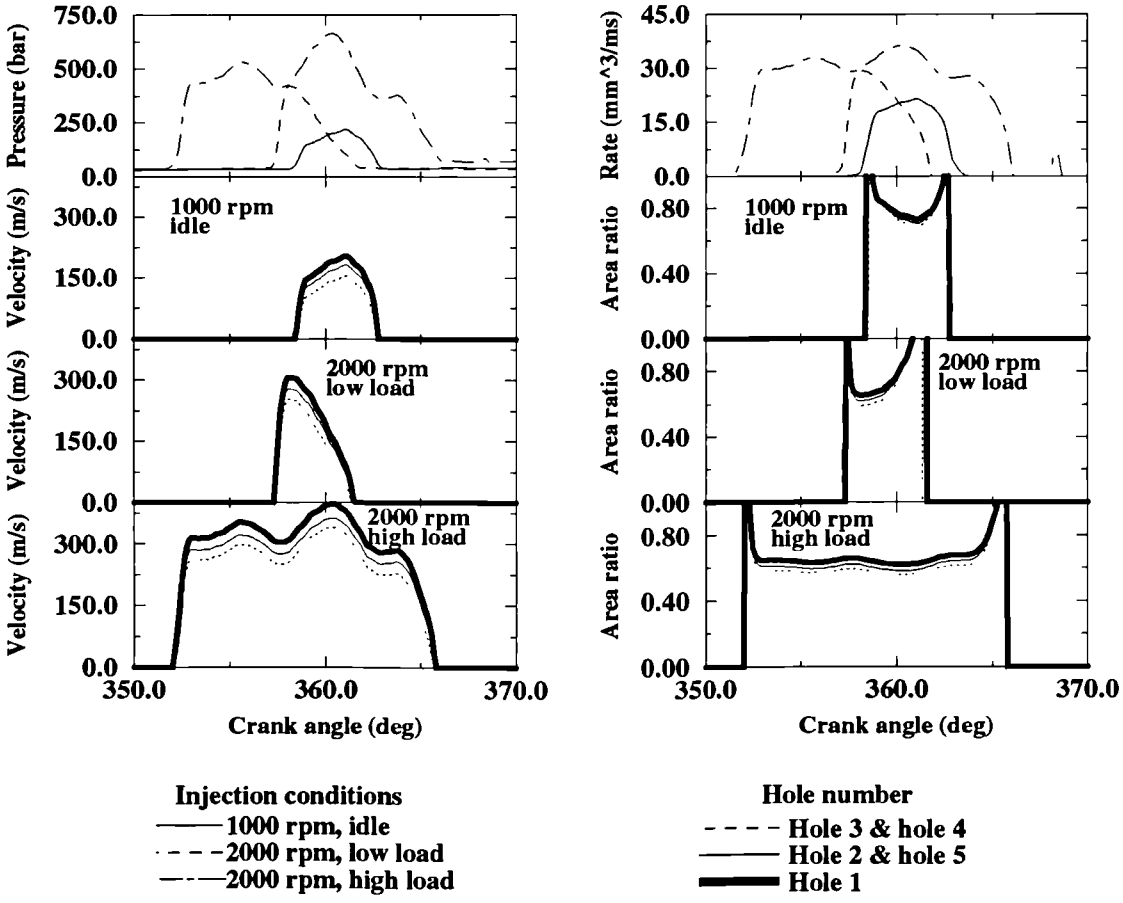

Figure 5–38 : Injection pressure, injection rate, injection velocity and effective hole area ratio for the three different injection conditions and the three different groups of holes, as calculated by the FIE model

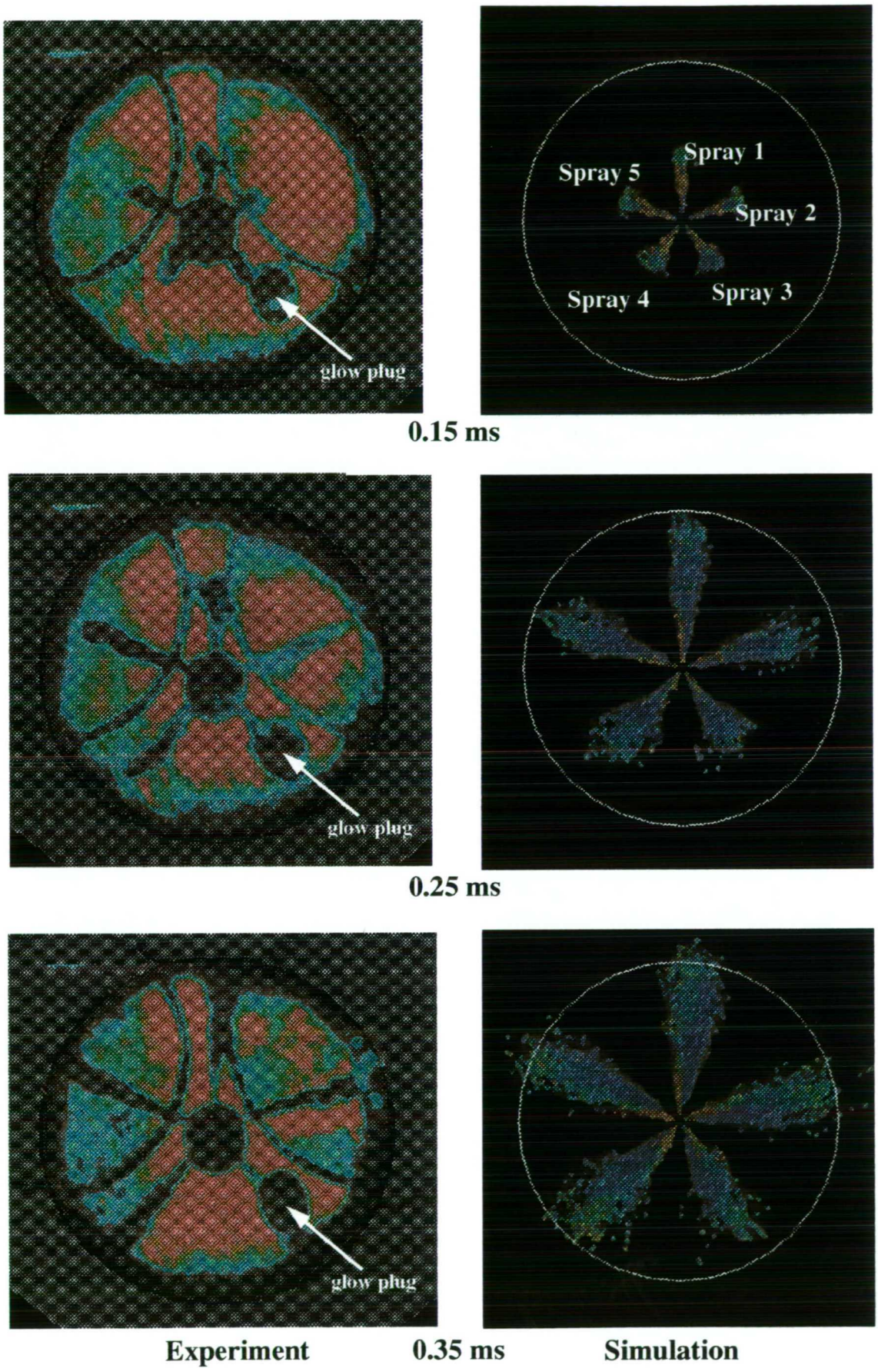

Figure 5–39 : Comparison between computational and experimental results of all five individual sprays inside the piston bowl of the DI Diesel engine.

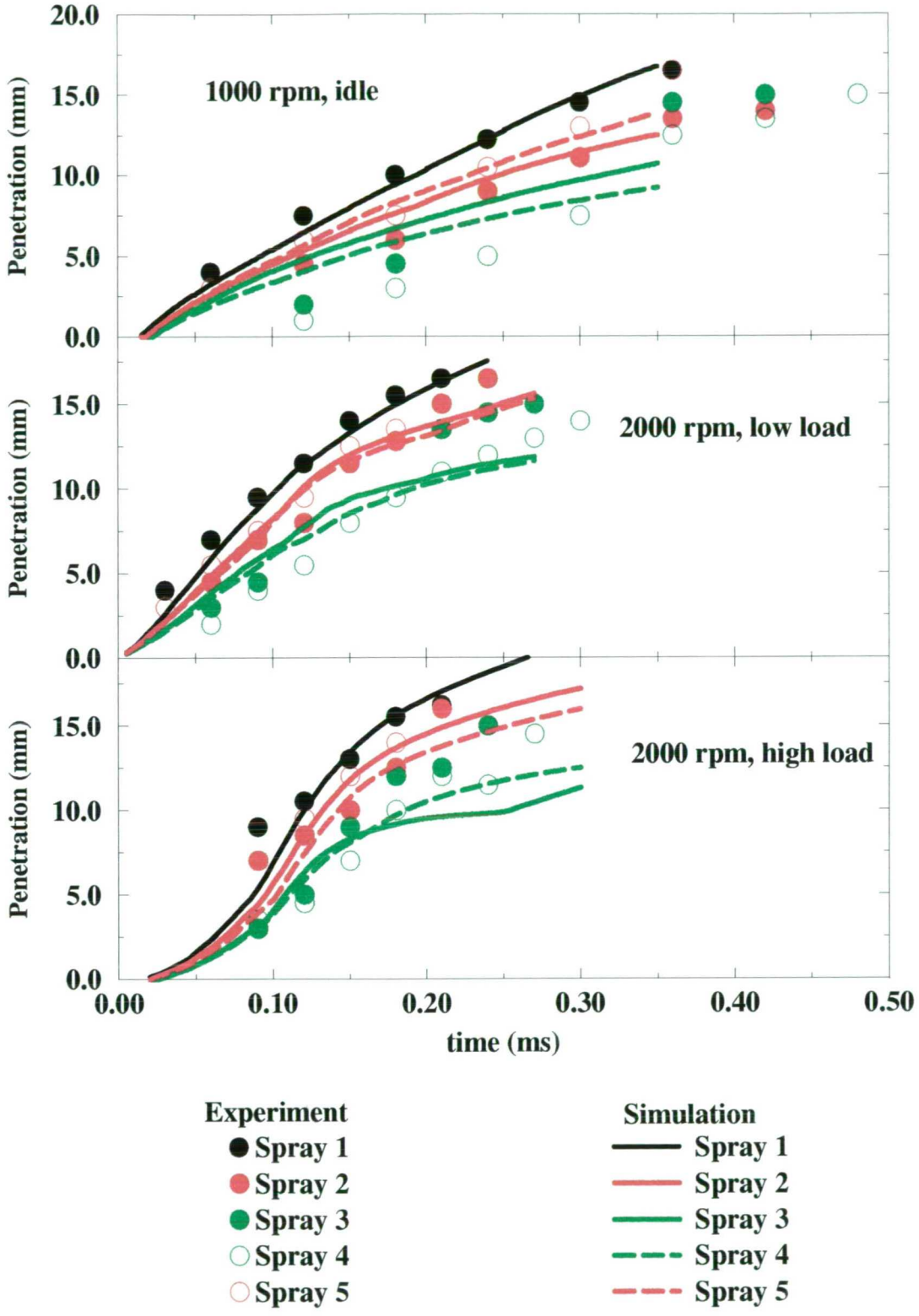

Figure 5–40 : Comparison between computational and experimental results for the spray tip penetration of all five individual sprays in the combustion chamber of the DI Diesel engine.

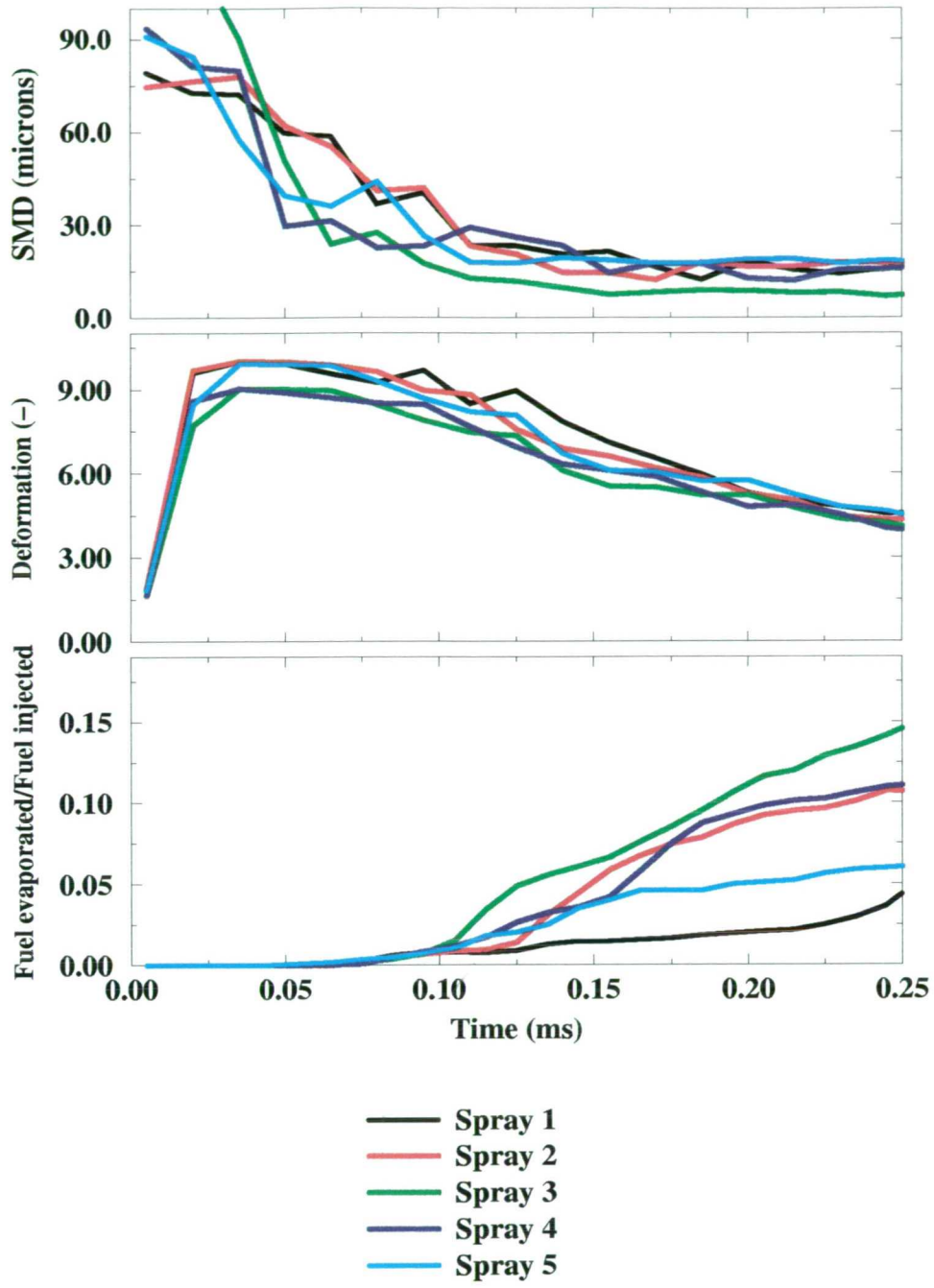

Figure 5–41 : Calculated droplet SMD, droplet deformation and fuel evaporated for all five individual sprays (pump speed 1000 rpm, idle)

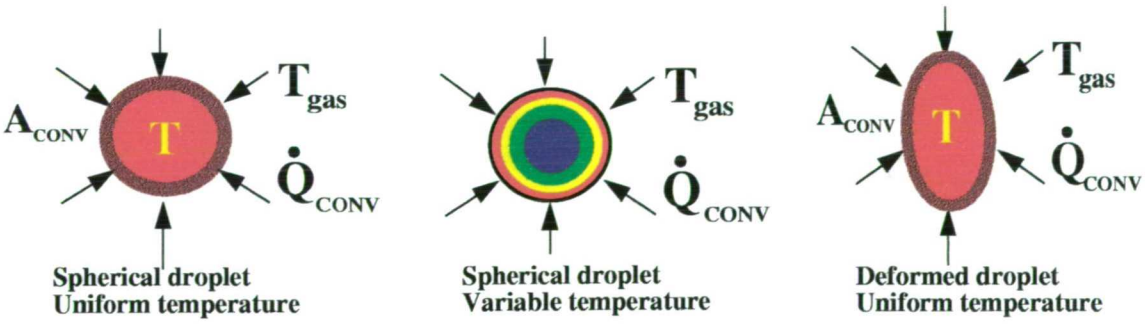

Figure 5–42 : Schematic representation of the droplet evaporation models used

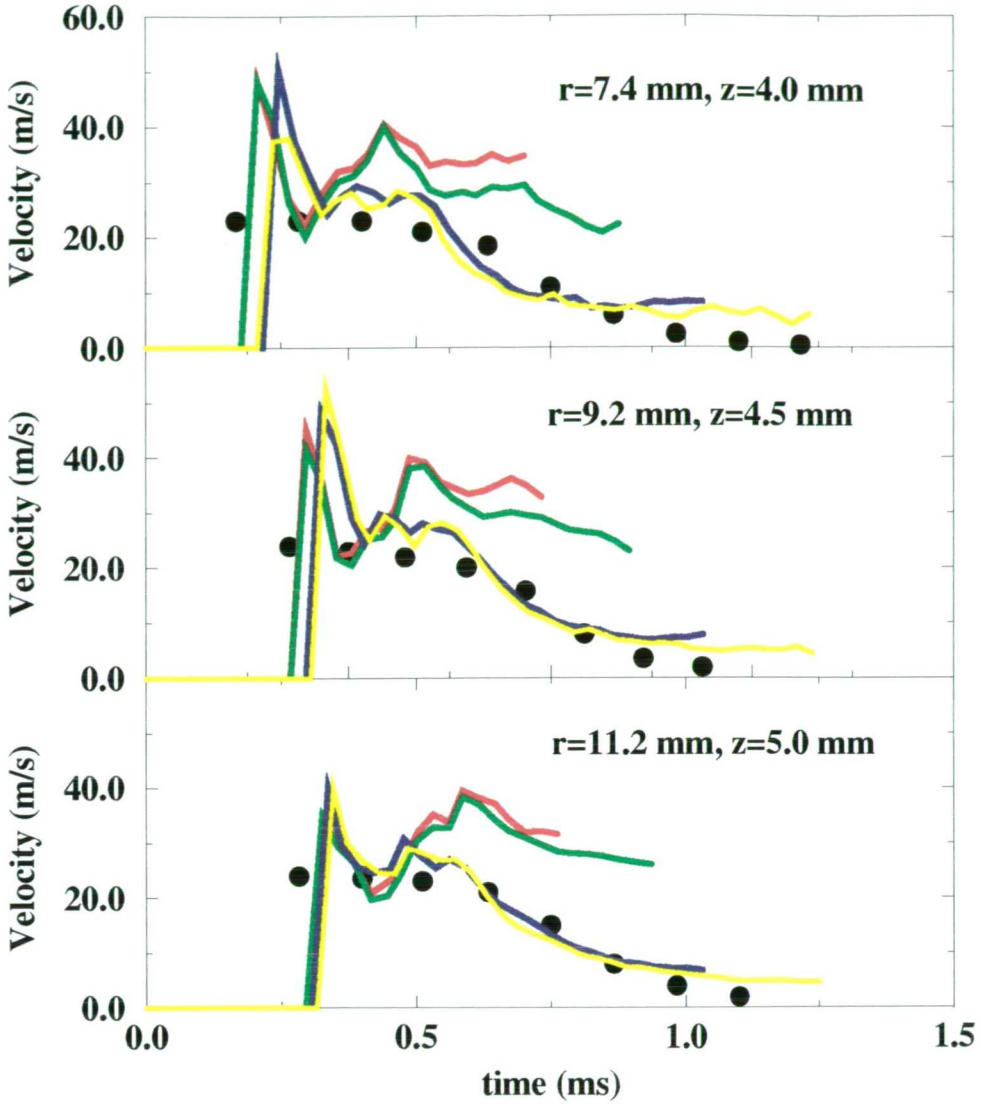

● **Experiment**
Simulation – Uniform temperature, drag of spherical droplet
Simulation – Variable temperature, drag of spherical droplet
Simulation – Uniform temperature of spherical droplet, drag of deformed droplet
Simulation – Uniform temperature of deformed droplet drag of deformed droplet

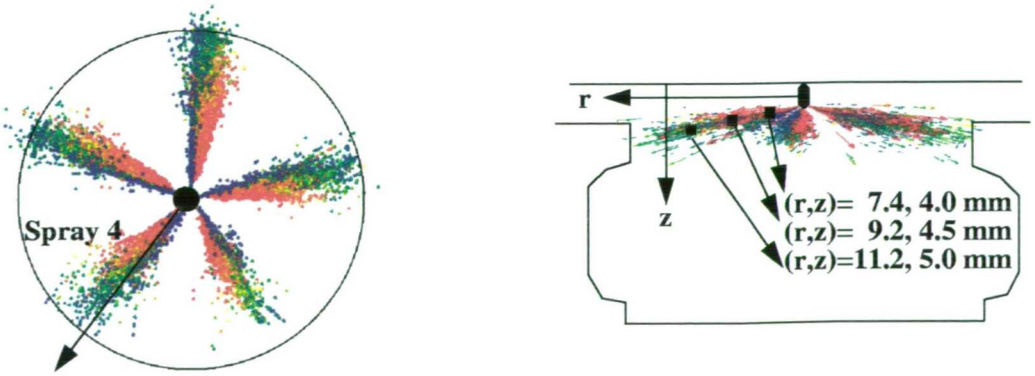

Figure 5–43 : Comparison between computational and experimental results for the mean droplet velocities of spray 4 at three different points inside the piston bowl of the DI Diesel engine, using various droplet evaporation and droplet drag coefficient models (pump speed 1000 rpm, idle)

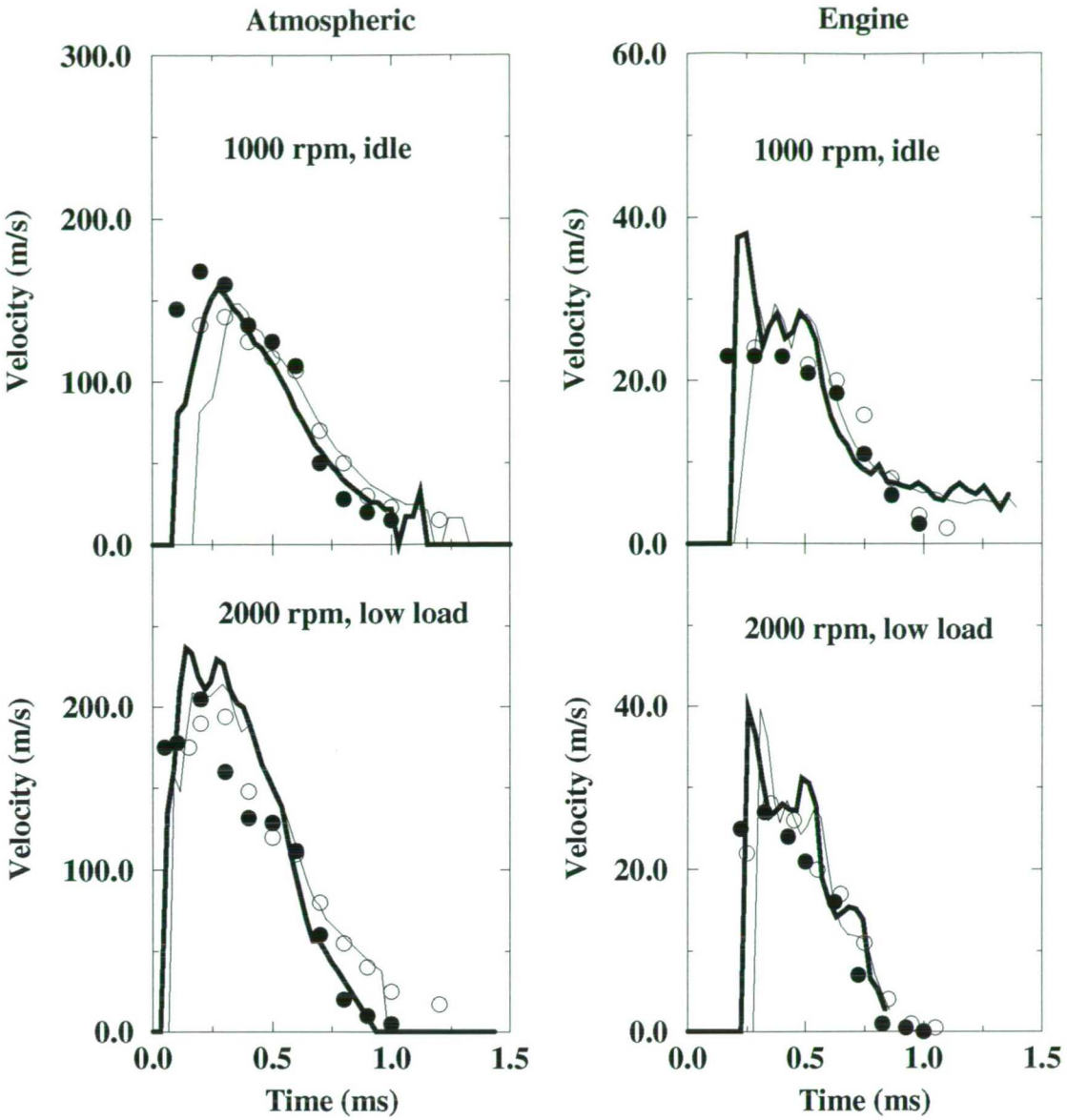

Figure 5–44 : Comparison between computational and experimental results for the temporal variation of the droplet mean axial velocities for two different injection conditions (pump speed 1000 rpm, idle and pump speed 2000 rpm, low load) and surrounding conditions corresponding to both engine and atmospheric sprays

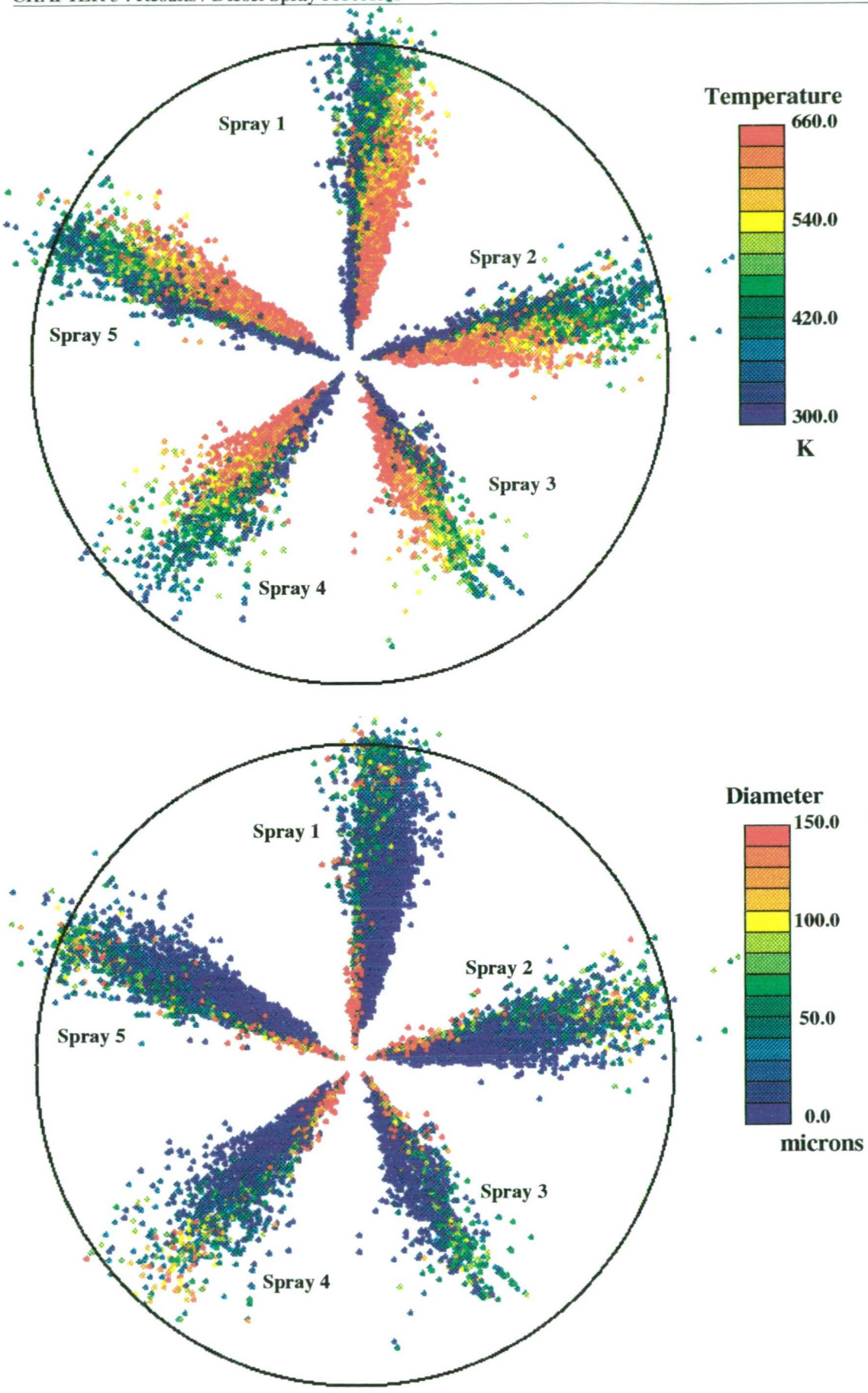

Figure 5–45: Calculated droplet positions with the color represending the (a) droplet temperature and (b) droplet size at 0.35 ms after the start of injection (pump speed 1000 rpm, idle)

CHAPTER 6

When one hears for a sudden and unexpected discovery - a lighting in the blue sky - be sure that it came from the influence of one person to another and it is this interaction which makes every scientific progress possible. Science is never based on the ideas of one person, it is the combined knowledge of thousands.

E. Rutherford

Conclusions and Recommendations for Future Work

This is the last chapter of the present thesis and it is divided into two sections. The first one summarizes the most important conclusions from this work while the second one makes some recommendations for future work.

6.1 Conclusions

During this investigation a combined FIE-spray model was developed and validated against experimental data over a wide range of pump operating and surrounding gas conditions. The sub-models developed or implemented during the present investigation have included:

- a one-dimensional model simulating the transient compressible flow development in hydraulic systems. Any combination of the physical elements assumed to represent the geometry of the system can be specified by the user. In addition, emphasis was given to the hole flow pattern under cavitating conditions and a simple one-dimensional model calculating the effective hole area at the exit of the holes was implemented into the FIE model.
- An existing three-dimensional single-phase CFD model was used to predict the flow distribution inside the sac volume and the injection holes under non cavitating conditions. This model was extended in this investigation to include the developed two-phase diesel spray model which included:
- The development of a cavitation-induced atomization model and its implementation into the code together with existing aerodynamic-induced atomization and jet turbulence-induced atomization models.

- The development of a droplet secondary break-up model combined with a maximum entropy based size distribution model. In addition, three existing droplet break-up models have been implemented into the CFD model.
- The implementation of models for the droplet collisions and droplet turbulent dispersion.
- The implementation of droplet drag coefficient models based on both spherical and deformed droplets.
- The implementation of four droplet-wall interaction models for impinging sprays reported in the open literature.
- The implementation of droplet evaporation models assuming either uniform droplet temperature or its variation within the volume of the droplet. In addition, correlations estimating the effect of droplet deformation on the droplet evaporation were also implemented into the CFD model.

The previous chapters have demonstrated that the developed models in combination with the experimental results can offer valuable information on the performance of fuel injection systems, on the effect of design parameters on the nozzle exit characteristics, on the features of particular spray sub-models and also on the gas-spray evolution under various conditions. In addition, parameters not easily obtained from experimentation have been estimated from the mathematical model giving unique information about the physics involved during the spray development. Although the detailed results have been extensively assessed and discussed in the previous chapters, the most important comments/conclusions are summarized below:

- The flow in diesel fuel injection systems can be considered as one-dimensional. Predictions of the pressure development and the flow rate in such hydraulic systems were found to be in satisfactory agreement with the experimental data.
- 1-D models can be developed in such a way as to easily represent new systems or to allow investigation of the effect that various design parameters have on the performance of the system. In addition, such models can also be used to represent the effect of manufacturing tolerances on the nozzle exit characteristics.
- The flow pattern in the sac volume and the injection holes is strongly affected by the details of the local geometry of this region which is also a function of the manufacturing process. CFD models can be used to obtain information in this area

even under transient flow conditions, since detailed flow measurements in real-size injectors is a particularly difficult task.

- In the present study the validation of the CFD model was based on LDV measurements obtained in a large scale transparent injection nozzle under steady-state conditions.
- Hole cavitation seems to occur in the injection holes under certain operating conditions and can have a strong effect on the spray characteristics. Profound effects such as the increase of the injection velocity due to the volume occupied by the cavitation bubbles at the hole exit can be estimated from one-dimensional considerations.
- The flow pattern inside the injection holes of inclined injectors varies significantly between the holes and depends strongly on the hole inclination angle relative to the needle seat axis while it causes significant differences in the total fuel injected and the injection velocity between the various holes. These differences can be estimated using empirical correlations for the discharge coefficient of each individual injection hole.
- The atomization of the emerging liquid from the injection hole seems to be controlled and enhanced by the presence of cavitation within the injection holes.
- Classical atomization theories based on either the aerodynamic-induced atomization or the jet turbulence-induced atomization have failed to predict the measured droplet size distribution close to the injection hole during the injection period. However, even when phenomenological models simulating the cavitation-induced atomization are introduced, the subsequent physical processes expected to take place during the spray development require special attention and further development.
- The radial distribution of the droplets within the spray cone angle was found to be a function of the inertia of the formed droplets. Larger droplets with higher velocities are located close to the spray axis and smaller ones at the periphery of the spray. This trend was simulated by using a simple radial droplet distribution model within the spray cone angle during the atomization process.
- Droplet secondary break-up is an important mechanism having significant effects on the structure of diesel sprays. Predictions with the model developed during the present investigation and incorporating correlations estimating the droplet deformation and deformed droplet drag coefficient over a wide range of Weber

numbers seems to give more realistic predictions than existing models in the open literature.

- The aforementioned model when combined with a sub-model estimating the droplet size distribution of the formed droplets during their secondary break-up based on the concept of maximum entropy has eliminated the need for using an assumed droplet size distribution function.
- Stripping break-up was found to be the dominant droplet break-up regime under injection conditions and back (chamber) pressures of practical interest.
- When bimodal droplet size distributions were introduced into the stripping break-up model, significant differences in the predicted structure of the diesel spray were observed. The frequently observed 'Christmas tree' spray structure was represented and attributed to both the modulation in the injection conditions caused by the wave dynamics within the fuel injection system and to the bimodal droplet size distributions resulting during the stripping break-up regime.
- Droplet deformation was predicted to exhibit higher values for larger droplets in non-evaporating sprays; however, when injected into a high temperature chamber, the variation of the liquid physical properties as a function of its temperature was found to have an important effect on the deformation process of the evaporating droplets. These at the latest stages of their existence as droplets were becoming highly distorted and evaporated rapidly.
- Most of the fuel evaporated from the spray was found to originate from small heated droplets, which implies that the droplet deformation process should be given further attention and their effect on the evaporation process should be considered.
- A model taking into account the change of the gas-liquid interface contact area between the evaporating droplets and the surrounding gas as a function of the droplet deformation rate was found to predict more accurately the measured droplet characteristics inside the piston bowl of a DI diesel engine.
- Droplet evaporation models assuming spherical symmetry and a temperature variation inside the volume of the droplets can not be justified on the basis of the calculated by the break-up model droplet shape. In addition, calculation of the droplet drag coefficient should also be based on droplet deformation since only under these circumstances the droplet velocities were reasonably well predicted.

- Spray to spray variations resulting from the flow pattern inside the sac volume and the injection holes of inclined injectors were predicted reasonably well by the combined FIE-spray model. These consistent variations, experimentally identified in terms of individual spray tip penetration inside the piston bowl of the DI diesel engine, were reasonably well predicted by the combined model.
- The processes involved during the impingement of diesel sprays on a flat wall were found to be not only a function of the hydrodynamics of the single-droplet impingement process, but also of the dynamics of the impinging spray as a whole. These include the increased collision frequency at the impinging region, due to the opposite directed streams of the impinging and the ejected from the wall droplets, and the secondary atomization of the droplets resulting from the head vortex formation and its development along the wall direction.
- Overall, the numerical models appear to be attractive since they provide important information not easily obtained from experiments, have limitations resulting from the discretization procedure. The computational results were found to depend on the number of computational parcels used to represent the spray. It seems that a very large number, which in some cases is practically unrealistic, is required in order to obtain statistically independent results. The grid resolution also affects the accuracy of the results. Special emphasis has to be given to the assumptions involved in the formulation of the Eulerian-Lagrangian approach used to represent the spray. For example, when the void fraction becomes zero (i.e. when the liquid occupies the whole computational cell) then the method collapses; thus, special attention has to be given very close to the nozzle exit where these conditions may prevail.

6.2 Recommendations for Future Work

It should be clear by now that the processes involved during the injection and the development of diesel sprays in engines are complicated and involve the influence of a significant number of parameters. As a result, further research in this field will be guided not only by the scientific aspects of the various sub-processes involved, but also by the engine and fuel injection system manufacturers, or in other worlds, by the requirements that future engines have to satisfy. Irrespective of that, there are still many parameters affecting the physical processes of fuel injection which require further work.

Far from implying that there are no other areas which require further investigation, some important topics are summarized below:

- The detailed physics involved during and after the onset of cavitation in the injection holes remains an ill-understood problem. Thus, experiments have to be performed in representative geometries since the details of the flow in this area govern the atomization process of the injected liquid. Experiments are in progress at Imperial College aiming to visualize cavitation in a large scale nozzle and to obtain quantitative information about the bubble concentration and the slip velocity between the two phases. Depending on the results of this investigation, experiments will be designed focusing on the visualization of cavitation in real size nozzles under realistic operating conditions.
- Data obtained from such experiments can be used for the development and validation of three-dimensional CFD models able to simulate the two-phase cavitating flow. Although direct numerical simulation (DNS) seems to be closer to reality as a mathematical approach for this type of flows, CFD models incorporating sub-models for the mass exchange between the two phases and the effect of the presence of cavitating bubbles on the molecular and turbulent mixing are expected to be developed in the next few years but will require extensive validation against experimental data.
- Studies on the hole flow pattern should be combined with simultaneous visualization of the atomization process, since all subsequent spray calculations depend on the results of the atomization sub-model. Thus, experiments should be directed towards the visualization of the mechanisms causing the atomization of the emerging jets, which will provide the basis for further theoretical modeling, but also for the quantification of the characteristics of the droplets resulting from this process, which will be used for the validation of the refined models.
- Experiments should also be addressed towards the investigation of the detailed spray characteristics under higher back (chamber) pressures and temperatures; such studies can provide information for validation of existing models under very high injection pressures, which seems to be the trend in all future fuel injection systems, and under turbocharged engine operation.
- It is of significant importance to develop techniques capable of estimating not only the droplet velocity and droplet sizes but also the mass flux associated with these

droplets, since that still remains an unsolved problem; models should be able to predict accurately the fuel mass distribution since this is of major importance for the refinement of existing combustion models.

- Further research should be directed towards the investigation of the phenomena of single droplet motion. Processes like droplet deformation and break-up, droplet evaporation and collision between droplets should be further investigated not only experimentally but also computationally; DNS studies in this area can now be used with the existing computer power to provide correlations which can then be implemented as sub-models into the CFD spray models.
- Finally, phenomena associated with the spray/wall interaction process seem to be another area where many problems remain to be solved; these include the wall film formation and its interaction with the impinging droplets, the effect of increasing wall temperature and the hydrodynamics of single droplet impingement, both spherical and distorted, on walls under variable conditions.
- Although the Eulerian-Lagrangian approximation is an attractive technique, it can not be used in very high flow rates at the areas close to the injection holes due to the locally very high liquid concentration. Thus, on the numerical side, other approximations have to be introduced in order to calculate the liquid and gas properties under such high-load conditions and be combined with this method for the prediction of the far spray characteristics.

Overall, this study should be regarded as another step towards the simulation of all the processes taking place in diesel engines and in many other fluid mechanics applications, through the building of a comprehensive tool for their prediction. It is hoped that the conclusions of this work will be of benefit to modelers, experimentalists and industrial manufacturers alike and will contribute to the design of more fuel efficient and environmentally-friendly diesel engines.

REFERENCES

Abramzon B. and Sirignano W.A. "Droplet vaporization model for spray combustion calculations", Int. J. Heat and Mass Transfer, Vol. 32, No 9, pp. 1605-1618, 1989

Adey A.J., Cunliffe F. and Mardell J.E. "Rotary Fuel Injection Pump Developments for High Speed Diesel Engines", SAE Paper 810516, 1981

Ahmadi G. and Goldschmidt V.W. "Kinematic computer simulation of the turbulent dispersion of newtrally buoyant particles", Developments in mechanics, Proceedings of the 11th Midwestern Mechanics conf, eds. H.J. Weiss, D.F.Young, W.F.Riley and T.R.Roggie, vol.5, pp. 201-214, Iowa State University Press, Ames, 1969

Ahmadi M. and Sellens R.W. "A simplified maximum-entropy-based drop size distribution" Atomization and Sprays, Vol. 3, pp. 291-310, 1993

Ahmadi-Befrui B., Uchil N., Gosman A.D. and Issa R. "Modeling and Simulation of Thin Liquid Films Formed by Spray-Wall Interaction", SAE Paper 960627, 1996

Ahmadi-Befrui B., Wiesler B., and Winklhofer E. "The propagation of Fuel Sprays in a Research Diesel Engine - A Joint Numerical and Experimental Analysis", SAE Paper 910181, 1991

Al-Roub M., Farrell P. and Senda J. "Near Wall Interaction in Spray Impingement", SAE Paper 960863, 1996

Amsden A.A., O'Rourke P.G. and Butler T.D. "KIVA-II : A computer program for chemically reactive flows with sprays", Los Alamos report LA-11560-MS, May 1989

Andrews M.J. and O'Rourke P.J. "The Multiphase Particle-In-Cell (MP - PIC) Method for Dense Particulate Flows", Int. J. Multiphase Flow, Vol. 22, No 2, pp 379-402, 1996

Anno J.N. The Mechanics of Liquid Jets, D.C.Heath and Company, 1977

Arai M. and Amagai K. "Experimental study on a diesel spray of multi-stage injection", COMODIA 1994, Kobe, Japan, July 1994

Arai M., Tabata M., Hiroyasu H., and Shimizu M. "Disintegration Process and Spray Characterization of Fuel Jet Injected by a Diesel Nozzle", SAE Paper 840275, 1984

Araki K. and Moriyama A. "Deformation behavior of a liquid droplet impinging on a hot surface", Int. Conf. on Liquid Atomization and Spray Systems. ICLASS-82, 1982

Arcoumanis C. and Baniasad M.S. "Analysis of Consecutive Fuel Injection Rate Signals Obtained by the Zeuch and Bosch Methods", SAE Paper 930921, 1993

Arcoumanis C. and Baniasad M.S. "Analysis of transient response of diesel fuel injection systems", Proc. IMechE Seminar on Diesel Fuel Injection Systems, pp. 99-113, London, 28-29 Sept. 1995

Arcoumanis C. and Chang J-C. "Flow and Heat Transfer Characteristics of an Impinging Transient Diesel Spray", SAE Paper 940678, 1994

Arcoumanis C. and Chang J-C. "Heat transfer between a heated plate and an impinging transient diesel spray", Experiments in Fluids 16, 105-119, 1993

Arcoumanis C. and Cutter P.A. "Flow and Heat Transfer Characteristics of Impinging Diesel Sprays Under Cross-Flow Conditions", SAE Paper 950448, 1995

Arcoumanis C. and Fairbrother R.J. "Computer Simulation of Fuel Injection Systems for DI Diesel Engines", SAE Paper 922223, 1992

Arcoumanis C., Gavaises M, Yamanishi M., and Oiwa J. 'Application of a FIE computer model to an in-line pump based injection system for diesel engines', SAE Paper 970348, 1997

Arcoumanis C., Bae C., Nagwaney A., and Whitelaw J.H. "Effect of EGR on Combustion Development in a 1.9L DI Diesel Optical Engine", SAE Paper 950850, 1995

Arcoumanis C., Begleris P., Gosman A.D. and Whitelaw J.H. "Measurements and Calculations of the Flow in a Research Diesel Engine", SAE Paper 861563, 1986

Arcoumanis C., Chang C-J. and Morris T. "Spray Characteristics of Single- and Two- Spring Diesel Fuel Injectors", SAE Paper 930922, 1993

Arcoumanis C., Fairbrother R.J., Gavaises M., Flora H. and French B. "Development and validation of a computer simulation model for diesel fuel injection systems", D05594@IMechE, (Part D: Journal of Automotive Engineering), Vol. 210, pp. 149-160, 1996

Arcoumanis C., Gavaises M., Bostock P.G. and Horrocks R.W. "Evaluation of Pump Design Parameters in Diesel Fuel Injection Systems", SAE Paper 950078, 1995

Arcoumanis C., Hentschel W. and Schindler K-P. "Flow and combustion in a transparent 1.9 litre direct injection diesel engine", Proc Instn Mech Engrs, Vol 208, D03293@IMechE, 1994

Arcoumanis C., Khezzar L., Whitelaw D.S., Warren B.C.H. "Breakup on Newtonian and Non-Newtonian Fluids in Air Jets", Experiments in Fluids 17, pp. 405-414, 1994

Arcoumanis C., Nagwaney A., Hentschel W. and Ropke S. "Effect of EGR on Spray Development, Combustion and Emmisions in a 1.9L Direct-Injection Diesel Engine", SAE Paper 952356, 1995

Arcoumanis C., Nouri J.M. and Andrews R.J. "Application of refractive index matching to a diesel nozzle internal flow", Proc. IMechE Seminar on Diesel Fuel Injection Systems, April 14-15, 1992

Ashgriz N. and Givi P. "Binary collision dynamics of fuel droplets", Int. J. Heat and Fluid Flow, Vol. 8, 205-210, 1987

Assanis D., Gavaises M. and Bergeles G. "Calibration and validation of the Taylor Analogy Break-up Model for diesel spray calculations", ASME, Houston, January 1993

Avedisian C.T. and Koplik J. "Leidenfrost boiling of methanol droplets on hot porous/ceramic surfaces", Int. J. Heat Mass Transfer, Vol 30, pp. 379-393, 1987

Ayoub N.S. and Reitz R.D. "Multidimensional Computation of Multicomponent Spray Vaporization and Combustion", SAE Paper 950285, 1995

Bai. C. "Modelling of spray impingement processes", Ph.D. thesis, University of London, Imperial College, 1996

Bai C. and Gosman A.D. "Development and Methodology for Spray Impingement Simulation", SAE Paper 950284, 1995

Bai C. and Gosman A.D. "Mathematical Modelling of Wall Films Formed by Impinging Sprays", SAE Paper 960626, 1996

Batchelor G.K. "A new theory of the instability of a uniform fluidized bed", J. Fluid. Mech., 193, 75-110, 1988

Baumeister K.J. and Simon F.F. "Leidenfrost temperature - its correlation for liquid metals, cryogens, hydrocarbons and water", Int. J. Heat Mass Transfer, Vol. 16, 166-173, 1973

Bayvel L. and Orzechowski Z. , Liquid Atomization, Taylor & Fransis, 1993

Bazari Z. "A DI Diesel Combustion and Emission Predictive Capability for Use in Cycle Simulation", SAE Paper 920462, 1992

Bazari Z. "Diesel Exhaust Emissions Prediction Under Transient Operating Conditions", SAE Paper 940666, 1994

Bazari Z. and French B. "Performance and Emissions Trade - Offs for a HSDI Diesel Engine - An Optimization Study", SAE Paper 930592, 1993

Becchi G. and Guglielmotti A. "Influence of some particular fuel injection phenomena on diesel engine performances", Proc Instn Mech Engrs, Vol. 184, Pt 3J, 1969-70

Bergwerk W. "Flow pattern in diesel nozzle spray holes", Proc. Instn. Mech Engrs, Vol 173, No 25, pp 655-674, 1959

Beshay K.R., Gosman A.D. and Watkins A.P. "Assessments of Multidimensional diesel spray predictions", SAE Paper 861570, 1986

Betamio de Almeida A. and Koelle E. Fluid Transients in Pipe Networks, Computational Mechanics Publications, Elsevier Science Publishers Ltd, 1992

Bhatia J.C., Domnick J., Durst F., Tropea C. "Phase-Doppler-Anemometry and the Log-Hyperbolic Distribution applied to Liquid Sprays", Part. Part. Syst. Charact. 5, 153-164, 1988

Bitone G. "Experiences sur la Forme et sur la Direction des Veines des Courants d'Eau Lances par Diverses Ouvertures", Imprimeric Royale, Turin, pp. 1-136, 1829

Bo T., Clerides D., Gosman A.D. and Theodosopoulos P. "Prediction of the flow and spray processes in an automobile DI diesel engine", SAE Paper 970882, 1997

Booth R.A. and Borman G.L. "Geometry of the Fuel Cloud Created by Impingement of a Diesel Jet onto a Small Heated Target", SAE Paper 941950, 1994

Borgnakke C., Davis G.C. and Tabaczynski R.J. "Prediction of In - Cylinder Swirl Velocity and Turbulence Intensity for an Open Chamber Cup in Piston Engine", SAE Paper 810224, 1981

Bosch W. "The Fuel Rate Indicator: A New Measuring Instrument for Display of the Characteristics of Individual Injection", SAE Paper 660749, 1966

Bourke M.C. and Evers L.W. "Fuel Film Dynamics in the Intake Port of a Fuel Injected Engine", SAE Paper 940446, 1994

Bower G.R. and Foster D.E. "A comparison of the Bosch and Zeuch Rate of Injection Meters", SAE Paper 910724, 1991

Bower G.R. and Foster D.E. "Data from a Variable Rate Shape High Pressure Injection System Operating in an Engine Fed Constant Volume Combustion Chamber", SAE Paper 902082, 1990

Bracco F.V. "Modeling of Engine Sprays", SAE Paper 850394, 1985

Brazier-Smith P.R., Jennings S.G. and Latham J. "The interaction of falling water drops: coalescence", Proc. R. Soc. Lond. A. 326, 393-408, 1972

Brennen C.E. Cavitation and bubble dynamics, Oxford University Press, 1995

Brennen H. "The slow motion of shere through a viscous fluid towards a plane surface", Chem. Engng Sci., 16, 242-251, 1961

Brown P.S. "An empirical implicit scheme for efficient solution of the coalescence/collision break-up equation", J. Comp. Phys., 58, 417-431, 1985

Bruni G. and Laforgia D. "Study of the flow field of a multihole valve covered orifice (V.C.O.) nozzle and effects on spray" FED-Vol. 178/HTD-Vol. 270, Fluid Mechanics and Heat Transfer in Sprays, ASME 1993

Bruni G., Fiore A., Laforgia D. and Fiorentino L. "3-D Analysis of the Flow Through a Multihole V.C.O. Nozzle for D.I. Diesel Engine", SAE Paper 950085, 1995

Campanella R., Laforgia D., Ficarella A., and Damiani V. "Spray Characteristics of Five-Hole V.C.O. Nozzles of a direct Electro-Injector", SAE Paper 940192, 1994

Carey V.P., Liquid-Vapor Phase-Change Phenomena, Hemishre Publishing Corporation, 1992

Castman R.A. "The mechanism of the atomization accompanying solid injection", NACA Report 440, 1932

Chandra S. and Avedisian C.T. "On the collision of a droplet with a solid surface", Proc. R. Soc. Lond. A, 432, 13-41, 1991

Chandra S. and Avedisian C.T. "Observations of droplet impinging on a ceramic porous surface", Int. J. Heat Mass Transfer, 35, 2377-2388, 1992

Chang J-C. "Diesel spray characteristics and spray/wall heat transfer", Ph.D. thesis, University of London, Imperial College, 1993

Chaves B.J., Obermeier H., Schneider F. "Influence of cavitation in a turbulent nozzle flow an atomization and spray formation of a liquid jet", AutoTech Exhibition & Congress, Integrated Diesel European Action (IDEA), C399/13 Seminar, 1989

Chaves H. and Obermeier F. "Modelling the Effect of Modulations of the Injection Velocity on the Structure of Diesel Sprays", SAE Paper 961126, 1996

Chaves H., Bode J., Hentschel W., Kubitzek A., Obermeier F., Schindler K.P., Schneider T. "Fuel Spray in Diesel Engines Part I: Spray Formation", Proceedings of the 3rd Int. Conf. Innovation and Reliability in Automotive Design and Testing, paper 2.6.2, 1995

Chaves H., Hentschel W., Obermeier F., Schindler K.P., Weiss D. "Fuel Spray in Diesel Engines Part II: Spray Propagation and Wall Interaction" Proceedings of the 3rd Int. Conf. Innovation and Reliability in Automotive Design and Testing, paper 2.6.3, 1995

Chaves H., Knapp M., Kubitzek A., Obermeier F., and Schneider T. "Experimental Study of Cavitation in the Nozzle Hole of Diesel Injectors Using Transparent Nozzles", SAE Paper 950290, 1995

Chehroudi B., Onuma Y., Chen S.-H. and Bracco F.V. "On the intact core of full-cone sprays", SAE Paper 850126, 1985

Chein R.R. "Numerical simulation of droplet dispersion and evaporation in turbulent shear flows", Int. Conf. on Mechanics of Two-Phase Flows, Taiwan, ROC, 1989

Chen F.Y. Mechanics and Design of Cam Mechanisms, Pergamon Press, 1982

Chen Y. and Kittelson D.B. "Geometric Optimization of Nozzles for inclined Injectors for DI Diesel Engines", SAE Paper 960869, 1996

Chigier N.A. "The atomization and combustion of liquid fuel sprays", Pros. Energy Combust. Sci., Vol. 2, pp. 97-114, 1976

Chigier N.A. "The physics of atomization", ICLASS-91, Gaithersburg, MD, U.S.A., 1991

Ching B., Golay M.W. and Johnson T.J. "Droplet impacts upon liquid surfaces", Science, 226(4674), 535-537, 1984

Chisholm D., Two - phase flow in pipelines and heat exchangers, George Godwin an impint of Longman Group Limited, 1983

Choi K.J. and Yao S.C. "Mechanisms of film boiling heat transfer of normally impacting spray" Int. J. Heat Mass Transfer, Vol. 30, No 2, pp. 311-318, 1987

Choi K.Y. and Lee H.J. "Experimental studies on the dynamics and evaporation of tandem liquid droplets in a hot gas flow", Int. J. Heat Mass Transfer, 35, 2921-2929, 1992

Choi Y.D. and Chung M.K. "Analysis of Turbulent Gas-Solid Suspension Flow in a Pipe", ASME Journal of Fluids Engineering, vol. 105, pp. 329-334, 1983

Clerides D. "Numerical simulation of spray processes in diesel engines", Ph.D. thesis, University of London, Imperial College, 1997

Clift R., Grace J.R., Weber M.E. Bubbles, drops, and Particles, Academic Press, Inc., 1978
Curtis and Farrell "A numerical study of high-pressure droplet vaporization", Combustion and Flame, 90, 85-102, 1992

Cossali G.E., Coghe A. and Brunello G. "Effect of Spray-Wall Interaction on Air Entrainment in a Transient Diesel Spray", SAE Paper 930920, 1993

Cossali G.E., Gerla A., Coghe A. and Brunello G. "Effect of Gas Density and Temperature on Air Entrainment in a Transient Diesel Spray", SAE Paper 960862, 1996

Cutter P. "Diesel spray characteristics, spray/wall interaction and heat transfer", Ph.D. thesis, University of London, Imperial College, 1996

Dahneke B. "Diffusion deposition of particles", J. Colloid Interface Sci, 48, 520-522, 1974

Daidzic N., Kohnen G. and Sommerfeld M. "A New Spray Evaporation Model based on Droplet Interface Phenomena", Proceedings of The 2nd International Conference on Multiphase Flow, Kyoto, Japan, April 1995

Date K., Manabe M., Kano H., Kato M., and Oya T. "Contribution of Fuel Flow Improvement in Nozzle to Spray Formation", SAE Paper 920622, 1996

Date K., Nobechi H., Kano H., Kato M., and Oya T. "Experimental Analysis of Fuel Flow Characteristics in the Nozzle for Direct Injection Engines", SAE Paper 931002, 1993

Davis G.C. and Borgnakke C. "The Effect of In - Cylinder Flow Processes (Swirl, Squish and Turbulence Intensity) on Engine Efficiency - Model Predictions", SAE Paper 820045, 1982

Delplanque J.-P. and Sirignano W.A. "Numerical study of the transient vaporization of the oxygen droplet at sub- and super-critical conditions", Int. J. Heat Mass Transfer, Vol. 36, No. 2, pp. 303-314, 1993

Diez J.A., Gratton R., Thomas L.P. and Marino B. "Laplace pressure driven drop spreading", Phys. Fluids, 6, 24-33, 1994

Dodge L.G., Ryan T.W., and Ryan M.G. "Effects of Different Injector Hole Shapes on Diesel Sprays", SAE Paper 920623, 1992

Domnick J., Dorfner V., Xu T.-H. "Analyzing Atomizer Defects using Phase-Doppler Anemometry and the Three-parameter Log-Hyperbolic Distribution", presented at the 5th Europ. Symp. Particle Characterization, Nurnberg, 1992

Domnick J., Tropea C. and Wagner R. "A miniaturized semiconductor optic phase-Doppler anemometer (DFPDA) with applications to liquid sprays", Meas. Sci. Technol. 4, 411-415, 1993

Dreeben T., Millen L., Wells M., and Woolworth J. "Effect os Sac Volume on Injector Performance", SAE Paper 920680, 1992

Drew D.A. "Mathematical Modelling of Two-Phase Flow", Ann. Rev. Fluid Mech, 15, 261-291, 1983

Dukowicz J.K. "A Particle-Fluid Numerical Model for Liquid Sprays", J. Comp. Physics, vol. 35, pp. 229-253, 1980

Eckhause J.E. and Reitz R.D. "Modeling heat transfer to impinging fuel sprays in direct-injection engines" Atomization and Sprays, Vol. 5, pp. 213-242, 1995

El Wakil M.M., Ugehara O.A. and Myers P.S. "A theoretical investigation of the heating-up period of injected fuel droplets vaporizing in air", NACA TN 3179, 1954

Faeth G.M. "Current studies of droplet and liquid combustion", Progress in Energy and combustion Science 3, 191-224, 1977

Faeth G.M. "Evaporation and combustion of sprays", Prog. Energt Combust. Sci., 1-76, 1983

Faeth G.M. "Mixing, transport and combustion in sprays", Prog. Energy Combust. Sci., 13, 293-345, 1987

Faeth G.M. and Hsiang L.-P. "Drop deformation and breakup due to shock wave and steady disturbances", Int. J. Multiphase Flow, Vol. 21, No 4. pp. 545-560, 1995

Faeth G.M., Hsiang L-P. and Wu P.-K. "Structure and Breakup properties of sprays", Int. J. Multiphase Flow, Vol. 21, Suppl. pp. 99-127, 1995

Farrell P.V., Chang C.T. and Su T.F. "High Pressure Multiple Injection Spray Characteristics", SAE Paper 960860, 1996

Fairbrother R.J. 'Computer simulation of fuel injection for direct-injection diesel engines', Ph.D. thesis, Imperial College, University of London, 1994

Faxen H. "Die Bewegun einer Starren Kugel Langs der Achse eines mit Zaher Flussigkeit getullten Rohres", Arkiv. Mat. Astron. Fys., 17, 1-28, 1923

Frank T. and Schulze I. "Numerical simulation of Gas-Droplet flow around a nozzle in a cylindrical chamber using a lagrangian model based on a multigrid Navier-Stokes solver", FED-Vol. 185, Numerical Methods in Multiphase Flows, ASME 1994

Frossling N. "On the evaporation of falling droplets", Gerlands Beitr. Geophys., Vol. 52, pp. 170-216, 1938

Fujimoto H., Nishikori T., Hojyo Y., Tsukamoto T. and Senda J. "Modelling of Atomization and Vaporization Process in Flash Boiling Spray", SAE Paper 941925, 1994

Fujimoto H., Sugihara H., Tanabe H. and Sato G. "Investigation on combustion in medium-speed marine diesel engines using model chambers", 14th Inter. Cong. on Combustion Engines, Helsinki, 1981

Gavaises M., Theodorakakos A. and Bergeles G. "Modelling wall impaction of diesel sprays", Int. J. Heat and Fluid Flow, Vol. 17, pp. 130-138, 1996

Gavaises M., Theodorakakos A. and Bergeles G. "Evaluation of the effect of droplet collisions on spray mixing", Proc. IMechE, Vol.2, pp. 465-475, 1996

Gavaises M. and Bergeles G. "Validation of a spray model for diesel engine calculations", Entropie No. 200, pp. 43-52, 1997

Gavanagh E.J. 'Simulation of automotive diesel fuel injection equipment', Ph.D. thesis, University of Southampton, 1984

Ghadiri H. "Raindrop impact, soil splash and creating", Ph.D. thesis, University of Reading, 1978

Gibson D.H. 'A flexible fuel injection simulation', SAE Paper 861567, 1986

Gidaspow D. "Hydrodymanics of fluidization and heat transfer: supercomputer modeling", Appl. Mech. Rev., 39, 1-22, 1986

Gidaspow D. Multiphase Flow and Fluidization Continuum and Kinetic Theory Descriptions, Academic Pres, Boston, MA, 1994

Gillespie D.T. "An exact method for numerically simulating the stochastic coalescence process in a cloud", J. atmos. Sci., 76, 541-556, 1975

Gillespie D.T. and List R. "Effects of collision-induced break-up on drop size distributions in steady state rainshafts", Pure appl. Geophys., 1117, 559-626, 1979

Gillespie T. and Rideal E. "On the adhesion of drops and particles on impact at solid surfaces II", J. Colloid Sci., 10, 281-298, 1955

Giorgio F.D., Laforgia D. and Damiani V. "Investigation of Drop Size Distribution in the Spray of a Five-Hole, V.C.O. Nozzle at High Feeding Pressure", SAE Paper 950087, 1995

Glushkov V.I. "Interaction between liquid droplets and a solid wall", Povysheniye effectinosti transport gaya (Improving the efficiency of gas transport), Moscow, 90-98, 1975

Goldsmith M. and Penner S.S. "On the burning of single drops of fuel in a oxidizing atmosphere", J. Propul. 24, 245-251, 1954

Gosman A.D. and Harvey P.S. "Computer Analysis of Fuel - Air Mixing and Combustion in an Axisymmetric D.I. Diesel", SAE Paper 820036, 1982

Gosman A.D. and Ioannides E. "Aspects of Computer Simulation of Liquid Fueler Combustors", J. Energy, Vol.7, No 6, 1983

Gosman A.D. The Thermodynamics and Gas-Dynamics of Internal Combustion Engines, Clarendon Press, Oxford, 1983

Gottfried B.S., Lee C.J. and Bell K.J. "The Leidenfrost phenomenon : Film boiling of liquid droplets on a flat plate", Int. J. Heat Mass Transfer, Vol. 9, pp. 1167-1182, 1967

Goyal M. "Modular Approach to Fuel Injection System Simulation", SAE Paper 78062, 1978

Green G.A., Irvine T.F., Gyves T. and Smith T. "Drag relationships for liquid droplets setting ina continuous liquid", AIChE J., 39(1), 37-41, 1993

Gregory P.H., Guthrie E.J. and Bunce M.E. "Experiments on splash dispersal of fungus spores", J. Gen. Microbiol., 20, 328-354, 1959

Gukhman A.A., Vdynets A.Z., Rozhdestvenskii A.V. and Brazhnikov S.M. "Features of heat transfer in the impact of a drop against a hot surface", J. Eng. Phys., 49, 1178-1180, 1985

Hamady F.J., Hahn J.P., Hellman K.H., and Gray C.L. "High-Speed / High - Resolution Imaging of Fuel Sprays from Various Injector Nozzles for Direct Injection Engines", SAE Paper 950289, 1995

Hansell D., Kennedy I. and Kollmann W. "A simulation of particle dispersion in a turbulent jet", Int.J. multiphase Flow, 18(4), 559-576, 1992

Hardalupas Y. and Whitelaw J.H. "The characteristics of sprays produced by coaxial airblast atomisers", AIAA 93-0698, 1993

Hardalupas Y., Okamoto S., Taylor A.M.P.K. and Whitelaw J.H. "Application of a Phase Doppler Anemometer to a Spray Impinging on a Disk", Proceedings of the 6th International Symposium on Laser Techniques and Applications in Fluid Mechanics, Lisbon, Portugal, 20-23 July, 1992

Hardalupas Y., Taylor A.M.P.K., Whitelaw J.H., Ishii K., Miyano H., and Urata Y. "Influence of Injection Timing on In - Cylinder Fuel Distribution in a Honda VTEC-E Engine", SAE Paper 950507, 1995

Harlow F.H. and Amsden A.A. "Numerical Calculation of Multiphase Flow", J. Comp. Physics, vol. 17, pp. 19-52, 1975

Harris S.E and Crighton D.G. "Solitons, solitary waves, and voidage disturbances in gas-fluidized beds", F. Fluid Mech, 266, 243-276, 1994

Henein N.A, Singh T. and Rozanski J. 'Characterization and simulation of a unit injector', SAE Paper 750773, 1975

Hestroni G. handbook of multiphase systems, Hemisphere Publishing Corporation, 1982

Heymann F.J. "High-Speed Impact between a Liquid Drop and a Solid Surface", Journal of Applied Physics, Vol. 40, No 13, pp. 5113-5122, 1969

Heywood J.B. Internal Combustion Engine Fundamentals, Automotive Technology Series, McGraw Hill Book Company Inc., 1988

Hinze J.O. "Turbulent Fluid and Particle Interaction", Int.J.Heat Mass Transfer, vol. 6, pp. 433-452, 1972

Hinze J.O. Turbulence, 2nd ed. Mc-Graw Hill Book Company, 1975

Hiroyasu H. "Experimental and theoretical studies on the structure of fuel sprays in diesel engines", ICLASS-91, Gaithersburg, MD, U.S.A., 1991

Hiroyasu H. and Arai M. "Structures of Fuel Sprays in Diesel Engines", SAE Paper 900475, 1990

Hiroyasu H., Arai M. and Shimizu M. "Break-up length of a Liquid jet and Internal flow in a nozzle" ICLASS-91 Gaithersburg, MD, U.S.A. July 1991

Hiroyasu H., Arai M. and Tabata M. "Empirical Equations for the Sauter Mean Diameter of a Diesel Spray", SAE Paper 890464, 1989

Hiroyasu H., Smimizu M. and Arai M. "The breakup of ahigh speed jet in a high pressure gaseous environment", ICLASS-82, University of Wisconsin, Madison, 1982

Hobbs P.V. and Osheroff T. "Splashing of Drops on Shallow Liquids", Science, Vol. 158, 1184-1186, 1967

Hohmann S., Klingsporn M. and Renz U. "An Improved Model to Describe Spray Evaporation Under Diesel-Like Conditions", SAE Paper 960639, 1996

Holman J.P. Heat transfer, McGraw - Hill Book Company, Fourth edition, 1976

Hori H., Ogawa T., and Kuriyama T. "CFD In - Cylinder Flow Simulation of an Engine and Flow Visualization", SAE Paper 950288, 1995

Hosoya H. and Obokata T. "Effect of Nozzle Configuration on Characteristics of Steady-State Diesel Spray", SAE Paper 930593, 1993

Hou Z.-H., Abraham J. and Siebers D.L. "Three-dimensional Computations of Diesel Sprays in a Very High Pressure Chamber", SAE Paper 941896, 1994

Hou Z.-X. and Abraham J. "Three-Dimensional Modeling of Soot and NO in a Direct-Injection Diesel Engine", SAE Paper 950608, 1995

Hou Z.-X., Abraham J., and Siebers D.L. "Modeling of Diesel Sprays in a Very High Pressure Chamber, Part II : Effects of Combustion", SAE Paper 950603, 1995

Hsiang L.-P. and Faeth G.M. "Drop properties after secondary breakup", Int. J. Multiphase Flow, Vol 19, No 5, pp 721-735, 1993

Hsiang L.-P. and Faeth G.M. "Near limit drop deformation and secondary breakup", Int. J. Multiphase Flow, 18, 635-652, 1992

Huang P.G. and King E.W. "The accurate Simulation of Diesel Spray Structures", Int. Conf. on Mechanics of Two-Phase Flows, Taiwan, ROC, 1989

Huh J.-C., Lee G.-Y. and Yang O.-Y. "An experimental study on initial behaviour of diesel fuel spray characteristics", ICLASS-91, Gaithersburg, MD, U.S.A., 1991

Huh K.Y. and Gosman A.D. "A Phenomenological Model of Diesel Spray Atomization" Proceedings of The International Conference on Multiphase Flows '91-Tsukuba, September 24 - 27, Tsukuba, Japan, 1991

Ikonomou E. "A computational study of diesel sprays and combustion", Ph.D. thesis, University of London, Imperial College, 1996

Inada S., Miyasaka Y., Sakamoto K. and Hojo K. "Liquid-solid contact state and fluctuation of the vapor film thickness of a drop impinging on a hot surface", J. Chem. Engng. Japan, 21, 463-468, 1988

Ishiwata H. "Recent Progress in High Pressure Injection and Rate Shaping Technology for Diesel In-Line Pumps", International Symposium on Advanced Spray Combustion, July 6-8, Hiroshima, Japan, 1994

Ishiwata H., Li X., Yoshikawa H., and Kitahara N. "Recent Progress in Rate Shaping Technology for Diesel In - Line Pumps", SAE Paper 940194, 1994

Jayaratne O.W. and Mason B.J. "The coalescence and bouncing of water drops at an air/water interface", Proc. Royal Soc. (London), A280, 545 - 565, 1964

Jia H. and Gogos G. "High pressure droplet vaporization; effects of liquid-phase gas solubility", Int. J. Heat Mass Transfer, Vol. 36, No. 18, pp. 4419-4431, 1993

Jiang Y.J., Umemura A. and Law C.K. "An experimental investigation on the collision behaviour of hydrocarbon droplets", J. Fluid Mech., Vol. 234, pp 171-190, 1992

Johnen T. and Haug M. "Spray Formation Observation and Fuel Film Development Measurements in the Intake of a Spark Ignition Engine", SAE Paper 950511, 1995

Jones P. and Junday J.S. "Full Cycle Computational Fluid Dynamics Calculations in a Motored Four Valve Pent Roof Combustion Chamber and Comparison with Experiments", SAE Paper 950286, 1996

Jordan D.W. Brit. J. Appl. Phys. 3, 194, 1954

Kakac S. Heat conduction, 3rd Ed. 1993

Kampmann S., Dittus B., Mattes P., and Kirner M. "The Influence of Hydro Grinding at VCO Nozzles on the Mixture Preparetion in a DI Diesel Engine", SAE Paper 960867, 1996

Kano H., Kato M., Kojima T. and Katagiri M. "Contribution of Optimum Design for Nozzle Configuration to Spray Formation", SAE Paper 900824, 1990

Karasawa T., Shiga S., Tanaka M., Nakamura H. and Kurabayashi T. "Relationship between Atomization Behavior and the Nozzle Inlet - Shape of a Steady - Jet" International Symposium on Advanced Spray Combustion, July 6-8, Hiroshima, Japan, 1994

Karl A., Anders K. and Frohn A. "Disintegration of Droplets Colliding with Hot Walls", Proceedings of The 2nd International Conference on Multiphase Flow, Kyoto, Japan, 1995

Kashiwaya M., Kosuge T., Nakagawa K., and Okamoto Y. "The Effect of Atomization of Fuel Injectors on Engine Performance", SAE Paper 900261, 1990

Katsura N., Saito M., Senda J., Fujimoto H. "Characteristics of Diesel Spray Impinging on a Flat Wall", SAE Paper 890264, 1989

Kegl B."An Improved Mathematical Model of Conventional FIE Processes", SAE Paper 950079, 1995

Kegl B. "Optimal design of conventional in - line fuel injection equipment", D00994@IMechE 1995

Khalighi B., Tahry S.H., Haworth D.C., and Huebler M.S. "Computation and Measurement of Flow and Combustion in a Four-Valve Engine with Intake Variations", SAE Paper 950287, 1995

Kitron A., Elperin T. and Tamir A. "Stochastic modelling of the effects of liquid droplet collisions in impinging stream absorbers and combustors", Int. J. Multiphase Flow, Vol. 17, No 2, pp 247-265, 1991

Kitsha J. and Kocamustafaogullari G. "Breakup criteria for fluid particles", Int. J. Multiphase Flow, Vol. 15, No. 4, pp 573-588, 1989

Klee A. and Treybal R.E. "Rate of rise or fall of liquid drops", AIChE J., 2, 444, 1956

Knapp R.T., Daily J.W., Hammit F.G. Cavitation, McGraw Hill Book Company, 1970

Kneer R., Schneider M., Noll B. and Wittig S. "Diffusion controlled evaporation of a multicomponent droplet: theoretical studies on the importance of variable liquid properties", Int. J. Heat Mass Transfer, Vol. 36, No. 9, pp. 2403-2415, 1993

Knox-Kelecy A.L. and Ferrell P.V. "Spectral Characteristics of Turbulent Flow in a Scale Model of a Diesel Fuel Injector Nozzle", SAE Paper 930924, 1993

Kohnen G., Ruger M. and Sommerfeld M. "Convergence behaviour for numerical calculations by the Euler/Lagrange method for Strongly coupled phases", FED-Vol. 185, Numerical Methods in Multiphase Flows, ASME 1994

Komiyama K., Okazaki T., Togashi K., Hashimoto H. "Electronically Controlled High Pressure Injection Systems for Heavy Duty Diesel Engine - KOMPICS", SAE Paper 810997, 1981

Koo J.Y. and Martin J.K. "Near-Nozzle Characteristics of a Transient Fuel Spray" Atomization and Sprays, Vol. 5, pp107-121, 1995

Kowalewicz A., Combustion Systems of High - Speed Piston I.C. Engines, Wydawnictwa Komunikacji I Lacznosci, 1984

Kralj C. "Numerical simulation of diesel spray processes", Ph.D. thesis, University of London, Imperial College, 1995

Krzeczkowski S.A. "Measurement of liquid droplet disintegration mechanisms", Int. J. Multiphase Flow, Vol. 6, pp 227-239, 1980

Kuniyoshi H., Tanabe H., Sato G. and Fujimoto H. "Investigation of the Characteristics of Diesel Fuel Spray", SAE Paper 800968, 1980

Kuo K.K. Principles of Combustion, John Wiley & Sons, Inc, 1986

Ladommatos N. "Mechanisms of heat transfer to liquid films in the manifold of port-injected petrol engines", Proc. Instn. Mech Engrs, Vol 207, pp 211 - 222, D03592@IMechE, 1993

Landahl M.T. and Mollo-Christensen E., Turbulence and Random Processes in Fluid Mechanics, Second edition, Cambridge University Press, 1992

Launder E.B. and Spalding B.D. Mathematical models of turbulence, Academic Pres., London, 1974

Lebrere L. and Dillies B. "Engine Flow Calculations Using a Reynolds Stress Model in the Kiva-II Code", SAE Paper 960636, 1996

Lee H.-K. 'Modelling and prediction of the filling characteristics of modern diesel fuel injection equipment', Ph.D. thesis, University of Southampton, 1994

Lefebvre A.H. "Properties of sprays", Int. Conf. on Mechanics of Two-Phase Flows, Taiwan, ROC, 1989

Lefebvre A.H. Atomization and Sprays, Combustion: An International Series, by Hemisphere Corporation, 1989

Levin Z. and Hobbs P.V. "Splashing of water drops on solid and wetted surfaces: Hydrodynamics and charge separation", Philosophical transactions of the Royal Society of London A, Vol. 269, pp. 555-585, 1971

Li X. and Tankin R.S. "Prediction of Droplet Size and Velocity Distribution in Sprays Using Maximum Entropy Principle", Combust. Sci and Tech., Vol 68, pp. 147-155, 1989

Li X., Chin L.P., Tankin R.S., Jackson T., Stutrud T.J., Switzer G. "Comparison Between Experiments and Predictions Based on Maximum Entropy for Sprays from a Pressure Atomizer", Combustion and Flame 86: 73-89, 1991

Lian Z.W. and Reitz R.D. "The Effect of Vaporization and Gas Compressibility on Liquid Jet Atomization" Atomization and Sprays, Vol. 3, pp. 249-264, 1993

Lipkea W. and DeJoode A.D. "Direct Injection Diesel Engine Soot Modeling: Formulation and Results", SAE Paper 940670, 1994

Lock G.S.H. Latent heat transfer, an Introduction to fundamentals, Oxford University Press, 1994

Long W.Q., Hosoya H., Mashimo T., Kobayashi K., Obokata T., Durst F. and Xu T.-H. "Analytical Functions to Match Size Distributions in Diesel Sprays", International Symposium COMODIA 94, 1994

Lush P.A. "Cavity dynamics in a duct flow", C191/83@IMechE, 1983

Macklin W.C. and Hobbs P.V. "Subsurface Phenomena and the splashing of Drops on Shallow Liquids", Science, Vol. 166, 107-108, 1969

Makino K. and Michiyoshi I. "The behaviour of a water droplet on heated surfaces", Int. J. Heat and Mass Trans. 27, 781-791, 1984

Marcic M. 'Computer simulaiton of the diesel fuel injection nozzle', SAE Paper 930925, 1993

Matsuoka S., Yokota K., Kamimoto T. and Igoshi M. 'A study of fuel injection systems in diesel engines; Parts I & II, SAE Papers 760551 and 760552, 1976

Maude A.D. "End effects in a falling-sphere viscometer", Br. J. Appl. Phys., 12, 293, 1961

McCarthy M.J. and Molloy N.A. "Review of Stability of Liquid Jets and the Influence of Nozzle Design", The Chemical Engineering Journal, 7, 1-20, 1974

Mehta P.S., Dent J.C. and Gupta A.K. "Computational schemes for atomization and evaporation of diesel fuel spray", ICLASS-85, 1985

Miller and Majumdar "Role of under-relaxation in momentum interpolation for calculating of flow with non-staggered grids", Num. Heat Transfer, Vol. 13, p. 125, 1988

Minami K. and Shoham O. "Transient two-phase flow behaviour in pipelines - experiment and modeling", Int. J. Multiphase Flow, Vol. 20, No. 4, pp. 739-752, 1994

Minami T., Takeuchi K., and Smimazaki N. "Reduction of Diesel Engine Nox Using Pilot Injection", SAE Paper 950611, 1995

Miura A. and Yamaguchi Y. "Injection Rate Control of In-Line Injection Pump - Cam Design Through Injection Process Simulation", SAE Paper 950606, 1995

Modarress D., Tan H. and Elgobashi S. "Two-Component LDA Measurements in a Two-Phase Turbulent Jet", AIAA 21st Aerospace Sciences Meeting, Reno, Nev., Paper No AIAA-83-0052, 1983

Modarress D., Wuerer J. and Elgobashi S. " An experimental study of a Turbulent Round Two-Phase Jet", AiAA/ASME 3rd Joint Thermophysics, Fluids, Plasma and Heat Transfer Conference, St. Louis, Mo., Paper No. AIAA-82-0964, 1982

Modarress D., Wuerer J. and Elgobashi S. "An experimental Study of a Turbulent Round Two-Phase Jet", Chemical Eng. Communications, vol. 28, pp. 341-354, 1984

Mostafa A.A. and Elghobashi S.E. "A two-equation turbulence model for jet flows laden with vaporizing droplets", Int. J. Multiphase Flow, 11, 515-533, 1985

Mostafa A.A. and Mongia H.C. "Eulerian and Lagrangian Predictions of Turbulent Evaporating Sprays", AIAA-86-0452, 1986

Mostafa A.A. and Mongia H.C. "On the modelling of turbulent evaporating sprays:Eulerian versus Lagrangian approach", Int. J. Heat Mass Transfer. 30, 2583-2593, 1987

Moureau J.C.L., Bolle L. and Giot M. "Influence of the droplet size distribution on the spray cooling efficiency", Two-Phase Momentum, Heat and Mass Transfer, 1, 171-184, 1979

Mulholland J.A., Srivastava R.K. and Wendt J.O.L. "Influence of droplet spacing on drag coefficient in non-evaporating, monodisperse streams", AIAA J., 26, 1231-1237, 1988

Mundo C., Lackermeier U., Sommerfeld M. and Tropea C. "Numerical and experimental studies of the splashing and deposition of spray droplets on surfaces", ICLASS 1995, Two Phase Flow Modell. and Exp., Rome, 1995

Mundo C., Sommerfeld M. and Tropea C. "Droplet-Wall collisions: experimental studies of the deformation and breakup process" Int. J. Multiphase Flow, Vol. 21, No 2, pp. 151-173, 1995

Mundo C., Sommerfeld M. and Tropea C. "Numerical and experimental investigation of spray characteristics in the vicinity of a rigit wall", ICLASS 1995, Two Phase Flow Modell. and Exp., Rome, 1995

Mutchler C.K. "Parameters for describing raindrop splash", J. Soil and Water Cons, 22, 91-94, 1967

Mutchler C.K. "Splash droplet production by waterdrop impact", Water Resources Research, 7, 1024-1030, 1970

Naber J., Enright B. and Farrell P. "Fuel Impingement in a Direct Injection Diesel Engine", SAE Paper 881316, 1988

Naber J.D. and Farrell R.V. "Hydrodynamics of Droplet Impingement on a Heated Surface", SAE Paper 930919, 1993

Naber J.D. and Reitz R.D. "Modelling Engine Spray/Wall Impingement", SAE Paper 880107, 1988

Naber J.D. and Siebers D.L. "Effects of Gas Density and Vaporizaion on Penetration and Dispersion of Diesel Sprays", SAE Paper 960034, 1996

Nagaoka M., Kawazoe H., and Nomura N. "Modeling Fuel Spray Impingement on a Hot Wall for Gasoline Engines", SAE Paper 940525, 1994

Naitoh K., Takagi Y., Kokita H., Kuwahara K. "Numerical Prediction of Fuel Secondary Atomization Behavior in SI Engine based on the Oval-Parabola Trajectories (OPT) Model", SAE Paper 940526, 1994

Nagwaney A. "Spray and combustion development in a diesel engine incorporating exhaust gas recirculation", Ph.D. thesis, University of London, Imperial College, 1996

Nakahira T., Komori M., Nishida M. and Taujimura K. "The Shock Wave Generation Around the Diesel Fuel Spray with High Pressure Injection", SAE Paper 920460, 1992

Nehmer D.A. and Reitz R.D. "Measurement of the Effect of Injection Rate and Split Injections on Diesel Engine Soot and Nox Emissions", SAE Paper 940668, 1994

Nguyen Q.-V., Rangel R.H. and Dunn-Rankin D. "Measurement and Prediction of Trajectories and collision of Droplets", Int. J. Multiphase Flow, Vol. 17, No 2, pp 159-177, 1991

Nguyen T.K. and Avedisian C.T. "Numerical solution for film evaporation of a spherical liquid droplet on an isothermal and adiabatic surface", Int. J. Heat Mass Transfer, Vol. 30, pp. 1497-1507, 1987

Nicholls J. "Stream and droplet breakup by shock waves", NACA SP-194, 1972

Nigmatulin R.I. Dynamics of Multiphase Media, Revised and Augmented ed., Vol. 1, Hemisphere Publishing Corporation, New York, 1991. Originally published by Nauka Noscow under the title : Dinamika Mnogofaznyky Sred

Nishida K. and Hiroyasu H. "Simplified Three-Dimensional Modeling of Mixture Formation and Combustion in a D.I. Diesel Engine", SAE Paper 890269, 1989

Nishio S. and Hirate M. "Study on the Leidenfrost temperature-2nd report, behaviour of liquid-solid contact surface and Leidenfrost temperature", Trans. japan Soc. Mech. Engrs, 44(380), 1335-1346, 1978

O'Rourke P.J. "Collective drop effects in vaporizing fuel sprays", Ph.D. thesis, Prinseton University, 1980

O'Rourke P.J. "Statistical Properties and Numerical Implementation of a Model for Droplet Dispersion in a Turbulent Gas", J. Comp. Physics, vol. 83, 345-360, 1989

O'Rourke P.J. and Amsden A.A. "The TAB method for numerical calculation od spray droplet breakup", SAE Paper 872089, 1987

O'Rourke P.J. and Amsden A.A. "Three Dimensional Numerical Simulations of the UPS-22 Stratified Charge Engine", SAE Paper 870597, 1987

O'Rourke P.J. and Bracco F.V. "Modelling of drop interactions in thick sprays and a comparison with experiments", IMechE C404/80, Conference on Stratified charge automotive engines, November 1980

O'Rourke P.J. and Brackbill J.U. "On Particle-Grid Interpolation and Calculating Chemistry in Particle-in-Cell Methods", J. Comp. Physics, vol. 109, pp. 37-52, 1993

Oesterle B. and Peritjean A. "Simulation of particle-to-particle interactions in gas-solid flows", Proc. Int. Conf. of Multiphase Flows, Tsukuba, Japan, 1991

Ofner H. and Egartner W. "Identification of flow phenomena in fuel injection systems for diesel engines from dynamic measurements", C499/053@IMechE 1996

Ohnesorge W., "Formation of drops by Nozzles and the Breakup of Liquid Jets", Z. Angew. Math. Mech., Vol. 16, pp. 355-358, 1936

Ohrn T.R., Senser D.W., and Lefebvre A.H. "Geometrical Effects on Discharge coefficients for Plain - Orifice Atomizers", Atomization and Sprays, vol. 1, no. 2, pp. 137-153, 1991

Oishi Y., Miura A., Hamazaki N. and Watanabe Y. "A computational study into the effect of the injection nozzle inclination angle on the flow characteristics in nozzle holes", SAE Paper 920580, 1992

Okajima M., Kato M., Kano H., Tojo S., and Katagiri M. "Contribution of Optimum Nozzle Design to Injection Rate Control", SAE Paper 910185, 1991

Ormancey A. and Martinon J. "Prediction of particle dispersion in turbulent flows", Physicochem Hydrodynam. 5, 229-244, 1984

Oza R.D. and Sinnamon J.F. "An Experimntal and Analytical Study of Flash - Boiling Fuel Injection", SAE Paper 830590, 1983

Ozdemir B.I. and Whitelaw J.H. "Impingement of an unsteady two-phase jet on unheated and heated flat plates" J. Fluid Mech., Vol. 252, pp. 499-523, 1993

Park B.S. and Lee S.Y. "An experimental investigation of the flash atomization mechanism", Atomization and sprays, vol. 4, pp. 159-179, 1994

Payri F., Desantes J.M. and Arregle J. "Characterization of D.I.Diesel Sprays in High Density Conditions", SAE Paper 960774, 1996

Pearson H. J., Valioulis I.A. and List E.J. "Monte Carlo simulation of coagulation in discrete particle-size distributions. Part I. Brownian motion and fluid shearing", J. Fluid Mech. 143, 367-385, 1984

Pearson H. J., Valioulis I.A. and List E.J. "Monte Carlo simulation of coagulation in discrete particle-size distributions. Part 2.Interparticle forces and the quasi-station equilibrium hypothesis", J. Fluid Mech. 143, 387-411, 1985

Pedersen C.O. "An experimental study of the dynamic behavior and heat transfer characteristics of water droplets impinging upon a heated surface", Int. J. Heat Mass Transfer, Vol. 13, pp. 369-381, 1970

Phinney R.E. "The breakup of a turbulent liquid jet in a Gaseous atmosphere", J. Fluid Mech., 60, 689-701, 1973

Pierpont D.A. and Reitz R.D. "Effects of Injection Pressure and Nozzle Geometry on D.I. Diesel Emissions and Performance", SAE Paper 950604, 1995

Pilch M. and Erdman C.A. "Use of breakup time data and velocity history data to predict the maximum size of stable fragments for acceleration - induced breakup of a liquid drop", Int. J. Multiphase Flow, Vol 13, No 6, pp. 741-757, 1987

Potz D., Kreh A., and Warga J. "Variable Orifice Geometry Verified on the Two - Phase Nozzle (VRD)", SAE Paper 950081, 1995

Press W.H., Flannery B.P., Teukolsky S.A. and Vetterling W.T. Numerical recipes, The Art of Scientific Computing (FORTRAN Version), Cambridge University Press, 1989

Pzuppacher H.R. and Klett J.D. "Microphysics of Clouds and Precipitation", Reidel, Dordrecht, 1978

Qiao J., Dent J.C. and Garner C.P. "Diesel Engine Modelling Under Steady and Transient Conditions Using a Transputer Based Concurrent Computer", SAE Paper 922226, 1992

Quoc H.X. and Brun M. "Study on Atomization and Fuel Drop Size Distribution in Direct Injection Diesel Spray", SAE Paper 940191, 1994

Raju M.S. and Sirignano W.A. "Interaction between two vaporising droplets in an intermediate Reynolds number flow", Phys. Fluids. A, 2, 1780-1796, 1990

Rallison J.M. "The deformation of small viscous drops and bubbles in shear flows", Ann. Rev. Fluid Mech., 16, 45-66, 1984

Ramos J.I., Internal Combustion Engine Modelling, Hemisphere Publishing Corporation, 1989

Ranger A.A and Nicholls J.A. "Aerodynamic Shattering of Liquid Drops", AIAA Journal, Vol. 7, No 2, February 1969

Ranz W.E. and Marshall W.R. "Evaporation from drops", Chem. Eng. Prog., Vol. 48, Part I, pp. 141-146, Part II, pp. 173-180, 1952

Rayleigh, Lord, "On the Instability of Jets", Proc. London Math. Soc., Vol. 10, pp. 4-13, 1878

Reid R., Prausnitz J. and Poling B. The properties of gases and liquids, McGraw-Hill Inc., 4th ed., 1987

Reitz R.D. "Modeling Atomization Processes in High - Pressure Vaporizing Sprays" Atomisation and Spray Technology 3, 309 - 337, 1987

Reitz R.D. and Bracco F.V. "Mechanism of Atomization of a Liquid Jet", Phys. Fluids, Vol. 25, No. 2, pp. 1730-1741, 1982

Reitz R.D. and Diwakar R. "Effect of drop breakup on fuel sprays", SAE Paper 860469, 1986

Reitz R.D. and Diwakar R. "Structure of High-Pressure Fuel Sprays", SAE Paper 870598, 1987

Rhie M.C. and Chow L.W. "A numerical study of the turbulent flow past an isolated airfoil with trailing edge separation", AIAA-82-0998, 1982

Rizk M.A. "Mathematical modelling of densely loaded, particle-ladeb turbulent flows", Atom. Sprays, 3, 1-27, 1993

Rochester M.C. and Brunton J.H. "Surface pressure distribution during impingement", the 4th International Conference on rain Erosion and Related Phenomena, 371-393, Meersburg, Germany, 1974

Roosa V.D., Hess T.D., Walker J.W. "The Roosa Master Nozzle: Another Step in Symplifying Fuel Injection", SAE Paper 907 B, 1964

Rowe G.A. and Henwood G.A. "Drag forces in a hydraulic model of a fluidized bed: Part I. Trans. Inst. Chem. Eng. 39, 43-54, 1961

Ruff G.A., Sagar A.D., and Faeth G.M. "Structure and Mixing Properties of Pressure-Atomized Sprays", AIAA Journal, Vol. 27, No 2, July 1989

Russell M.F. and Lee H.K. "Modelling injection rate control devices", Proc. IMechE Seminar on Diesel Fuel Injection Systems, London, 28-29, pp. 115 - 132, Sept. 1995

Saffman P.G. "The lift on a small sphere in a slow shear flow", J. Fluid Mech, vol 22, part 2, pp. 385-400, 1965

Sankagiri N. and Ruff G.A. "Extension of Spray Nozzle Correlations to the Prediction of Drop Size Distributions Using Principles of Maximum Entropy", AIAA-93-0899, 1993

Santangelo P.J. and Sojka P.E. "A holographic investigation of the near - nozzle structure of an effervescent atomizer - produced spray", Atomization and sprays, Vol. 5, pp. 137-155, 1995

Savart F. Ann. Chim. Phys., Vol.53, pp. 337-386, 1833

Schlichting H. Boundary layer theory, McGraw Hill, 7th ed., 1979

Schweimer G.W., Schindler K.P., Oetting H. "The Physics of Fuel Injection in Diesel Engines", International EAEC Conference on New Developments in Power Train and Chaisis Engineering, Shasberg, 3-5 June, 1987

Scullen R.S. and Hames R.J. 'Computer simulation of the GM unit injector', SAE Paper 780161, 1978

Seki M., Kawamura H. and Sanokawa K. "Transient temperature profile of a hot wall due to an impinging liquid droplet", AMSE J. Heat Transfer, 100, 167-169, 1978

Sellens R.W. and Brzustowski T.A. "A Prediction of the Drop Size Distribution in a Spray from First Principles", Atomization and Spray Technology 1, 89-102, No. 2, 1985

Senda J., Kobayashi M., Iwashita S., Fujimoto H. "Modeling of Diesel Spray Impingement on a Flat Wall", SAE Paper 941894, 1994

Senda J. "Characteristics of Diesel Spray Impinging on a Flat Wall" International Symposium on Advanced Spray Combustion, July 6-8, Hiroshima, Japan, 1994

Senda J., Yamada K., Fujimoto H. and Miki H. "The Heat - Transfer Characteristics of a Small Droplet Impinging upon a Hot Surface" Paper No. 86-0103 A, JSME International Journal, Series II, Vol. 31, No 1, 1988

Senda J., Yamaguchi M., Nishikori T., Tsukamoto T., and Fujimoto H. "Characteristics of flash boiling spray under low-pressure field", Proc. Int. Conf. on Multiphase Flows, Tsukuba, Japan, 1991

Servati H. and Herman E.W. "Spray/Wall Interactions Simulation", SAE Paper 890566, 1989

Shavit U. and Chigler N. "The effects of dynamic surface tension on drop size, intact length, and wave characteristics in sprays", FED-Vol. 178/HTD-Vol. 270, Fluid Mechanics and Heat Transfer in Sprays, ASME 1993

Shearer A.J., Tamura H. and Faeth G.M. "Evaluation of a Locally Homogeneous Flow Model of Spray Evaporation", J. Energy, Vol.3, No.5, pp. 271-278, 1979

Shih L. and Assanis D. "Implementation of a Fuel Spray Wall Interaction Model in KIVA-II", SAE Paper 911787, 1991

Silverman I. and Sirignano W.A. "Multi-droplet interaction effects in dence sprays", Int. J. Multiphase Flow, Vol. 20, No. 1, pp. 99-116, 1994

Simmons H.S. "The correlation of Drop-Size Distributions in Fuel Nozzle Sprays, Part I: The Drop-Size/Volume-Fraction Distribution", ASME Trans, Journal of Engineering for Power, July 1977

Simmons H.S. "The correlation of Drop-Size Distributions in Fuel Nozzle Sprays, Part I: The Drop-Size/Number Distribution", ASME Trans, Journal of Engineering for Power, July 1977

Sirignano W.A. "Fuel droplet vaporization and spray combustion theory", Prog. Energy Combust. Sci., Vol. 9, pp. 291-32, 1983

Smith W.J. and Timoney D.J. "On the relative roles of fuel spray kinetic energy and engine speed in determining mixing rates in D.I. Diesel engines", ASME 1995, Internal Combustion Engine Division Spring Technical Conference, April 1995

Snyder H.E. and Reitz R.D. "Gas Efficient Liquid Atomization Using Micro-Machined Spray Nozzles", SAE Paper 960859, 1996

Solomon A.S.P., Rupprecht S.D., Chen L.-D. and Faeth G.M. "Flow and Atomization in Flashing Injectors", Atomization and Spray Technology 1, pp. 53-76, 1985

Sommerfeld M. "Modelling of particle - wall collisions in confined gas - particle flows", Int. J. Multiphase Flow, Vol. 18, No. 6, pp. 905 - 926, 1992

Soteriou C.C.E. 'Modeling and prediction of the filling characteristics of modern diesel fuel injection equipment', Ph.D. thesis, University of Southampton, 1990

Soteriou C.C.E., and Andrews R.J. "Cavitation, hydraulic flip and atomization in direct injection diesel sprays", C465/051@IMechE 1993

Soteriou C.C.E., Andrews R.J., and Smith M. "Direct Injection Diesel Sprays and the Effect of Cavitation and Hydraulic flip on Atomization", SAE Paper 950080, 1995

Spalding D.B. Some fundamentals of Combustion, Academic Press, New York, Butterworths Scientific Publications, London 1955

Spiegler P., Hopenfeld J., Silberberg M., Bumpus C.F. and Norman A. "Onset of Stable Film Boiling and the Foam Limit", Int. J. Heat Mass Transfer, Vol. 6, pp. 987-994, 1963

Spurk J.H., Betzel T. and Simon N. "Interaction of Nonlinear Dynamics and Unsteady Flow in Fuel Injectors", SAE Paper 920621, 1992

Stanton D.W. and Rutland C.J. "Modeling Fuel Film Formation and Wall Interaction in Diesel Engines", SAE Paper 960628, 1996

Stokes G.G. Scientific Papers, University Press, Cambridge, 1901

Stone H.A. "Dynamics of drop deformation and breakup in viscous fluids", Ann. Rev. Fluid Mech, 26, 65-102, 1994

Stow C.D. and Hadfield M.G. "An experimental investigation of fluid flow resulting from the impact of water drop with an unyielding dry surface", Proc. R. Soc. London A, Vol. 373, pp. 419-441, 1981

Stow C.D. and Stainer R.D. "The physical products of a splashing water drop", Journal of the Meteorological Society of Japan, 55, 518-531, 1977

Strauss T.S., Schweimer G.W., and Ritscher U. "Combustion in a Swirl Chamber Diesel Engine Simulation by Computation of Fluid Dynamics", SAE Paper 950280, 1995

Su T.F. and Farrell P. "Characterization of High Pressure Diesel Sprays with Relation to Particulate and Nox Emissions", Submitted to Atomization and Sprays, 1996

Su T.F., Farrell P.V. and Nagarajian R.T. "Nozzle Effect on High Pressure Injection", SAE Paper 950083, 1995

Su T.F., Patterson M.A., Reitz R.D. and Farrell P.V. "Experimental and Numerical Studies of High Pressure Multiple Injection Sprays", SAE Paper 960861, 1996

Suresh K. Aggarwal "Modeling of a dilute vaporizing multicomponent fuel spray", Int. J. Heat Mass Transfer. Vol. 30, No. 9, pp. 1949-1961, 1987

Suzuki K., Honda A., Sumi S. and Kibune M. "Study of Abnormal Fuel Delivery Characteristics in High Pressure Injection Systems", SAE Paper 821073, 1982

Tabata M., Fujii H., Arai M., Nishida K. and Hiroyasu H. "Pulced laser diffraction method for measuring the mean drop size of a diesel spray in an evaporation process", ICLASS-91, Gaithersburg, MD, USA, July 1991

Tabata T., Ishii Y., Takatsuki T., and Yokota K. "Numerical Calculation of Spray Mixing Process in a D.I. Diesel Engine and Comparison with Experiments", SAE Paper 950853, 1995

Takaishi T., Tateishi M., Kunimoto E., Matsuo T., Nagae Y., and Oikawa H. "Prediction of Cavitation Erosion in Diesel Engine Fuel Injection Systems", SAE Paper 871631, 1987

Takeda Y., Ishikawa N., Komori M., and Tsujimura K. "Diesel Combustion Improvement and Emissions Reduction Using VCO Nozzles with High Pressure Fuel Injection", SAE Paper 940899, 1994

Takeuchi K., Senda J. and Sato Y. "Experimental Studies on the behavior of a small droplet impinging upon a hot surface" ICLASS 82, 14-4, 1982

Talbot L., Cheng R.K., Schefer R.W. and Willis D.R. "Thermophoresis of particles in aheated boundary layer", J. Fluid Mech., vol. 101, part 4, pp. 737-758, 1980

Tambour Y. "Coalescence of vaporizing kerosene fuel sprays in a turbulent jet", Atom. Spray Techol., 1, 125-146, 1985b

Tanner F.X. and Boulouchos K. "A Computational Investigation of the Spray-Induced Flow and its Influence on the Fuel Distribution for Continuous and Intermittent DI-Diesel Sprays", SAE Paper 960631, 1996

Tennekes H. and Lumley J.L. A First Course in Turbulence, The MIT Press, 1972

Theodorakakos A. "Numerical simulation of the induction and compression strokes in reciprocating internal combustion engines", Ph.D. thesis, National Technical University of Athens, 1997 (in Greek)

Tomonaga T., Murai K., Takano T. and Sami H. "A study on combustion behaviour of a Diesel Fuel spray Impinging on a wall", SAE Paper 960028, 1996

Travis J.R., Harlow F.H. and Amsden A.A. "Numerical Calculation of Two-Phase Flows", Nuclear Science and Engineering: 61, 1-10, 1976

Tsurutani K., Yao M., Senda J. and Fujimoto M. "Numerical Analysis of the Deformation Process of a Droplet Impinging upon a Wall", JSME International Journal, Series II, Vol. 33, No 3, 1990

Tullis J.P. Hydraulics of Pipelines, John Wiley & Sons, Inc. 1989

Van Der Geld C.W.M. and Vermeer H. "Prediction of drop size distributions in sprays using the maximum entropy formalism: the effect of satellite formation", Int. J. Multiphase Flow, Vol. 20, No. 2, pp. 363-381, 1994

Van Wylen G.J. and Sonntag R.E. Fundamentals of Classical Thermodynamics, John Wiley & Sons, Inc., 3rd Edition, 1985

Varnavas C. and Assanis D.N. "A High Temperature and High Pressure Evaporation Model for the KIVA-3 Code", SAE Paper 960629, 1996

Wachters L.H.J. and Westerling N.A.J. "The heat transfer from a hot wall to impinging water drops in the spheroidal state" Chemical Engineering Science, Vol. 21, pp. 1047-1056, 1966

Wachters L.H.J., Smulders L., Vermulen J.R. and Kleiweg H.C. "The heat transfer from a hot wall to impinging mist droplets in the spheroidal state", Chemical Engineering Science, Vol. 21, pp. 1231-1238, 1966

Wallis G.B., One - dimensional Two - phase Flow, McGraw Hill Inc., 1969

Wang D.M. and Watkins A.P. "Numerical modeling of diesel spray wall impaction phenomena" Int. J. Heat and Fluid Flow, Vol. 14, No 3, September 1993

Wannewetsch P. and Egler W. 'A user-friently program system for digital simulation of hydraulic equipment', SAE Paper 850532, 1985

Watanabe H., Yamada M., Imai K., Ishi Y., and Sasaki S."Cavitation in the Fuel Injection System of Diesel Engines", International Symposium on Cavitation, Sendai, Japan, April 1986

Watkins A.P. "Computation of Diesel Sprays by a Non-Iterative Implicit Solution Scheme", Atomization and Spray Technology, Vol.3, pp. 261-290, 1987

Watkins A.P. and Park K. "Assessment and application of a new spray wall impaction model" C499/004@IMechE 1996

Weber C., "Disintegration of Liquid Jets", Z. Angew. Math. Mech., Vol. 11, No. 2, pp. 136-159, 1931

Whalley P.B. Boiling, Condensation and Gas-Liquid Flow, Clarendon Press, Oxford, 1987

White F.M. Fluid Mechanics, McGraw - Hill International Editions, Second Edition, 1988

Wierzba A. "Deformation and breakup of liquid drops in a gas stream an nearly critical Weber numbers", Experiments in Fluids 9, 59-64, 1990

Williams A. Combustion of Liquid Fuel Sprays, Butterworth & Co (Publishers) Ltd, 1990

Williams D. "The Desigh of In - Line Fuel Injection Equipment for Automotive Diesel Engines", SAE Paper 780769, 1978

Williams F.A. Combustion Theory, The Benjamin/Cummings Publishing Company, Inc., 1985

Wing R.D. "The rotary fuel - injection pump as a source of cyclic variation in diesel engines, and its effect on nitric oxide emissions", Proceedings IMechE, vol 189 50/75. 1975

Winklhofer E., Ahmadi-Befrui B., Wiesler B., and Cresnoverh G. "The influence of injection rate shaping on diesel fuel sprays - an experimental study", Proc Instn Mech Engrs Vol 206, D04591, 1992

Wong S.-C. and Lin A.-C. "Internal temperature distributions of droplets vaporizing in high-temperature convective flows", J. Fluid Mech., vol. 237, pp. 671-687, 1992

Worthington A.M. "Impact with a liquid Surface, Studied by the Aid of Instantaneous Photography", Proc., Roy. Soc., vol. 25, 1877

Wright A.C. "A physically-based model of the dispersion of splash droplets ejected from a water drop impact", Earth Surface Pocesses and Landforms, Vol. 11, 351-367, 1986

Wu P.-K. and Faeth G.M. "Aerodynamic Effects on Primary Breakup of Turbulent Liquids" Atomization and Sprays, Vol. 3, pp. 265-289, 1993

Wu P.-W., Miranda R.F. and Faeth G.M. "Effects of initial flow conditions on primary breakup of nonturbulent and turbulent round liquid jets", Atomization and sprays, vol. 5, pp. 175-196, 1995

Wylie E.B., Bolt J.A. and El-Erian M.F. 'Diesel fuel injection systen for simulation and experimental correlations', SAE Paper 710569, 1971
Xianguo Li "Mechanism of Atomization of a Liquid Jet" Atomization and Sprays, Vol. 5, pp. 89-105, 1995

Xiong T.Y. and Yuen M.C. "Evaporation of a liquid droplet on a hot plate", Int. J. Heat Mass Transfer, 34, 1881-1894, 1991

Xu M., Nishida K. and Hiroyasu H. "A practical Calculation Method for Injection Pressure and Spray Penetration in Diesel Engines", SAE Paper 920624, 1992

Xu T.-H., Durst F., and Tropea C. "The three - parameter log - hyperbolic distribution and its application to particle sizing", Atomization and Sprays, vol. 3, pp. 109-124, 1993

Yao S.C. and Cai K.Y. "Dynamics and heat transfer of drops impacting on a hot surface at small angles", Proceedings of the 3rd International conference on liquid atomization and spray systems, Imperial College, London, ICLASS-85, 1985

Yarin A.L. and Weiss D.A. "Impact of drops on solid surfaces: self-similar capilarry waves, and splashing as a new type of kinematic discontinuity", J. Fluid Mech., vol. 283, pp. 141-173, 1995

Yoshizaki T., Nishida K. and Hiroyasu H. "Approach to Low Nox and Smoke Emission Engines By Using Phenomenological Simulation", SAE Paper 930612, 1993

Young F.R. Cavitation, McGraw Hill Book Company, 1989

Young J.B. and Hanratty T.H. "Optical studies on the turbulent motion of solid particles in a pipe flow", J. Fluid Mech., vol. 231, pp. 665-688, 1991

Yuen M.C. and Chen L.W. "On the drag of evaporating liquid droplets", Comb. Sci. Tech., 14, 147-154, 1976

Yule A.J., Mo S. Thaw S.Y. and Aval S.M. "Diesel spray structure", Proc. ICLASS-85, Inst. Energy, London, 1985

Yule A.J. and Aval S.M. "Cyclic variations of diesel sprays", Fuel, Vol 68, 1989

Yule A.J. and Filipovic I. "On the break-up times and lengths of diesel sprays", Int. J. Heat & Fluid Flow, Vol. 13, No. 2, 1992

Yule A.J. and Salters D.G. "On the distance required to atomize diesel sprays injected from orifice - type nozzles", Proc Instn Mech Engrs Vol 209, D02194@IMechE 1995

Zeigerson-Katz M. and Sher E. "Fuel Atomization by flashing of a Volatile Liquid in a Liquid Jet", SAE Paper 960111, 1996

Zhang S. and Gogos G. "Film evaporation of a spherical droplet over a hot surface: fluid mechanics and heat/mass transfer analysis", J. Fluid Mech., vol. 222, pp. 543-563, 1991

Zhbankova S.L. and Kolpakov A.V. "Collision of water drops with a plane water surface", Fluid Dyn., 25, 470-473, 1991

Zhen H., Yiming S., Shiga S., Nakamura H., Karasawa T. "The orifice flow pattern, pressure characteristics, and their effects on the atomization of fuel containing dissolved gas", Atomization and Sprays, vol. 4, pp. 123-133, 1994

Zurlo J.R. and Chigier N. "Impinging Diesel Spray Dynamics" Atomization and Sprays, Vol 1, pp. 303-318, 1991